Towards understanding the catalytic reactivity of metal-ceria interfaces

Towards understanding the catalytic reactivity of metal-ceria interfaces

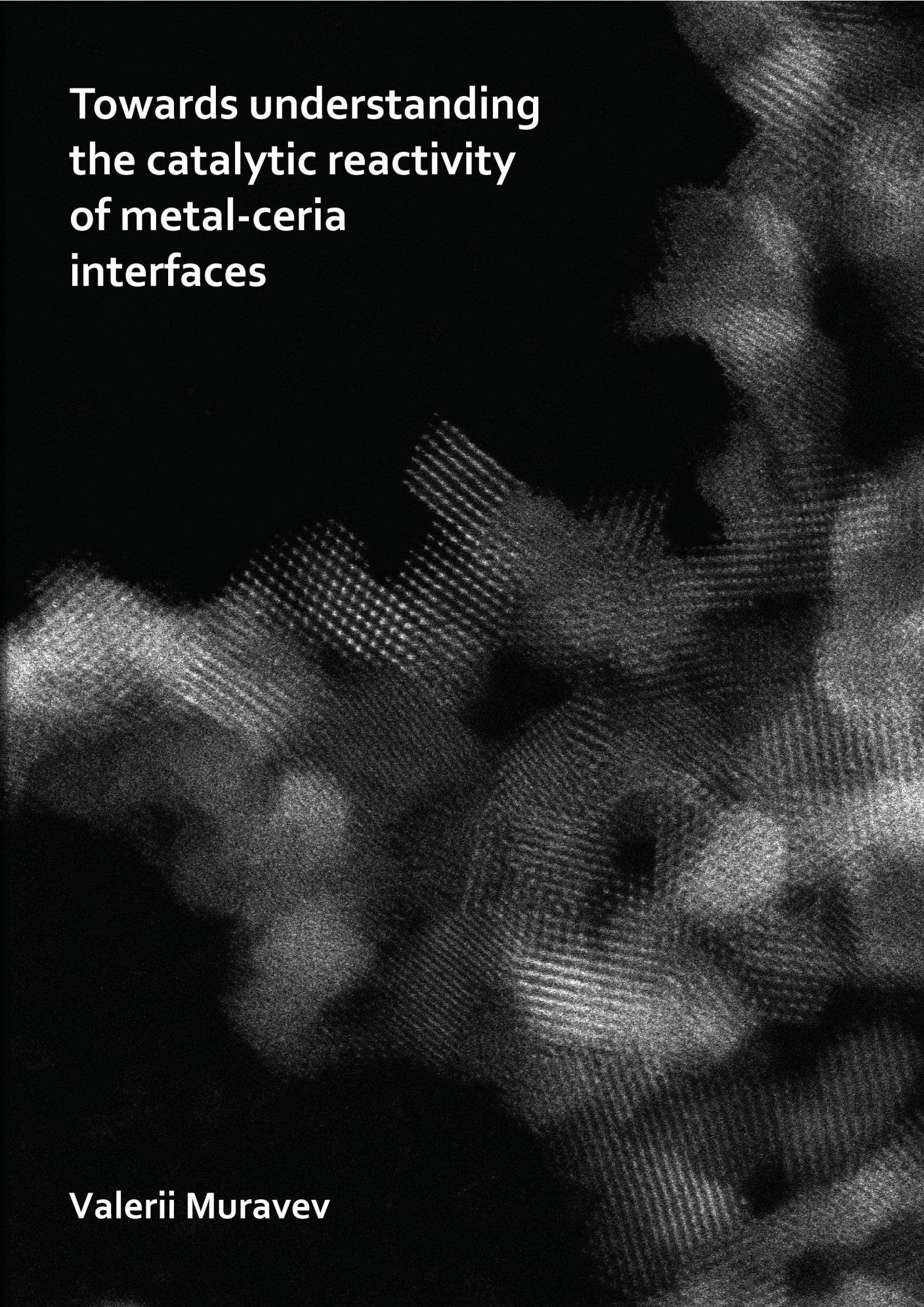

Valerii Muravev

Towards understanding the catalytic reactivity of metal-ceria interfaces

PROEFSCHRIFT

ter verkrijging van de graad van doctor aan de Technische Universiteit Eindhoven, op gezag van de rector magnificus prof.dr.ir. F.P.T. Baaijens, voor een commissie aangewezen door het College voor Promoties, in het openbaar te verdedigen op vrijdag 26 november 2021 om 16:00 uur

door

Valerii Muravev

geboren te Biysk, Rusland

Dit proefschrift is goedgekeurd door de promotoren en de samenstelling van de promotiecommissie is als volgt:

voorzitter:	prof.dr.eng. F. Gallucci
1e promotor:	prof.dr.ir. E.J.M. Hensen
2e promotor:	prof.dr. A.K. Datye (University of New Mexico)
copromotor(en):	dr. N. Kosinov
leden:	prof.dr. J.A. van Bokhoven (ETH Zürich)
	prof.dr. J.-D. Grunwaldt (Karlsruher Institut für Technologie)
	prof.dr.ir. J. van der Schaaf
	prof.dr. Th. Weber

Het onderzoek of ontwerp dat in dit proefschrift wordt beschreven is uitgevoerd in overeenstemming met de TU/e Gedragscode Wetenschapsbeoefening.

To my parents

Valerii Muravev

Towards understanding the catalytic reactivity of metal-ceria interfaces

A catalogue record is available from the Eindhoven University of Technology Library

ISBN: 978-90-386-5405-8

The work described in this thesis has been carried out at the Laboratory of Inorganic materials and Catalysis, Eindhoven University of Technology, The Netherlands. This work was financially supported by the Dutch Research Council (NWO) through Vici grant 13708 and the Netherlands Center for Multiscale Catalytic Energy Conversion (MCEC), an NWO Gravitation programme funded by the Ministry of Education, Culture and Science of the government of the Netherlands.

Cover design: Valerii Muravev

Original image: Nathalie Claes (University of Antwerp)

Printed by: Gildeprint - Enschede, The Netherlands

Contents

Chapter 1. Introduction and scope 1

Chapter 2. Metal-support interfaces in ceria-based catalysts 11

Chapter 3. Transforming Pt single atoms on CeO_2 into highly active catalysts for low-temperature CO oxidation 57

Appendix A 80

Chapter 4. Interface dynamics of Pd-CeO_2 single-atom catalysts during CO oxidation 89

Appendix B 114

Chapter 5. Operando spectroscopy unveils the catalytic role of different Pd oxidation states in CO oxidation on Pd/CeO_2 catalysts 157

Appendix C 179

Chapter 6. Tuning CO oxidation activity of Pd/CeO_2 catalysts by the size of the CeO_2 support 201

Appendix D 228

Summary and outlook 241

Acknowledgements 249

List of publications 255

Curriculum Vitae 257

Chapter 1

Introduction and scope

1.1 Heterogeneous catalysis

Catalysis plays a vital role in modern chemical industry. More than 90% of chemical products are produced with the aid of catalysts. The term catalysis has been redefined for many years since it was introduced by Berzelius in 1835. Phenomenologically, catalysis is most commonly defined as the change of the rate of chemical reaction under the action of certain substances that are not converted themselves – catalysts[1]. In practice, it means that catalysts allow the desired chemical reaction to occur under milder conditions, *e.g.*, pressure and temperature, which typically benefits both conversion and selectivity. Heterogeneous catalysts are particularly relevant for the large-scale chemical processes used in industry, as the reactants and products, usually gases or liquids, can be efficiently separated from the catalyst, typically present in a solid phase.

The development of heterogenous catalytic processes has shaped the world as we know it. Perhaps the most prominent example of the importance of catalysis for the society pertains to ammonia synthesis. At the end of the 19th century the agriculture heavily relied on nitrogen compounds whose sources were limited by deposits of saltpeter in Chile and guano from tropical islands. The lack of nitrogen-based fertilizers threatened the world population with hunger, prompting the nascent chemical industry to innovate. With the help of catalysts, the chemical inertness of atmospheric nitrogen was overcome and synthesis of ammonia, a building-block molecule for nitrogen compounds, was developed by Haber and Bosch by the end of 1910s[1]. Since then, over one third of the world's population has been supported by the nitrogen fertilizers produced from the Haber-Bosch process[2]. The industrial production of polymers – ubiquitous materials in modern society – was also stimulated by discovery of suitable heterogeneous catalysts, for which Ziegler and Natta were awarded the Nobel Prize in 1963[3,4]. Modern transportation powered by internal combustion engines would not exist without the use of catalysts. The production of the most types of transportation fuels relies on large-scale heterogeneous catalytic processes such as fluid catalytic cracking and hydrodesulfurization[5]. Significant advances in abatement

of toxic gases such as CO[6,7], NO_x [8,9], SO_x[10,11] are also due to the development of efficient heterogenous catalysts.

Heterogeneous catalysis is expected to play an even more important role in the future, as the growing concerns related to environmental pollution[12–14] and especially climate change[15] call for the development of new sustainable chemical processes. Valorization of greenhouse gases such as CO_2[16] and CH_4[17,18], efficient and sustainable production of hydrogen[19], electrochemical production of ammonia[20] and catalytic recycling of plastics[21] are only a few of the challenges that heterogeneous catalysis can aid to tackle. Exemplified by the development of Haber-Bosch process, the screening-based approach in engineering of heterogenous catalysts can be very successful. However, this method can also be very time-consuming – it took almost a decade to test more than 4000 compositions before a suitable formulation for ammonia synthesis catalyst could be discovered[22]. The growing concern about climate change necessitate urgent measures including the design of novel processes for which catalyst design based on high-throughput synthesis and testing may not offer sufficiently fast solutions. Fundamental understanding of the chemical phenomena taking place during catalytic reaction can help rational design of novel and more effective heterogeneous catalysts[23]. Remarkable developments in spectroscopy and electronic structure calculations seen in the past decades provided the tools for studying catalytic materials on the molecular level[24]. As a result, catalysis evolved from a chemical engineering discipline to a molecular chemical science. The establishment of structure-performance relationships with the aid of spectroscopic characterization and computational chemistry, has become the guiding principle of the modern catalytic research[25,26].

1.2 Catalytic CO oxidation on noble metals

The considerable progress in fundamental insights into heterogeneous catalysis phenomena are to a great extent due to the decades of extensive research on the "fruit fly" catalytic reaction – CO oxidation[27,28]. This prototypical reaction of heterogeneous catalysis is one of the most studied and often used as a probe reaction in catalytic research[29,30]. The noble metals Pt, Pd and Rh are the benchmark CO oxidation catalysts[31,32]. As in heterogeneous catalysis only the surface atoms are exposed to reactants, typical noble metal catalysts consist of nanoparticles of the active component dispersed over the solid support. The role of the inert support is to provide the anchoring sites for metal

nanoparticles and increase the mechanical and thermal stability of the catalyst under operating conditions.

CO oxidation over noble metals deposited on common inert metal-oxide supports, such as SiO_2, Al_2O_3 or ZrO_2, typically follows a Langmuir-Hinshelwood mechanism[32]. This implies that O_2 molecules dissociatively adsorb on the metal surface and react with coadsorbed CO to produce CO_2, which then leaves the surface. Due to strong adsorption of CO on noble metals, the surface of the catalyst is predominantly covered with CO and the activation of O_2 is inhibited at low temperatures (< 150 °C). This leads to low activity of noble metals deposited on inert supports in low-temperature CO oxidation. A high CO oxidation activity at near-ambient temperatures is particularly important for automotive exhaust neutralizers, where noble metals are used as catalysts since the 1970s[7]. Incomplete conversion of CO and other toxic exhaust gases in the first minutes after ignition of the car engine constitute the cold-start problem of automotive catalysis[7]. This issue becomes even more relevant now due to the growing use of hybrid-powered vehicles. The frequent start-stop cycles of the engine during short trips require very active catalysts operating at low temperatures[33]. The activity of noble metals towards CO oxidation can be substantially improved by using reducible oxides as the support[34].

1.3 Noble metals supported on reducible oxides

Reducible metal oxides such as TiO_2, FeO_x, MnO_x and CeO_2 are increasingly recognized as promising supports for many catalytic applications[35]. The ability of reducible supports to respond to the redox stimuli by creating or healing the oxygen vacancies provides extra possibilities for catalysis[36]. For example, noble metals supported on reducible oxides can display high activity towards low-temperature CO oxidation[34]. The activation of oxygen can take place at the metal-support interface instead of metallic surface, which allows for circumventing the CO poisoning at low temperatures[34,37]. The active participation of the support in CO oxidation in providing lattice oxygen atoms is a characteristic feature of a Mars-van Krevelen mechanism[38].

The unusual reactivity of the atoms at the metal-support interface[39,40] arises from the intricate interactions between the metal and the support[41]. Charge-transfer phenomena[42] and spillover effects[43,44] render the interfacial sites different from other atoms in a supported nanoparticle. Strong metal-support interactions can help stabilization of noble metals in a

dispersed form, beneficial in view of efficient use of noble metals[45,46]. In some cases, these interactions are so strong that atomic dispersion of noble metals can be achieved[46]. The strategy for developing a catalyst in which all the atoms of expensive noble metals are utilized is very appealing[47]. This is particularly desired for the automotive exhaust aftertreatment systems, leading to cost reduction due to decreased use of noble metals[48]. Due to their rich defect chemistry, reducible oxides such as FeO_x, TiO_2 and CeO_2 are well-suited supports for single atoms of noble metals[49]. Among Pt, Pd and Rh catalysts for CO oxidation, catalysts comprising single atoms of Pt are the most studied[50]. This is in part for practical reasons because Pt can be easier distinguished from the atoms of the support in transmission electron microscopy due to its higher atomic number. It has, for instance, been shown that atomically dispersed Pt on FeO_x is very active in low-temperature CO oxidation[29]. Isolated Pt atoms on TiO_2 have twice the intrinsic activity of Pt nanoparticles in CO oxidation[51]. Hydrothermally-treated Pt/CeO_2 single-atom catalysts display remarkable stability and high activity in low-temperature CO oxidation[52]. The catalytic properties of ceria-supported single-atom catalysts will be discussed in more detail in **Chapter 2** of this thesis.

1.4 Automotive emission catalysis

Owing to the global economic growth, the number of transport vehicles has immensely increased in the past decades. The modern transportation sector heavily relies on the internal combustion engine (ICE). ICE vehicles powered by mainly gasoline and diesel daily serve for our comfort but at the same time produce toxic emissions of particulate matter (PM), CO, hydrocarbons (HC) and NO_x. Strict control over exhaust emissions started in 1970s with the US Clean Air Act[7]. Since then, catalytic technology led to a reduction of automotive emissions by over 90%, making the development of catalytic convertors a success story of heterogenous catalysis[53]. The car exhaust catalytic convertor is now the most common catalytic reactor in the world.

State-of-the art commercial exhaust emission control systems are complex and typically tailored to the needs of a specific type of engine/exhaust system. **Figure 1.1** displays typical configurations for gasoline and diesel engines. In gasoline-powered vehicles, CO, HC and NO_x gases are converted in three-way catalysts (TWC), while a catalyzed gasoline particulate filter (cGPF) is used for removing PM. For diesel aftertreatment, the CO and HC are removed

by a diesel oxidation catalyst (DOC) or a lean NO_x trap (LNT). The next stage of the system contains a diesel particulate filter (DPF), followed by a selective reduction catalyst (SCR), which requires injection of a urea-based diesel exhaust fluid (DEF). Finally, the excess of ammonia is removed by an ammonia slip catalyst (ASC).

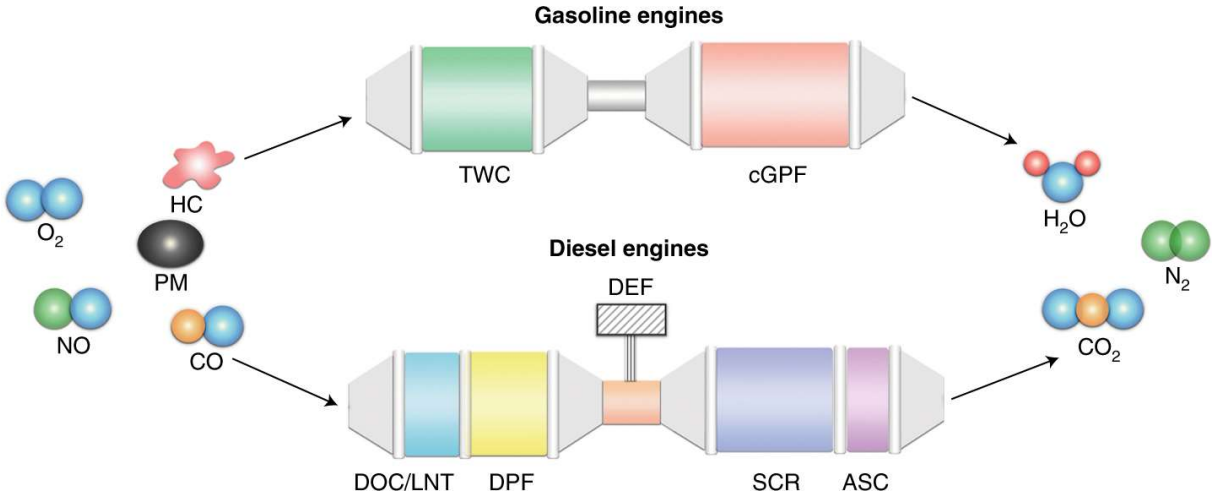

Figure 1.1. Typical configurations of modern gasoline and diesel emission control systems. Adapted from ref.[54].

Despite the significant advancements in automotive exhaust catalysis achieved in the past decades, there is enough room for improvement. The current expectations from the automotive exhaust catalyst imply full conversion of the harmful gases at 150 °C and below[53]. Incomplete conversion of CO and other toxic gases in the first minutes after ignition of the car engine constitute the cold-start problem of automotive catalysis[7]. This issue becomes even more relevant due to the growing use of hybrid-powered vehicles. The frequent start-stop cycles of the engine during short trips require very active catalysts operating at low temperatures[33].

Noble metals are the most common catalysts for exhaust aftertreatment, but their poisoning by CO at low temperature significantly contributes to the cold-start problem. Accordingly, current efforts pertain to the development of highly active noble metal catalysts supported on reducible oxides. Ceria is the key component of exhaust aftertreatment catalysts[7]. The unique redox properties of ceria-based catalysts give rise to their high oxygen storage capacity, which allows the catalysts to maintain its catalytic efficiency under changing reducing/oxidizing conditions in the exhaust. Furthermore, ceria can stabilize noble metals in highly dispersed form (down to single atoms) due to strong metal-support interactions.

Single-atom noble metal catalysts supported on ceria (see **Chapter 2**) are a promising class of materials that can play a major role in the future of automotive catalysis[48,55].

1.5 Scope

Abatement of car exhaust emissions containing toxic gases such as CO is an important environmental problem for which heterogeneous catalysts already provide a solution. Small nanoparticles of noble metals (Pt, Pd, Rh) supported on ceria (CeO_2) are benchmark catalysts used in three-way car exhaust neutralizers. The high efficiency of these metal-ceria catalysts in CO oxidation at low operating temperatures arises from the peculiar catalytic properties of the interfacial sites. Understanding the chemical phenomena taking place at the interface between metal (Pt, Pd) and support (CeO_2) during CO oxidation is the main goal of this work. Conventional and advanced synthesis methods such as flame-spray pyrolysis (FSP) are employed to prepare CeO_2-supported catalysts with Pt and Pd in the form of nanoparticles, clusters and single atoms. In contrast to Pt, oxidized Pd single atoms display high CO oxidation activity at low temperatures. By combining spectroscopic methods and reaction kinetics studies, structure-activity relationships in CO oxidation are established.

Chapter 2 is an overview of the properties of ceria as a support for heterogeneous catalysts. We discuss how the surface structure and size of CeO_2 can influence the performance of the ceria-based catalysts. Special attention is paid to the aspects of metal-support interactions and how their manifestations can be distinguished using advanced spectroscopic tools. Finally, we discuss the differences and similarities between the catalytic behaviour of metal nanoparticles and single metal atoms supported on CeO_2.

In **Chapter 3** we focus on the engineering of the Pt-CeO_2 interface for low-temperature CO oxidation. The as-synthesized Pt single-atom catalysts (SACs) display modest activity at low temperatures. This is attributed to the strong CO adsorption on ionic Pt sites. Reductive pretreatment of Pt-CeO_2 SACs gives rise to highly active catalysts comprising metallic Pt clusters. Using *in situ* spectroscopic techniques, the particularly high activity of a catalyst prepared by atom-trapping was linked to facile lattice oxygen removal from the ceria support.

Chapter 4 demonstrates that, in contrast to Pt, Pd-CeO_2 SACs do not require a reductive treatment to efficiently oxidize CO at low temperature. Well-defined Pd-CeO_2(111) single-atom catalysts prepared by wet impregnation of nanorods and one-step flame spray

pyrolysis (FSP), display much higher activity in low-temperature CO oxidation than Pd clusters supported on a commercial CeO_2 support. The Pd single atoms in FSP samples are more stable than on nanorods-CeO_2 under reaction conditions. The higher stability of single-atom Pd-oxo species in FSP-made catalysts can be linked to the higher lattice oxygen mobility in such materials. The redox chemistry of Pd-CeO_2 interface was probed by a combination of surface- and bulk-sensitive *in situ* spectroscopic tools.

Chapter 5 employs a set of advanced *operando* spectroscopic tools to distinguish the active Pd species from spectators during CO oxidation on a conventional Pd-CeO_2 catalyst. A combination of reaction kinetics studies and transient spectroscopic experiments reveals that oxidized Pd single atoms supported on large CeO_2 particles (30 nm) are active in low-temperature CO oxidation but unstable. The *in situ* formed metallic Pd clusters can catalyse CO oxidation by virtue of interfacial sites, but the number of such sites is limited in conventional Pd/CeO_2 catalysts.

Chapter 6 explores how the size-dependent intrinsic properties of CeO_2 support influences the catalytic performance of FSP-made Pd-CeO_2 SACs. We prepare a set of catalysts where the support size was varied from 4 to 18 nm. This has a profound effect on the low-temperature CO oxidation activity. We demonstrate that the redox properties of CeO_2 in prepared composites are size-dependent. Pd speciation and oxygen mobility at the Pd-CeO_2 interface dictate the kinetics of CO oxidation that can be tuned by the support size.

The last chapter summarizes the key findings of this work and provides an outlook.

1.6 References

1. Boreskov, G. K. *Heterogeneous catalysis*, Nova Science Publishers (2003)
2. Erisman, J. W., Sutton, M. A., Galloway, J., Klimont, Z. & Winiwarter, W. *Nat. Geosci.* **1,** 636–639 (2008).
3. Sinn, H. & Kaminsky, W. *Adv. Organomet. Chem.* **18,** 99–149 (1980).
4. Fisch, A. G. Ziegler-Natta Catalysts. *Kirk-Othmer Encyclopedia of Chemical Technology* 1–22 (2019).
5. Kaufmann, T. G., Kaldor, A., Stuntz, G. F., Kerby, M. C. & Ansell, L. L. *Catal. Today* **62,** 77–90 (2000).
6. Datye, A. K. & Votsmeier, M. *Nat. Mater. 2020* **20,** 1049–1059 (2020).
7. Farrauto, R. J., Deeba, M. & Alerasool, S. *Nat. Catal.* **2,** 603–613 (2019).
8. Roy, S., Hegde, M. S. & Madras, G. *Appl. Energy* **86,** 2283–2297 (2009).
9. Rezaei, F., Rownaghi, A. A., Monjezi, S., Lively, R. P. & Jones, C. W. *Energy Fuels* **29,** 5467–5486 (2015).
10. Centi, G., Ciambelli, P., Perathoner, S. & Russo, P. *Catal. Today* **75,** 3–15 (2002).
11. Asghar, U., Rafiq, S., Anwar, A., Iqbal, T., Ahmed, A., Jamil, F., Khurram, M. S., Akbar, M. M., Farooq, A., Shah, N. S. & Park, Y.-K. *J. Environ. Chem. Eng.* **9,** 106064 (2021).
12. Driscoll, C. T., Buonocore, J. J., Levy, J. I., Lambert, K. F., Burtraw, D., Reid, S. B., Fakhraei, H. & Schwartz, J. *Nat. Clim. Change* **5,** 535–540 (2015).
13. Apte, J. S., Messier, K. P., Gani, S., Brauer, M., Kirchstetter, T. W., Lunden, M. M., Marshall, J. D., Portier, C. J., Vermeulen, R. C. H. & Hamburg, S. P. *Environ. Sci. Technol.* **51,** 6999–7008 (2017).
14. Lelieveld, J., Evans, J. S., Fnais, M., Giannadaki, D. & Pozzer, A. *Nature* **525,** 367–371 (2015).
15. van Vuuren, D. P., Stehfest, E., Gernaat, D. E. H. J., van den Berg, M., Bijl, D. L., de Boer, H. S., Daioglou, V., Doelman, J. C., Edelenbosch, O. Y., Harmsen, M., Hof, A. F. & van Sluisveld, M. A. E. *Nat. Clim. Change* **8,** 391–397 (2018).
16. Vogt, C., Monai, M., Kramer, G. J. & Weckhuysen, B. M. *Nat. Catal.* **2,** 188–197 (2019).
17. Horn, R. & Schlögl, R. *Catal. Lett.* **145,** 23–39 (2014).
18. Olivos-Suarez, A. I., Szécsényi, À., Hensen, E. J. M., Ruiz-Martinez, J., Pidko, E. A. & Gascon, J. *ACS Catal.* **6,** 2965–2981 (2016).
19. Fajrina, N. & Tahir, M. *Int. J. Hydrog. Energy* **44,** 540–577 (2019).
20. Kyriakou, V., Garagounis, I., Vasileiou, E., Vourros, A. & Stoukides, M. *Catal. Today* **286,** 2–13 (2017).
21. Vollmer, I., Jenks, M. J. F., Roelands, M. C. P., White, R. J., Harmelen, T. van, Wild, P. de, Laan, G. P. van der, Meirer, F., Keurentjes, J. T. F. & Weckhuysen, B. M. *Angew. Chem. Int. Ed.* **59,** 15402–15423 (2020).
22. Dumesic, J. A., Huber, G. W. & Boudart, M. *Handbook of Heterogeneous Catalysis* **1.1** (2008).
23. Vojvodic, A. & Nørskov, J. K. *Natl. Sci. Rev.* **2,** 140–143 (2015).
24. van Santen, R.A. & Neurock, M. *Molecular Heterogeneous Catalysis: A Conceptual and Computational Approach*, *Wiley-VCH Verlag GmbH &Co, KGaA* (2009)
25. Meirer, F. & Weckhuysen, B. M. *Nat. Rev. Mater.* **3,** 324–340 (2018).
26. Kondrat, S. A. & van Bokhoven, J. A. *Top. Catal.* **62,** 1218–1227 (2019).
27. Freund, H.-J., Meijer, G., Scheffler, M., Schlögl, R. & Wolf, M. *Angew. Chem. Int. Ed.* **50,** 10064–10094 (2011).
28. Gustafson, J., Balmes, O., Zhang, C., Shipilin, M., Schaefer, A., Hagman, B., Merte, L. R., Martin, N. M., Carlsson, P.-A., Jankowski, M., Crumlin, E. J. & Lundgren, E. *ACS Catal.* **8,** 4438–4445 (2018).
29. Qiao, B., Wang, A., Yang, X., Allard, L. F., Jiang, Z., Cui, Y., Liu, J., Li, J. & Zhang, T. *Nat. Chem.* **3,** 634–641 (2011).
30. Cargnello, M., Doan-Nguyen, V. V. T., Gordon, T. R., Diaz, R. E., Stach, E. A., Gorte, R. J., Fornasiero, P. & Murray, C. B. *Science* **341,** 771–773 (2013).
31. Engel, T. & Ertl, G. *Adv. Catal.* **28,** 1–78 (1979).
32. Royer, S. & Duprez, D. *ChemCatChem* **3,** 24–65 (2011).
33. Alvarez, R. & Weilenmann, M. *Fuel* **97,** 119–124 (2012).
34. An, K., Alayoglu, S., Musselwhite, N., Plamthottam, S., Melaet, G., Lindeman, A. E. & Somorjai, G. A. *J. Am. Chem. Soc.* **135,** 16689–16696 (2013).
35. Pinto, F. M., Suzuki, V. Y., Silva, R. C. & la Porta, F. A. *Front. Mater.* **6,** 260 (2019).

36. Puigdollers, A. R., Schlexer, P., Tosoni, S. & Pacchioni, G. *ACS Catal.* **7,** 6493–6513 (2017).
37. Kopelent, R., van Bokhoven, J. A., Szlachetko, J., Edebeli, J., Paun, C., Nachtegaal, M. & Safonova, O. v. *Angew. Chem. Int. Ed.* **54,** 8728–8731 (2015).
38. Mars, P. & van Krevelen, D. W. *Chem. Eng. Sci.* **3,** 41–59 (1954).
39. Rodriguez, J. A., Grinter, D. C., Liu, Z., Palomino, R. M., Senanayake, S. D. *Chem. Soc. Rev.* **46,** 1824–1841 (2017).
40. Bruix, A., Rodriguez, J. A., Ramírez, P. J., Senanayake, S. D., Evans, J., Park, J. B., Stacchiola, D., Liu, P., Hrbek, J. & Illas, F. *J. Am. Chem. Soc.* **134,** 8968–8974 (2012).
41. van Deelen, T. W., Hernández Mejía, C. & de Jong, K. P. *Nat. Catal.* **2,** 955–970 (2019).
42. Lykhach, Y., Kozlov, S. M., Skála, T., Tovt, A., Stetsovych, V., Tsud, N., Dvořák, F., Johánek, V., Neitzel, A., Mysliveček, J., Fabris, S., Matolín, V., Neyman, K. M. & Libuda, J. *Nat. Mater.* **15,** 284–288 (2016).
43. Karim, W., Spreafico, C., Kleibert, A., Gobrecht, J., VandeVondele, J., Ekinci, Y. & van Bokhoven, J. A. *Nature* **541,** 68–71 (2017).
44. Vayssilov, G. N., Lykhach, Y., Migani, A., Staudt, T., Petrova, G. P., Tsud, N., Skála, T., Bruix, A., Illas, F., Prince, K. C., Matolı´n, V., Neyman, K. M. & Libuda, J. *Nat. Mater.* **10,** 310–315 (2011).
45. Tauster, S. J., Fung, S. C., Baker, R. T. K. & Horsley, J. A. *Science* **211,** 1121–1125 (1981).
46. Liu, L. & Corma, A. *Chem. Rev.* **118,** 4981–5079 (2018).
47. Bruix, A., Lykhach, Y., Matolinova, I., Neitzel, A., Skala, T., Tsud, N., Vorokhta, M., Stetsovych, V., Sevcikova, K., Myslivecek, J., Fiala, R., Vaclavu, M., Prince, K. C., Bruyere, S., Potin, V. V., Illas, F., Matolin, V., Libuda, J. J., Neyman, K. M. *Angew. Chem. Int. Ed.* **53,** 10525–10530 (2014).
48. Datye, A. K. & Guo, H. *Nat. Commun.* **12,** 1–3 (2021).
49. Lang, R., Du, X., Huang, Y., Jiang, X., Zhang, Q., Guo, Y., Liu, K., Qiao, B., Wang, A. & Zhang, T. *Chem. Rev.* **120,** 11986–12043 (2020).
50. Kaiser, S. K., Chen, Z., Akl, D. F., Mitchell, S. & Pérez-Ramírez, J. *Chem. Rev.* **120,** 11703–11809 (2020).
51. DeRita, L., Dai, S., Lopez-Zepeda, K., Pham, N., Graham, G. W., Pan, X. & Christopher, P. *J. Am. Chem. Soc.***139,** 14150–14165 (2017).
52. Nie, L., Mei, D., Xiong, H., Peng, B., Ren, Z., Hernandez, X. I. P., DeLaRiva, A., Wang, M., Engelhard, M. H., Kovarik, L., Datye, A. K. & Wang, Y. *Science* **358,** 1419–1423 (2017).
53. Lambert, C. K. *Nat. Catal,* **2,** 554–557 (2019).
54. Wang, A. & Olsson, L. *Nat. Catal.* **2,** 566–570 (2019).
55. Beniya, A. & Higashi, S. *Nat. Catal.* **2,** 590–602 (2019).

Chapter 2

Metal-support interfaces in ceria-based catalysts

Abstract

Over the past decades ceria (CeO_2) has gained a widespread attention of the researchers from the diverse scientific fields including fundamental inorganic chemistry, catalysis, and materials science. Unique chemical properties of ceria are linked to the facile $Ce^{3+} \rightleftarrows Ce^{4+}$ redox transformations that are particularly relevant for catalytic applications. Herein we overview the structure–properties relationships in ceria materials in the context of heterogeneous catalysis. Interactions between active component (metal) and the support (ceria) give rise to the interface catalysis when both constituents are involved in chemical conversion. We emphasize how the latest developments in spectroscopic techniques and imaging allow for deeper understanding of the chemical phenomena taking place in ceria-based catalysts. The two principal classes of interface catalysts are overviewed: supported metal nanoparticles and metal single atoms. This chapter introduces the basic concepts of the catalysis by ceria-based materials and discusses the current challenges in the rapidly emerging field of interface catalysis.

This chapter is based on the following publication:

Muravev, V., Kosinov, N., Hensen, E.J.M. *Comprehensive Inorganic Chemistry III* (book chapter). Elsevier, Amsterdam, 2021. *doi: 10.1016/B978-0-12-823144-9.00024-8*.

2.1 Introduction

Ceria (CeO_2) is the oxide of the most abundant of the rare-earth metals – cerium. Over the past decades, ceria has attracted widespread attention from industry and academia as an exceptional material for diverse applications. Initially spurred by the emerging automotive exhaust after-treatment technology in the 1970s, the interest in ceria-based materials is now coming from diverse scientific fields including fundamental inorganic chemistry, catalysis, and materials science. Several studies and comprehensive reviews have covered the peculiarities of ceria for distinct applications. Herein, we focus on the role of ceria-based materials in modern heterogenous catalysis. In the first part, we review the main chemical properties of cerium dioxide that render it a ubiquitous support in heterogenous catalysis. We then discuss the most common methods to prepare ceria and highlight several novel approaches for nanoscale-controlled synthesis of ceria-supported catalysts. The second part is devoted to spectroscopic tools that are typically used for studying ceria-based catalysts with a focus on cerium's redox chemistry in operating catalysts as can be captured by X-ray-based *in situ* and *operando* techniques. In the third part, we focus on ceria-supported metal catalysts and discuss the interactions between the support and active metal phase, usually consisting of nanoparticles (NPs). Next, the intricate chemistry of the metal-ceria interface is discussed in the context of the rapidly emerging field of single-atom catalysis. Valuable mechanistic understanding of catalytic reactions can be gained by studying single-atom catalysts (SACs), capable of bridging the gap between classical model systems and complex nanosized interface catalysts. Finally, we summarize the main concepts of catalysis by ceria-based materials.

2.2 Structure and redox properties

Cerium dioxide has the cubic fluorite ($Fm\bar{3}m$) structure (**Figure 2.1**). The Ce cations occupy the octahedral sites in the corresponding face-centered cubic array, while the O anions reside in the tetrahedral sites. As a result, Ce and O are 8-fold and 4-fold coordinated, respectively. The simple cubic arrangement leads to the high stability of the CeO_2 structure, even in the presence of point defects such as oxygen vacancies or heteroatom substituents in the cation sublattice. These two aspects define the rich chemistry of ceria-based materials. The ability of ceria to accommodate a high concentration of oxygen vacancies is related to reversible transformation of Ce^{4+} into Ce^{3+}. By virtue of facile $Ce^{4+} \rightleftarrows Ce^{3+}$ transitions, ceria is

known as a redox-active support with a high oxygen storage capacity. Ceria can store and release oxygen, depending on the redox potential of the surrounding medium. This aspect makes ceria widely used as a support material in automotive exhaust catalysts. Lattice oxygen mobility in these catalysts defines the efficiency of conversion of oxygen-containing gases such as CO and NO_x under transiently changing reducing (rich) and oxidative (lean) conditions of the engine exhaust. The redox-active catalyst can adapt to these changes via reversible cycling between Ce^{3+} and Ce^{4+} and releasing/storing lattice oxygen. Another manifestation of this property is the ionic conductivity of ceria due to the formation of oxygen vacancies under reducing conditions. This has triggered the widespread application of ceria as an electrolyte in solid-oxide fuel cells. The high tolerance of ceria structure to the introduction of other cations, such as Ga^{2+}, Sm^{3+}, and Pr^{3+} has led to significant advances in material design of solid electrolytes based on CeO_2[1]. Tuning the extent of doping and the nature of dopants allows tailoring the properties of the final material for specific applications. A large body of theoretical and experimental literature dedicated to the effects of introduction of other transition metals into ceria lattice is available[2]. Below we will show that the oxygen transfer in ceria-based catalysts has important implications in virtually all catalytic processes where CeO_2 based catalysts are used.

The surface termination of cerium dioxide crystals has a substantial impact on the redox chemistry. The most thermodynamically stable (110), (111) and (100) surfaces of ceria[3] are shown in **Figure 2.1**. Density functional theory (DFT) calculations confirm that (111) is the most stable one, followed by the (110) and (100) surfaces[4]. The (111) surface contains 7-fold coordinated Ce atoms and 3-fold coordinated O atoms, while the (110) and (100) surfaces contain 6-fold coordinated Ce with 3- and 2-fold coordinated O atoms, respectively. The differences in local structure result in different band gaps, which are decreasing in the order: bulk CeO_2 (2.35 eV) > (111) surface (2.02 eV) > (100) surface (1.69 eV) and (110) surface (1.67 eV)[5]. The narrowing of the band gap for surfaces with more coordinatively unsaturated atoms decreases the energy cost for electron transfer from O to Ce. This results in lower barriers for surface oxygen vacancy formation and thus in a higher reducibility of the surface[6]. It explains why ceria-based materials exposing different facets exhibit different reactivities in heterogeneous catalytic reactions[7–11]. The possible transformation of one type of facet into another one due to the surface reconstruction upon thermal treatment brings another level of complexity into the surface chemistry of cerium dioxide[12]. When the goal is

to understand facet-dependent surface chemistry of inorganic crystal phases, it is important to develop advanced synthetic approaches that allow preferential exposure of particular facets. Significant advances in our understanding of structure-activity relationships in catalysis by ceria-based materials have been achieved in the past decades, owing to the development of shape-controlled synthesis of CeO_2[13]. The main insights derived from these efforts will be discussed later in this chapter.

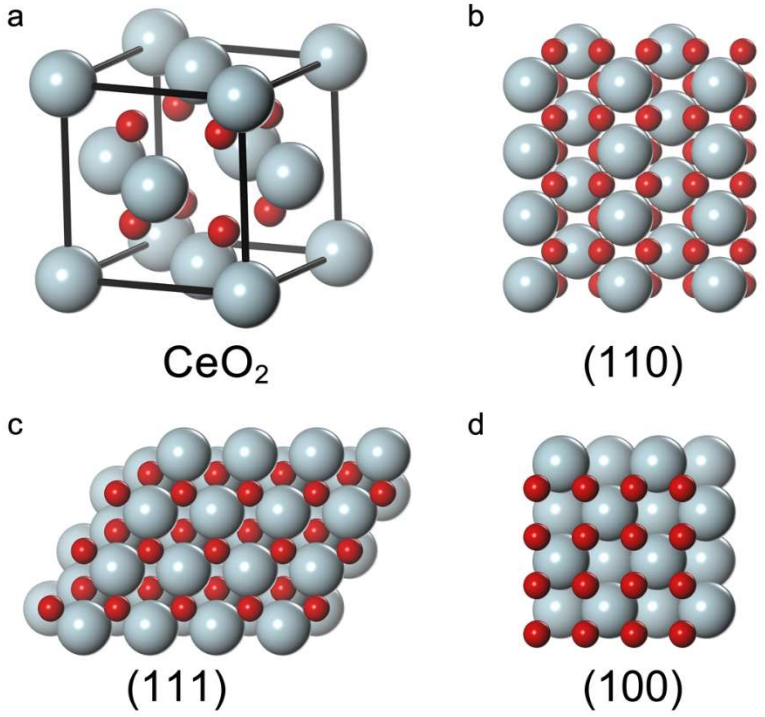

Figure 2.1. Structure of bulk CeO_2 a) and the most common surface terminations b) (110), c) (111) and d) (100).

The ceria crystal size is another important parameter that can significantly influence its catalytic properties[14,15]. Smaller crystallites of ceria usually contain a higher concentration of oxygen defects[16,17]. Moreover, it has been observed that the reducibility of ceria also changes as a function of the particle size, with smaller NPs being more reducible than larger ones[18]. In a series of comprehensive DFT studies, Neyman and co-workers investigated the quantum size-effect on the reactivity of ceria[19–21]. The energy cost for oxygen vacancy formation of ceria NPs with a size in the 1-4 nm range is substantially lower than of ceria NPs with typical sizes larger than 10 nm (**Figure 2.2**). Recently, the same group combined computational modeling and a surface science approach to shed light on oxygen transport phenomena at the Pt-CeO_2 interface[22]. A particularly important finding is that oxygen can efficiently migrate

from the ceria support to Pt clusters on nanosized CeO_2, while this process is energetically unfavorable for Pt on relatively large ceria particles. The reverse oxygen spillover process for nanosized ceria suggested by these experiments can explain the high activity observed by metal NPs supported on nanocrystalline ceria[23,24].

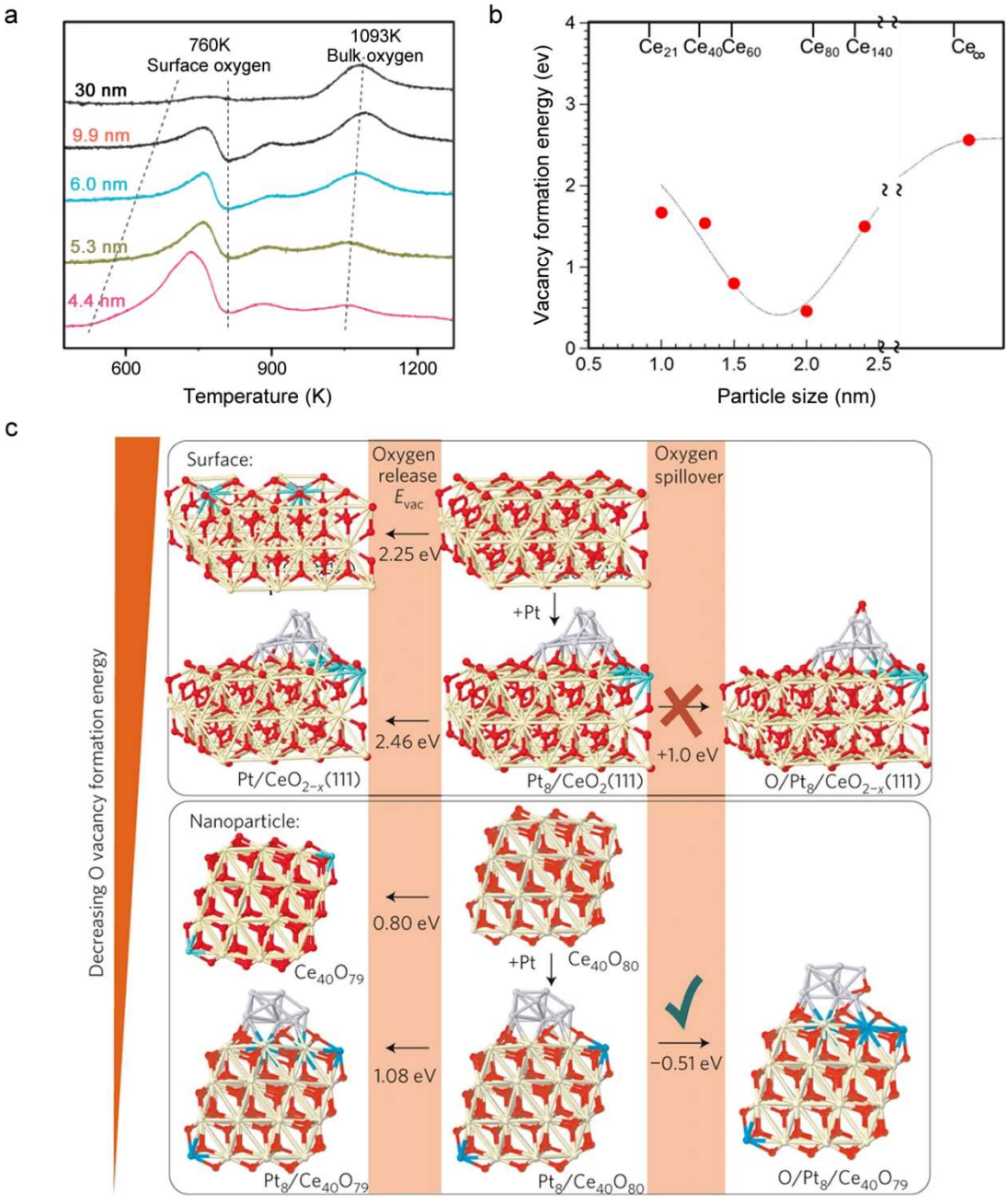

Figure 2.2. Size effects in CeO_2. a) Ceria reducibility probed by hydrogen temperature-programmed reduction (H_2-TPR). Adapted from ref.[18]. b) DFT-derived energetics of oxygen vacancy formation for a series of Ce_nO_{2n} nanoclusters differing in size. Adapted from ref.[25]. c) Reverse oxygen spillover from CeO_2 to the Pt cluster on nano-sized ceria and extended CeO_2 surfaces. Data from ref.[22].

It has also been observed by a combination of XRD, neutron pair-distribution function (nPDF) and Raman spectroscopy that nanosized CeO_2 undergoes anomalous thermal

expansion below 0 °C[26]. Such lattice expansion has not been observed for bulk ceria. The conductivity measurements together with results of DFT simulations suggested that the counter-intuitive lattice expansion upon cooling is linked to the unusual charge-transfer dynamics between oxygen vacancies and Ce 4f orbitals in nanosized ceria.

So far, we have summarized several of the main structural and chemical aspects of ceria relevant to catalysis without aiming to be comprehensive. Many other peculiarities of the ceria structure have been reviewed by the groups of Trovarelli[27] and Fornasiero[28]. Mullins presented an extensive overview of the redox properties of ceria as investigated by a classical surface science approach[3]. The importance of such aspects of the surface structure, redox dynamics and the size of ceria will be further discussed throughout this chapter in the context of preparation, characterization and performance of ceria-based catalytic systems.

2.3 Synthesis of ceria

The most widespread use of ceria in catalysis is in automotive emissions neutralizers. Ceria-supported catalysts also display promising performance for the water-gas shift (WGS) reaction[29] and solar thermochemical water splitting[30], while solid-oxide fuel cells typically contain ceria as a solid electrolyte[1]. As with all catalytic supports, industrial scale production of ceria requires straightforward and reproducible synthesis recipes. Most of the current syntheses are based on wet chemistry methods. Metal loading of ceria-based catalysts is usually achieved using impregnation, resulting in the formation of (transition) metal NPs or clusters. A high metal dispersion typically requires a high surface area of the support material. Ceria with high surface area can be prepared by precipitation[31,32]. This approach has the advantage that other (transition) metals can be co-precipitated, resulting in high dispersion of the added transition metal, possibly in the ceria lattice as a solid solution[33–35]. Ceria-zirconia ($Ce_xZr_{1-x}O_{2-\delta}$), which is the most studied mixed oxide of ceria, is typically obtained by co-precipitation. Ceria-zirconia is widely used in the automotive industry[36] and in heterogeneous catalysis in general[33,34]. Facile preparation, excellent thermal stability, and enhanced oxygen storage capacity with respect to ceria are the main reasons for its widespread use as a catalyst support[33,34].

Use of templates in combination with precipitation allows increasing the surface area of ceria. The work of Terribile et al. demonstrated that the utilization of an amphiphilic surfactant such as cetyltrimethylammonium bromide (CTAB) can result in an ordered

mesoporous structure of cerium dioxide[37]. Due to the very strong but reversible adsorption of CO_2 on ceria, such porous materials with large exposed surface are promising candidates to support CO_2 conversion catalysts[38]. Sol-gel synthesis is another wet chemistry method widely used for the preparation of ceria-based systems with high surface area[39]. A recent report of Hyeon and co-workers demonstrates the unprecedent versatility of the sol-gel route for the size- and shape-controlled synthesis of very small ceria crystallites (**Figure 2.3**)[40]. Datye and co-workers showed that the sol-gel method can be also used for the preparation of high-surface-area ceria that is homogeneously doped with transition metals such as Ni, Fe, Mn, and Cu[41]. Apart from the large surface area, the sol-gel method brings the advantage of its versatility in preparing thin films and coatings. This aspect is exploited in solid-oxide fuel cells, in photo- and electrochemistry and in corrosion protection.

The development of spectroscopic techniques and especially of atomic-resolved microscopic imaging has led to notable progress in establishing structure-function relationships of ceria-based catalysts. Using state-of-the-art imaging and spectroscopy, we are now able to resolve the surface structure of powder catalysts at the atomic level[42]. Before, such profound insights could only be gained with surface science model systems. While earlier a large surface area of the support was the main target in catalyst preparation, we now understand that crystallites shape and surface termination can have a substantial impact on the overall catalytic performance[8,11,43]. Such a control over the surface termination is therefore an important element of current and future investigations aimed at optimizing ceria-based catalysts. In recent years, extensive research of hydrothermal synthesis of ceria has led to many examples of shape control in the synthesis of ceria nanostructures[12,25,44]. The seminal work of Li and co-workers involved a fairly simple hydrothermal synthesis of ceria nanorods predominantly exposing (110) surfaces, while conventional precipitation method yielded CeO_2 NPs with dominant (111) facets[45]. Although the total surface area of the obtained materials was rather similar, the CO oxidation performance was markedly different. The authors explained the higher activity of their nanorod-shaped ceria by the higher reducibility of exposed (110) surfaces as compared to (111) ones. In later work, Mai et al. showed that by changing the concentration of the precipitation agent (NaOH) and temperature of the synthesis, other shapes of ceria can be obtained (**Figure 2.3**)[46]. For instance, ceria nanocubes are preferentially (100) faceted and exhibit higher reducibility than polyhedra of ceria, featuring predominantly (111) surfaces. Detailed high-resolution

transmission microscopy (HR-TEM) analysis revealed that CeO_2 (100) and (110) surfaces can reconstruct into more stable ones, and usually the (111) one. The combination of HR-TEM with IR spectroscopy of low-temperature adsorbed adsorption was used to unambiguously conclude that ceria nanorods are predominantly enclosed by (111) facets (**Figure 2.3**)[44]. The same conclusion was drawn by Datye and co-workers based on the catalytic activity of nanorods in the WGS reaction[10].

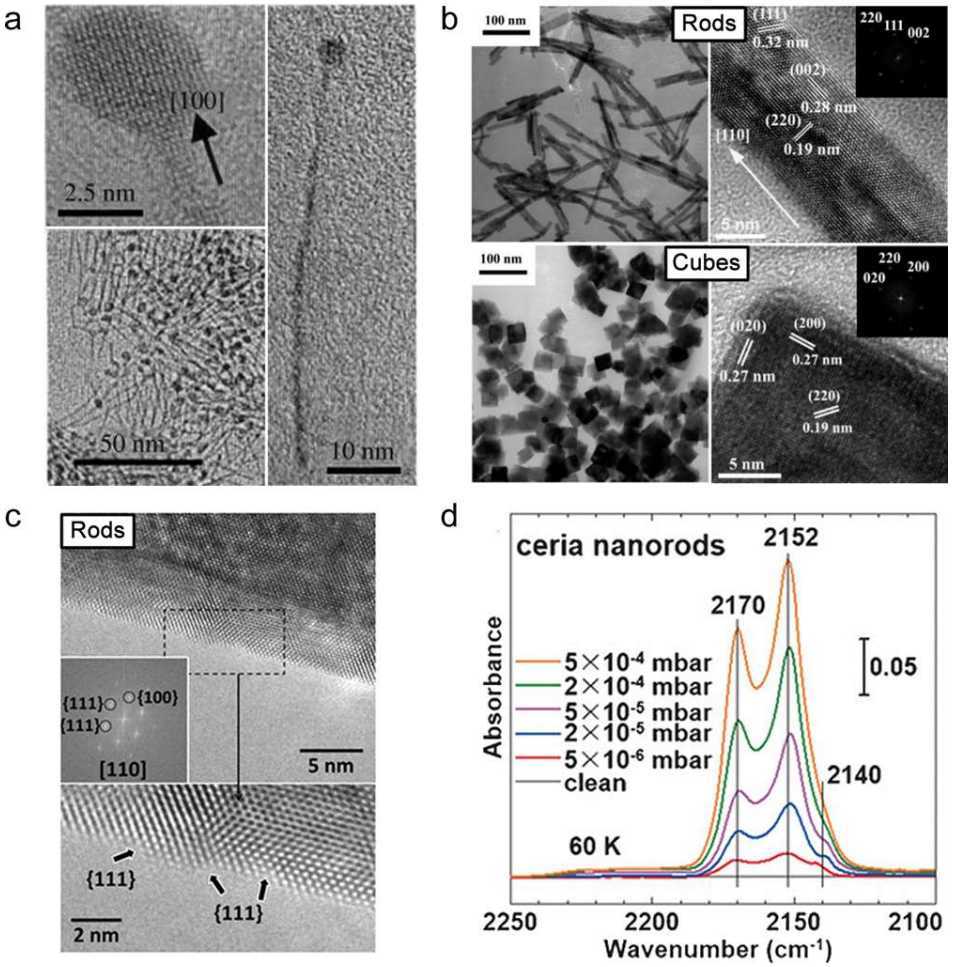

Figure 2.3. Nano-shaped ceria crystals: a) nanowires prepared by sol-gel methods, adapted from ref.[40]; b) rod- and cube-shaped ceria prepared by hydrothermal synthesis, adapted from ref.[46]. Elucidation of the predominant faceting of CeO_2 nanorods: c) HRTEM images showing (111) surfaces and d) IR spectra of low-temperature CO adsorption on ceria exhibiting bands at 2152 cm^{-1} and 2170 cm^{-1}related to CO on Ce^{4+} sites of (111) and (110) facets, respectively (adapted from ref.[44]).

More complex morphologies, such as core-shell structures, are also within reach for ceria. Cargnello et al. demonstrated that coating/encapsulation of Pd NPs in CeO_2 remarkably enhances their thermal stability and activity towards methane oxidation (**Figure 2.4**)[47]. Recently, it was shown that similar structures can be prepared by a facile and direct self-assembly strategy[48]. Confinement in such core-shell structures has also been exploited for

hydrogenation reactions. For instance, Ni NPs encapsulated in ceria(-zirconia) showed better stability and catalytic performance in CO_2 methanation[49]. A modular design strategy paves the way to the development of catalysts with unconventional metal-support interactions. The increased stability and activity of such modular catalysts can outweigh their higher complexity and cost of preparation.

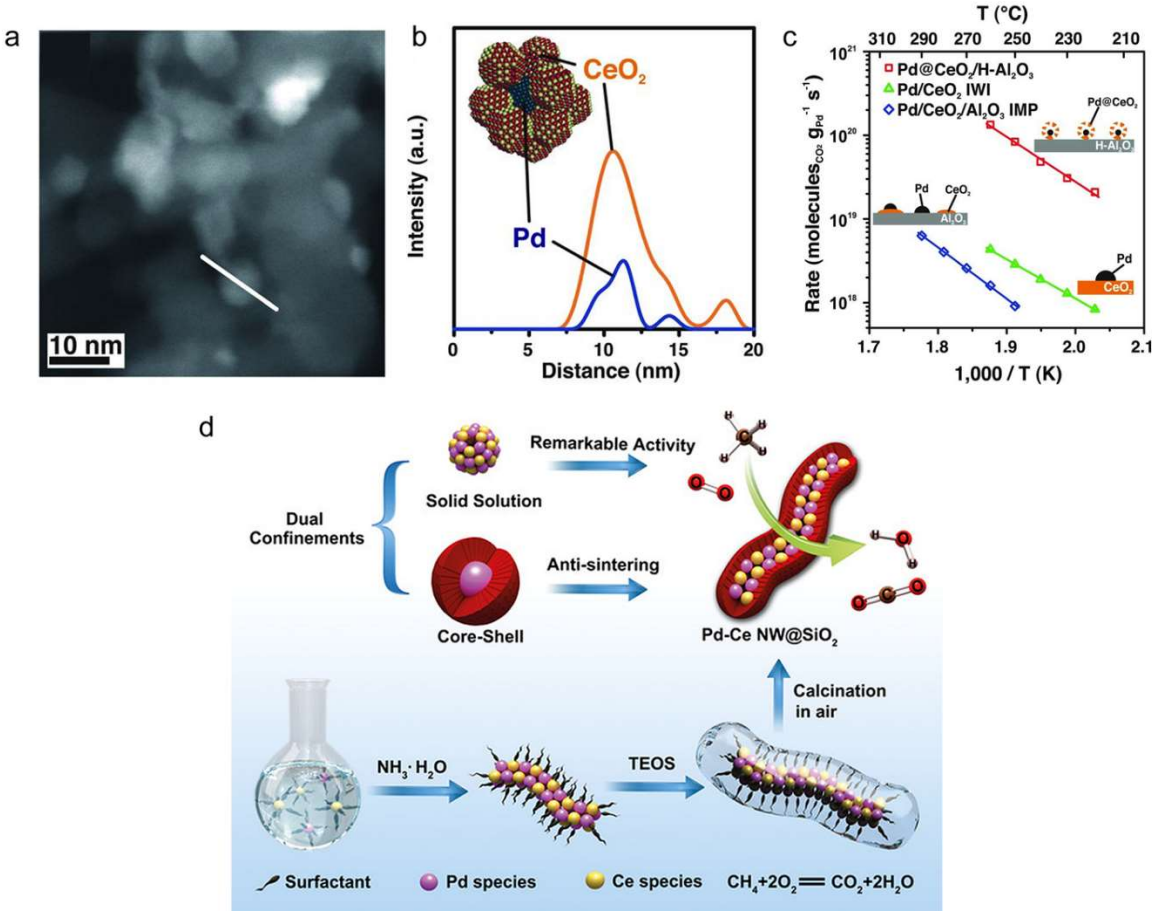

Figure 2.4. Core-shell ceria structures. (a) TEM images of Pd@CeO_2 composites, (b) element analysis line profile displaying the Pd-core and CeO_2-shell, (c) beneficial effect of core-shell structure on activity of composites in methane combustion (adapted from ref.[47]). (d) Dual-confinement concept for stabilization of metal-oxide interfaces (reproduced from ref.[48]).

Preparation of ceria-based materials by combustion and mechanochemical approaches appears to be a promising alternative to conventional wet chemistry methods. Some of the disadvantages of wet chemistry routes are the involvement of multiple steps such as precipitation, washing, drying, calcination, and impregnation, and the large amount of solvent used during washing steps. Recently, the group of Trovarelli demonstrated that ball-milling of commercially available low-surface-area precursors of Ce and Pd yields highly-active and stable catalysts for methane combustion[50]. The cost-efficiency and flexibility, with respect to the choice of precursors, and the simplicity of this preparation method are

appealing from the perspective of scale-up. The same group also used a solution-combustion synthesis method to prepare Pd-CeO_2[51]. The resulting materials are $Pd_xCe_{1-x}O_{2-\delta}$ solid solutions obtained in a single step. Despite their low surface area (<20 m^2/g), these catalysts displayed higher methane oxidation activity than conventional impregnated Pd/CeO_2 catalysts.

Another combustion method for the single-step preparation of ceria and its derivatives is flame spray pyrolysis (FSP). In contrast to the majority of solution-combustion methods, FSP allows obtaining ceria with a very large surface area (~150-200 m^2/g). FSP is a versatile preparation method fit for scale-up[52]. The basic principle of FSP synthesis lies in the injection of liquid precursors containing the metals of interest into a methane-oxygen flame (**Figure 2.5**). The temperature in the flame (typically, 1500-2000 ºC) can be tuned by using solvents and precursors with different enthalpies of combustion. The high temperature results in fast evaporation of the solution droplets, which shortens the residence time in the flame and, thus, limits the sintering of the resulting metal oxide and/or metal nanomaterials. The high temperature of FSP synthesis also ensures full decomposition of the precursors, which has the advantage that the resulting materials can be directly used without further drying or calcination. FSP is also ideally suited to prepare mixed metal oxides and solid solutions of two or more metals[53,54]. Wet chemical methods, such as coprecipitation, often lead to inhomogeneous doping of ceria because of the different pH regions of precipitation of cerium and transition metal dopants. In FSP synthesis, salts of several transition metals can be solubilized in suitable organic solvents, contributing to a homogenous mixing of the metal ions in the resulting material. Another advantage of FSP applied to ceria preparation is that the products are highly crystalline. It is typically observed that FSP of ceria precursors leads to particles with a well-defined octahedral shape exposing predominantly the thermodynamically most stable (111) surface (**Figure 2.5**)[55].

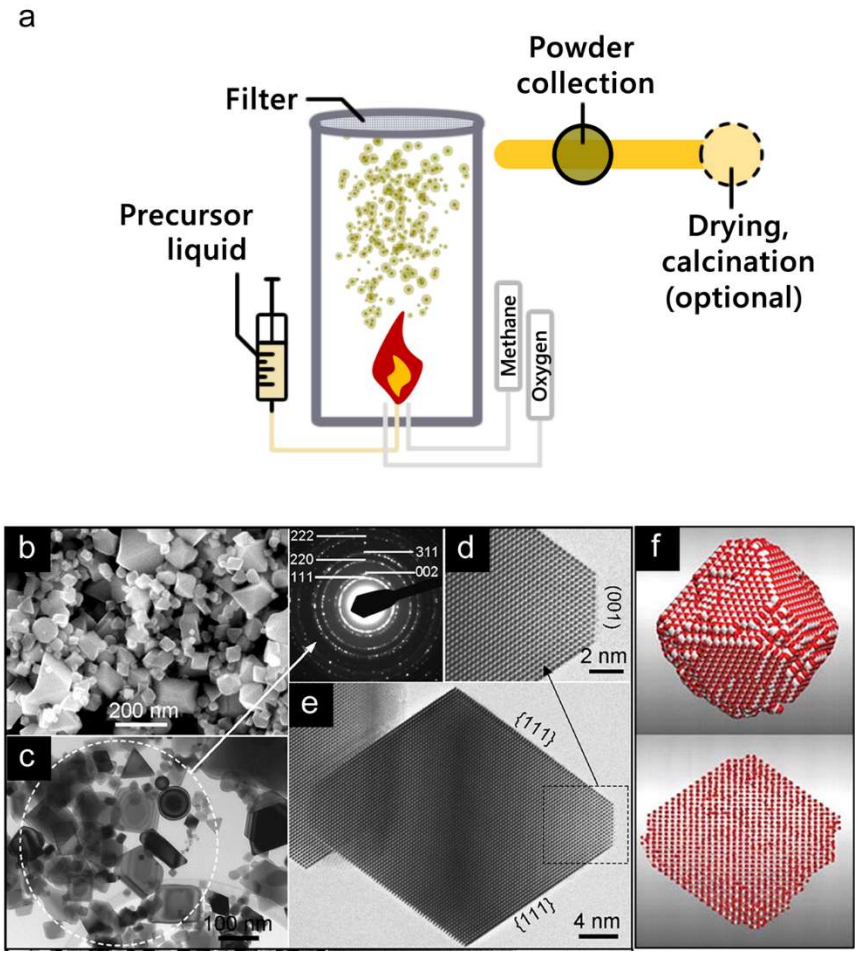

Figure 2.5. Flame spray pyrolysis (FSP) synthesis. a) Schematic representation of FSP synthesis. b) - e) Highly crystalline (111) faceted CeO_2 prepared by FSP; f) CeO_2 nanoparticle morphology predicted by molecular dynamics simulations of the annealing process. Adapted from ref.[55].

The group of Sayle has successfully developed computational tools to simulate synthesis, generating atomistic models in quantitative agreement with experimentally observed crystallite morphologies[56]. In brief, an amorphous precursor structure is melted at very high temperature (~2000 K), followed by rapid cooling to facilitate the crystallization of the framework. The appeal of these simulations is that they allow to predict the faceting of for instance ceria nanorods, exposing primarily (111) facets with a small fraction of (100) ones. Simulating crystallization of ceria doped with Ti atoms led to core-shell structure of the nanocomposites, which was validated by experiment. Coupling molecular dynamics simulations with experiments provides unique insights into the mechanism of crystal growth and will stimulate the knowledge-driven design of ceria nanomaterials with controlled morphology and nanostructure.

2.4 Characterization of ceria materials

In recent decades, the fast development of *operando* spectroscopy tools has led to unprecedented insights into the chemistry of ceria. Many of the older literature is focused on understanding the role of ceria in automotive exhaust emissions[57]. Thus, such reactions as CO oxidation, NO reduction, oxidation of hydrocarbons and the water-gas shift reaction are typically used to evaluate the catalytic performance of ceria-based catalysts. The surface science approach, which depends on the use of model systems such as thin films and single crystals with a well-defined surface structure, substantially contributed to understanding of metal-support interactions (MSI) in ceria-based catalysts[58]. However, this research is typically limited by "pressure" and "material" gaps. The former refers to the use of characterization techniques that require high-vacuum conditions where the pressure can be up to ~10 orders of magnitude lower than the pressure under real reaction conditions. Moreover, the chemistry of model systems may differ significantly from the chemistry of nano-sized powder catalysts containing defects and other imperfections, which is referred to as the "material gap". Recent developments of spectroscopy techniques and the advancement of synchrotron radiation facilities allowed studying of catalysts in the *operando* regime. As such, it has already become possible to follow the dynamics of catalysts during the actual chemical reaction under close-to-practical conditions. A key element of this approach is to analyze the reaction products, allowing the establishment of firm structure-performance relationships. Detailed accounts of the *operando* methodology in catalysis can be found in excellent reviews by Lukashuk and Foettinger[59] and Weckhuysen[60]. Traditionally, the use of *operando* spectroscopy is aimed at unveiling the speciation of the active components in catalysts, which are typically metal NPs or clusters on a support. For ceria-based catalysts, the support can directly participate in the catalytic cycle and, thus, it is often considered a part of the active phase. Therefore, in this section we will particularly focus on the spectroscopy tools that allow following the chemistry of Ce.

The most important techniques to characterize ceria-based catalysts are X-ray diffraction (XRD), Raman spectroscopy, Fourier-transformed infrared spectroscopy (FTIR), X-ray photoelectron spectroscopy (XPS), X-ray absorption spectroscopy (XAS) and transmission electron microscopy (TEM). Although almost all of these techniques are now available for *in situ* investigations, the majority of previous studies were carried out in an *ex situ* manner,

implying the inherent limitation that the structure and state of catalysts were determined before and/or after the catalytic reaction.

XRD is typically used to study the structure and phase purity of ceria. By using the Scherrer equation, it is possible to estimate the average crystallite size, while Rietveld refinement of XRD patterns can provide information about lattice parameters and strain. Such data are especially relevant to understand the influence of dopants on the structure of mixed oxides and solid solutions of ceria[61]. *In situ* XRD can be used to unveil the phase transitions of the supported transition metals and also provide insight into the redox chemistry of CeO_2 (**Figure 2.6**)[62]. Senanayake and co-workers showed that lattice expansion of ceria under reducing conditions is related to reduction of Ce^{4+} to Ce^{3+}. The larger ionic radius of Ce^{3+} together with the electrostatic repulsion between oxygen vacancies and the surrounding cations lead to an expansion of the lattice, which can be followed by XRD. In this way, we can probe Ce^{3+}/Ce^{4+} redox processes under *operando* conditions. Moreover, using synchrotron radiation, one can follow such processes with high temporal resolution. A disadvantage of this methodology, however, is the bulk sensitivity of XRD. In this respect, the use of ceria supports with relatively small particle size to maximize the number of atoms exposed to reactants seems to be a promising direction for studying redox dynamics in these systems by diffraction-based techniques.

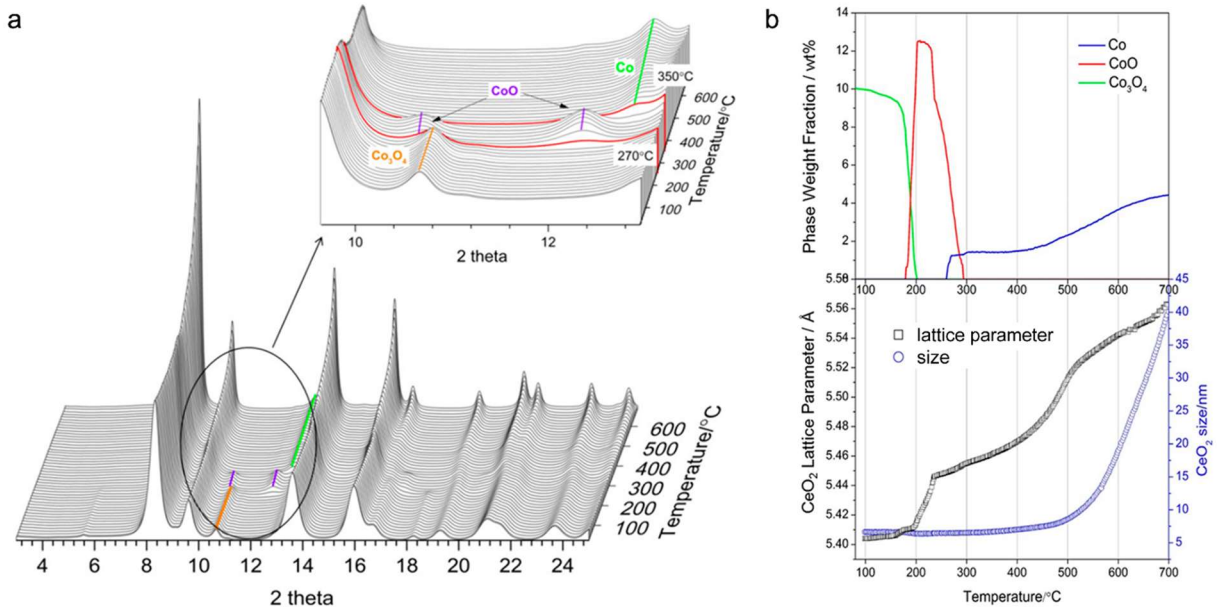

Figure 2.6. *In situ* XRD of Co-CeO_2 catalyst. a) The XRD patterns resolve cobalt oxide and ceria reduction features; b) ceria lattice expansion due to Ce^{3+} formation upon reduction. Adapted from ref.[62].

Raman spectroscopy is another scattering technique widely used to interrogate the structural and redox properties of ceria. As this technique can probe vibrational modes, it is much more sensitive to short-range order than XRD. Spectral changes related to vibrational features can be used to investigate disorder in defective nanomaterials such as ceria. As it relatively easy to simulate vibrational spectra, Raman spectroscopy is a good choice for studying the structural properties of ceria[63]. The red-shift of the main F_{2g} band (~460 cm^{-1}) in the Raman spectrum of ceria can be correlated to lattice strains and the presence of structural defects. In turn, the width of the band was shown to be inversely proportional to the crystallite size[64]. The broad band in the range of 550-560 cm^{-1} is a signature of nanocrystalline ceria. This D band is related to point defects in the ceria lattice. The formation of oxygen vacancies and reduction of Ce^{4+} to Ce^{3+} are some of the reasons for the local lattice disorder, allowing the observation of vibrational modes that are normally symmetry-forbidden. Using the intensity of the D band as a proxy for concentration of oxygen vacancies, it is possible to follow the redox behavior of the support in an *operando* manner. As Raman is a vibrational spectroscopy, it is also very sensitive to isotope exchange, which opens up possibilities for studying the oxygen mobility in ceria lattice using labelled oxygen atoms. Recently, Schilling et al. elegantly proved a pivotal role of oxygen of the support in the WGS reaction over gold-ceria catalysts using isotopic labelling and *operando* Raman spectroscopy[65]. An important benefit of Raman spectroscopy for ceria characterization is the ability to detect peroxo (O_2^{2-}, 820-890 cm^{-1}) and superoxo (O_2^{-}, 1120-1140 cm^{-1}) species, which are vital intermediates in various oxidation reactions[66]. One of the disadvantages is its strong dependence on the optical absorption properties of the material, which can often change as a function of the reaction conditions. Irradiation damage by the laser source is another issue that can complicate data interpretation in Raman spectroscopy. Further information on the application of Raman spectroscopy for investigation of ceria-based catalysts can be found in a recent review by Loridant[67].

FTIR spectroscopy is one of the key techniques to characterize catalytic materials. In the context of heterogeneous catalysts, it is mostly applied in combination with probe molecules. For example, IR analysis of chemisorbed CO is a widely used method for studying catalytic surfaces. The vibrational frequency of adsorbed CO is sensitive to the geometric and electronic structure of the adsorption site. CO adsorption FTIR spectroscopy can be considered an *operando* technique, if CO is one of the reactants or products of the reaction.

In some cases, it is preferred to avoid reactions of CO, which can be achieved by cooling to very low temperatures. The low CO adsorption strength on surface sites of metal-oxides, such as ceria, is another reason for performing low-temperature CO adsorption. The group of Wöll studied CO adsorption on different surfaces of ceria single crystals and shaped nanocrystallites[44]. They concluded that IR spectroscopy of low-temperature CO adsorption is a suitable method to distinguish between the most relevant facets of ceria, *i.e.* (111), (110) and (110), based on the frequency of the observed carbonyl IR bands. The position of these IR bands also depends on the oxidation state of Ce atoms. This approach led to unambiguous determination of the primary faceting of nano-shaped ceria crystallites. IR spectroscopy of methanol adsorption is a less common method, but it is also sensitive to ceria surface termination[68]. The C-H and C-O stretching frequencies of adsorbed methanol molecules can also be used to determine the surface structure of CeO_2 (**Figure 2.7**).

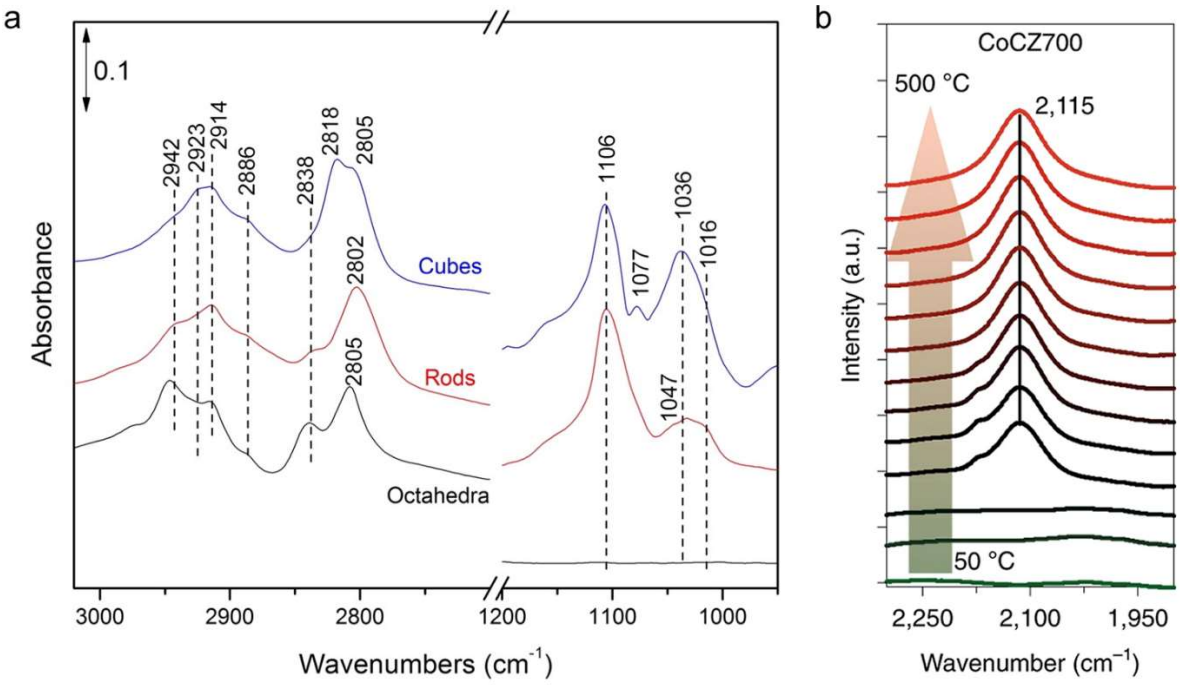

Figure 2.7. IR probes for the surface termination and electronic state of ceria. a) C-H and C-O regions of methoxy groups IR spectrum over nano-shaped ceria. Reproduced from ref.[68]. b) Ce^{3+} formation, as manifested by the 2115 cm^{-1} band ($^2F_{5/2} \rightarrow {}^2F_{7/2}$) during the reduction of cobalt-ceria-zirconia catalyst (adapted from ref.[70]).

It should be noted that the ceria surface can be reduced by methanol, even at room temperature. IR spectroscopy of adsorbed probe molecules is a powerful methodology which, however, does not directly probe the electronic structure and redox properties of ceria. The O-H region of the ceria IR spectrum can also be used to follow surface

reduction/oxidation phenomena, although the interpretation is not very straightforward[69]. A direct probe for Ce^{3+} states is the broad band at ~2120 cm^{-1}, which is due to $^2F_{5/2} \rightarrow {}^2F_{7/2}$ electronic transition. Recently, Parastaev et al. successfully used this IR signature to study the Ce^{3+}/Ce^{4+} redox dynamics of cobalt-ceria-zirconia interface[70]. Yet, the weak intensity of the adsorption band and its appearance only at high degree of ceria reduction significantly limits the use of this spectroscopic method. Further details into the characterization of ceria-based materials by IR spectroscopy can be found elsewhere[69].

XPS has become a very valuable technique for studying heterogenous catalysts. The importance of XPS to especially heterogenous catalysis arises from its surface sensitivity (typically 2-10 nm). Using synchrotron radiation, it is now possible to vary the sample probing depth (from tens to fractions of nm) by tuning the incident photon energy. The photoelectron lines in XPS spectra are specific to the elements and can thus be employed for elemental analysis, while the use of appropriate relative sensitivity factors allows quantifying the surface composition of the sample. Analysis of the binding energy of the core-line electrons can be used to identify the valence state of the surface atoms. This is especially relevant for ceria-based systems, where the redox Ce^{3+}/Ce^{4+} dynamics are of particular interest. Conventional XPS analysis is done in ultra-high vacuum (UHV), required by the technical considerations and to minimize the attenuation of electrons escaping the solid. Under such conditions the samples can be characterized *ex situ*. An often employed approach is to characterize samples *quasi in situ,* referring to a particular pretreatment of a sample followed by transfer to the UHV analysis chamber of the spectrometer without exposure to the ambient atmosphere. Although such approaches are an improvement over conventional *ex situ* analysis, the characterization of ceria in this way remains problematic, especially for the study of Ce redox dynamics. A main reason for this is that Ce^{3+} can be readily oxidized at relatively low partial pressure of oxygen. Another issue relates to the reduction of Ce^{4+} to Ce^{3+} upon prolonged exposure to UHV conditions and especially under X-ray irradiation, resulting in erroneous determination of the surface valence state[71]. Recent advances in the development of *in situ* near-ambient pressure XPS (NAP-XPS) or ambient pressure XPS (AP-XPS) resolved such challenges to a large extent[72]. Modern NAP-XPS systems allow studying the catalysts at pressures of up to 100 mbar, which is very close to real conditions of many important catalytic reactions. The combination of high photon flux and tunable energy of the excitation radiation available at synchrotrons makes NAP-XPS an

ultimate tool for studying surface redox dynamics in ceria-based materials. Bluhm and co-workers[73] have recently analyzed the Ce 3d core-line spectra with the aim of following the Ce valence as a function of applied potential in a working solid-oxide electrochemical cell (**Figure 2.8**). This example is very illustrative of how dramatic the changes in surface Ce^{3+}/Ce^{4+} ratio can be due to the applied (electro)chemical conditions. By means of lab-based NAP-XPS study, Parastaev et al. demonstrated oxygen spillover from and to the support at cobalt-ceria-zirconia interface[70]. Kato et al. obtained another important insight into the chemistry of Ce^{3+} and oxygen vacancies[74]. Using a tunable photon energy, the authors showed that catalytically relevant Ce^{3+} ions and oxygen vacancies reside in the top-most surface layers of Pt-CeO_2 catalysts. This study underpins the vital importance of (i) an *in situ* approach to follow the Ce^{3+}/Ce^{4+} dynamics and (ii) the surface sensitivity for accurate probing of the catalytically relevant charge states in ceria. With respect to the latter, the use of resonance photoelectron spectroscopy (RPES) of Ce 4d → 4f transitions to quantify the Ce^{3+} states at the very surface, appears to be very promising[75]. Yet, this approach has not been used at near-ambient pressure and on realistic samples.

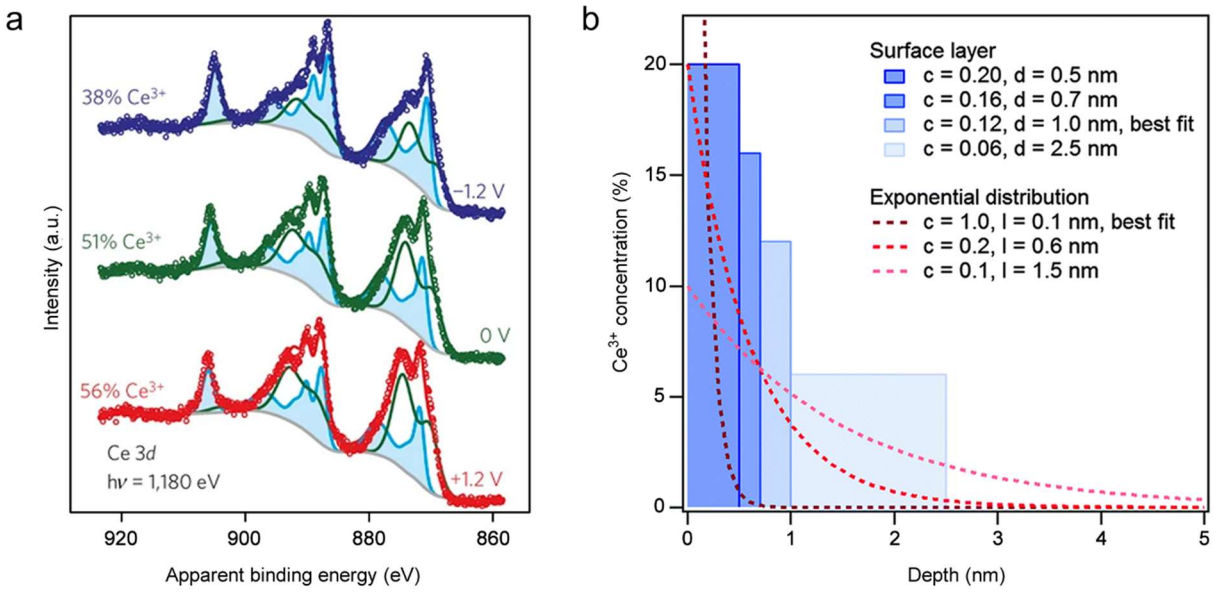

Figure 2.8. *In situ* NAP-XPS data. a) Ce 3d core-line spectra exhibiting different Ce^{3+} fractions at the surface of the operating solid-oxide electrochemical cell as a function of applied bias. Adapted from ref.[73]; b) Spatial distribution of Ce^{3+} as a function of probing depth – majority of the oxygen vacancies reside on the very surface (adapted from ref.[74]).

Hard X-ray absorption spectroscopy (XAS) is a synchrotron-based technique, which provides insights into element-specific electronic and atomic structure of the materials. XAS has become an important analytical tool in materials chemistry and, in particular, in catalysis

research. High sensitivity (with some fluorescence detectors possibly down to sub-ppm concentrations) and flexibility with respect to pressure and temperature are the key reasons for its popularity in heterogeneous catalysis. Although the main principles of XAS remain the same regardless of the incident photon energy, it is convenient to separate two types of X-ray absorption using soft (< 5 keV) and hard (> 10 keV) X-rays. With high-energy X-rays, it is feasible to perform *operando* spectroscopic studies (almost) without any compromises with regards to reaction conditions. X-ray absorption near edge structure (XANES) spectroscopy allows following the electronic structure of the element (*e.g.*, valence state) as function of time, reaction conditions and other stimuli. Another benefit of hard X-rays is the possibility to obtain information about the local structure around the absorbing atoms, resulting from the photoelectron scattering by the neighboring atoms. This spectroscopy method is called extended X-ray absorption fine structure (EXAFS). After proper data reduction, local structural parameters of the absorbers, including the nature of neighboring atoms, their number and interatomic distances, can be resolved. For structural studies of ceria-based materials, the Ce K-edge (~ 40 keV) is commonly used. It is also very useful to use XANES to directly probe Ce^{3+}/Ce^{4+} redox transformations and interrogate the electronic structure of Ce. Typically, this is done at the Ce L_3-edge (~5.7 keV), which is sensitive to the valence state of Ce due to dipole allowed 2p→5d transitions. The fine structure of the XANES region can be obtained by using high-energy resolution fluorescence detection (HERFD). This technique allows reaching an energy resolution below the one dictated by the core-hole lifetime broadening. Such high spectral resolution is especially valuable for studying CeO_2 NPs, whose electronic structure is markedly different from their bulk counterparts[76]. Better signal quality comes, however, at a cost, because HERFD-XAS requires energy-dispersive detectors or crystal analyzers, complicated in use and not so often available at XAS beamlines. Therefore, conventional Ce L_3 XANES still remains a workhorse for studying oxidation-reduction processes in ceria. Using this approach, Ganzler et al.[77] demonstrated that nano-sized ceria in Pt-CeO_2-Al_2O_3 composites undergoes reduction by CO already at temperatures as low as 100 °C. Such low-temperature lattice oxygen removal provides strong evidence for the high oxygen mobility in nano-sized ceria (**Figure 2.9**). The small size of CeO_2 NPs used in this study (~5 nm) is particularly suitable due to the high surface-to-bulk atom ratio, since XAS employed in normal incidence geometry is a bulk-sensitive technique. The size-dependent reducibility of ceria NPs was also validated by Ce L_3 XANES[78]. By

following the formation of Ce^{3+} as a function of temperature, the authors showed that small NPs of ceria can be reduced by CO at a lower temperature than their bulkier counterparts.

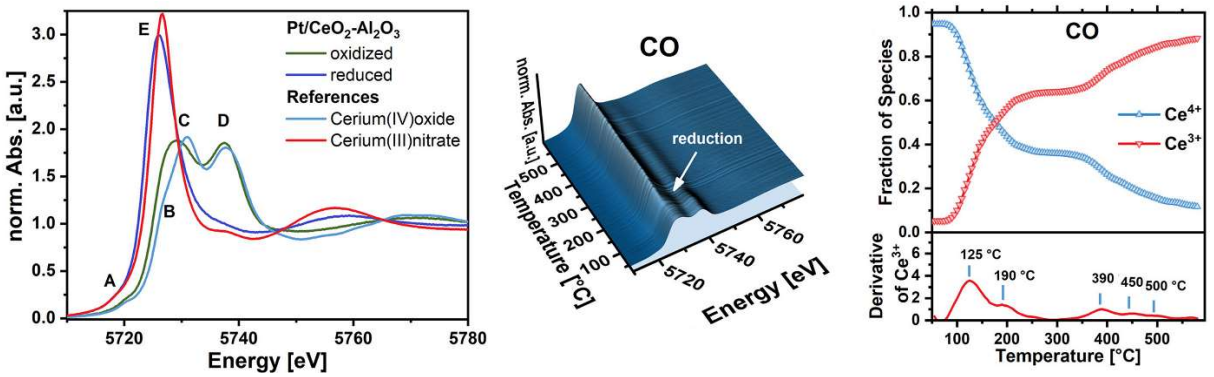

Figure 2.9. Following the reduction of Ce^{4+} to Ce^{3+} by CO using *in situ* XANES at Ce L_3-edge. Adapted from ref.[77].

Another effective technique to follow minute changes in the population of Ce^{3+} states is resonant X-ray emission spectroscopy (RXES). Under optimized conditions, Safonova and co-workers pushed the sensitivity limit down to 0.3% of Ce^{3+} while operating at sub-second time resolution (**Figure 2.10**)[79]. X-ray emission techniques require rather complicated analyzers and a high flux of incident photons, in return providing exceptional sensitivity to the changes in valence states with high temporal resolution.

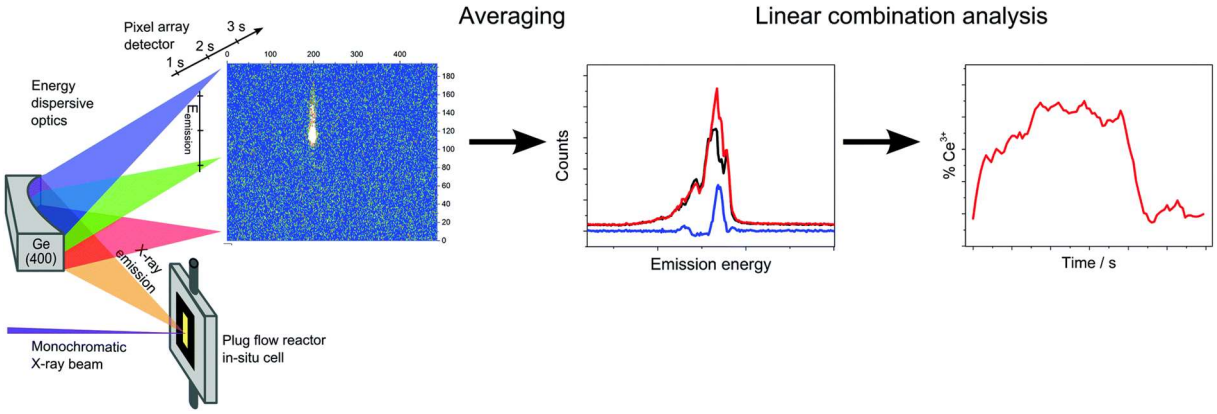

Figure 2.10. Schematic representation of the approach by Safonova and co-workers for time-resolved Ce^{3+} detection using RXES. Reproduced from ref.[79].

Electron microscopy has evolved into a very powerful tool for imaging the nanoscale properties and the combination with other spectroscopy tools provides very valuable insights into local structure including its physico-chemical aspects. With the development of aberration-corrected electron microscopes, exact atomic arrangements at the surface of materials can be visualized. This kind of knowledge is indispensable for developing structure-activity relationships for ceria-based catalysts. Using atomically resolved

transmission electron microscopy, Wöll and colleagues demonstrated that calcination of ceria nano-cubes leads to significant surface reconstructions[12] (**Figure 2.11**). Refaceting of (100) and (110) surfaces towards thermodynamically more stable (111) surfaces upon calcination caused the experimentally observed increase of CO oxidation activity of annealed samples.

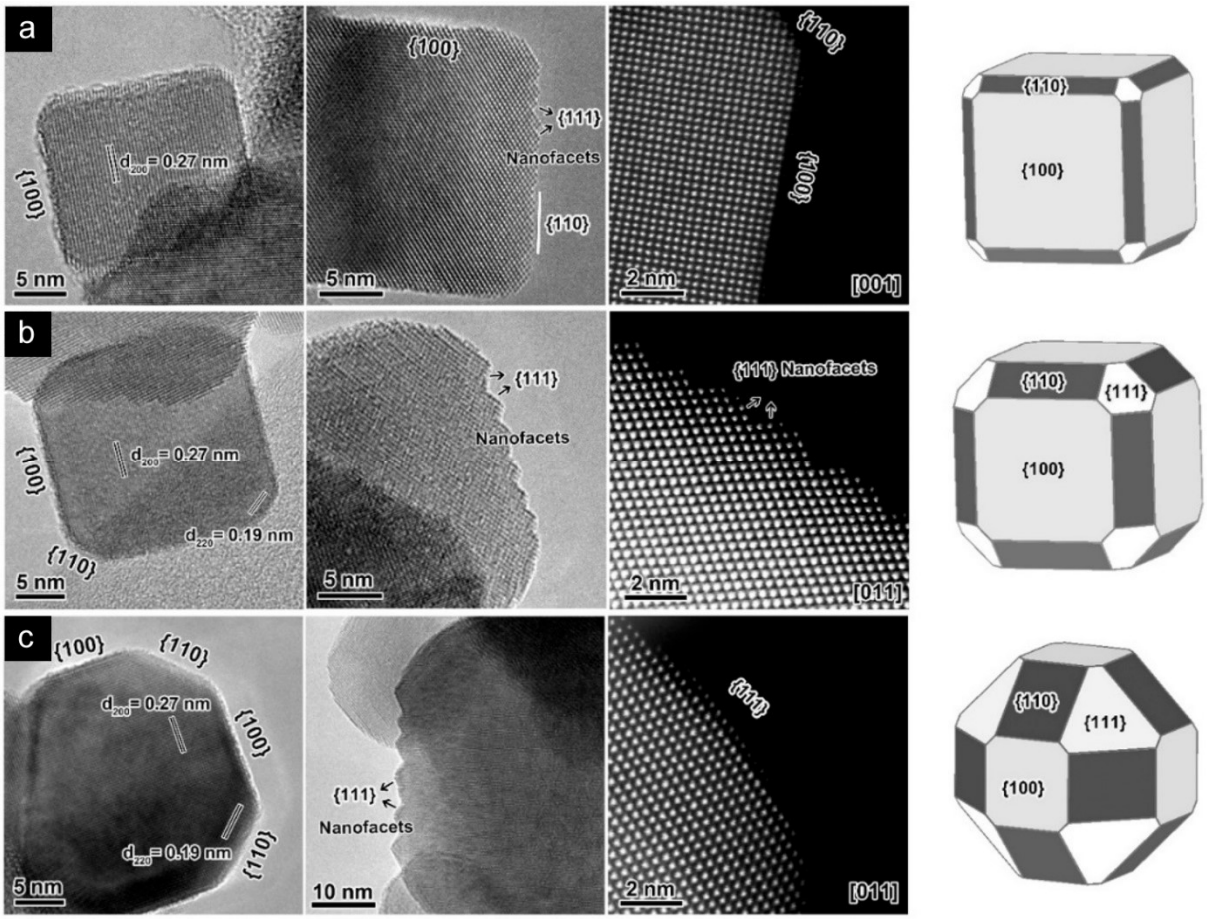

Figure 2.11. Surface refaceting of ceria cubic nanostructures induced by the thermal treatment at a) 500 °C, b) 600 °C, c) 700 °C. Reproduced from ref.[12].

Impressive possibilities in atomic scale imaging with elemental and valence state analysis can be derived by combining EM with electron energy loss spectroscopy (EELS). Current aberration-corrected TEM/STEM techniques allow imaging of isolated single atoms as well as acquiring spectroscopic information from a single atomic column. The valence states of Ce atoms in ceria nano-structures can be spatially resolved with close-to-atomic precision. Van Tendeloo and co-workers successfully employed STEM-EELS for mapping the Ce^{3+} and Ce^{4+} states in ceria NPs (**Figure 2.12**), using the Ce $M_{4,5}$ edges as a fingerprint[80]. They found that (100) surfaces are substantially richer in oxygen vacancies (up to ~6 atomic layers deep) as reflected by a higher Ce^{3+}/Ce^{4+} ratio than (111) facets where only 1-2 underlying atomic

layers are of mixed valence state. These findings are in line with the DFT-predicted lower barriers for oxygen vacancy formation and the higher reducibility of the (100) surface in comparison to the (111) one.

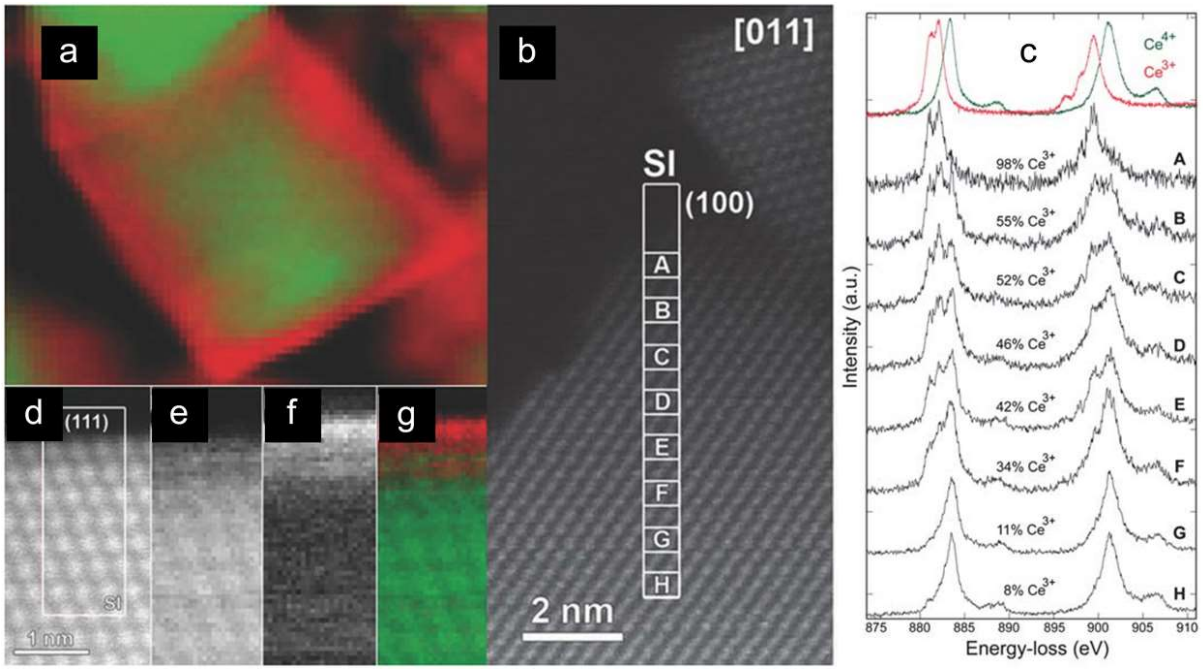

Figure 2.12. STEM-EELS color map of CeO_2 NPs with Ce^{3+} (red) and Ce^{4+} (green). a) Overview of the entire nanoparticle. b) HAADF-STEM image showing the (100) surface truncation and the scan region indicated. c) Averaged Ce $M_{4,5}$ spectra from regions A-H together with reference spectra for Ce^{3+} and Ce^{4+}. The fitted weight of Ce^{3+} is given for each spectrum. High resolution HAADF-STEM image showing the d) (111) surface and the EELS scan region. e) Ce^{4+} map. f) Ce^{3+} map. g) Color map with Ce^{3+} (red) and Ce^{4+} (green). Reproduced from ref.[81].

Pioneering EM work of Takeda and colleagues[82] revealed the dynamic reconstruction of ceria-supported Au NPs in the presence of CO and O_2 already at room temperature (**Figure 2.13**). By adapting the energy of incident electron beam, these researchers could observe CO adsorbed on the reconstructed surface of gold nanoparticles. Even such level of detail, however, did not allow to unambiguously answer the important issue of identifying the metal-support interface or metallic sites as the active sites for low-temperature CO oxidation. For further details on the latest advancements in microscopy imaging of ceria-based materials, the reader is referred to an excellent review by the group of Van Tendeloo[81].

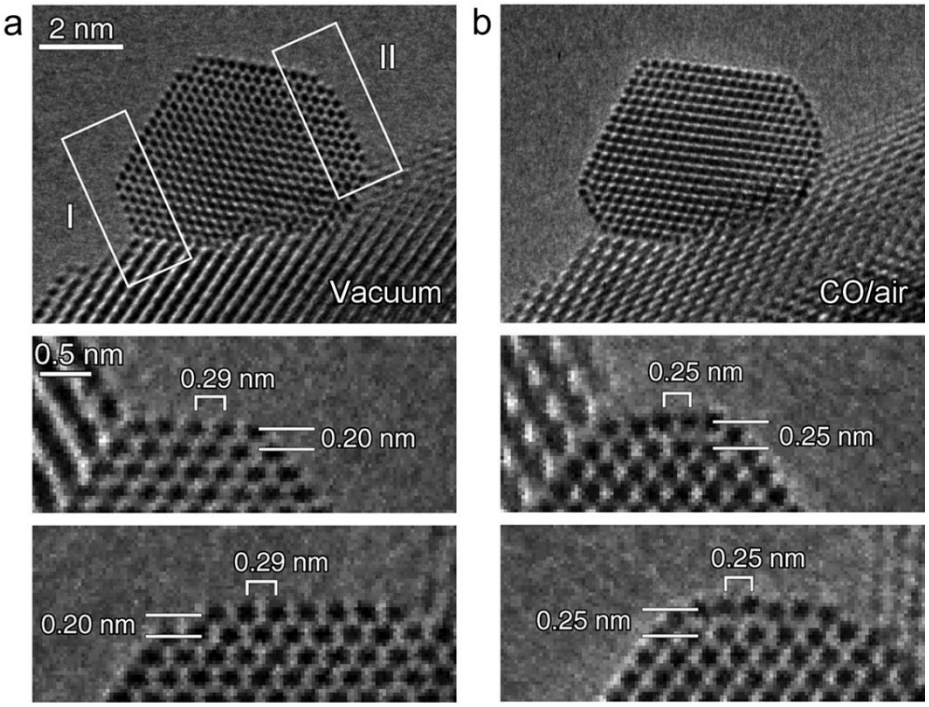

Figure 2.13. TEM images of Au supported on CeO_2 in a) vacuum and b) reaction environment (1 vol% CO in air gas mixture at 45 Pa at room temperature). The (100) facets are indicated by areas I and II. Enlarged images of these regions in vacuum and in the CO in air gas mixture are shown at the bottom. Adapted from ref.[82].

For completeness, we mention some of the other frequently used tools to characterize the electronic and structural properties of ceria. UV-Vis spectroscopy can be applied to determine the band gap structure and the Ce^{3+} to Ce^{4+} charge transfer transitions (~570 nm) in the *operando* regime[83]. Yet, direct quantification of Ce^{3+} states cannot be performed in this manner. In electron paramagnetic resonance (EPR), a characteristic line with g ~1.97 has been used to quantify Ce^{3+} states (or oxygen vacancies). However, a recent report of Rakhmatullin et al.[84] suggests that this assignment is a misinterpretation, *i.e.*, the EPR signal is rather due to an electron trapped near the surface Ce^{3+}/Ce^{4+} redox pair. Solid-state NMR using ^{17}O as a probe can be considered a potent method for studying the surface structure and defect chemistry of ceria NPs[85]. The high cost associated with enriching ceria with ^{17}O in gaseous $^{17}O_2$ limits its wide application for studying catalytic systems, although isotopic exchange with $H_2{}^{17}O$ appears to be a cheaper alternative.

Despite the significant advances in the characterization of ceria, there are many remaining challenges in understanding the chemistry of these unique materials. In the next sections we will discuss how the toolbox of advanced synthesis techniques together with the state-

of-the-art spectroscopy and imaging can help us to understand and improve the catalytic functions of ceria-based materials.

2.5 Metal-support interfaces in ceria catalysts

Nanoparticles of transition metals, mostly of the platinum group, dispersed over ceria-containing support materials are widely used as catalysts in car exhaust neutralizers. The strong interactions between the metal and the ceria support can result in a high metal dispersion during preparation and the use of the catalyst. In some cases, the metal-support interaction (MSI) is so strong that the supported metals can be atomically dispersed, giving rise to a new class of materials – single-atom catalysts, which will be the subject of the next section. Decades after the first reports about strong MSI[86], there remains a lack of detailed atomistic understanding about the origin and nature of these interactions. The challenge to comprehend MSI arises from the difficulty to disentangle its chemical origins from the many manifestations. Such ambiguities can be overcome by establishing firm structure-performance relationships. The latest developments in spectroscopy and imaging hold promise to resolve many of the underlying physico-chemical aspects of MSI.

In a recent review, De Jong and colleagues discussed the main concepts underlying the chemistry of MSI[87]. Applied to ceria-based catalysts, the morphology of the support and metal NPs, charge transfer and spillover effects are identified as the most important consequences of MSI. These interactions at the metal-support interface cause the interfacial sites (metal atoms in close proximity to the supporting oxide) to be distinctly different from other surface atoms of the supported NPs. The charge transfer between metal and support (known as electronic MSI or EMSI) causes the perturbations of the electronic structure of atoms at the metal–oxide interface[88]. Such interactions can give rise to a new type of sites, whose catalytic properties are markedly different from conventional metallic sites. This was for instance shown for the WGS reaction by Bruix et al.[89]. Following the classical surface science approach, the authors engineered model Pt-CeO_2 interfaces, which are substantially more active than extended Pt surfaces or conventional Cu/ZnO catalysts. Detailed photoemission spectroscopy study revealed that the valence state of ceria-supported Pt clusters is different from bulk Pt metal, which is caused by the charge transfer from Pt to Ce. In a seminal work, Lykhach and coworkers quantified these charge-transfer phenomena using Pt-CeO_2 as a model system[90]. They first prepared an (111) oriented thin film of CeO_2 on

which the Pt atoms were deposited at a controlled rate. By tracking the valence states of Ce and Pt atoms as a function of Pt coverage using surface-sensitive RPES and XPS, it was possible to count the number of electrons transferred from Pt^0 to Ce^{4+} atoms. As follows from **Figure 2.14**, the size of the deposited Pt clusters strongly influences the extent of the EMSI, the smallest ones (<2 nm) being the most sensitive to charge redistribution. Similar charge-transfer phenomena were also observed for Cu clusters deposited on ceria[91]. These results pave the way to understanding of the size-induced effects in structure-property relationships of metal NPs supported on ceria.

Spillover effects are another class of phenomena occurring at the interface between metals and the reducible ceria support. Conceptually, the term spillover implies the process in which certain species are activated on the metal surface and then transferred to the support, which is typically a metal oxide. Despite being already observed in the 1960s[92], the actual understanding of hydrogen spillover is far from complete[93]. Van Bokhoven and colleagues elegantly used the state-of-the-art *in situ* X-ray photoemission electron microscopy (X-PEEM) to follow the hydrogen spillover from metal to metal oxides[94]. The authors first prepared a suitable model system, employing electron beam lithography to produce well-defined Pt NPs of platinum and iron oxide on typical reducible (titania) and non-reducible (alumina) supports (**Figure 2.15**). By varying with nanometer precision the distance between nanoparticles of Pt and FeO_x, hydrogen spillover could be monitored by studying the reduction of iron oxide. When supported on alumina, only the reduction of iron oxide NPs in close proximity (<15 nm) to Pt was observed. On the contrary, when supported on titanium oxide, the reduction of iron oxide occurred to the same extent regardless of the distance from Pt. This is a clear illustration of the prominent hydrogen spillover effect on reducible oxides. Lykhach et al. demonstrated the relevance of hydrogen spillover on ceria as well, showing Ce^{3+} formation at the surface of Pt-CeO_2 model system when exposed to hydrogen[95].

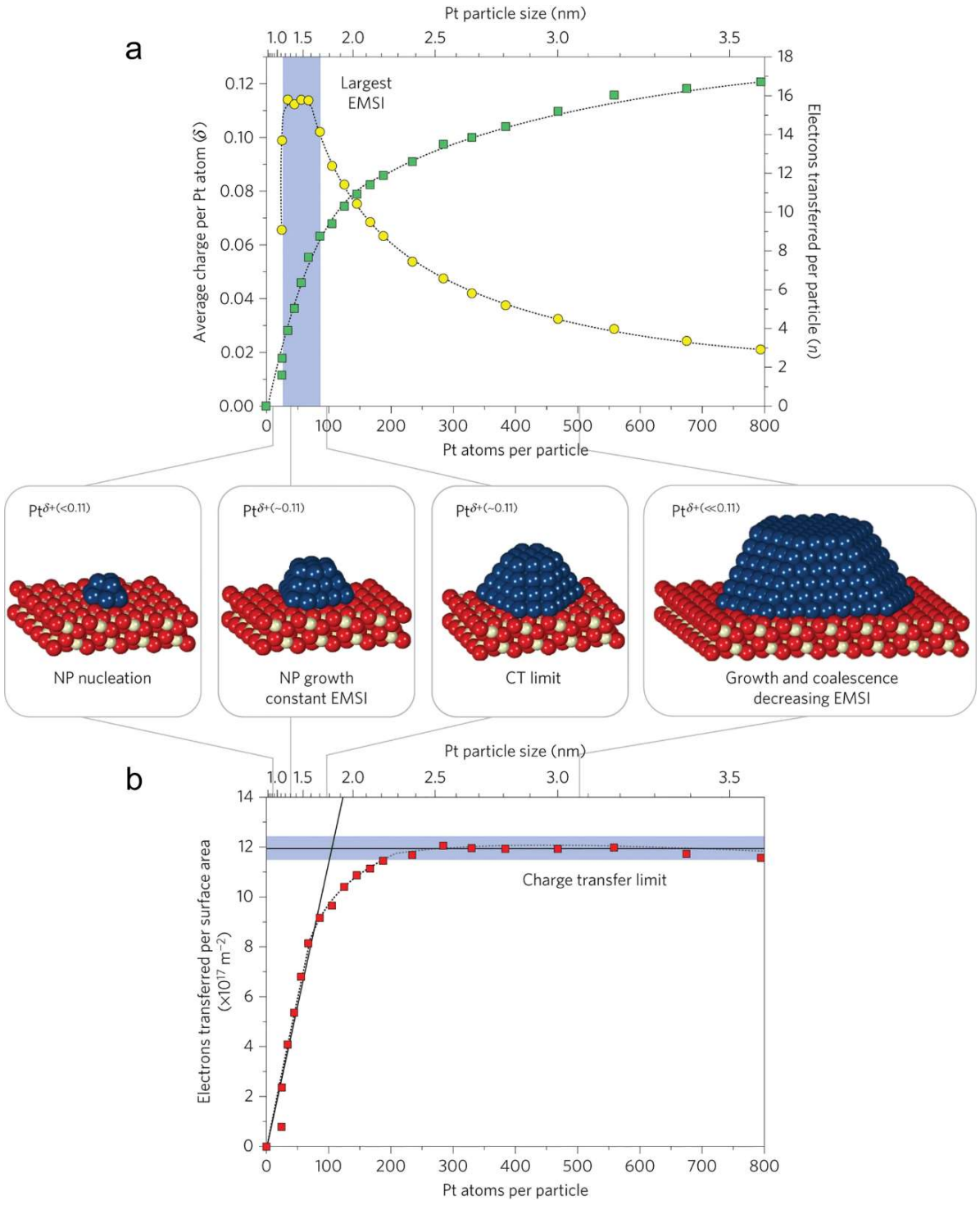

Figure 2.14. Charge-transfer phenomena at Pt-CeO_2 interface. a) The number of electrons transferred per Pt particle to the ceria support increases with increasing particle size (green squares). The partial charge per Pt atom reaches a maximum for particles with 30 to 70 atoms (yellow circles). b) At higher Pt coverage the total amount of transferred charge approaches a limit – "charge transfer limit" (red squares). The atomic models show schematically the average particle sizes in the different regions. Reproduced from ref.[90].

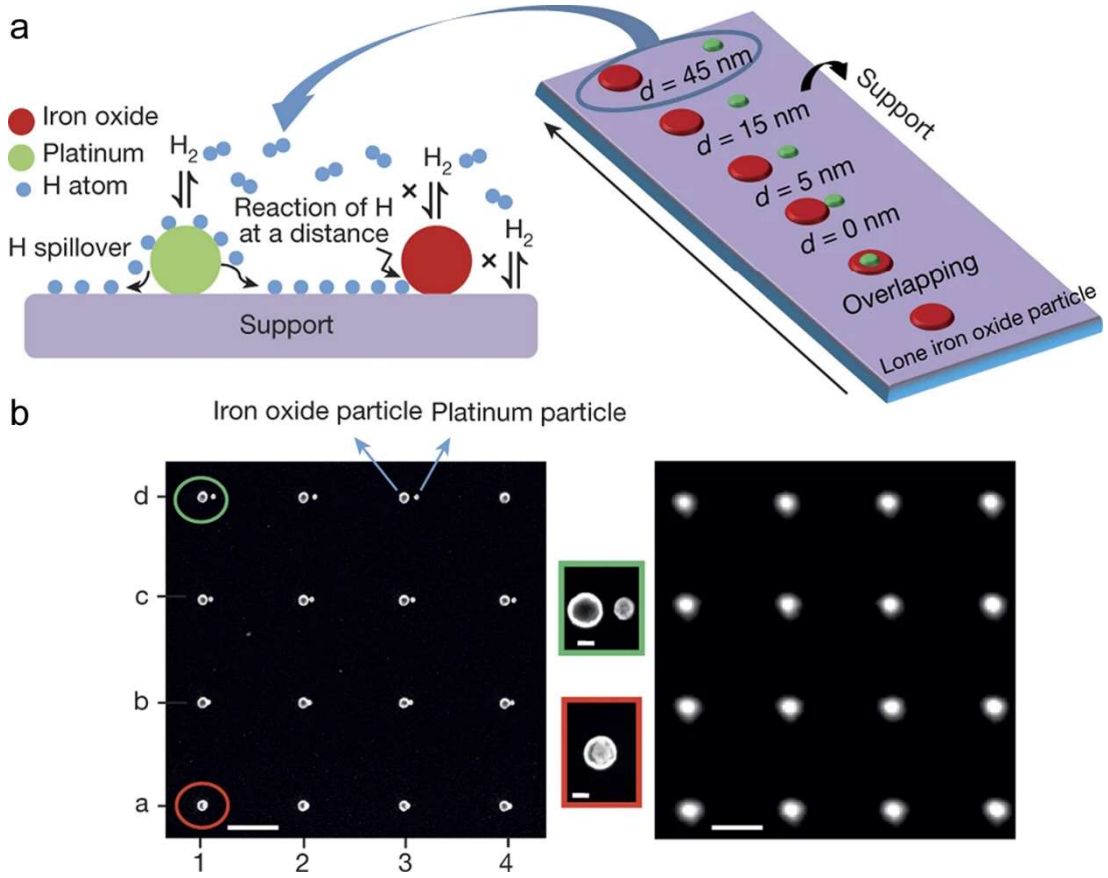

Figure 2.15. Hydrogen spillover. a) Scheme of hydrogen spillover from platinum to an iron oxide particle over a titanium oxide or aluminum oxide support. b) SEM image (left) and X-PEEM (right) of the nanofabricated model system on an aluminum oxides support, with 15 such pairs and a single iron oxide particle over an area of $3 \times 3\ \mu m^2$ (scale bar, 500 nm). The iron oxide particles have a diameter of 60 nm, while the platinum particles have a diameter of 30 nm. The distance between the pairs is 1 µm. Higher-magnification SEM images (scale bars, 25 nm) of pairs 'd1' and 'a1', encircled in green and red, respectively. Adapted from ref.[94].

Facile hydrogen spillover is an important property of ceria-based catalysts, particularly relevant for hydrogenation reactions, *e.g.,* CO_2 methanation. In principle, not only hydrogen but also oxygen atoms can be spilled over to the support, as was demonstrated recently for cobalt-ceria-zirconia catalysts[70]. This is likely caused by the participation of the cobalt-ceria interface in CO_2 and CO dissociation. The reverse spillover process can also occur, entailing that active species are transferred from the support (reducible metal oxide) to the interfacial sites of the deposited metal. Typically, this concerns oxygen atoms leaving the ceria lattice positions with the formation of oxygen vacancies and adjunct Ce^{3+} cations. Key examples of reverse oxygen spillover were captured in a surface science study of Gorte and Zafiris[96], who demonstrated the transfer of oxygen atoms from ceria to Rh NPs. Using CO adsorption and temperature-programmed desorption (TPD) experiments, they showed that a substantial fraction of adsorbed CO molecules leaves the surface as CO_2 due to oxidation by interfacial

oxygen atoms. Later, Smirnov and Graham[97] showed by XPS that heating in UHV conditions leads to oxidation of Pd clusters on the surface of ceria due to facile oxygen transport from the support to metal species. Finally, Neyman and colleagues[22] directly observed reverse oxygen spillover in model Pt-CeO_2 nanocomposites (**Figure 2.16**).

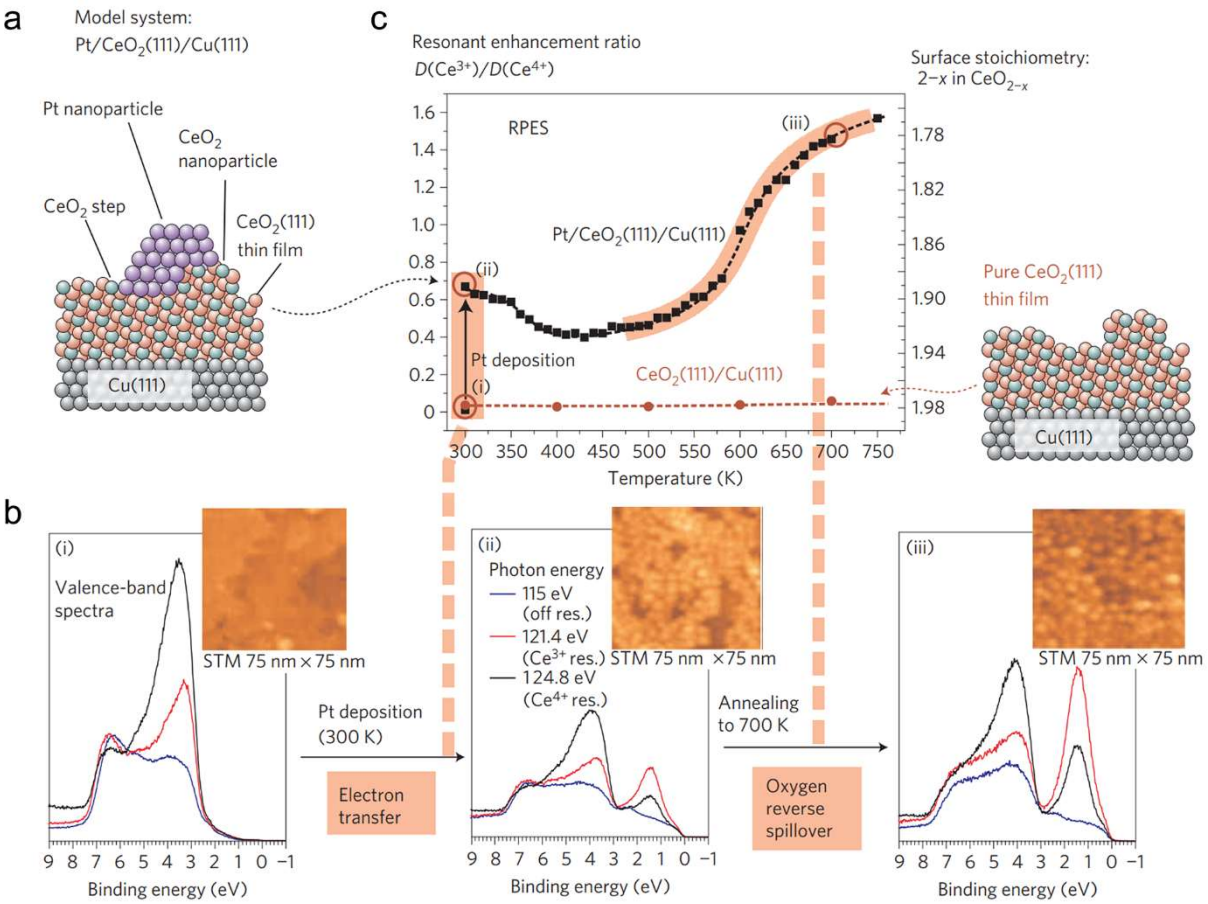

Figure 2.16. Reverse oxygen spillover effect. a) Schematics of Pt–CeO_2/Cu(111) model catalyst (left). Reference measurements are made on a pure CeO_2 film on Cu(111) (right). b) Changes in the ceria oxidation state monitored by RPES. Three selected situations are shown: (i) the pristine CeO_2 film; (ii) after deposition of Pt at 300 K; (iii) after subsequent annealing to 700 K. The insets show representative scanning tunneling microscopy images of the model systems. c) The resonant enhancement ratio from RPES, reflecting the Ce^{3+} concentration, reveals two individual processes: Spontaneous Ce^{3+} formation on Pt deposition at 300 K—attributed to a purely electronic metal-oxide interaction—and an abundant further formation of Ce^{3+} on annealing above 500 K—attributed to the activated process of oxygen reverse spillover. The right axis shows the surface stoichiometry of CeO_{2-x} as determined from the RER. In the absence of Pt, no reduction is observed. Adapted from ref.[22].

The authors first showed that in the absence of a metal-support interface (*i.e.,* without deposited Pt NPs) reduction of Ce^{4+} to Ce^{3+}, as a proxy for oxygen vacancies formation, did not occur upon heating the model catalyst in vacuum. However, by depositing Pt clusters on a thin film of ceria, the redox properties were dramatically changed. Thermal treatment

of the Pt-CeO_2 (111) composite led to Ce^{3+} formation, as monitored using the high surface and valence state sensitivity of RPES. Their experimental findings were rationalized by DFT calculations, pointing at size-dependent oxygen mobility (via reverse spillover). These spillover effects significantly broaden the scope of mechanistic steps that has to be considered in catalytic cycles over ceria-based materials. Understanding spillover effects and other phenomena underlying the MSI is pivotal for knowledge-driven design of novel interfaces with tailored catalytic properties.

Next, we will discuss some illustrative examples of catalytic reactions, where the chemistry is dominated by the MSI phenomena at the interface between metal NPs and ceria. A prominent example is found in the work of Cargnello et al., who prepared a set of well-defined ceria-supported Pd, Pt and Ni NPs of different size using colloidal synthesis (**Figure 2.17**)[98]. The advantage of this modular synthesis approach is the uniformity of the deposited particles, which usually cannot be achieved by conventional methods such as impregnation. A specific feature of metal NPs supported on ceria is that they are already active in CO oxidation at much lower temperature than metal NPs supported on non-reducible supports. Extensive HR-TEM analysis and careful kinetic studies provided insights into the relation between the size of the metal NPs and the CO oxidation activity. Specifically, the authors concluded that interfacial metal atoms – despite not necessarily being metallic – are the most active sites for low-temperature CO oxidation, which can be explained by the active participation of oxygen of the ceria support via a Mars-van Krevelen-type of mechanism. The normalized reaction rates and apparent activation energies for ceria-supported Pt, Pd and Ni NPs were very similar, yet markedly different from those of metal NPs supported on alumina. This study revealed the crucial role of metal-support interface in catalysis by ceria systems. Another good example of interfacial synergy between metal NPs and ceria was provided by Chen et al.[99]. By depositing well-defined Pd NPs on the surface of ceria nanorods, they found that the catalytic activity in CO oxidation is substantially higher as compared to the activities of the separate components. The synergetic effect was explained by electron charge transfer at the metal-support interface, which was demonstrated by Ce L_3-edge XAS. Kopelent et al. used time-resolved RXES to directly prove the involvement of ceria in CO oxidation at low temperatures[100]. RXES was used to follow the Ce^{3+}/Ce^{4+} dynamics as a function of transient switches between feeds of $CO+O_2$ and CO over impregnated catalysts comprising small Pt NPs on CeO_2. The initial rate of Ce^{3+} formation (upon a switch

to CO) is markedly slower than the subsequent reoxidaton to Ce^{4+}, when O_2 is co-fed with CO again. The working hypothesis was that CO oxidation occurs at the Pt-CeO_2 interface, in which Pt atoms serve as CO adsorption sites, while O_2 molecules are activated at the oxygen vacancies transiently formed in the reaction cycle. The Ce^{4+}-to-Ce^{3+} reduction due to the reverse oxygen spillover to Pt sites was concluded to be a rate-limiting step in the overall process. This mechanistic proposal was further corroborated by the similarity between the steady-state apparent activation energy and the one derived from the transient experiments using Ce reduction kinetics. As such, this work forms an excellent example of how advanced spectroscopy with temporal resolution, comparable to the rate of elementary reaction steps, can resolve key mechanistic details governing the overall kinetics.

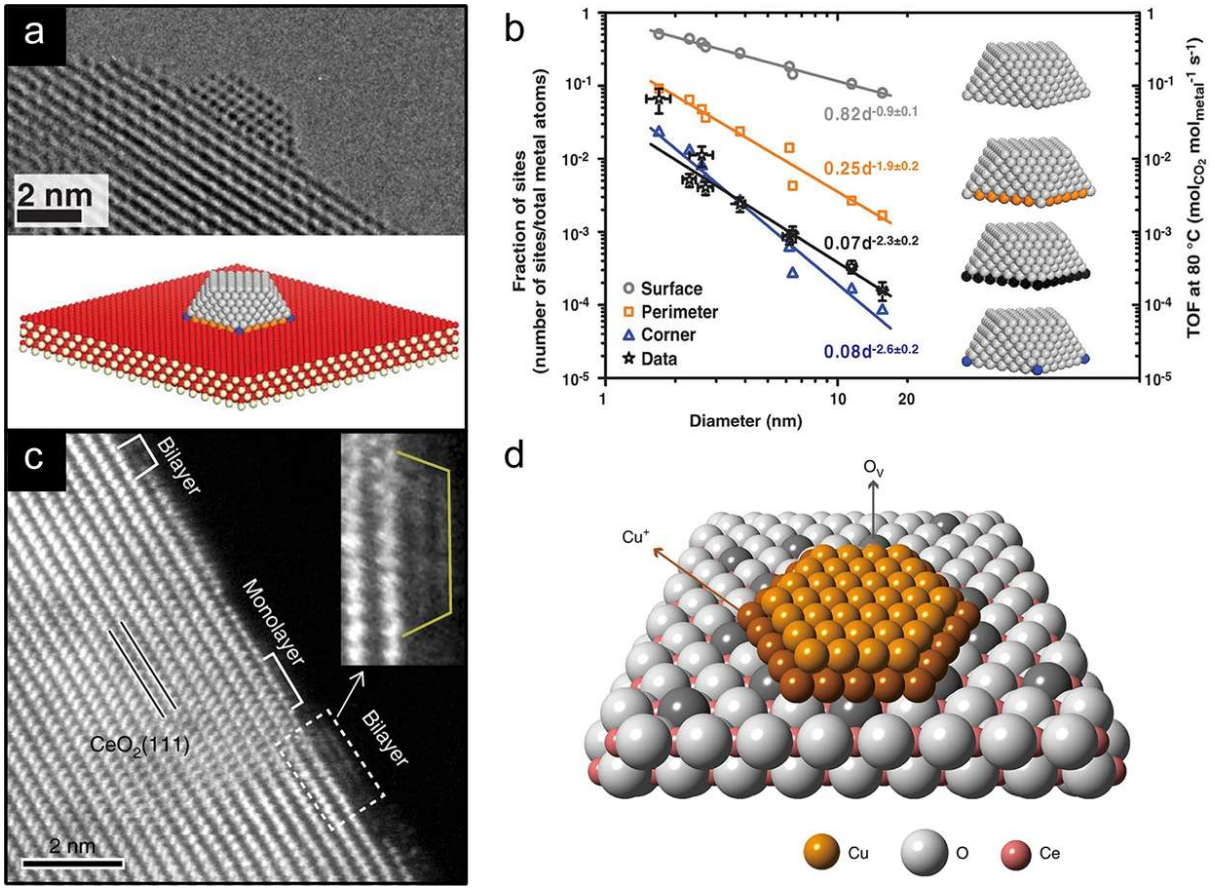

Figure 2.17. Catalysis by metal-support interfaces. a) HR-TEM of CeO_2 supported Pd NPs; b) intrinsic CO oxidation activity as a function of metal particle size and relation to the number of interfacial sites (adapted from ref.[98]). c) The atom-resolved HAADF-STEM images of copper clusters on ceria rods show the atomic configurations of copper domains, monolayers and bilayers; d) a schematic illustration of the Cu bilayer on ceria (adapted from ref.[101]).

The group of Shen demonstrated the relevance of interfacial sites in copper-ceria catalysts for the low-temperature WGS reaction[101]. Using state-of-the-art microscopy and IR spectroscopy, they concluded that the reaction takes place at the perimeter of the Cu

clusters (**Figure 2.17**). An important finding was that the actual interfacial copper sites are not metallic, but positively charged Cu^+ atoms. These atoms provide adsorption sites for CO molecules that can further react with OH groups situated on ceria to form CO_2 and hydrogen. Adsorbed water then dissociates at the oxygen vacancies, which are formed as a result of hydrogen spillover, and regenerates the OH groups closing the catalytic cycle.

The ability of ceria to maintain a high dispersion of metal NPs in comparison to irreducible (stoichiometric) oxides is a well-known manifestation of strong MSI. Despite its prominence, it has only recently been explained in a quantitative manner. Campbell and Farmer[102] used calorimetric measurements to demonstrate that the sintering resistance of silver NPs is strongly dependent on their size with the smallest ones (<2 nm) being identified as the most stable on a ceria surface rich in oxygen vacancies. The large adhesion energy of smaller silver NPs to ceria was explained by lattice strain effects caused by strong metal-oxide bonding. Later, this explanation was generalized for other oxide supports and the observed trend suggests that higher adhesion energies of a metal are also linked to a higher heat of formation of the corresponding metal oxide[103]. The ability of ceria to stabilize highly dispersed metal NPs under transiently changing reaction conditions is especially important for the catalysis in automotive industry. Using state-of-the-art time-resolved *operando* XAS, Nagai et al.[104] demonstrated that the size of the Pt NPs supported on ceria-zirconia can change as a function of reaction conditions. They observed that agglomeration of Pt under reducing conditions can be reversed through redispersion during the oxidizing cycle. Such self-regenerative behavior can explain the higher stability and activity of ceria-supported catalysts. When Pt is supported on alumina, it sinters during reduction-oxidation treatments, leading to catalyst deactivation. Cargnello and co-workers[105] used mild oxidative treatments of ceria-supported Ru NPs to tune the selectivity in CO_2 hydrogenation. Ru NPs can be dispersed into single-atom species through such an oxidative pretreatment. This transformation in turn led to dramatic changes in the catalytic performance. Atomically dispersed Ru species showed ~90% selectivity towards CO in CO_2 hydrogenation, while the same catalyst without oxidative pretreatment showed >90% selectivity towards methane under the same reaction conditions. Interestingly, substantially lower selectivity towards CO after the mild oxidative pretreatment was found for TiO_2- and Al_2O_3-supported catalysts. This finding was explained by incomplete redispersion of initially deposited Ru NPs on these supports, which points at the exceptional ability of CeO_2 to strongly anchor noble metal

atoms. The redispersion of metallic species on ceria does not always require the actual reoxidation of the supported NPs. Newton et al. in a combined time-resolved EXAFS/DRIFTS *operando* study revealed a non-oxidative route for Pd redispersion upon switching CO and NO reactants over a ceria-based catalyst[106]. The strong MSI in ceria catalysts seems to be the driving force for these peculiar transformations of metal speciation.

Facet-dependent catalysis by ceria-based materials is an explicit manifestation of how the support structure can influence the catalytic behavior of the system. Wang et al. prepared nanostructured ceria supports with predominant (111) and (110) faceting to study the crystal plane effect in CO oxidation catalyzed by supported copper oxide clusters[107]. When deposited on (111) ceria facets, these copper oxide clusters are more prone to reduction (from Cu^{2+} to Cu^{+}) as compared to those on (110) facets. This in turn led to substantially different CO oxidation performance, copper oxide clusters on (111) ceria surfaces being the most active at low temperature. For CO_2 hydrogenation, on the contrary, (111) faceting of ceria seems to be unfavorable[108]. It was shown that small ruthenium clusters supported on (100) ceria facets were the most active in CO_2 methanation. Higher activity of Ru-CeO_2 (100) catalyst stems from easier oxygen vacancy formation in (100) surfaces than in (110) and (111) ones, as was concluded from Raman and TPR data. On the other hand, the role of support faceting on the catalytic performance appeared to be relatively small for CO_2 hydrogenation to methanol over Cu NPs supported on nanoshaped CeO_2[109]. It is clear that many aspects of the facet-dependent chemistry related to metal-ceria interfaces are yet to be systematized and mechanistically understood.

Seminal work of Corma and colleagues[23] demonstrated how the size of support particles can impact the catalytic activity of supported metal NPs via MSI. Gold NPs deposited on large ceria particles were found to be nearly inactive in low-temperature CO oxidation. On the contrary, small (~4 nm) Au NP supported on small CeO_2 nanocrystallites (~5 nm) exhibited exceptional activity in CO oxidation already at 10 ^{o}C. In a follow-up publication, it was shown that the ability of nanosized ceria to accommodate peroxide and superoxide species on its surface plays a decisive role in efficient CO oxidation[110]. Parastaev et al. have recently shown that the optimal size of support NPs is key to strong MSI in cobalt-ceria-zirconia (CoCZ) catalysts for CO_2 methanation[70]. Specifically, the Co dispersion depended strongly on the particle size of the support. While relatively small and large CZ support particles resulted in low dispersion of Co NPs, medium-sized CZ support gave rise to the highest methanation

activity due to a high dispersion of Co NPs. The enlarged metal-support interface in optimal catalyst was found to be beneficial for C-O bond dissociation at interfacial sites. To maximize metal-support interface, Tsang and colleagues encapsulated Pt NPs within a thin layer of CeO_2[111]. Such nanoarchitecture was completely inactive for CO methanation, while it was exceptionally active and selective towards the WGS reaction. This work is an elegant example of how knowledge-driven engineering of the metal-support interfaces can be used to fine-tune catalytic performance.

In this section we discussed the role of the metal-support interface in catalysis by ceria-based materials. Synthesis of well-defined interfaces and extensive characterization including *operando* spectroscopy techniques can play a key role in identifying the reasons and effects of the MSI. The physical and chemical phenomena underlying the metal-support interactions are complex and difficult to unravel. Nonetheless, current knowledge already can be applied for fine-tuning the catalyst architecture for specific reactions. Truly inspiring example was recently demonstrated by groups of Somorjai and Yang, who used different functions of metal-support interfaces to direct two chemical reactions into a controlled tandem[112]. Combining colloidal synthesis and self-assembly, they engineered a catalyst, where each platinum nanoparticle had both Pt-SiO_2 and Pt-CeO_2 interfaces (**Figure 2.18**).

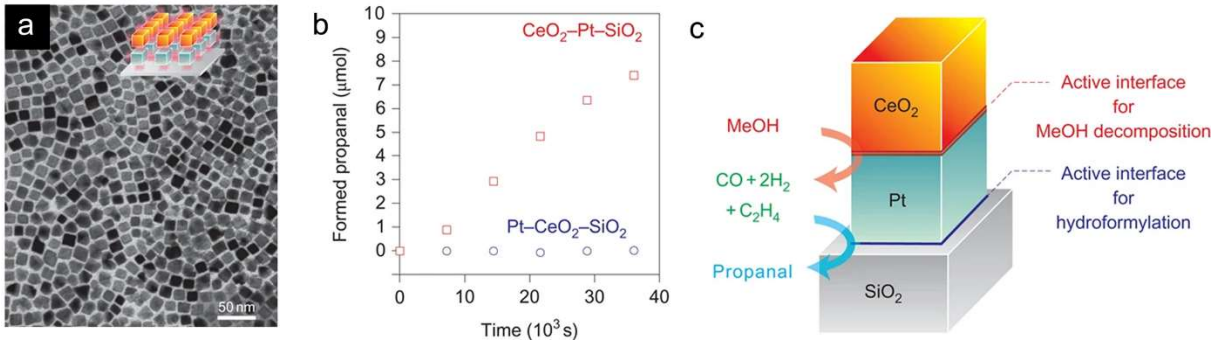

Figure 2.18. Interfacial tandem catalysis. a) TEM image of CeO_2 nanocube monolayer on a Pt monolayer forming a double interface system. b) Propanal produced as a function of reaction time over CeO_2–Pt–SiO_2 and Pt–CeO_2-SiO_2 bilayers from ethylene and MeOH. c) Illustration of the CeO_2–Pt–SiO_2 tandem catalyst. Adapted from ref.[112].

Each interfacial region serves its purpose: platinum-ceria catalyzes methanol decomposition into CO and H_2, while platinum-silica stimulates hydroformylation of ethylene. Altogether this unique structure exhibits very high selectivity towards propanal, which is not accessible with separate metal-oxide interfaces. We believe that many more examples of such multifunctional nanostructured catalysts are yet to be explored once fundamental understanding of the metal-support interface chemistry is developed.

2.6 Catalysis by single-atom ceria-based catalysts

Recently, single-atom catalysts (SACs) have been actively investigated by the heterogeneous catalysis community[113–116]. Single-atom catalysts refer to supported catalysts in which the active metal phase is present as isolated atoms. In such catalysts, strong MSI play a crucial role in order to achieve and maintain atomic dispersion of the active metal. The approach to atomically disperse often-expensive transition metals (*e.g.,* PGMs) on an oxide support also provides a strategy to tune the activity and selectivity of catalytic reactions. An obvious application area is in automotive exhaust systems, where there remains a need for cheap, robust, and efficient catalysts for the foreseeable future[117]. Other catalytic processes involving the use of expensive metals can also benefit from the maximized atom efficiency and the unusual reactivity offered by the interface between the single metal atom and the support. The SACs are also interesting model systems for studying MSI, because all metal atoms are part of the interface; thus, the influence of MSI is maximized. The uniformity in metal speciation renders SACs suitable for studying the mechanistic steps of catalytic reactions[118]. In the following section, we will discuss several examples that highlight how the use of isolated metal atoms on ceria can contribute to our understanding of ceria chemistry in heterogeneous catalysts.

One of the first examples of ceria-based SACs was provided by the group Flytzani-Stephanopolous, who studied the WGS performance of nanoparticles of Au and Pt on ceria[119]. While it was well accepted that metal sites in Pt/CeO_2 catalyze the WGS reaction, the elegant approach to remove a large part of metallic species using cyanide (*e.g.*, nearly 90% of all Au atoms can be removed in this way from Au/CeO_2) indicated that the WGS activity is caused by a small fraction of the active metal in a highly dispersed form. The importance of a small fraction of highly dispersed metal was supported by the unaltered kinetic parameters after leaching. The strong MSI in ceria resulted in the dominance of cationic Au and Pt species in cyanide-leached samples as probed by XPS. Another important observation was that the cationic metal species activate the ceria surface oxygen atoms. Such ceria surface defects and highly dispersed Pt and Au cations, possibly embedded in the ceria surface, were considered to be pivotal to the WGS activity. This seminal work showed the importance of MSI affecting not only the dispersion but also the electronic state of the metal.

Datye and coworkers provided another evidence for the exceptional ability of ceria to anchor atomically dispersed noble metals[120]. High-temperature calcination typically leads to sintering of the support and the active metal phase in noble-metal catalysts supported on non-reducible oxides. As CeO_2 strongly interacts with most metals, it can maintain a high metal dispersion. During ageing at 800 ºC of a physical mixture of La-modified alumina-supported Pt and CeO_2, volatile PtO_2 species can be trapped on the surface of CeO_2 (**Figure 2.19**). The resulting Pt phase on CeO_2 is atomically dispersed, which resulted in sinter-resistant catalysts even under CO oxidation conditions.

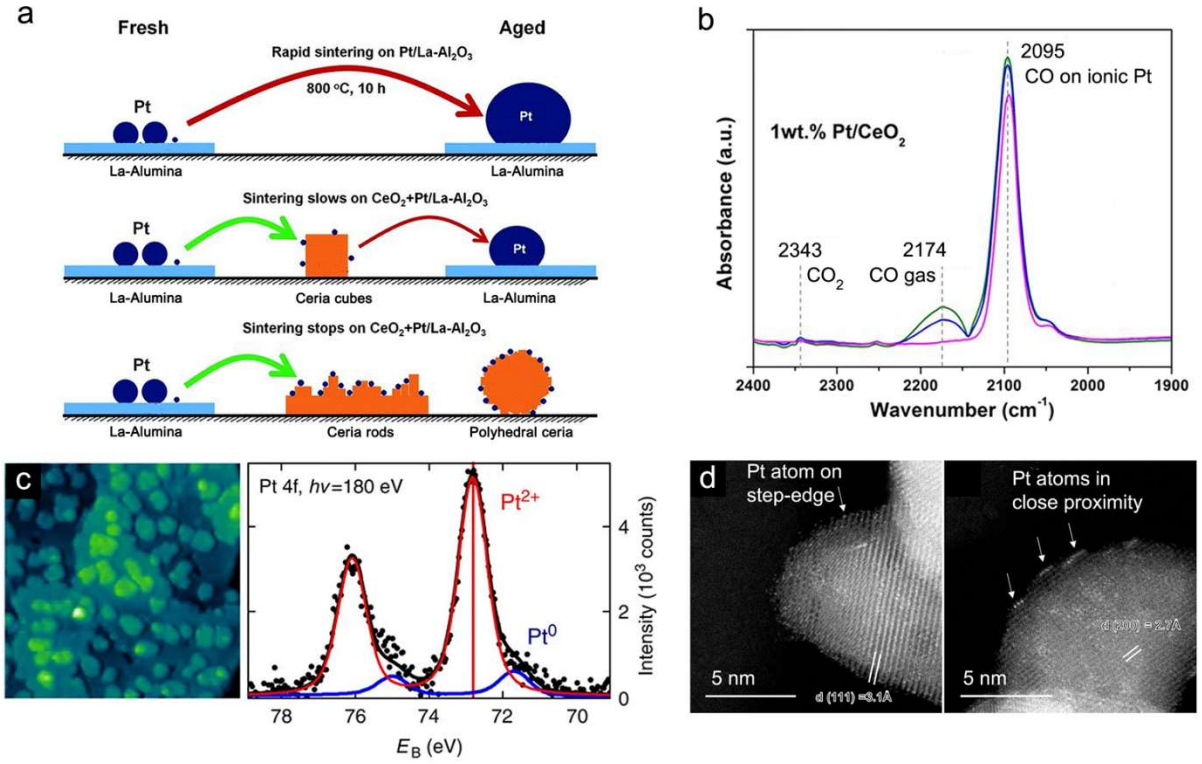

Figure 2.19. Pt-CeO_2 single-atom catalysts. a) Atom-trapping of volatile Pt species transferred from the alumina supported Pt NPs; b) *in situ* DRIFTS during CO oxidation over the Pt-CeO_2 SAC. One major band at ~2095 cm^{-1} and absence of bridged carbonyls manifest the atomic dispersion of Pt under reaction conditions. Adapted from ref.[120]. c) Atomically dispersed Pt on step-edges of CeO_2 (111). No Pt NP discerned from scanning tunneling microscopy image (left); Pt single-atoms are trapped at steps as (2+) cations, as derived from XPS spectrum (right). Adapted from ref.[121]. d) Pt single atoms localize at step-edges of ceria in powder catalysts. Adapted from ref.[122].

Another interesting finding is the dependence of the trapping of single Pt atoms on the CeO_2 facet. While nanocubes enclosed by (100) surfaces were shown to lessen the extent of Pt sintering, nanorods and polyhedra, exposing (111) surfaces, completely suppressed Pt agglomeration. As discussed earlier, the extent of MSI in CeO_2-based catalysts is highly-dependent on the exact ceria surface structure. Dvorak et al. used a classical surface science approach to show that Pt single atoms preferentially occupy the step-edge sites on the (111)

ceria surfaces[121]. XPS evidenced that Pt is present in the 2+ oxidation state (**Figure 2.19**). The strong interaction with the support stabilizes dispersed Pt^{2+} ions via formation of Pt-O-Ce bonds. In a subsequent work, Datye and colleagues used aberration corrected-scanning transmission electron microscopy (AC-STEM) to confirm the isolated nature of Pt trapped on ceria steps after high-temperature annealing of real powder catalysts[122]. Although challenging, advanced TEM techniques allow distinguishing between Pt and Ce atoms using for instance HAADF-STEM. Compared to Pt, lighter transition metals of interest such as Pd and Rh are more difficult to be discerned from Ce by techniques such as HAADF-STEM.

A systematic spectroscopic study by Neitzel et al. provides unique insight into the stability and redox chemistry of ceria-supported single atoms of Pt, Pd, and Ni[123]. By preparing thin films of model catalysts using simultaneous physical vapor deposition of ceria and the active phase as the metal oxide, a set of materials was obtained with the active phase ranging in size from single atoms to clusters. Low-loaded model catalysts (up to ~10 mol%) showed distinct features in XPS spectra related to highly-dispersed Pt^{2+}, Pd^{2+}, and Ni^{2+} on CeO_2. To probe their reactivity, the catalysts were then exposed to hydrogen (~10^{-7} mbar) under stepwise heating. Simultaneously, the valence state of the metals under study was monitored by surface-sensitive XPS, while the Ce electronic state was probed by RPES. Atomically dispersed, Pt, Pd, and Ni are practically inert towards reduction by hydrogen at temperatures as high as 400 °C. However, the use of higher loadings of Pt and Pd led to the formation of some metal oxide clusters on the surface and a dramatic change in the redox properties of the system. Exposure of such high-loaded samples to hydrogen led to a substantial reduction of Ce^{4+} to Ce^{3+} already at 125 °C, likely via hydrogen spillover from the agglomerated metallic species, followed by reduction of single atoms of supported metals. From these data, the authors concluded that in contrast to metallic species, cationic single-atom species cannot activate H_2. It should be noted, however, that the hydrogen partial pressure used in this work is orders of magnitude lower than in actual catalytic hydrogenation reactions. Such detailed spectroscopic insights into the redox chemistry of ceria-supported SACs, gained under more relevant conditions (at least in a mbar range), can further improve our understanding of these complex catalysts.

Despite the high atom efficiency, the activity offered by ceria-based SACs is not always on par with conventional catalysts based on metal nanoparticles supported by CeO_2. For example, it has been reported that Pt single atoms on CeO_2 exhibit a low CO oxidation

activity at temperature below 150 ºC [124]. The low activity has been linked to the very strong CO adsorption on Pt single atoms. Using CO reduction at 275 °C, Datye and colleagues demonstrated that Pt-CeO_2 SACs can be transformed in a very active and stable catalyst in which the initially single-atom Pt species agglomerated into small Pt clusters, which strongly interact with the CeO_2 support. The CO oxidation activity at low temperature can be associated with the lability of ceria lattice oxygen atoms at the metal-support interface. An *in situ* NAP-XPS study of the Pt and Ce valence states upon switches between CO/O_2 and CO gas feeds demonstrated that CeO_2 reduction with creation of oxygen vacancies can occur at temperatures as low as 50 ºC. Together with TPR-CO and DRIFTS characterization, the authors concluded that CO is oxidized by mobile oxygen associated with the Pt-CeO_2 interface. Wang et al. suggested that the formation of distinct Pt NPs is not necessary and, instead, very small clusters of Pt-O-Pt, obtained by a mild reductive pretreatment of a Pt/CeO_2 SAC, are responsible for the higher CO oxidation activity than SAC parent[125]. A recent report by the group of Grunwaldt emphasizes the importance of using *operando* characterization for studying the dynamic Pt-CeO_2 interface[126]. Although *ex situ* characterization suggested that the active sites remain virtually unaltered, this work revealed that the Pt speciation changes during the reaction. By employing *operando* HERFD-XANES, it was shown that reduction of atomically dispersed Pt^{2+} species to $Pt^{\delta+}$ results in formation of few-atom Pt clusters during heating in a CO and O_2 mixture (**Figure 2.20**). Their presence was linked to a rapid increase in CO oxidation activity, pointing at participation of the semi-reduced Pt species in CO oxidation at elevated temperatures (>200 ºC). Importantly, such small Pt clusters are prone to redispersion into Pt single atoms upon cooling in the same reaction mixture. This finding underpins the essential role of *operando* methodology in attempts to understand the metal-support interfaces in dynamic metal-ceria catalysts.

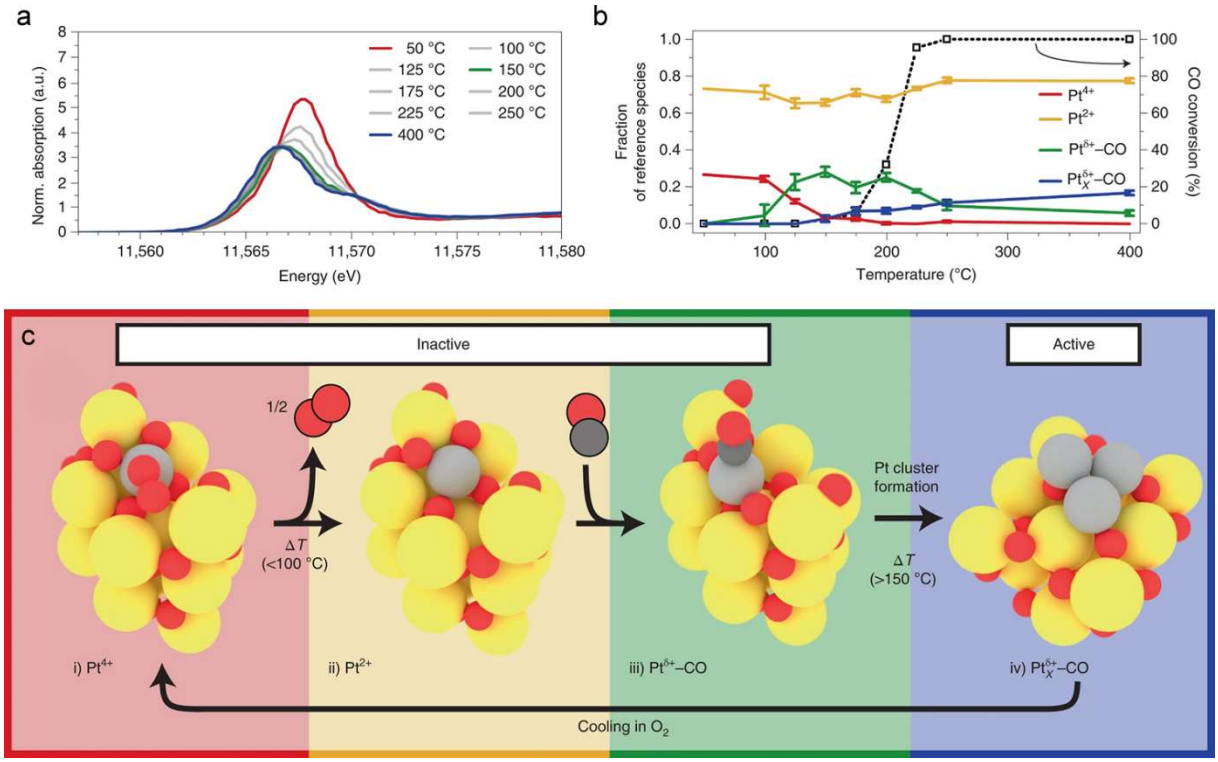

Figure 2.20. Tracking the interface dynamics in Pt-CeO_2 SACs. a) *Operando* HERFD-XAS of Pt L_3-edge upon heating in reaction mixture. b) Catalytic activity during the HERFD-XAS and Pt speciation during the CO oxidation tests. c) Proposed scheme for the reversible formation of the catalytically active $Pt_X^{\delta+}$ cluster based on *operando* HERFD-XANES analysis (grey, Pt; yellow, Ce; red, O; dark grey, C). Adapted from ref.[126].

The activity of Pt single atoms supported on ceria in oxidation reactions can be efficiently tuned by changing the oxidation state of Pt atoms[127]. The authors prepared a system in which Pt atoms are trapped on highly defective nanosized CeO_2 particles dispersed over an alumina support. Next, by straightforward H_2 reduction of as-prepared SACs at different temperatures, the oxidation state of Pt single atoms could be controlled, circumventing their agglomeration into clusters or NPs as evidenced by XAS. The different oxidation states of Pt species caused dramatic differences in the oxidation of CO, CH_4 and NO. The optimal catalyst, reduced at 300 ºC, contained ~70% of metallic Pt species, which remained intact even after prolonged catalytic testing. Temperature-programmed desorption experiments shed light on the origin of the performance differences with Pt oxidation state. The adsorption strength of reactants was shown to be strongly dependent on the oxidation state of Pt centers, which can be linked to the activity trends. Another interesting approach to control the electronic structure of the metal and thus the performance of Pt-CeO_2 SACs was illustrated by Yanfu et al.[128]. Doping the surface of ceria nanorods with phosphorous altered the valence state of the supported Pt atoms due to the charge-transfer from Pt to P. This led

to an almost one order of magnitude higher activity of the P-doped catalyst in the hydrogenation of styrene, cyclohexane, phenylacetylene and nitrobenzene. Such enhancement in hydrogenation was linked to more pronounced hydrogen spillover for the P-doped system.

The work of Cargnello et al. demonstrated that Pd and Pt atoms located at the interface between metallic NPs and ceria display similar catalytic behavior in low-temperature CO oxidation[98]. However, when dispersed as single atoms, Pt and Pd catalysts exhibit distinctly different catalytic activity. In contrast to Pt, atomically dispersed Pd-O species on the surface of ceria are highly active in low-temperature CO oxidation[129]. Spezzati et al. found that Pd single atoms on the surface of ceria nanorods, exposing (111) surfaces, are stabilized exclusively in the oxidized form according to XAS. However, exposure to the reaction feed led to the formation of semi-reduced Pd clusters already at 50 °C, as follows from the presence of bridged carbonyls in CO IR spectra. Later work of the same authors[8] unveiled that the stabilizing effect of ceria on atomically dispersed Pd depended on the facet exposed by ceria. When Pd was deposited on ceria nanorods and nanocubes, exposing predominantly (111) and (100) surfaces respectively, PdO NPs were accompanying Pd single atoms in the nanocubes case. Pd supported on CeO_2 nanocubes was found to be substantially less active in low-temperature CO oxidation than nanorod-supported Pd-CeO_2 SACs. These differences in reactivity were linked to intrinsically different redox properties of (111) and (100) facets, with (100) ones being less favorable for the stabilization of oxidized single-atom Pd-O moieties responsible for CO oxidation at low temperatures. Another example of the influence of ceria surface termination on the activity of single-atom Pd species was evident for electrocatalytic oxidation of formic acid[130]. Here, however, polar (100) surfaces of ceria cubes were catalytically favored over (111) and (110) surfaces exposed by nanorod and spherical ceria. On the basis of DFT calculations and *in situ* NAP-XPS results, the authors concluded that on (100) facets oxygen vacancies can be generated easier through a reverse oxygen spillover to Pd sites. CO stripping voltammetry indicated a key role of spilled-over oxygen in circumventing poisoning of Pd by CO, which is the product of the unwanted process of formic acid dehydration. These examples demonstrate the pronounced effects of MSI on the redox properties, the reactivity, and the stability of ceria-supported SACs.

Finally, a recent report by the group of Lee demonstrated a viable strategy to stabilize noble metals as single atoms and clusters of low nuclearity on nanosized ceria under harsh reaction conditions[131]. They developed a nanoarchitecture in which Pt, Pd and Rh were dispersed over defect-rich ceria NPs (~5 nm) stabilized on alumina (**Figure 2.21**).

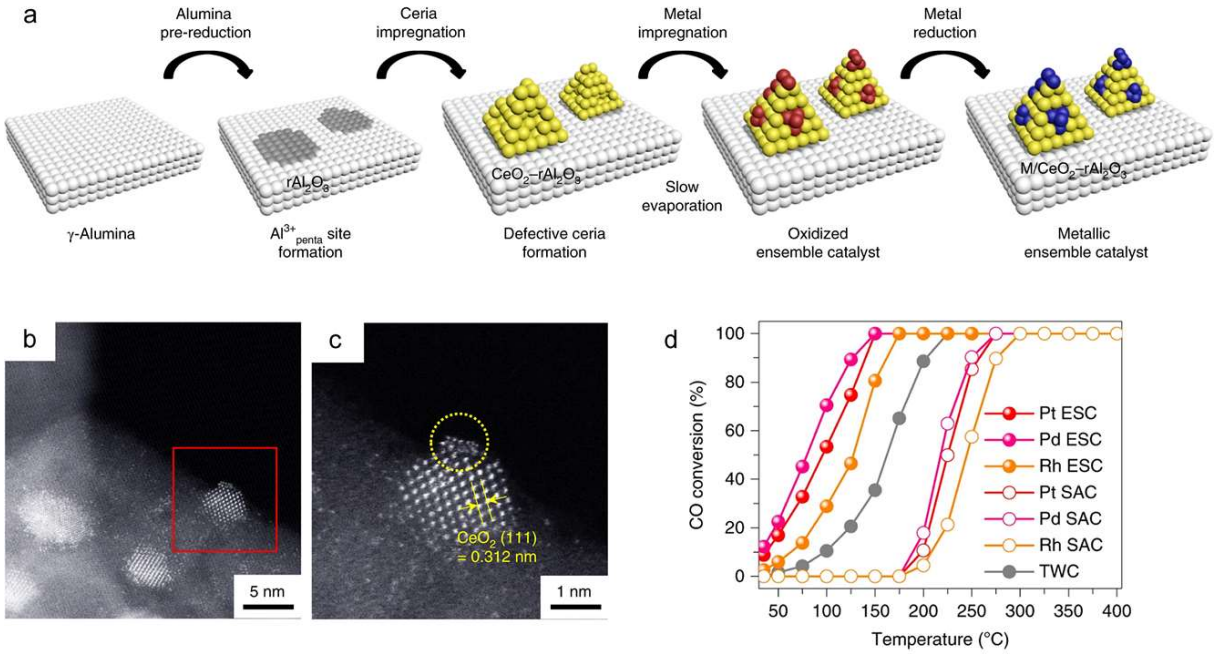

Figure 2.21. Highly durable metal ensemble catalysts. a) Synthetic procedure of metal ensemble catalysts (ESC) with full dispersion and reduced metallic states. b) and c) HAADF-STEM images of Pt ESC. d) CO oxidation performance during simultaneous CO, C_3H_6, C_3H_8 and NO conversion. Adapted from ref.[131].

Depending on the impregnation temperature, reduction of these nanocomposites in hydrogen led to either single atoms or clusters of noble metals, as demonstrated by CO IR and EXAFS analysis. Catalytic testing with a model exhaust feed revealed that clustered metal catalysts significantly outperform their SAC counterparts during the simultaneous conversion of CO, C_3H_6, C_3H_8 and NO at low temperature. This was explained by competitive adsorption of CO and NO with unreacted hydrocarbons on single atoms of noble metals. Surprisingly, the clustered catalysts maintained a high activity, even after harsh hydrothermal aging at 900 ºC, making them comparable in performance with the most durable and efficient catalysts for exhaust aftertreatment reported so far[132]. It still remains unclear what are the intrinsic reasons for such exceptional activity and stability of these complex nanoarchitectures. An explanation can be sought in the peculiar properties of nanosized ceria. As we discussed earlier, using model systems as an example, nanostructured ceria displays facile oxygen transfer at the metal-support interface via

spillover[22]. This oxygen mobility can play an important role in redox reactions. In addition, lattice strain effects and the presence of defects characteristic for small ceria NPs lead to repulsive interactions between small metal clusters, preventing them from sintering[102]. It is clear that novel catalysts based on nanosized ceria such as developed by Lee and coworkers require further in-depth mechanistic studies in order to explain and fully utilize their peculiar properties.

In this section, we discussed various aspects of metal-ceria interfaces where the metal phase is limited to a single metal atom. This represents a burgeoning field of modern heterogeneous catalysis. The exceptional ability of ceria to maintain noble metals in highly dispersed form, even under harsh reaction conditions, is one of the key reasons for the widespread application of ceria as a support for SACs. The research on ceria-based SACs is mostly related to PGMs due to the significant interest in developing novel atom-efficient and stable catalysts for automotive exhaust neutralizers. The presence of PGMs in such catalysts seems to be inevitable. Therefore, innovations in the design of catalysts containing atomically dispersed PGM and ceria need to be sought. From a perspective of fundamental studies, the undercoordinated nature of supported single atoms maximizes the influence of MSI, which in turn can be studied in greater detail using well-defined SACs. One should be cautious, however, with propagating the knowledge of the properties of single atoms to interfacial sites in NPs and *vice versa* – the contrasting cases of Pt and Pd for low-temperature CO oxidation illustrate this limitation. Nevertheless, ceria-based materials with atomically dispersed metal species appear to be a promising class of catalysts, for which many aspects remain to be discovered.

2.7 Summary

The unique properties of ceria have made it a widely used support material in heterogeneous catalysts. The tunable redox chemistry, which is intimately related to the surface structure and the crystallite size of ceria, allows optimizing the surface reactivity for specific catalytic applications. Ceria is a well-suited support for transition metals because of the relatively strong ceria-metal interactions. Ceria is particularly known for its rich interfacial chemistry. The reactivity and exact properties of the interfacial sites are yet be understood, but the rapidly growing body of knowledge points to a key role of the metal-support interface in a large number of reactions catalyzed by ceria-supported catalysts. Aiming at better understanding of the individual steps in the underlying reaction mechanisms, it is critical to prepare well-defined interfaces between ceria and metal phases. Novel synthetic approaches together with advances in *operando* spectroscopy and microscopic imaging can push the boundaries in the development of structure-function relationships in these catalyst systems. Single atoms of noble metals dispersed on ceria hold a promise of maximizing the use of such PGMs, which are key in combatting harmful automotive emissions. When prepared in a uniform manner, such single-atom catalysts can serve as a bridge between classical surface science models and technical powder catalysts in fundamental studies in which material and pressure gaps are overcome.

2.8 References

1. Jaiswal, N., Tanwar, K., Suman, R., Kumar, D., Uppadhya, S. & Parkash, O. *J. Alloys. Compd.* **781,** 984–1005 (2019).
2. Kim, H. J., Lee, G., Jang, M. G., Noh, K. & Han, J. W. *ChemCatChem* **11,** 2288–2296 (2019).
3. Mullins, D. R. *Surf. Sci. Rep.* **70,** 42–85 (2015).
4. Nolan, M., Grigoleit, S., Sayle, D. C., Parker, S. C. & Watson, G. W. *Surf. Sci.* **576,** 217–229 (2005).
5. van Santen, R. A., Tranca, I. & Hensen, E. J. M. *Catal. Today* **244,** 63–84 (2015).
6. Duchoň, T., Hackl, J., Mueller, D. N., Kullgren, J., Du, D., Senanayake, S. D., Mouls, C., Gottlob, D. M., Khan, M. I., Cramm, S., Veltruská, K., Matolín, V., Nemšák, S. & Schneider, C. M. *J. Mater. Chem. A* **8,** 5501–5507 (2020).
7. Wu, Z., Li, M. & Overbury, S. H. *J. Catal.* **285,** 61–73 (2012).
8. Spezzati, G., Benavidez, A. D., DeLaRiva, A. T., Su, Y., Hofmann, J. P., Asahina, S., Olivier, E. J., Neethling, J. H., Miller, J. T., Datye, A. K. & Hensen, E. J. M. *Appl. Catal. B: Environ.* **243,** 36–46 (2019).
9. Paier, J., Penschke, C. & Sauer, J. *Chem. Rev.* **113,** 3949–3985 (2013).
10. Agarwal, S., Lefferts, L., Mojet, B. L., Ligthart, D. A. J. M., Hensen, E. J. M., Mitchell, D. R. G., Erasmus, W. J., Anderson, B. G., Olivier, E. J., Neethling, J. H. & Datye, A. K. *ChemSusChem* **6,** 1898–1906 (2013).
11. Zhao, E. W., Zheng, H., Zhou, R., Hagelin-Weaver, H. E. & Bowers, C. R. *Angew. Chem. Int. Ed.* **54,** 14270–14275 (2015).
12. Yang, C., Capdevila-Cortada, M., Dong, C., Zhou, Y., Wang, J., Yu, X., Nefedov, A., Heißler, S., López, N., Shen, W., Wöll, C. & Wang, Y. *J. Phys. Chem. Lett.* **11,** 7925–7931 (2020).
13. Wu, Q., Zhang, F., Xiao, P., Tao, H., Wang, X., Hu, Z. & Lü, Y. *J. Phys. Chem. C* **112,** 17076–17080 (2008).
14. Tsunekawa, S., Wang, J. T. & Kawazoe, Y. *J. Alloys. Compd.* **408–412,** 1145–1148 (Elsevier, 2006).
15. Tsunekawa, S., Sahara, R., Kawazoe, Y. & Ishikawa, K. *Appl. Surf. Sci.* **152,** 53–56 (1999).
16. Zhou, X. D. & Huebner, W. *Appl. Phys. Lett.* **79,** 3512–3514 (2001).
17. Chen, L., Fleming, P., Morris, V., Holmes, J. D. & Morris, M. A. J. Phys. Chem. C **114**, 12909-12919 (2010).
18. Xu, J., Harmer, J., Li, G., Chapman, T., Collier, P., Longworth, S. & Tsang, S. C. *Chem. Commun.* **46,** 1887–1889 (2010).
19. Migani, A., Vayssilov, G. N., Bromley, S. T., Illas, F. & Neyman, K. M. *J. Mater. Chem.* **20,** 10535–10546 (2010).
20. Sk, M. A., Kozlov, S. M., Lim, K. H., Migani, A. & Neyman, K. M. *J. Mater. Chem. A* **2,** 18329–18338 (2014).
21. Bruix, A. & Neyman, K. M. *Catal. Lett.* **146,** 2053–2080 (2016).
22. Vayssilov, G. N., Lykhach, Y., Migani, A., Staudt, T., Petrova, G. P., Tsud, N., Skála, T., Bruix, A., Illas, F., Prince, K. C., Matolı´n, V., Neyman, K. M. & Libuda, J. *Nat. Mater.* **10,** 310–315 (2011).
23. Carrettin, S., Concepción, P., Corma, A., López Nieto, J. M. & Puntes, V. F. *Angew. Chem. Int. Ed.* **43,** 2538–2540 (2004).
24. Puigdollers, A. R., Schlexer, P., Tosoni, S. & Pacchioni, G. *ACS Catal.* **7,** 6493–6513 (2017).
25. Trovarelli, A. & Llorca, J. *ACS Catal.* **7,** 4716–4735 (2017).
26. Zhu, H., Yang, C., Li, Q., Ren, Y., Neuefeind, J. C., Gu, L., Liu, H., Fan, L., Chen, J., Deng, J., Wang, N., Hong, J. & Xing, X. *Nat. Commun.* **9,** 1–8 (2018).
27. Trovarelli, A. *Catal. Rev. Sci. Eng.* **38,** 439–520 (1996).
28. Montini, T., Melchionna, M., Monai, M. & Fornasiero, P. *Chem. Rev.* **116,** 5987–6041 (2016).
29. Gorte, R. J. *AIChE J.* **56,** 1126-1135 (2010).
30. le Gal, A. & Abanades, S. *J. Phys. Chem. C* **116,** 13516–13523 (2012).
31. Chen, P-L., & Chen, I-W. *J. Am. Ceram. Soc.* **76,** 1577–1583 (1993).
32. Zhou, X. D., Huebner, W. & Anderson, H. U. *Appl. Phys. Lett.* **80,** 3814–3816 (2002).
33. di Monte, R. & Kašpar, J. *Catal. Today* **100,** 27–35 (Elsevier, 2005).
34. Devaiah, D., Reddy, L. H., Park, S. E. & Reddy, B. M. *Catal. Rev. Sci. Eng.* **60,** 177–277 (2018).
35. Mukherjee, D. & Reddy, B. M. *Catal. Today* **309,** 227–235 (2018).
36. Wang, J., Chen, H., Hu, Z., Yao, M. & Li, Y. *Catal. Rev.* **57,** 79–144 (2015).

37. Terribile, D., Trovarelli, A., Llorca, J., de Leitenburg, C. & Dolcetti, G. *J. Catal.* **178,** 299–308 (1998).
38. Boaro, M., Colussi, S. & Trovarelli, A. *Front. Chem.* **7,** 28 (2019).
39. Laberty-Robert, C., Long, J. W., Lucas, E. M., Pettigrew, K. A., Stroud, R. M., Doescher, M. S. & Rolison, D. R. *Chem. Mater.* **18,** 50–58 (2006).
40. Yu, T., Joo, J., Park, Y.I. & Hyeon, T. *Angew. Chem. Int. Ed.* **44,** 7411–7414 (2005).
41. Riley, C., Canning, G., de La Riva, A., Zhou, S., Peterson, E., Boubnov, A., Hoffman, A., Tran, M., Bare, S. R., Lin, S., Guo, H. & Datye, A. *Appl. Catal. B: Environ.* **264,** 118547 (2020).
42. Zhang, Y., Bals, S. & van Tendeloo, G. *Part. Part. Syst. Charact.* **36,** 1800287 (2019).
43. Aneggi, E., Wiater, D., de Leitenburg, C., Llorca, J. & Trovarelli, A. *ACS Catal.* **4,** 172–181 (2014).
44. Yang, C., Yu, X., Heißler, S., Nefedov, A., Colussi, S., Llorca, J., Trovarelli, A., Wang, Y. & Wöll, C. *Angew. Chem. Int. Ed.* **56,** 375–379 (2017).
45. Zhou, K., Wang, X., Sun, X., Peng, Q. & Li, Y. *J. Catal.* **229,** 206–212 (2005).
46. Mai, H. X., Sun, L. D., Zhang, Y. W., Si, R., Feng, W., Zhang, H. P., Liu, H. C. & Yan, C. H. *J. Phys. Chem. B* **109,** 24380–24385 (2005).
47. Cargnello, M., Jaen, J. J. D., Garrido, J. C. H., Bakhmutsky, K., Montini, T., Gamez, J. J. C., Gorte, R. J. & Fornasiero, P. *Science* **337,** 713–717 (2012).
48. Peng, H., Rao, C., Zhang, N., Wang, X., Liu, W., Mao, W., Han, L., Zhang, P. & Dai, S. *Angew. Chem. Int.l Ed.* **57,** 8953–8957 (2018).
49. Vrijburg, W. L., van Helden, J. W. A., Parastaev, A., Groeneveld, E., Pidko, E. A. & Hensen, E. J. M. *Catal. Sci. Technol.* **9,** 5001–5010 (2019).
50. Danielis, M., Colussi, S., de Leitenburg, C., Soler, L., Llorca, J. & Trovarelli, A. *Angew. Chem. Int.l Ed.* **57,** 10212–10216 (2018).
51. Colussi, S., Gayen, A., Camellone, M. F., Boaro, M., Llorca, J., Fabris, S. & Trovarelli, A. *Angew. Chem. Int. Ed.* **48,** 8481–8484 (2009).
52. Gröhn, A. J., Pratsinis, S. E., Sánchez-Ferrer, A., Mezzenga, R. & Wegner, K. *Ind. Eng. Chem. Res.* **53,** 10734–10742 (2014).
53. Seo, D. J., Ryu, K. O., Park, S. bin, Kim, K. Y. & Song, R. H.. *Mat. Res. Bull.* **41,** 359–366 (2006).
54. Strobel, R., Baiker, A. & Pratsinis, S. E. *Adv. Powder Technol.* **17,** 457–480 (2006).
55. Feng, X., Sayle, D. C., Wang, Z. L., Paras, M. S., Santora, B., Sutorik, A. C., Sayle, T. X. T., Yang, Y., Ding, Y., Wang, X. & Her, Y.-S. *Science* **312,** 1504–8 (2006).
56. Sayle, D. C., Feng, X., Ding, Y., Zhong, L. W. & Sayle, T. X. T. *J. Am. Chem. Soc.* **129,** 7924–7935 (2007).
57. Kašpar, J., Fornasiero, P. & Hickey, N. *Catal. Today* **77,** 419–449 (Elsevier, 2003).
58. Rodriguez, J. A., Grinter, D. C., Liu, Z., Palomino, R. M. & Senanayake, S. D. *Chem. Soc. Rev.* **46,** 1824–1841 (2017).
59. Lukashuk, L. & Foettinger, K. *Johnson Matthey Technol. Rev.* **62,** 316–331 (2018).
60. Weckhuysen, B. M. *Phys. Chem. Chem. Phys.* **5,** 4351–4360 (Royal Society of Chemistry, 2003).
61. Anirban, S., Paul, T. & Dutta, A. *RSC Adv.* **5,** 50186–50195 (2015).
62. Zhang, F., Liu, Z., Zhang, S., Akter, N., Palomino, R. M., Vovchok, D., Orozco, I., Salazar, D., Rodriguez, J. A., Llorca, J., Lee, J., Kim, D. H., Xu, W., Frenkel, A. I., Li, Y., Kim, T. & Senanayake, S. D. *ACS Catal.* **8,** 3550–3560 (2018).
63. Schilling, C., Hofmann, A., Hess, C. & Ganduglia-Pirovano, M. V. *J. Phys. Chem. C* **121,** 20834–20849 (2017).
64. Kosacki, I., Suzuki, T., Anderson, H. U. & Colomban, P. *Solid State Ion.* **149,** 99–105 (2002).
65. Schilling, C. & Hess, C. *ACS Catal.* **9,** 1159–1171 (2019).
66. Choi, Y. M., Abernathy, H., Chen, H. T., Lin, M. C. & Liu, M. *ChemPhysChem* **7,** 1957–1963 (2006).
67. Loridant, S. *Catal. Today* (2020).
68. Wu, Z., Li, M., Mullins, D. R. & Overbury, S. H. *ACS Catal.* **2,** 2224–2234 (2012).
69. Binet, C., Daturi, M. & Lavalley, J. C. *Catal. Today* **50,** 207–225 (1999).
70. Parastaev, A., Muravev, V., Huertas Osta, E., van Hoof, A. J. F., Kimpel, T. F., Kosinov, N. & Hensen, E. J. M. *Nat. Catal.* **3**, 526-533 (2020).
71. Zhang, F., Wang, P., Koberstein, J., Khalid, S. & Chan, S. W. *Surf. Sci.* **563,** 74–82 (2004).

72. Salmeron, M. & Schlögl, R. *Surf. Sci. Rep.* **63,** 169–199 (2008).
73. Zhang, C., Grass, M. E., McDaniel, A. H., Decaluwe, S. C., Gabaly, F. el, Liu, Z., McCarty, K. F., Farrow, R. L., Linne, M. A., Hussain, Z., Jackson, G. S., Bluhm, H. & Eichhorn, B. W. *Nat. Mater.* **9,** 944–949 (2010).
74. Kato, S., Ammann, M., Huthwelker, T., Paun, C., Lampimäki, M., Lee, M.-T., Rothensteiner, M. & van Bokhoven, J. A. *Phys. Chem. Chem. Phys.* **17,** 5078–5083 (2015).
75. Skála, T., Šutara, F., Prince, K. C. & Matolín, V. *J. Electron Spectros. Relat. Phenomena* **169,** 20–25 (2009).
76. Cafun, J.-D., Kvashnina, K. O., Casals, E., Puntes, V. F. & Glatzel, P. *ACS Nano.* **7,** 10726–10732 (2013).
77. Gänzler, A. M., Casapu, M., Maurer, F., Störmer, H., Gerthsen, D., Ferré, G., Vernoux, P., Bornmann, B., Frahm, R., Murzin, V., Nachtegaal, M., Votsmeier, M. & Grunwaldt, J. D.. *ACS Catal.* **8,** 4800–4811 (2018).
78. della Mea, G. B., Matte, L. P., Thill, A. S., Lobato, F. O., Benvenutti, E. v., Arenas, L. T., Jürgensen, A., Hergenröder, R., Poletto, F. & Bernardi, F. *Appl. Surf. Sci.* **422,** 1102–1112 (2017).
79. Kopelent, R., van Bokhoven, J. A., Nachtegaal, M., Szlachetko, J. & Safonova, O. v. *Phys.Chem. Chem. Phys.* **18,** 32486–32493 (2016).
80. Turner, S., Lazar, S., Freitag, B., Egoavil, R., Verbeeck, J., Put, S., Strauven, Y. & van Tendeloo, G. *Nanoscale* **3,** 3385–3390 (2011).
81. Zhang, Y., Bals, S. & van Tendeloo, G. *Part. Part. Syst. Charact.* **36,** 1800287 (2019).
82. Yoshida, H., Kuwauchi, Y., Jinschek, J. R., Sun, K., Tanaka, S., Kohyama, M., Shimada, S., Haruta, M. & Takeda, S. *Science* **335,** 317–319 (2012).
83. Schilling, C. & Hess, C. *J. Phys. Chem. C* **122,** 2909–2917 (2018).
84. Rakhmatullin, R. M., Semashko, V. V., Korableva, S. L., Kiiamov, A. G., Rodionov, A. A., Tschaggelar, R., van Bokhoven, J. A. & Paun, C. *Mater. Chem. Phys.* **219,** 251–257 (2018).
85. Wang, M., Wu, X.-P., Zheng, S., Zhao, L., Li, L., Shen, L., Gao, Y., Xue, N., Guo, X., Huang, W., Gan, Z., Blanc, F., Yu, Z., Ke, X., Ding, W., Gong, X.-Q., Grey, C. P. & Peng, L. *Sci. Adv.* **1** (2015)
86. Tauster, S. J., Fung, S. C. & Garten, R. L. *J. Am. Chem. Soc.* **100,** 170–175 (1978).
87. van Deelen, T. W., Hernández Mejía, C. & de Jong, K. P. *Nat. Catal.* **2,** 955–970 (2019).
88. Campbell, C. T. *Nat. Chem.* **4**, 597-598 (2012).
89. Bruix, A., Rodriguez, J. A., Ramírez, P. J., Senanayake, S. D., Evans, J., Park, J. B., Stacchiola, D., Liu, P., Hrbek, J. & Illas, F. *J. Am. Chem. Soc.* **134,** 8968–8974 (2012).
90. Lykhach, Y., Kozlov, S. M., Skála, T., Tovt, A., Stetsovych, V., Tsud, N., Dvořák, F., Johánek, V., Neitzel, A., Mysliveček, J., Fabris, S., Matolín, V., Neyman, K. M. & Libuda, J. *Nat. Mater.* **15,** 284–288 (2016).
91. Szabová, L., Skála, T., Matolínová, I., Fabris, S., Farnesi Camellone, M. & Matolín, V. *Surf. Sci.* **267,** 12–16 (2013).
92. Khoobiar, S. *J. Phys. Chem.* **68,** 411–412 (1964).
93. Prins, R. *Chem. Rev.* **112,** 2714–2738 (2012).
94. Karim, W., Spreafico, C., Kleibert, A., Gobrecht, J., VandeVondele, J., Ekinci, Y. & van Bokhoven, J. A. *Nature* **541,** 68–71 (2017).
95. Lykhach, Y., Staudt, T., Vorokhta, M., Skála, T., Johánek, V., Prince, K. C., Matolín, V. & Libuda, J. *J. Catal.* **285,** 6–9 (2012).
96. Zafiris, G. S. & Gorte, R. J. *J. Catal.* **139,** 561–567 (1993).
97. Smirnov, M. Y. & Graham, G. W. *Catal. Lett.* **72,** 39–44 (2001).
98. Cargnello, M., Doan-Nguyen, V. V. T., Gordon, T. R., Diaz, R. E., Stach, E. A., Gorte, R. J., Fornasiero, P. & Murray, C. B. *Science* **341,** 771–773 (2013).
99. Chen, Y., Chen, J., Qu, W., George, C., Aouine, M., Vernoux, P. & Tang, X. *Chem. Commun.* **54,** 10140–10143 (2018).
100. Kopelent, R., van Bokhoven, J. A., Szlachetko, J., Edebeli, J., Paun, C., Nachtegaal, M. & Safonova, O. V. *Angew. Chem. Int. Ed.* **54,** 8728–8731 (2015).
101. Chen, A., Yu, X., Zhou, Y., Miao, S., Li, Y., Kuld, S., Sehested, J., Liu, J., Aoki, T., Hong, S., Camellone, M. F., Fabris, S., Ning, J., Jin, C., Yang, C., Nefedov, A., Wöll, C., Wang, Y. & Shen, W. *Nat. Catal.* **2,** 334–341 (2019).
102. Farmer, J. A. & Campbell, C. T. *Science* **329,** 933–936 (2010).
103. Hemmingson, S. L. & Campbell, C. T. *ACS Nano.* **11,** 1196–1203 (2017).

104. Nagai, Y., Dohmae, K., Ikeda, Y., Takagi, N., Tanabe, T., Hara, N., Guilera, G., Pascarelli, S., Newton, M. A., Kuno, O., Jiang, H., Shinjoh, H. & Matsumoto, S. *Angew. Chem. Int. Ed.* **47,** 9303–9306 (2008).
105. Aitbekova, A., Wu, L., Wrasman, C. J., Boubnov, A., Hoffman, A. S., Goodman, E. D., Bare, S. R. & Cargnello, M. *J. Am. Chem. Soc.***140,** 13736–13745 (2018).
106. Newton, M. A., Belver-Coldeira, C., Martínez-Arias, A. & Fernández-García, M. *Nat. Mater.* **6,** 528–532 (2007).
107. Wang, W. W., Yu, W. Z., Du, P. P., Xu, H., Jin, Z., Si, R., Ma, C., Shi, S., Jia, C. J. & Yan, C. H. *ACS Catal.* **7,** 1313–1329 (2017).
108. Wang, F., Li, C., Zhang, X., Wei, M., Evans, D. G. & Duan, X. *J. Catal.* **329,** 177–186 (2015).
109. Zhu, J., Su, Y., Chai, J., Muravev, V., Kosinov, N. & Hensen, E. J. M. *ACS Catal.* **10,** 11532–11544 (2020).
110. Guzman, J., Carrettin, S. & Corma, A. *J. Am. Chem. Soc.* **127,** 3286–3287 (2005).
111. Yeung, C. M. Y., Yu, K. M. K., Fu, Q. J., Thompsett, D., Petch, M. I. & Tsang, S. C. *J. Am. Chem. Soc.* **127,** 18010–18011 (2005).
112. Yamada, Y., Tsung, C.-K., Huang, W., Huo, Z., Habas, S. E., Soejima, T., Aliaga, C. E., Somorjai, G. A. & Yang, P. *Nat. Chem.* **3,** 372–376 (2011).
113. Wang, A., Li, J. & Zhang, T. *Nat. Rev. Chem.* **2,** 65-81 (2018).
114. Qiao, B., Wang, A., Yang, X., Allard, L. F., Jiang, Z., Cui, Y., Liu, J., Li, J. & Zhang, T. *Nat. Chem.* **3,** 634–641 (2011).
115. Gates, B. C. *Chem. Rev.* **95,** 511–522 (1995).
116. Flytzani-Stephanopoulos, M. & Gates, B. C. *Annu. Rev. Chem. Biomol. Eng.* **3,** 545–574 (2012).
117. Beniya, A. & Higashi, S. *Nat. Catal.* **2,** 590–602 (2019).
118. Resasco, J., Derita, L., Dai, S., Chada, J. P., Xu, M., Yan, X., Finzel, J., Hanukovich, S., Hoffman, A. S., Graham, G. W., Bare, S. R., Pan, X. & Christopher, P. *J. Am. Chem. Soc.* **142,** 169–184 (2020).
119. Fu, Q. *Science* **301,** 935–938 (2003).
120. Jones, J., Xiong, H., DeLaRiva, A. T., Peterson, E. J., Pham, H., Challa, S. R., Qi, G., Oh, S., Wiebenga, M. H., Pereira Hernandez, X. I., Wang, Y. & Datye, A. K. *Science* **353,** 150–154 (2016).
121. Dvořák, F., Camellone, M. F., Tovt, A., Tran, N., Negreiros, F. R., Vorokhta, M., Skála, T., Matolínová, I., Mysliveček, J., Matolín, V. & Fabris, S. *Nat. commun.* **7,** 1–8 (2016).
122. Kunwar, D., Zhou, S., Delariva, A., Peterson, E. J., Xiong, H., Pereira-Hernández, X. I., Purdy, S. C., ter Veen, R., Brongersma, H. H., Miller, J. T., Hashiguchi, H., Kovarik, L., Lin, S., Guo, H., Wang, Y. & Datye, A. K. *ACS Catal.* **9,** 3978–3990 (2019).
123. Neitzel, A., Figueroba, A., Lykhach, Y., Skala, T., Vorokhta, M., Tsud, N., Mehl, S., Sevcikova, K., Prince, K. C., Neyman, K. M., Matolin, V. & Libuda, J. *J. Phys. Chem. C* **120,** 9852–9862 (2016).
124. Pereira-Hernández, X. I., DeLaRiva, A., Muravev, V., Kunwar, D., Xiong, H., Sudduth, B., Engelhard, M., Kovarik, L., Hensen, E. J. M., Wang, Y. & Datye, A. K. *Nat. Commun.* **10,** 1358 (2019).
125. Wang, H., Liu, J. X., Allard, L. F., Lee, S., Liu, J., Li, H., Wang, J., Wang, J., Oh, S. H., Li, W., Flytzani-Stephanopoulos, M., Shen, M., Goldsmith, B. R. & Yang, M. *Nat. Commun.* **10,** 1–12 (2019).
126. Maurer, F., Jelic, J., Wang, J., Gänzler, A., Dolcet, P., Wöll, C., Wang, Y., Studt, F., Casapu, M. & Grunwaldt, J.-D. *Nat. Catal.* **3,** 824–833 (2020).
127. Jeong, H., Shin, D., Kim, B.-S., Bae, J., Shin, S., Choe, C., Han, J. W. & Lee, H. *Angew. Chem. Int. Ed.* **59,** 20691-20696 (2020).
128. Ma, Y., Chi, B., Liu, W., Cao, L., Lin, Y., Zhang, X., Ye, X., Wei, S. & Lu, J. *ACS Catal.* **9,** 8404–8412 (2019).
129. Spezzati, G., Su, Y., Hofmann, J. P., Benavidez, A. D., DeLaRiva, A. T., McCabe, J., Datye, A. K. & Hensen, E. J. M. *ACS Catal.* **7,** 6887–6891 (2017).
130. Ye, L., Mahadi, A. H., Saengruengrit, C., Qu, J., Xu, F., Fairclough, S. M., Young, N., Ho, P.-L., Shan, J., Nguyen, L., Tao, F. F., Tedsree, K. & Tsang, S. C. E. *ACS Catal.* **9,** 5171–5177 (2019).
131. Jeong, H., Kwon, O., Kim, B. S., Bae, J., Shin, S., Kim, H. E., Kim, J. & Lee, H. *Nat. Catal.* **3,** 368-375 (2020).
132. Datye, A. K. & Votsmeier, M. *Nat. Mater.* **20,** 1049-1059 (2020).

Chapter 3

Transforming Pt single atoms on CeO_2 into highly active catalysts for low-temperature CO oxidation

Abstract

Single-atom catalysts (SACs) have attracted a lot of interest due to the promise of high atom efficiency, superior reactivity and selectivity. Although ionic Pt single atoms on CeO_2 are inactive for low-temperature (<150 °C) CO oxidation, they can serv as a precursor for a highly active Pt/CeO_2 catalyst upon treatment in a reducing atmosphere (*Nat. Commun.* 10 (2019) 1358). In this work, we investigated the factors responsible for improved low-temperature CO oxidation reactivity by using near-ambient pressure X-ray photoelectron spectroscopy (NAP-XPS), diffuse reflectance infrared Fourier transform spectroscopy (DRIFTS), high-angle annular dark-field scanning transmission electron microscopy (HAADF-STEM) and temperature-programmed reduction in CO (CO-TPR). Pt/CeO_2 catalysts were prepared by: (i) conventional wet chemical synthesis (strong electrostatic adsorption – SEA); (ii) high-temperature vapor-phase synthesis (atom trapping – AT) and (iii) flame-spray pyrolysis (FSP). All prepared catalysts initially contain atomically dispersed Pt species. Reducing pretreatment in CO at 275 °C leads to enhanced reactivity for all catalysts, but the AT catalyst exhibited much higher CO oxidation activity than others, achieving 100% CO conversion below 70 °C (T_{100} <70 °C) at a GHSV of 232,500 ml g_{cat}^{-1} h^{-1}. The high reactivity can be related to the absence of CO poisoning of Pt and the ability of the CeO_2 support to readily provide oxygen to the active sites at lower temperatures. High-temperature vapor-phase synthesis provides a novel approach for tuning the reactivity of the CeO_2 support.

This chapter is based on the following publication:

Pereira-Hernández, X.I.*, DeLaRiva, A.*, **Muravev, V.*,** Kunwar, D., Xiong, H., Sudduth, B., Engelhard, M., Kovarik, L., Hensen, E.J.M., Wang, Y. & Datye, A.K. *Nature Communications* **10,** 1358 (2019). *doi: 10.1038/s41467-019-09308-5*. (* equal contribution)

3.1 Introduction

Achieving 90% conversion of critical pollutants at a temperature (T_{90}) of 150 °C or lower is the current goal for automotive exhaust treatment technologies[1]. In addition to high reactivity at low operating temperatures, thermal durability is essential to survive the harsh conditions encountered in automotive exhaust. A strategy to achieve high reactivity is to use single-atom catalysts (SACs), which also provide efficient utilization of scarce platinum group metals (PGMs). Current synthesis methods such as strong electrostatic adsorption (SEA), ion exchange, co-precipitation, impregnation or deposition-precipitation use low metal loading (~0.2 wt.%) to generate single-atom catalysts (SACs)[2–5]. Generally, operating temperatures with SACs are limited (<300 °C) to prevent agglomeration of single atoms into nanoparticles[3,6,7]. SACs with high thermal stability are of relevance to automotive emission treatment technologies in which PGMs are used. The International Organization of Motor Vehicle Manufacturers (OICA) reported that the world vehicle production in 2016 was over 95 million[8]. To increase efficiency and reduce costs of catalytic converters that protect the environment and human health, it is desirable to keep the PGMs highly dispersed, even when the catalyst is subjected to temperatures as high as 800°C during accelerated aging protocols[9].

Ceria is a commonly used component in automotive exhaust catalysts. It was recently shown that ceria can provide sites for trapping Pt single atoms that are thermally stable at 800 °C in air[10]. However, such Pt atoms in atomically dispersed and ionic form are not active for low-temperature CO oxidation[10]. This was already recognized in 1992 by Nunan et al. who pointed out that catalyst activity declined after oxidation and that reduction of the catalyst was necessary to achieve high reactivity[11]. Gänzler et al.[12] used extended X-ray absorption fine structure (EXAFS) and environmental transmission electron microscopy (ETEM) to demonstrate that formation of Pt nanoparticles was necessary to achieve high reactivity. In a later study, Gänzler et al.[13] concluded that 1.4 nm Pt particles represent the optimal size. On the other hand, Gatla et al.[14] concluded that, to achieve room temperature CO oxidation activity, the Pt particles should be very small. The characteristic feature of these small particles was their tendency to spread when exposed to the electron beam. In a recent work, Gatla et al.[15] reported that the particle size of Pt in the most active catalyst (reduced at 300 °C in H_2) is too small to detect by TEM. The observation of Pt^{2+} by XPS shows that oxidized Pt may be responsible for the high reactivity. Care should be taken, because XPS was

performed on air-exposed samples. It is clear that there is a need for *in situ* XPS studies under conditions of low-temperature CO oxidation, which will help elucidate the nature of the active sites.

With regard to Pt particle size, it is well known that the vibrational frequency of adsorbed CO decreases with decreasing particle size of Pt, while the strength of CO binding to Pt increases[16,17]. Hence, very small particles may not be desired for this reaction, because they are subject to strong CO binding leading to CO poisoning. Indeed, it was recently found that very small Pt particles (and single atoms) may not be effective[13]. However, other work suggests that even isolated single atoms of Pt[3,18] or corner atoms on Pt nanoparticles[19] are active for CO oxidation. From these studies, it can be inferred that particle size may not be the sole criterion for achieving high CO oxidation activity. Another important aspect is the nature of the support, specifically its ability to provide oxygen species to the active sites. The unique properties of ceria to change the oxidation state from Ce^{4+} to Ce^{3+} and its role in CO oxidation kinetics were originally demonstrated by Bunluesin et al.[20–22]. In recent work, Kopelent et al.[23] pointed out that ceria reduction is a kinetically relevant step during CO oxidation. Previous studies have focused on the size of ceria particles and their exposed surface facets to improve CO oxidation activity[24–26]. As the reducibility of ceria is influenced by the nature of metal-support interactions, here we studied several methods of catalyst preparation, leading to different extent of interaction between Pt and CeO_2.

A conventional catalyst preparation involving adsorption of the precursor on the support (SEA)[4] was used with a moderate calcination temperature (350 °C in air). With the SEA catalyst preparation, Pt is initially bound to the surface through ligands, which are removed during calcination[27]. In contrast, the AT method involves calcination of the adsorbed precursor at 800 °C in air, which causes the Pt to form covalent bonds with the surface oxygen atoms[28,29]. The high-temperature synthesis can also cause restructuring of the ceria support as ceria becomes mobile and loses surface area at elevated temperatures[10]. Flame spray pyrolysis (FSP) is a high-temperature synthesis method that allows strong anchoring of noble metal ions on the surface and in the lattice of ceria[30–32]. In this work, ceria powders with large surface area (>100 m^2/g) and highly dispersed Pt species were prepared in a single step using FSP.

Catalytic activity measurements show that as-synthesized AT, SEA and FSP catalysts are not active in low-temperature CO oxidation. *In situ* DRIFTS pointed at strong adsorption of CO

on Pt single atoms, which limits low-temperature CO oxidation activity. A pretreatment in CO at 275 °C notably improves the catalytic performance of the as-synthesized catalysts due to formation of small Pt nanoparticles (<2 nm). CO molecules adsorbed on metallic Pt are more reactive than on ionic Pt sites, as followed from *in situ* DRIFTS. Despite the similar size of Pt nanoparticles in all activated samples, the AT catalyst achieves the highest activity in CO oxidation at low temperature. Spectroscopic and microscopic characterization suggests that the AT synthesis leads to a stronger interaction between Pt and ceria, which results in the activation of support oxygen at lower temperatures than in SEA and FSP catalysts. This finding was further corroborated by *in situ* NAP-XPS data, which evidenced ceria reduction in CO already at 50 °C in activated AT catalyst. Facile oxygen transfer from ceria to metallic Pt explains why the onset of CO oxidation on this sample occurs near room temperature, a temperature at which metallic Pt is poisoned by CO.

3.2 Results and Discussion

3.2.1 CO oxidation activity of the AT, SEA and FSP catalysts

Figure 3.1 shows CO oxidation light-off curves for the catalysts synthesized by AT and SEA using tetraammineplatinum nitrate (TAPN) as a precursor and FSP before activation (called as-synthesized). The activity of all as-synthesized catalysts is very low, showing a T_{90} of ~280 °C, which has been reported previously on isolated ionic Pt species supported on ceria[10,12]. The AT, SEA and FSP catalysts pretreated at 275 °C in CO (called activated) showed a substantial increase in low-temperature CO oxidation activity. The activated AT catalyst displays significantly higher reactivity and reaches 90% conversion at 64 °C, while the activated SEA and FSP catalysts achieve 90% conversion at 120-130 °C. The same trend was observed for the AT and SEA catalysts synthesized using chloroplatinic acid (CPA) precursor (**Figure A1**). Furthermore, the activated AT catalyst retains high activity after repeated CO oxidation runs (**Figure A2**). It is also important to consider that this catalyst was synthesized by heating in air at 800 °C, which satisfies the requirements for accelerated aging set by the US DRIVE partnership for Diesel Oxidation Catalysts (DOCs)[9].

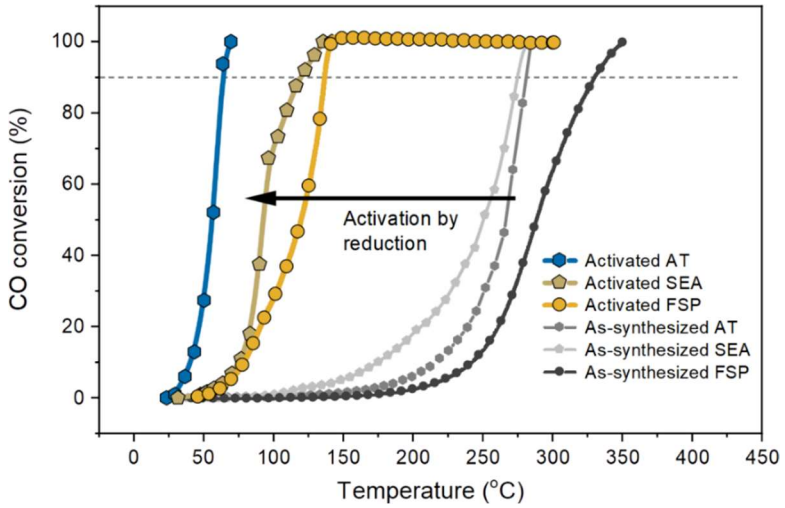

Figure 3.1. CO oxidation light-off curves for 1 wt% Pt/CeO_2 catalysts synthesized by AT and SEA using TAPN as a precursor, and by FSP before and after activation.

3.2.2 TEM of activated catalysts

Figure 3.2 shows HAADF-STEM images of the as-synthesized and activated AT, SEA and FSP catalysts. In the as-synthesized state, the AT and SEA catalysts show only Pt single atoms. This is in line with XPS data acquired on the as-synthesized samples (**Fig. A3**). For all catalysts, only Pt^{2+} and Pt^{4+} species are observed[33,34], confirming that the as-synthesized state only contains ionic Pt species. After activation in CO, Pt transforms into nanoparticles, exhibiting comparable particle size for AT, SEA and FSP catalysts. **Figures A4** and **A5** show the particle size distribution (PSD) for the activated catalysts. Results indicate that Pt nanoparticles have a mean particle size of 1.7 ± 0.3 nm and 1.6 ± 0.3 nm, for the activated AT and SEA catalysts prepared with the TAPN precursor, respectively. In the case of the activated AT and SEA catalysts prepared with the CPA precursor, these values are 1.1 ± 0.2 nm and 1.7 ± 0.4 nm, respectively. The FSP-derived ceria consists of relatively small nanoparticles (~9 nm, **Fig. A6**), which hinders detailed analysis of Pt particle size by HAADF-STEM (**Fig. 3.2g**). Thus, energy-dispersive X-ray spectroscopy (EDX) was used for Pt mapping (**Fig. 3.2h**). For the activated FSP catalyst, the size of Pt nanoparticles is slightly larger (1.9 ± 0.3 nm) than those for the AT and SEA catalysts. Despite the significant differences in the catalytic performance of the activated AT, SEA and FSP catalysts, the Pt particles are comparable in size and under 2 nm, the size at which Cargnello et al.[19] observed the highest reactivity in their study of particle size effects. Thus, other effects may also play a role. Negative effects of Cl on the activity of ceria-supported transition metal catalysts have been

reported previously[35,36]. In order to avoid an influence of Cl, we focus on TAPN and FSP catalysts.

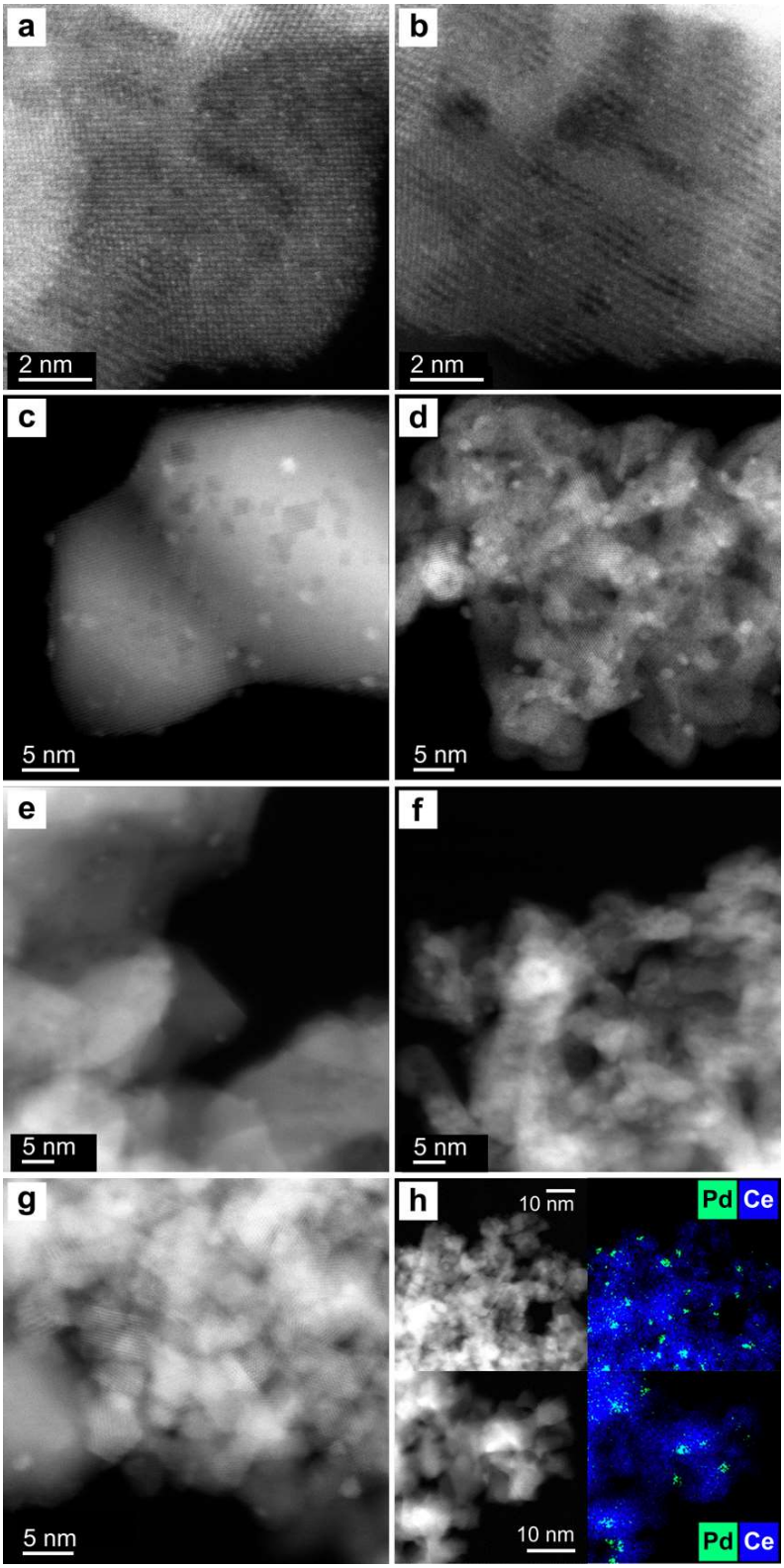

Figure 3.2. HAADF-STEM images of the 1 wt% Pt/CeO_2 catalysts: a) as-synthesized AT (CPA), b) as-synthesized SEA (CPA), c) activated AT (CPA), d) activated SEA (CPA), e) activated AT (TAPN), f) activated SEA (TAPN), g) activated FSP, h) EDX mapping of activated FSP.

3.2.3 Probing Pt-CO interaction with IR spectroscopy

Adsorbed CO species were monitored using *in situ* DRIFTS to probe the surface of the as-synthesized and activated catalysts during CO oxidation. The as-synthesized AT and FSP catalysts show a well-defined peak at 2091 cm^{-1} (**Figure 3.3a** and **3.3c**). The as-synthesized SEA catalyst shows a similar feature at a slightly different wavenumber of 2105 cm^{-1} (**Figure 3.3b**). Based on previous work[10], these peaks at high wavenumber (2091 cm^{-1} and 2105 cm^{-1}) can be assigned to CO adsorbed on ionic Pt species, corresponding to Pt single atoms supported on CeO_2. The difference in peak position between catalysts suggests there is a different interaction between the metal and the support. There is little change in the peak intensity after CO was stopped and He or O_2 were flowed over the catalyst, indicating that CO is strongly bound to the ionic Pt. This is the likely reason for the low activity of these catalysts in the as-synthesized state (**Figure 3.1**). This strong bond between CO and ionic Pt single atoms has been reported previously[37]. The spectra of the AT and SEA catalysts also contain weak carbonyl bands at 2041 cm^{-1} and 2056 cm^{-1}, respectively. Even though these peaks fall in the range for CO on Pt nanoparticles, it is found that CO adsorbed on these Pt sites cannot be removed after the CO flow is replaced by either He or O_2 flows (**Figs. 3.3a** and **b**). As CO adsorbed on metallic Pt nanoparticles reacts readily with oxygen, the peaks at low wavenumber (2041 and 2056 cm^{-1}) can be assigned to oxidized Pt sites[17,37].

Figures 3.3d, e and **f** show IR spectra for CO oxidation at 50 °C for the activated AT, SEA and FSP catalysts, respectively. At this temperature, the AT catalyst shows ~20% conversion of CO, while the SEA and FSP catalysts show < 3% CO conversion (**Fig. 3.1**). The activated AT catalyst shows two prominent bands at 2093 cm^{-1} and 2078 cm^{-1} due to CO adsorption on metallic Pt nanoparticles[37–51]. These peaks disappear as soon as the CO flow is replaced by a He flow, indicating that CO is weakly bound to Pt nanoparticles. A smaller peak at 2109 cm^{-1} is assigned to CO adsorbed on ionic Pt[17,37]. This site binds CO very strongly, as it is stable in He and O_2 flows. Nevertheless, the nature of these ionic Pt species is likely different from the ionic Pt single atoms observed in the as-synthesized state. This is supported by the blueshift in the wavenumber compared to the peak in the as-synthesized state for ionic Pt single atoms and an observable redshift during desorption. Others have earlier attributed this peak to CO on Pt-oxide clusters[52]. Spectra recorded during the activation treatment at 275 °C with CO (**Fig. A7**) and for CO adsorption at 125°C before CO oxidation (**Fig. A8**) do not show the same peak observed in **Figure 3.3d**. This suggests that the peak at 2109 cm^{-1} is formed

during CO oxidation due to exposure to O_2, supporting its assignment to Pt oxide clusters. The activated SEA catalyst shows similar behavior to the activated AT catalyst (**Fig 3.3e**). During CO oxidation and desorption experiments, peaks for CO on Pt nanoparticles are observed at 2095 cm^{-1} and 2080 cm^{-1}, while a peak for CO on ionic Pt is also found at 2109 cm^{-1}. For the FSP catalysts, CO bands related to Pt nanoparticles give rise to main peaks at 2088 cm^{-1} and 2076 cm^{-1}, which quickly disappear when the reaction mixture is switched to helium (**Fig. 3.3f**). Yet, similarly to AT and SEA catalysts, a band at 2100 cm^{-1} (inset in **Fig. 3.3f**) related to ionic Pt species remains even in O_2, pointing at strong CO adsorption on these sites. It should be noted that the disappearance of CO bands in He during the first 3 min is substantially faster for the FSP catalyst, which suggests a weaker CO adsorption. However, this is related to a notably faster replacement of the gas phase upon switches during the *in situ* DRIFTS experiments performed on the FSP catalysts (**Fig. A9**). The higher total flow and the use of a gas rig system with minimized dead volume results in much shorter gas holdup time with respect to experiments performed on the AT and SEA catalysts.

Altogether, the *in situ* DRIFTS results show that an increase in the reactivity of the catalysts after CO reduction is related to the formation of Pt nanoparticles and the ease with which adsorbed CO can be reacted away. These results are consistent with previous reports that CO on metallic Pt reacts readily with O_2, unlike CO on ionic Pt that does not react unless heated to higher temperatures[3,10,19,37]. As the Pt particle size (**Fig. 3.2**) and the nature of the adsorbed CO molecules is similar for the studied catalysts, the much higher reactivity of AT catalysts with respect to SEA and FSP counterparts might be related to the catalyst support.

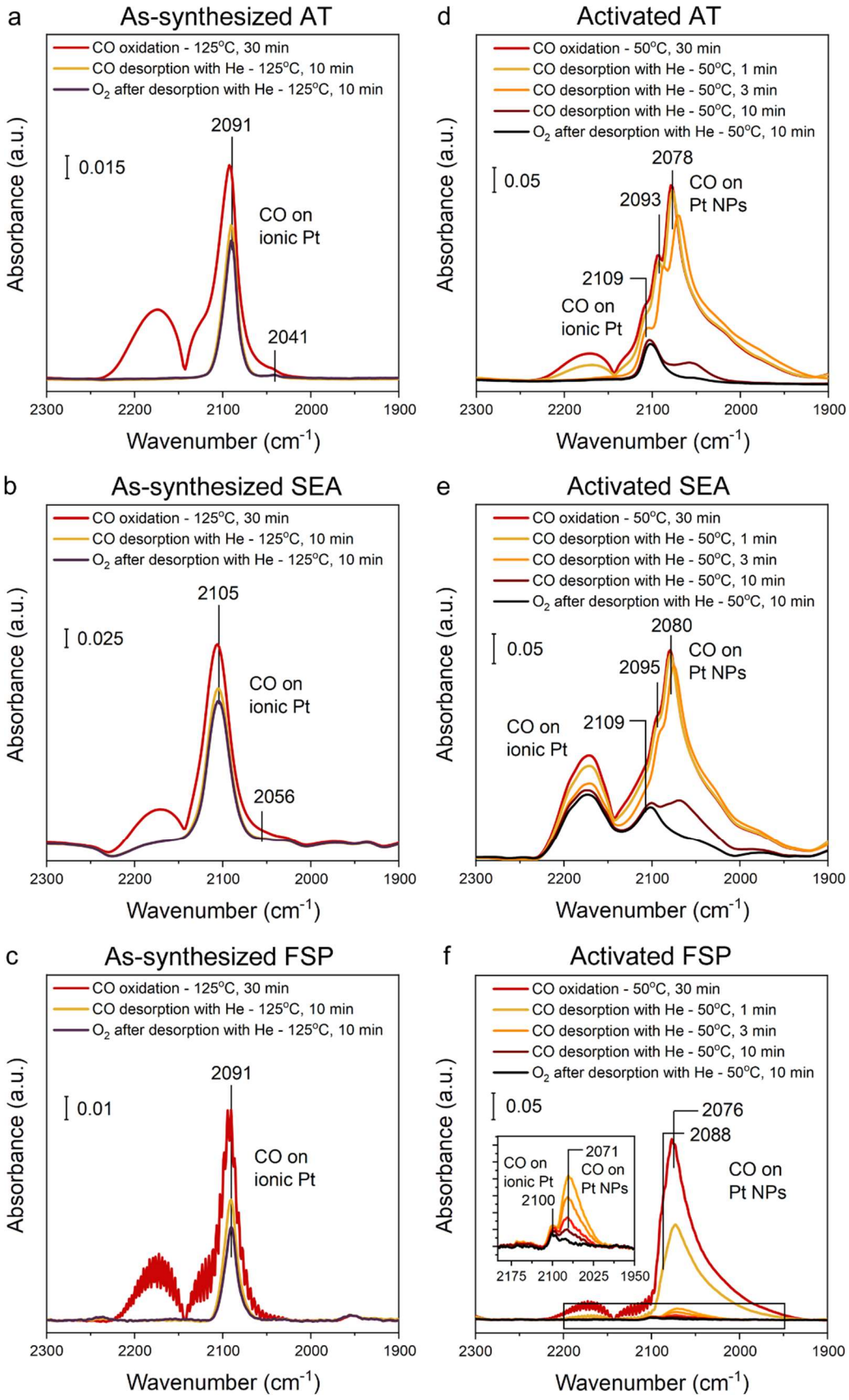

Figure 3.3. CO oxidation reaction monitored by *in situ* DRIFTS on the 1 wt% Pt/CeO_2 catalysts: a) as-synthesized AT (TAPN) at 125 °C, b) as-synthesized SEA (TAPN) at 125 °C, c) as-synthesized FSP at 125 °C, d) activated AT (TAPN) at 50 °C, e) activated SEA (TAPN) at 50 °C, f) activated FSP at 50 °C.

3.2.4 Surface oxygen reactivity monitored by reduction with CO

Previous studies on ceria-supported Pt catalysts have revealed that CO oxidation follows a Mars-van Krevelen (MvK) reaction mechanism with positive effect of surface oxygen activation on the oxidation of CO[23,39,53]. It has also been observed that the relevant step during CO oxidation in a MvK reaction mechanism is the reaction between CO adsorbed on Pt and oxygen from the ceria lattice[46]. Furthermore, previous work found that the amount and type of Pt species deposited on the support can play a role during the activation of surface oxygen[54]. Considering that the AT and SEA catalysts are synthesized at different temperatures, it is reasonable to expect a different interaction between Pt and CeO_2 for the two catalysts. Furthermore, due to the single-step nature of synthesis of the FSP catalyst, Pt ions can be doped inside the ceria lattice[55], thus affecting the redox properties of the catalyst. Therefore, CO-TPR was used to study the differences in the reaction between CO and oxygen from the catalysts.

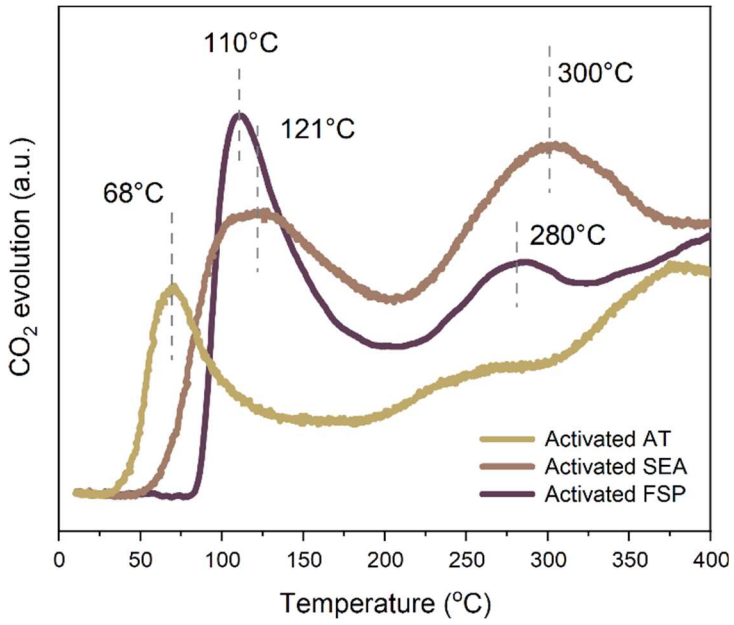

Figure 3.4. CO-TPR of the activated AT (TAPN), SEA (TAPN) and FSP 1 wt% Pt/CeO_2 catalysts.

The as-synthesized AT, SEA and FSP catalysts were exposed to CO to study the initial reduction of the catalyst, as reported in **Figure A10**. The ease of reducibility of the AT catalyst is evident already in the as-synthesized state. A separate aliquot of the catalyst was next activated via CO reduction at 275 °C, then exposed to an oxidation at 200 °C to remove any adsorbed species and to replenish the oxygen on the support. **Figure 3.4** shows the formation of CO_2 during CO-TPR for the activated catalysts. The AT catalyst exhibits CO_2

formation at lower temperature (68 °C) than the SEA (121 °C) and FSP (110 °C) counterparts. As all catalysts were exposed to an oxidative treatment prior to the CO-TPR, the formation of CO_2 must stem from reactive oxygen species. These results demonstrate that AT synthesis creates ceria sites that are reducible at low temperature, at which the AT catalyst is highly active for CO oxidation. The SEA and FSP catalysts can be reduced only at higher temperatures. Previous work by Gatla et al.[14] suggested that strong interaction between Pt and CeO_2 can cause a reduction of the energy cost to remove oxygen between Pt and Ce. Therefore, the results presented here suggests that the interaction between Pt and CeO_2 is stronger in the AT catalyst than in the SEA and FSP ones. This is not completely unexpected, considering that the interaction between Pt and CeO_2 has to be strong enough to keep Pt as single atoms during the calcination at 800 °C. Although the temperature achieved in the flame during FSP synthesis is much higher (~2000 °C)[56] than during AT synthesis, this method apparently does not lead to the specific interaction between Pt and CeO_2 phases that gives rise to enhanced reducibility of lattice oxygen. We speculate that the difference is due to the location of Pt on the CeO_2 surface. During AT synthesis, Pt is transported through the gas phase and likely trapped by defects on ceria such step edges[10]. Rapid quenching during FSP synthesis[57] might lead to a less specific localization of Pt atoms on the surface of CeO_2. The facile oxygen transport from ceria to Pt sites in AT catalyst can explain its high reactivity towards CO oxidation at low temperature. It should be noted that the high-temperature AT synthesis is beneficial only when Pt is already present on the support and the synthesis is made in an oxygen-rich environment like air. Previous work by Bunluesin et al.[58] showed that calcining bare CeO_2 at high temperature (900 °C) followed by deposition of Pd leads to low catalytic activity due to a large increase in crystallite size of the support. Therefore, support activation is likely not induced by high-temperature treatment of CeO_2 but by the strong interaction between Pt and CeO_2 caused by high-temperature treatment. This interaction leads to volatile PtO_2 being trapped on CeO_2[10], creating the catalytic sites for oxygen activation at low temperature.

3.2.5 Surface oxygen reactivity monitored by NAP-XPS

To better understand the reason for high CO oxidation activity of the Pt species in AT catalyst, *in situ* NAP-XPS was performed on the activated samples. **Figures 3.5a** and **3.5b** show the Pt 4f and Ce 3d regions, respectively, for the activated AT catalyst after exposure to different gas environments. Spectra after consecutive *in situ* activation at 275 °C and

exposure to CO at 50 °C show that the Pt phase is dominated by Pt^0 species (% Pt^0 ~ 83%). Continuous exposure to a mixture of CO and O_2 at 50 °C leads to the partial reoxidation of Pt (% Pt^0 ~ 68%). This is due to the small particle size of the Pt nanoparticles and in line with the assignment of the 2109 cm^{-1} peak (**Figure 3.3d**) to Pt oxide clusters. Further exposure to CO and CO + O_2 at 50 °C do not significantly change the fraction of Pt^0 species. On the other hand, the amount of Ce^{3+} species after activation with CO at 275 °C is ~ 28%, while after exposure to the reaction mixture at 50 °C, this fraction decreases to 9%. Exposing the catalyst to CO at 50 °C increases the amount of Ce^{3+} to 14%, suggesting that even at 50 °C oxygen can be easily removed leaving behind vacancies and forming Ce^{3+} species. Further exposure to the reaction mixture at 50 °C reduces the fraction of Ce^{3+} species to 7%, suggesting these changes are reversible at 50 °C. The composition of the gas during the NAP-XPS experiments monitored by mass spectrometry (MS) (**Figure A11**) confirms the formation of CO_2 when the catalyst is exposed to the reaction mixture at 50 °C.

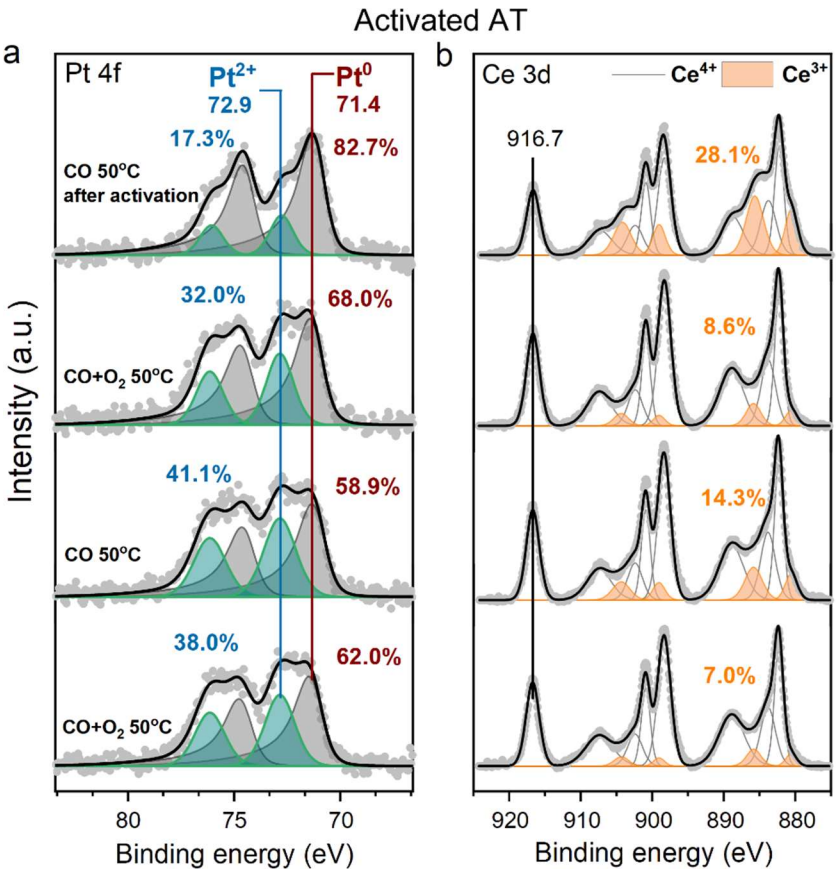

Figure 3.5. NAP-XPS results for the 1 wt% Pt/CeO_2 TAPN catalyst synthesized by AT after activation in CO at 275°C: a) Pt 4f region, b) Ce 3d region. The catalyst was sequentially exposed to different gas environments, starting at the top. The Pt/Ce atomic ratio remained at ~0.030 throughout the experiment.

Figures 3.6a and **3.6b** show the Pt 4f and Ce 3d regions, respectively, for the SEA catalyst activated with CO at 275 °C, after exposure to different gas environments during NAP-XPS. The SEA catalyst also has Pt^0 as the primary species (% Pt^0 ~ 75%). However, compared to the AT catalyst, the SEA catalyst shows more reoxidation of Pt (% Pt^0 ~ 41%), which remain stable after further exposure to CO and CO + O_2 at 50 °C. The most pronounced difference between the AT and SEA catalysts is the reducibility of CeO_2. The amount of Ce^{3+} after activation is similar to the AT catalyst (~25%). Once the SEA catalyst is exposed to the reaction mixture at 50 °C, the Ce^{3+} contribution decrease to 9% and successive exposure to CO at 50 °C does not lead to a significant increase of Ce^{3+} (~10%). This indicates that oxygen vacancies are not easily formed in the SEA catalyst under these low temperature reaction conditions, different from the AT catalyst. Further exposure to the reaction mixture leads to a similar amount of Ce^{3+} species (8.7%). As the SEA catalyst is less active than the AT catalyst, the temperature was increased to 100 °C in order to monitor CO_2 formation by MS and confirm the operating state of the catalyst during NAP-XPS experiment (**Figure A11**).

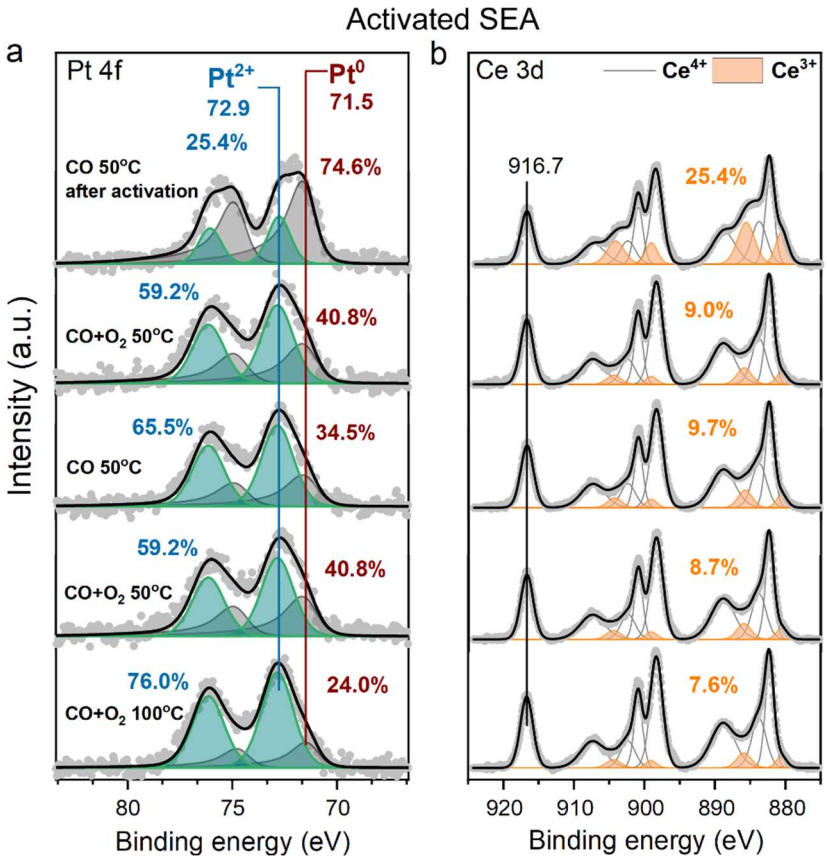

Figure 3.6. NAP-XPS results for the 1wt.% Pt/CeO_2 TAPN catalyst synthesized by SEA after activation in CO at 275°C: a) Pt 4f region, b) Ce 3d region. The catalyst was sequentially exposed to different gas environments, starting at the top. The Pt/Ce atomic ratio remained at ~0.015 throughout the experiment.

To probe the strength of the interaction between Pt and CeO_2 for AT and SEA catalysts, a harsh reduction treatment with CO at 450 °C for 8 h was performed (**Figure A12**). The amount of Ce^{3+} species was found to be higher in the AT catalyst than in the SEA catalyst, in line with the higher reducibility of the former. Pt in the SEA catalyst is fully reduced whereas a fraction of Pt^{2+} species remains present in the AT catalyst. Therefore, the XPS data indicate that the interaction between Pt and CeO_2 in the AT catalyst is stronger than in the SEA catalyst. The highly active AT catalyst was further studied by *in situ* Raman spectroscopy (**Figure A13**). The spectrum of the sample in the as-synthesized state shows peaks at 555 cm^{-1} associated with Pt-O-Ce and at 662 cm^{-1} attributed to Pt-O[59–61]. The lower intensity of these peaks upon activation of the catalyst indicates that the low-temperature peak observed during CO-TPR for the AT catalyst is associated with the reduction of the Pt-O-Ce bond. Previous theoretical studies on the reducibility of ceria-supported Pt catalysts showed that Pt^{2+} species had an effect on the reducibility of ceria. Pt^{2+} species can replace a Ce^{4+} cation and adopt a square-planar coordination, creating an oxygen vacancy and leaving three three-coordinate oxygen atoms that can be removed easier[62,63]. Thus, despite the atomically dispersed ionic nature of Pt in the as-synthesized state, the bonds between Pt and CeO_2 in the AT, SEA and FSP catalysts are different.

3.2.6 Establishing structure-function relationships

Figure 3.7 shows a schematic description of the AT catalyst at the different stages explored in this study. The synthesis of the AT catalyst take place at high temperature (800 °C), which results in the stabilization of Pt single atoms on the surface of CeO_2 as confirmed by STEM (**Figure 3.2**) and DRIFTS (**Figure 3.3**). Activation of the catalyst in CO at 275 °C leads to the partial transformation of Pt single atoms into Pt nanoparticles, which was evidenced by STEM (**Figure 3.2**), DRIFTS (**Figure 3.3**) and NAP-XPS (**Figure 3.5**). The NAP-XPS spectra show a higher fraction of oxidized Pt species as compared with DRIFTS. This is likely due to the presence of ionic Pt at the interface between metallic Pt nanoparticles and the support. As the escape depth of the photoelectrons exceeds the size of Pt nanoparticles, XPS can probe the Pt atoms within the nanoparticles that are in contact with ceria. In contrast, DRIFTS can only probe sites at the surface. As furthermore the extinction coefficients of the CO bands can vary significantly with Pt speciation, it can be stated that NAP-XPS is more appropriate to probe the state of the activated AT catalyst. **Figure 3.7** also shows why the AT catalyst has a high activity for low-temperature CO oxidation with a T_{90} of 64 °C (**Figure**

3.1). The facile reaction of ceria surface oxygen with CO in activated the AT catalyst was demonstrated by NAP-XPS (**Figure 3.5**), where the fraction of Ce^{3+} changes as oxygen is switched on and off at 50 °C. The formation and healing of oxygen vacancies that can react with CO can explain the low-temperature reactivity of the AT catalyst.

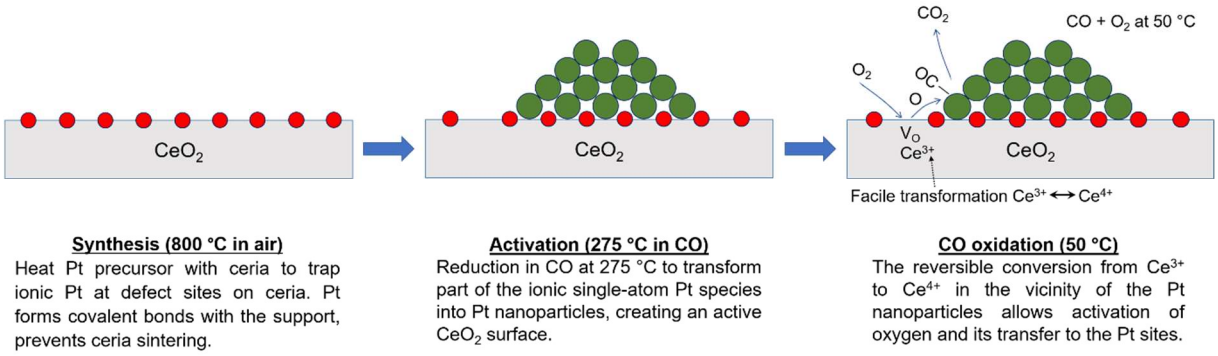

Figure 3.7. Transforming Pt single-atom catalyst into nanoparticles creates active sites on the ceria support (red: ionic Pt, green: metallic Pt)

The SEA and FSP syntheses also result in single-atom Pt species on CeO_2. Further activation of the catalysts in CO at 275 °C leads to similar transformation of Pt single atoms into Pt nanoparticles (**Figures 3.2, 3.3** and **3.6**). Nevertheless, the SEA and FSP catalysts display notably lower CO oxidation activities than the AT catalyst. The NAP-XPS data for SEA catalysts (**Figure 3.6**) shows that, unlike in the AT catalyst, CeO_2 does not provide oxygen to react with CO at 50 °C, evidenced by the negligible change in the amount of Ce^{3+} species when exposed to CO and CO+O_2. The CO-TPR data clearly demonstrated that the reaction of surface oxygen in FSP and SEA samples with CO requires higher temperatures compared with the AT catalyst. In other words, only AT-synthesis conditions followed by activation at 275 °C in CO can lead to high reactivity of the oxygen in the support at low temperature.

The strong interaction between Pt and CeO_2, required to stabilize Pt as single atoms, also reduces the sintering of CeO_2. This is observed by the larger BET surface area (**Table A1**) and smaller ceria crystallite size (**Figure A14**) of CeO_2 in the Pt/CeO_2 catalyst compared to pure CeO_2. This stronger interaction between Pt and CeO_2 in the AT catalyst is further confirmed by measuring the amount of ionic Pt species by XPS after a harsh reduction treatment in CO at 450 °C for 8 h (**Figure A12**). Pt in the SEA catalyst is completely reduced, whereas the AT catalyst still contains Pt^{2+} species. Even after such harsh reduction treatment, the Pt particle size did not increase significantly in the AT catalyst (1.9 ± 0.4 nm in **Figure A15**). However, a significant decrease in the activity was observed, which can be explained by a loss of

reactivity of surface oxygen at low temperature (**Figure A15**). The loss of activity and reactivity of surface oxygen along with a decrease in the amount of Pt single-atom species may suggest that ionic Pt single-atom species in ceria, left behind after CO activation, are important for the activation of oxygen at low temperature.

3.3 Conclusions

Single-atom Pt/CeO_2 catalysts prepared by SEA, AT and FSP display limited low-temperature CO oxidation activity due to strong adsorption of CO on ionic Pt as evidenced by *in situ* DRIFTS. Reductive treatment in CO at 275 °C leads to a strong improvement in the activity owing to the formation of small Pt nanoparticles (<2 nm). *In situ* DRIFTS showed that the removal of CO adsorbed on these Pt clusters is much faster than on Pt single atoms, correlating with the catalytic activity. Among the activated catalysts, the AT-synthesized one displayed much higher activity than those prepared by SEA and FSP. CO-TPR data indicated that oxygen atoms in the activated AT catalyst can be removed at much lower temperature than in the activated SEA and FSP catalysts. *In situ* NAP-XPS data revealed that ceria lattice oxygen in AT catalyst can be removed by CO already at 50 °C, explaining the high activity of this sample. The high-temperature treatment during AT synthesis leads to specific interactions between Pt and CeO_2, which benefit the CO oxidation activity owing to creation of labile lattice oxygen.

3.4 Materials and Methods

Catalyst synthesis and activation

The 1 wt% Pt/CeO_2 catalysts were synthesized by incipient wetness impregnation as described previously[10]. To prepare the 1 wt% Pt/CeO_2 catalyst, cerium oxide powder support was synthesized via thermal decomposition of cerium (III) nitrate hexahydrate (99.999% purity, Sigma-Aldrich) at 350 °C for 2 h. The TAPN catalysts were synthesized using tetraammineplatinum nitrate (Sigma-Aldrich, 99.999% purity). After impregnation, the catalysts were directly calcined at 350 °C for 1 h and 800 °C 10 h, respectively, in flowing air. These two catalysts calcined at 350 °C and 800 °C are called "as-synthesized" SEA and AT catalysts, respectively. To achieve a high-activity state, the catalysts are further reduced at 275 °C for 1 h using 6 ml/min CO and 70.5 ml/min of He. These catalysts are called "activated" SEA and AT catalysts, respectively. CPA catalysts where synthesized using chloroplatinic acid solution 8 wt% in H_2O (Sigma-Aldrich) and followed the same synthesis conditions described for the TAPN catalysts.

FSP synthesis was performed using a TETHIS NPS10 apparatus. An appropriate amount of Pt (II) acetylacetonate (Sigma-Aldrich, 99% purity) was dissolved together with cerium (III) acetate hydrate (Sigma-Aldrich, 99.9% purity) in a mixture (50:50 vol%) of glacial acetic acid and 2-ethylhexanoic acid to yield a 0.15 M (based on Ce) precursor solution.To ensure complete solubility, the mixture was mildly heated to 60-70 °C and stirred for 1 h. After cooling to ambient temperature, the solution was used to fill the syringe of FSP apparatus. To sustain the flame, flows of 1.5 l/min of methane and 3.0 l/min of oxygen were used. Oxygen also served as a dispersion gas at a rate of 5 l/min. An injection rate of 5 ml/min was used and an overpressure at the nozzle was fixed to 2.5 bar.

Activity measurements

CO oxidation experiments on AT and SEA catalysts were carried out using a Varian CP-4900 Micro-GC. 20 mg of sample was packed in between quartz wool inside a stainless-steel reactor tube (I.D. 1/8"). The CO oxidation flow rates consisted of 1.0 ml/min O_2, 1.5 ml/min CO, and 75 ml/min He (~232,500 ml g_{cat}^{-1} h^{-1}). The samples were heated to 300 °C at 2 °C/min and cooled back down to room temperature in the reaction mixture to test for reproducibility. CO oxidation tests over FSP samples were performed on a home-bulit setup equipped with mass-spectrometer (Balzer TPG 300). Approximately 50 mg of the catalyst

sieved fraction (125-250 µm) was mixed with silicon carbide (200-300 mg) and enclosed between two quartz wool plugs in a quartz reactor. The catalysts were pretreated *in situ* under a flow of 20 vol% O_2 in He at 300 ºC for 1 h and then cooled to room temperature. Then to achieve a high-activity state, the catalysts are further reduced at 275 °C for 1 h using 6 ml/min CO and 70.5 ml/min of He. These catalysts are called "activated" FSP. The CO oxidation flow consisted of 2.6 ml/min O_2, 3.9 ml/min CO, and 193 ml/min He (~240,000 ml g_{cat}^{-1} h^{-1}). CO conversion was estimated from the mass-spectrometry data by following the CO (*m/z*=28), O_2 (*m/z*=32) and CO_2 (*m/z*=44) signals (*m/z*=44).

Characterization

HAADF-STEM **i**mages of the AT and SEA samples were acquired using an Aberration Corrected FEI Titan 80-300 Transmission Electron Microscope with an HAADF detector. STEM samples were prepared by dispersing the crushed Pt/CeO_2 powder on a copper grid with holey carbon film. The powder was transferred onto the Cu grids in a dry form, without the use of a dispersing solution. Additional measurements were done using a JEOL 2010F TEM/STEM operated at 200 kV. For FSP catalysts, transmission electron microscopy imaging was performed using a probe corrected JEOL ARM 200F microscope operated at 200 kV and equipped with a 100 mm^2 Centurio SDD EDX detector. Imaging was performed in HAADF-STEM mode.

XRD measurements were done on a Rigaku SmartLab using a Bragg-Brentano geometry and a DTex high-speed detector. The diffractograms were collected using the 2Theta scan axis between 25° and 80°, using a rate of 1°/min at a step of 0.01°. The radiation used was Cu Kα with a wavelength of 0.154 nm.

Specific surface area measurements using a Brunauer, Emmett and Teller (BET) method were performed on a Micromeritics Gemini 2360 multipoint analyzer using N_2 adsorption at -196 ˚C.

Raman spectra were collected using a Horiba LabRAM HR Raman/FTIR microscope equipped with a 532 nm (Ventus LP 532) laser source and Synapse CCD (Charge Coupled Device) detector, and an *in situ* cell (Linkam CCR1000). The presented spectra correspond to the average of three scans, each one with a 60 s acquisition time. No changes over time were detected in the sample due to laser exposure.

CO-TPR measurements for SEA and AT catalysts were performed using an Autochem 2920 from Micromeritics. Approximately 50 mg of catalyst were used for each experiment. The exhaust line was connected to a QMS from Pfeiffer Vacuum (described above) to analyze the products. CO_2 formation was monitored on the mass-to-charge (*m/z*) ratio of 44. The as-synthesized catalysts were exposed to an oxidative pretreatment (300 °C, 10 vol% O_2, 30 min) before the CO-TPR experiments. The activated catalysts were exposed to an oxidative pretreatment (200 °C, 10 vol% O_2, 30 min) after activation to replenish the oxygen on the support. The temperature in this case was only 200 °C to avoid possible redispersion of the Pt nanoparticles. A total flowrate of 50 ml/min with a concentration of 5 vol% CO, 2.5 vol% Ar in He was used during the temperature ramp (10 °C/min) and during the data processing the CO_2 signal (*m/z*=44) was normalized by the signal for the Ar tracer (*m/z*=40). For FSP catalysts a home-built setup equipped with mass-spectrometer (Balzer TPG 300) was used to perform CO-TPR experiments. The as-synthesized catalysts were exposed to an oxidative pretreatment (300 °C, 10 vol% O_2, 30 min) before the CO-TPR experiments. To perform CO-TPR tests over activated state of the catalyst, the as-synthesized FSP samples were first exposed to an oxidative pretreatment (300 °C, 10 vol% O_2, 30 min) then reduced at 275 °C for 1 h using 6 ml/min CO and 70.5 ml/min of He and then exposed to an oxidative pretreatment (200 °C, 10% O_2, 30 min) after activation to replenish the oxygen on the support. The temperature in this case was only 200 °C to avoid possible redispersion of the Pt nanoparticles. For CO-TPR over as-synthesized and activated FSP a total flowrate of 50 ml/min with a concentration of 5 vol% CO in He was used during the temperature ramp (10 °C/min). The CO_2 signal (*m/z*=44) was used to plot the CO_2 evolution traces.

DRIFTS was used to monitor CO oxidation reaction over the studied catalysts. For AT and SEA samples, Tensor 27 from Bruker FT IR spectrometer, coupled with a Praying Mantis™ Diffuse Reflection Accessory from Harrick was used. The experiment started by loading the catalyst in the cell. The temperature was increased to 300 °C under He. Once at 300 °C, a pretreatment with 10 vol% O_2 was performed for 30 min. The gas was switched to He and background spectra of the catalysts were taken at 275 °C, 125 °C and 50 °C. CO oxidation was performed for 30 min using 15 ml/min of 10 vol% CO, 10 ml/min of 10 vol% O_2 and 15 ml/min of He. CO desorption with He was performed for 10 min using 40 ml/min of He. Then O_2 flow (40 ml/min of 10 vol% O_2) after desorption with He was introduced for 10 min. During the reduction step at 275 °C, a flow of 40 ml/min of 10 vol% CO was used and followed by

desorption with 40 ml/min of He at the same temperature. For FSP-made samples, DRIFTS was carried out using Bruker Vertex 70V with an MCT-detector and Harrick-design *in situ* DRIFTS cell. The sample powder was placed in the cell and pretreated in 20 vol% O_2/He flow (100 ml/min) at 300 °C. A background spectrum was then acquired. For achieving the "activated" state, catalysts were reduced at 275 °C in 4 vol% CO in He (100 ml/min). For CO oxidation, the reaction mixture consisted of a 100 ml/min flow of 1.5 vol% CO, 1 vol% O_2 in He. For CO desorption experiments, the reaction mixture was switched to pure He flow (100 ml/min). After desorption in He, a flow of 1 vol% O_2 in He (100 ml/min) was introduced for 10 min.

The surface chemistry of Pt/CeO_2 catalysts was characterized in a lab-based SPECS NAP-XPS system. *In situ* XPS measurements at pressures of up to 2 mbar are possible due to the incorporation of a reaction cell in the UHV chamber of the NAP-XPS spectrometer. The gases flow through the cell and exit through the outlet port and aperture of the nozzle that interfaces the gas phase in the reaction cell and the vacuum environment of the pre-lens system. The aperture of the 0.3-mm nozzle is close to the spot size of the X-ray beam. A high vacuum in the lens system and electron analyzer (SPECS Phoibos 150 NAP) is maintained via a system of differentially pumped stages. Gases are fed into the NAP-cell via calibrated mass-flow controllers. The overall pressure inside the reaction cell was kept at 2 mbar via a back-pressure controller installed at the outlet of the cell. Prior to the reaction, catalysts were pretreated in 2 mbar of pure CO (2 ml/min) at 275 °C in order to activate the catalyst. A reaction mixture of 1.5 ml/min of CO and 1 ml/min of O_2 was used, keeping the same ratio between the reactants as for the catalytic studies. High-purity gases were used for the *in situ* XPS measurements. A standard residual gas analyzer (QMS MKS e-Vision 2) placed in the second differential pumping stage allowed following the catalytic activity during XPS measurements. Spectra were obtained using monochromatic Al Kα irradiation (1486.6 eV) of an Al anode operating at 50 W. The total acquisition time of the survey spectrum, O 1s, C 1s, Ce 3d, and Pt 4f regions took around 60–70 min. A pass energy of 40 eV with a step size of 0.1 eV and a dwell time of 0.5 s were typically used for acquiring the core-line spectra. Pt 4f and Ce 3d regions were energy-corrected according to the U''' component of the Ce 3d core line with a characteristic binding energy of 916.7 eV[64–66]. The peak position of this component is independent of the Ce^{3+} to Ce^{4+} ratio (as long as Ce^{4+} is present), which makes it possible to calibrate the spectra throughout the experiment. Atomic ratios were estimated

following the standard procedure, involving a Shirley background subtraction and raw area normalization by using relative sensitivity factors. Spectral lines were fitted using a symmetric pseudo-Voigt function denoted by a GL (30) line shape in the CasaXPS software. Pt 4f spectra containing a metallic Pt component were fitted using an asymmetric pseudo-Voigt function (LF (0.56, 1.5, 55, 150)). The Ce 3d line was fitted according to a model described elsewhere[65,67]. All the spectra are presented without normalization of the areas. In order to follow possible sintering/segregation of Pt, the Pt/Ce atomic ratios at every temperature were estimated.

Quasi *in situ* XPS measurements were carried out with a Kratos AXIS Ultra spectrometer, equipped with a monochromatic Al Kα x-ray source and a delay-line detector. Spectra were obtained using the aluminum anode Al Kα = 1486.6 eV operating at 150 W. The background pressure was in the range of 10^{-9} mbar. Ex situ treatments were performed in the preparation chamber of the spectrometer in 55 mbar of CO at 450 °C for 8 h. After the treatment the sample was transferred without the exposure to the air to the analysis chamber of the spectrometer, where the spectra were acquired. The acquisition parameters of the spectra were kept as in case of NAP-XPS studies.

3.5 Contribution statement

This chapter is based on the following publication: Pereira-Hernández, X.I.*, DeLaRiva, A.*, **Muravev, V.*,** Kunwar, D., Xiong, H., Sudduth, B., Engelhard, M., Kovarik, L., Hensen, E.J.M., Wang, Y. & Datye, A.K. *Nature Communications* 10**,** 1358 (2019). V. Muravev was responsible for performing *in situ* NAP-XPS and *quasi in situ* XPS experiments and interpreting the data. Synthesis, catalytic testing as well as XRD, XPS, TPR-CO and *in situ* DRIFTS characterization of PdFSP samples was performed by V. Muravev. He was also involved in writing of the original manuscript.

3.6 References

1. Office of Energy Efficiency and Renewable Energy, Advanced Combustion and Emission Control Roadmap. *Energy.gov* (2018).
2. De Jong, K. Synthesis of Solid Catalysts, *Wiley-VCH Verlag GmbH & Co. KGaA* (2009).
3. Qiao, B., Wang, A., Yang, X., Allard, L. F., Jiang, Z., Cui, Y., Liu, J., Li, J. & Zhang, T. *Nat. Chem.* **3,** 634–641 (2011).
4. Lambert, S., Job, N., D'Souza, L., Pereira, M. F. R., Pirard, R., Heinrichs, B., Figueiredo, J. L., Pirard, J. P. & Regalbuto, J. R. *J. Catal.* **261,** 23–33 (2009).
5. Liu, J. Catalysis by Supported Single Metal Atoms. *ACS Catal.* **7,** 34–59 (2016).

6. Lin, J., Wang, A., Qiao, B., Liu, X., Yang, X., Wang, X., Liang, J., Li, J., Liu, J. & Zhang, T. J. *Am. Chem. Soc.***135,** 15314–15317 (2013).
7. Yang, M., Li, S., Wang, Y., Herron, J. A., Xu, Y., Allard, L. F., Lee, S., Huang, J., Mavrikakis & M. Flytzani-Stephanopoulos. *Science* **346,** 1498–1501 (2014).
8. International Organization of Motor Vehicle Manufacturers. World Vehicle Production 2016. *oica.net/category/production-statistics/2016-statistics (2016).*
9. U.S. D.R.I.V.E. Partnership. Aftertreatment Protocols for Catalyst Characterization and Performance Evaluation: Low-Temperature Oxidation Catalyst Test Protocol, *cleers.org/wp-content/uploads/2015_LTATOxidation-Catalyst-Characterization-Protocol.pdf.* (2015).
10. Jones, J., Xiong, H., DeLaRiva, A. T., Peterson, E. J., Pham, H., Challa, S. R., Qi, G., Oh, S., Wiebenga, M. H., Pereira Hernandez, X. I., Wang, Y. & Datye, A. K. *Science* **353,** 150–154 (2016).
11. Nunan, J. G., Robota, H. J., Cohn, M. J. & Bradley, S. A. *J. Catal.* **133,** 309–324 (1992).
12. Gänzler, A. M., Casapu, M., Vernoux, P., Loridant, S., Cadete Santos Aires, F. J., Epicier, T., Betz, B., Hoyer, R. & Grunwaldt, J. D. *Angew. Chem. Int. Ed.* **56,** 13078–13082 (2017).
13. Gänzler, A. M., Casapu, M., Maurer, F., Störmer, H., Gerthsen, D., Ferré, G., Vernoux, P., Bornmann, B., Frahm, R., Murzin, V., Nachtegaal, M., Votsmeier, M. & Grunwaldt, J. *ACS Catal.* **8,** 4800–4811 (2018).
14. Gatla, S., Aubert, D., Agostini, G., Mathon, O., Pascarelli, S., Lunkenbein, T., Willinger, M. G. & Kaper, H. *ACS Catal.* **6,** 6151–6155 (2016).
15. Gatla, S., Aubert, D., Flaud, V., Grosjean, R., Lunkenbein, T., Mathon, O., Pascarelli, S. & Kaper, H. *Catal. Today* **333,** 105-112 (2018).
16. Lykhach, Y., Bruix, A., Fabris, S., Potin, V., Matolínová, I., Matolín, V., Libuda, J. & Neyman, K. M.. *Catal. Sci. Technol.* **7,** 4315–4345 (2017).
17. Thang, H. V., Pacchioni, G., DeRita, L. & Christopher, P. *J. Catal.* **367,** 104–114 (2018).
18. DeRita, L., Dai, S., Lopez-Zepeda, K., Pham, N., Graham, G. W., Pan, X. & Christopher, P. *J. Am. Chem. Soc.* **139,** 14150–14165 (2017).
19. Cargnello, M., Doan-Nguyen, V. V. T., Gordon, T. R., Diaz, R. E., Stach, E. a., Gorte, R. J., Fornasiero, P. & Murray, C. B. *Science* **341,** 771–773 (2013).
20. Bunluesin, T., Putna, E. S. & Gorte, R. J. *Catal. Lett.* **41,** 1–5 (1996).
21. Bunluesin, T., Cordatos, H. & Gorte, R. J. *J. Catal.* **157,** 222–226 (1995).
22. Bunluesin, T., Gorte, R. J. & Graham, G. W. *Appl. Catal. B: Environ.* **15,** 107–114 (1998).
23. Kopelent, R., van Bokhoven, J. A., Szlachetko, J., Edebeli, J., Paun, C., Nachtegaal, M. & Safonova, O. V. *Angew. Chem. Int. Ed.* **127,** 8852–8855 (2015).
24. Gao, Y., Wang, W., Chang, S. & Huang, W. *ChemCatChem* **5,** 3610–3620 (2013).
25. Ho, C., Yu, J. C., Kwong, T., Mak, A. C. & Lai, S. *Chem. Mater.* **17,** 4514–4522 (2005).
26. Valechha, D., Lokhande, S., Klementova, M., Subrt, J., Rayalu, S. & Labhsetwar, N. *J. Mater. Chem.* **21,** 3718–3725 (2011).
27. Regalbuto, J. R. Strong Electrostatic Adsorption of Metals onto Catalyst Supports, *Catalyst preparation* **2,** 297–318, *CRC Press* (2007).
28. Wang, X., Van Bokhoven, J. A. & Palagin, D. *Phys. Chem. Chem. Phys.* **19,** 30513–30519 (2017).
29. Datye, A. & Wang, Y. *Natl. Sci. Rev.* **5,** 630–632 (2018).
30. Stark, W. J., Grunwaldt, J.-D., Maciejewski, M., Pratsinis, S. E. & Baiker, A. *Chem. Mater.* **17,** 3352-3358 (2005).
31. Cavusoglu, G., Miao, D., Lichtenberg, H., Carvalho, H. W. P., Xu, H., Goldbach, A. & Grunwaldt, J. D. *Appl. Catal. A: Gen.* **504,** 381–390 (2015).
32. Steiner, C., Gänzler, A. M., Zehentbauer, M., Hagen, G., Casapu, M., Müller, S., Grunwaldt, J.-D. & Moos, R.. *Top. Catal.* **62,** 227–236 (2018).
33. Lykhach, Y., Kozlov, S. M., Skála, T., Tovt, A., Stetsovych, V., Tsud, N., Dvořák, F., Johánek, V., Neitzel, A., Mysliveček, J., Fabris, S., Matolín, V., Neyman, K. M. & Libuda, J. *Nat. Mater.* **15,** 1–6 (2016).
34. Dvořák, F., Camellone, M. F., Tovt, A., Tran, N., Negreiros, F. R., Vorokhta, M., Skála, T., Matolínová, I., Mysliveček, J., Matolín, V. & Fabris, S. *Nat. Commun.* **7,** 1–8 (2016).
35. Oran, U. & Uner, D. *Appl. Catal. B: Environ.* **54,** 183–191 (2004).
36. Okal, J., Zawadzki, M., Kraszkiewicz, P. & Adamska, K. *Appl. Catal. A: Gen.* **549,** 161–169 (2018).

37. Ding, K., Gulec, A., Johnson, A. M., Schweitzer, N. M., Stucky, G. D., Marks, L. D. & Stair, P. C. *Science* **350,** 189–192 (2015).
38. Pozdnyakova, O., Teschner, D., Wootsch, A., Kröhnert, J., Steinhauer, B., Sauer, H., Toth, L., Jentoft, F. C., Knop-Gericke, A., Paál, Z. & Schlögl, R. *J. Catal.* **237,** 1–16 (2006).
39. Wang, C., Gu, X. K., Yan, H., Lin, Y., Li, J., Liu, D., Li, W. X. & Lu, J. *ACS Catal.* **7,** 887–891 (2017).
40. Bazin, P., Saur, O., Lavalley, J. C., Daturi, M. & Blanchard, G. *Phys. Chem. Chem. Phys.* **7,** 187–194 (2005).
41. Busca, G., Finocchio, E. & Escribano, V. S. *Appl. Catal. B: Environ.* **113–114,** 172–179 (2012).
42. Jardim, E. O., Rico-Francés, S., Coloma, F., Anderson, J. A., Silvestre-Albero, J. & Sepúlveda-Escribano, A. *J. Colloid Interface Sci.* **443,** 45–55 (2015).
43. Lentz, C., Jand, S. P., Melke, J., Roth, C. & Kaghazchi, P. *J. Mol. Catal. A: Chem.* **426,** 1–9 (2017).
44. Moses-Debusk, M., Yoon, M., Allard, L. F., Mullins, D. R., Wu, Z., Yang, X., Veith, G., Stocks, G. M. & Narula, C. K. *J. Am. Chem. Soc.* **135,** 12634–12645 (2013).
45. Kaftan, A., Kollhoff, F., Nguyen, T. S., Piccolo, L., Laurin, M. & Libuda, J. *Catal. Sci. Technol.* **6,** 818–828 (2016).
46. Liu, H. H., Wang, Y., Jia, A. P., Wang, S. Y., Luo, M. F. & Lu, J. Q. *Appl. Surf. Sci.* **314,** 725–734 (2014).
47. Aleksandrov, H. A., Neyman, K. M., Hadjiivanov, K. & Vayssilov, G. N. *Phys. Chem. Chem. Phys.* **18,** 22108–22121 (2016).
48. Royer, S. & Duprez, D. *ChemCatChem* **3,** 24–65 (2011).
49. Korányi, T. I., Mihály, J., Pfeifer, E., Németh, C., Yuzhakova, T. & Mink, J.. *J. Phys. Chem. A* **110,** 1817–1823 (2006).
50. Brummel, O., Waidhas, F., Faisal, F., Fiala, R., Vorokhta, M., Khalakhan, I., Dubau, M., Figueroba, A., Kovács, G., Aleksandrov, H. A., Vayssilov, G. N., Kozlov, S. M., Neyman, K. M., Matolín, V. & Libuda, J.. *J. Phys. Chem. C* **120,** 19723–19736 (2016).
51. Happel, M., Mysliveček, J., Johánek, V., Dvořák, F., Stetsovych, O., Lykhach, Y., Matolín, V. & Libuda, J. *J. Catal.* **289,** 118–126 (2012).
52. DeRita, L., Dai, S., Lopez-Zepeda, K., Pham, N., Graham, G. W., Pan, X. & Christopher, P. *J. Am. Chem. Soc.* **139,** 14150–14165 (2017).
53. Nie, L., Mei, D., Xiong, H., Peng, B., Ren, Z., Pereira Hernandez, X. I., DeLaRiva, A., Wang, M., Engelhard, M. H., Kovarik, L., Datye, A. K. & Wang, Y. *Science* **358,** 1419–1423 (2017).
54. Mullins, D. R. *Surf. Sci. Rep.* **70,** 42–85 (2015).
55. Zhang, L., Spezzati, G., Muravev, V., Verheijen, M. A., Zijlstra, B., Filot, I. A. W., Su, Y.-Q., Chang, M.-W. & Hensen, E. J. M. *ACS Catal.* **11,** 5614–5627 (2021).
56. Teoh, W. Y., Amal, R. & Mädler, L. *Nanoscale* **2,** 1324–1347 (2010).
57. Koirala, R., Pratsinis, S. E. & Baiker, A. *Chem. Soc. Rev* **45,** 3053 (2016).
58. Bunluesin, T., Gorte, R. J. & Graham, G. W. *Appl. Catal. B: Environ.* **14,** 105–115 (1997).
59. Morfin, F., Nguyen, T. S., Rousset, J. L. & Piccolo, L. *Appl. Catal. B: Environ.* **197,** 2–13 (2016).
60. Lin, W., Herzing, A. A., Kiely, C. J. & Wachs, I. E. *J. Phys. Chem. C* **112,** 5942–5951 (2008).
61. Murrell, L. L., Tauster, S. J. & Anderson, D. R. *Stud. Surf. Sci. Catal.* **75,** 681–690 (1993).
62. Lykhach, Y., Figueroba, A., Skála, T., Duchon, T., Tsud, N., Aulická, M., Neitzel, A., Veltruská, K., Prince, K. C., Matolín, V., Neyman, K. M. & Libuda, J. *J. Mater. Chem. A.* **5,** 9250–9261 (2017).
63. Scanlon, D. O., Morgan, B. J. & Watson, G. W. *Phys. Chem. Chem. Phys.* **13,** 4279–4284 (2011).
64. Artiglia, L., Orlando, F., Roy, K., Kopelent, R., Safonova, O., Nachtegaal, M., Huthwelker, T. & van Bokhoven, J. A. *J. Phys. Chem. Lett.* **8,** 102–108 (2017).
65. Skála, T., Šutara, F., Prince, K. C. & Matolín, V. *J. Electron Spectros. Relat. Phenomena* **169,** 20–25 (2009).
66. Stadnichenko, A. I., Muravev, V. V., Koscheev, S. V., Zaikovskii, V. I., Aleksandrov, H. A., Neyman, K. M. & Boronin, A. I. *Surf. Sci.* **679,** (2019).
67. Kato, S., Ammann, M., Huthwelker, T., Paun, C., Lampimäki, M., Lee, M.-T., Rothensteiner, M. & van Bokhoven, J. A. *Phys. Chem. Chem. Phys.* **17,** 5078–5083 (2015).

3.7 Appendix A

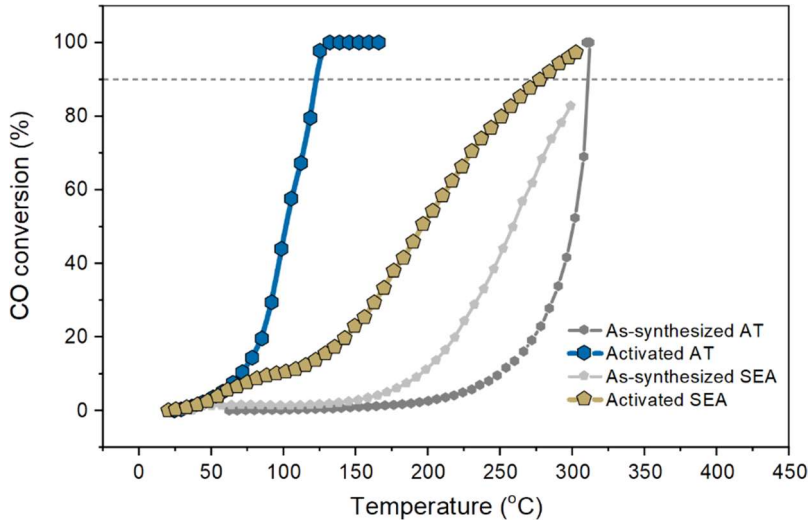

Figure A1. CO oxidation light-off curves for 1 wt% Pt/CeO_2 catalysts synthesized by AT and SEA using CPA as a precursor before and after activation.

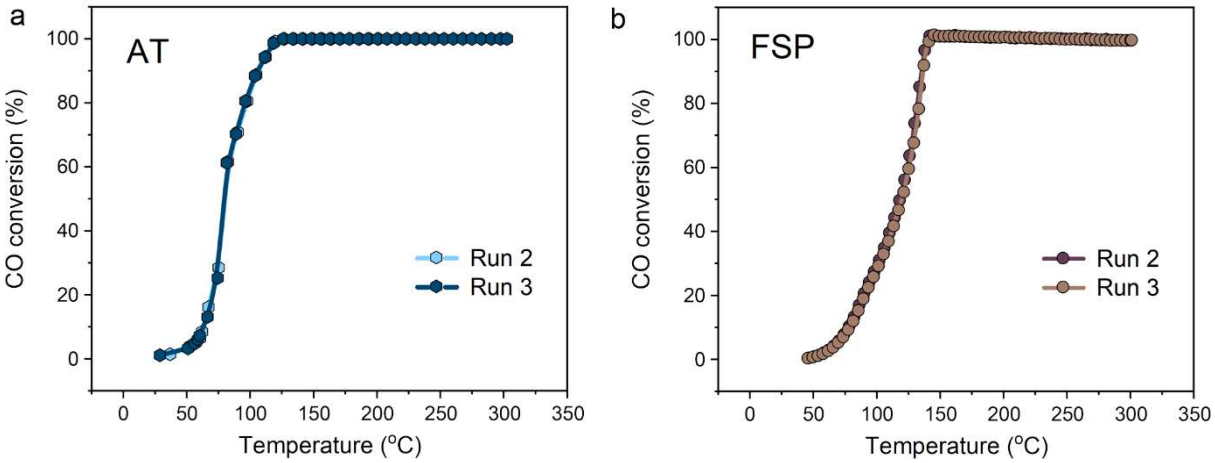

Figure A2. Consecutive CO oxidation light-off curves for the 1 wt% Pt/CeO_2 activated catalysts: AT (TAPN) and FSP.

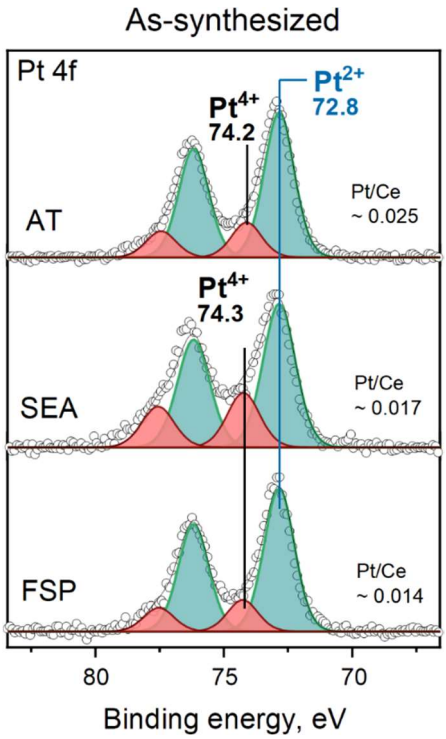

Figure A3. XPS of as-synthesized 1 wt% Pt/CeO_2 AT and SEA using TAPN as a precursor and FSP catalysts.

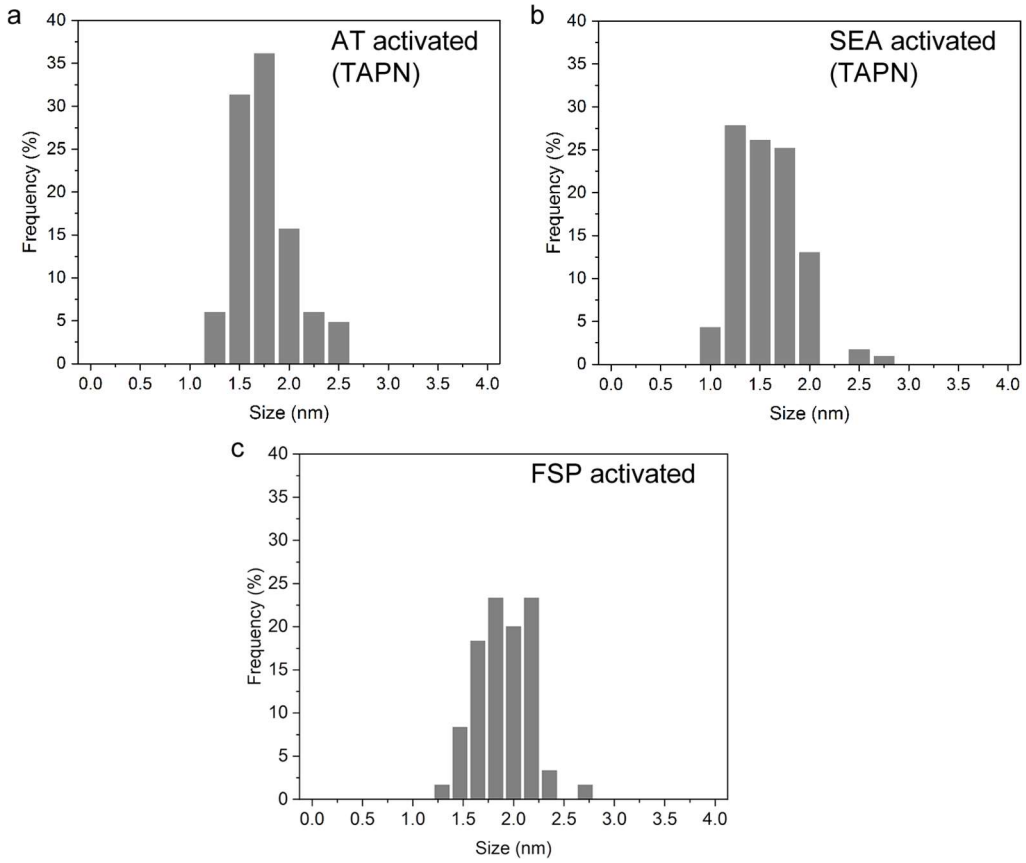

Figure A4. Pt Particle size distributions (PSD) for the activated 1 wt% Pt/CeO_2 TAPN catalysts: a) AT and b) SEA. The mean particle size and standard deviation for the AT and SEA catalysts are 1.68 ± 0.3 nm and 1.58 ± 0.33 nm, respectively.

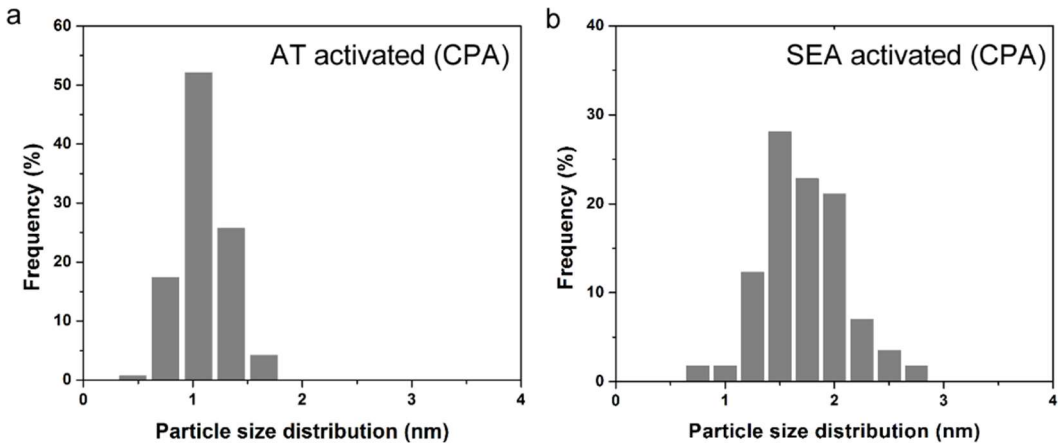

Figure A5. Pt Particle size distributions (PSD) for the activated 1 wt% Pt/CeO_2 CPA catalyst: a) AT and b) SEA. The mean particle size and standard deviation for the AT and SEA catalysts are 1.05 ± 0.2 nm and 1.72 ± 0.36 nm, respectively.

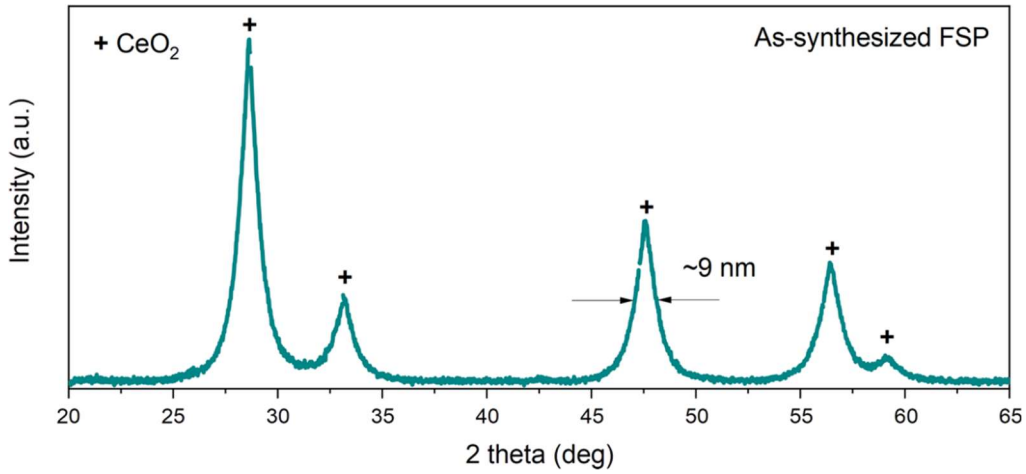

Figure A6. X-ray powder diffraction pattern for as-synthesized 1 wt% Pt/CeO_2 FSP sample.

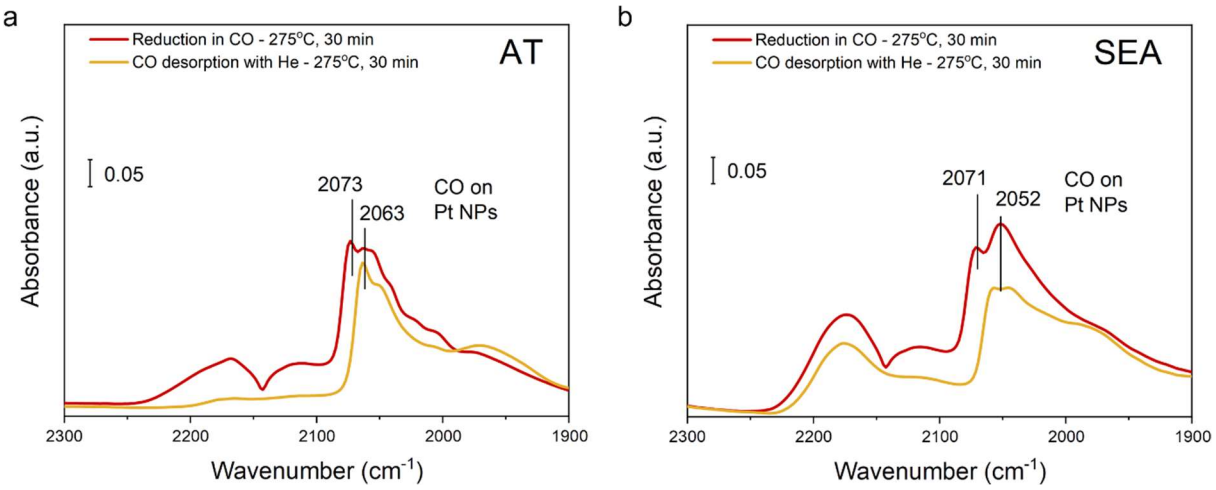

Figure A7. CO reduction at 275 °C monitored by DRIFTS on the 1 wt% Pt/CeO_2 TAPN catalysts: a) AT, b) SEA. The CO is strongly bound and only partially removed in flowing He.

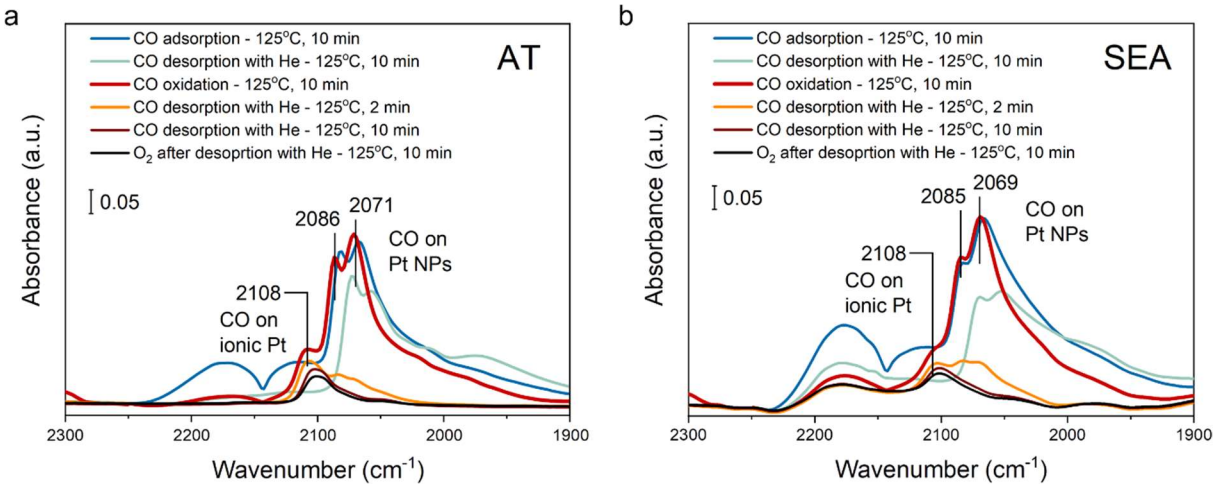

Figure A8. CO adsorption/desorption previous to CO oxidation reaction at 125 °C monitored by DRIFTS on the activated 1 wt% Pt/CeO_2 TAPN catalysts: a) AT, b) SEA. When CO flow is stopped after CO exposure at 125 °C, the CO band persists, but after CO oxidation the CO is readily removed, presumably because the ceria support has acquired the oxygen that it provides to react with the adsorbed CO.

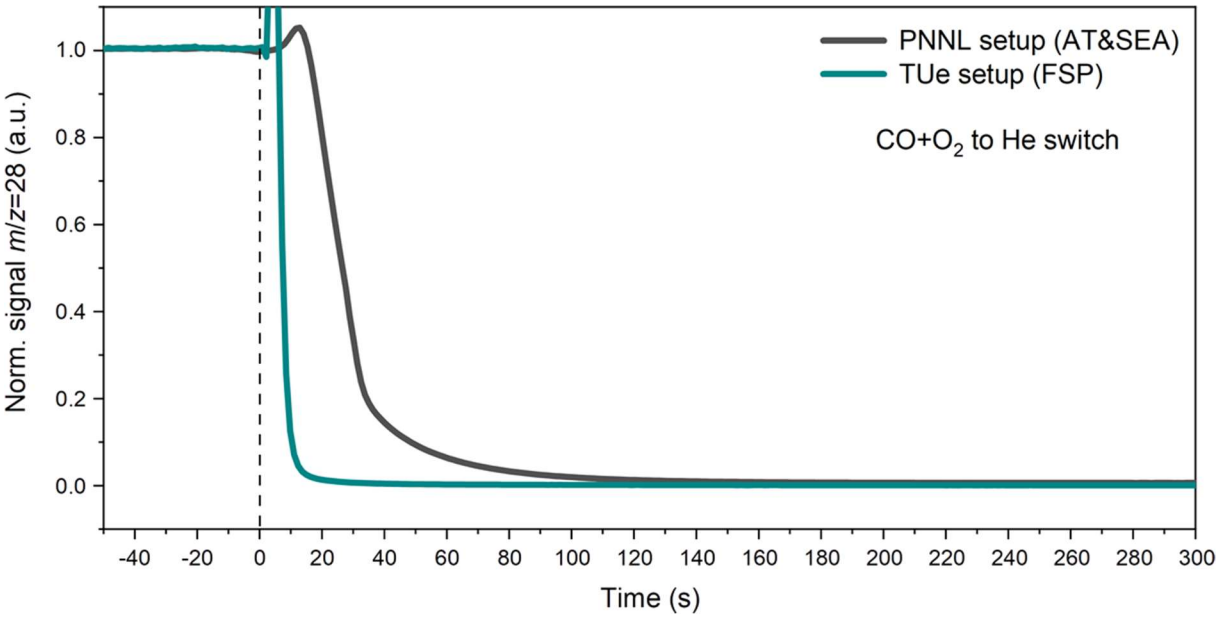

Figure A9. Mass-spectrometry data showing the time difference in gas holdup time in different DRIFTS setups during a typical switch.

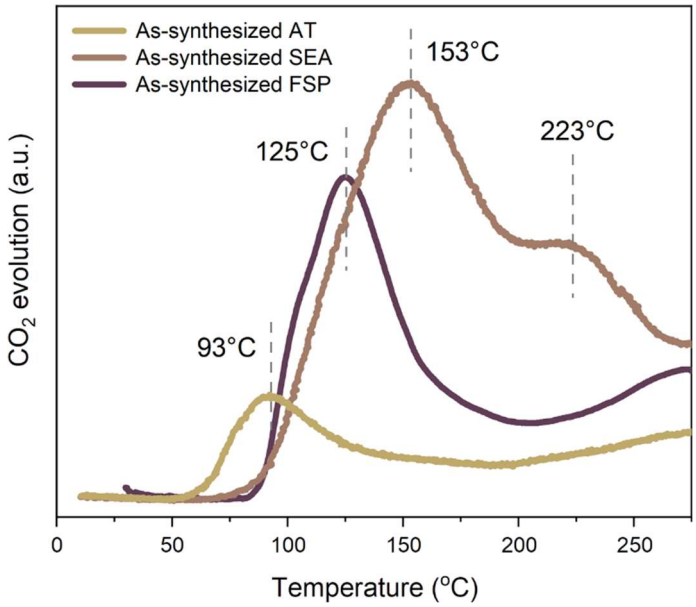

Figure A10. CO-TPR of the 1 wt% Pt/CeO_2 TAPN as-synthesized AT and SEA catalysts and as-synthesized FSP. The SEA and FSP catalysts have a higher surface area since they were not calcined at 800 °C, explaining in part, the difference in peak areas with respect to AT catalyst. The lower temperature peak indicates easier reduction of the trapped ionic Pt and the ceria lattice in the AT catalyst.

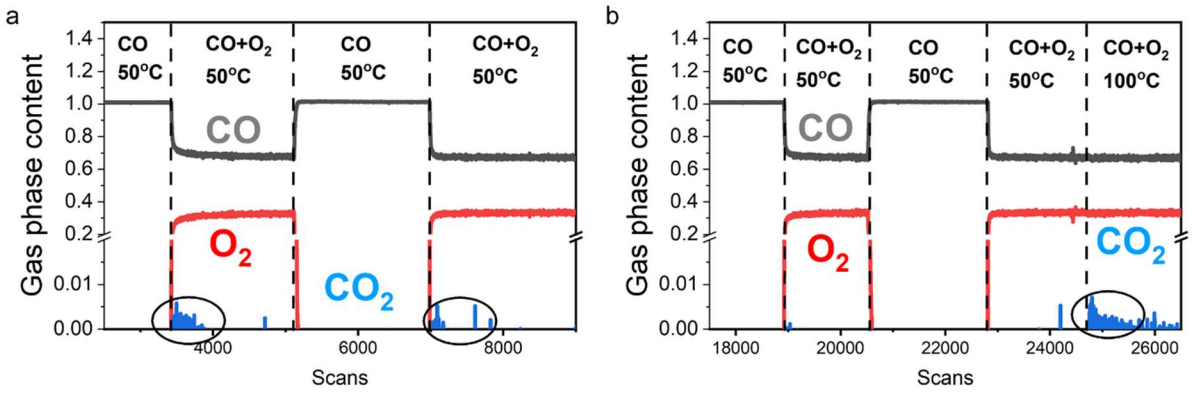

Figure A11. Mass spectrometry results during NAP-XPS experiments for the activated 1 wt% Pt/CeO_2 catalysts a) AT, b) SEA, showing the higher reactivity for the AT catalyst at 50 °C. The SEA catalyst shows evidence of reaction only at 100 °C.

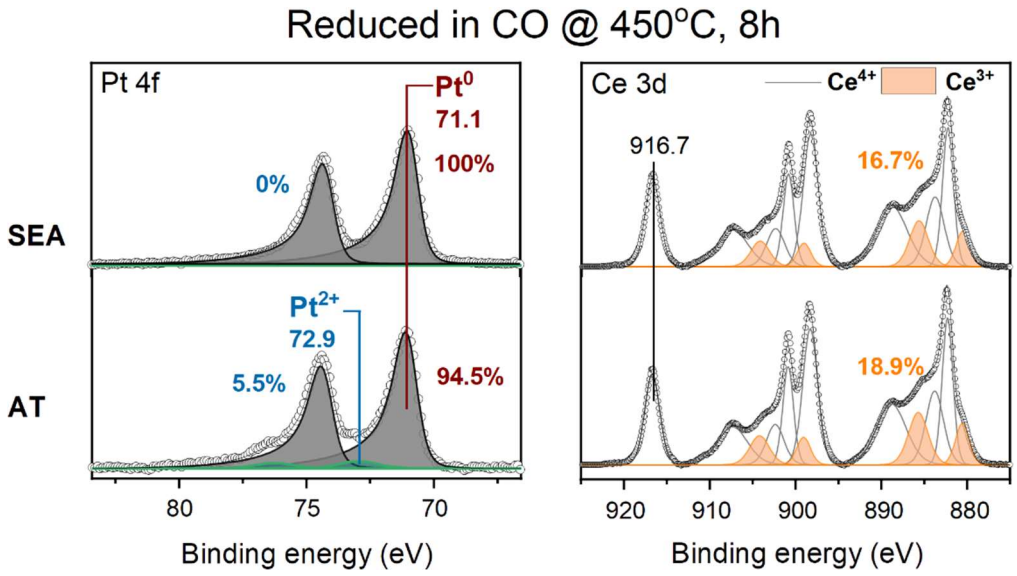

Figure A12. *Quasi in situ* XPS results after UHV transfer for 1 wt% Pt/CeO_2 TAPN catalysts after reduction at 450 °C for 8 h: Pt 4f region for the AT and SEA catalysts (left), Ce 3d region for the AT and SEA catalysts (right). The Pt/Ce ratio changed from 0.025 to 0.021 and 0.017 to 0.038 for the AT and SEA catalysts, respectively, after reduction at 450 °C in CO for 8 h. The doubling in the Pt/Ce ratio for the SEA catalyst is attributed to the sintering of CeO_2 particles. This is not observed in the AT catalyst since it has already been exposed previously to a temperature of 800 °C during the AT synthesis.

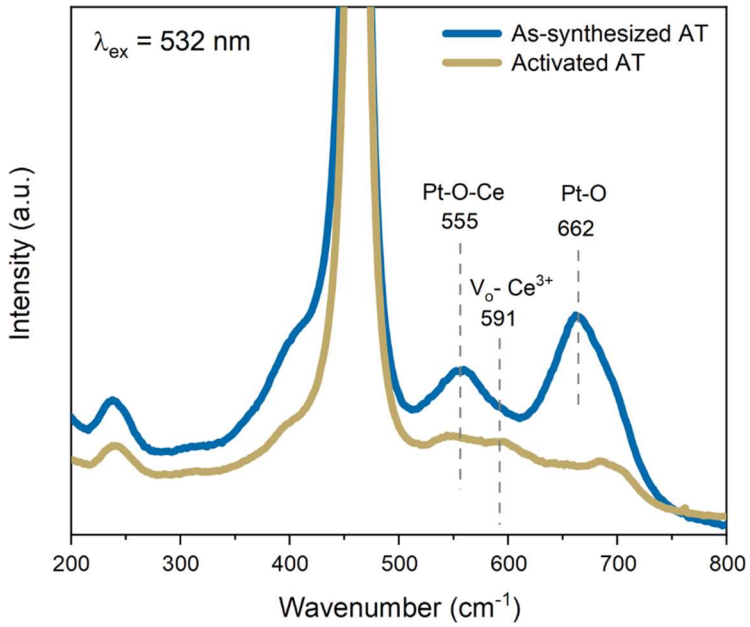

Figure A13. Raman spectra of the 1 wt% Pt/CeO_2 TAPN catalyst synthesized by AT, as-synthesized and activated.

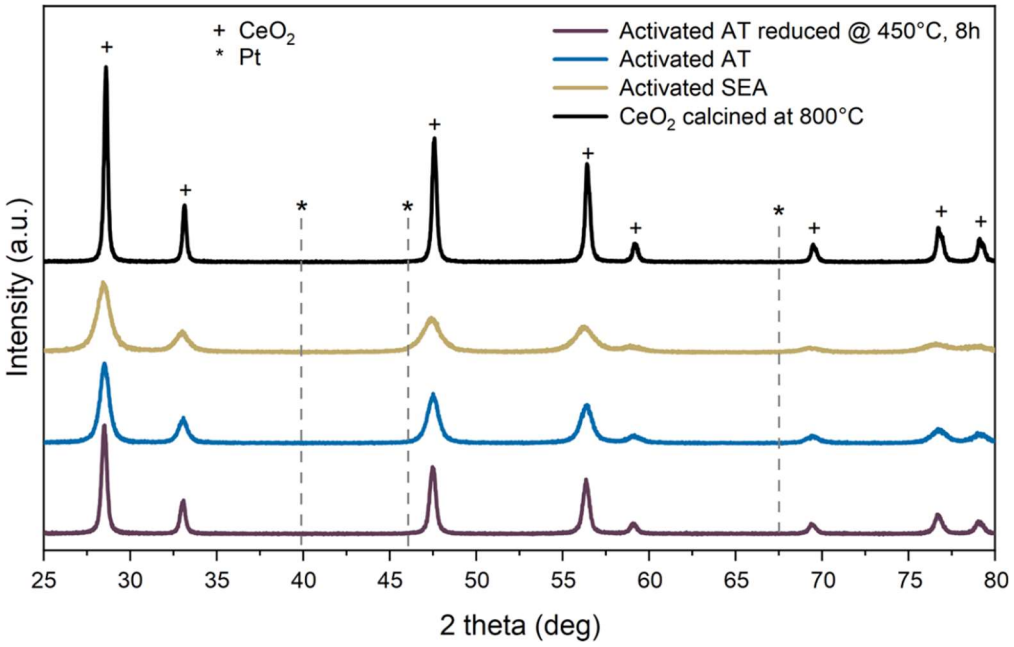

Figure A14. XRD pattern for bare CeO_2 calcined at 800 °C for 10 h, the AT and SEA catalysts activated at 275 °C and the AT catalyst activated at 450 °C for 8 h. No diffraction peaks are observed for Pt even after a harsh reduction treatment at 450 °C for 8 h.

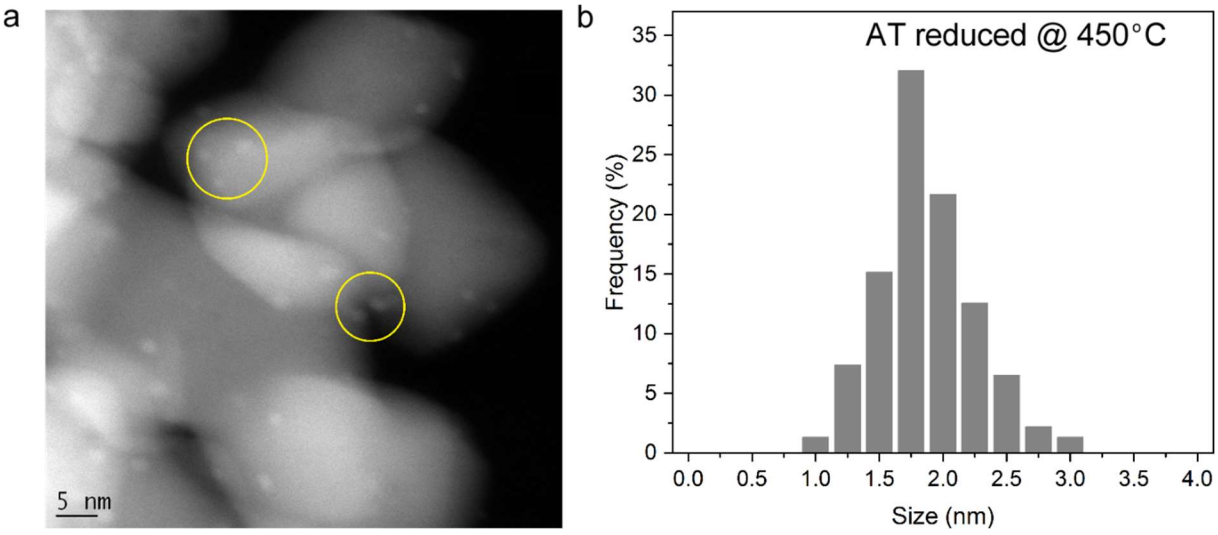

Figure A15. Pt particle size after activation of the 1 wt% Pt/CeO_2 TAPN catalyst synthesized by AT at 450 °C for 8 h: a) HAADF-STEM image, b) Pt PSD. The mean particle size and standard deviation are 1.87 ± 0.38 nm.

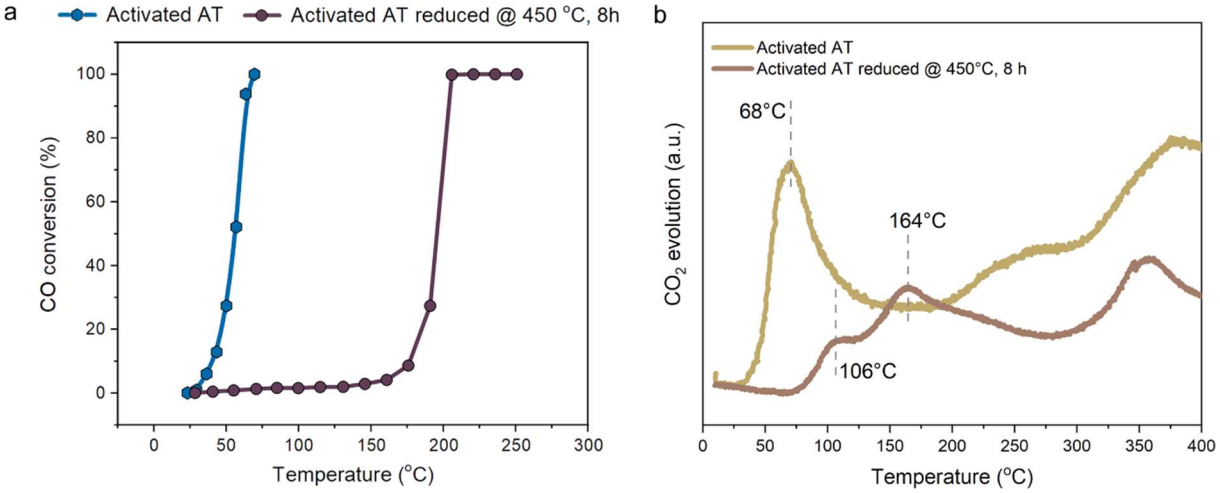

Figure A16. Effect of activation at 450 °C on the activity and reducibility of the 1 wt% Pt/CeO_2 catalyst synthesized by AT: a) Light-off curves after activation at 275 °C (regular activation treatment) and 450 °C for 8 h (harsher activation treatment) and b) CO-TPR after activation at 275 °C (regular activation treatment) and 450 °C for 8 h (harsher activation treatment). The lower reactivity on the 450 °C activated catalyst is correlated with the loss of the low temperature CO-TPR peak.

Table A1. BET surface area of pure CeO_2 and the 1 wt% Pt/CeO_2 TAPN catalyst synthesized by AT as a function of synthesis temperature. Pure CeO_2 retains only 12% of the surface area after being calcined at 800 °C while in the 1 wt% Pt/CeO_2 catalyst, CeO_2 retains 40% of the surface area.

Synthesis temperature	**400°C**	**500°C**	**600°C**	**700°C**	**800°C**
Surface area CeO_2 (m^2/g)	83	80	68	33	10
Surface area 1wt%Pt/CeO_2 (m^2/g)	94	87	80	63	38

Chapter 4

Interface dynamics of Pd-CeO_2 single-atom catalysts during CO oxidation

Abstract

In recent years, noble metals atomically dispersed on solid oxide supports have become a frontier of heterogeneous catalysis. In pursue of ultimate atom efficiency, the stability of single atom catalysts (SACs) is pivotal. Here, we compare two Pd/CeO_2 SACs that are active in low-temperature CO oxidation and display drastically different structural dynamics under reaction conditions. These catalysts were obtained by conventional impregnation on hydrothermally synthesized CeO_2 and one-step flame spray pyrolysis (FSP). The oxidized Pd atoms in the impregnated catalyst are prone to reduction and sintering during CO oxidation, whereas they remain intact on the surface of FSP-derived Pd-doped CeO_2. Detailed *in situ* characterization links the stability of Pd single atoms to the reducibility of the Pd-CeO_2 interface and the extent of reverse oxygen spillover. Understanding these chemical phenomena underlying the metal-support interactions is crucial to the rational design of stable SACs.

This chapter is based on the following publication:

Muravev, V., Spezzati, G., Su, Y., Parastaev, A., Chiang, F., Longo, A., Escudero, C., Kosinov, N. & Hensen E.J.M. *Nature Catalysis* **4,** 469-478 (2021). *doi: 10.1038/s41929-021-00621-1*.

4.1 Introduction

Metal-support interactions (MSI) are a central topic in heterogeneous catalysis [1,2]. By controlling the extent of MSI, we can tune the size of supported metal nanoparticles (NPs), which is often decisive for the catalytic performance [3–7]. Small supported clusters can display catalytic behavior very different from larger NPs, owing to quantum size effects[8,9] and changes in the electronic structure under the influence of the support [10,11]. In search of atom-efficient use of often expensive transition metals, a new trend bridging heterogeneous catalysis, homogeneous catalysis, and material science has emerged: catalysis by single atoms [12,13]. Supported single-atom catalysts (SACs) often display remarkable catalytic activity originating from the coordinatively unsaturated nature of the single atom, which is favorable for the activation of reactants [14]. Similar to non-innocent ligands in homogeneous catalysts, the support not only stabilizes the single metal atom but also influences its reactivity and can even play a role in the catalytic cycle [15,16]. Reducible oxide supports such as TiO_2, Fe_2O_3, and CeO_2 are especially suitable for stabilizing single atoms due to strong MSI [13,17–19]. CeO_2 is known for its ability to disperse platinum group metals, which are key components of modern automotive exhaust catalysts. The unique Ce^{3+}/Ce^{4+} redox properties, associated with the reversible formation of oxygen vacancies, render CeO_2 a widely used support in modern heterogeneous and single-atom catalysis [20–25].

Pivotal to tail gas treatment of internal combustion engines, oxidation of CO is one of the most studied reactions for CeO_2-based catalysts [14,26–29]. For example, remarkable advances in understanding structure-activity relationships in Pt/CeO_2 CO oxidation catalysts have been achieved. As-prepared ionic Pt-species in Pt/CeO_2 SACs display limited activity in low-temperature CO oxidation, while a reductive pretreatment of such catalysts results in highly active small Pt clusters [26,27,30,31] The reaction is thought to take place at the metal-support interface: CO molecules are adsorbed on Pt clusters, while transiently formed oxygen vacancies on the ceria surface activate O_2 [28]. A key aspect of this chemistry is facile dissociation of O_2, circumventing the problem of CO poisoning of extended Pt surfaces.

For practical applications in exhaust clean-up systems of petrol-powered vehicles, Pd and Pt are similarly attractive, and the choice of the key component is often determined by metal price differences [32]. When dispersed as single atoms, however, Pt and Pd behave quite differently in catalytic CO oxidation. Unlike Pt, isolated Pd atoms do not require reduction to

become active in CO oxidation. Peterson et al. demonstrated in an operando X-ray absorption study that oxidized Pd atoms are the active sites for low-temperature CO oxidation. During the reaction, however, oxidized single atoms were reduced, which led to sintering and a loss of the high activity [33]. Parkinson et al. scrutinized the dynamic behavior of Pd single atoms supported on Fe_3O_4 under CO exposure [34]. The authors argued that sintering of Pd atoms was induced by the migration of Pd-carbonyl species. In a previous work, we found that oxidized Pd single atoms supported on CeO_2 nanorods are active low-temperature CO oxidation catalysts [35,36]. Jeong et al. reported that, by anchoring Pd to small CeO_2 NPs dispersed over alumina, a close-to-atomic Pd dispersion can be preserved even after hydrothermal ageing at 900 °C [37]. Despite these peculiar findings, the activity and stability descriptors of Pd SACs remain elusive due to the dynamic nature of the Pd-support interface in the presence of reactants. Such MSI phenomena as charge transfer between the support and the metal atom[10,11,15], oxygen spillover[38,39], and reactions at the interface[17,40] are relevant aspects of the underlying chemistry. As demonstrated by Christopher and co-workers, careful synthesis of well-defined SACs and application of suitable *in situ* characterization techniques are critical for establishing accurate structure-activity relationship for these systems [16,29].

Herein, we report a simple one-step synthesis of high-surface area Pd/CeO_2 SACs using flame spray pyrolysis (FSP) [41,42]. This preparation method results in catalysts that are more active for low-temperature CO oxidation than previously reported single-atom Pd-CeO_2-nanorod systems [35]. Comparable activation energies and reaction orders of low-temperature CO oxidation suggest a similar nature of the active sites. However, *in situ* IR, near-ambient pressure X-ray photoelectron and X-ray absorption spectroscopy reveal drastically different dynamic behavior of Pd-CeO_2 interfaces. Pd impregnated on nanorods is prone to reduction, which leads to sintering of metal under the applied reaction conditions. In contrast, the isolated nature of Pd^{2+} species is preserved in FSP-derived catalysts. The enhanced stability is linked to the higher mobility of surface lattice oxygen in the Pd-doped FSP catalysts. Altogether, the obtained results demonstrate that FSP is an appealing strategy for the synthesis of highly loaded stable single-atom catalysts, relevant for automotive exhaust neutralizers [43].

4.2 Results and Discussion

4.2.1 Preparation and characterization of Pd/CeO_2 SACs

Ceria nanorods were prepared following a hydrothermal synthesis procedure reported earlier (**Fig. B1**) [19,35]. The surface of nanorods was found to be predominantly enclosed by (111) CeO_2 surfaces (additional data and related discussion in **Figs. B3, B18 and B22**). Wet impregnation with palladium nitrate yielded 1 wt% Pd/CeO_2 sample (1PdRods). High-resolution high-angle annular dark-field scanning transmission electron microscopy (HAADF-STEM) evidenced the absence of Pd/PdO clusters on the CeO_2 surface (**Fig. 4.1a** and **Fig. B2**). Energy dispersive X-ray spectroscopy (EDX) mapping confirmed a close to atomic dispersion of Pd in the as-prepared catalysts. To obtain Pd/CeO_2 SACs in a single step, we employed flame spray pyrolysis using cerium and palladium acetylacetonates as precursors (**Fig. B1**). Besides being fast, robust and scalable[44], this approach results in crystalline CeO_2 with a high surface area [41,42]. As shown in **Fig. 4.1b**, the FSP-derived 1 wt% Pd/CeO_2 sample (1PdFSP) comprises small (~5 nm) octahedrally-shaped ceria NPs, preferentially exposing (111) facets (**Fig. B4**). Similar with 1PdRods, HAADF-STEM and EDX point to the presence of atomically dispersed Pd. The shift of the characteristic CeO_2 XRD reflections of 1PdFSP sample towards higher angles (**Fig. B5**) together with the red-shift and broadening of F_{2g} band in Raman spectrum (**Fig. B6**), imply that some Pd^{2+} ions are introduced into the ceria lattice during the FSP preparation [45]. X-ray absorption spectroscopy (XAS) at Pd K-edge was used to study the local coordination environment and chemical state of Pd. The extended X-ray absorption fine structure (EXAFS) spectra shown in **Fig. 4.1c** exhibit an intense first Pd-O coordination shell for both samples, indicative of the oxidized nature of Pd. EXAFS data analysis (**Table B1**) confirms the atomic dispersion of Pd in the 1PdRods and 1PdFSP samples. The EXAFS spectrum of 1PdRods was fitted using the Pd_1O_2 model (**Fig. B7**), representative of the oxidized Pd single atoms on the surface of CeO_2 [35,36]. To fit the EXAFS spectrum of 1PdFSP we used a square planar Pd_1O_4 motif, which was previously determined to be a stable structure of Pd doped in CeO_2 by density functional theory calculations (**Fig. B7**) [46]. A weak second-shell feature at 3.2 Å, different from the Pd-Pd distances in PdO (**Table B1**) is observed for both samples and can be assigned to the Pd-O-Ce coordination [47–49]. To summarize, FSP presents a suitable method to prepare Pd/CeO_2 SACs. Compared to conventional impregnation, requiring support preparation, drying, impregnation, and

calcination of the final catalyst, FSP involves a single preparation step (**Fig. B1**) and yields materials with a higher surface area (**Table B2**). A potential drawback of the FSP method is that a part of Pd is embedded in the bulk of the CeO_2 support. These doped Pd atoms should be inaccessible for surface reactions and thus would not be directly involved in CO oxidation catalysis. In the following, we will link the structure of 1PdFSP and 1PdRods catalysts to their CO oxidation performance.

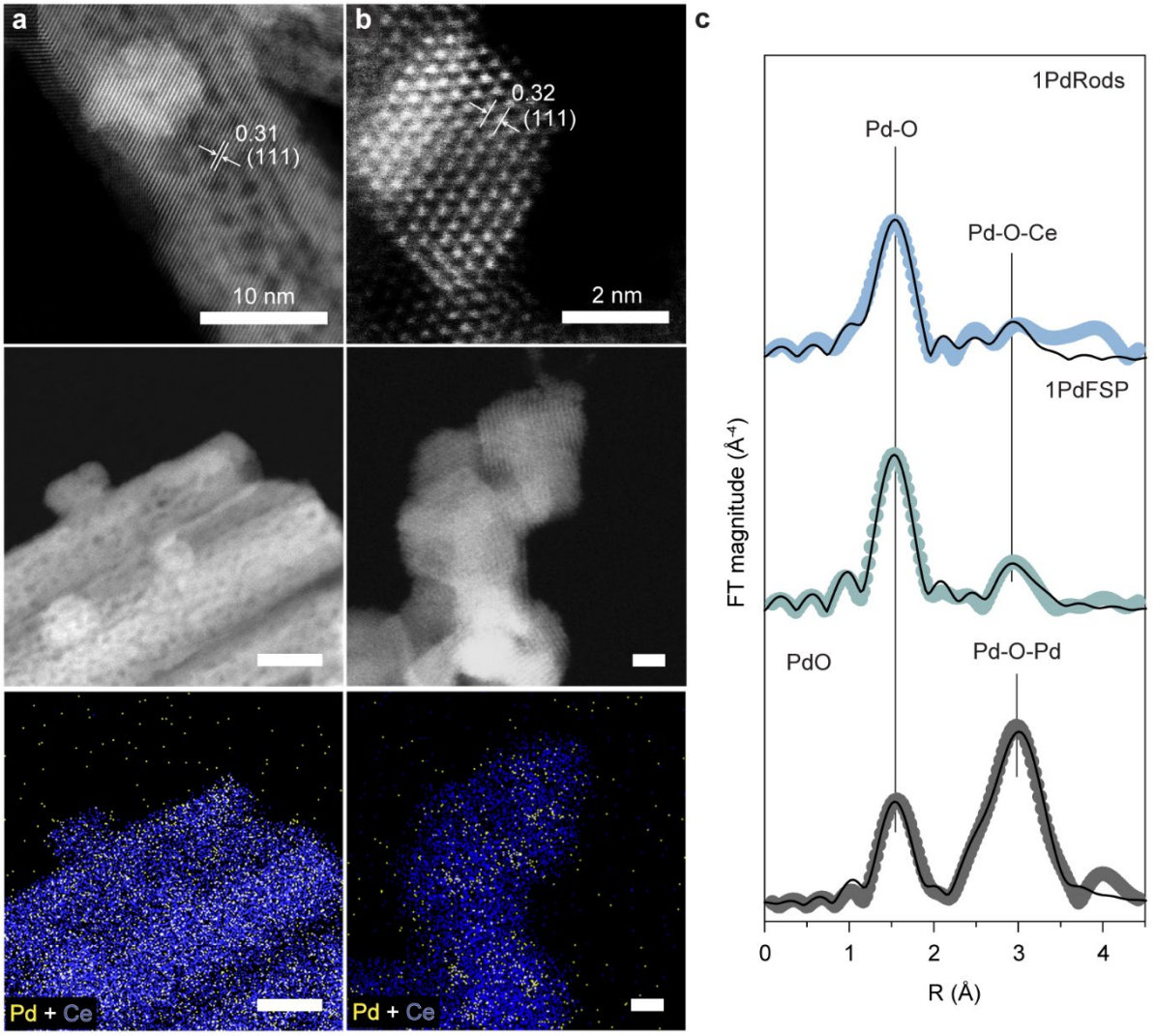

Figure 4.1. Structure of as-prepared ceria supported Pd SACs. a, b, HAADF-STEM and EDX-mapping images of a) 1PdRods , b) 1PdFSP. The spacing of corresponding crystal planes is indicated in nm. c) The k^3-weighted FT-EXAFS spectra (Pd K-edge) of 1PdFSP (turquoise), 1PdRods (blue), reference PdO (grey), circles represent the data and solid lines - fit.

4.2.2 Kinetics of CO oxidation

Catalytic activity measurements of CO oxidation in the steady-state regime are presented in **Fig. 4.2a**. The prepared Pd SACs are already active at room temperature and exhibit higher activity than reference Pd-loaded catalysts (**Fig. B9** and **Note B2**). Although it is expected

that there is less Pd on the surface of 1PdFSP due to doping, its low-temperature activity is higher than that of 1PdRods (insets in **Fig. 4.2a** and **Fig. B10**). The CO oxidation kinetics also exhibited a lower apparent activation energy for 1PdFSP (~50 kJ mol^{-1}, **Fig. B11**) in comparison with 1PdRods (~60 kJ mol^{-1}). These values are typical for CO oxidation on Pd/CeO_2 [40,48,50]. A higher reaction order in CO (+0.25 *vs.* +0.16) and a lower reaction order in O_2 (-0.14 *vs.* -0.08) were observed for the 1PdFSP sample (**Fig. 4.2b**), implying a lower coverage of CO and more facile oxygen activation on 1PdFSP [14,51]. The observed reaction orders for both Pd SACs are different from classical Langmuir-Hinshelwood CO oxidation kinetics on metals (negative order in CO, positive order in O_2), where poisoning by CO suppresses adsorption and activation of O_2. The positive reaction orders in CO point to the Mars-van Krevelen mechanism, typical for reducible oxide-based catalysts, where O_2 activation proceeds at the metal-support interface [17,40,52]. Cargnello et al. concluded that the interfacial atoms in direct contact with CeO_2 are the most active sites for CO oxidation in Ni/CeO_2, Pt/CeO_2 and Pd/CeO_2 catalysts [40]. From this perspective, all surface Pd atoms in the as-prepared Pd SACs are interfacial sites, although variations in the local structure can influence the reaction mechanism. To obtain further mechanistic insights, we studied the transient responses of 1PdRods and 1PdFSP catalysts to a step change in the reactant mixture from $CO+O_2$ to O_2 under isothermal conditions. As shown in **Fig. 4.2c**, there is a sharp increase in CO_2 concentration for the 1PdRods sample once the CO partial pressure drops to almost zero. This behavior is characteristic for the oxidation of CO adsorbed on metallic sites (**Note B3**). The CO_2 peak is significantly lower for the 1PdFSP sample, pointing to a different Pd speciation in these catalysts under reaction conditions. Comparison of reaction orders at elevated temperature emphasized the mechanistic differences between the catalysts (**Fig. 4.2d**). For 1PdFSP, the reaction order at 175 °C remained negative in O_2 (-0.06) and increased in CO (+1.36) compared to 50 °C, indicating facile oxygen activation and a low CO coverage. The 1PdRods sample demonstrated a nearly unchanged reaction order in CO (+0.19) and an increased order in O_2 (+0.29). We explain this difference by the participation of metallic Pd sites in CO oxidation at elevated temperature (**Note B4**).

Altogether, these (transient) kinetic data indicate that $Pd\text{-}CeO_2$ interface is involved in low-temperature CO oxidation in both Pd SACs. The high-temperature CO oxidation activity of 1PdRods is likely influenced by aggregated metallic Pd species formed *in situ*, whose contribution is negligible in 1PdFSP. The limited stability of supported single atoms under

operating conditions is often an issue due to the undercoordinated nature of the metal atoms in SACs [16,33,53]. To link the activity and stability of the prepared Pd SACs to their structure, we will next employ a set of spectroscopic tools.

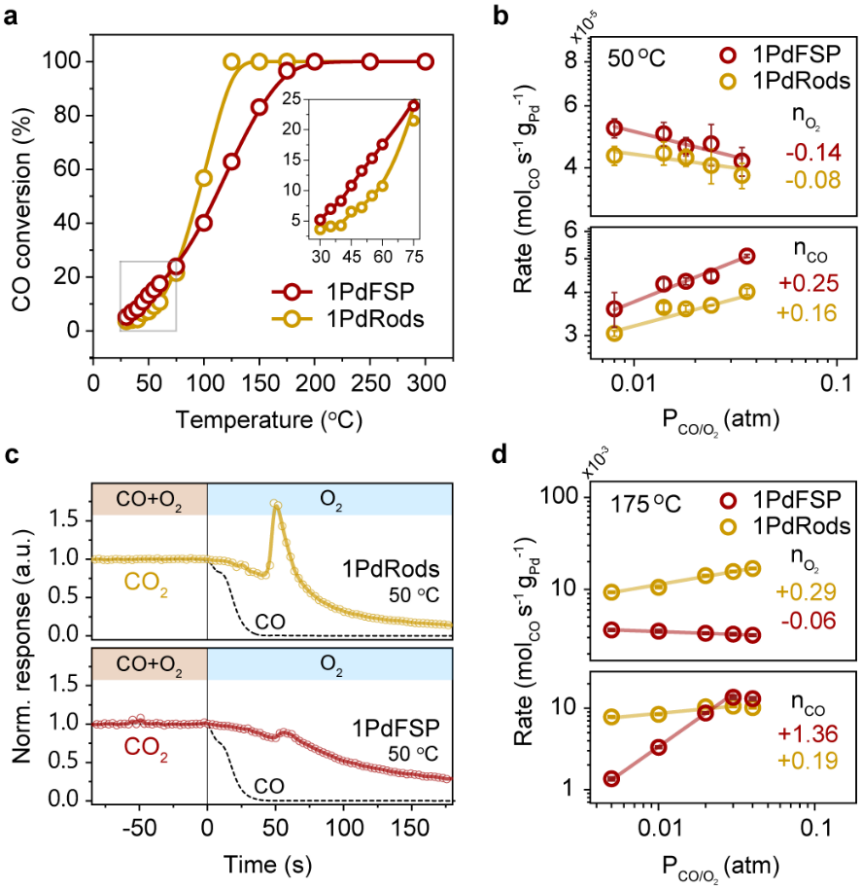

Figure 4.2. CO oxidation kinetics. a) Steady-state CO conversion plots (1%CO, 1%O_2, He balance, GHSV of 60,000 mL h^{-1} g_{cat}^{-1}). b) Reaction rate as a function of CO or O_2 partial pressure measured at 50 °C. When O_2 partial pressure was varied (from 8 to 34 mbar), the partial pressure of CO was fixed (12 mbar). When CO partial pressure was varied (from 8 to 36 mbar) the partial pressure of O_2 was fixed (12 mbar). Reaction orders (n_x) estimated as slopes of the linear fit. Error bars represent standard deviation of the three subsequent measurements at given pressure. c) Transient kinetic step-response of CO_2 during the switch from CO+O_2 to O_2 feed at 50 °C. d) Reaction rate as a function of CO or O_2 partial pressure measured at 175 °C. When O_2 partial pressure was varied (from 5 to 40 mbar), the partial pressure of CO was fixed (10 mbar). When CO partial pressure was varied (from 5 to 40 mbar) the partial pressure of O_2 was fixed (10 mbar). Reaction orders (n_x) estimated as slopes of the linear fit. Error bars represent standard deviation of the five subsequent measurements at given pressure.

4.2.3 Structure and dynamics of Pd/CeO_2 SACs during CO oxidation

The EXAFS spectrum of the used 1PdRods catalyst shown in **Fig. 4.3a** is notably different from the one of the as-prepared sample (**Fig. 4.1c**). The decrease in the Pd-O CN from 3.1 to 2.6 and the appearance of an intense Pd-Pd shell at ~2.7 Å with CN of ~3 (**Table B1**) indicate partial reduction and clustering of the initially atomically dispersed Pd-oxo species during

CO oxidation. In contrast, the EXAFS spectrum of used 1PdFSP catalyst is similar to that of the as-prepared sample, suggesting a much higher stability of the FSP-prepared SAC. This is in line with the transient step-response experiment (**Fig. 4.2c**) and the reaction orders at 175 °C (**Fig. 4.2d**), which indicated the absence of metallic/reduced Pd species in 1PdFSP under reaction conditions.

The observed structural dynamics of the Pd SACs call for an *in situ* spectroscopy approach. We will use *in situ* near-ambient pressure X-ray photoelectron spectroscopy (NAP-XPS) to follow the surface electronic structure of working catalysts and *in situ* IR spectroscopy to probe the interaction of the surface sites with the reacting molecules. The NAP-XPS spectrum of the Pd 3d core-line shown in **Fig. 4.3b** reveals that the 1PdRods catalyst contains two Pd states during CO oxidation at 50 °C. The more intense component at 337.8 eV corresponds to atomically dispersed Pd^{2+} ions covalently bonded to CeO_2 [54–56]. The second one located at ~336 eV is attributed to small PdO_x clusters with a lower average oxidation state as compared to bulk PdO (~337 eV, **Fig. B13**) [57]. Hence, even under mild reaction conditions, Pd single atoms supported on nanorods are prone to reduction and agglomeration. At a reaction temperature of 300 °C almost half of the Pd turned into metallic (335.4 eV) and semi-oxidized (~336 eV) Pd species, which is in good agreement with the EXAFS (**Fig. 4.3a**) and X-ray absorption near edge structure (XANES) (**Fig. B14**) data. On the contrary, corresponding NAP-XPS spectra for the 1PdFSP sample contain only one state of Pd – atomically dispersed Pd^{2+} species – independent of the applied reaction conditions (**Fig. 4.3b**). According to the NAP-XPS results, the Pd speciation did not change even during CO oxidation at 300 °C.

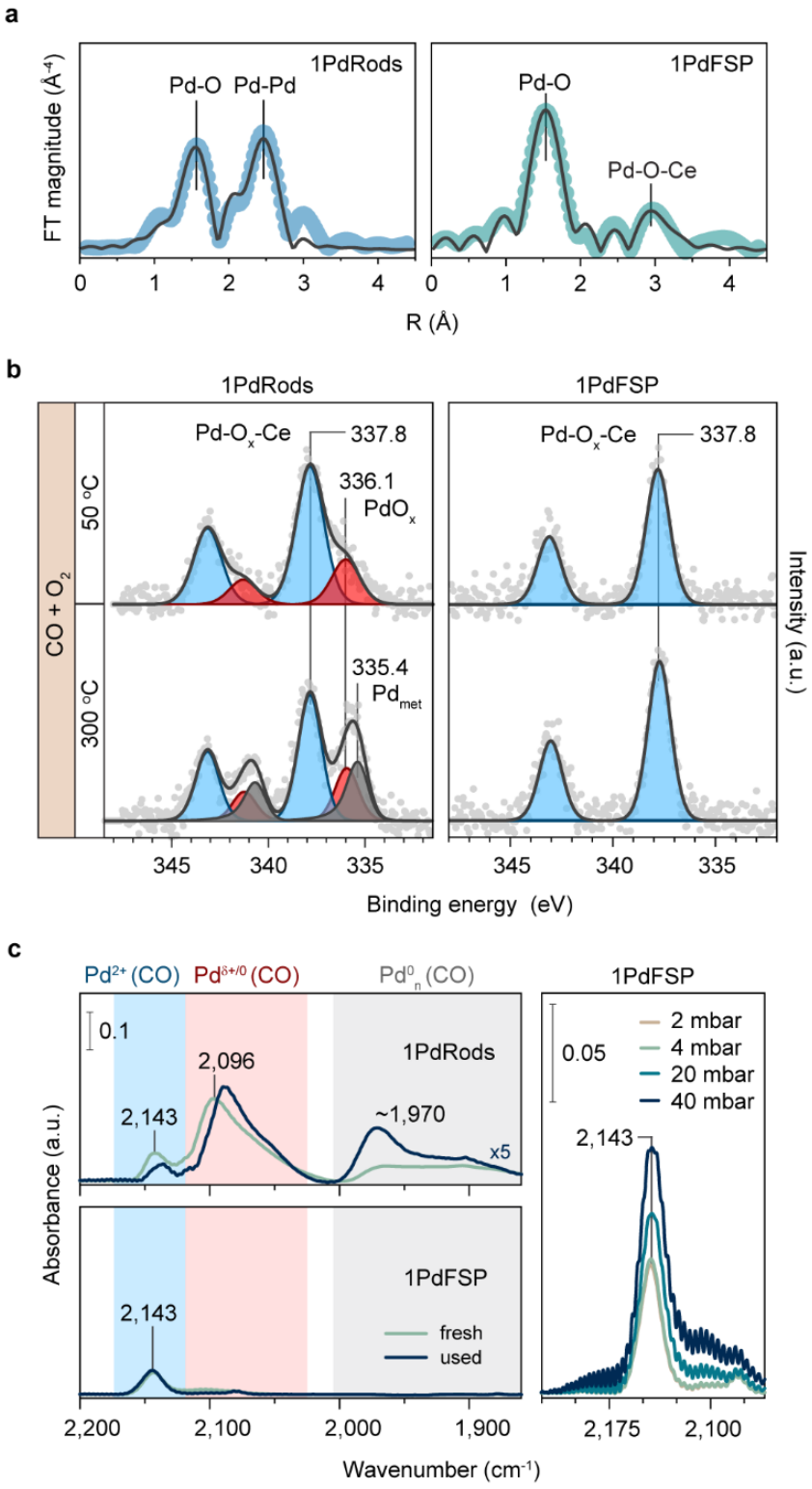

Figure 4.3. Reaction induced structural changes of the Pd sites**.** a) The k^3-weighted FT-EXAFS spectra (Pd K-edge) of catalysts after one reaction run up to 300 °C, circles represent the data and solid lines - fit. b) *In situ* NAP-XPS of Pd 3d core-line as a function of reaction conditions. Total pressure in the NAP cell was fixed to 2 mbar ($CO:O_2$ = 1:1). c) *In situ* DRIFTS spectra of fresh and used catalysts (after one light-off cycle up to 300 °C) at RT and 2 mbar of reactants ($CO:O_2$ = 1:1, 3.5 ml/min flow mode). Right panel shows an evolution of 2143 cm^{-1} band for 1PdFSP sample as a function of reactant pressure (CO to O_2 ratio was fixed to 1, total pressure is indicated).

In situ diffuse reflectance Fourier-transformed IR spectroscopy (DRIFTS) using CO as a probe molecule is sensitive to the electronic structure and nuclearity of the surface metal species in working catalysts [16,29]. Consistent with our previous findings [35], three major CO IR bands were observed for 1PdRods under reaction conditions (**Fig. 4.3c**). The band at 2143 cm^{-1} is assigned to CO adsorbed on Pd single atoms bound to CeO_2 via two bridged oxygens (Pd_1O_2) [35]. The band centered around 2096 cm^{-1} can be attributed to Pd single atoms bound to CeO_2 via one oxygen atom (Pd_1O_1) [35]. During CO oxidation, additional carbonyl bands appear at ~2060 cm^{-1} and ~1900 cm^{-1} (**Fig. B15**), which can be related to semi-oxidized and metallic Pd clusters, respectively [35]. The formation of these species can be caused by CO-assisted migration of Pd single atoms [34]. Comparing DRIFTS spectra of the fresh and used 1PdRods samples, we note a more pronounced contribution of bands related to metallic Pd species, in agreement with *in situ* NAP-XPS data (**Fig. 4.3b**). In contrast, 1PdFSP exhibited only one carbonyl band at 2143 cm^{-1}, corresponding to oxidized Pd single atoms, throughout the whole experiment. Increasing the CO partial pressure (**Fig. 4.3c**) did not lead to a shift in this IR band, indicating the absence of lateral interactions[17], and thereby further confirming the isolated nature of Pd sites in 1PdFSP. The superior structural stability of 1PdFSP in comparison to 1PdRods reveals stronger metal-support interactions in the former sample.

Structure-activity relationships of Pd/CeO_2 catalysts under study can be established by correlating the reaction kinetics and *in situ* spectroscopy results. The positive reaction orders in CO observed for both Pd SACs at low temperature (50 °C) point to the non-metallic nature of active Pd sites [14,51]. The low-temperature performance of 1PdRods catalyst during repeated CO oxidation runs was nearly unaffected by the increased fraction of reduced $Pd^{\delta+/0}$ species formed during the first run (**Figure B16** and **Note B5**). From this, we infer that these species do not contribute to the low-temperature activity. This is in line with step-response experiments (**Fig. 4.2c**) that indicated that a substantial fraction of Pd sites in 1PdRods are poisoned by CO at low reaction temperature. However, at elevated temperature (>100 °C) these $Pd^{\delta+/0}$ species, characterized by Pd $3d_{5/2}$ components with E_b < 337 eV in XPS and carbonyls below 2100 cm^{-1} in IR spectra, become active (**Fig. 4.2d**). In 1PdFSP sample the persistent carbonyl IR signature at 2143 cm^{-1} and the spectral component at 337.8 eV of the Pd $3d_{5/2}$ core-line confirm the oxidized nature of the Pd single-atom active sites. Together with the XAS data, these results prove that, irrespective of the applied reaction temperature, 1PdFSP is a structurally stable SAC.

4.2.4 Effect of Pd loading

A conventional approach to obtain stable SACs often involves decreasing the surface concentration of metal atoms down to one metal atom per support particle [16,17]. The 1PdFSP sample contains about 30 Pd atoms per particle, but the actual surface concentration of Pd is lower due to the partial inclusion of Pd into the CeO_2 bulk. Both XPS and CO chemisorption results confirm this (see **Note B6** and **Table B2**). The lower density of Pd single atoms on the surface of the 1PdFSP sample in principle, can explain its high stability during CO oxidation. To test this hypothesis, we prepared an additional set of catalysts with a higher Pd surface density by loading 5 wt% Pd on the two used ceria supports (denoted as 5PdFSP and 5PdRods, see **Note B7**). The 5PdFSP sample displayed a substantially higher low-temperature activity than 5PdRods. Although some PdO clusters were observed by TEM in both as-prepared catalysts (**Figs. B19, 21-23**), the apparent activation energies and reaction orders were similar to those of their 1 wt% Pd SACs counterparts (**Note B8** and **Figs. B25-26**). *In situ* NAP-XPS analysis of the 5PdFSP catalyst (**Fig. 4.4a**) revealed that isolated Pd^{2+} in Pd-O-Ce moieties (337.7 eV) are the dominant species in O_2 at 300 ºC. Remarkably, exposure to CO oxidation conditions below 200 ºC did not change the XPS spectra of the operating catalyst (see **Fig. B29** for MS-data), while higher temperatures led to the appearance of a small contribution (~5%) of metallic Pd. In contrast, extensive reduction of Pd species was observed for the 5PdRods sample already at 100 ºC (**Fig. 4.4b**). The strong stabilization of oxidized Pd single atoms on the surface of the 5PdFSP sample is also corroborated by *in situ* DRIFTS data (**Fig. B30**). The intensity of carbonyl band at 2143 cm^{-1} remained the same, even after reaction at 300 ºC. In contrast, the 5PdRods sample showed a lower intensity of the 2143 cm^{-1} band after the reaction as compared to the as-prepared state, explaining the partial loss of the low-temperature activity in the repeated reaction cycle (**Fig. B27**). Noteworthy, even a much lower loading of 0.2 wt% Pd on CeO_2 nanorods (0.2PdRods sample, **Figs. B31-32**) did not lead to a stable Pd SAC.

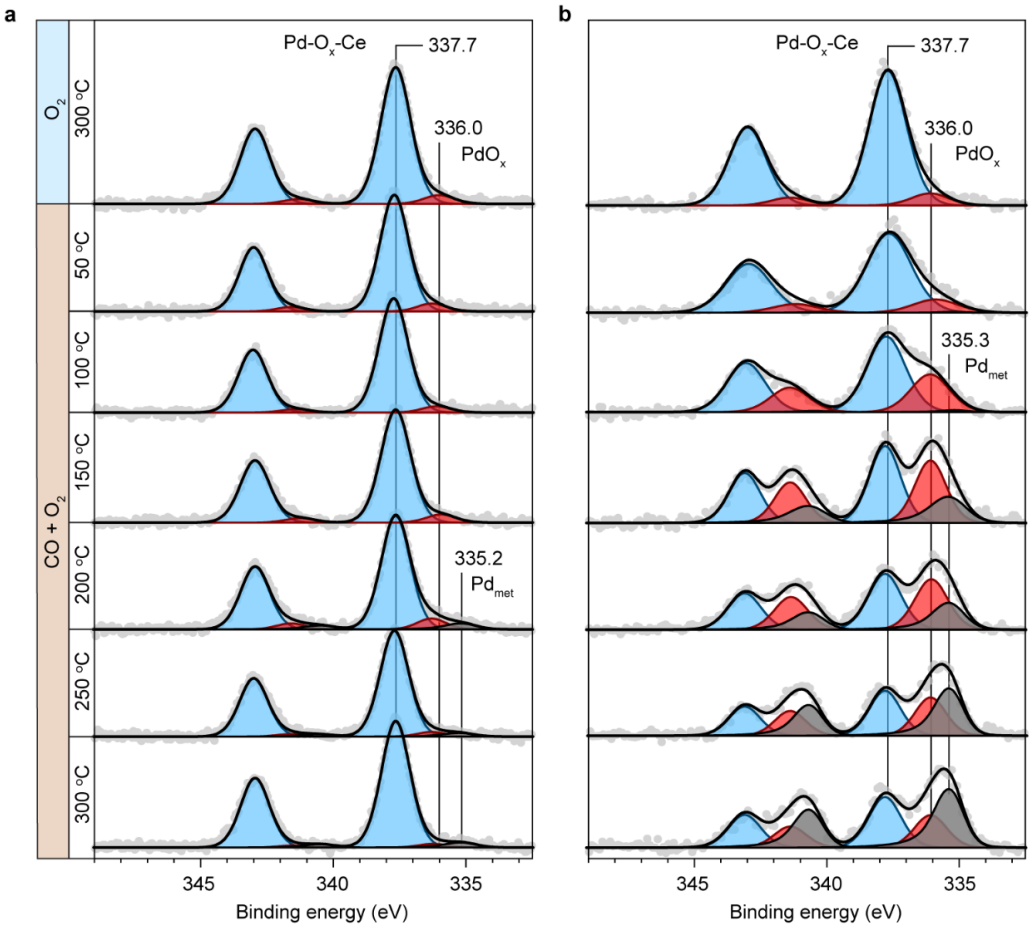

Figure 4.4. Pd speciation followed by *in situ* NAP-XPS. Pd 3d core-line spectra as a function of reaction conditions for a) 5PdFSP and b) 5PdRods. Total pressure in the NAP-cell was fixed to 2 mbar.

Based on the obtained results, we argue that the higher stability of Pd single atoms in FSP-derived catalysts is not related to the low Pd surface concentration. Instead, we attribute this to stronger MSI in the PdFSP materials. As both the FSP and Rods supports exhibit preferential (111) faceting, the effect of crystal termination cannot explain the difference between the PdFSP and PdRods samples (**Figs. B3-4** and **22-23**). The strength of the MSI has often been correlated with the redox properties of the support [4,30,39,58]. Doping with transition metals is known to influence the reducibility of ceria [25,46,59]. As a fraction of Pd atoms is doped into the CeO_2 lattice in the PdFSP catalysts, we surmise that the superior stability of surface Pd single atoms stems from the modified redox properties of the PdFSP samples. In the next section we will investigate the redox phenomena at the Pd-CeO_2 interface.

4.2.5 Reducibility of the Pd-CeO_2 interface

We first studied the reactivity of Pd-CeO_2 interface in the Pd SACs using CO titration followed by *in situ* DRIFTS as depicted in **Figs. B33-34**. In the absence of O_2, the Pd^{2+} single atoms

readily react with CO at 50 °C to form metallic species. Quantitative data were obtained by CO pulsing titration at the same temperature, according to the scheme: $PdO_x + CO \rightarrow Pd + CO_2$. The $[O_{titr}]$/Pd ratio was considerably higher than unity (**Table B3**). Assuming that Pd is atomically dispersed, it can be estimated from these titration results that two reactive oxygen atoms exist per Pd site in the fresh 1PdRods catalyst. This agrees with the DFT-supported structure of $Pd_1O_2/CeO_2(111)$ reported in a previous work (**Fig. B7**) and which was used here to fit the EXAFS data [35]. For the 1PdFSP sample, the same procedure results in three reactive oxygen atoms per Pd atom, suggesting a different structure of the Pd sites. The involvement of oxygen atoms of the CeO_2 support in CO oxidation, which was indicated by negative reaction orders in O_2, can explain the titration results. Thus, in the following part we will focus on the redox dynamics of the two components of the metal-support interface, *i.e.*, Pd and CeO_2.

Using lab-based *in-situ* NAP-XPS, we did not observe significant changes in the Ce^{3+} concentration as a proxy for the formation of oxygen vacancies under CO oxidation conditions (**Fig. B28**). Although this may indicate that ceria reduction does not take place, we need to consider that short-lived reactive Ce^{4+}/Ce^{3+} sites can be present in low concentrations during steady-state reaction [28]. Moreover, as Ce^{3+} is preferentially located in the top-most surface layers[60], a conventional lab-based X-ray source (Al K_α, hν = 1486.7 eV) may not offer sufficient surface sensitivity. Therefore, more valuable information can be obtained by probing the system as a function of the reactant chemical potential[28] and at lower excitation energy. To follow the formation of Ce^{3+} at the very surface, we turned to synchrotron radiation-based (resonant) photoelectron spectroscopy. Access to the low excitation energies allows *in situ* probing Pd and Ce electronic states in the outermost layers at a depth less than ~10 Å. In turn, the use of resonant photoelectron spectroscopy (RPES) offers substantially higher sensitivity to changes in Ce^{3+} concentration at the very surface as compared to conventional Ce 3d core-line spectroscopy [38,54]. Ce-related electronic states were characterized by analyzing the Ce 4d-4f transitions, which resonate at specific energies. The exact thresholds were experimentally determined by mapping of the valence band as a function of incident photon energy (**Fig. B35**). Intense features, appearing in the valence band at photon energies of 124 eV and 120 eV, correspond to Ce^{4+} and Ce^{3+} states, respectively. Off-resonance spectra recorded at 114 eV were used to estimate the Ce^{3+}/Ce^{4+} ratios (**Fig. 4.5b**).

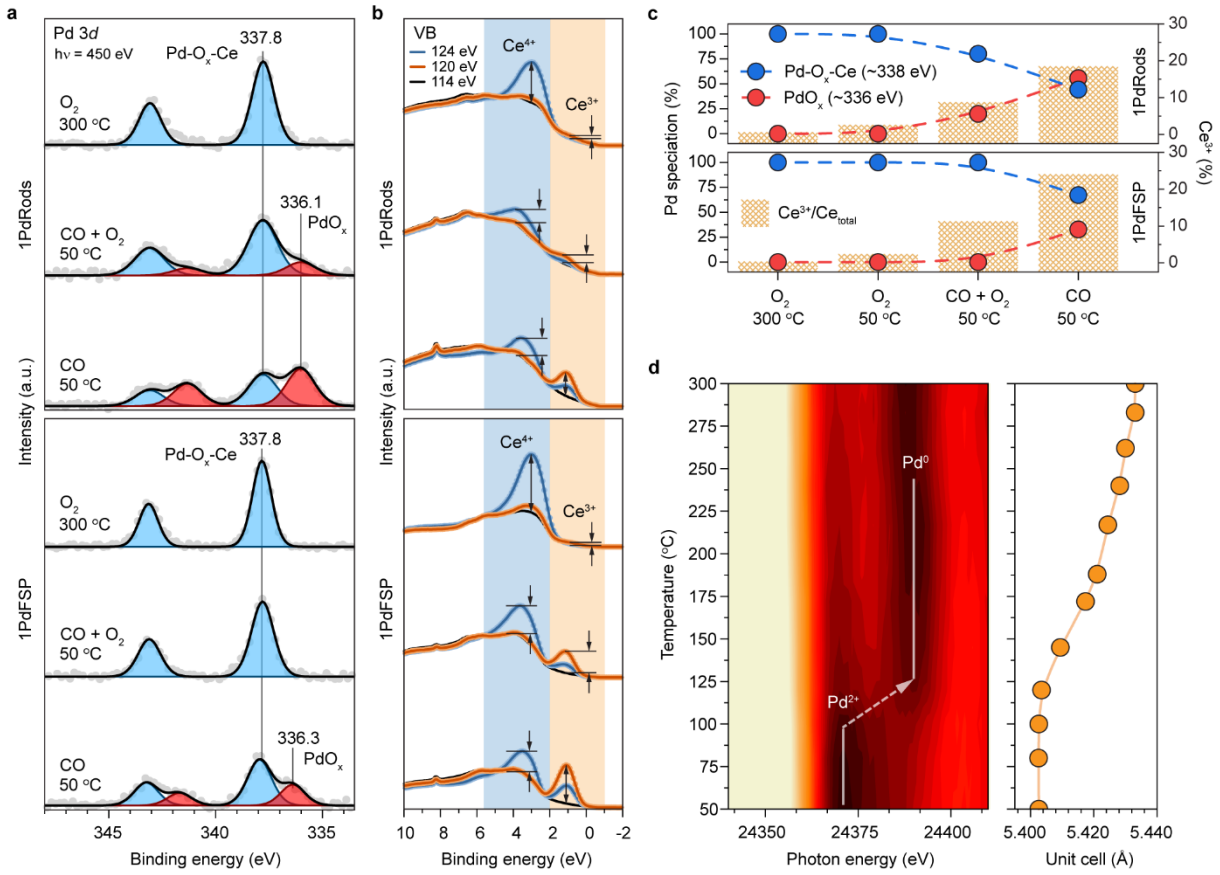

Figure 4.5. Redox chemistry of Pd-CeO_2 interface probed by *in situ* spectroscopy. *In situ* NAP-XPS and RPES data acquired in 0.1 mbar of reactants for 1PdRods and 1PdFSP: a) Pd 3d core-line region and b) valence band region. The intensities of Ce^{4+} and Ce^{3+} related features, appearing at respective resonant energies, were used for estimation of Ce^{3+} atomic fraction. c) Pd and Ce oxidation state dynamics derived from XPS and RPES data. d) Evolution of Pd K-edge XANES and CeO_2 unit cell parameter of 5PdFSP sample during TPR-CO monitored by *in situ* XAS/WAXS.

As shown in **Figs. 4.5a-b**, both Pd SACs contain exclusively oxidized Pd^{2+} single atoms on a nearly stoichiometric CeO_2 surface (Ce^{3+} ~ 1%, **Fig. 4.5c**) under oxidizing conditions. Exposure of the 1PdRods sample to the reaction mixture at 50 °C led to the formation of semi-oxidized Pd clusters. In contrast, the isolated Pd^{2+} state was preserved in 1PdFSP sample. The high surface sensitivity of RPES resolves even subtle differences in the Ce^{3+} concentration under reaction conditions (11% of Ce^{3+} for 1PdFSP and 9% for 1PdRods). Switching the reaction feed to pure CO resulted in a deeper reduction of Pd in 1PdRods than in 1PdFSP, in line with the DRIFTS findings (**Figs. B33-34**). The reverse was observed for the Ce reduction degree. Upon CO exposure 24% and 19% of Ce^{3+} was formed at the surface of 1PdFSP and 1PdRods, respectively. Under identical conditions the surface of the bare FSP support contained 17% of Ce^{3+}. In line with CO titration results, the higher concentration of oxygen vacancies confirms that Pd increases the surface reducibility of the 1PdFSP catalyst. (**Fig. B36**). The high oxygen mobility at the Pd-CeO_2 interface can explain the strong

stabilization of oxidized Pd single atoms. Altogether, these observations point to the importance of the reverse oxygen spillover from the support to Pd single atoms. In this way, the isolated ionic Pd sites can be preserved even under reducing conditions due to a sufficient oxygen supply from the support, as previously seen for Pt/CeO_2 SACs [61].

To complete the investigation of the redox properties of the Pd-CeO_2 interface, we studied the 5 wt% Pd catalysts by a combination of *in situ* XAS and wide-angle X-ray scattering (WAXS). These bulk-sensitive techniques simultaneously probe the speciation of Pd via XANES at the Pd K-edge and Ce via WAXS analysis of the unit cell parameter, which increases upon Ce^{3+} formation [62]. As follows from **Fig. 4.5d**, for the FSP-derived sample Pd reduction in a CO flow starts at 80 ºC, while ceria lattice expansion, indicative of bulk Ce^{3+} formation, is delayed. Once sufficient metallic Pd has been formed, *i.e.*, ~50% of all Pd species, Ce^{3+} starts to emerge at ~125 °C as manifested by the shift of CeO_2 reflections towards lower angles (**Figs. B37-38**) [62]. The bulk reduction of ceria, induced by the formation of Pd metal, is another indication of reverse oxygen spillover [38,58]. Notable Ce^{3+} formation in the bulk for the impregnated 5PdRods catalyst was observed only at ~200 ºC, which points to a lower mobility of oxygen in this sample (**Figs. B39-40**). Importantly, thermal treatment in O_2 or $CO+O_2$ did not lead to substantial shifts in the diffraction patterns apart from those related to thermal lattice expansion (**Fig. B42**). This is in line with the lab-based NAP-XPS findings, emphasizing a low Ce^{3+} concentration under these conditions.

To conclude, we demonstrated that the oxygen mobility in the PdFSP system is higher both in the bulk and at the surface. Previous DFT studies predicted substantially lower barriers for oxygen vacancy formation in the vicinity of the doped square-planar Pd_1O_4 structural motif [46,59]. In turn, surface reducibility of the support is key for the stabilization of noble metals anchored in ionic single-atom form [4,61]. Oxygen atoms spilled over from the support to Pd single atoms suppress their reduction under the reaction conditions, which is crucial for preservation of the isolated nature of Pd-oxo species. Our earlier theoretical findings[35] revealed that reduced Pd adatoms are prone to migration over the ceria surface and form metallic clusters inactive in low-temperature CO oxidation. Facile oxygen transport at the Pd-CeO_2 interface, enabled by doping of nanosized ceria with Pd, explains the stability of oxidized Pd single atoms on the surface of FSP-derived catalysts.

4.3 Conclusions

Herein, we demonstrate that two Pd/CeO_2 SACs, which are similar in the as-prepared state, evolve in a different manner under reaction conditions. Isolated ionic Pd species, obtained by impregnation on the surface of CeO_2 nanorods, undergo swift reduction and agglomeration into metallic clusters during CO oxidation (**Fig. 4.6a**). Pd/CeO_2 SACs with high surface area can be prepared by a single-step FSP method. The surface Pd single atoms on FSP-derived catalysts show a high resistance against sintering under CO oxidation conditions (**Fig. 4.6b**). Analysis of the transient and steady-state CO oxidation kinetics combined with *in situ* NAP-XPS, DRIFTS and EXAFS revealed that isolated surface Pd^{2+} sites are responsible for the low-temperature CO oxidation in both catalysts, while reduced $Pd^{\delta+/0}$ species become active at elevated temperature. By following the Ce^{4+}/Ce^{3+} and $Pd^{2+}/Pd^{\delta+/0}$ redox dynamics, we established that doping by Pd ions activates lattice oxygen of the CeO_2 support and facilitates reverse oxygen spillover at the Pd-O-Ce interface. The mobility of oxygen at the metal-support interface has a strong impact on the stability and reactivity of the Pd SACs. These findings open up an alternative approach for the rational design of active and stable single-atom catalysts, where lattice oxygen can be activated by doping the support with transition metals. The insight that the speciation of the supported metal is strongly influenced by the redox properties of the support is also relevant to other catalytic reactions involving metal-support interface such as methane dry reforming, the water gas-shift reaction and CO_2 hydrogenation

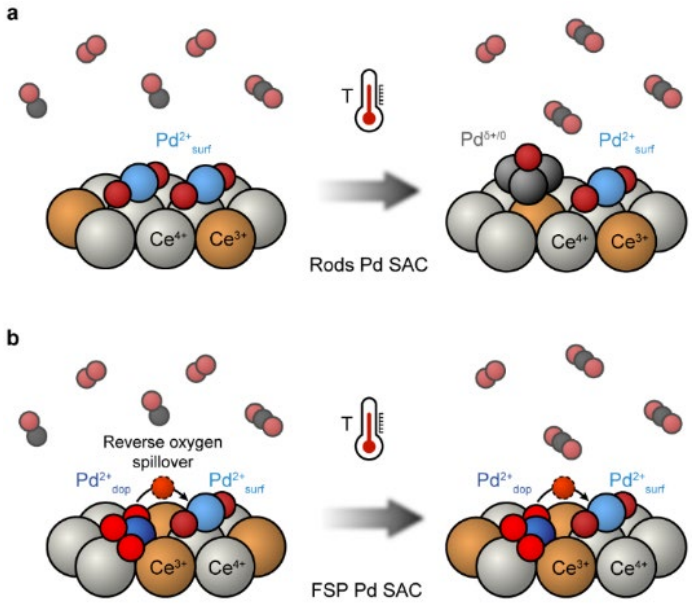

Figure 4.6. Schematic overview of the SACs evolution during CO oxidation revealed by *in situ* spectroscopy. a) Oxidized Pd single atoms on the surface of CeO_2 nanorods undergo reduction and agglomeration into metallic clusters at elevated temperatures. b) Pd-doped sites, inherently present in FSP-derived catalysts, facilitate oxygen mobility at the Pd-CeO_2 interface and via reverse oxygen spillover preserve oxidized Pd single-atom moieties.

4.4. Materials and Methods

Catalyst synthesis

All chemicals were purchased from Sigma-Aldrich and used without further purification. CeO_2 nanorods were prepared according to the procedure reported elsewhere.[35,36] The synthesis scheme is depicted in **Figure B1**. In brief, 25 g of NaOH (reagent grade, ≥ 98%) was dissolved in 30 mL of demineralized water. An aqueous solution of 2.17 g of $Ce(NO_3)_3{\cdot}6H_2O$ (99% purity) in 5 mL was prepared. Consequently, two solutions were poured together, and the obtained slurry was stirred at room temperature for 1 h. Next, the volume was increased to ~ 100 mL by adding demineralized water and the slurry was transferred into a 125 mL Teflon liner. This liner was then sealed in a stainless-steel autoclave, which was placed in the oven for 24 h at 100 ºC. After cooling in a water bath, the obtained precipitate was washed by 5 cycles of centrifugation, decantation and redispersion until pH ~ 7-8 was obtained. The resulting solid was dried in a vacuum oven for 2 h at 80 ºC and then calcined in air at 500 ºC. Subsequently, wet impregnation of CeO_2 nanorods using $Pd(NO_3)_2{\cdot}2H_2O$ as Pd precursor was performed. An appropriate amount of Pd salt was dissolved in demineralized water (10 mL) and poured onto the calcined CeO_2 powder. The resulting mixture was vigorously stirred for 30 minutes at room temperature and then slowly heated to evaporate the water without boiling. The obtained solid was dried overnight at 110 ºC and subsequently calcined in air at 300 ºC. The calcined samples were denoted as 1PdRods and 5PdRods, depending on the intended Pd loading.

Flame-spray pyrolysis (FSP) synthesis was performed using a commercial TETHIS NPS10 apparatus. The principle scheme of the synthesis setup can be found in **Figure B1**. The precursor solution was prepared by dissolving $Ce(acac)_3{\cdot}H_2O$ (99.9% purity) and $Pd(acac)_2{\cdot}H_2O$ (99% purity) salts in glacial acetic acid (99.7% purity), giving rise to 0.1 M Ce precursor solution, while the Pd molarity was varied targeting a particular Pd loading. To increase the solubility of the salts, the solution was slightly heated to ~ 50 ºC and stirred for 0.5 h. The fully transparent solution was then transferred into the syringe of the FSP setup. The solution was injected at a feed rate of 5 mL min^{-1} into the methane/oxygen flame (1.5 L min^{-1} of methane and 3.0 L min^{-1} of oxygen). An oxygen flow of 5.0 L min^{-1} was used for the dispersion of the solution, giving rise to an overpressure at the nozzle of ~ 2.5 bar. Upon pyrolysis in the flame the nanoparticles are formed and deposited on the quartz fibre filter

in the upper part of the setup. The powders collected from the filter were denoted as 1PdFSP and 5PdFSP depending on the intended Pd loading.

Activity measurements

Catalytic activity was evaluated using a high-throughput setup with a 10-tube parallel flow reactor. The catalysts were sieved with a fraction between 125 and 250 µm. The catalyst bed was packed between quartz wool plugs in each quartz tube reactor. Typically, 50 mg of catalyst (if not stated otherwise) was mixed with 250 mg of SiC of the same sieved fraction as an inert diluent material. The catalytic testing was performed at atmospheric pressure. The catalysts were pretreated for 1 h at 300 °C in a 20% O_2/80% He flow (50 mL min^{-1} per reactor). After cooling down to RT, the reaction mixture of 1% CO + 1% O_2 in He was fed for 0.5 h. Subsequently, stepwise heating to 300 °C at a rate of 5 °C min^{-1} was performed. Each measurement point was acquired isothermally after 15 min of stabilization. The effluent gas was analyzed by online gas chromatography using an Interscience Compact GC equipped with Plot and Molsieve columns and thermal conductivity detectors (TCD). Catalytic data used for Arrhenius plots were measured in the light off regime (5 °C min^{-1}, 1% CO + 1% O_2 in He, 200 mL min^{-1}) using a mass spectrometer. High gas-hourly space velocities (up to 1,200,000 mL g_{cat}^{-1} h^{-1}), dilution with SiC and low loading of catalysts were used to ensure differential conditions with conversion levels below 5% (see **Note B1**). Further details of catalytic activity measurements can be found in the captions of the figures.

Step-response studies were performed using the setup designed for the transient kinetic experiments. Two parallel gas lines were connected to a four-way valve, which allows rapidly switching between the two feed flows. Pressure difference between the two feed flows did not exceed 0.02 mbar. A low dead-volume stainless-steel tubular reactor of 5 mm inner diameter and 80 mm bed length was used. The catalytic activity in steady state was determined by online gas chromatography (VARIAN CP-3800 equipped with TCD and FID). The concentrations of CO (m/z = 28), O_2 (m/z = 32), CO_2 (m/z = 44), Ne (m/z = 22), and Ar (m/z = 40) were monitored by an online quadrupole mass spectrometer (GeneSys). Typically, 20 mg of sample diluted with SiC was loaded in the stainless-steel reactor. Prior to reaction, the sample was pretreated in O_2 flow (20% O_2 in Ar, 50 mL min^{-1} in total) at 300 °C using a heating rate of 10 °C min^{-1} and atmospheric pressure for 2 h. Subsequently, the sample was cooled to 50 °C in an O_2 flow (3.5% in Ar, 50 mL min^{-1} in total) and the pressure was increased to 1.5 bar. Thereafter, the feed was switched to a flow containing a mixture of CO (1 vol%),

O_2 (3.5 vol%), and Ar (50 mL min^{-1} in total) for ~48 h to ensure steady-state conversion. Then the switch to O_2 flow (3.5% in Ar, 50 mL min^{-1} in total) was performed.

Characterization

Atomic resolution high-angle annular dark-field scanning transmission electron microscopy (HAADF-STEM) images of various samples were acquired by JEOL JEM ARM200F with Cs-corrected (probe) operating at 200 kV. The samples for analysis were dispersed in ethanol followed by addition of a few drops on lacey carbon films supported on copper grids. Energy-dispersive X-ray spectroscopy (EDX) data were obtained using an Oxford Instruments X-Max 100TLE system.

N_2-physisorption at 77 K was employed using a Micromeritics TriStar II 3020 instrument. Typically, 100 mg of sample were kept in N_2 flow at 150 °C overnight to desorb water and other impurities. The Brunauer-Emmet-Teller (BET) method was utilized to determine the surface area.

The Pd weight loading was determined using inductively coupled plasma optical emission spectrometry (ICP-OES) with a Spectroblue, AMETEK Inc. instrument. Nanorod-shaped catalysts were dissolved in concentrated H_2SO_4 under vigorous stirring at 250 °C. Once fully transparent, solution was cooled and further diluted with demineralized water for analysis. FSP-derived samples often contain some residues from the quartz fibre filter from which the powders were collected. Therefore, a melting process of the sample and $K_2S_2O_7$ was employed using a Bunsen burner The melt was subsequently dissolved in concentrated H_2SO_4 and 4% HF was added to dissolve any glass fibres. The resulting solutions were further diluted for analysis. The measurements were performed *in duplo*.

Powder X-ray diffraction was used to determine the crystalline structure of the as-prepared materials. Bruker D2 Phaser diffractometer with Cu Kα (1.54 Å) radiation was used.

In situ near-ambient pressure photoelectron spectroscopy (NAP-XPS) was performed on SPECS system. The core-line spectra were acquired using monochromatized Al Kα (1,486.6 eV) irradiation generated by Al anode (SPECS XR-50) operating at 50 W. A differential pumping system of the electron analyser (SPECS Phoibos NAP-150) allows normal emission XPS measurements in the presence of gases (up to ~20 mbar). To avoid sample charging (see **Note B10**) the catalyst powder was pelletized with a conductive diluent and directly

fixed onto the stainless-steel sample holder. The NAP-cell was operated in a flow mode keeping constant total pressure of 2 mbar using an electronic back-pressure regulator. Gas mixtures were fed using calibrated mass-flow controllers with a maximum total flow of 2 mL min^{-1}. All the gasses were of high purity (99.999%). For pretreatment, O_2 was fed into the cell followed by heating the sample to 300 °C. After cooling to room temperature, oxygen was replaced by the reaction mixture ($CO:O_2$ = 1:1). Whilst recording the spectra, the gas-phase composition was followed using a standard residual gas analyser (MKS e-Vision 2) located in the differential pumping system. All XPS spectra were recorded isothermally. The total acquisition time of the survey spectrum, including the O 1s, C 1s, Ce 3d and Pd 3d regions, was around 1.5 h. A pass energy of 40 eV was typically used with a step size of 0.1 eV and a dwell time of 0.5 s. The binding energies were corrected to the U''' component of the Ce 3d line with a characteristic position of 916.7 eV[26,50,60], allowing reliable energy calibration of the photoelectron spectra at different reaction conditions. To estimate atomic surface ratios, a standard procedure including use of atomic sensitivity factors and subtraction of the Shirley background was applied. Spectral lines were fitted using a symmetric pseudo-Voigt function referred to as GL(30) using the CasaXPS software. Pd 3d spectra containing a metallic Pd component were fitted using an asymmetric pseudo-Voigt function (LF (0.76, 1.5, 55, 300)). The Ce 3d line was fitted according to a model described elsewhere [60,63].

Surface-sensitive *in situ* resonant photoelectron spectroscopy (RPES) and NAP-XPS were performed at NAPP endstation of CIRCE beamline, ALBA Synchrotron. Spectra acquisition was done with a SPECS Phoibos NAP-150 electron analyser equipped with a differential pumping system allowing XPS measurements in a gaseous environment (up to ~ 20 mbar). A take-off angle of ~45° was used to enhance surface sensitivity. The analysis chamber (backfilling design) was pressurized up to ~0.1 mbar using mass-flow controllers and high purity gases. Pretreatment and reaction mixtures were identical to the ones used for lab-based NAP-XPS study. Switches between gaseous environments were performed without evacuation to high vacuum conditions. The Pd 3*d* core-line was recorded at 450 eV incident photon energy, giving rise to a probing depth of ~10 Å. After linear background subtraction, spectral lines were fitted in a similar manner to lab-based NAP-XPS data. For RPES study, variable photon energy allowed selective excitation of Ce 4*d*-4*f* transitions directly related to the concentration of Ce^{3+} and Ce^{4+} [10,38,63]. By mapping the valence band region as a function of the incident photon energy, we determined the energies required for resonant

enhancement of Ce^{3+} and Ce^{4+} features (see details in **Fig. B35**). The heights of the respective resonant peaks were used to obtain Ce^{3+}/Ce^{4+} ratios, according to the procedure reported earlier. Using this approach, the Ce^{3+} concentration at the very surface (~ 10 Å) can be obtained [10,38,63].

Conventional UHV XPS was performed using a K-Alpha XPS spectrometer (Thermo Scientific) equipped with an Al anode (Al Kα = 1486.68 eV) monochromatized X-ray source. Powder samples were placed on double-sided carbon tape and spectra were acquired using the flood-gun source to account for surface charging. All spectra were analysed using the CasaXPS software package. The same data processing approach was used as in case of XPS measurements performed on SPECS instruments described above.

In situ DRIFT spectroscopy was employed using a Bruker Vertex 70v Fourier transform (FT) infrared spectrometer equipped with a mercury-cadmium-telluride (MCT) detector. Each spectrum was collected by averaging 100 scans with a resolution of 4 cm^{-1} in 4,000-400 cm^{-1} range. The experiments were performed using a Praying Mantis accessory and a commercial in-situ cell (Harrick). Fine powder samples were put in the cell dome without dilution and the thermocouple was located in the centre of the catalyst bed. Gases were introduced in the cell using calibrated mass-flow controllers and pressure in the cell was regulated by the back- pressure controller. First, the samples were pretreated in 40 mbar of oxygen at 300 °C and then cooled to room temperature, followed by recording a background spectrum. Then, either pure CO (2 mbar) or $CO+O_2$ (2 mbar) were introduced and spectra were collected. All measurements were performed under flow and fixed total pressure. Transmission FTIR low-temperature CO adsorption was performed using Bruker Vertex 70v spectrometer equipped with a deuterated-triglycine sulfate (DTGS) detector. A home-built environmental transmission infrared cell was used. Self-supporting pellets were made by pressing approximately 10 mg of a sample in a disc with a diameter of 13 mm. Each spectrum was collected by averaging 64 scans with a resolution of 2 cm^{-1} in the 4,000–1,000 cm^{-1} range. The samples were pretreated in 200 mbar of O_2 at 300 °C, then cooled to room temperature and evacuated. Subsequently, the cell was cooled to -160 °C via internally circulating liquid N_2 and background spectra was recorded. CO was dosed to the cell and spectra were recorded. Afterwards, CO desorption was performed by gradual heating of the sample to room temperature.

X-ray absorption spectroscopy (XAS) was performed at the DUBBLE BM26A beamline at the ESRF and the B18 beamline at the Diamond Light Source. Data was collected at the Pd K-edge (24350 eV) in fluorescence mode. Energy calibration was performed using Pd foil. Collected XAFS data were background-subtracted, normalized, and fitted using linear combination fitting (LCF) as implemented in the Athena software package. EXAFS analysis on k^3-weighted Pd K-edge data was performed with Artemis. Scattering paths were calculated with FEFF6 using crystal structures of PdO and the DFT-optimized Pd models [35, 46]. The amplitude reduction factor S_0^2 was determined by fitting the first and second shell Pd-O and Pd-Pd scattering paths, fixing the coordination numbers to 4 and 12, respectively, of a PdO reference sample.

A simultaneous *in situ* wide-angle X-ray scattering (WAXS) and XAS study was performed at the DUBBLE BM26A beamline at the ESRF. 2D X-ray patterns were collected with a CCD detector (FReLoN) at an X-ray beam wavelength of 0.51 Å. The instrumental parameters were calibrated using NIST LaB_6 as a standard reference. Fit2D software was used for integration of the 2D patterns and GSAS-II was applied for Rietveld refinement using pseudo-Voigt function for the peak shape. XANES spectra at Pd K-edge were measured in fluorescence mode and processed with Athena software. Both XAS and WAXS data were acquired as a function of temperature. A capillary Clausen cell reactor was used for the *in-situ* measurements. Fine powder of pure sample (~2-3 mg) was loaded between two quartz wool plugs. The thermocouple was in direct contact with catalyst bed. For pretreatment, 1.5 mL min^{-1} O_2 and 2 mL min^{-1} He were fed over the sample upon heating to 300 °C at a rate of 10 °C min^{-1}. After cooling to 50 °C, the reaction mixture (0.5 mL min^{-1} CO, 0.5 mL min^{-1} O_2, 2 mL min^{-1} He) was fed to the sample, while heating to 300 °C at a rate of 10 °C min^{-1}. After cooling to 50 °C, 0.5 mL min^{-1} CO and 2 mL min^{-1} He was flowed under heating to 300 °C at a ramp rate of 5 °C min^{-1} (TPR-CO regime).

CO pulsing chemisorption and titration experiments were utilized using a Micromeritics Autochem II 2920 instrument. Typically, 50 mg of the catalyst was loaded in tubular quartz reactor. The sample was pretreated at 300 °C in 20 vol% O_2 in He at a flow rate 50 mL min^{-1}. For the chemisorption experiments, after cooling to room temperature the reactor was flushed with He for 40 min and a NaCl-ice bath was used to reach -20 °C. After the TCD signal was stable, pulses (50 µL) of pure CO were dosed into the He feed until saturation (*i.e,* when

no changes of the peak area were observed anymore). The amount of CO adsorbed on the sample was calculated from the peak areas of the TCD signal. For the titration experiments, ~50 mg of catalyst was loaded in U-shape quartz reactor. After pretreatment at 300°C in 20 vol% O_2 in He a flow rate of 50 mL min^{-1}, the sample was cooled to 50°C and flushed with He for 40 min. After TCD signal stabilised, pulses (50 µL) of pure CO were dosed into the He flow until saturation. Quantification was performed in the same manner as for the CO chemisorption procedure.

4.5 References

1. van Deelen, T. W., Hernández Mejía, C. & de Jong, K. P. *Nat. Catal.* **2,** 955–970 (2019).
2. O'Connor, N. J., Jonayat, A. S. M., Janik, M. J. & Senftle, T. P. *Nat. Catal.* **1,** 531–539 (2018).
3. Hackett, S. F. J., Brydson, R. M., Gass, M. H., Harvey, I., Newman, A. D., Wilson, K. & Lee, A. F. *Angew. Chem. Int. Ed.* **46,** 8593–8596 (2007).
4. Lang, R., Xi, W., Liu, J.-C., Cui, Y.-T., Li, T., Lee, A. F., Chen, F., Chen, Y., Li, L., Li, L., Lin, J., Miao, S., Liu, X., Wang, A.-Q., Wang, X., Luo, J., Qiao, B., Li, J. & Zhang, T. *Nat. Commun.* **10,** 234 (2019).
5. Herzing, A. A., Kiely, C. J., Carley, A. F., Landon, P. & Hutchings, G. J. *Science* **321,** 1331–1335 (2008).
6. Le, Y., Mehmood, F., Lee, S., Greeley, J., Lee, B., Seifert, S., Winansl, R. E., Elám, W., Meyer, R. J., Redfern, P. C., Teschner, D., Schlö'Gl, R., Pellin, M. J., Curtiss, L. A. & Vajda, S. *Science* **328,** 224–228 (2010).
7. Parastaev, A., Muravev, V., Huertas Osta, E., van Hoof, A. J. F., Kimpel, T. F., Kosinov, N. & Hensen, E. J. M. *Nat. Catal.* **3,** 526-533 (2020).
8. Yang, X. F., Wang, A., Qiao, B., Li, J., Liu, J. & Zhang, T. *Acc. Chem. Res.* **46,** 1740–1748 (2013).
9. Li, J., Li, X., Zhai, H. J. & Wang, L. S. *Science* **299,** 864–867 (2003).
10. Lykhach, Y., Kozlov, S. M., Skála, T., Tovt, A., Stetsovych, V., Tsud, N., Dvořák, F., Johánek, V., Neitzel, A., Mysliveček, J., Fabris, S., Matolín, V., Neyman, K. M. & Libuda, J. *Nat. Mater.* **15,** 284–288 (2016).
11. Campbell, C. T. *Nat. Chem.* **4,** 597-598 (2012).
12. Flytzani-Stephanopoulos, M. & Gates, B. C. *Annu. Rev. Chem. Biomol. Eng.* **3,** 545–574 (2012).
13. Qiao, B., Wang, A., Yang, X., Allard, L. F., Jiang, Z., Cui, Y., Liu, J., Li, J. & Zhang, T. *Nat. Chem.* **3,** 634–641 (2011).
14. Yu, W.-Z., Wang, W.-W., Li, S.-Q., Fu, X.-P., Wang, X., Wu, K., Si, R., Ma, C., Jia, C.-J. & Yan, C.-H. *J. Am. Chem. Soc.* **141,** 17548-17557 (2019).
15. Li, J., Guan, Q., Wu, H., Liu, W., Lin, Y., Sun, Z., Ye, X., Zheng, X., Pan, H., Zhu, J., Chen, S., Zhang, W., Wei, S. & Lu, J. *J. Am. Chem. Soc.* **141,** 14515–14519 (2019).
16. DeRita, L., Resasco, J., Dai, S., Boubnov, A., Thang, H. V., Hoffman, A. S., Ro, I., Graham, G. W., Bare, S. R., Pacchioni, G., Pan, X. & Christopher, P. *Nat. Mater.* **18,** 746-751 (2019).
17. DeRita, L., Dai, S., Lopez-Zepeda, K., Pham, N., Graham, G. W., Pan, X. & Christopher, P. *J. Am. Chem. Soc.* **139,** 14150–14165 (2017).
18. Lin, J., Wang, A., Qiao, B., Liu, X., Yang, X., Wang, X., Liang, J., Li, J., Liu, J. & Zhang, T. *J. Am. Chem. Soc.* **135,** 15314–15317 (2013).
19. Jones, J., Xiong, H., DeLaRiva, A. T., Peterson, E. J., Pham, H., Challa, S. R., Qi, G., Oh, S., Wiebenga, M. H., Pereira Hernandez, X. I., Wang, Y. & Datye, A. K. *Science* **353,** 150–154 (2016).
20. Trovarelli, A. *Catal. Rev.* **38,** 439–520 (1996).
21. Montini, T., Melchionna, M., Monai, M. & Fornasiero, P. *Chem. Rev.* **116,** 5987–6041 (2016).
22. Bruix, A., Lykhach, Y., Matolinova, I., Neitzel, A., Skala, T., Tsud, N., Vorokhta, M., Stetsovych, V., Sevcikova, K., Myslivecek, J., Fiala, R., Vaclavu, M., Prince, K. C., Bruyere, S., Potin, V. V., Illas, F., Matolin, V., Libuda, J. J., Neyman, K. M. *Angew. Chem. Int. Ed.* **53,** 10525–10530 (2014).
23. Dvořák, F., Camellone, M. F., Tovt, A., Tran, N., Negreiros, F. R., Vorokhta, M., Skála, T., Matolínová, I., Mysliveček, J., Matolín, V. & Fabris, S. *Nat. Commun.* **7,** 1–8 (2016).

24. Sarma, B. B., Kim, J., Amsler, J., Agostini, G., Weidenthaler, C., Pfänder, N., Arenal, R., Concepción, P., Plessow, P., Studt, F. & Prieto, G. *Angew. Chem. Int. Ed.* **59,** 5806-5815 (2020).
25. Riley, C., Zhou, S., Kunwar, D., de La Riva, A., Peterson, E., Payne, R., Gao, L., Lin, S., Guo, H. & Datye, A. *J. Am. Chem. Soc.* **140,** 12964–12973 (2018).
26. Pereira-Hernández, X. I., DeLaRiva, A., Muravev, V., Kunwar, D., Xiong, H., Sudduth, B., Engelhard, M., Kovarik, L., Hensen, E. J. M., Wang, Y. & Datye, A. K. *Nat. Commun.* **10,** 1358 (2019).
27. Gänzler, A. M., Casapu, M., Vernoux, P., Loridant, S., Cadete Santos Aires, F. J., Epicier, T., Betz, B., Hoyer, R. & Grunwaldt, J.-D. *Angew. Chem. Int.Ed.* **56,** 13078–13082 (2017).
28. Kopelent, R., van Bokhoven, J. A., Szlachetko, J., Edebeli, J., Paun, C., Nachtegaal, M. & Safonova, O. V. *Angew. Chem. Int. Ed.* **54,** 8728–8731 (2015).
29. Resasco, J., Derita, L., Dai, S., Chada, J. P., Xu, M., Yan, X., Finzel, J., Hanukovich, S., Hoffman, A. S., Graham, G. W., Bare, S. R., Pan, X. & Christopher, P. *J. Am. Chem. Soc.* **142,** 169–184 (2020).
30. Gänzler, A. M., Casapu, M., Maurer, F., Störmer, H., Gerthsen, D., Ferré, G., Vernoux, P., Bornmann, B., Frahm, R., Murzin, V., Nachtegaal, M., Votsmeier, M. & Grunwaldt, J. D. *ACS Catal.* **8,** 4800–4811 (2018).
31. Wang, H., Liu, J. X., Allard, L. F., Lee, S., Liu, J., Li, H., Wang, J., Wang, J., Oh, S. H., Li, W., Flytzani-Stephanopoulos, M., Shen, M., Goldsmith, B. R. & Yang, M. *Nat. Commun.* **10,** 1–12 (2019).
32. Golunski, S. E. *Platin. Met. Rev.* **51,** 162 (2007).
33. Peterson, E. J., DeLaRiva, A. T., Lin, S., Johnson, R. S., Guo, H., Miller, J. T., Hun Kwak, J., Peden, C. H. F., Kiefer, B., Allard, L. F., Ribeiro, F. H. & Datye, A. K. *Nat. Commun.* **5,** 4885 (2014).
34. Parkinson, G. S., Novotny, Z., Argentero, G., Schmid, M., Pavelec, J., Kosak, R., Blaha, P. & Diebold, U. *Nat. Mater.* **12,** 724–728 (2013).
35. Spezzati, G., Su, Y.-Q., Hofmann, J. P., Benavidez, A. D., Delariva, A. T., McCabe, J., Datye, A. K. & Hensen, E. J. M., *ACS Catal.* **7,** 6887-6891 (2017).
36. Spezzati, G., Benavidez, A. D., DeLaRiva, A. T., Su, Y., Hofmann, J. P., Asahina, S., Olivier, E. J., Neethling, J. H., Miller, J. T., Datye, A. K. & Hensen, E. J. M. *Appl. Catal. B: Environ.* **243,** 36–46 (2019).
37. Jeong, H., Kwon, O., Kim, B. S., Bae, J., Shin, S., Kim, H. E., Kim, J. & Lee, H. *Nat. Catal.* **3,** 368-375 (2020).
38. Vayssilov, G. N., Lykhach, Y., Migani, A., Staudt, T., Petrova, G. P., Tsud, N., Skála, T., Bruix, A., Illas, F., Prince, K. C., Matolin, V., Neyman, K. M. & Libuda, J. *Nat. Mater.* **10,** 310–315 (2011).
39. Puigdollers, A. R., Schlexer, P., Tosoni, S. & Pacchioni, G. *ACS Catal.* **7,** 6493–6513 (2017).
40. Cargnello, M., Doan-Nguyen, V. V. T., Gordon, T. R., Diaz, R. E., Stach, E. A., Gorte, R. J., Fornasiero, P. & Murray, C. B. *Science* **341,** 771–773 (2013).
41. Mädler, L., Stark, W. J. & Pratsinis, S. E. *J. Mater Res.* **17,** 1356–1362 (2002).
42. Koirala, R., Pratsinis, S. E. & Baiker, A. *Chem. Soc. Rev* **45,** 3053 (2016).
43. Beniya, A. & Higashi, S. *Nat. Catal.* **2,** 590–602 (2019).
44. Gröhn, A. J., Pratsinis, S. E., Sánchez-Ferrer, A., Mezzenga, R. & Wegner, K. *Ind. Eng. Chem. Res.* **53,** 10734–10742 (2014).
45. Liang, H., Raitano, J. M., He, G., Akey, A. J., Herman, I. P., Zhang, L. & Chan, S. W. *J. Mater. Sci.* **47,** 299–307 (2012).
46. Su, Y.-Q., Filot, I. A. W., Liu, J.-X. & Hensen, E. J. M. ACS Catal. **8,** 75-80 (2017).
47. Hinokuma, S., Fujii, H., Okamoto, M., Ikeue, K. & Machida, M. *Chem.Mater.* **22,** 6183–6190 (2010).
48. Wang, X., Chen, J., Zeng, J., Wang, Q., Li, Z., Qin, R., Wu, C., Xie, Z. & Zheng, L. *Nanoscale* **9,** 6643–6648 (2017).
49. Jeong, H., Bae, J., Han, J. W. & Lee, H. *ACS Catal,* **7,** 7097–7105 (2017).
50. Slavinskaya, E. M., Gulyaev, R. v, Zadesenets, A. v, Stonkus, O. A., Zaikovskii, V. I., Shubin, Y. v, Korenev, S. v & Boronin, A. I. *Appl. Catal. B, Environ.* **166–167,** 91–103 (2015).
51. Lu, Y., Wang, J., Yu, L., Kovarik, L., Zhang, X., Hoffman, A. S., Gallo, A., Bare, S. R., Sokaras, D., Kroll, T., Dagle, V., Xin, H. & Karim, A. M. *Nat. Catal.* **2,** 149–156 (2019).
52. Zafiris, G. S. & Gorte, R. J. *J. Catal.* **143,** 86–91 (1993).
53. Su, Y.-Q., Wang, Y., Liu, J.-X., Filot, I. A. W., Alexopoulos, K., Zhang, L., Muravev, V., Zijlstra, B., Vlachos, D. G. & Hensen, E. J. M. *ACS Catal.* **9,** 3289–3297 (2019).
54. Neitzel, A., Figueroba, A., Lykhach, Y., Skala, T., Vorokhta, M., Tsud, N., Mehl, S., Sevcikova, K., Prince, K. C., Neyman, K. M., Matolin, V. & Libuda, J. *J. Phys. Chem. C* **120,** 9852–9862 (2016).

55. Boronin, A. I., Slavinskaya, E. M., Danilova, I. G., Gulyaev, R. V., Amosov, Yu. I., Kuznetsov, P. A., Polukhina, I. A., Koscheev, S. V., Zaikovskii, V. I. & Noskov, A. S. *Catal. Today* **144,** 201–211 (2009).
56. Chen, Y., Chen, J., Qu, W., George, C., Aouine, M., Vernoux, P. & Tang, X. *Chem. Commun.* **54,** 10140–10143 (2018).
57. Slavinskaya, E. M., Gulyaev, R. v., Zadesenets, A. v., Stonkus, O. A., Zaikovskii, V. I., Shubin, Y. v., Korenev, S. v. & Boronin, A. I. *Appl. Catal. B: Environ.* **166–167,** 91–103 (2015).
58. Nilsson, J., Carlsson, P. A., Fouladvand, S., Martin, N. M., Gustafson, J., Newton, M. A., Lundgren, E., Grönbeck, H. & Skoglundh, M. *ACS Catal.* **5,** 2481–2489 (2015).
59. Su, Y. Q., Zhang, L., Muravev, V. & Hensen, E. J. M. *Chinese J. Catal.* **41,** 977–984 (2020).
60. Kato, S., Ammann, M., Huthwelker, T., Paun, C., Lampimäki, M., Lee, M.-T., Rothensteiner, M. & van Bokhoven, J. A. *Phys. Chem. Chem. Phys.* **17,** 5078–5083 (2015).
61. Tovt, A., Bagolini, L., Dvořák, F., Tran, N. D., Vorokhta, M., Beranová, K., Johánek, V., Farnesi Camellone, M., Skála, T., Matolínová, I., Mysliveček, J., Fabris, S. & Matolín, V. *J. Mater. Chem. A* **7,** 13019–13028 (2019).
62. Zhang, F., Liu, Z., Zhang, S., Akter, N., Palomino, R. M., Vovchok, D., Orozco, I., Salazar, D., Rodriguez, J. A., Llorca, J., Lee, J., Kim, D. H., Xu, W., Frenkel, A. I., Li, Y., Kim, T. & Senanayake, S. D. *ACS Catal.* **8,** 3550–3560 (2018).
63. Skála, T., Šutara, F., Prince, K. C. & Matolín, V. *J. Electron Spectros Relat. Phenomena* **169,** 20–25 (2009).

4.6 Appendix B

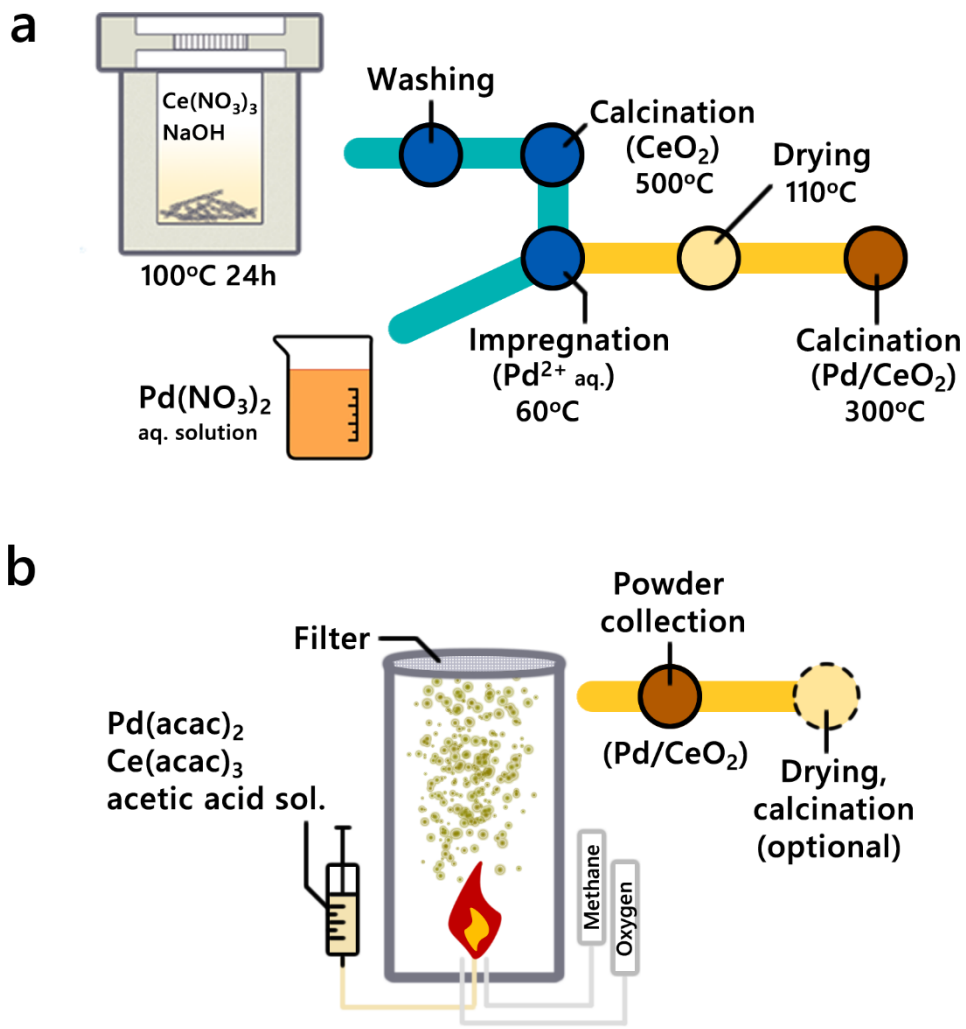

Figure B1. Synthesis scheme of: Pd/CeO_2 nanorod (a) and Pd/CeO_2 FSP (b) catalysts. Injection of the precursor solution into methane-oxygen flame leads to pyrolysis and formation of crystalline nanoparticles. The resulting catalyst material is collected from the quartz filter.

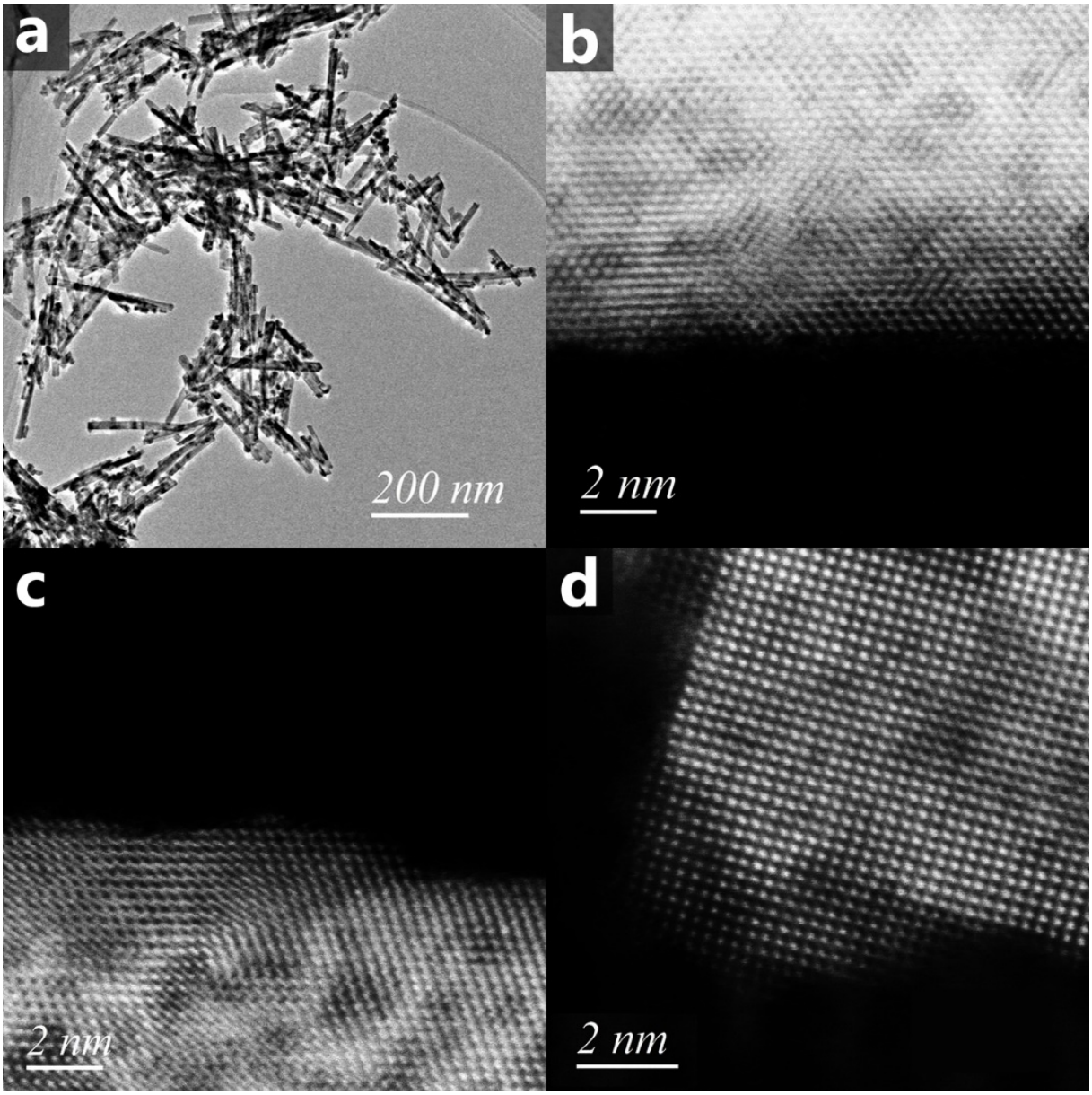

Figure B2. Representative bright field STEM (a) and atomically resolved HAADF-STEM (b-d) images of Pd/CeO_2 nanorod catalysts with 1 wt% Pd (1PdRods). No PdO NPs and/or clusters were found.

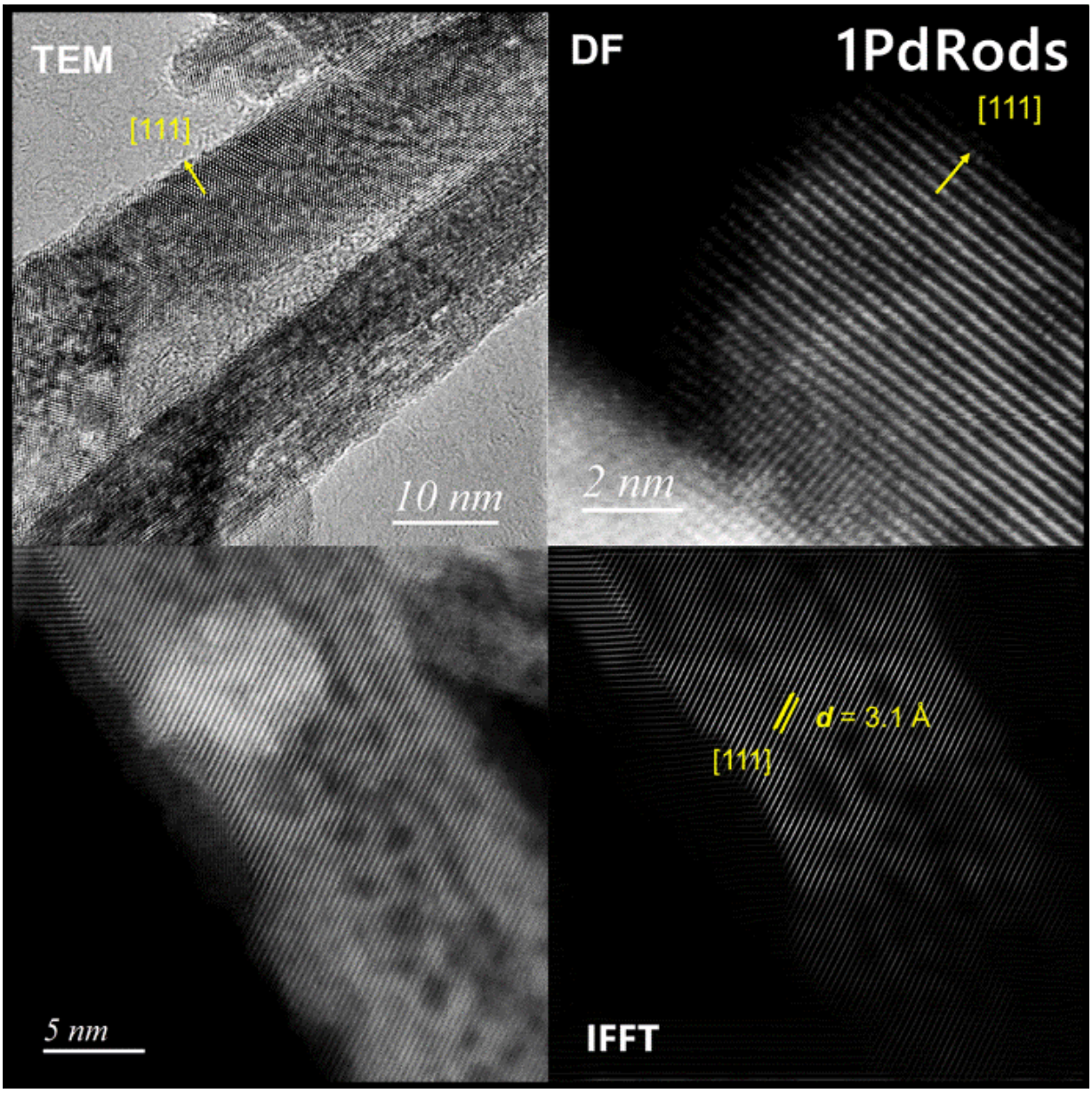

Figure B3. HRTEM images of 1PdRods sample showing predominant (111) faceting. Preferential (111) faceting of the prepared catalysts was further confirmed by low-temperature CO adsorption monitored by FTIR (see **Figure B18**).

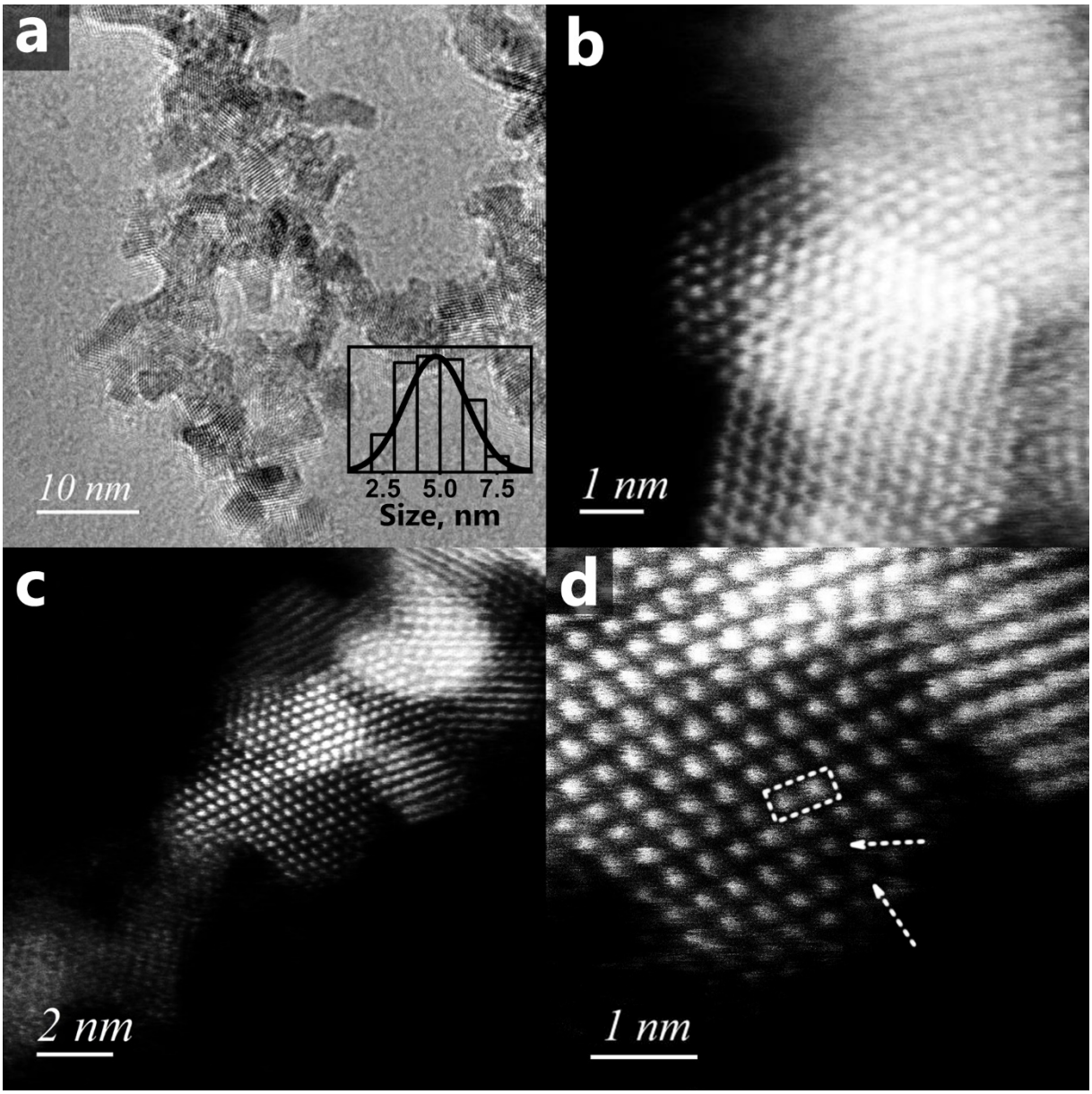

Figure B4. Representative bright-field STEM (a) and atomically resolved HAADF-STEM (c-d) of Pd/CeO_2 flame-spray pyrolysis derived catalysts with 1 wt% Pd. Mean Pd/CeO_2 particle size ~4.8 nm, 150 particles were counted. Dashed area displays structural defects. Arrows indicate atom columns with substantially lower contrast, possibly due to the Pd substitution. No PdO NPs and/or clusters were found.

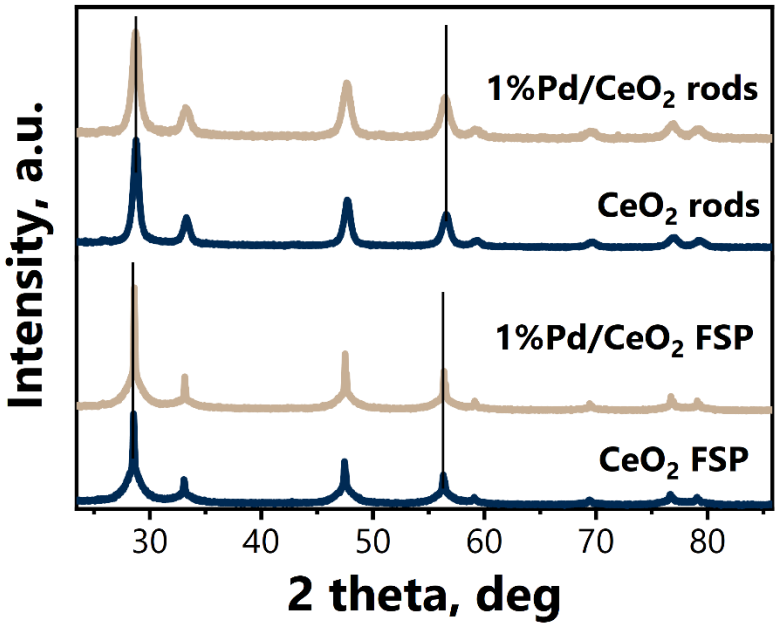

Figure B5. XRD patterns of as prepared catalysts. Vertical lines illustrate a slight shift of CeO_2 reflections towards higher angles for the FSP-derived Pd/CeO_2, which suggests Pd doping in CeO_2 lattice.

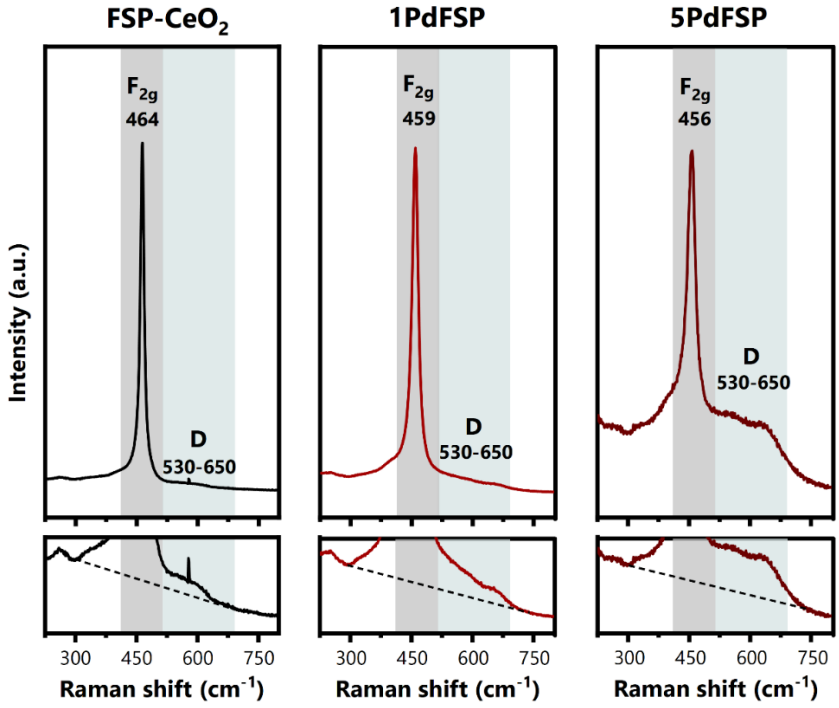

Figure B6. Raman spectroscopy data for FSP-derived samples. Loading with Pd led to a systematic red-shift and broadening of the F_{2g} band, accompanied by a substantial increase in relative (with respect to F_{2g}) intensity of the D-band. This evolution of spectral features can be linked to increased disorder and higher concentration of point defects in CeO_2 structure. These structural changes in CeO_2 lattice upon Pd addition can be explained by the inclusion of Pd atoms into ceria [1–3].

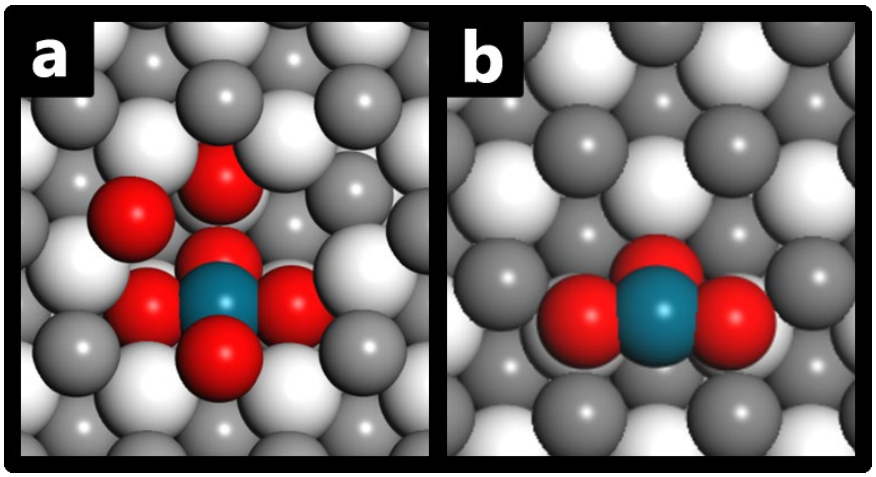

Figure B7. DFT derived structures of (a) Pd-doped model (Pd_1O_4)[4] and (b) surface Pd single-atom model (Pd_1O_2)[5] used for the fitting of EXAFS spectra of FSP-derived and rods-supported samples respectively. Pd-cyan, O-red. (111) CeO_2 surface is shown in black and white colour code: white -Ce, grey – O atoms.

Note B1. Absence of heat and mass transfer limitations.

First, we ensured the plug-flow behavior by the following relations:

$$\frac{d_t}{d_p} = \frac{4\times10^{-3}\ m}{175\times10^{-6}\ m} \approx 23 > 10 \quad (1) \quad \text{and} \quad \frac{L_b}{d_p} = \frac{2\times10^{-2}\ m}{175\times10^{-6}\ m} \approx 114 > 50 \ (2),$$

where d_t – reactor tube diameter, d_p – particle diameter, L_b – bed length.

Secondly, sieved fraction of catalyst powder with particle size $125\ \mu m < d_p < 250\ \mu m$ was diluted with a large amount of SiC – keeping the ratio of SiC to catalysts by weight not less than 5. This is a common practice to avoid the hot spots and interphase diffusion limitations[6].

Mears criterion for the interphase heat transfer limitations:

$$\frac{|\Delta H_R|\ r_{obs}\ R_p\ E_a}{R_g\ h\ T_b^2} < 0.15 \quad (3)$$

Where ΔH_R – reaction heat ($\frac{J}{mol}$), r_{obs} – rate per catalyst volume ($\frac{mol}{m_{cat}^3\ s}$), R_p – particle radius ($\frac{d_p}{2}$), E_a – activation energy ($\frac{J}{mol}$), R_g – ideal gas constant ($\frac{J}{mol\ K}$), h – gas-solid heat transfer coefficient ($\frac{W}{m^2\ K}$), T_b – temperature of bulk fluid (K).

$$h = \frac{2\ \lambda_g}{d_p} \quad (4)$$

Where λ_g – thermal conductivity of the gas,

$$\lambda_g = y_{CO}\lambda_{CO} + y_{O_2}\lambda_{O_2} + y_{He}\lambda_{He} = 0.01(0.027) + 0.01(0.028) + 0.98(0.165) = 0.16\ \frac{W}{m\ K}\ (0.20\ @448K) \quad (5),$$

$$\text{giving}\ \ h = \frac{2\times0.16}{175\times10^{-6}} = 1829\ \frac{W}{m^2\ K}\ (2286\ @\ 448K) \quad (6)$$

$\Delta H_R = 283 \times 10^3 \ \frac{J}{mol}$; $r_{obs} = \ 0.26 \ \frac{mol}{m_{cat}^3 \, s}$ $(41.81@448K)$; $R_p = 0.5 * 175 \times 10^{-6} \, m$; $E_a \sim 50 \times 10^3 \ \frac{J}{mol}$; $R_g = 8.314 \ \frac{J}{mol \, K}$; $T_b = 323K \ (448K)$; the apparent (poured) density of the catalyst (sieved fraction): $\rho_c = 1.91 \times 10^6 \ \frac{g}{m^3}$.

Mears criterion at 50ºC:

$$\frac{|\Delta H_R| \, r_{obs} \, R_p \, E_a}{R_g \, h \, T_b^2} = \frac{283{\times}10^3 * 0.26 * \frac{175{\times}10^{-6}}{2} * 55{\times}10^3}{8.314 * 1829 * 323^2} \approx 2.2 \times 10^{-4} < 0.15 \qquad (7)$$

Therefore, our experimental conditions satisfy the Mears criterion for the absence of heat transfer limitations (at 175 ºC Mears criterion is 0.0149 < 0.15).

Mears criterion for the mass transport limitations:

$$\frac{r_{obs} \, R_p}{k_c C_{Ab}} < 0.15 \quad (8)$$

k_c – mass transfer coefficient of the reactant ($\frac{m}{s}$), C_{Ab} – concentration of the reactant in the bulk gas phase ($\frac{mol}{m^3}$). Since $Re \ll 1$,

$$k_c \sim \frac{2D_{CO-He}}{d_p} \quad (9)$$

D_{CO-He} – diffusion coefficient of CO in He ($\frac{m^2}{s}$). $k_c = \frac{2 * 1.2{\times}10^{-5}}{175{\times}10^{-6}} \approx 0.14 \ \frac{m}{s}$ $(0.24@448K)$ $C_{Ab} = 0.38 \ \frac{mol}{m^3}$ $(0.27@448K)$

$$\frac{r_{obs} \, R_p}{k_c C_{Ab}} = \frac{0.26 * \frac{175{\times}10^{-6}}{2}}{0.14 * 0.38} = 4.3 \times 10^{-4} < 0.15 \quad (10)$$

Therefore, our experimental conditions satisfy the Mears criterion for the absence of external mass transfer limitations (at 175 ºC Mears criterion is 0.0564 < 0.15).

Experimental diagnostic tests:

To further validate that the catalytic data was obtained in the kinetic regime, we performed additional diagnostic tests using our most active catalyst (per g_{cat} basis) – 5PdFSP. We varied the amount of catalyst loaded in the reactor and the overall flow, keeping the constant ratio between the flow rate and catalyst weight [6]. As shown in **Figure B8** the reaction rate profiles are nearly identical, meaning that the reaction kinetics is not affected by the transport phenomena.

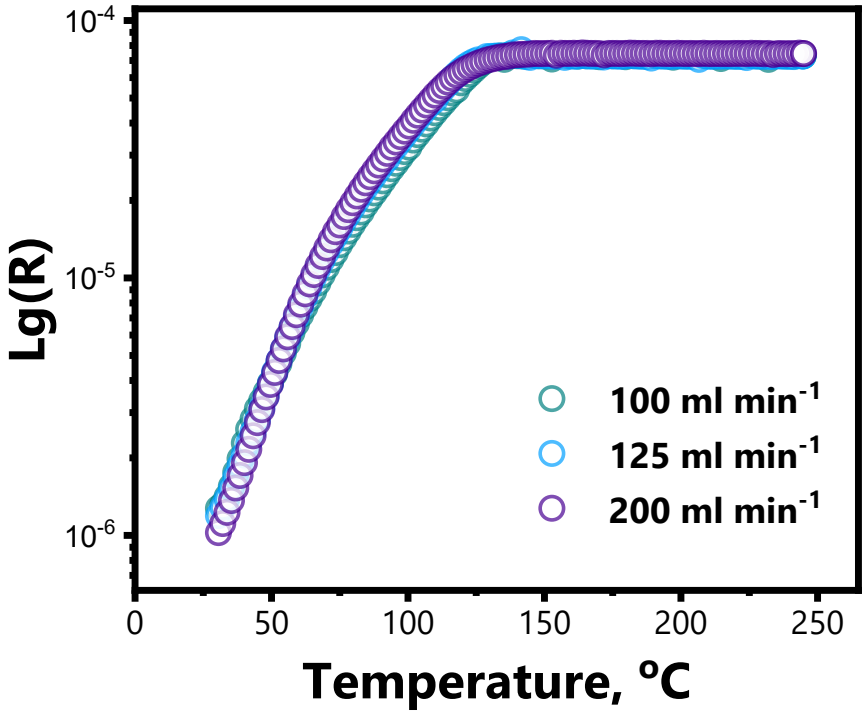

Figure B8. Diagnostic CO oxidation tests for 5PdFSP sample. The reaction feed: 1%CO + 1%O_2 in He flow. Overall flow was varied from 100 to 200 ml/min. The weight of the catalyst loaded in the reactor was varied accordingly, keeping the GHSV 600,000 ml h^{-1} g_{cat}^{-1} For the measurements sieved fractions (125 to 250 µm) were diluted with ~300 mg of SiC. All the catalysts were pretreated in 20% O_2/He at 300 °C for 1 h, cooled down to RT and flushed with He for 30 minutes. Then reaction mixture of 1%CO + 1% O_2 in He was fed. The temperature was ramped up at a rate of 5 °C/min.

Note B2. Catalytic performance of Pd catalysts in CO oxidation.

First, we prepared and tested bare supports (Rods and FSP CeO_2). As can be seen from the **Fig. B9** contribution of the support to the low temperature CO oxidation activity is negligible. Next, a high surface area silica (Sipernat® 50) was loaded with 5 wt% Pd via wetness impregnation to represent PdO nanoparticles dispersed on the inert support. This catalyst, denoted as 5PdSiO_2, showed limited activity at low temperatures and notable conversion was observed only at T> 175 °C, in line with a recent report [7]. Finally, a commercial ceria support (Sigma-Aldrich) was loaded with 1 wt% of Pd via wetness impregnation and the resulting catalyst is denoted as 1PdCeO_2 (SA). This sample exhibited better activity in low-temperature CO oxidation than 5PdSiO_2, which points to the beneficial effect of the Pd-CeO_2 interface on the performance, in accordance with earlier works [8,9]. Single-atom Pd/CeO_2 catalysts (1PdRods and 1PdFSP) exhibit a much higher CO oxidation activity than other tested catalysts under identical reaction conditions. As explained in the manuscript, the higher activity of these samples stems from the presence of Pd-O single-atom species, highly active in low-temperature CO oxidation [5,10–13].

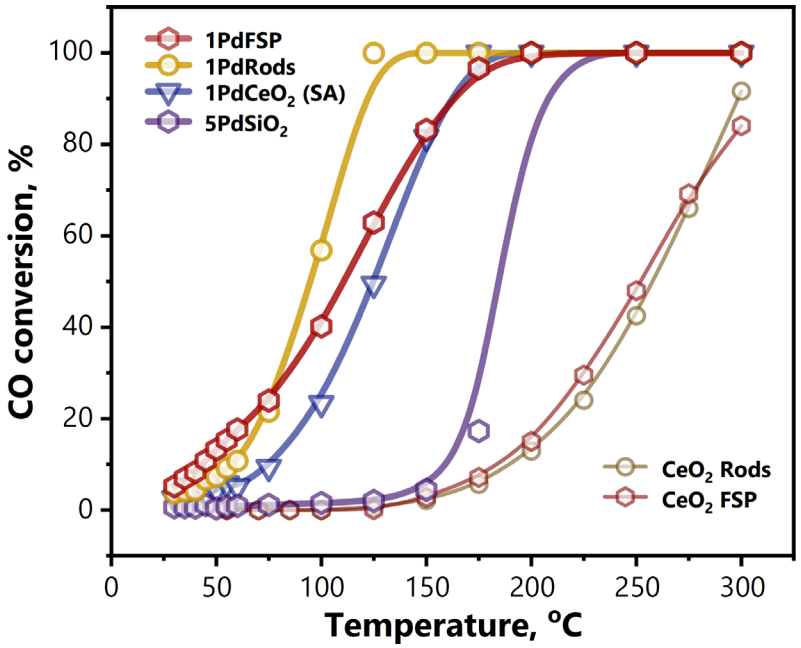

Figure B9. Steady-state plots of CO oxidation activity. Sieved fractions (125 to 250 µm) were diluted with ~250 mg of SiC. All catalysts were pre-treated in 20% O_2/He at 300 °C for 1 h and cooled down to RT. Then the reaction mixture of 1% CO + 1% O_2 in He (50 ml/min, GHSV ~60,000 ml/ g_{cat} h^{-1}) was fed. After 30 minutes dwell at RT, stepwise heating was initiated with 5 °C/min. Each measurement was performed after 15 minutes of stabilisation at every temperature point.

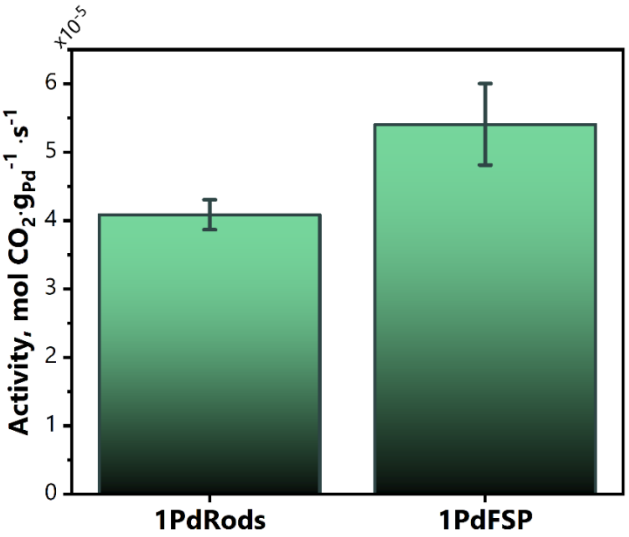

Figure B10. Mass-specific activity of the catalysts at 50 °C. Error bars represent standard deviation obtained in three subsequent measurements. For the measurements sieved fractions (125 to 250 µm) were diluted with ~250 mg of SiC. The amount of catalyst was adjusted in order to keep the conversion below 5%. All the catalysts were pre-treated in 20% O_2/He at 300 °C for 1 h, cooled down to RT and flushed with He for 30 minutes. Then reaction mixture of 1%CO + 1% O_2 in He (100 ml/min, GHSV ~120,000 ml g_{cat}^{-1} h^{-1}) was fed and temperature was slowly increased up to 50°C. The catalysts were exposed to the reaction feed for 4 hours prior to the measurements.

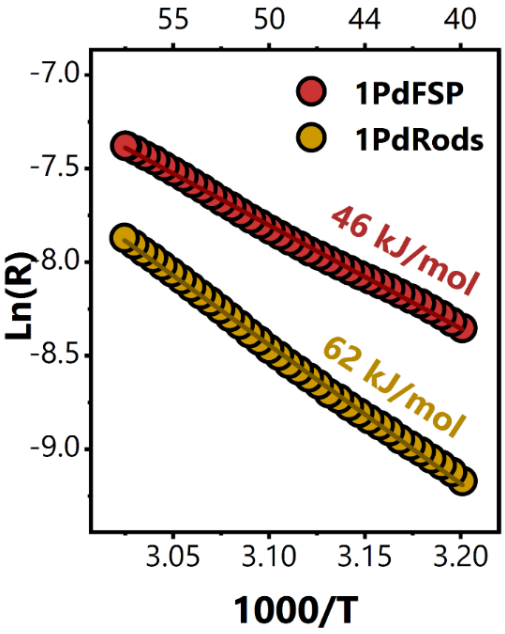

Figure B11. Arrhenius plot of reaction rate (mol CO converted/ g_{pd} s^{-1}). Sieved fractions (125 to 250 µm) were diluted with ~250 mg of SiC. The catalysts were pre-treated in 20% O_2/He at 300 ºC for 1h. Reaction feed: 1% CO + 1% O_2 in He, ramp rate 5 ºC/min. Conversion was kept below 20% and accordingly the amount of catalyst was adjusted. Flow rate: 200 ml/min and total GHSV of 240,000 ml/ g_{cat} h^{-1}.

Note B3. Step-response experiments.

Previously[14], we found that the metallic nature of small Pd clusters results in a low activity for CO oxidation at low temperature, which was explained by too strong CO adsorption. To prove the spectator nature of the reduced/semi-reduced Pd species during low-temperature CO oxidation, we performed a transient kinetic step-response study. By following the response of a catalyst to a transient change in the reactant mixture under isothermal conditions, we can distinguish between different types of sites present on the surface of the catalysts. Here we employed a switch from the CO + O_2 feed to a feed only containing O_2 at 50 ºC. The figure below (**Fig. B12**) shows a markedly different response of 1PdRods and 1PdFSP samples to such switch. For the 1PdRods sample (top graph), we see that the initial decrease in the concentration of the CO_2 product is followed by a steep increase at the moment, when the CO concentration in the reactor becomes very low. This sharp CO_2 peak is related to oxidation of residual CO molecules in the almost pure oxygen feed. This behavior is characteristic for metallic sites [15,16]. At low temperature and under the steady-state conditions (constant partial pressure of reactants), these metallic sites are poisoned by CO and the overall CO oxidation reaction is inhibited. However, the reaction can proceed in large excess of oxygen, when the CO concentration in the gas-phase drops to nearly zero. With this experiment we demonstrate that the reduced/semi-reduced Pd species, formed during the reaction at low temperature in 1PdRods, do not (significantly) contribute to the low-temperature activity. In stark contrast, a similar transient experiment for the 1PdFSP sample did not lead to a steep increase in CO_2 concentration, which suggests that the number of reduced/semi-reduced spectator Pd species in this sample is very low. This finding is in line with our *in situ* DRIFTS, NAP-XPS and *ex situ* EXAFS data, which will be discussed later.

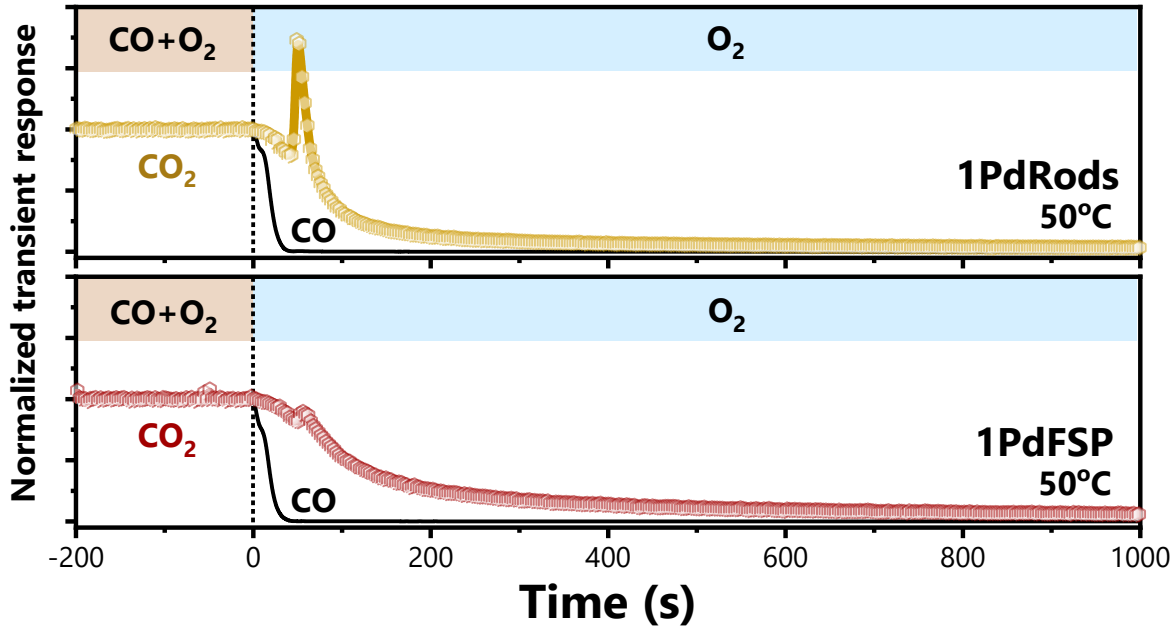

Figure B12. Transient kinetic step-response of CO_2 upon the switch from $CO+O_2$ to O_2 at 50 °C for 1PdRods (top graph) and 1PdFSP (bottom graph). Sieved fractions (125 to 250 µm) were diluted with ~2 g of SiC. The catalysts were pre-treated in 20% O_2/He at 300 °C for 1h. After cooling down to 50 °C, the reaction mixture was fed for ~48 h to ensure the stable steady-state regime. Reaction feed: 1% CO +3.5% O_2 in He, with overall flow of 50 ml/min. Conversion was kept below 5%.

Note B4. Reaction orders measurements at elevated temperature.

To demonstrate that the reduced Pd sites might play an important role in CO oxidation at elevated temperature, we performed an additional reaction order study for the 1PdRods and 1PdFSP samples at 175 °C. In the **Figure 4.2d**, we show how the reaction orders change when the reaction temperature increases from 50 °C to 175 °C. We found that the reaction order in O_2 is negative (-0.06) for the 1PdFSP sample at both temperatures. This observation points to a facile oxygen supply to the active sites and a high coverage of oxygen. At the same time the reaction order in CO increases from +0.25 at 50 °C to +1.36 at 175 °C, suggesting that CO coverage is low at elevated temperature. The presence of the metallic Pd species is usually characterized by low CO reaction orders, due to the substantially stronger CO adsorption on metallic sites as compared to oxidized clusters or single atoms. Metal nanoparticles or clusters supported on redox-active supports typically exhibit reaction orders of ~0 in CO and >0 in O_2 (~ 0 to +0.5).[9,17,18] Therefore, taking into account *in situ* NAP-XPS, DRIFTS and *ex situ* XAS data showing only oxidized Pd state for the 1PdFSP sample, we can conclude that only a negligible amount of metallic/reduced Pd species are formed and/or involved in CO oxidation in this catalyst even at elevated temperature.

In line with the catalytic results presented in **Figure 4.2a**, the 1PdRods sample is markedly more active than the 1PdFSP sample at 175°C. At the same time, the reaction order in O_2 for 1PdRods is higher than that for 1PdFSP and it increases from -0.08 at 50°C to +0.29 at 175°C. This is a strong indication of a lower oxygen coverage and less facile oxygen activation by 1PdRods in comparison to 1PdFSP. As mentioned above, positive (~ 0 to +0.5) reaction orders in oxygen are typical for metals on reducible oxides, where a Mars-van Krevelen type of mechanism takes place at the metal-support interface. Knowing from the spectroscopic data that under these conditions a substantial fraction of

Pd is reduced, we can explain the change in the oxygen reaction order from negative to positive by the involvement of the metallic species into CO oxidation at elevated temperature. This is the reason for the substantially higher activity of the 1PdRods sample at elevated temperature. Since the 1PdFSP sample lacks the reduced/metallic Pd sites, its activity at high temperature might be limited by the weaker CO adsorption on oxidized Pd single atoms, which results in the observed high reaction order in CO. In the 1PdRods sample, oxidized and reduced Pd species coexist. While the latter ones are inactive at low temperatures, they come into play at elevated temperature. The +0.19 reaction order in CO for 1PdRods at 175ºC sample arises from the presence of two types of active sites: Pd single atoms, which under these conditions display a positive order (+1.36 for 1PdFSP), and reduced/semi-reduced Pd clusters, which show ~0 order in CO when supported on reducible oxides. The reaction order in O_2 for 1PdRods can be also explained by a superposition of reduced Pd sites giving a ~0.5 reaction order and oxidized Pd single atoms displaying -0.09. This kinetic approach was recently elegantly used by Karim and co-workers to quantify the different types of sites using exclusively the reaction order measurements [19,20].

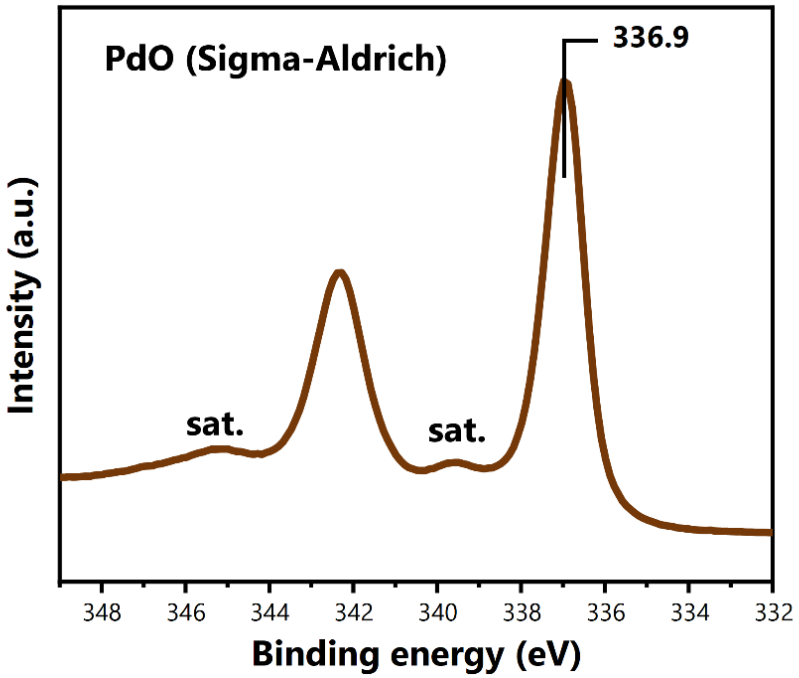

Figure B13. Pd 3d XPS spectra acquired in UHV (K-alpha Thermo, flood gun on) for commercial PdO (Sigma-Aldrich). The absence of satellite feature and shift of the main component towards higher binding energies (~1.8eV) suggest principal difference of Pd electronic state in 1PdFSP and 1PdRods samples from the Pd in PdO, in line with XAS data.

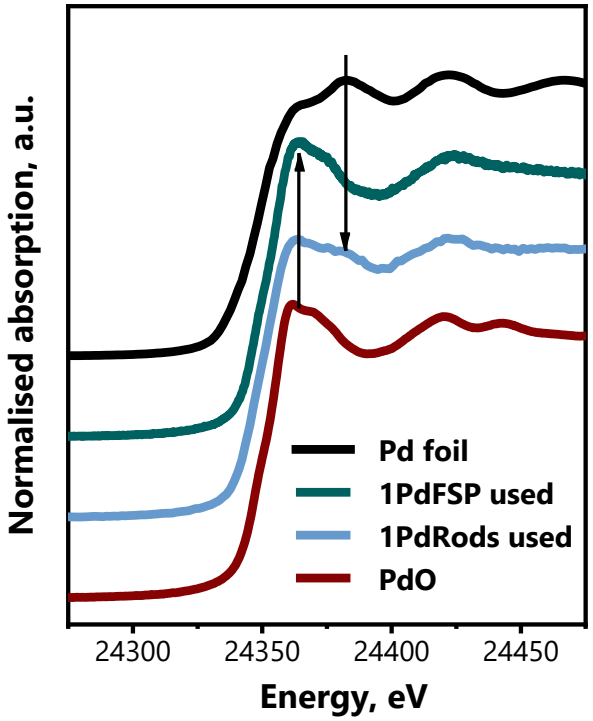

Figure B14. Pd K-edge XANES of 1PdFSP and 1PdRods after CO oxidation cycle (used). Decreased white line intensity for 1PdRods spectrum and additional feature at ~24380 eV indicate partial reduction of Pd species in line with EXAFS data. In contrast, spectrum of 1PdFSP manifests oxidized nature of Pd species.

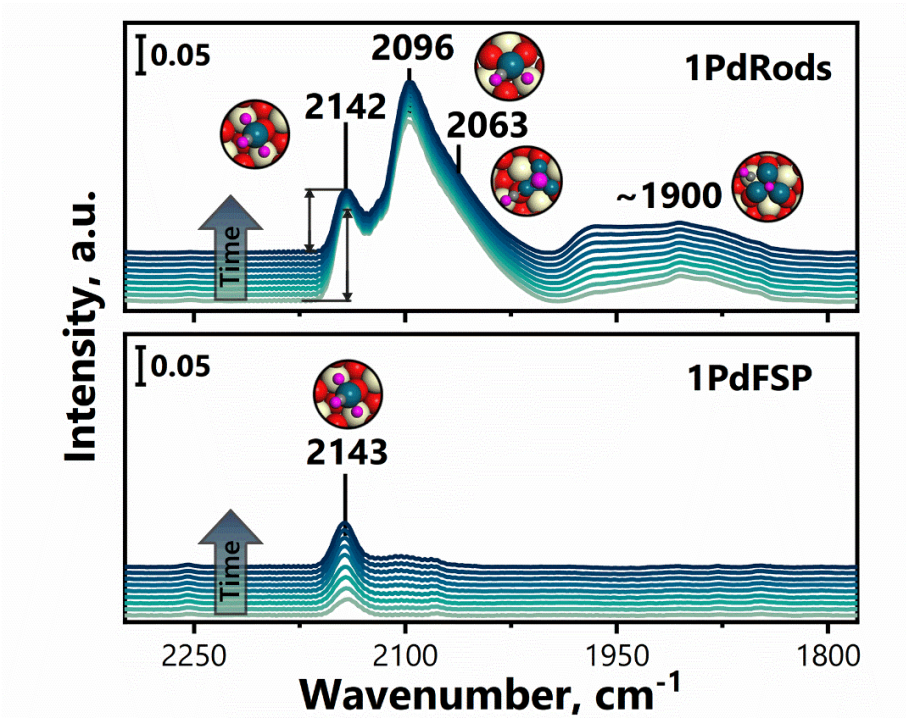

Figure B15. Development of *in situ* DRIFT spectra of fresh catalysts (after pre-treatment in O_2 at 300 °C) during exposing them to 2 mbar of reactants ($CO:O_2$=1:1, 3.5 ml/min flow mode) at RT. Time period between first and last spectra is ~20 min. As shown in the top panel, Pd speciation in 1PdRods changes during CO oxidation. The intensity of 2143 cm^{-1} band decreases, accompanied by a growth of the contribution of cluster species. Circled images represent the DFT-derived structures matching the observed bands. Color code: Pd-turquoise, O-purple (of PdO), C-grey; support – (111) CeO_2 surface, Ce-white, O-red. Band assignment and detailed description of DFT models is reported in our previous work[5].

Note B5. The effect of Pd speciation on low-temperature activity after CO oxidation at elevated temperature.

The comparable CO oxidation performance of 1PdFSP sample during repeated CO oxidation cycles (**Figure B16**) can be explained by the stable single-atom nature of Pd active sites described in the main text. In contrast, the partial transformation of oxidized Pd to metallic/semi-reduced Pd that occurs during CO oxidation at elevated temperature in 1PdRods sample was captured by several characterization techniques: (i) *ex situ* EXAFS and XANES point to a mixture of Pd^0 and Pd^{2+} being present in 1PdRods after CO oxidation at 300 ºC (**Figure 4.3** and **Figure B14**); (ii) *in situ* DRIFTS indicates an increased fraction of carbonyls related to $Pd^{\delta+/0}$ clusters after the reaction at 300 ºC (**Figure 4.3**). At the same time, the CO band attributed to single-atom Pd species (2143 cm^{-1}), responsible for low-temperature CO oxidation, remained visible in the spectrum even after the reaction at 300 ºC. These observations are in line with the preserved low-temperature activity of 1PdRods during the second reaction run (**Figure B16**). In turn, the similar CO oxidation activities at T > 100 ºC during the first and second reaction cycle stem from the fact that reduced/semi-reduced Pd species are formed already at low temperature (as shown in **Figure B15**) during initial stages of steady-state CO oxidation activity measurements. These Pd clusters, which are active at elevated temperatures, can undergo semi-reversible reduction/oxidation (as a function of temperature) under reaction conditions, thus influencing the $Pd^{+/\delta+}$ to Pd^0 ratio. This was demonstrated by *in situ* NAP-XPS study of 1PdRods sample (**Figure B17**). The ratio between Pd^0 and $Pd^{+/\delta+}$, derived from the analysis of Pd 3d spectra, varies as a function of reaction conditions and can be explained by the formation of Pd_nO_x clusters with different O/Pd stoichiometries. This ratio can influence the observed ("average") oxidation state of Pd. In our earlier work[14], we demonstrated that Pd_8O_x clusters (x = 0 , 6 ,12) supported on CeO_2 exhibit notably different catalytic CO oxidation activity at low temperature (near RT), while an increase in reaction temperature leads to smaller differences between them due to overall weaker CO adsorption. In other words, the CO oxidation performance at elevated temperature is less sensitive to the exact stoichiometry of Pd_8O_x, which relates to the experimentally determined $Pd^0/Pd^{+/\delta+}$ ratio from XPS. Therefore, even incomplete transformation of Pd^0 to $Pd^{+/\delta+}$ in small Pd clusters upon cooling in reaction mixture does not significantly affect the activity of CO oxidation at high temperature. The apparent dynamic behaviour of different Pd phases as a function of the reaction conditions underpins the importance of *in situ* and *operando* approaches for studying Pd-CeO_2 catalysts.

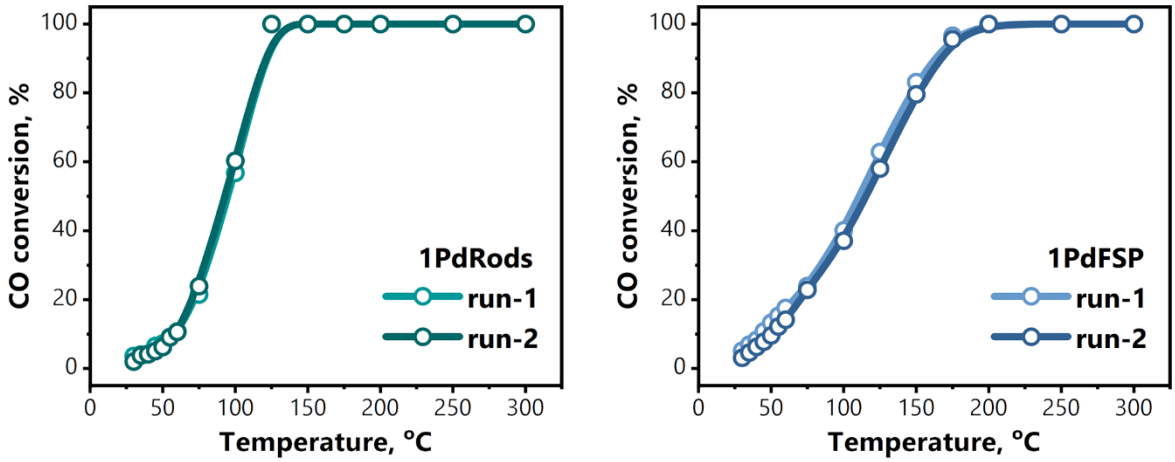

Figure B16. Steady-state plots of CO oxidation activity. Sieved fractions (125 to 250 µm) were diluted with ~250 mg of SiC. Both catalysts were pre-treated in 20% O_2/He at 300ºC for 1h and cooled down to RT. Then the reaction mixture of 1%CO + 1% O_2 in He (50 ml/min, GHSV ~60,000 ml/ g_{cat} h^{-1}) was fed. After 30 minutes dwell at RT, stepwise heating was initiated with 5 ºC/min. Each measurement was performed after 15 minutes of stabilisation at every temperature point.

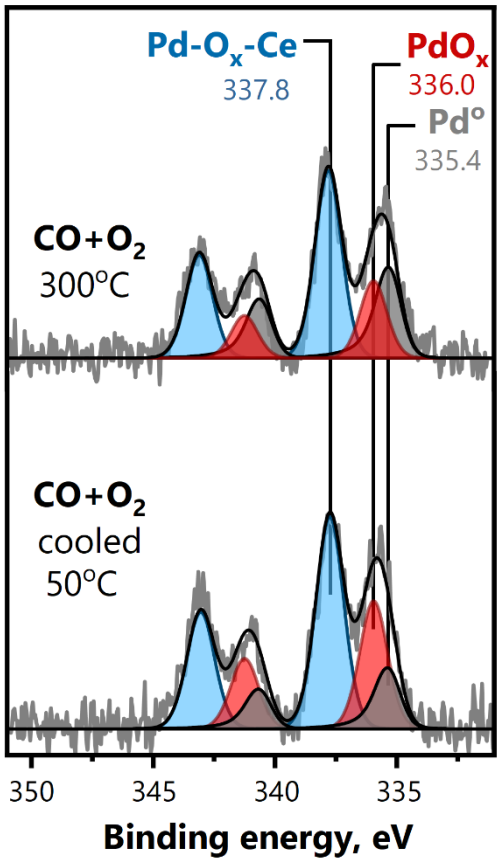

Figure B17. *In situ* NAP-XPS data for 1PdRods sample: Pd 3d core-line spectra as a function of temperature under reaction conditions (2 mbar $CO:O_2$ = 1:1, 2 ml/min flow). Metallic Pd species (grey component), which are clearly observed at elevated temperature under reaction conditions, can be partly re-oxidized upon cooling in the same reaction mixture (red component). These data indicate that the transformation of PdO_x ($Pd^{+/\delta+}$) to Pd^0 is reversible to a certain extent. In turn, this could explain why the consecutive CO oxidation runs over 1PdRods exhibit a comparable CO oxidation performance at elevated temperatures (see extended discussion in **Note B5**)

Note B6. Quantification of Pd surface species.

To understand the origin of the higher stability of Pd single atoms on the surface of the 1PdFSP catalyst, it would be useful to estimate the fraction of accessible/surface Pd atoms. Conventional lab-based XPS cannot provide a sufficiently accurate absolute atomic surface concentration, as its analysis depth (~5 nm) probes also the subsurface layers of the FSP made Pd-CeO_2 particles. However, the relative surface atomic ratios (*i.e.,* Pd/Ce) can be used to determine the elemental distribution within the probing depth and were shown to agree well with other highly surface sensitive techniques [21]. Using XPS, we found a higher Pd surface concentration in case of impregnated nanorods compared to one-step FSP-made samples (**Table B2**). Nevertheless, a higher Pd/Ce ratio derived from XPS (0.032) than expected from the loading (0.016) in PdFSP sample suggests near-surface localisation of the Pd. In other words, using the FSP-method it is possible to dope the surface and sub-surface layers of ceria with Pd atoms.

To get quantitative information about the surface concentration of Pd on the very surface of catalysts, we employed CO pulsing chemisorption. In contrast to XPS, CO chemisorption probes only the sites, which are accessible for CO adsorption, *i.e*. potential active sites for CO oxidation. Conventional approach to CO chemisorption involves reduction of the catalysts in hydrogen prior to the measurements. The reduction leads to inevitable changes in the local environment of the active sites even when low loading of metal and mild reduction conditions are used [17,22]. In addition, for reducible supports such as CeO_2, more complicated procedures involving, for example, CO_2 pre-adsorption are required[23,24]. Otherwise, the number of the accessible metal sites can be overestimated due to chemisorption of CO on the reduced support. To conclude, any treatment of the catalyst prior to the chemisorption, which is different from the actual pre-treatment before the catalytic testing, would most certainly result in different properties of the catalyst. Since our CO oxidation testing protocol features only an oxidative pre-treatment of the catalyst (20% O_2 in He, 300 ^oC), we precluded the use of H_2 reductive step for the chemisorption studies. CO chemisorption was performed at -20 ^oC, *i.e.* at a temperature low enough to supress the possible oxidation of CO by oxidized surface Pd species. In turn, at a temperature substantially lower than -20 °C a notable adsorption of CO on the CeO_2 was observed (see Ce-related bands in **Figure B18**), thus -20 ^oC was chosen. As follows from **Table B2**, nearly all Pd atoms in the 1PdRods sample are available for CO chemisorption (94%, assuming only on top CO ads.) in agreement with the isolated nature and preferential surface localization of Pd sites. Surprisingly, the 1PdFSP sample exhibits extremely low CO adsorption, comparable with that of bare ceria support. Therefore, we conclude that a certain fraction of Pd atoms are present as doped sites within the lattice of CeO_2 and are not accessible for CO adsorption. The lower amount of Pd single atoms on the surface of the 1PdFSP sample, as compared to impregnated 1PdRods, could possibly explain the stability of isolated Pd species during the reaction. A similar effect was recently demonstrated with the low-loaded materials reported by Christopher and co-workers [17]. Therefore, as described in the main text, we prepared 5 wt% Pd samples using the same preparation methods as for the 1 wt% samples (see **Table B2** for BET surface area and Pd loading). As follows from XPS, a nearly 5-fold increase in Pd to Ce ratios was found for both impregnated 5PdRods and 5PdFSP samples. Having these samples, we could study the effect of Pd surface site density/concentration on the stability of isolated Pd^{2+} species using *in situ* NAP-XPS (**Figure 4.4** and **Figures B28-29**) and DRIFTS (**Figure B30**).

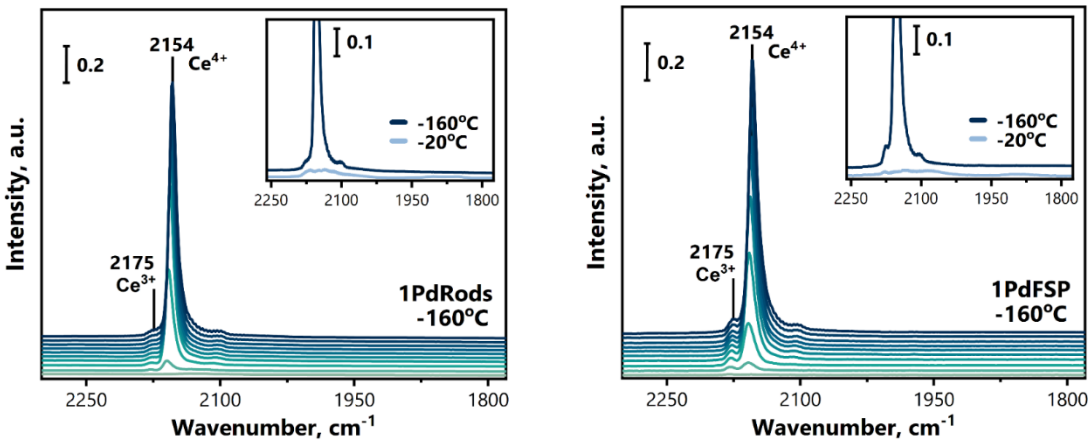

Figure B18. Transmission FTIR spectra of fresh catalysts upon CO adsorption at -160 °C. For the measurements the samples were first pre-treated in O_2 at 300 °C and then cooled down to RT and evacuated. Further cooling was performed via circulation of liquid nitrogen within the sample holder. After reaching -160 °C CO was dosed up to a pressure of 10 mbar. Similar spectra were obtained for both fresh catalysts. Sharp bands at 2175 and 2154 cm^{-1} correspond to CO adsorbed on Ce^{3+} and Ce^{4+} sites, respectively[25]. It can be seen that 1PdFSP sample comprises higher concentration of surface Ce^{3+}. It is important to note that the main band at 2154 cm^{-1} corresponds to CO adsorbed on oxidized (111) CeO_2 surface[26]. This finding further confirms the predominant (111)-faceting of the prepared PdRods and PdFSP samples. No bands attributed to CO adsorbed on metallic Pd (~1900 cm^{-1}) were found at -160 °C, suggesting that as prepared samples contain only oxidized Pd species. Stepwise heating revealed that at -20 °C a neglible amount of CO is adsorbed on the Ce sites, thus this temperature was chosen for CO chemisorption measurements. Significantly lower intensity of CO bands attributed to Pd carbonyls compared to DRIFTS spectra is due to the transmission mode measurements, whereas multiple reflection and absorption events take place within the sample in the diffuse reflectance mode amplifying the signal.

Note B7. Structure of 5 wt% Pd samples: 5PdRods and 5PdFSP.

The EXAFS spectrum of the 5 wt% Pd-CeO_2 FSP sample (5PdFSP) did not show any Pd-Pd scattering, indicating that the majority of the Pd species are atomically dispersed (**Figure B19**) and resemble the Pd_1O_4 doped structure (fitting results presented in **Table B1**). Surprisingly, the same holds true even for the higher loaded 10 wt% Pd-CeO_2 FSP sample (10PdFSP) (**Figure B20**). Yet, we note that the presence of "EXAFS-invisible"[27] sub-nm clusters, as observed by high resolution HAADF-STEM (**Figures B19** and **B23**), cannot be ruled out for such high Pd loadings. In contrast to FSP-derived materials, EXAFS spectra of the 5PdRods (**Figure B19**) shows both second and third shells of Pd-Pd scattering at ~3.0 and ~3.4 Å. These scattering paths are similar to the ones found for bulk PdO reference, however, with substantially lower coordination number (CN) of ~6 (compared to 12 in PdO). This finding goes in line with the microscopy data, indicating the presence of small crystalline Pd oxide NPs on the surface of highly loaded nanorods (**Figures B19, 21, 22**). However, these PdO NPs were not detected by XRD (**Figure B24**), likely due to the very small size and/or their amorphous nature. Similar to the case of 1PdFSP sample, we note a slight shift in CeO_2 reflections for the 5PdFSP sample, indicative of Pd inclusion into the CeO_2 lattice in line with the Raman spectroscopy results.

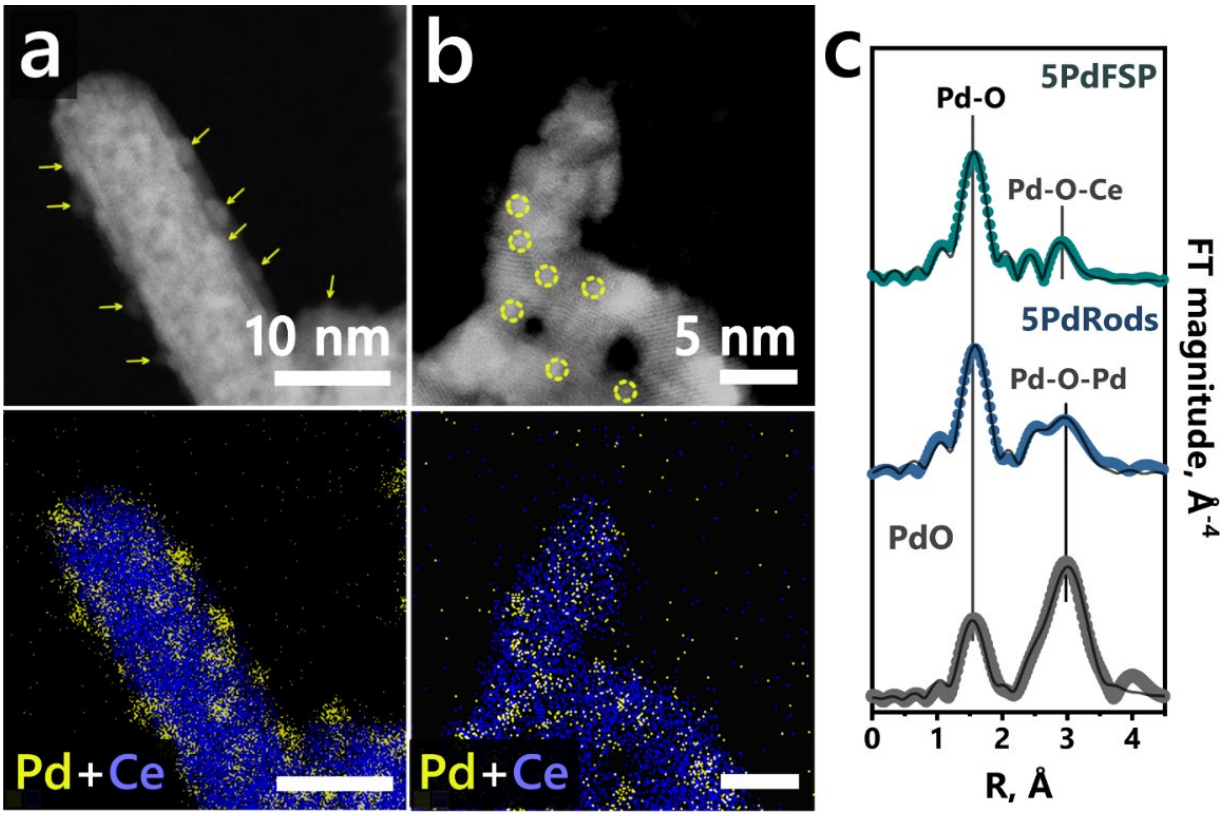

Figure B19. Structure of as-prepared 5 wt% Pd/CeO_2 catalysts. a, b, HAADF-STEM and energy dispersive X-ray spectroscopy (EDX) images of 5PdRods (a), 5PdFSP (b). c, The k^3-weighted FT-EXAFS spectra (Pd K-edge) of 5PdFSP (turquoise), 5PdRods (blue), reference PdO (grey), circles represent the data and solid lines – fit. Fitting details are reported in **Table B1**.

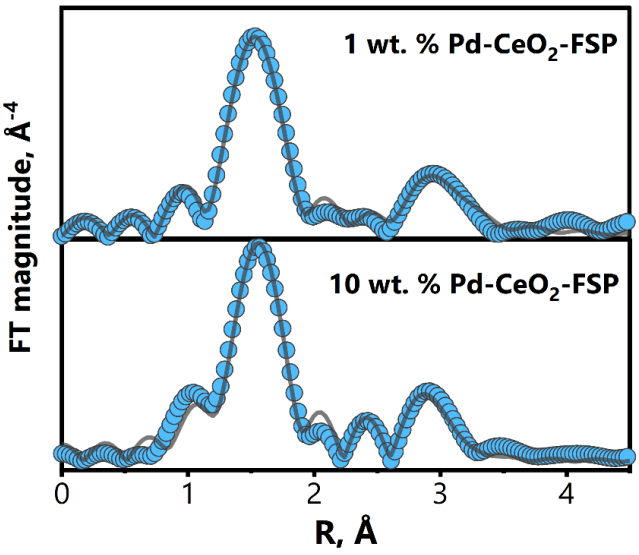

Figure B20. The k^3-weighted FT-EXAFS spectra (Pd K-edge) of 1PdFSP (top), 10PdFSP (bottom). Solid line stands for the fit and circles for the data. Fitting details are reported in **Table B1**.

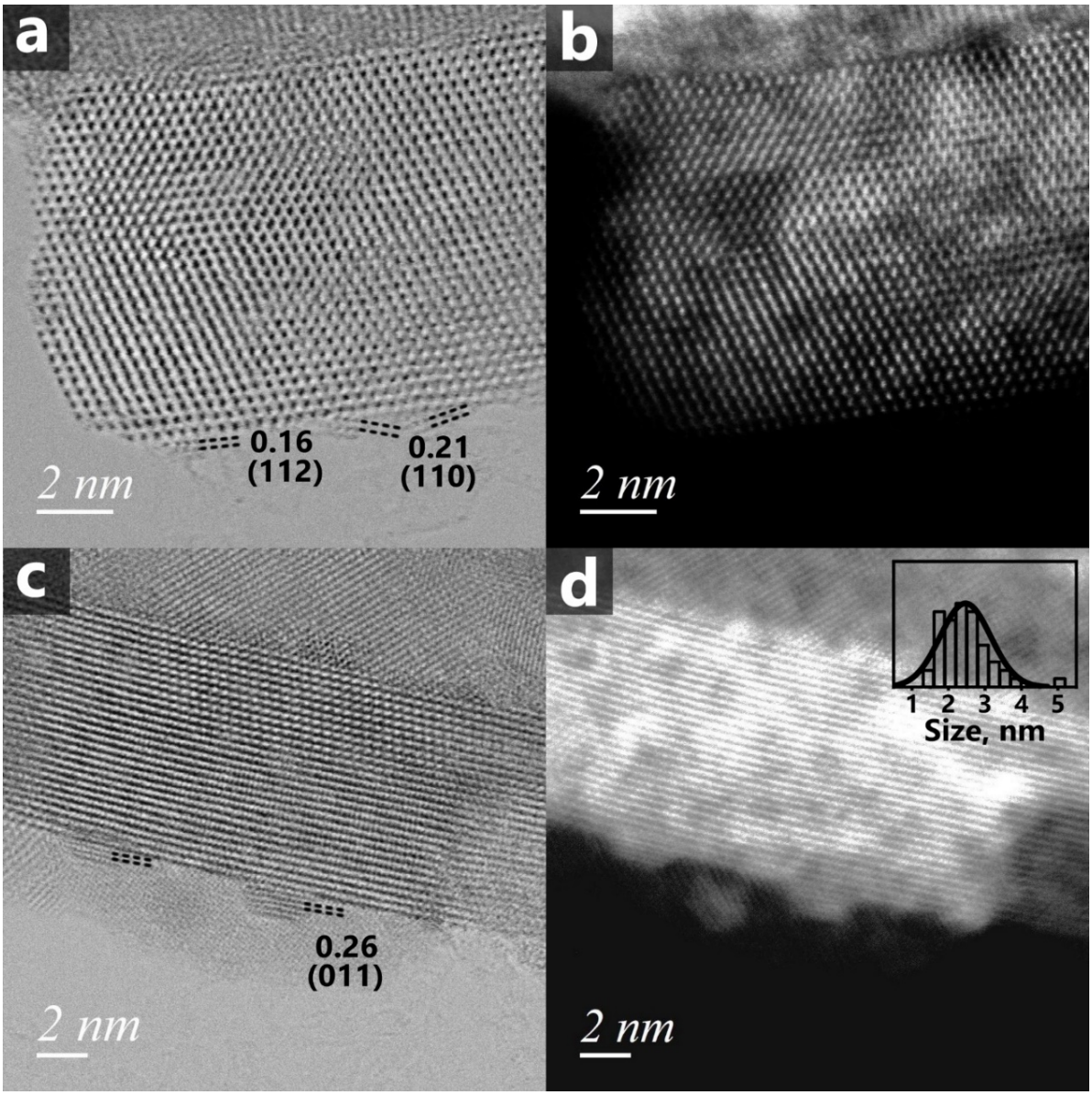

Figure B21. Atomically resolved bright-field (a, c) and HAADF-STEM (b, d) of Pd/CeO_2 nanorod catalysts with 5 wt% Pd (5PdRods). Clearly small nanoparticles and clusters can be seen (mean. size ~2.4 nm, 50 NPs were counted). Spacing corresponds to PdO phase.

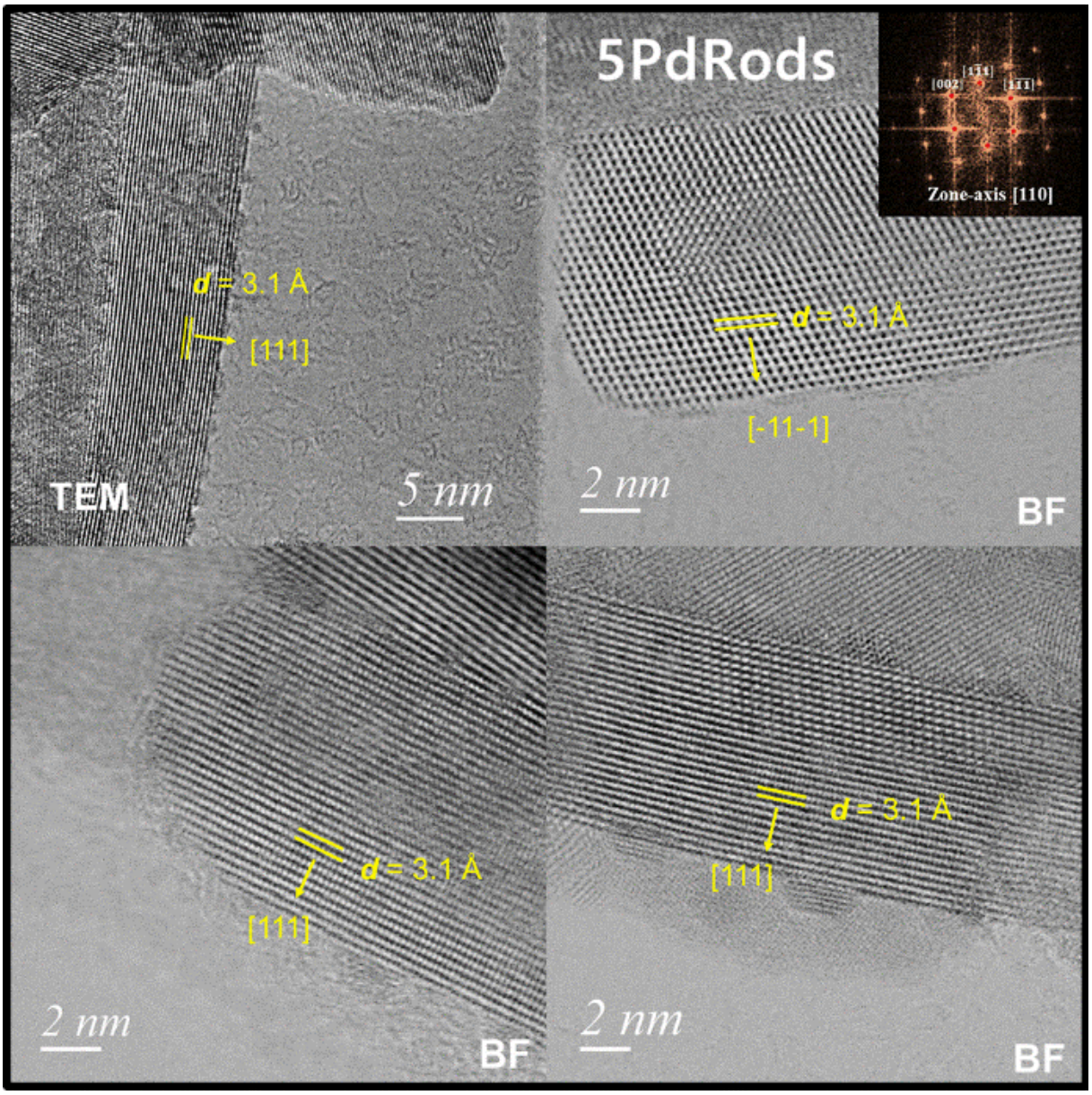

Figure B22. HRTEM images of 5PdRods sample showing predominant (111) faceting.

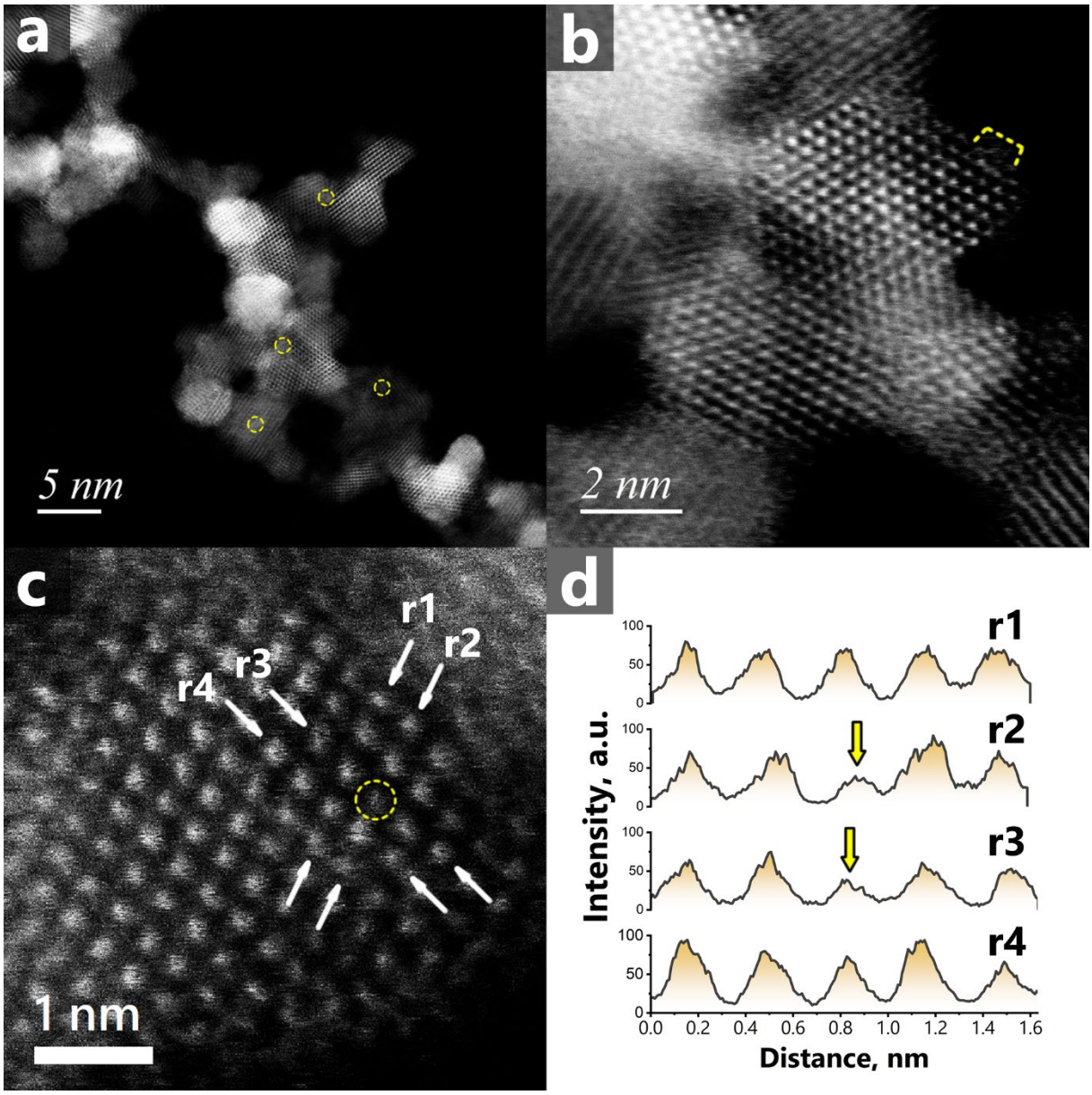

Figure B23. Atomically resolved HAADF-STEM (a-c) of Pd/CeO_2 flame-spray pyrolysis derived catalysts with 5 wt% Pd (5PdFSP). Sub-nm clusters (yellow dashed line) of palladium oxide found with EDX are difficult to locate with the dark-field TEM. Intensity analysis of atomic rows indicates possible location of Pd-doped sites (Pd scattering intensity is lower than that of Ce) or structural defects.

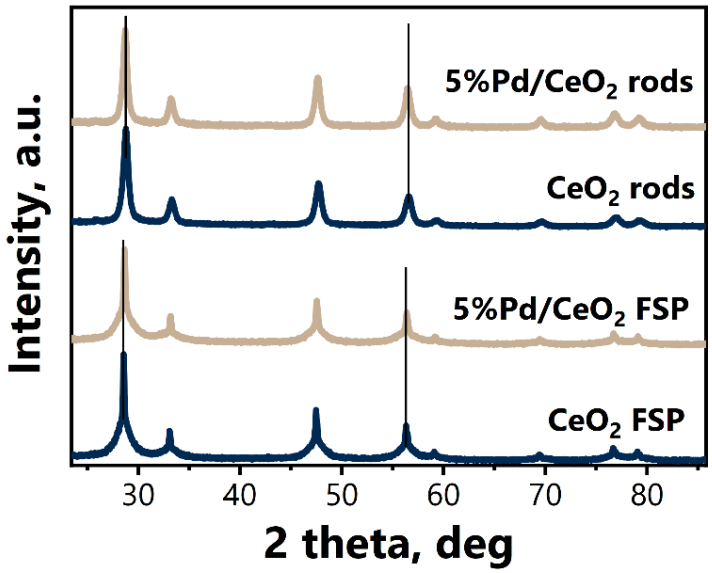

Figure B24. XRD patterns for as prepared catalysts. Vertical lines indicate a slight shift of CeO_2 reflections towards higher angles for one-step flame-spray pyrolysis made Pd/CeO_2. No reflections of PdO/Pd were found even for high-loaded samples.

Note B8. CO oxidation kinetics of 5PdRods and 5PdFSP.

As shown in **Figure B25**, on a Pd atom basis both Pd SACs (1PdRods and 1PdFSP) outperform their 5 wt% Pd counterparts in CO oxidation at 50 °C. The presence of small Pd oxide clusters and NPs leads to decreased mass specific activity. Thus, atomic dispersion Pd is essential to maximize the efficiency of CO oxidation at low temperature. The interfacial nature of Pd active sites (atoms in close vicinity to CeO_2) explains why similar kinetics of low-temperature CO oxidation (apparent activation energy and reaction orders, **Figure B26**) was observed for all studied catalysts, including single atoms and aggregated species. The nature of the active sites might be similar, but the efficiency of the material utilization is different. Similar conclusions were drawn by Christopher and co-workers, who studied Pt/TiO_2 catalysts where isolated Pt atoms and small NPs showed similar reaction orders and activation energies.[17]

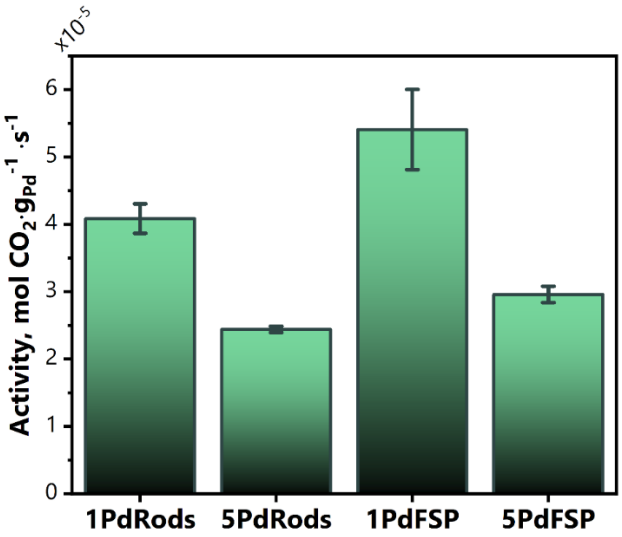

Figure B25. Mass-specific activity of the catalysts at 50ºC. Error bars represent standard deviation of the three subsequent measurements. Sieved fractions (125 to 250 µm) were diluted with ~250mg of SiC. Amount of the catalysts was adjusted in order to keep the conversion below 5%. All the catalysts were pre-treated in 20% O_2/He at 300ºC for 1h, cooled down to RT and flushed with He for 30 minutes. Then the reaction mixture of 1%CO + 1% O_2 in He (100 ml/min, GHSV ~120,000 ml/ g_{cat} h^{-1} for 1PdRods, 1PdFSP and 5PdRods; ~600,000 ml/ g_{cat} h^{-1} for 5PdFSP) was fed and temperature was slowly increased up to 50 ºC. The catalysts were exposed to the reaction feed for 4 hours prior to the activity measurements.

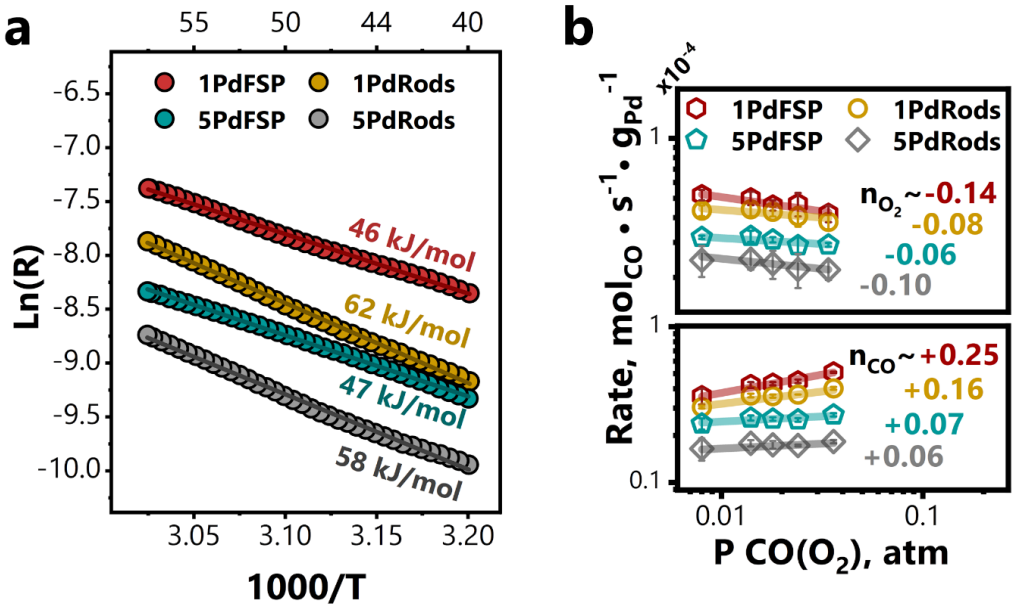

Figure B26. (a) Arrhenius plot of reaction rate (mol CO converted/ g_{pd} s^{-1}). Sieved fractions (125 to 250 µm) were diluted with ~250 mg of SiC. All catalysts were pre-treated in 20% O_2/He at 300 ºC for 1h. Reaction feed: 1% CO +1% O_2 in He, ramp rate 5ºC/min. Conversion kept below 20%, accordingly the amount of the catalysts was adjusted. Flow rate: 200ml/min, yielding GHSV 240,000 to 1,200,000 ml/ g_{cat} h^{-1}. (b) Reaction rate as a function of CO or O_2 partial pressure measured at 50 ºC. Reaction orders (n_x) estimated as slopes of the linear fit. Error bars represent standard deviation of the three subsequent measurements at each partial pressure. Sieved fractions (125 to 250 µm) were diluted

with ~250 mg of SiC. The amount of the catalysts was adjusted in order to keep the conversion below 5%. All the catalysts were pre-treated in 20% O_2/He at 300 °C for 1h, cooled down to RT and flushed with He for 30 minutes. Then reaction mixture of 1%CO + 1% O_2 in He (100ml/min, GHSV ~120,000 ml/ g_{cat} h^{-1} for 1PdRods, 1PdFSP and 5PdRods; ~600,000 ml/ g_{cat} h^{-1} for 5PdFSP) was fed and temperature ramped to 50 °C. Before reaction order measurements catalysts were kept on stream for 5h for stabilisation.

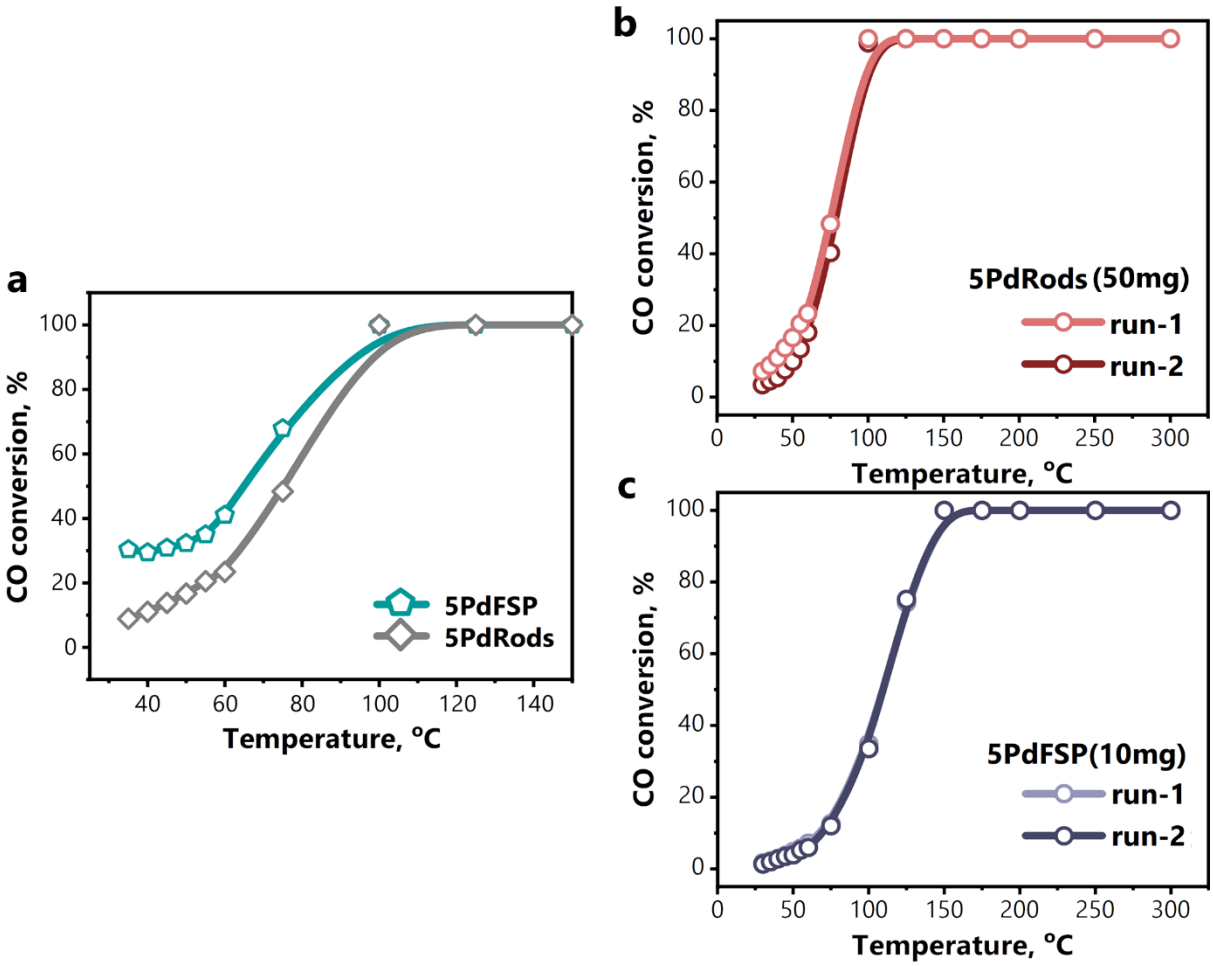

Figure B27. Steady-state plots of CO oxidation activity: (a) comparison of 5 wt% Pd samples (GHSV ~ 60,000 ml/ g_{cat} h^{-1}), (b) Repeated reaction cycles for 5PdRods (GHSV ~ 60,000 ml/ g_{cat} h^{-1}), (c) Repeated reaction cycle for 5PdFSP (GHSV ~ 300,000 ml/ g_{cat} h^{-1}). Sieved fractions (125 to 250 µm) were diluted with ~250mg of SiC. All the catalysts were pre-treated in 20% O_2/He at 300°C for 1h and cooled down to RT. Then reaction mixture of 1%CO + 1% O_2 in He was fed. After 30 minutes of dwell at RT, stepwise heating was initiated with 5 °C/min. Each measurement was performed after 15 minutes of stabilisation at any temperature point. Second run was performed after cooling to 30°C in the reaction mixture overnight. Total time on stream ~ 24h.

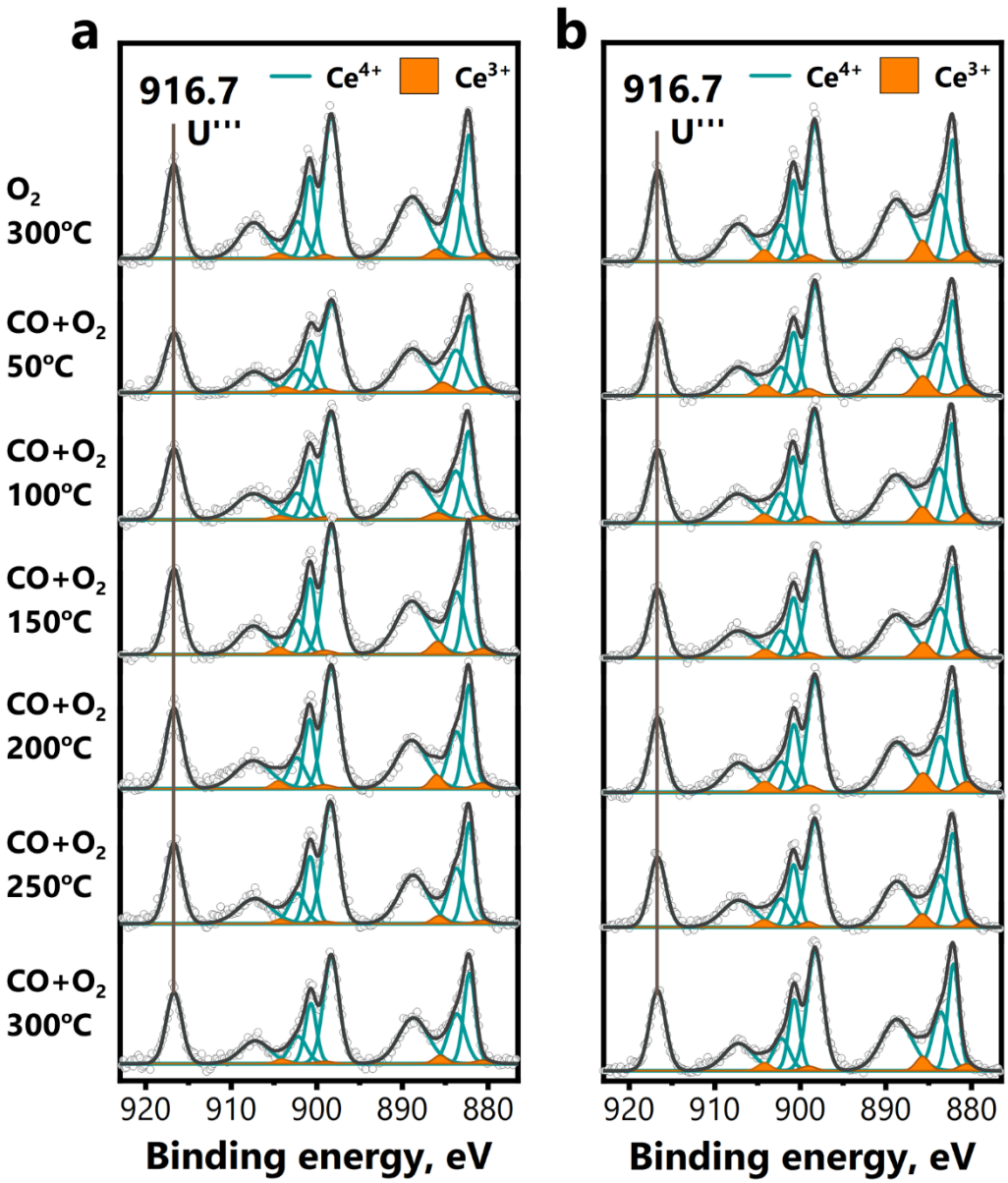

Figure B28. NAP-XPS of Ce 3d core-line region for (a) 5PdRods and (b) 5PdFSP. Each spectrum was recorder at isothermal conditions. Pressure of reactants (CO and/or O_2) was fixed to 2 mbar. All spectra were energy corrected by the U''' component at 916.7 eV. Spectra fitting model is based on reported by Skala et al.[28] As can be concluded from the Ce 3d core-line fitting, only minute changes in Ce^{3+} can be observed under reaction conditions. However, we note a slightly higher Ce^{3+} concentration for 5PdFSP (b) sample, as compared to 5PdRods (a) at similar conditions.

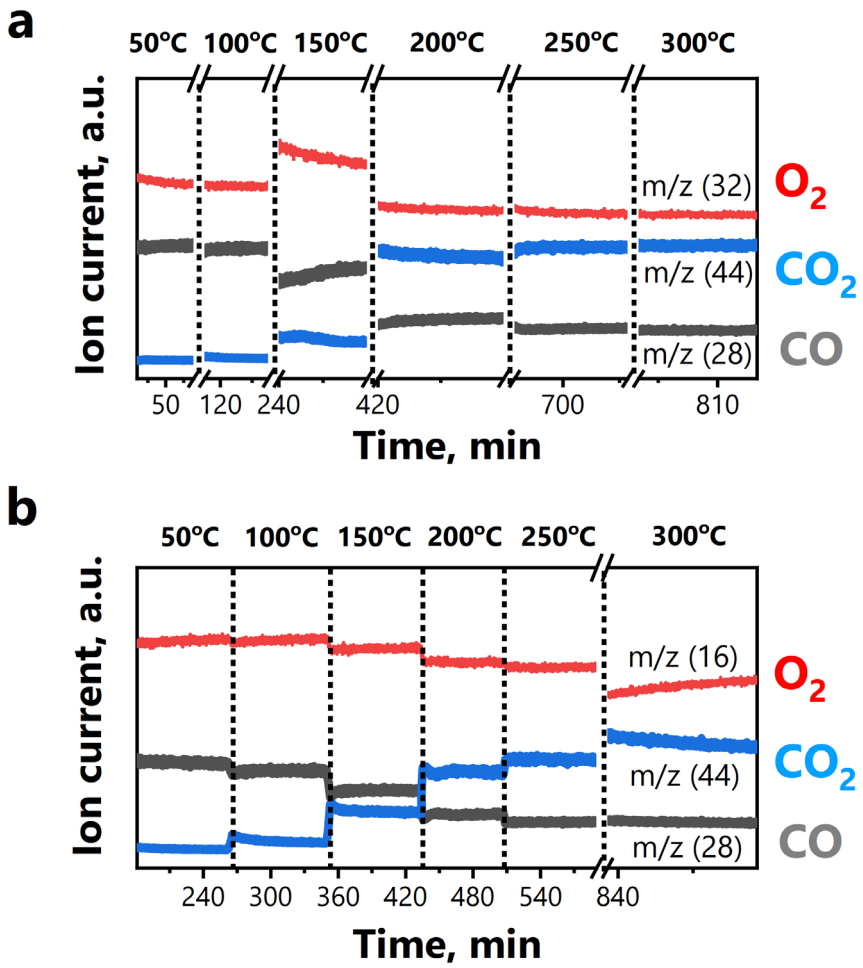

Figure B29. Mass-spectrometry data collected during NAP-XPS measurements for (a) 5PdRods and (b) 5PdFSP samples. RGA mass-spectrometer is located in the second differential pumping stage of the analyzer. Overall flow in the *in situ* cell was fixed to 2 ml/min. The overall pressure of 2 mbar was adjusted by the automatic back pressure controller. As follows from the MS-data, *in situ* cell design allows following the operation of catalyst during the measurements. However, we note that these data can be used only to obtain qualitative trends.

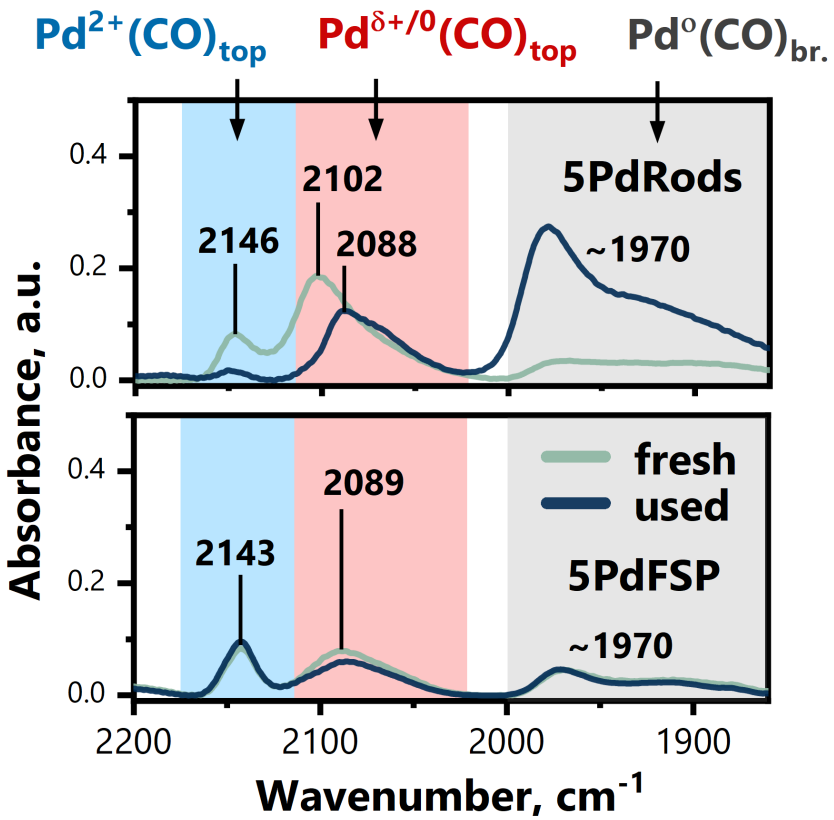

Figure B30. *In situ* DRIFT spectra of fresh and used catalysts (after one light-off cycle up to 300 °C) at 50 °C and 2 mbar of reactants ($CO:O_2$=1:1, 3.5 ml/min flow mode). For 5PdFSP catalyst, the intensity of the 2143 cm^{-1} band remains the same even after reaction at 300 °C, in stark contrast to 5PdRods sample. The lower fraction of Pd single atoms after the first cycle of reaction observed for 5PdRods explains the partial loss in low temperature activity during the second cycle of reaction (**Figure B27**). This finding suggests that even in case of high-loaded samples, where PdO clusters are also present, FSP-derived Pd-doped ceria can stabilize the highly dispersed Pd^{2+} forms, in line with the NAP-XPS results (**Figure 4.4**).

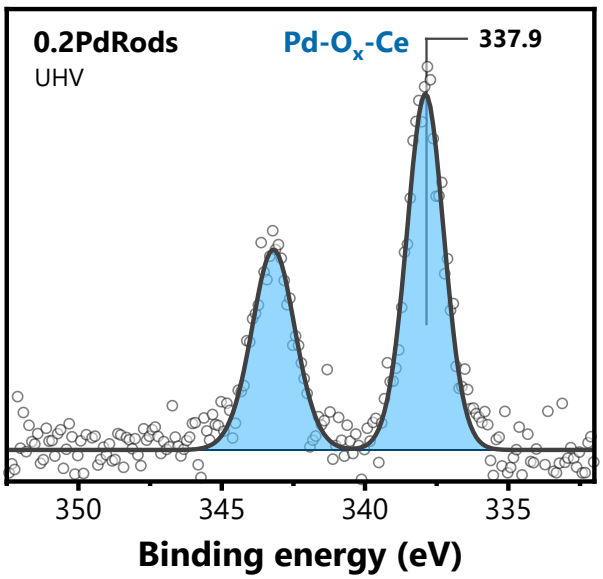

Figure B31. Conventional UHV XPS spectrum of Pd 3d core-line of the 0.2 wt% Pd/CeO_2-nanorods sample (0.2PdRods). The main doublet is attributed to the Pd-O_x-Ce moieties suggesting a highly dispersed nature of Pd in this sample in the as-prepared state.

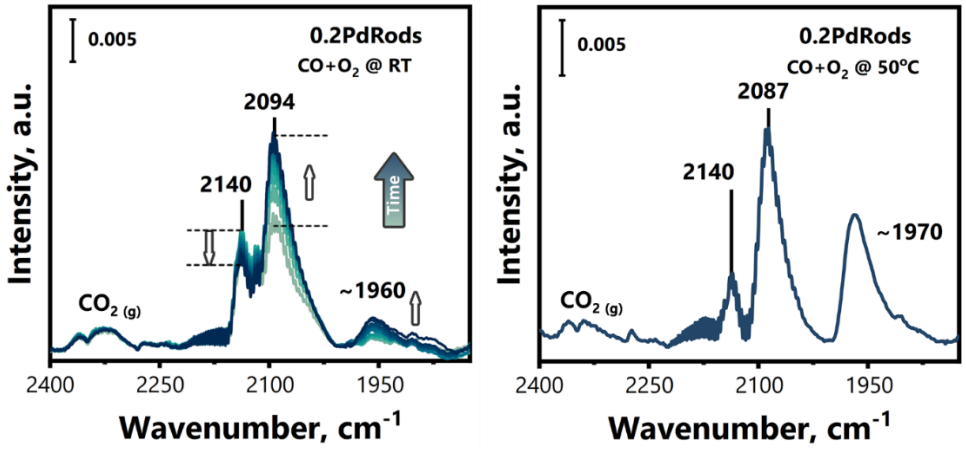

Figure B32. *In situ* DRIFT spectra of 0.2PdRods exposed to reaction mixture (2 mbar of $CO:O_2$ = 1:1, 3.5 ml/min, flow mode) at room temperature (left graph) and 50 °C (right graph). Overall, the behavior of the 0.2PdRods sample is very similar to the one of 1PdRods (**Fig. B15**), although the contribution of bridged carbonyls is markedly lower. This can be explained by the lower amount of Pd on the surface and, thus, the lower extent of sintering of the Pd single atoms. However, when the temperature increases to 50 °C (right graph), further reduction takes place and the overall spectrum contains similar features as those in the 1PdRods sample (**Figure 4.3**). Thus, we can conclude that the effect of lowering the Pd surface concentration on the stability of PdRods catalyst is minor.

Note B9. CO titration experiments.

The catalysts were subjected to the flow of CO and He (partial pressure of CO was 2 mbar) in the DRIFTS cell and the spectra were collected as a function of time. As shown in **Figure B33** (top panel) after the first 15 minutes of CO exposure several bands emerged. These bands located at 2143 cm^{-1}, 2089 cm^{-1} and ~1900 cm^{-1}, as discussed earlier[5], correspond to Pd^{2+} single-atoms, reduced $Pd^{+/\delta+}$ species and metallic Pd clusters, respectively. Upon reduction the intensity of the 2143 cm^{-1} band decreases, while the broad band at ~1900 cm^{-1} grows. We can conclude that Pd^{2+} single-atom species readily react with CO at 50 °C and agglomerate to form metallic clusters. Comparison of these data with the DRIFT spectra obtained under reaction conditions, *i.e.* in the presence of O_2 (**Figure 4.3c** and **Figure B15**), points to the vital role of the gas-phase oxygen on the stability of single-atom Pd species (attributed to 2143 cm^{-1} band). Turning now to the 1PdFSP SAC, we note a substantially lower intensity of the observed carbonyl bands, which is related to the lower fraction of surface Pd atoms in this sample (**Figure B34**). Similarly, to 1PdRods, we observed a reduction of oxidized Pd single atoms accompanied by their clustering. However, in case of 1PdFSP, considerably lower of bridged carbonyls at 1973 cm^{-1} was observed, pointing to a lesser extent of Pd agglomeration. Furthermore, **Figure B34** (bottom panel) displays a notable relative contribution of ionic isolated species (2143 cm^{-1} CO band in the final spectrum remains at 30% of its initial intensity), whereas in case of 1PdRods reduced species dominate (**Figure B33**, bottom panel).

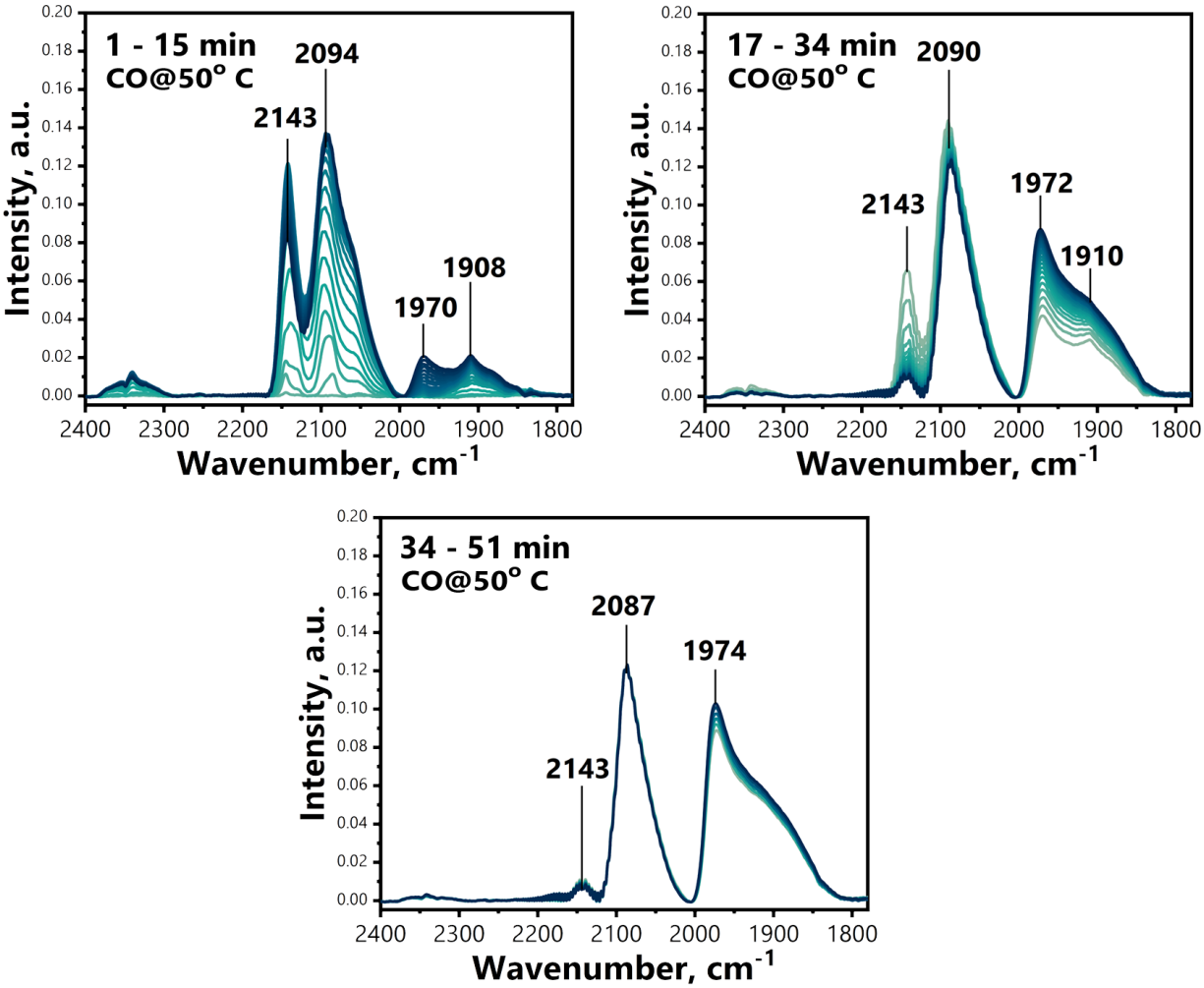

Figure B33. *In situ* DRIFT spectra of 1PdRods upon CO exposure at 50 °C as a function of time. Fresh catalyst was pre-treated in O_2 at 300 °C, cooled down to 50 °C and then evacuated. Subsequently 3.5 ml/min flow of CO/He was fed with constant 2 mbar partial pressure of CO in the cell. DRIFT spectra were recorded as a function of time. The intensity of 2143 cm^{-1} band decreases, accompanied by growth in the contribution of sub-oxidized cluster species. First doses of CO show multiple adsorption bands prior to appearance of bridged carbonyls. This observation might indicate the initial site heterogeneity/inequality of Pd single atoms, probably due to the different local coordinative environment of anchored Pd atoms on different surface defects of nanorods.

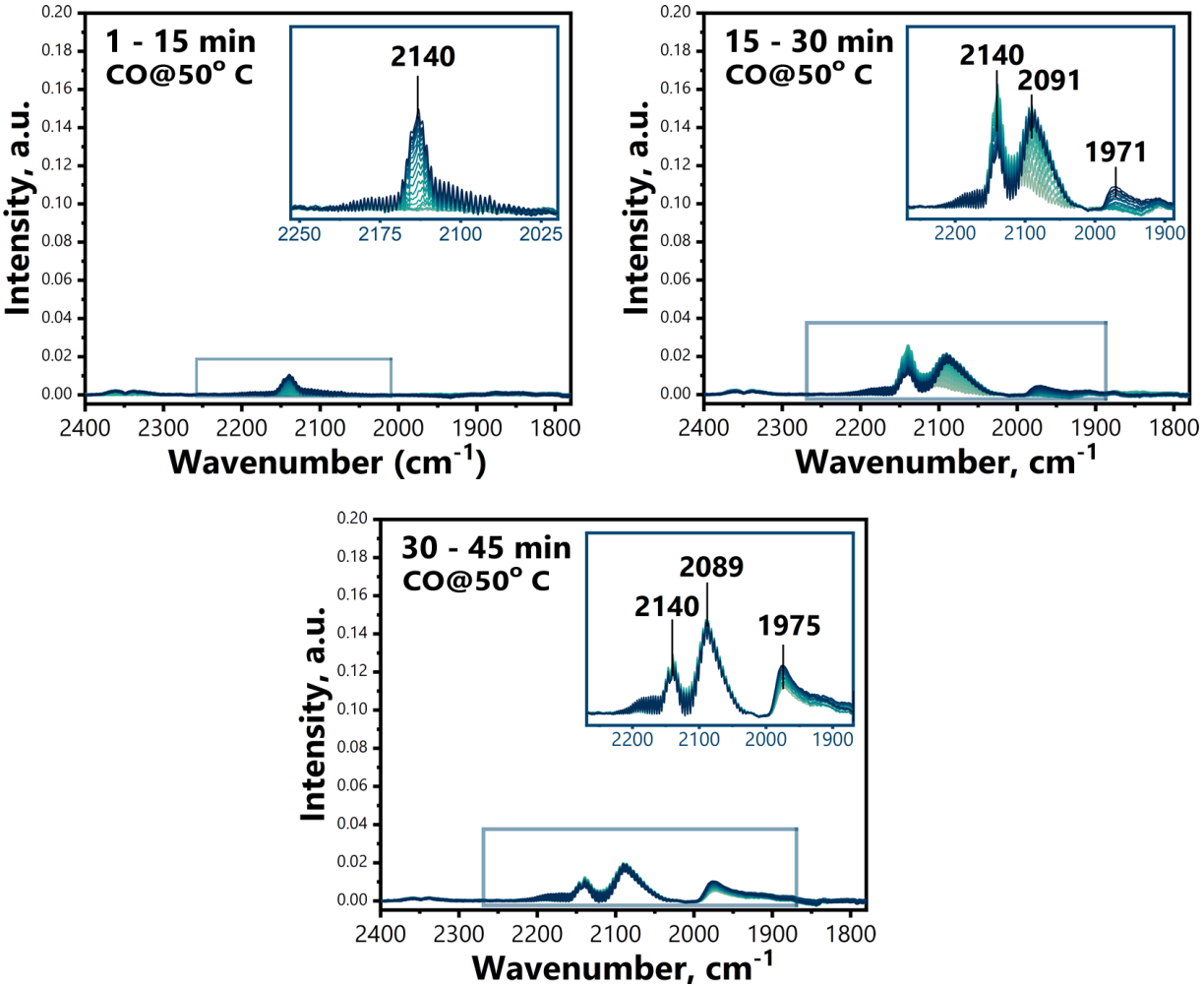

Figure B34. *In situ* DRIFT spectra of 1PdFSP upon CO exposure at 50 °C as a function of time. Fresh catalyst was pre-treated in O_2 at 300 °C, cooled down to 50 °C and then evacuated. Subsequently 3.5 ml/min flow of CO/He was fed with constant 2 mbar partial pressure of CO in the cell. DRIFT spectra were recorded as a function of time. The intensity of 2143 cm^{-1} band decreases, accompanied by growth in the contribution of sub-oxidized cluster species. Substantially lower intensity of CO adsorption bands compared to 1PdRods sample is likely due to the lower concentration of Pd single atoms on the surface, as was evidenced by CO chemisorption and XPS.

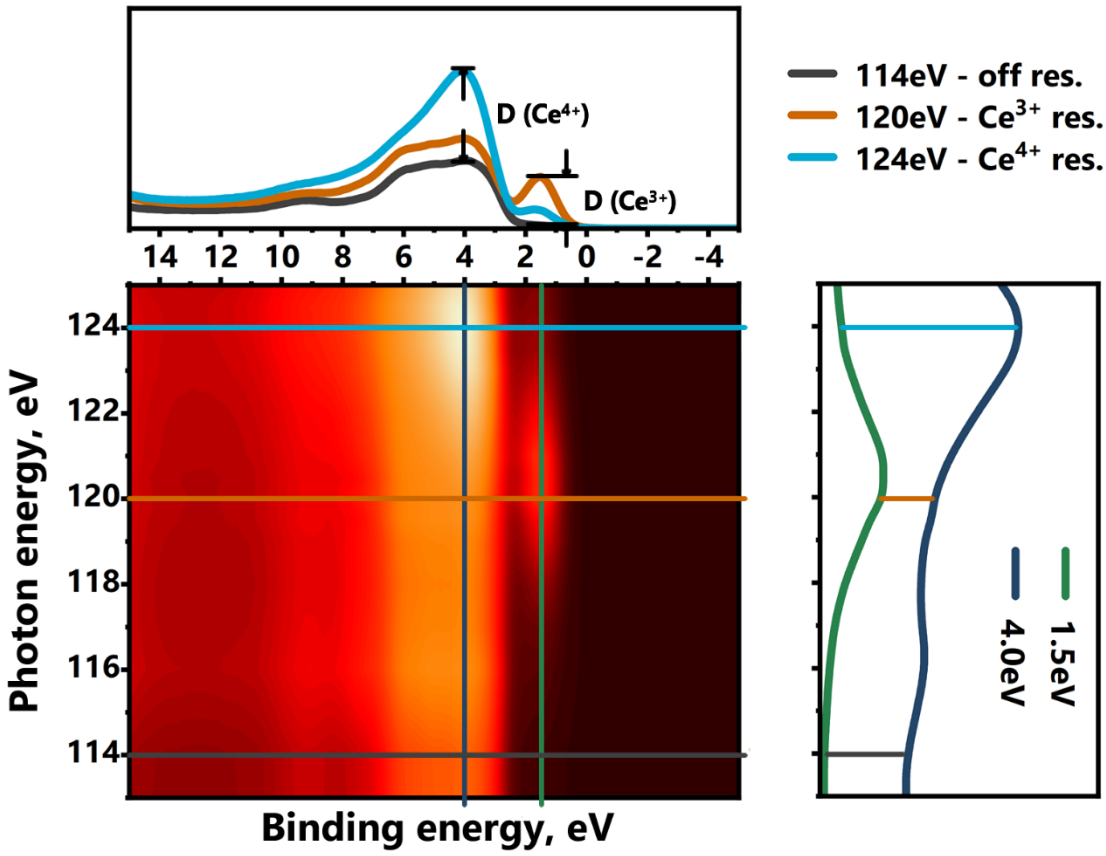

Figure B35. Valence band region resonance photoelectron spectroscopy (RPES) of bare FSP-made CeO_2 support in UHV. Resonant energies were found experimentaly via tunning the incident photon energy and acquiring the respective VB spectra. Resonant VB features of Ce^{4+} (~ 4 eV) and Ce^{3+} (~ 1.5 eV) occurred at 124 eV and 120 eV of incident photon energy respectively. Off-resonance spectra, *i.e.* below the Ce 4d level threshold, were measured at 114 eV photon energy. The resonant ratio of $D(Ce^{3+})/D(Ce^{4+})$ was determined by the heights of corresponding maxima. The Ce^{3+}/Ce^{4+} ratio was estimated via the formulae proposed by Lykhach et al. [29]: $Ce^{3+}/Ce^{4+}= D(Ce^{3+})/(5.5*D(Ce^{4+}))$. Further methodological details can be found in the same paper.

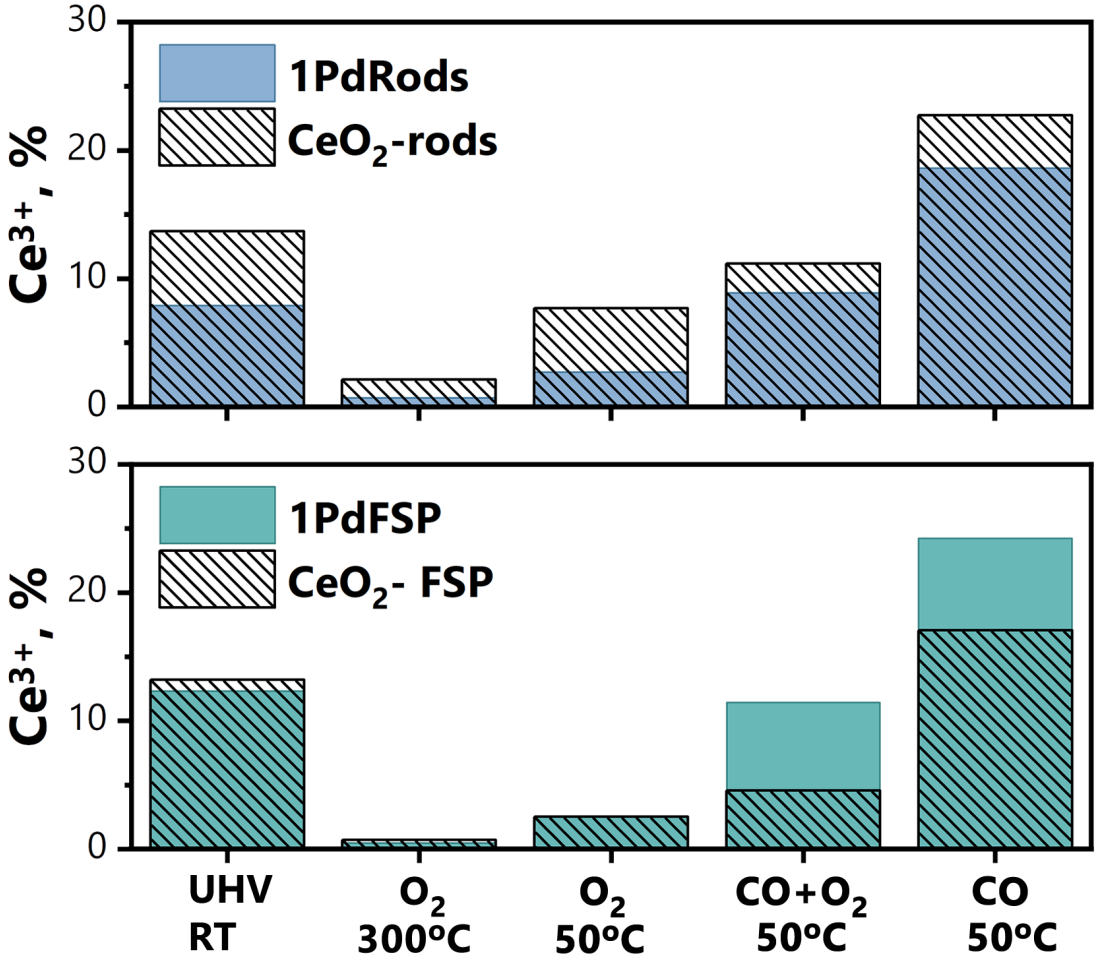

Figure B36. Ce^{3+} concentration at the surface (probing depth ~1 nm) derived from the RPES data. The data were collected for Pd-loaded samples and bare supports to follow the effect of Pd addition on the surface reducibility of the CeO_2. In case of impregnated nanorod CeO_2 we can observe a systematically lower Ce^{3+} fraction. In other words, in this temperature regime, Pd does not facilitate the CeO_2 surface oxygen removal in case of impregnated 1PdRods SAC. However, we found a pronounced effect in case of FSP-derived system, which showed substantial increase in Ce^{3+} concetration under reducing conditions. These findings support DFT results reported by us and other groups[4,30], which suggested that Pd inclusion into the CeO_2 lattice increases its reducibility and provides reactive oxygen already at low temperature.

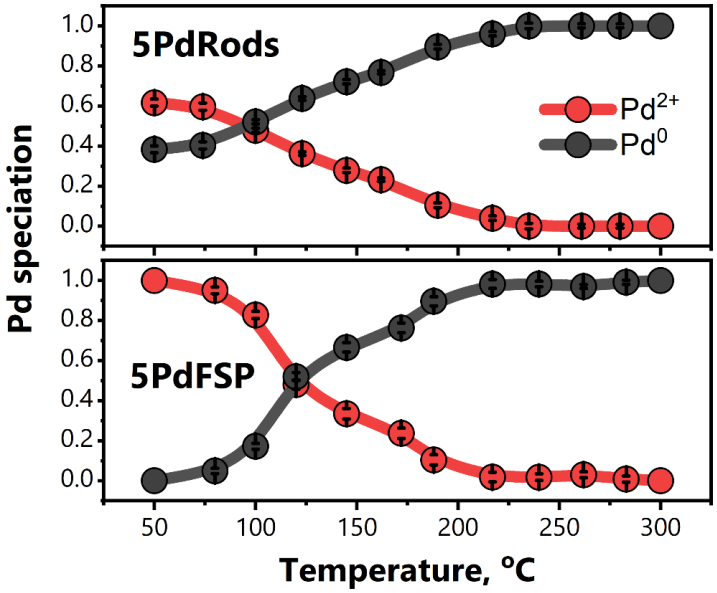

Figure B37. Linear combination fitting of Pd K-edge XANES data acqired during *in situ* XAS/WAXS study of samples in TPR-CO regime. Error bars represent standard deviation of the linear combination fit using two spectra as standards: oxidized (just before CO was introduced) and reduced (final spectra obtained in CO at 300 °C – **Figure B43** for 5PdRods). In case of FSP no substantial changes at 50 °C were observed (**Figure B44**), thus the first spectrum was used as a standard for linear combination fitting.

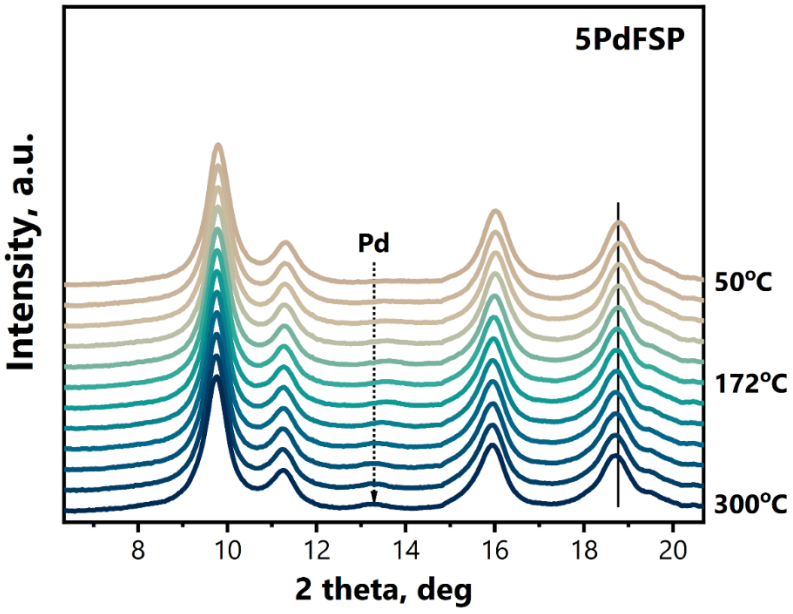

Figure B38. WAXS data acquired during *in situ* XAS/WAXS study of 5PdFSP sample in TPR CO regime. Depicted region of scattering angles was used for Rietveld refinement and determination of lattice parameter. Solid line emphasize the shift of the ceria phase reflections, due to the lattice expansion upon Ce^{3+} formation.

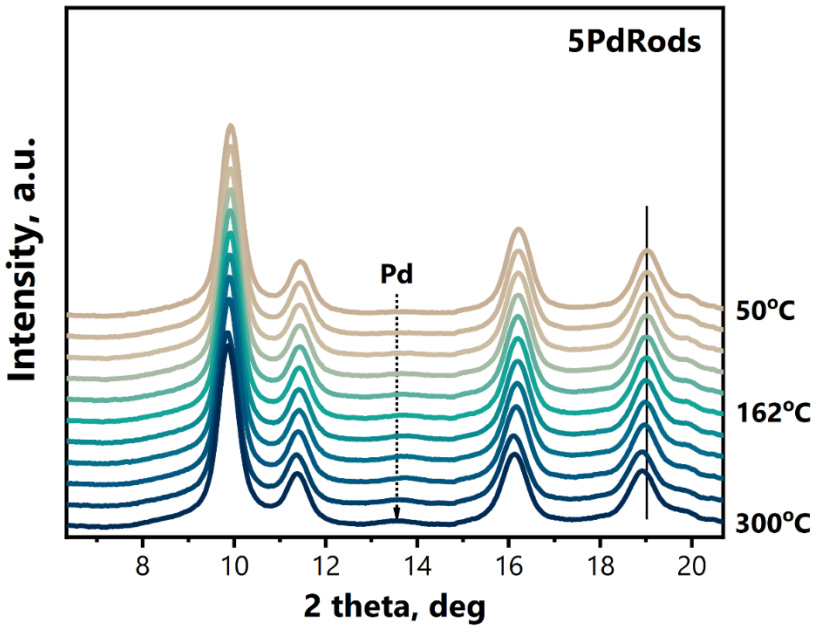

Figure B39. WAXS data acquired during *in situ* XAS/WAXS study of 5PdRods sample in TPR CO regime. Depicted region of scattering angles was used for Rietveld refinement and determination of lattice parameter. Solid line emphasize the shift of the ceria phase reflections, due to the lattice expansion upon Ce^{3+} formation.

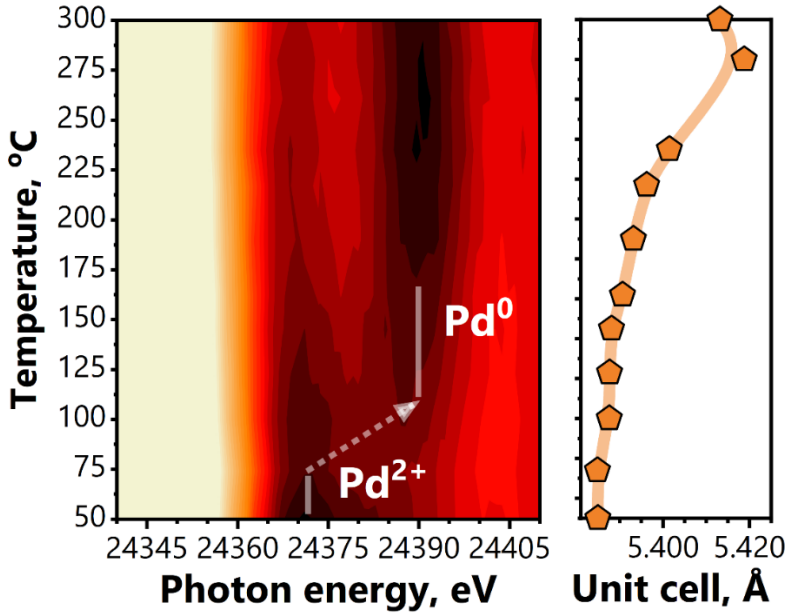

Figure B40. Combined *in situ* XAS/WAXS study of 5PdRods sample in TPR-CO regime: left panel shows Pd XANES region and right panel unit cell parameter (*a*) derived from the Rietveld refinement (**Figure B41**).

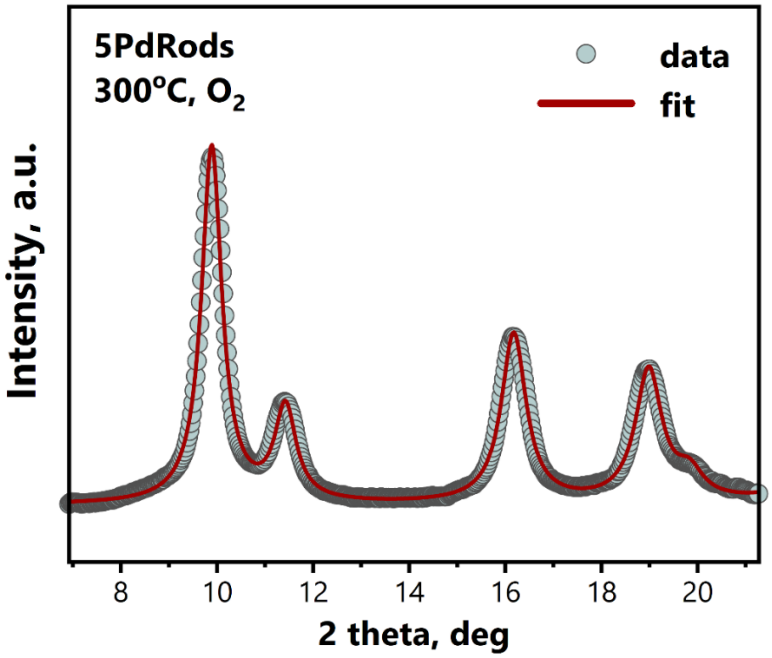

Figure B41. Example of the data region used for Rietveld refinement.

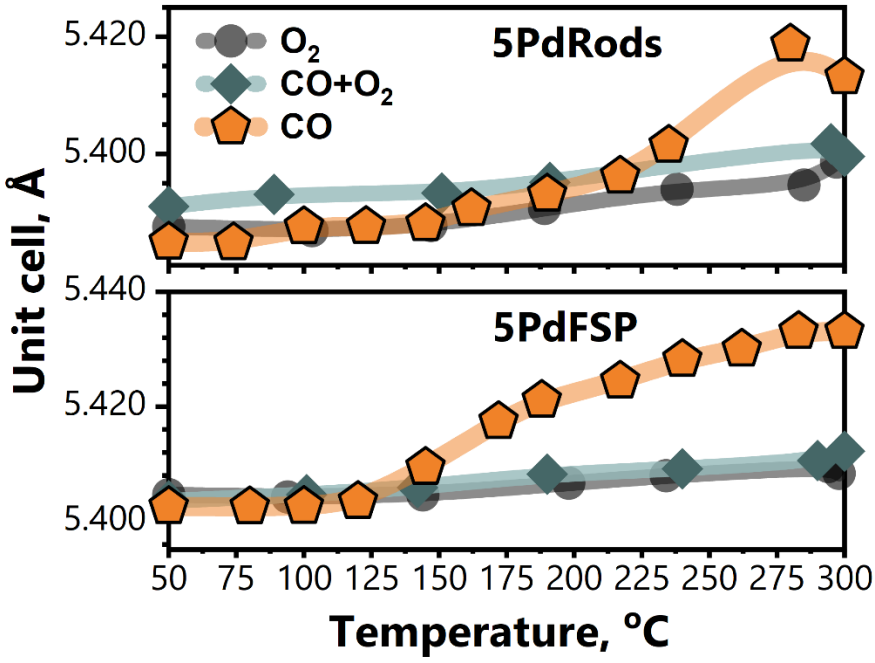

Figure B42. Lattice parameter *a* (related to Ce^{3+} formation) as a function of reaction conditions determined via the Rietveld refinement of CeO_2 diffraction patterns. Prior to TPR-CO, samples were thermally treated in oxygen and reaction mixture with no notable expansion due to the Ce^{3+} formation, indicative of low population of oxygen vacancies in the bulk of CeO_2.

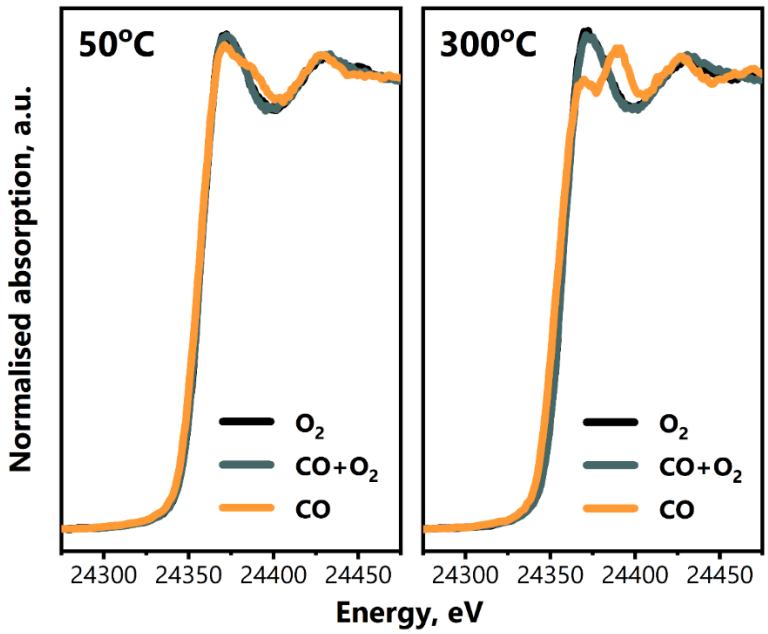

Figure B43. XANES spectral region of Pd K-edge for 5PdRods sample exposed to different conditions. Under reaction conditions at elevated temperature no Pd metal is seen. This finding suggests that Pd metal observed in NAP-XPS locates only on the very surface, while the core of the Pd NPs remains oxidized. Alternatively, different partial pressures of oxygen in NAP-XPS conditions and in XAS/WAXS study can explain variation in average Pd oxidation state. Notably, exposure to CO at 50 °C already leads to spectral changes in XANES data for 5PdRods.

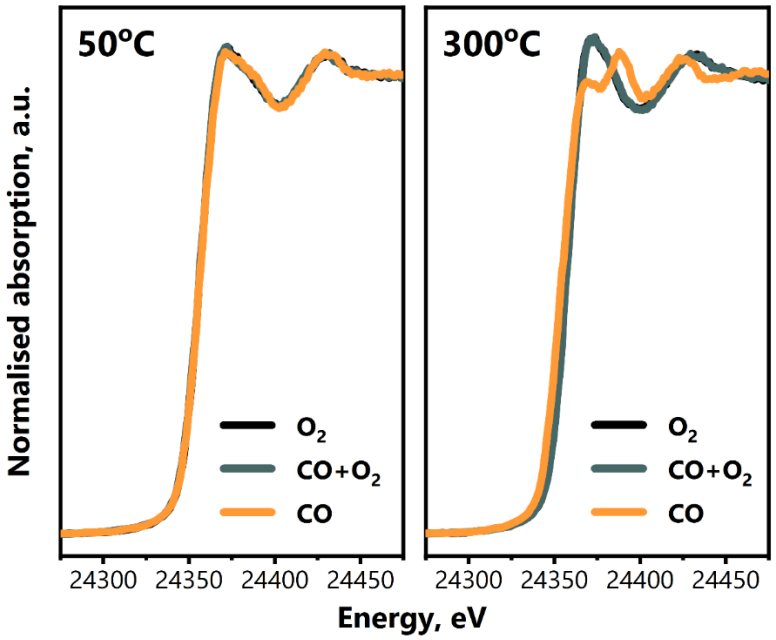

Figure B44. XANES spectral region of Pd K-edge for 5PdFSP sample exposed to different conditions. No changes under reaction conditions correlate with *in situ* NAP-XPS data. These results indicate high stability of oxidized Pd species. Exposure to CO at 50 °C did not lead to substantial spectral changes in XANES data for 5PdFSP.

Note B10. Sample conductivity necessary for NAP-XPS measurements.

XPS often requires sufficient conductivity of the samples to study the oxidation states of the elements present on the surface. [31,32] Using a flood gun, which is a filament generating low energy electrons and/or ions to compensate for the surface charging, analysis of even insulating samples can be achieved.[31] While useful for high-vacuum conditions, such an approach, however, is technically not feasible for *in situ* measurements. Thus, *in situ* XPS measurements of insulating and semi-conducting samples pose a serious challenge. Here we used an aproach of using conductive diluent, namely carbon (Printex U, or model soot). Carbon was mixed with catalyst powder (diluent:catalyst – 1:20 for lab-based XPS and 1:5 for synchrotron-based XPS) and pelletized. This diluent is inert towards oxidation at temperatures below 300 °C. [33,34] No CO_2 formation, apart from the desorption at low temperature (~150 °C), was detected upon heating diluted 5PdFSP sample in pure O_2 (**Figure B45**). Therefore, the pretreatment step ensures that all loosely bound species and reactive carbon moieties are removed. Under pretreatment conditions even an undiluted sample is sufficiently conductive, largely due to the elevated temperature[31] and partial charge compensation by the gaseous molecules, resulting in high-quality photoelectron spectra of both Pd 3d and Ce 3d lines (top spectra in **Figure B46**). It can be seen that the presence of diluent does not change the chemical speciation of Pd and Ce (spectra p and d). At lower temperature, substantial distortion of the spectral features occur (*e.g.,* no spectra can be recorded below at T<100 °C, regardless of gas composition) for the undiluted powder. The arrows 1 and 2 indicate broadenning and assymetry of the components induced by the charging even at 100 °C. Spectra of such quality (cyan) cannot provide reliable information, as extra components necessary for fitting can correspond to charging rather than to the actual chemical states. Much narrower spectral features (identical to a pure sample at high temperature) were found for diluted sample (dark cyan), which allows proper fitting and assignment of the spectral components. Using this method one can obtain spectroscopic data free from sample charging (**Figure B47**) under reaction conditions even at low temperature, relevant in particular for CO oxidation studies. At elevated temperature under reaction conditions both samples (blue spectra) are sufficiently conductive and we can note that dilution with carbon leads to a slightly underestimated fraction of reduced Pd species (70% in pure sample *vs.* 65% in diluted sample). This effect likely stems from the partial coverage of catalyst particles with the diluent, which hinders the reaction with the gas phase molecules. Using the same dilution method to compare different samples reliable systematic trends can be obtained, although the absolute values of charge states distributions (within the spectral line) should be taken with care.

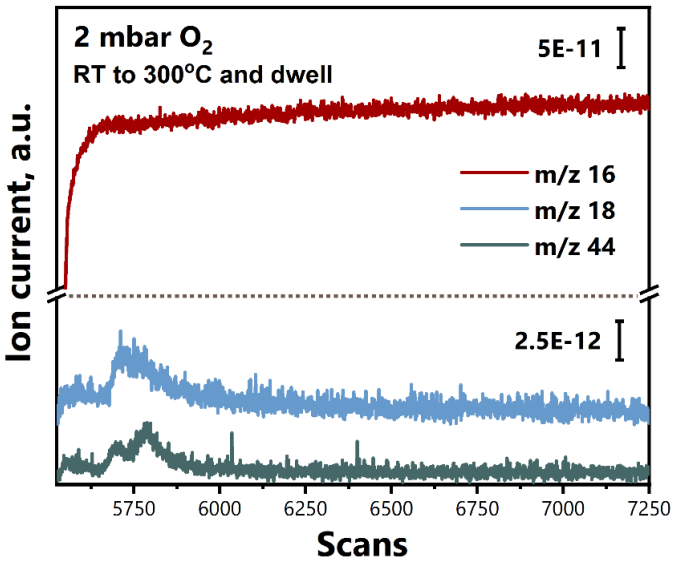

Figure B45. Mass spectrometry data recorded upon pretreatment of the 5PdFSP carbon-diluted sample in the NAP-XPS reaction cell. 2 mbar of oxygen were dosed into the *in situ* cell and then the MS data is recorded as a function of increasing temperature: from RT to 300 °C. As follows from the 44 and 18 m/z signals, water and CO_2 are detected when the temperature reaches ~150 °C. This can be explained by the desorption of water and loosely bound CO_2 from the sample and diluent. Afterwards no increase in water or CO_2 signals was noted, proving the absence of carbon (diluent) oxidation up to 300 °C.

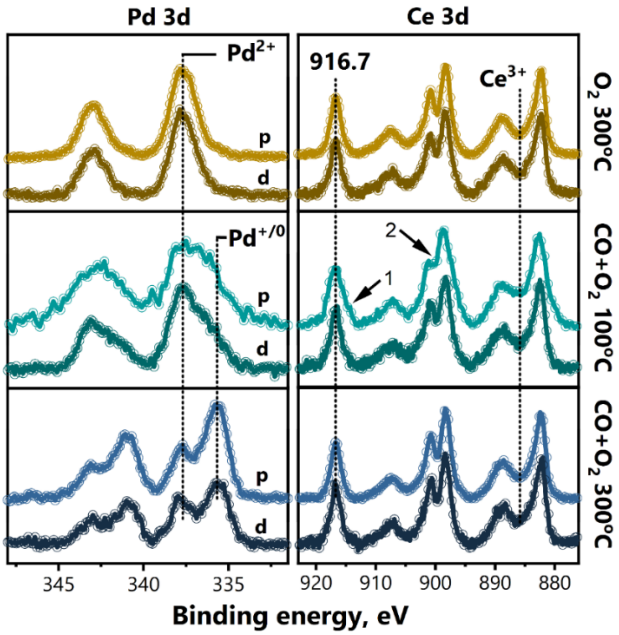

Figure B46. Pd 3d and Ce 3d core-lines for 5PdRods exposed to different conditions. The catalyst powder was grounded and pressed into pellet, which was further attached to a sample holder and transferred into the NAP-cell. This sample is denoted as (p). Another portion of the same powder was diluted with 5 wt% of Printex U carbon, to provide sufficient conductivity and pressed into pellet. This sample was denoted as (d).

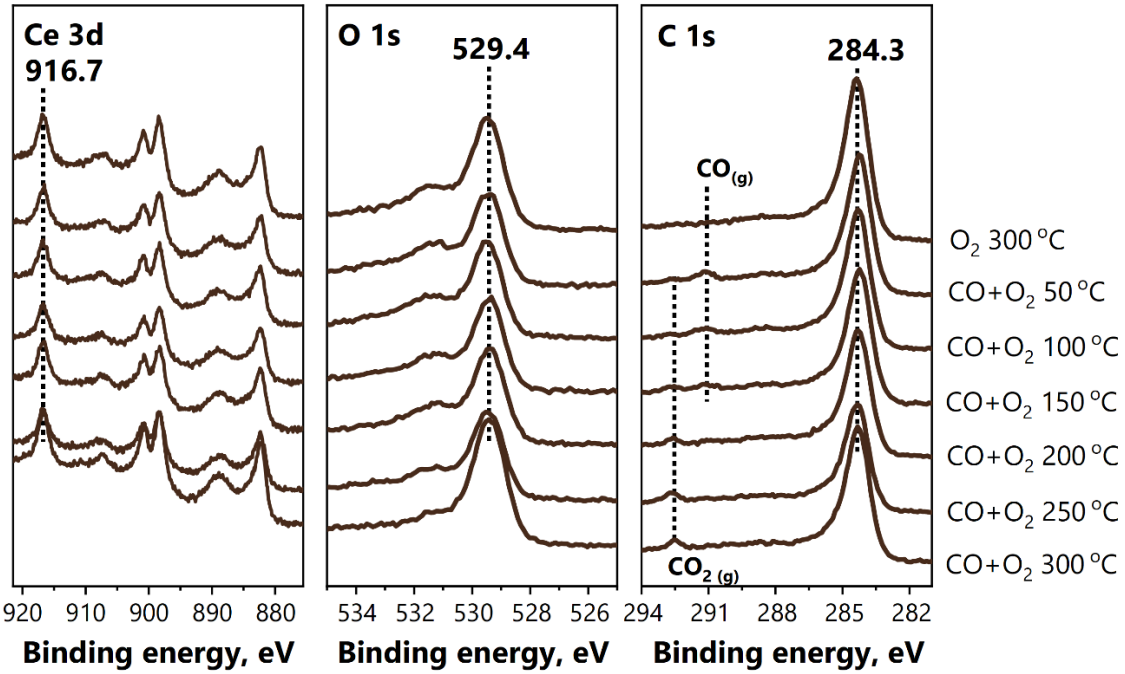

Figure B47. Example of NAP-XPS data acquired for a carbon-diluted sample (5PdFSP) energy corrected by the position of the U''' component of the Ce 3d core-line.

Table B1. EXAFS fitting results. S_0^2 values (0.68 for B18, Diamond and 0.70 for DUBBLE, ESRF) were derived from fitting the PdO reference (Sigma-Aldrich) and used for the fitting of Pd-CeO_2 samples. ΔE_0 was shared for all the shells, while σ^2 and ΔR values were shared within each shell for the same type of back-scattering atoms. The errors indicate the uncertainties of fitting results derived from Artemis software.

Sample	Path	R (Å)	CN	σ^2 (Å^2)	ΔE_0 (eV)	R-factor (%)
1PdRods	Pd-O	2.02 ± 0.01	3.1 ± 0.7	0.005 ± 0.002	1.5 ± 2.3	2.8
	Pd-Ce (surf. model)	3.24 ± 0.03	3.2 ± 2.4	0.014 ± 0.007		
1PdRods used	Pd-O	1.99 ± 0.01	2.6 ± 0.7	0.003 ± 0.002	-0.9 ± 2.2	2.5
	Pd-Pd (metal)	2.74 ± 0.01	2.9 ± 0.9	0.007 ± 0.002		
1PdFSP	Pd-O	2.01 ± 0.01	4.0 ± 0.5	0.001 ± 0.001	2.0 ± 1.5	2.1
	Pd-Ce (doped model)	3.19 ± 0.01	4.1 ± 1.8	0.009 ± 0.003		
1PdFSP used	Pd-O	2.00 ± 0.01	4.1 ± 0.7	0.001 ± 0.001	1.7 ± 1.9	1.7
	Pd-Ce (doped model)	3.22 ± 0.02	3.6 ± 2.2	0.009 ± 0.004		
5PdRods	Pd-O	2.02 ± 0.06	4.4 ± 0.6	0.001 ± 0.001	5.3 ± 1.8	1.2
	Pd-Pd (oxide)	3.04 ± 0.01	3.2 ± 1.4	0.006 ± 0.002		
	Pd-Pd (oxide)	3.43 ± 0.01	2.9 ± 1.1	0.006 ± 0.002		
5PdFSP	Pd-O	2.01 ± 0.01	4.1 ± 0.5	0.001 ± 0.001	3.3 ± 1.3	1.3
	Pd-Ce (doped model)	3.22 ± 0.01	5.1 ± 2.0	0.012 ± 0.003		
10PdFSP	Pd-O	2.01 ± 0.01	4.6 ± 0.5	0.002 ± 0.001	2.5 ± 1.3	1.5
	Pd-Ce (doped model)	3.20 ± 0.01	5.7 ± 2.3	0.012 ± 0.003		
PdO	Pd-O	2.02 ± 0.01	4.0	0.001 ± 0.001	-2.3 ± 1.7	1.6
	Pd-Pd (oxide)	3.05 ± 0.01	4.0	0.003 ± 0.001		
	Pd-Pd (oxide)	3.44 ± 0.02	8.0	0.003 ± 0.001		

Table B2. CO pulsing chemisorption, surface area, Pd loading and XPS data quantification. The errors indicate a standard deviation of measurements performed *in duplo*.

	CO adsorbed, $\mu mol/g_{cat}$	mol CO/mol Pd (ICP)	Pd_{surf}/Pd_{total}, %*	Pd/Ce XPS	Pd loading (ICP-OES), wt. %	BET surface area, m^2/g
CeO_2-nanorods	9	-	-	-	-	-
1PdRods	87	0.937	94	0.050	0.99 ± 0.01	64
5PdRods	82	0.178	18	0.285	4.9 ± 0.2	45
CeO_2-FSP	12	-	-	-	-	-
1PdFSP	7	0.069	7	0.032	1.02 ± 0.02	164
5PdFSP	196	0.404	40	0.172	5.14 ± 0.04	142

* Assuming only linear CO adsoprtion (Pd/CO = 1)

Table B3. Quantification of pulsing CO titration at 50°C

	CO consumed, $\mu mol/g_{cat}$	$CO_{cons.}$ / Pd_{total}, mol/mol
CeO_2-nanorods	7	-
1PdRods	219	2.34
5PdRods	165	0.36
CeO_2-FSP	~ 0 (0.4)	-
1PdFSP	312	3.24
5PdFSP	698	1.44

4.7 Appendix B references

1. Sartoretti, E., Novara, C., Giorgis, F., Piumetti, M., Bensaid, S., Russo, N. & Fino, D. *Sci. Rep.* **9,** 1–14 (2019).
2. McBride, J. R., Hass, K. C., Poindexter, B. D. & Weber, W. H *J. Appl. Phys.* **76,** 2435–2441 (1994).
3. Schilling, C. & Hess, C. *ACS Catal.* **9,** 1159–1171 (2019).
4. Su, Y. Q., Filot, I. A. W., Liu, J. X. & Hensen, E. J. M. *ACS Catal.* **8,** 75–80 (2018).
5. Spezzati, G., Su, Y., Hofmann, J. P., Benavidez, A. D., DeLaRiva, A. T., McCabe, J., Datye, A. K. & Hensen, E. J. M. *ACS Catal.* **7,** 6887–6891 (2017).
6. Zhang, M., Wang, M., Xu, B. & Ma, D. *Joule* **3,** 2876–2883 (2019).
7. Hill, A. J., Seo, C. Y., Chen, X., Bhat, A., Fisher, G. B., Lenert, A. & Schwank, J. W. *ACS Catal.* **10,** 1731–1741 (2020).
8. Bunluesin, T., Putna, E. S. & Gorte, R. J. *Catal. Lett.* **41,** 1–5 (1996).
9. Cargnello, M., Doan-Nguyen, V. V. T., Gordon, T. R., Diaz, R. E., Stach, E. A., Gorte, R. J., Fornasiero, P. & Murray, C. B. *Science* **341,** 771–773 (2013).
10. Peterson, E. J., DeLaRiva, A. T., Lin, S., Johnson, R. S., Guo, H., Miller, J. T., Hun Kwak, J., Peden, C. H. F., Kiefer, B., Allard, L. F., Ribeiro, F. H. & Datye, A. K. *Nat. Commun.* **5,** 4885 (2014).
11. Alcala, R., DeLaRiva, A., Peterson, E. J., Benavidez, A., Garcia-Vargas, C. E., Jiang, D., Pereira-Hernández, X. I., Brongersma, H. H., Veen, R. ter, Staněk, J., Miller, J. T., Wang, Y. & Datye, A. *Appl. Catal. B: Environ.* **284,** 119722 (2021).
12. Wang, X., Chen, J., Zeng, J., Wang, Q., Li, Z., Qin, R., Wu, C., Xie, Z. & Zheng, L. *Nanoscale* **9,** 6643–6648 (2017).

13. Jeong, H., Kwon, O., Kim, B. S., Bae, J., Shin, S., Kim, H. E., Kim, J. & Lee, H. *Nat. Catal.* **3,** 368-375 (2020).
14. Liu, J. X., Su, Y., Filot, I. A. W. & Hensen, E. J. M. *J. Am. Chem. Soc.* **140,** 4580–4587 (2018).
15. Zhou, X., Barshad, Y. & Gulari, E. *Chem. Eng. Sci.* **41,** 1277–1284 (1986).
16. Barshad, Y. & Gulari, E. *AIChE Journal* **31,** 649–658 (1985).
17. DeRita, L., Dai, S., Lopez-Zepeda, K., Pham, N., Graham, G. W., Pan, X. & Christopher, P. *J. Am. Chem. Soc.* **139,** 14150–14165 (2017).
18. Zafiris, G. S. & Gorte, R. J. *J. Catal.* **143,** 86–91 (1993).
19. Lu, Y., Kuo, C. te, Kovarik, L., Hoffman, A. S., Boubnov, A., Driscoll, D. M., Morris, J. R., Bare, S. R. & Karim, A. M. *J. Catal.* **378,** 121–130 (2019).
20. Lu, Y., Wang, J., Yu, L., Kovarik, L., Zhang, X., Hoffman, A. S., Gallo, A., Bare, S. R., Sokaras, D., Kroll, T., Dagle, V., Xin, H. & Karim, A. M. *Nat. Catal.* **2,** 149–156 (2019).
21. Kunwar, D., Zhou, S., Delariva, A., Peterson, E. J., Xiong, H., Pereira-Hernández, X. I., Purdy, S. C., ter Veen, R., Brongersma, H. H., Miller, J. T., Hashiguchi, H., Kovarik, L., Lin, S., Guo, H., Wang, Y. & Datye, A. K. *ACS Catal.* **9,** 3978–3990 (2019).
22. DeRita, L., Resasco, J., Dai, S., Boubnov, A., Thang, H. V., Hoffman, A. S., Ro, I., Graham, G. W., Bare, S. R., Pacchioni, G., Pan, X. & Christopher, P. *Nat. Mater.* **18,** 746-751 (2019).
23. Takeguchi, T., Manabe, S., Kikuchi, R., Eguchi, K., Kanazawa, T., Matsumoto, S. & Ueda, W. *Appl. Catal. A: Gen.* **293,** 91–96 (2005).
24. Zhu, J., Su, Y., Chai, J., Muravev, V., Kosinov, N. & Hensen, E. J. M. *ACS Catal.* **10,** 11532–11544 (2020).
25. Chen, A., Yu, X., Zhou, Y., Miao, S., Li, Y., Kuld, S., Sehested, J., Liu, J., Aoki, T., Hong, S., Camellone, M. F., Fabris, S., Ning, J., Jin, C., Yang, C., Nefedov, A., Wöll, C., Wang, Y. & Shen, W.. *Nat. Catal.* **2,** 334–341 (2019).
26. Yang, C., Yin, L.-L., Bebensee, F., Buchholz, M., Sezen, H., Heissler, S., Chen, J., Nefedov, A., Idriss, H., Gong, X.-Q. & Wöll, C. *Phys. Chem. Chem. Phys.* **16,** 24165–24168 (2014).
27. Feng, K., Zhang, H., Gao, J., Xu, J., Dong, Y., Kang, Z. & Zhong, J. *Appl. Phys. Lett.* **116,** 191903 (2020).
28. Skála, T., Šutara, F., Prince, K. C. & Matolín, V. *J. Electron Spectros. Relat. Phenomena* **169,** 20–25 (2009).
29. Lykhach, Y., Kozlov, S. M., Skála, T., Tovt, A., Stetsovych, V., Tsud, N., Dvořák, F., Johánek, V., Neitzel, A., Mysliveček, J., Fabris, S., Matolín, V., Neyman, K. M. & Libuda, J. *Nat. Mater.* **15,** 284–288 (2016).
30. Scanlon, D. O., Morgan, B. J. & Watson, G. W. *Phys. Chem. Chem. Phys* **13,** 4279–4284 (2011).
31. Coln Santana, J. A. & Coln Santana, J. A., *Quantitative Core Level Photoelectron Spectroscopy*, Morgan & Claypool Publishers (2014).
32. Yu, X. & Hantsche, H. *Fresenius J Anal Chem* **346,** 233-236 (1993).
33. Machida, M., Murata, Y., Kishikawa, K., Zhang, D. & Ikeue, K. *Chem. Mater.* **20,** 4489–4494 (2008).
34. Aneggi, E., Wiater, D., de Leitenburg, C., Llorca, J. & Trovarelli, A. *ACS Catal.* **4,** 172–181 (2014).

Chapter 5

Operando spectroscopy unveils the catalytic role of different Pd oxidation states in CO oxidation on Pd/CeO_2 catalysts

Abstract

Identification of structure-activity relationships of heterogenous catalysts has become a central topic of catalytic research. Aiming at knowledge-driven design of novel metal-ceria catalysts for automotive exhaust abatement, current efforts mostly pertain to the synthesis and understanding of well-defined systems. In contrast, technical catalysts are often heterogenous in their metal speciation. Here, we unveiled rich structural dynamics of a conventional impregnated Pd/CeO_2 catalyst during CO oxidation. *In situ* X-ray photoelectron spectroscopy and *operando* X-ray absorption spectroscopy revealed presence of metallic and oxidic Pd states during the reaction. Using transient *operando* infrared spectroscopy, we were able to probe the nature and reactivity of the surface intermediates involved in CO oxidation. We found that while low-temperature activity is associated with sub-oxidized and interfacial Pd sites, the reaction at elevated temperatures involves metallic Pd. These results highlight the utility of the multi-technique *operando* approach for establishing structure-activity relationships of technical catalysts.

5.1 Introduction

Transition metals supported on metal oxides are major heterogeneous catalysts used to accelerate many chemical reactions. Understanding of their functioning is crucial for the design of efficient and sustainable catalytic processes. In search of guiding principles for catalyst design, identifying structure-performance relationships has become a main paradigm of modern catalysis research[1–3]. CO oxidation has been long used to probe the reactivity of metals[4–8]. Noble metal nanoparticles are typical catalysts for CO oxidation used in automotive exhaust neutralizers[9], gas sensors,[10] and fuel cells[11]. When deposited on inert supports such as alumina, silica or zirconia, noble metals suffer from CO poisoning, which limits their low-temperature performance[12–14]. Reducible oxide supports and especially ceria can be used to overcome this problem owing to specific catalytic sites at the metal-support interface[15–18].

Cargnello et al. showed that nanoparticles of Pt, Pd and Ni deposited on ceria are active in low-temperature CO oxidation (<150 ºC)[19]. Using uniform metal nanoparticles of controlled size and relatively simple geometrical considerations, the authors unequivocally demonstrated the key role of catalytic sites at the metal-ceria interface. Maximizing the contribution of interfacial sites can increase the overall activity of the catalyst and, at the same time, improve the utilization degree of often expensive transition metals. For instance, a number of works reported that ceria-supported Pd catalysts with a high metal dispersion display excellent CO oxidation activity[20–23]. Synthesis of well-defined Pd/CeO_2 single-atom catalysts has only recently been developed[24–27]. The high reactivity of these materials for low-temperature CO oxidation has been linked to the oxidized nature of isolated Pd atoms[24–26]. In the presence of other reactants (*i.e.*, in model exhaust gas feeds), however, few-atom Pd clusters deposited on CeO_2(-Al_2O_3) nanocomposites exhibited notably higher CO oxidation activity than single-atom catalysts[28].

Structure-activity relations obtained for metal-ceria systems with well-defined metal speciation provide a solid basis for designing practical CO oxidation catalysts based on Pd/CeO_2. Nonetheless, typical metal-oxide catalysts prepared by conventional preparation methods (*e.g.*, impregnation or precipitation) often lack uniformity and contain a mixture of metal nanoparticles, clusters, and single atoms already in the as-prepared state[29–32]. Moreover, these species can transform into each other depending on the reaction

conditions[33–36]. For Pd/CeO_2, several works demonstrated a coexistence and, in fact, synergy between PdO_x clusters and Pd atoms in the CeO_2 lattice for the oxidation of CO at low temperature[37–39]. Other reports stressed the importance of metallic Pd sites for optimal catalytic performance[40,41]. Despite all these efforts, the lack of *operando* spectroscopy data where structure and activity of Pd/CeO_2 are determined simultaneously hampers the understanding of the catalytic roles of different Pd species. Moreover, it remains unclear whether activity descriptors derived for well-defined nanoparticles or single atoms of Pd supported on ceria are applicable for catalysts prepared by conventional methods.

Here, a Pd/CeO_2 catalyst prepared by wet impregnation of a commercially available ceria support was studied by a set of complementary *operando* and *in situ* spectroscopy tools. We used *operando* X-ray absorption spectroscopy (XAS) to interrogate the changes in Pd speciation as a function of time, temperature, and composition of the reaction mixture. Using *in situ* near-ambient pressure X-ray photoelectron spectroscopy (NAP-XPS), we identified various Pd species during CO oxidation with high surface and chemical sensitivity. We applied time-resolved *operando* diffuse reflectance infrared Fourier transform spectroscopy (DRIFTS) to follow the evolution of adsorbates on Pd surface and determine the nature of active and spectator species in low-temperature CO oxidation. Finally, correlation of the spectroscopic data with results of steady-state and transient reaction kinetic experiments completed a mechanistic picture of the dynamic role of different Pd states in CO oxidation.

5.2 Results and Discussion

5.2.1 Structure and CO oxidation activity of Pd/CeO_2 catalyst

A commercial ceria support was loaded with 1 wt% Pd by wet impregnation using palladium nitrate as a precursor (sample denoted as Pd/CeO_2). No Pd or PdO phases were detected by powder X-ray diffraction and Raman spectroscopy in the as-prepared state of Pd/CeO_2 (**Fig. C1**). This points to a high Pd dispersion in the fresh sample. As shown in **Fig. 5.1a-b**, high-resolution high-angle annular dark-field scanning transmission electron microscopy (HAADF-STEM) together with energy-dispersive X-ray spectroscopy (EDX) mapping revealed a non-uniform speciation of Pd. While part of Pd is highly dispersed (**Fig. 5.1a and Fig. C2**), while also small nanoparticles of ~3 nm are present (**Fig. 5.1b**, **Fig. C3**). *Ex situ* X-ray absorption near-edge structure (XANES) analysis demonstrated that Pd is in the oxidic state in the as-prepared sample (**Fig. C4**). Fitting of extended X-ray absorption fine structure (EXAFS) data confirmed the high dispersion of Pd (CN_{Pd-Pd} ~ 4 *vs.* 12 in bulk PdO, **Table C1**). Thus, Pd-oxo species in the as-prepared catalyst are present in varying sizes from few-atom clusters to small nanoparticles. The steady-state CO oxidation activity was evaluated at 80 °C. The reaction orders with respect to CO and O_2 were +0.31 and +0.21, respectively (**Fig. 5.1c**). The positive reaction order in CO points to the absence of CO poisoning at low temperature, which has earlier been associated with CO oxidation taking place at the Pd-CeO_2 interface[18,19,24]. Previously, we reported that, unlike reduced metal nanoparticles, single Pd atoms on CeO_2 exhibited a positive order in CO, while the reaction order in O_2 was negative[24]. The positive reaction order in O_2 observed in the present work might therefore indicate that the fraction of single-atom Pd species in impregnated Pd/CeO_2 catalyst is low under reaction conditions. This is consistent with the lower activity of Pd/CeO_2 in low-temperature CO oxidation (**Fig. C5**) in comparison to a single-atom Pd_1/CeO_2 catalyst[24]. Repeated CO oxidation light-off cycles over the same catalyst revealed that the activity at low temperatures (<100 °C) decreased during the second light-off run (**Fig. 5.1d**). Together with a slight increase in apparent activation energies (41 *vs.* 53 kJ mol^{-1}), these results point to structural changes in the catalyst during CO oxidation. Accordingly, we employed *operando* X-ray absorption spectroscopy (XAS) at the Pd K-edge to follow the structure of Pd/CeO_2 during CO oxidation.

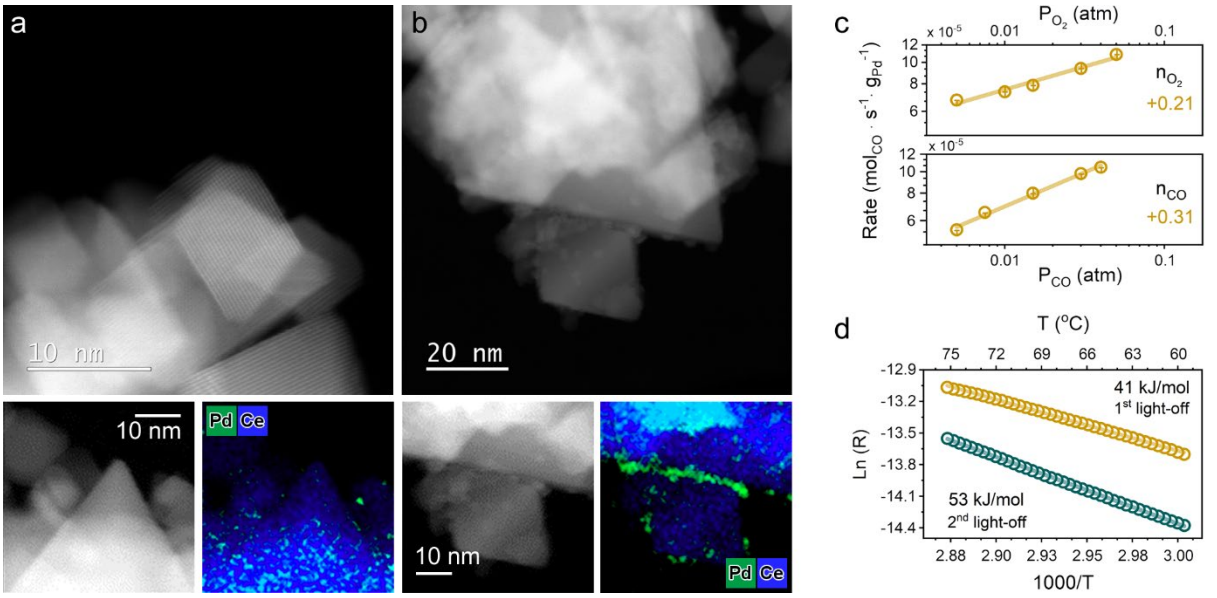

Figure 5.1. **Structure and activity of Pd/CeO_2 catalyst.** HAADF-STEM and EDX mapping of fresh Pd/CeO_2 catalyst: a) region with highly-dispersed Pd species; b) region with small clusters and nanoparticles of Pd oxide. c) Steady-state catalytic activity of the Pd/CeO_2 in CO oxidation as a function of pressure of reactants at 80 °C. When O_2 pressure was varied (5 to 50 mbar), the pressure of CO was constant (10 mbar). When CO pressure was varied (5 to 40 mbar), the pressure of O_2 was constant (10 mbar). GHSV ~240,000 ml g_{cat}^{-1} h^{-1}, conversion kept below 5%. Error bars represent five consequent measurements. d) Arrhenius plot for low-temperature catalytic activity of Pd/CeO_2 in CO oxidation. Yellow circles represent the low-temperature activity during the first light-off run (RT to 300 °C), cyan circles stand for the second run. Reaction conditions: 1% CO and 1% O_2 in He (GHSV ~180,000 ml g_{cat}^{-1} h^{-1}), conversion kept below 10%.

5.2.2 Structural dynamics of Pd/CeO_2 catalyst during low-temperature CO oxidation

Taking advantage of the high penetrating power of X-rays at the Pd K-edge, we could use a conventional quartz plug-flow reactor and high space velocities (~200,000 ml g_{cat}^{-1} h^{-1}) for XAS measurements. Complemented by online mass spectrometry (MS), this setup allows *operando* characterization of Pd in Pd/CeO_2 catalyst during CO oxidation. In the experiment the catalyst was pretreated in oxygen at 300 °C followed by cooling to 80 °C. Then the oxygen feed was swiftly switched to the reaction mixture – 1vol% CO and 1vol% O_2 in He. XANES analysis revealed substantial spectral changes upon a switch from O_2 to CO+O_2 (**Fig. 5.2a**). Using reference spectra of PdO and Pd metal for linear combination fitting, we found that the Pd oxide species initially present in Pd/CeO_2 catalyst were reduced (**Fig. 5.2b**). Within 30 min, around 30% of Pd^{2+} was transformed into $Pd^{0/\delta+}$ species. These changes in the Pd oxidation state are accompanied by a substantial decrease in the CO oxidation activity. While initially the CO conversion was around 90% (oscillations are explained in **Note C1**), the conversion decreased to ~5% after 40 min. These results indicate that highly dispersed

Pd-oxo species present in the fresh catalyst are highly active in CO oxidation but not stable. Comparison of the *in situ* EXAFS data acquired after stabilization of the catalyst in the reaction mixture to the one obtained for the pretreated sample (**Fig. 5.2c**) reveals that the deactivation goes together with the appearance of a Pd-Pd shell due to metallic Pd. The coordination numbers for Pd-Pd scattering paths for the Pd and Pd-oxide oxide species were below 6 (**Table C1**), suggesting that small metallic/sub-oxidized Pd nanoparticles are formed under low-temperature CO oxidation conditions. As EXAFS is a bulk averaging technique, we cannot distinguish a mixture of Pd-oxide and Pd metal from sub-oxide Pd phase that can be present on the surface under reaction conditions [42]. Thus, we studied the surface speciation of Pd by *in situ* NAP-XPS. After pretreatment in O_2, the Pd 3d spectrum (Fig. 2d) contains two principal components: (i) ~13% of Pd $3d_{5/2}$ at 337.9 eV due to highly dispersed Pd^{2+} in strong interaction with ceria (Pd-O_x-Ce) and (ii) ~87% Pd $3d_{5/2}$ at 336.6 eV related to sub-oxidized PdO_x species[20,24,43]. This shows that both highly dispersed and clustered Pd-oxo species are present in the pretreated catalyst. When the catalyst was exposed to the CO+O_2 reaction mixture in the NAP cell, partial reduction of Pd^{2+} took place resulting in ~35% of sub-oxidized and ~5% of metallic species. Owing to the high sensitivity of the 3d core-level XPS to intermediate charge states, we can conclude that at low reaction temperature most of Pd^{2+} reduced to sub-oxidized $Pd^{\delta+}$ state instead of metallic Pd^0. The absence of severe Pd sintering under low-temperature CO oxidation conditions is confirmed by similar values of atomic Pd/Ce ratios determined by XPS (~0.04) in both O_2 and CO+O_2 atmospheres.

Operando XAS and *in situ* NAP-XPS findings indicate the structural complexity of a seemingly simple Pd/CeO_2 catalyst synthesized by conventional wet impregnation method. The initial heterogeneity of the as-prepared Pd-oxo species and the changes in the oxidation state of Pd during CO oxidation led to the coexistence of different Pd oxidation states on the surface of the working catalyst, *i.e.*, oxidized and sub-oxidized Pd. In order to distinguish spectator Pd species from the actual active centers, we investigated CO reaction intermediates by transient FTIR.

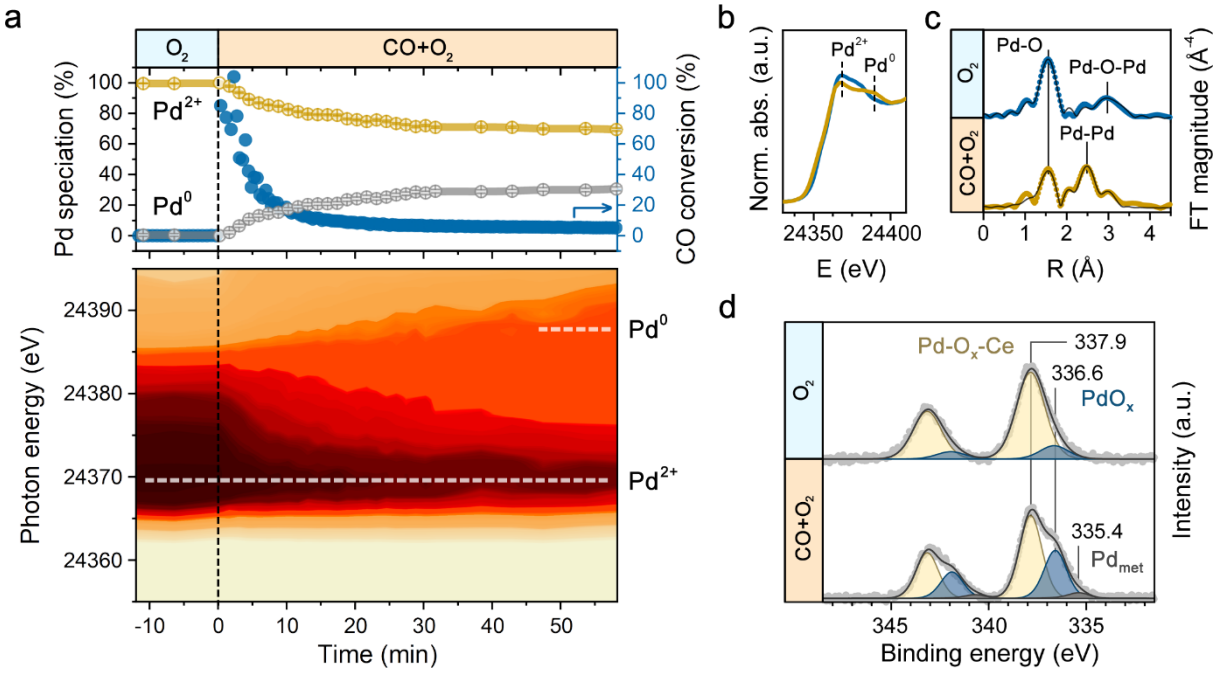

Figure 5.2. Reaction driven structural dynamics of Pd/CeO_2 catalyst. a) *Operando* XAS at Pd K-edge during a switch from O_2 to CO+O_2 at 80 °C. XAS data acquired in the middle of the catalyst bed. Top panel shows the distribution of Pd states derived from linear combination fitting and the CO conversion as a function of time after the switch. Bottom panel displays XANES region of Pd K-edge spectra as a function of time after the switch. Conditions: "O_2" – 20% O_2 in He; "CO+O_2" – 1% CO and 1% O_2 in He, total flow 100 ml/min. b) XANES spectra for the sample before the switch (blue) and after stabilization (amber) in the reaction mixture at 80 °C. c) R-space plot of EXAFS data for the sample before the switch and after stabilization in the reaction mixture at 80 °C. d) *In situ* NAP-XPS of Pd 3d core-level before and after the switch from O_2 to CO+O_2 at 80 °C. The total pressure in NAP-cell was fixed to 2 mbar, for the reaction mixture 1 mbar CO and 1 mbar of O_2 were used.

5.2.3 Probing the adsorbate bonding at Pd sites by time-resolved *operando* DRIFTS

Insights into the bonding and reactivity of CO molecules adsorbed on the surface of Pd were obtained from chemical transient kinetic experiments monitored by *operando* DRIFTS with high temporal resolution of 0.6 s^{-1}. **Figure 5.3a** shows the changes in the carbonyl absorption bands upon a switch from O_2 to CO+O_2 at 80 °C. We found that CO band at 2146 cm^{-1} was the dominant one during the first seconds of the reaction (**Fig. 5.3a-b**). This high-frequency band (denoted here as L_{HF}-CO) has been earlier assigned to linear carbonyl on single-atom Pd species[24–26]. These atomically dispersed oxidized Pd species are highly reactive but require a nanostructured ceria support with enhanced oxygen mobility to maintain their isolated nature during CO oxidation[24]. Clearly, on the surface of the relatively large ceria particles used in the present study the oxidized Pd single atoms are prone to reduction and clustering. The decrease in L_{HF}-CO goes together with the appearance of additional bands at ~2090 cm^{-1} and ~1980-1850 cm^{-1} due to linear (L-CO) and multi-bonded

(M-CO) carbonyls of sub-oxidized and metallic Pd, respectively[24–26]. The reduction and partial sintering of Pd-oxo species is accompanied by a significant decrease of the CO oxidation activity, as follows from the decrease of the IR band intensity of gas-phase CO_2 in the DRIFTS cell and the decrease of the *m/z* = 44 signal in MS (**Fig. C6**). These changes are consistent with the results of *operando* XAS characterization, showing that the initial high catalytic activity can be linked to highly dispersed Pd-oxo species.

After steady state CO oxidation was reached and no further changes in IR spectra of the operating catalyst were seen, the backward transient from $CO+O_2$ to O_2 was performed. As shown in **Fig. 5.3c-d**, CO is completely removed from the gas phase in about 8 s following the switch. In contrast, the removal of adsorbed CO is substantially slower, and the responses of the L-CO and M-CO carbonyls exhibited very different kinetics (**Fig. 5.3c**). By using rapid-scan FTIR, we could resolve two stages of carbonyl evolution during the switch from $CO+O_2$ to O_2. The first one ($t < 17$ s) was found to be linear in the semi-logarithmic coordinates (**Fig. 5.4a**) and gave rise to rate constants for L-CO and M-CO decomposition of ~0.057 s^{-1} and ~0.027 s^{-1}, respectively. Thus, the initial rate of removal of linearly adsorbed CO on sub-oxidized Pd sites is nearly twice faster than the removal of multi-bonded CO on metallic Pd. However, in the second stage ($t > 17$ s), M-CO decomposed much faster (k~0.145 s^{-1}) than L-CO (k~0.037 s^{-1}). When M-CO started to decay rapidly (at t~20 s), the decrease in L-CO band area slowed down (**Fig. C7**), likely due to the interconversion between multi-bonded and linearly adsorbed CO species[44,45]. The two-step nature of the carbonyl decomposition can be explained by differences in the CO oxidation mechanism at high and low coverage of CO. We hypothesize that during the first stage of $CO+O_2$ to O_2 transient, CO oxidation still proceeds mainly at the Pd-CeO_2 interface, because metallic sites remain poisoned due to the high CO coverage. In the second phase of the transient, the CO coverage decreases, allowing oxygen to adsorb on metallic Pd where oxidation of CO can take place. CO oxidation involving facile oxygen dissociation on bridge and/or hollow sites of metallic Pd surface[46], can also explain the fast decay of M-CO and the peak in CO_2 gas phase evolution at ~17 s after the switch (**Fig. 5.3c** and **Fig. C8**).

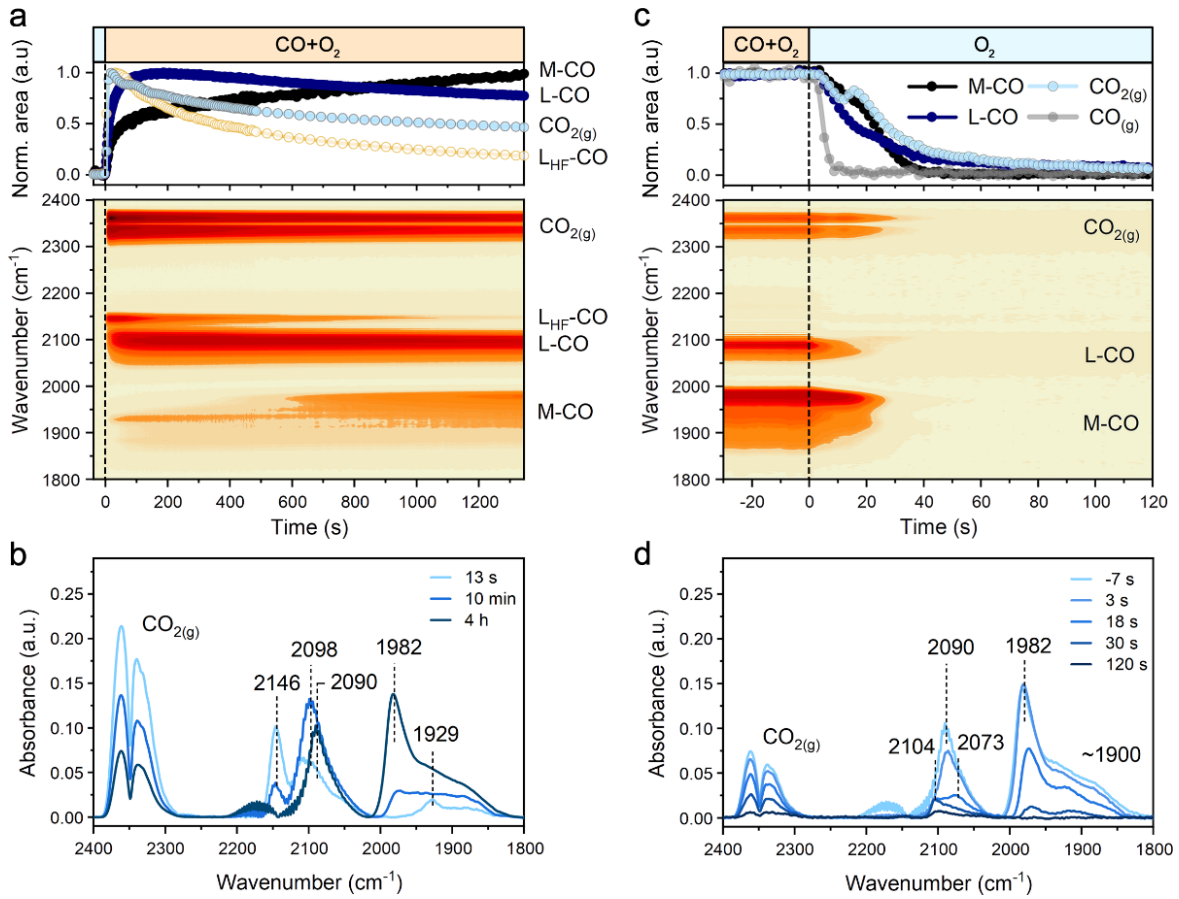

Figure 5.3. Response of Pd carbonyl species to chemical transients monitored by time-resolved DRIFTS. a) DRIFTS data acquired during a forward switch from O_2 to CO+O_2 at 80 ºC. The top panel displays the evolution of normalized band area intensity over the time. The bottom panel shows the changes in the respective spectral region as a function of time. b) Selected FTIR spectra acquired during a forward switch from O_2 to CO+O_2 at 80 ºC. c) DRIFTS data acquired during a backward switch from CO+O_2 to O_2 at 80 ºC. d) Selected FTIR spectra acquired during a backward switch from CO+O_2 to O_2 at 80 ºC. Conditions: "O_2" – 1% O_2 in He; "CO+O_2" – 1% CO + 1% O_2 in He; "CO" – 1% CO in He. Total flow 100 ml/min.

In order to understand the effect of CO desorption on the observed transient responses, we also performed a chemical transient experiment in which the CO+O_2 reaction mixture was replaced by inert He. The disappearance of Pd carbonyls proceeded much slower (~200 s, see **Fig. C9**) than upon the CO+O_2 to O_2 switch (~60 s) and with much lower rate constants (**Fig. 5.4b**) for the decays of L-CO (~0.038 s^{-1}) and M-CO (~0.018 s^{-1}) than for the backward O_2 transient (**Fig. 5.4a).** We attribute this difference to oxidation of adsorbed CO by O_2 in the CO+O_2 to O_2 transient. Recent works suggest that oxidation of chemisorbed CO at low temperature can also occur in inert atmosphere due to the supply of oxygen atoms from ceria to interface sites[17,47]. To deplete reactive oxygen atoms, the catalyst initially operated at steady state in a CO+O_2 mixture at 80 ºC was exposed to a feed of 1% CO in He. As a result of surface reduction, we observed a bathochromic shift (~7 cm^{-1}) of both L-CO and M-CO

bands and an increased intensity of multi-bonded carbonyls (**Fig. C10**). The total band area of Pd carbonyls for the catalyst exposed to CO is not very different from the $CO+O_2$ case, indicating that the CO coverage is high during steady-state CO oxidation. This is consistent with the mechanistic proposal that low-temperature CO oxidation at high CO coverages occurs at the Pd-CeO_2 interface, while the rest of Pd surface is poisoned by CO. When the intensity of the Pd carbonyl bands stabilized after exposure of the catalyst to CO, a switch from CO to He feed was performed. In this case, the removal of carbonyls took much longer (~600 s) than for the switches from $CO+O_2$ to O_2 (~60 s) and $CO+O_2$ to He (~200 s). The rate constants for decomposition of L-CO (~0.009 s^{-1}) and M-CO (~0.021 s^{-1}) in He after CO exposure (**Fig. 5.4c**) were much lower than upon the $CO+O_2$ to He switch. This difference can be attributed to stronger adsorption of CO on more reduced Pd sites or the depletion of reactive oxygen at the Pd-CeO_2 interface.

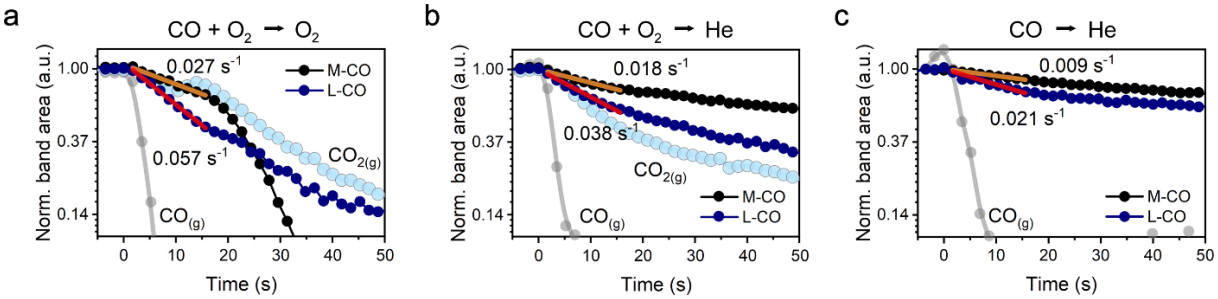

Figure 5.4. Kinetics of the removal of Pd carbonyls during chemical transient experiments. Semi-logarithmic plots of FTIR band areas as a function of time for: a) $CO+O_2$ to O_2 transient; b) $CO+O_2$ to He transient; c) CO to He transient. Conditions: "O_2" – 1% O_2 in He; "$CO+O_2$" – 1% CO + 1% O_2 in He; "CO" – 1% CO in He. Total flow 100 ml/min. The rate constants were estimated as slopes of the linear part of the decays.

To investigate the latter aspect, we performed an identical set of experiments on a reference sample in which lattice oxygen mobility and its impact on CO oxidation kinetics can be neglected. For this purpose, non-reducible ZrO_2 support[48] was impregnated with 1 wt% Pd (sample denoted as Pd/ZrO_2). As shown in **Fig. C11**, this catalyst was much less active than Pd/CeO_2 in low-temperature CO oxidation and followed a conventional Langmuir-Hinshelwood mechanism[49,50]. The presence of similar L-CO and M-CO bands under identical reaction conditions (**Fig. C12**) facilitates a comparison of the kinetics of Pd carbonyl removal from Pd/CeO_2 and Pd/ZrO_2. During the switch from $CO+O_2$ to O_2 over Pd/ZrO_2, carbonyl removal was much slower (~600 s) than for Pd/CeO_2. This difference can be explained by the absence of reactive lattice oxygen in ZrO_2. Strikingly, the kinetics of the disappearance of L-CO and M-CO bands for Pd/ZrO_2 during $CO+O_2$ to He (**Fig. C13**) and CO to He (**Fig. C14**)

switches were similar (~600 s). From this, we infer that reactive ceria lattice oxygen is the key to efficient low-temperature CO oxidation on supported Pd.

To summarize, we showed that, besides clusters of Pd oxide, atomically dispersed oxidized Pd species are present in fresh Pd/CeO_2. Although these species are highly active in low-temperature CO oxidation, they are unstable and prone to reduction and sintering as evidenced by XAS, NAP-XPS, and DRIFTS. The initially high activity of the catalyst could not be restored after exposure of the catalyst to an O_2 feed at 80 °C (**Fig. C15**). This is in line with earlier studies which suggest that *in situ* formed sub-oxidized and metallic Pd species can redisperse into single atoms only at high calcination temperatures[50]. Hence, under the actual reaction conditions the fraction of highly dispersed Pd on the surface of commercial CeO_2 is very small, limiting the low-temperature activity. Chemical transient experiments revealed two principal regimes of CO oxidation. At high CO coverage, CO oxidation takes place at the metal-ceria interface and involves CO linearly adsorbed on Pd and oxygen from the metal-support interface. In contrast, multi-bonded CO species are reactive at low CO coverages, when O_2 dissociation can take place on the liberated metallic surface sites. The response of the catalyst to chemical transients provides insight into the reactivity and bonding of adsorbed CO species. This allowed us to distinguish Pd species active in steady-state low-temperature CO oxidation from spectators. In the following section, we will investigate how the structure-activity relationships of Pd/CeO_2 in CO oxidation evolve as a function of the operating temperature.

5.2.4 Structural evolution of Pd during CO oxidation at elevated temperature

Pd/CeO_2 initially stabilized in a CO+O_2 mixture at 80 °C for ~1.5 h was characterized during heating to 225 °C using *operando* Pd K-edge XANES. **Fig. 5.5a** shows that heating to ~150 °C led to an increase in CO oxidation activity and a reduction of the Pd-oxo species. After a CO conversion of ~50% at around 160 °C was obtained, reduction of Pd-oxide stopped. Further heating led to reoxidation of $Pd^{0/\delta+}$ to Pd^{2+}. Oscillations in the catalytic activity caused by the exothermicity of the reaction (see **Note C1**) were not observed after full CO conversion was reached (~170 °C). After stabilization at 225 °C for 30 min, around 90% of Pd was oxidized. Reoxidation of Pd after ignition of CO oxidation has been observed before for Pd on redox-inactive alumina, suggesting that this phenomenon is related to the chemical nature of Pd-PdO clusters rather than to the ceria support specifically[51,52]. During subsequent

cooling, reduction of Pd started at ~165 °C, resulting in around 40% of Pd^{2+} at 80 °C (**Fig. 5.5b**). These light-off experiments show that the catalyst did not return to the initial state preceding ignition (~60% of Pd^{2+}). EXAFS analysis of the catalyst after cooling revealed a decrease in the Pd-O coordination number to ~2 and an increase in Pd-Pd coordination number to 7 (**Fig. 5.5c**) from respective initial values of ~4 and ~5 for the fresh catalyst. TEM images of the used catalyst showed that Pd was present as ~3 nm particles (**Fig. 5.6** and **Fig. C16**). The EDX mapping confirms that Pd is predominantly localized within small nanoparticles. The reduction and sintering of highly dispersed Pd-oxo species during CO oxidation at elevated temperature can explain the partial loss of low-temperature catalytic performance during the repeated light-off tests (**Fig. 5.1d**).

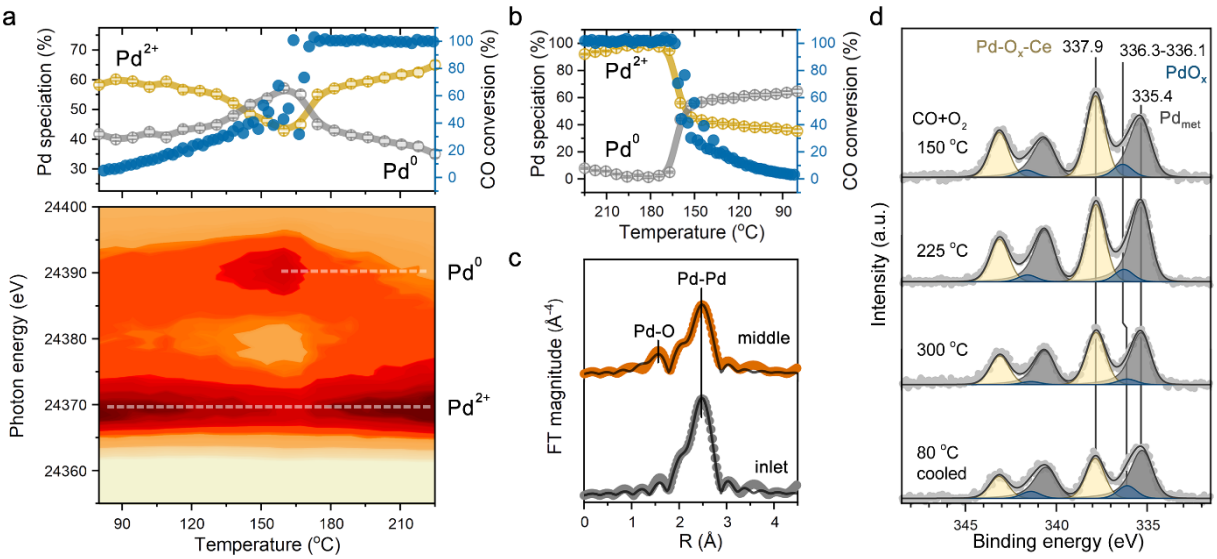

Figure 5.5. Evolution of Pd during CO oxidation as a function of temperature. a) *Operando* XAS at Pd K-edge during heating in 1% CO and 1% O_2 in He (total flow 100 ml/min). XAS data acquired close to the middle of the catalyst bed. Top panel shows the distribution of Pd states (Pd^0-grey, Pd^{2+}-yellow), derived from linear combination fitting, and the CO conversion as a function of temperature. Bottom panel displays XANES region of Pd K-edge spectra as a function of temperature. b) Evolution of Pd oxidation state upon cooling in reaction mixture after light-off test. The CO conversion (blue) depicted as a function of temperature. c) R-space EXAFS data for different parts of the catalyst bed cooled to 80 °C after the reaction. d) *In situ* NAP-XPS of Pd 3d core-level for the catalyst exposed to $CO+O_2$ mixture as function of temperature. The total pressure in NAP-cell was fixed to 2 mbar, for the reaction mixture 1 mbar CO and 1 mbar of O_2 were used

The temperature and concentration gradients along the catalyst bed that occur at high temperatures and/or high conversion levels can significantly contribute to heterogeneity in the Pd speciation[15,51,52]. After performing the CO oxidation light-off on Pd/CeO_2, XAS was performed close to the feed side (2 mm), in the middle (6 mm, standard position) and close to the exit (14 mm) of the catalyst bed (15 mm total). XANES indicated a significant difference

in Pd state at the inlet position (**Fig. C17**) as compared to the middle and the end of the bed, which appeared to be rather similar. Linear combination fitting analysis revealed an almost two times lower concentration of Pd^{2+} in the beginning of the catalyst bed with respect to the other segments. Fitting of the EXAFS spectrum (**Fig. 5.5c** and **Table C1**) acquired in this position reveals a more severe reduction and sintering of Pd species. This result indicates that at elevated temperature and full conversion of CO only the front part of the catalyst bed is used to convert the feed mixture, while the rest of the catalyst is only exposed to a mixture of O_2 and CO_2. This also explains a substantial degree of Pd reoxidation in the middle of the reactor observed above 170 °C. Accordingly, we can explain the observed reduction of Pd upon cooling from 225 °C to 80 °C (**Fig. 5.5b**). When the temperature decreases and CO is not fully converted anymore, the middle of the bed starts to be exposed to CO, which leads to Pd reduction.

To disentangle the reaction-driven changes in Pd speciation from the effects of local temperature and concentration gradients along the catalyst bed, we performed an *in situ* NAP-XPS study. Upon heating the catalyst from 80 °C to 150 °C in the reaction mixture, a considerable fraction of oxidized Pd-O_x-Ce and PdO_x species transformed into metallic Pd (**Fig. 5.5d**), in line with *operando* XAS data showing reduction of Pd (**Fig. 5.5a**). Further heating to 225 °C resulted in a slightly higher fraction of Pd metal (~53%), whereas nearly full reoxidation of Pd was observed during the *operando* XAS experiment in a catalytic bed. Even at 300 °C, no notable reoxidation of Pd was observed by NAP-XPS. This can be explained by the incomplete CO conversion in the NAP cell (**Fig. C18**), where the gases flow over the catalyst surface instead of passing through the catalyst bed as in *operando* XAS tests. The *in situ* determined Pd/Ce surface atomic ratio decreased at elevated temperatures (**Table C2**), pointing to sintering of metallic Pd. When the catalyst was cooled to 80 °C in the reaction mixture, only a slight decrease in the Pd^{2+} fraction (~9%) was seen by NAP-XPS. This is also in contrast to the notable reduction observed in the corresponding *operando* XAS measurements, which is due to the exposure of the whole catalyst bed to CO at incomplete conversion. Despite these differences, the average oxidation state of Pd in the used catalyst after the first light-off cycle determined by XPS and XAS were similar ($Pd^{\delta+}$, $\delta \sim 0.7$-0.8), indicating the minor effect of the pressure difference between the two techniques (2 mbar in NAP-XPS and 20 mbar in XAS).

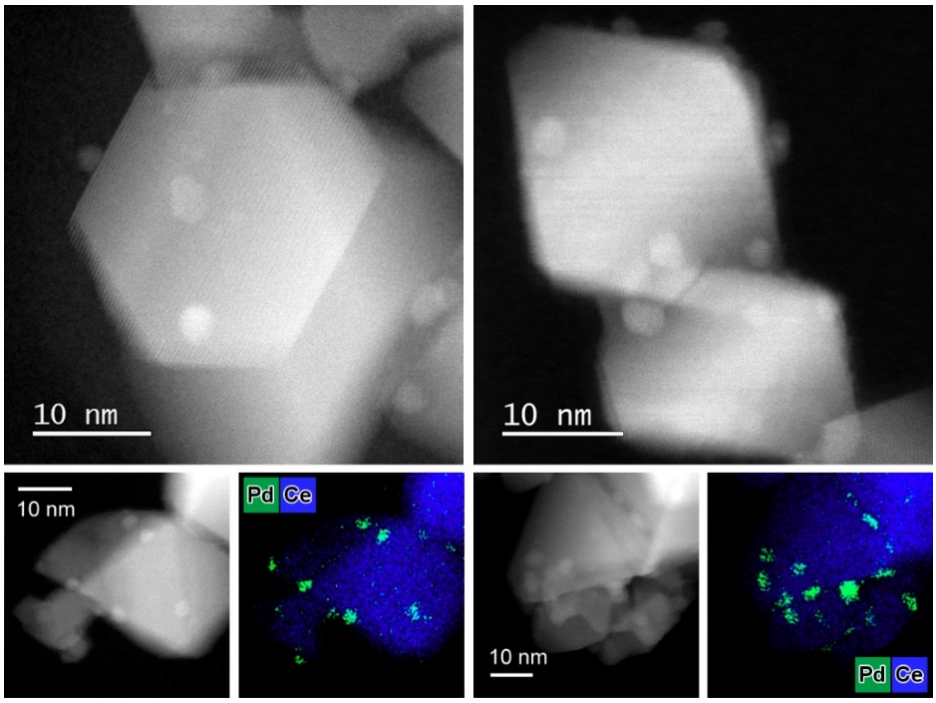

Figure 5.6. HAADF-STEM and EDX mapping of the Pd/CeO_2 catalyst after CO oxidation. In contrast to as-prepared state, Pd is predominantly present as Pd/PdO nanoparticles of ~ 3 nm size after CO oxidation at elevated temperature.

Based on the above results, we can conclude that substantial structural changes in Pd/CeO_2 take place during CO oxidation light-off. Small sub-oxidized Pd clusters formed at low temperature undergo partial reduction and sintering at elevated temperature. However, almost complete reoxidation of Pd can occur in a fixed-bed reactor when full CO conversion is reached. These observations highlight the importance of spatially-resolved *operando* experiments to draw unambiguous conclusions on the structure-activity relations[15,51–53]. Complementary surface-sensitive spectroscopic experiments allowed us to confirm the coexistence of metallic Pd^0, sub-oxidized $Pd^{\delta+}$ and oxidized Pd^{2+} species in strong interaction with CeO_2 in the catalyst operating at elevated temperature. Recently, it was shown that coexistence of Pt^0 and Pt^{2+} in ceria-supported Pt nanoparticles was due to the presence of Pt^{2+}-O-Ce interfacial sites[54]. From the finding that *operando* DRIFTS spectra did not exhibit any CO adsorbed on highly oxidized Pd sites in the used catalyst, we infer that Pd^{2+}-O-Ce moieties detected by X-ray based spectroscopy are located at the interface between Pd nanoparticles (~3 nm) and ceria. In line with this, the repeated CO oxidation cycle followed by *in situ* NAP-XPS and *operando* XAS revealed a slightly lower fraction of Pd^{2+}-O-Ce fragments due to the increased size of supported nanoparticles and thus lower contribution of interfacial sites (**Figs. C19-21**).

5.2.5 Correlating Pd oxidation states to CO oxidation kinetics

A set of *in situ* and *operando* spectroscopy experiments demonstrated that Pd is present in several oxidation states in Pd/CeO_2 catalyst during CO oxidation. Chemical transient experiments showed that metallic Pd species (M-CO) are spectators in low-temperature CO oxidation, while sub-oxidized Pd sites (L-CO) in proximity to Pd^{2+}-O-Ce interface are most likely the active sites. CO oxidation on these sub-oxidized Pd species exhibits a different mechanism than the conventional metal-catalyzed CO oxidation. This is consistent with the positive reaction order in CO (~0.3), indicating the absence of CO poisoning. Thus, the low-temperature CO oxidation activity can be linked to the Pd-CeO_2 interface (**Fig. 5.7, top**).

Furthermore, our *in situ* and *operando* experiments clearly demonstrated that the Pd speciation changes with reaction conditions. With increasing temperature, a higher fraction of metallic Pd nanoparticles is present, which in turn might influence the apparent reaction kinetics. The reaction orders measured at 80 °C and 165 °C for the Pd/CeO_2 catalyst (**Fig. C22**) were respectively 0.1 and 0.3 in CO, and 0.3 and 0.2 in O_2. These changes can be attributed to an increased contribution of Langmuir-Hinshelwood mechanism on metallic Pd[49,50] to the global kinetics of CO oxidation (**Fig. 5.7, middle**). At higher temperature of 225 °C, the contribution of metallic sites to the overall activity further increased, as indicated by a negative reaction order in CO (-0.1) and a more positive order in O_2 (+0.6) (**Fig. 5.7, bottom**). The importance of metallic Pd sites formed under reaction conditions for CO oxidation is also apparent from the higher activity at elevated temperature during the repeated light-off cycles (**Fig. C23**). These

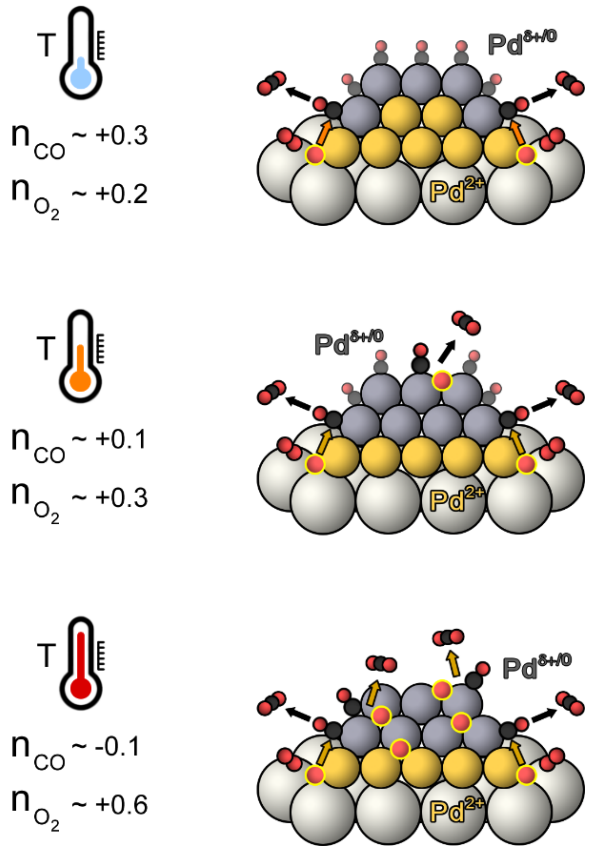

Figure 5.7. The kinetics of CO oxidation at different temperatures and schematics of Pd states involved. At low temperature (80 °C) oxidation of CO mostly occurs at the Pd-CeO_2 interface while metallic sites are poisoned (top panel). At medium temperature (165 °C) the surface coverage of CO decreases allowing dissociation of oxygen and its reaction with CO at metallic Pd sites. At high temperature (225 °C) reaction on metallic Pd surface significantly contributes to the global reaction rate.

results illustrate a complex and dynamic role of different Pd oxidation states during CO oxidation over Pd/CeO_2 catalysts.

5.3 Conclusions

In this work we demonstrated that a conventional impregnated Pd/CeO_2 catalyst contains various Pd-oxo species, ranging in size from single atoms to clusters and nanoparticles. Using a set of time-resolved *operando* and *in situ* spectroscopic techniques, we assessed the reactivity and stability of these different Pd species under reaction conditions. The oxidized Pd single atoms present in the as-prepared catalyst display high low-temperature activity but are prone to reduction under CO oxidation conditions at 80 °C. The *in situ* formed sub-oxidized and metallic Pd species display a much lower activity in low-temperature CO oxidation than oxidized Pd single atoms. The low activity of reduced Pd species can be explained by CO poisoning as demonstrated by *operando* DRIFTS. The analysis of *in situ* NAP-XPS and *operando* spatially-resolved XAS data revealed that CO oxidation at elevated temperature causes further reduction and sintering of Pd-oxo species. This results in the formation of a predominantly ~3 nm Pd nanoparticles with ca. 40% of Pd atoms in the oxidized state due to strong interaction with CeO_2. The change in reaction orders as a function of the reaction temperature clearly demonstrates the involvement of metallic Pd in CO oxidation at elevated temperatures. Thus, Pd species that are spectators at low temperature are important to the catalytic performance at higher temperature. This exemplifies the complexity of establishing the structure-activity relationships for technical catalysts that will typically contain different Pd states. The present study shows how a combination of appropriate *operando* and *in situ* characterization methods can resolve the dynamic active phase speciation under changing reaction conditions.

5.4 Materials and Methods

Catalyst preparation

To prepare the Pd/CeO_2 catalyst a commercial ceria powder (Sigma-Aldrich) was loaded with Pd by wet impregnation. An appropriate amount of $Pd(NO_3)_2{\cdot}2H_2O$ (Sigma-Aldrich) was dissolved in 30 mL of ammonia solution (30 wt%, Sigma-Aldrich) at room temperature. The obtained solution was then poured onto ~2 g of ceria powder. The resulting suspension was vigorously stirred till formation of the thick paste. This paste was then dried in air at 110 °C overnight and subsequently calcined at 300 °C. Similar procedure was used to obtain Pd/ZrO_2 except for higher calcination temperature (350 °C). Commercial zirconia powder (Alfa-Aesar) was used as a support.

Catalytic activity measurements

CO oxidation tests were performed in a quartz tube reactor. Effluent analysis was done by online mass-spectrometry (Balzers TPG-300) and gas chromatography (Interscience Compact GC 4.0), equipped with Plot and Molsieve columns and thermal conductivity detectors (TCDs) The samples were pressed, crushed and sieved between 125 µm and 250 µm to obtain the fraction for catalytic measurements. Sieved catalyst was then mixed with 250-300 mg of silicon carbide of the same fraction to avoid bypassing and formation of hot spots. The prepared mixture was then loaded between two quartz wool plugs. All catalysts were pretreated *in situ* under a flow of 20 vol% O_2 in He at 300 °C for 1 h. The light-off CO oxidation catalytic tests followed by mass-spectrometry were performed from room temperature to 300 °C at a ramp rate of 5 °C min^{-1}. The reaction mixture contained 1 vol% CO and 1 vol% O_2 in He, with a total flow of 150 mL min^{-1}. Repeated light-off cycles were performed on the same catalysts after cooling to room temperature. CO conversion was estimated on the basis of CO (*m/z*=28), O_2 (*m/z*=32) and CO_2 (*m/z*=44) signal evolution (*m/z*=44) in MS data and verified by gas chromatography. The reaction rates were plotted in Arrhenius coordinates using the regions of low conversion (<10%). To maintain low conversion levels the amount of loaded catalyst was varied. For reaction orders studies an appropriate amount of catalyst was loaded to maintain the CO conversion below 5% at all studied temperatures. Prior to changing the partial pressures of reactants (CO and O_2), the catalyst was stabilized in the reaction feed for at least 14 h to reach the steady state.

Characterization

Powder X-ray diffraction was performed using Bruker Phaser D2 diffractometer equipped with CuKα source. N_2 physisorption at -196 °C on a TriStar II 3020 apparatus was used to estimate the surface area of the prepared materials using Brunauer-Emmet-Teller method. The Pd loading in ceria and zirconia supported catalysts was determined using ICP-OES instrument (Spectroblue). The loading was estimated based on measurements performed *in duplo*. Raman spectra were acquired using Witec Alpha 300 Raman microscope equipped with 532 nm laser with a power of 2.5 mW and 10X Zeiss lens objective. Transmission electron microscopy was performed using a probe corrected JEOL ARM 200F microscope operated at 200 kV and equipped with a 100 mm^2 Centurio SDD EDX detector. Imaging was performed in HAADF-STEM mode.

Operando XAS experiments were performed at P65 beamline (PETRA III synchrotron, Hamburg). Double crystal Si (311) monochromator and beam size of ~ 0.2 mm x 1.0 mm were used. Spectra were measured at Pd K-edge in fluorescence mode using Si PIPS detector. Simultaneously Pd foil standard was measured in transmission mode to allow reliable energy calibration of the acquired data. Data reduction was performed using Athena software. Pd speciation during operando experiments was determined by linear combination fitting of the XANES data using spectra of Pd foil and powder PdO as standards. EXAFS fitting was performed in R-space for k^1, k^2, and k^3-weighted data using Artemis software The fitting ranges were Δk = 3-12 $Å^{-1}$ and ΔR = 1.0-3.0 Å. The spectra presented are k^3-weighted and not phase-corrected. Amplitude reduction factors were obtained from fitting of EXAFS spectrum of PdO. For *operando* experiments the catalyst powder was mixed with a sieved fraction (125 µm and 250 µm) of dry BN in a ratio of 1:2. The prepared mixture was fixed between two quartz wool plugs in the quartz reactor (O.D. 3 mm, 0.1 mm wall thickness). The catalyst bed length was about 15 mm. To control sample temperature, the thermocouple was placed inside the reactor in direct contact with the catalyst bed at the outlet side. For temperature control a standard PID thermocontroller (Eurotherm) and two resistive heating elements fixed ~1.5 mm above and below the quartz reactor were used. Unless stated otherwise, the X-ray beam was irradiating the sample near the middle of the catalyst bed. Other parts of the bed were probed by moving the sample stage. For pretreatment, the catalyst was heated from room temperature to 300 °C with a ramp rate of 5 °C min^{-1} and dwelled for 30 minutes in 20 vol% O_2 in He. After cooling to 80 °C a fast switch

from 20 vol% O_2 to 1 vol% CO and 1 vol% O_2 in He was performed using a four-way valve equipped with an electric actuator (VICI). The total flow was fixed to 100 mL min^{-1}. The outlet of the reactor was connected to the mass-spectrometer (Pfeiffer Omnistar) and CO (*m/z*=28), O_2 (*m/z*=32) and CO_2 (*m/z*=44) signals were used to calculate the CO conversion. During light-off measurements (80 – 225 ºC) the temperature was ramped at 5 ºC min^{-1}. The same rate for cooling was used. Ex situ XAS measurements at Pd K-edge were performed at the B18 beamline Diamond synchrotron (Didcot). Samples were pressed into pellets and analysed in fluorescence mode using a 9-element Ge detector.

For *in situ* NAP-XPS measurements a SPECS system was used. The monochromated Al Kα X-ray source operated at 20W with a spot size of ~0.3 mm. The differential pumping system of the SPECS Phoibos NAP-150 allows for acquisition of spectra directly in the presence of reactants. To avoid sample charging, catalyst powder was finely grounded and dispersed in ethanol. The obtained suspension was drop casted onto an Al-foil and fixed on a sample holder. After evacuation, the sample was transferred into the NAP-cell and pretreated in 2 mbar of O_2 at 300 ºC. Next the sample was cooled down and reaction mixture of 1 mbar of CO and 1 mbar of O_2 was introduced. Total flow of the gas feed in the cell was 2 mL min^{-1}. Pressure in the cell was regulated by electronic back-pressure controller. All the gasses used during experiments were of high purity (99.999%). The spectra were acquired isothermally upon step-wise heating. Acquisition time for the survey, Pd 3d, Ce 3d, O 1s and C1s spectra for each temperature step was around 2.5 h. A pass energy of 40 eV, step size of 0.1 eV (0.05 eV for Pd 3d) and dwell of 0.5 s were typically used. The binding energy scale was corrected using the U''' component of the Ce 3d core line located at 916.7 eV[55–57]. Shirley background for all spectra. The Pd to Ce surface atomic ratios were estimated using respective atomic sensitivity factors. Photoelectron spectra were fitted using symmetric pseudo-Voigt function, referred to as GL (30) in CasaXPS software. For the Pd 3d spectra containing metallic component, an asymmetric pseudo-Voigt function referred to as LF (0.76, 1.5, 55, 300) in CasaXPS was used. The Ce 3d spectra were fitted according to the models reported earlier[56,58].

Operando DRIFTS experiments were performed using BRUKER Vertex 70v FT infrared spectrometer equipped with a mercury–cadmium–telluride detector and mid-infrared laser source. We used a Praying Mantis accessory and a commercial cell (Harrick). A scheme of the setup is shown in **Fig. C24**. Catalyst powder (~50 mg) was placed on top of the quartz wool

plug and was in direct contact with sample thermocouple. To allow simultaneous acquisition of catalytic activity data, one of the windows of the dome of the cell was replaced by a steel window with a mounted capillary of the mass-spectrometer (Balzer, Prisma). The capillary of the MS was placed close to the sample surface (3-4 mm above) to ensure efficient gas probing. Gas inlet of the cell was located below the catalyst bed, while the outlet was connected to internal volume of the cell. Using this configuration, the fast gas replacement (~8-10 s) was achieved during the switches according to MS and IR signals. A home-made gas-delivery system allowed switches between two reaction feeds without significant pressure drops or perturbations of the flow. This was achieved using a four-way valve with two parallel feeds of reactants with equal flow rates (balanced by He and Ar). Electronic back-pressure regulators located at the outlet of the cell and the vent of the four-way valve were set to 200 mbar to prevent the pressure drop upon switches. For *operando* measurements a constant total flow of 100 ml min^{-1} was used. The catalyst was first pretreated in 20 vol% O_2 in He at 300 ^oC for 30 minutes. Then the catalyst was cooled down to 80 ^oC and the feed was changed to 1 vol% O_2 in He. After stabilization, a measurement was started and after ~30 s the four-way valve was activated by a remote control to feed the reaction mixture of 1 vol% CO and 1 vol% O_2 in He. Analogues to that switches to other mixtures were performed. After each switch the catalyst was stabilized under the flow at least for 30 minutes. The rapid-scan mode was used to increase the temporal resolution. To maximize the signal intensity an aperture of 8 cm^{-1} was set. Each spectrum was collected at a resolution of 2 cm^{-1} in the 3780-1000 cm^{-1} range. In each measurement first 300 spectra were acquired by averaging 8 scans with a frequency of 0.6 s^{-1} and the last 100 spectra were collected by averaging 40 scans with a frequency 0.12 s^{-1}. Spectra of the pretreated catalyst were used as a background. All spectra are shown in absorbance. Major IR bands were integrated, plotted over time after normalization and analysed in semi-logarithmic coordinates.

5.5 References

1. Meirer, F. & Weckhuysen, B. M. *Nat. Rev. Mater.* **3,** 324–340 (2018).
2. Topsøe, H. *J. Catal.* **216,** 155–164 (2003).
3. Kondrat, S. A. & van Bokhoven, J. A. *Top. Catal.* **62,** 1218–1227 (2019).
4. Freund, H. J., Meijer, G., Scheffler, M., Schlögl, R. & Wolf, M. *Angew. Chem. Int. Ed.* **50,** 10064–10094 (2011).
5. Valden, M., Lai, X. & Goodman, D. W. *Science* **281,** 1647–1650 (1998).
6. Ertl, G. *Science* **254,** 1750–1755 (1991).
7. Herzing, A. A., Kiely, C. J., Carley, A. F., Landon, P. & Hutchings, G. J. *Science* **321,** 1331–1335 (2008).
8. van Spronsen, M. A., Frenken, J. W. M. & Groot, I. M. N. *Chem. Soc. Rev.* **46,** 4347–4374 (2017).
9. Farrauto, R. J., Deeba, M. & Alerasool, S. *Nat. Catal.* **2,** 603–613 (2019).
10. Kocemba, I. & Rynkowski, J. *Sens. Actuators B: Chem.* **155,** 659–666 (2011).
11. Cao, L., Liu, W., Luo, Q., Yin, R., Wang, B., Weissenrieder, J., Soldemo, M., Yan, H., Lin, Y., Sun, Z., Ma, C., Zhang, W., Chen, S., Wang, H., Guan, Q., Yao, T., Wei, S., Yang, J. & Lu, J. *Nature* **565,** 631–635 (2019).
12. Zafiris, G. S. & Gorte, R. J. *J. Catal.* **143,** 86–91 (1993).
13. Pramhaas, V., Roiaz, M., Bosio, N., Corva, M., Rameshan, C., Vesselli, E., Grönbeck, H. & Rupprechter, G. *ACS Catal.* **11,** 208–214 (2021).
14. Ding, K., Gulec, A., Johnson, A. M., Schweitzer, N. M., Stucky, G. D., Marks, L. D. & Stair, P. C. *Science* **350,** 189–192 (2015).
15. Gänzler, A. M., Casapu, M., Doronkin, D. E., Maurer, F., Lott, P., Glatzel, P., Votsmeier, M., Deutschmann, O. & Grunwaldt, J. D. *J. Phys. Chem. Lett.* **10,** 7698–7705 (2019).
16. Gänzler, A. M., Casapu, M., Maurer, F., Störmer, H., Gerthsen, D., Ferré, G., Vernoux, P., Bornmann, B., Frahm, R., Murzin, V., Nachtegaal, M., Votsmeier, M. & Grunwaldt, J. D. *ACS Catal.* **8,** 4800–4811 (2018).
17. Pereira-Hernández, X. I., DeLaRiva, A., Muravev, V., Kunwar, D., Xiong, H., Sudduth, B., Engelhard, M., Kovarik, L., Hensen, E. J. M., Wang, Y. & Datye, A. K. *Nat. Commun.* **10,** 1358 (2019).
18. DeRita, L., Dai, S., Lopez-Zepeda, K., Pham, N., Graham, G. W., Pan, X. & Christopher, P. *J. Am. Chem. Soc.* **139,** 14150–14165 (2017).
19. Cargnello, M., Doan-Nguyen, V. V. T., Gordon, T. R., Diaz, R. E., Stach, E. A., Gorte, R. J., Fornasiero, P. & Murray, C. B. *Science* **341,** 771–773 (2013).
20. Boronin, A. I., Slavinskaya, E. M., Danilova, I. G., Gulyaev, R. V., Amosov, Yu. I., Kuznetsov, P. A., Polukhina, I. A., Koscheev, S. V., Zaikovskii, V. I. & Noskov, A. S. *Catal. Today* **144,** 201–211 (2009).
21. Gulyaev, R. v., Slavinskaya, E. M., Novopashin, S. A., Smovzh, D. v., Zaikovskii, A. v., Osadchii, D. Y., Bulavchenko, O. A., Korenev, S. v. & Boronin, A. I. *Appl. Catal. B: Environ.* **147,** 132–143 (2014).
22. Zhang, L., Spezzati, G., Muravev, V., Verheijen, M. A., Zijlstra, B., Filot, I. A. W., Su, Y.-Q., Chang, M.-W. & Hensen, E. J. M. *ACS Catal.* **11,** 5614–5627 (2021).
23. Bera, P., Patil, K. C., Jayaram, V., Subbanna, G. N. & Hegde, M. S. *J. Catal.* **196,** 293–301 (2000).
24. Muravev, V., Spezzati, G., Su, Y.-Q., Parastaev, A., Chiang, F.-K., Longo, A., Escudero, C., Kosinov, N. & Hensen, E. J. M. *Nat. Catal.* **4,** 469–478 (2021).
25. Spezzati, G., Su, Y., Hofmann, J. P., Benavidez, A. D., DeLaRiva, A. T., McCabe, J., Datye, A. K. & Hensen, E. J. M. *ACS Catal.* **7,** 6887–6891 (2017).
26. Jiang, D., Wan, G., García-Vargas, C. E., Li, L., Pereira-Hernández, X. I., Wang, C. & Wang, Y. *ACS Catal.* **10,** 11356–11364 (2020).
27. Datye, A. K. & Guo, H. *Nat. Commun.* **12,** 1–3 (2021).
28. Jeong, H., Kwon, O., Kim, B. S., Bae, J., Shin, S., Kim, H. E., Kim, J. & Lee, H. *Nat. Catal.* **3,** 368–375 (2020).
29. Rong, H., Ji, S., Zhang, J., Wang, D. & Li, Y. *Nat. Commun.* **11,** 1–14 (2020).
30. Herzing, A. A., Kiely, C. J., Carley, A. F., Landon, P. & Hutchings, G. J. *Science* **321,** 1331–1335 (2008).
31. Liu, K., Pritchard, J., Lu, L., van Putten, R., Verhoeven, M. W. G. M., Schmitkamp, M., Huang, X., Lefort, L., Kiely, C. J., Hensen, E. J. M. & Pidko, E. A. *Chem. Com.* **53,** 9761–9764 (2017).
32. Liu, S.; Xu, H.; Liu, D.; Yu, H.; Zhang, F.; Zhang, P.; Zhang, R.; Liu, W. *J. Am. Chem. Soc.* **143**, 15243–15249 (2021)

33. Gänzler, A. M., Betz, B., Baier-Stegmaier, S., Belin, S., Briois, V., Votsmeier, M. & Casapu, M. *J. Phys. Chem. C* **124,** 20090–20100 (2020).
34. Goodman, E. D., Johnston-Peck, A. C., Dietze, E. M., Wrasman, C. J., Hoffman, A. S., Abild-Pedersen, F., Bare, S. R., Plessow, P. N. & Cargnello, M. *Nat. Catal.* **2,** 748–755 (2019).
35. Lang, R., Xi, W., Liu, J.-C., Cui, Y.-T., Li, T., Lee, A. F., Chen, F., Chen, Y., Li, L., Li, L., Lin, J., Miao, S., Liu, X., Wang, A.-Q., Wang, X., Luo, J., Qiao, B., Li, J. & Zhang, T. *Nat. Commun.* **10,** 234 (2019).
36. Wang, Y.; Kalscheur, J.; Su, Y.-Q.; Hensen, E. J. M.; Vlachos, D. G. *Nat. Commun.*, **12**, 1–9 (2021).
37. Meng, L., Jia, A.-P., Lu, J.-Q., Luo, L.-F., Huang, W.-X. & Luo, M.-F. *J. Phys. Chem. C* **115,** 19789–19796 (2011).
38. Slavinskaya, E. M., Gulyaev, R. v., Zadesenets, A. v., Stonkus, O. A., Zaikovskii, V. I., Shubin, Y. v., Korenev, S. v. & Boronin, A. I. *Appl. Catal. B: Environ.* **166–167,** 91–103 (2015).
39. Stonkus, O. A., Kardash, T. Y., Slavinskaya, E. M., Zaikovskii, V. I. & Boronin, A. I. *ChemCatChem* **11,** 3505–3521 (2019).
40. Kurnatowska, M., Kepinski, L. & Mista, W. *Appl. Catal. B: Environ.* **117–118,** 135–147 (2012).
41. Hinokuma, S., Fujii, H., Okamoto, M., Ikeue, K. & Machida, M. *Chem. Mater.* **22,** 6183–6190 (2010).
42. Wu, C. H., Liu, C., Su, D., Xin, H. L., Fang, H. T., Eren, B., Zhang, S., Murray, C. B. & Salmeron, M. B. *Nat. Catal.* **2,** 78–85 (2019).
43. Neitzel, A., Figueroba, A., Lykhach, Y., Skala, T., Vorokhta, M., Tsud, N., Mehl, S., Sevcikova, K., Prince, K. C., Neyman, K. M., Matolin, V. & Libuda, J. *J. Phys. Chem. C* **120,** 9852–9862 (2016).
44. Meunier, F. C., Cardenas, L., Kaper, H., Šmíd, B., Vorokhta, M., Grosjean, R., Aubert, D., Dembélé, K. & Lunkenbein, T. *Angew. Chem. Int. Ed.* **60,** 3799–3805 (2021).
45. Gelin, P., Siedle, A. R. & Yates, J. T. *J. Phys. Chem.* **88,** 2978-2985 (1984).
46. Gao, F., Wang, Y. & Goodman, D. W. *J. Am. Chem. Soc.* **131,** 5734–5735 (2009).
47. Lu, Y., Thompson, C., Kunwar, D., Datye, A. K. & Karim, A. M. *ChemCatChem* **12,** 1726–1733 (2020).
48. Suchorski, Y.; Kozlov, S. M.; Bespalov, I.; Datler, M.; Vogel, D.; Budinska, Z.; Neyman, K. M.; Rupprechter, G. *Nat. Mater.*, **17**, 519–522, (2018).
49. Santra, A. K. & Goodman, D. W. *Electrochimica Acta* **47,** 3595–3609 (2002).
50. Peterson, E. J., DeLaRiva, A. T., Lin, S., Johnson, R. S., Guo, H., Miller, J. T., Hun Kwak, J., Peden, C. H. F., Kiefer, B., Allard, L. F., Ribeiro, F. H. & Datye, A. K. *Nat. Commun.* **5,** 4885 (2014).
51. Stewart, C., Gibson, E. K., Morgan, K., Cibin, G., Dent, A. J., Hardacre, C., Kondratenko, E. v., Kondratenko, V. A., McManus, C., Rogers, S., Stere, C. E., Chansai, S., Wang, Y. C., Haigh, S. J., Wells, P. P. & Goguet, A. *ACS Catal.* **8,** 8255–8262 (2018).
52. Dann, E. K., Gibson, E. K., Catlow, C. R. A., Celorrio, V., Collier, P., Eralp, T., Amboage, M., Hardacre, C., Stere, C., Kroner, A., Raj, A., Rogers, S., Goguet, A. & Wells, P. P. *J. Catal.* **373,** 201–208 (2019).
53. Singh, J.; Nachtegaal, M.; Alayon, E. M. C.; Stötzel, J.; van Bokhoven, J. A. Dynamic Structure Changes of a Heterogeneous Catalyst within a Reactor: Oscillations in CO Oxidation over a Supported Platinum Catalyst. *ChemCatChem* **2**, 653–657, (2010).
54. Li, Y., Kottwitz, M., Vincent, J. L., Enright, M. J., Liu, Z., Zhang, L., Huang, J., Senanayake, S. D., Yang, W.-C. D., Crozier, P. A., Nuzzo, R. G. & Frenkel, A. I. *Nat. Commun.* **12,** 914 (2021).
55. Stadnichenko, A. I., Muravev, V. V., Koscheev, S. V., Zaikovskii, V. I., Aleksandrov, H. A., Neyman, K. M. & Boronin, A. I. *Surf. Sci.* **679,** 273-283 (2019).
56. Kato, S., Ammann, M., Huthwelker, T., Paun, C., Lampimäki, M., Lee, M.-T., Rothensteiner, M. & van Bokhoven, J. A. *Phys. Chem. Chem. Phys.* **17,** 5078–5083 (2015).
57. Parastaev, A., Muravev, V., Huertas Osta, E., van Hoof, A. J. F., Kimpel, T. F., Kosinov, N. & Hensen, E. J. M. *Nat. Catal.* **3,** 526-533 (2020).
58. Skála, T., Šutara, F., Prince, K. C. & Matolín, V. *J. Electron. Spectros. Relat. Phenomena* **169,** 20–25 (2009).

5.6 Appendix C

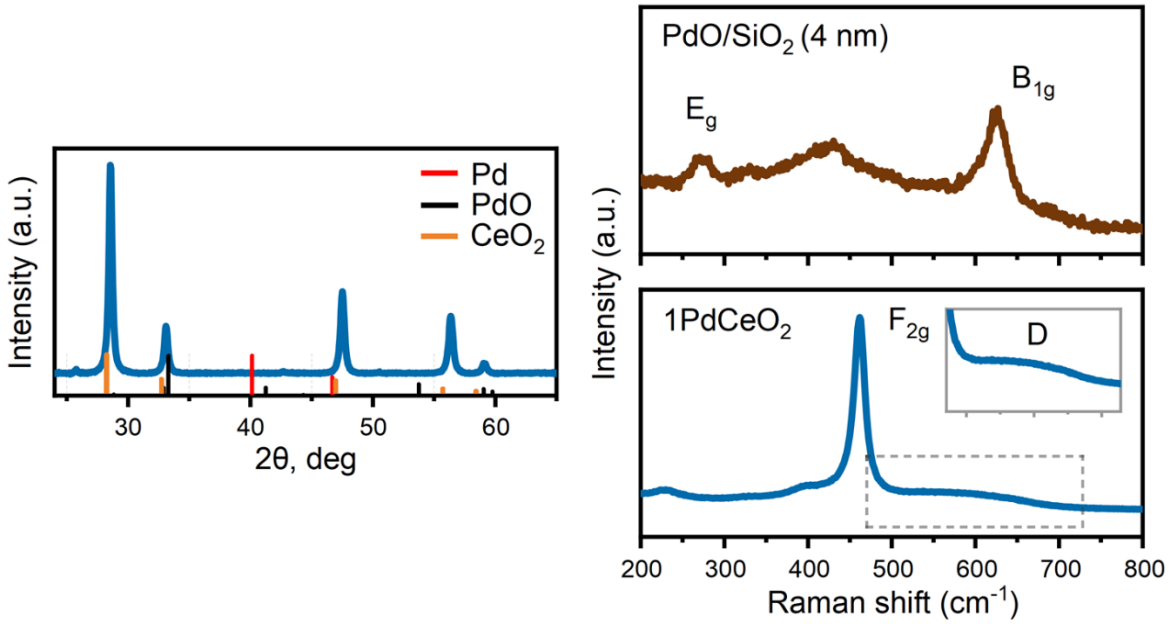

Figure C1. XRD and Raman characterization. No Pd/PdO phases were detected by XRD or Raman spectroscopy. PdO/SiO_2 reference sample was prepared by wet impregnation of a high surface area silica (Sipernat® 50) with palladium nitrate dissolved in deionized water, dried, and calcined at 300 ºC. The size of PdO domains on silica are ~4 nm in size as estimated from XRD data by Scherrer equation. The vibrational bands of PdO (E_g and B_{1g}) were not found in Raman spectrum of Pd/CeO_2 which suggests that Pd species are highly dispersed.

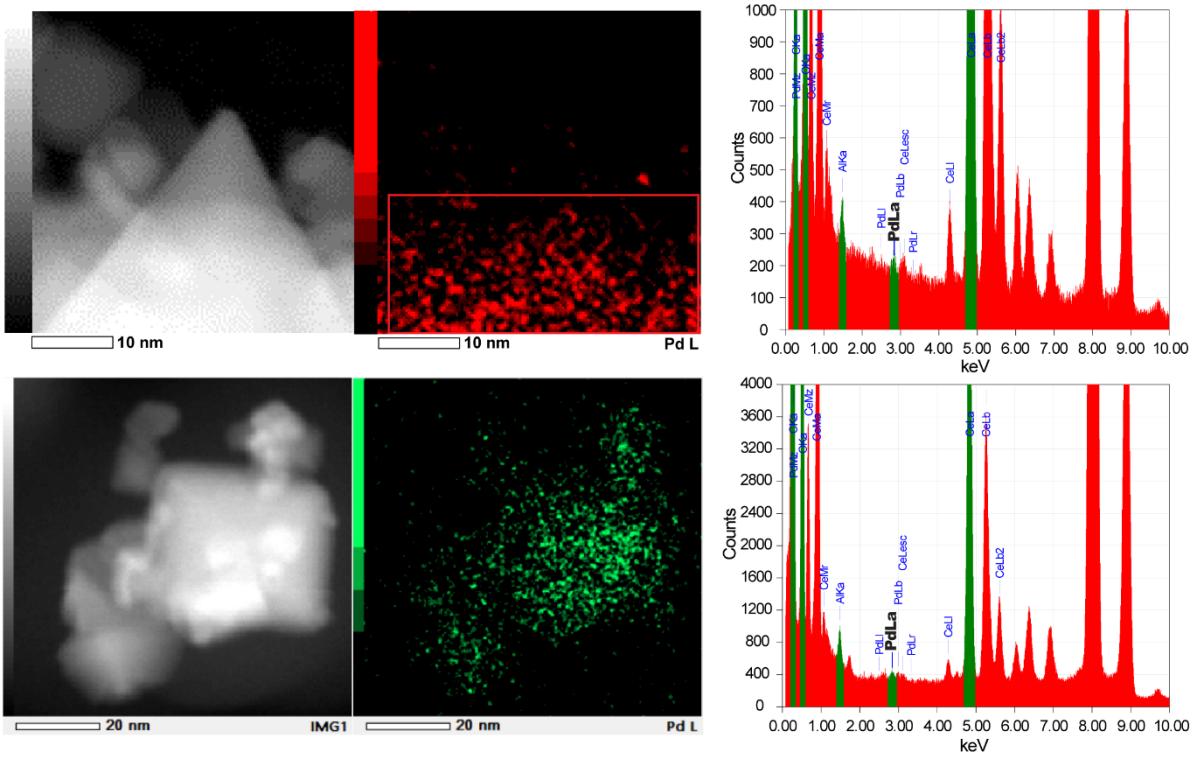

Figure C2. HAADF-STEM images and EDX spectroscopy data obtained for fresh Pd/CeO_2 sample. EDX data indicates that part of Pd is present in the form of highly dispersed species that cannot be identified by HAADF-STEM. In the regions where no particles/clusters of Pd can be seen, EDX spectra displays Pd-related components. Together with the images shown above these results suggest that in the as-prepared catalyst Pd nanoparticles, clusters and highly-dispersed species coexist with each other.

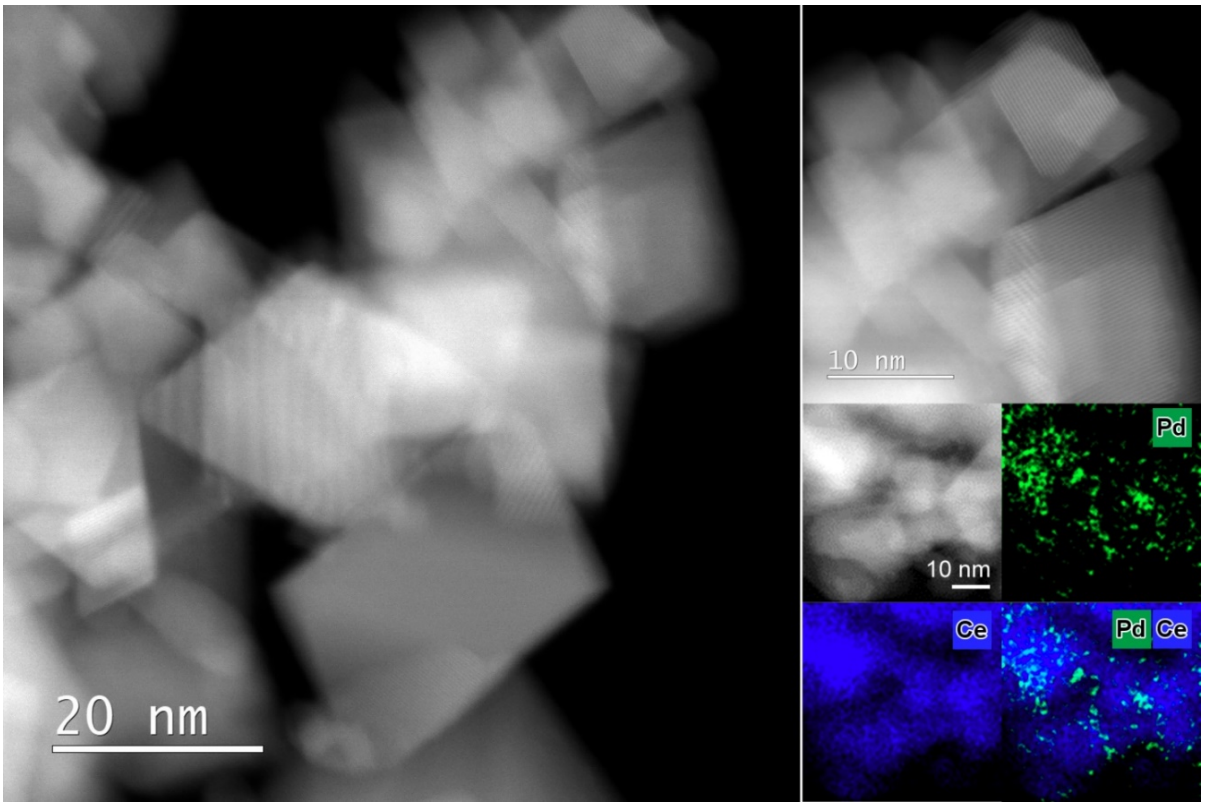

Figure C3. HAADF-STEM and EDX mapping images of fresh Pd/CeO_2 sample. Regions of homogeneous distribution of Pd over CeO_2 can be seen. Some clustered Pd species can also be identified.

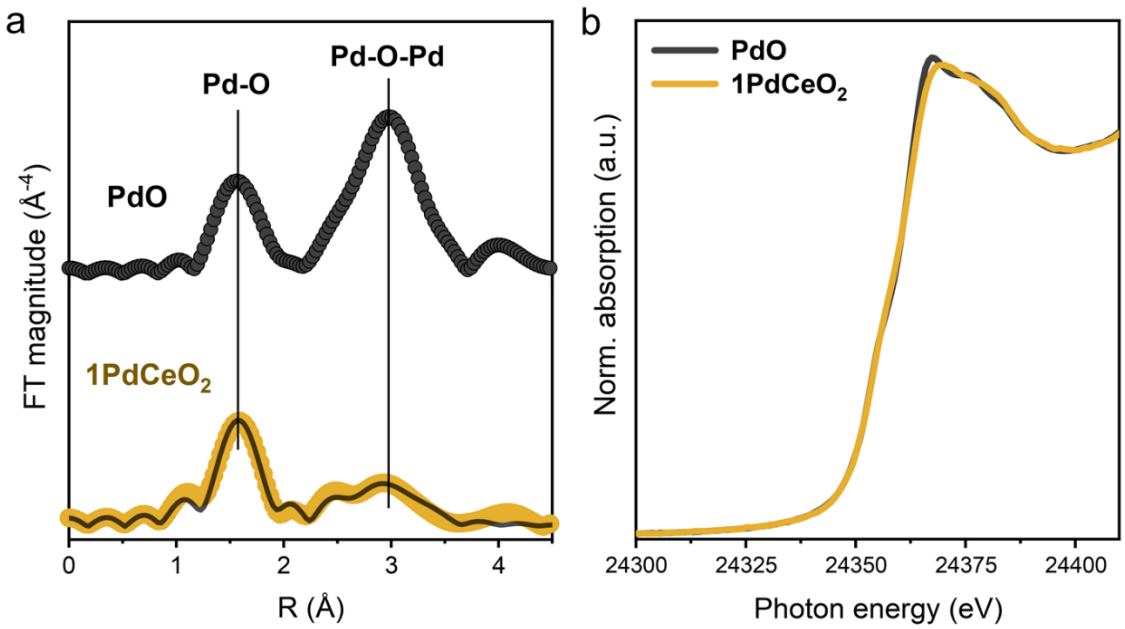

Figure C4. *Ex situ* XAS of fresh Pd/CeO_2 sample and PdO reference (Sigma-Aldrich): FT-EXAFS in R-space (a), XANES region (b). In contrast to PdO, the second shell scattering is diminished in Pd/CeO_2 sample, which implies high dispersion of Pd-oxo species. XANES region manifests a slight shift of the white-line maximum to higher energies for spectra of Pd/CeO_2 sample. The shape of the XANES spectrum of Pd/CeO_2 sample also differs from PdO, implying that electronic state of Pd is different, likely due to the strong interaction with ceria. The average oxidation state is close to Pd^{2+}.

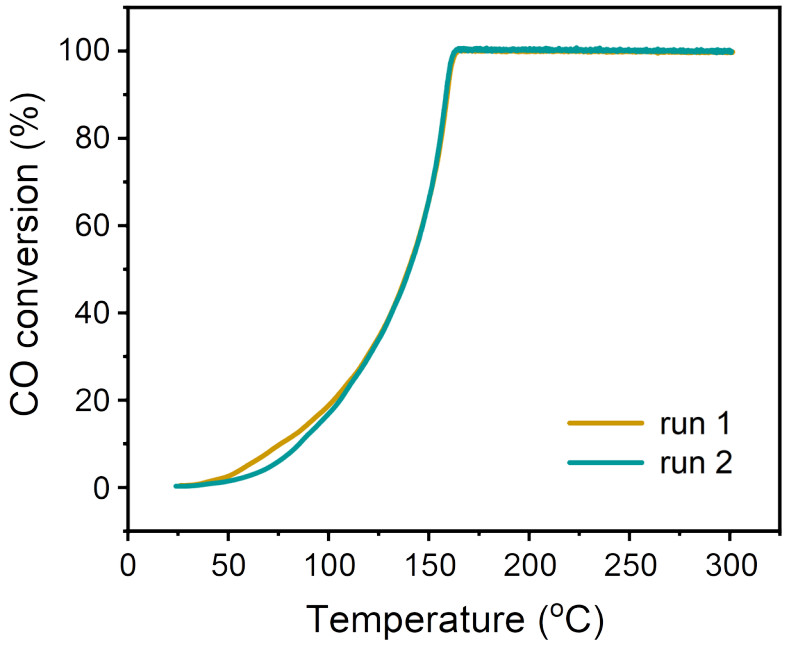

Figure C5. CO oxidation light-off measurements for Pd/CeO_2 sample. Sieved fraction (125 to 250 μm) was diluted with ~250 mg of SiC. The catalyst was pretreated in 20% O_2/He at 300 °C for 1h. Reaction feed: 1% CO + 1% O_2 in He, ramp rate 5 °C/min. Flow rate: 150 ml/min and total GHSV of 180,000 ml/g_{cat} h^{-1}.

Note C1. Fluctuation of CO conversion during operando XAS experiments.

The observed fluctuations of CO conversion during the first minutes after the switch from O_2 to $CO+O_2$ reaction mixture were caused by the superposition of several factors. The reaction of CO oxidation is highly exothermic, and the produced heat can effectively sustain the catalytic reaction and cause temperature fluctuations inside the catalyst bed. In the first instances after the switch the catalyst is exposed to reaction conditions and is highly reactive, due to the majority of Pd still being oxidized and well-dispersed. The produced heat is then sufficient to maintain the reaction till the point at which a certain fraction of Pd sites becomes reduced and CO conversion drops. During this stage the heating rods of the reactor setup (resistively heated wires wrapped around the ceramic cylinders) rapidly cool down, since the thermocouple, inserted in the middle of the bed, reads an increase in temperature caused by the exothermicity of the reaction. Once the conversion drops, due to the reduction of Pd, readings of the thermocouple decrease and then the heating unit starts to heat up the catalyst bed. Since the processes of ignition-extinction of the reaction are quite fast, the latency in the response of the heating system causes the mismatches between cooling-heating cycles of the catalyst bed and of the heating rods, which in turn lead to the observed fluctuation. As will be shown later these effects are also enhanced due to the reoxidation of Pd (and possible recovery of the active sites), when high CO conversion levels are reached. We should note, that high space velocities (100 ml/min, GHSV ~ 200,000 ml/g_{cat} h^{-1}) and dilution of the catalyst with a sieved fraction of BN (catalyst : BN = 1:2 by weight) were used to avoid the formation of hot spots and mimic the kinetic measurements. We assume that the main difference of the reactor cell used for XAS measurements which caused the observed phenomena is related to the heating system that is not thermally isolated from ambient air and is controlled by a thermocouple placed inside the bed. In our conventional reactor the thermocouple is located next to the quartz reactor. The slower response of this system to the overheating of the catalyst bed results in the absence of such fluctuations.

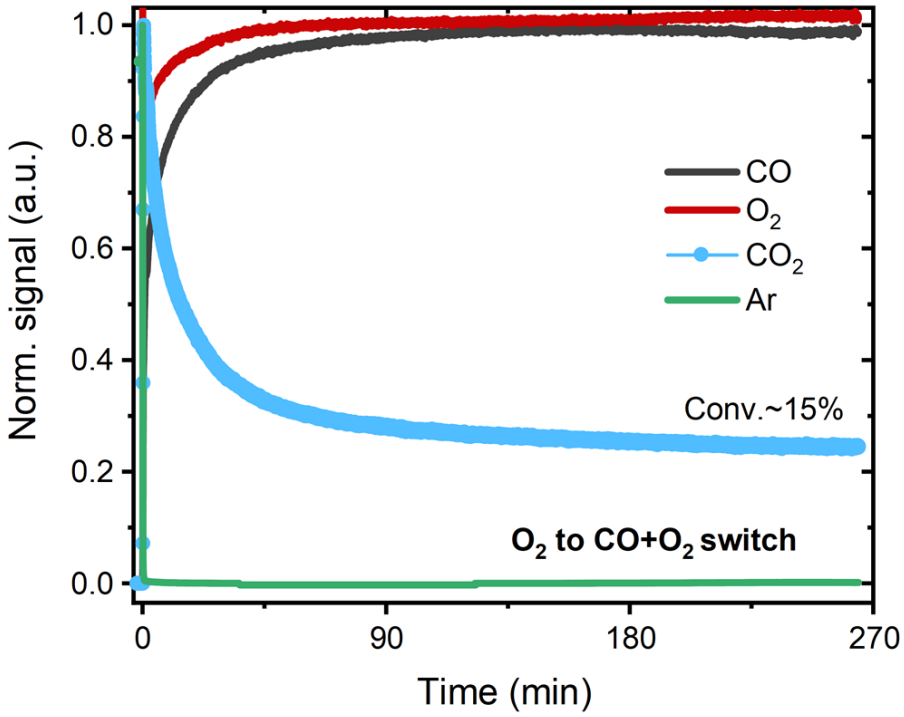

Figure C6. Mass-spectrometry data acquired during chemical transient from O_2 to $CO+O_2$ mixture at 80 °C followed by operando DRIFTS. Gas holdup time ~ 8 s. Conditions: "O_2" – 1% O_2 in He; "$CO+O_2$" – 1% CO + 1% O_2 in He, total flow 100 ml/min.

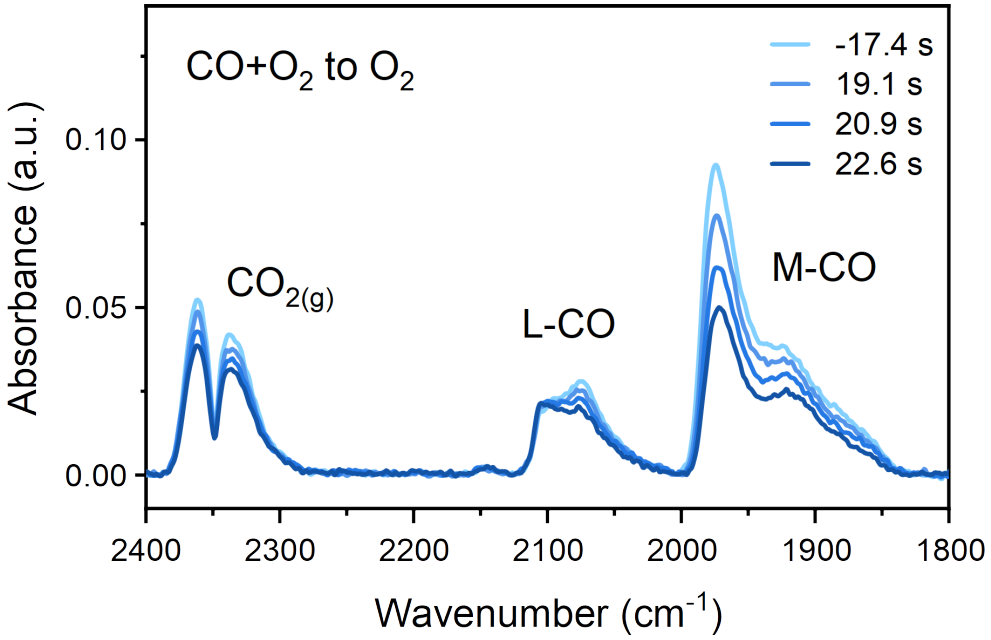

Figure C7. *Operando* DRIFTS spectra acquired during chemical transient from O_2 to $CO+O_2$ mixture at 80 ºC. In this time range, the removal of linear carbonyls was virtually slowed down, while the rate of removal of bridged and hollow carbonyls increased substantially. As explained in the main text, possible interconversion between carbonyls and ignition of the reaction at metallic sites due to facile oxygen dissociation are the likely reason for the observed phenomenon.

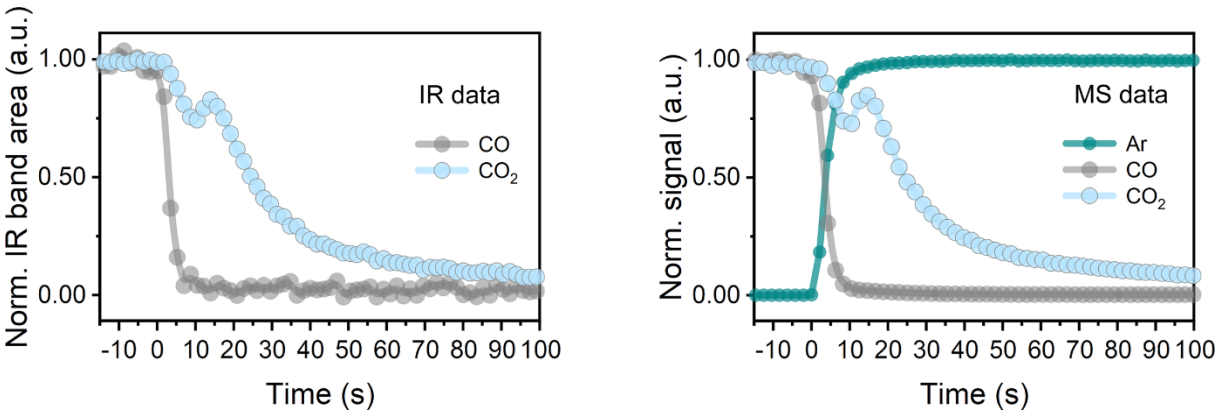

Figure C8. The extra peak of CO_2 formation, related to rapid oxidation of CO on metallic sites at low CO coverage, is seen both in IR and MS data. As shown here the MS and IR data on gas composition are identical, confirming the very fast gas-phase replacement under applied conditions.

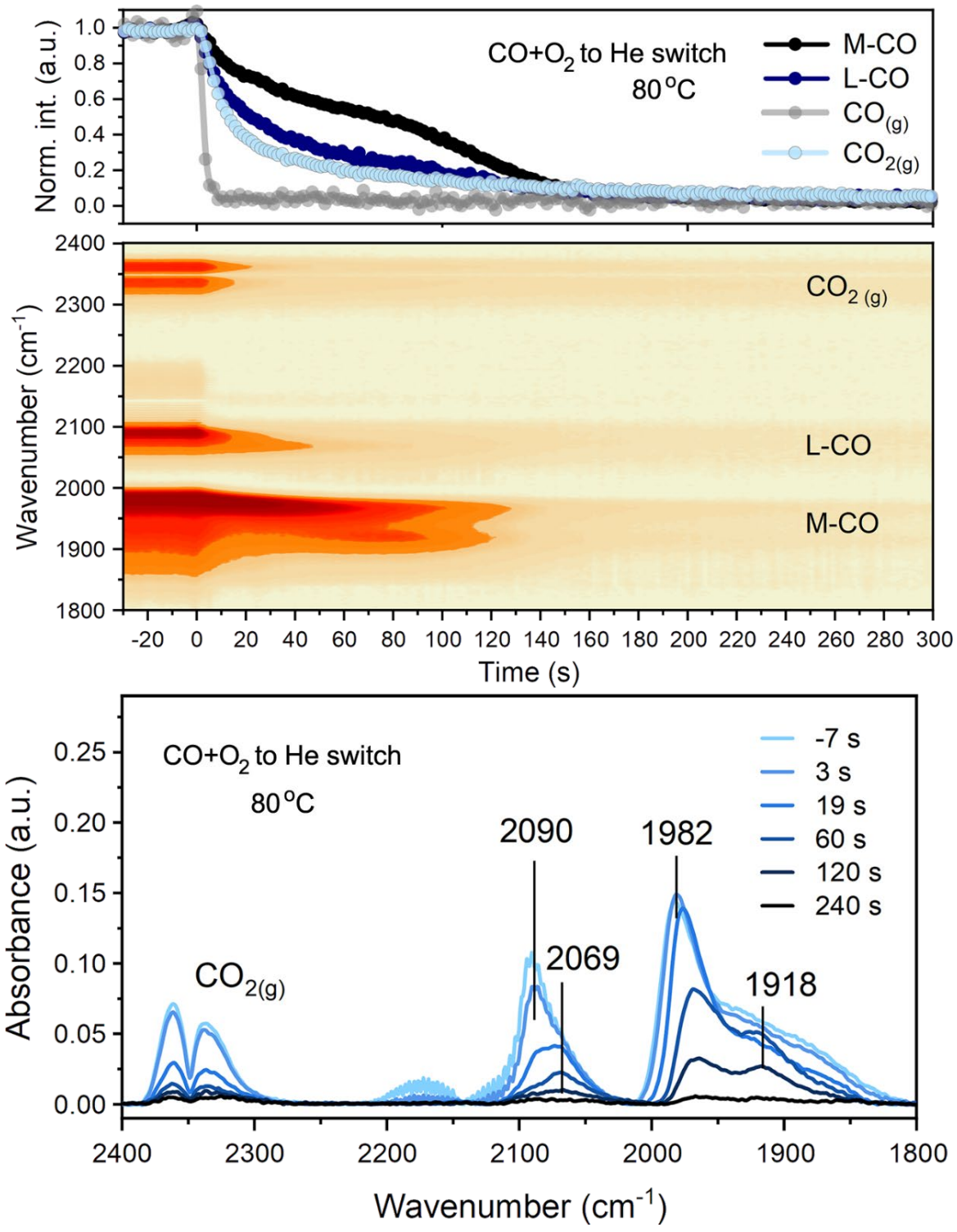

Figure C9. DRIFTS data for Pd/CeO_2 catalyst acquired during a switch from CO+O_2 to He at 80 °C. The top panel displays the evolution of normalized band area intensity over the time. The middle panel shows the changes in the respective spectral region as a function of time. The bottom panel display selected FTIR spectra acquired during the switch. Conditions: "CO+O_2" – 1% CO + 1% O_2 in He; total flow 100 ml/min.

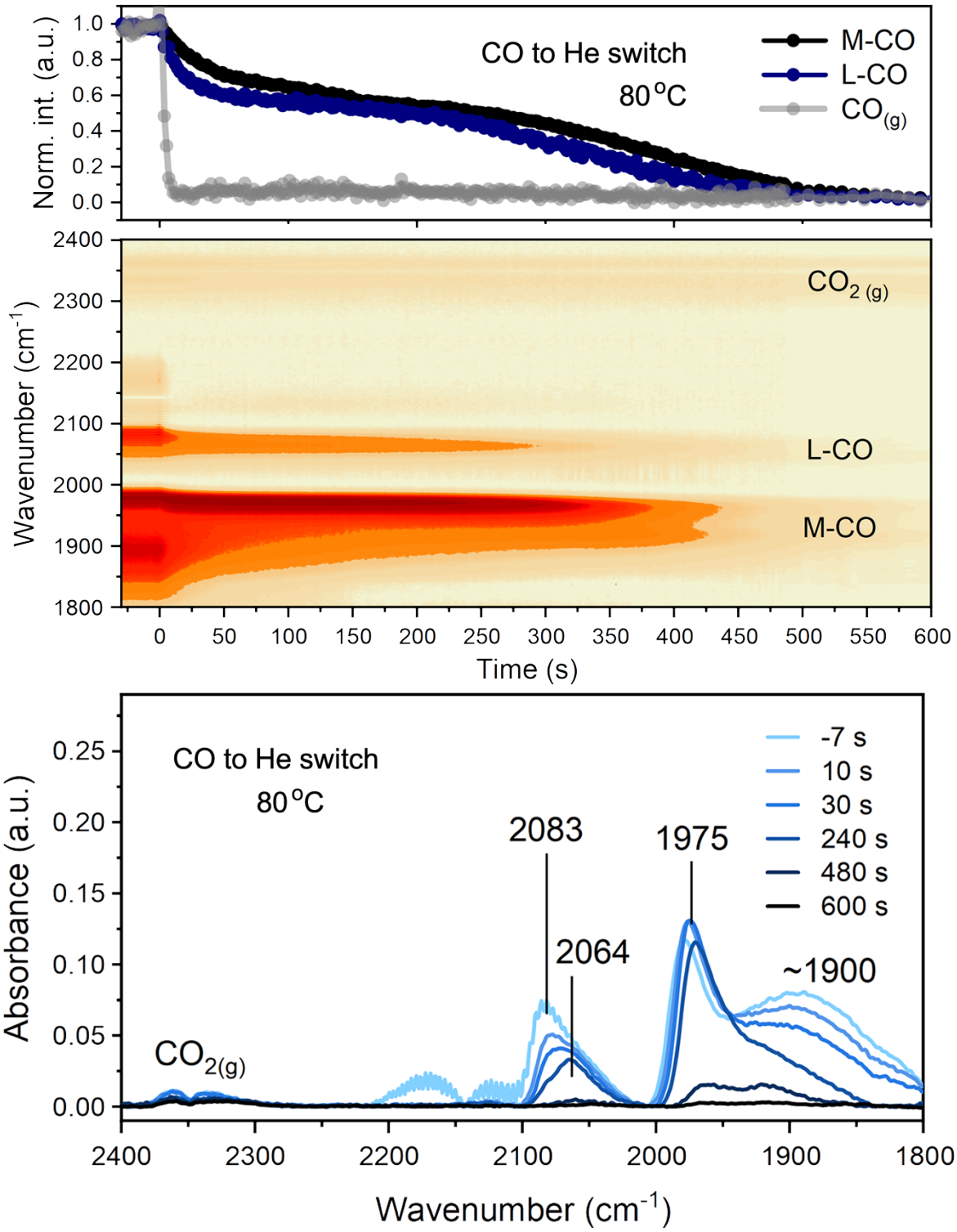

Figure C10. DRIFTS data for Pd/CeO_2 catalyst acquired during a switch from CO to He at 80 °C. The top panel displays the evolution of normalized band area intensity over the time. The middle panel shows the changes in the respective spectral region as a function of time. The bottom panel display selected FTIR spectra acquired during the switch. During exposure to pure CO the oxygen was depleted from the catalyst, as seen by the CO_2 band. Once the switch to He was performed, CO_2 signal vanished. Conditions: "CO" – 1% CO in He; total flow 100 ml/min.

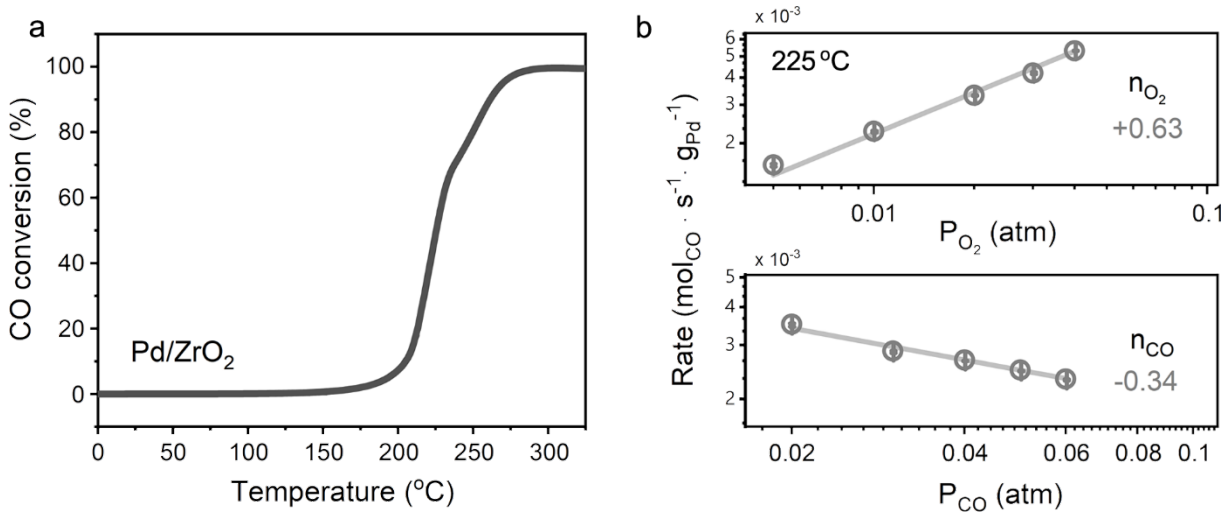

Figure C11. CO oxidation light-off measurements for Pd/ZrO_2 sample (a). Sieved fraction (125 to 250 µm) was diluted with ~250 mg of SiC. The catalyst was pretreated in 20% O_2/He at 300 ºC for 1h. Reaction feed: 1% CO + 1% O_2 in He, ramp rate 5 ºC/min. Flow rate: 150 ml/min and total GHSV of 180,000 ml/g_{cat} h^{-1}. (b) Reaction orders measurements. The catalyst was stabilized on the stream for ~ 16 h at 225 ºC to reach steady state. When O_2 pressure was varied (5 to 40 mbar), the pressure of CO was constant (20 mbar). When CO pressure was varied (20 to 60 mbar), the pressure of O_2 was constant (20 mbar). The lower partial pressures of CO were not used for estimation of reaction orders due to high CO conversion levels (>15%) in such CO-lean conditions.

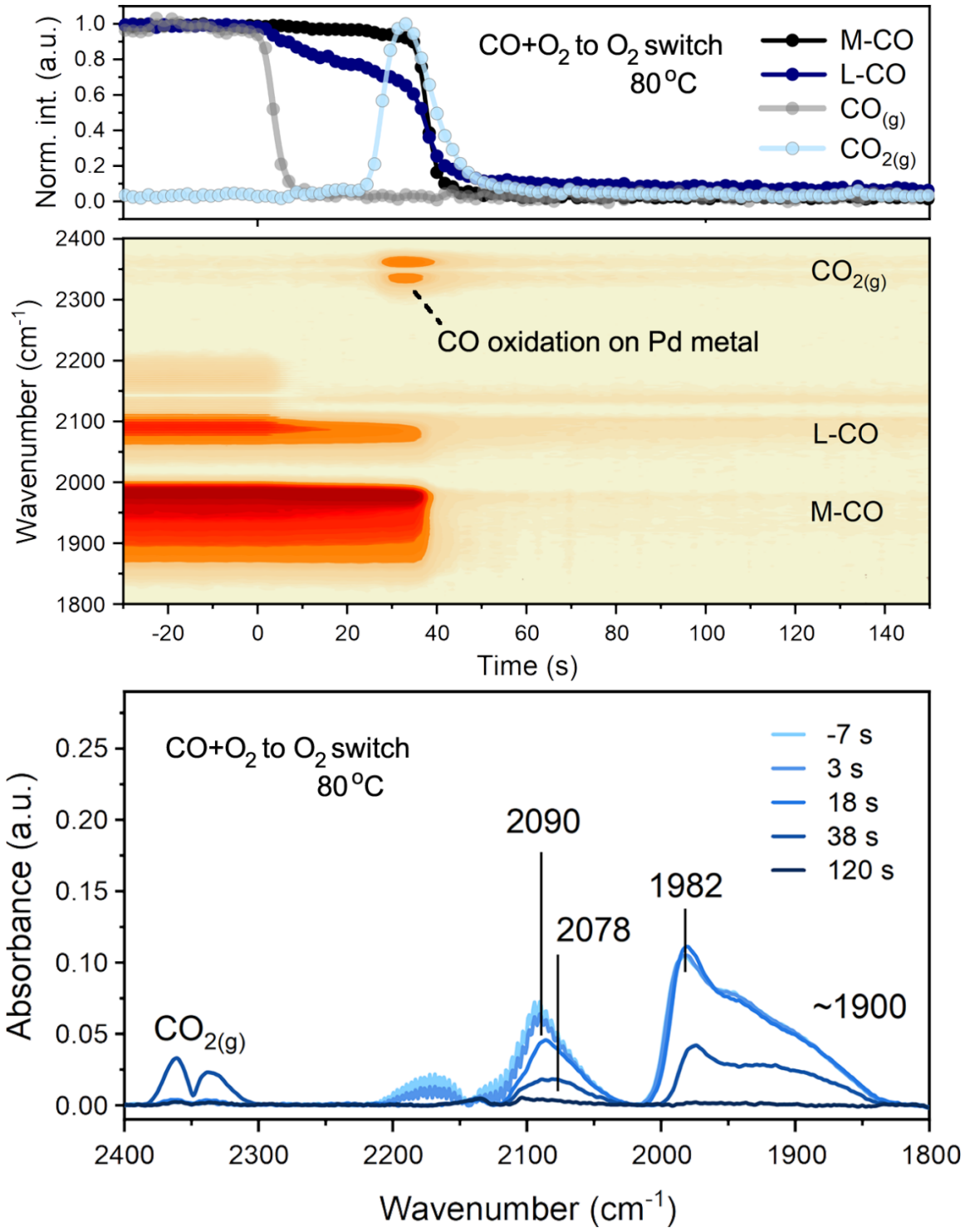

Figure C12. DRIFTS data for Pd/ZrO_2 catalyst acquired during a switch from $CO+O_2$ to O_2 at 80 °C. The top panel displays the evolution of normalized band area intensity over the time. The middle panel shows the changes in the respective spectral region as a function of time. The bottom panel display selected FTIR spectra acquired during the switch. In contrast to Pd/CeO_2, the Pd/ZrO_2 catalyst is nearly inactive at 80 °C. The positions of CO bands are, however, similar to the ones observed for ceria-supported catalyst. In contrast to Pd/CeO_2, CO oxidation over Pd/ZrO_2 takes place only in pure O_2 (at ~35s) due to poisoning of metallic sites by CO and absence of interface capable of providing reactive oxygen. Conditions: "$CO+O_2$" – 1% CO and 1% O_2 in He; "O_2" – 1% O_2 in He, total flow 100 ml/min.

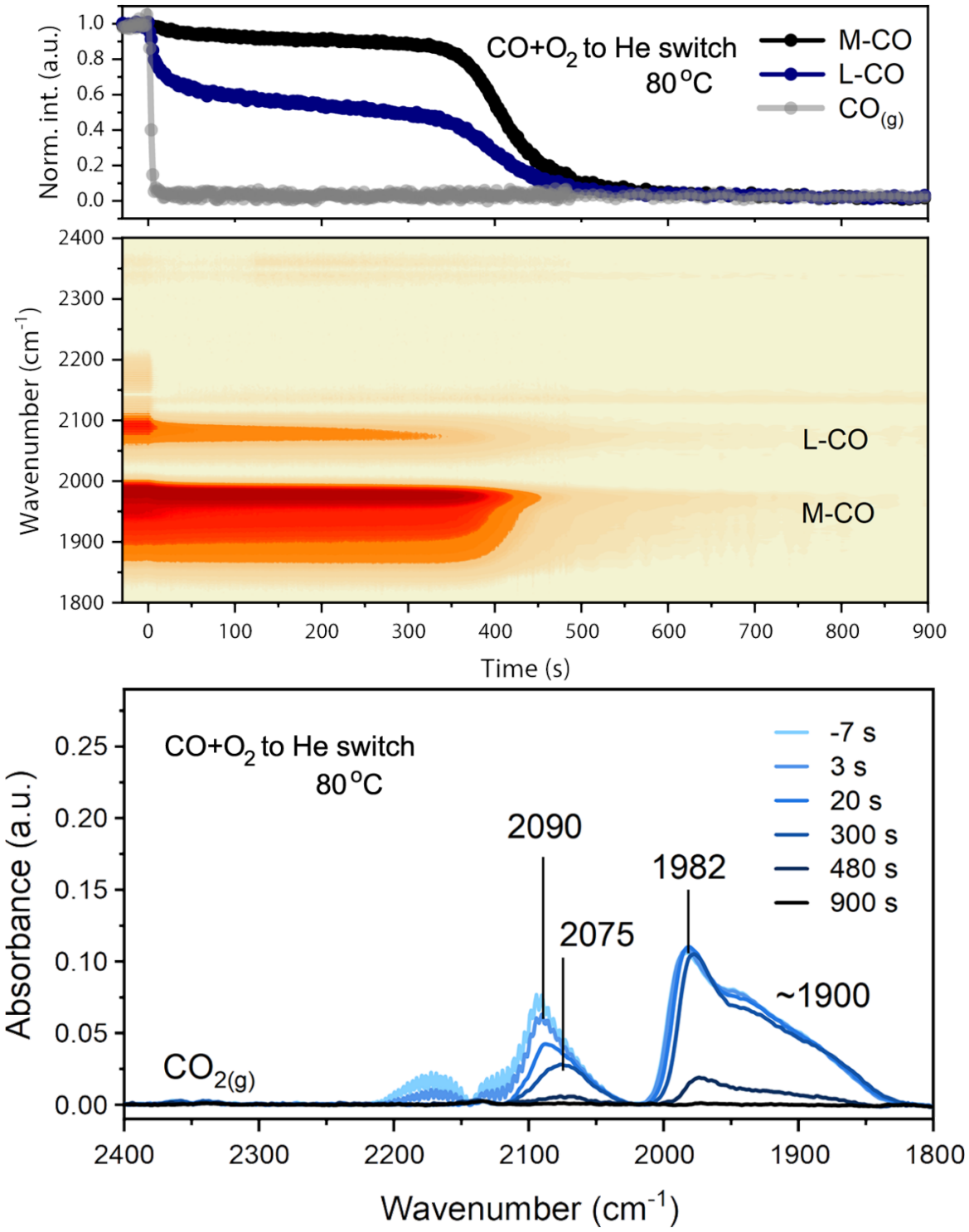

Figure C13. DRIFTS data for Pd/ZrO_2 catalyst acquired during a switch from CO+O_2 to He at 80 °C. The top panel displays the evolution of normalized band area intensity over the time. The middle panel shows the changes in the respective spectral region as a function of time. The bottom panel display selected FTIR spectra acquired during the switch. In contrast to Pd/CeO_2, the removal of carbonyls from Pd/ZrO_2 catalyst is much slower. Conditions: "CO+O_2" – 1% CO and 1% O_2 in He, total flow 100 ml/min.

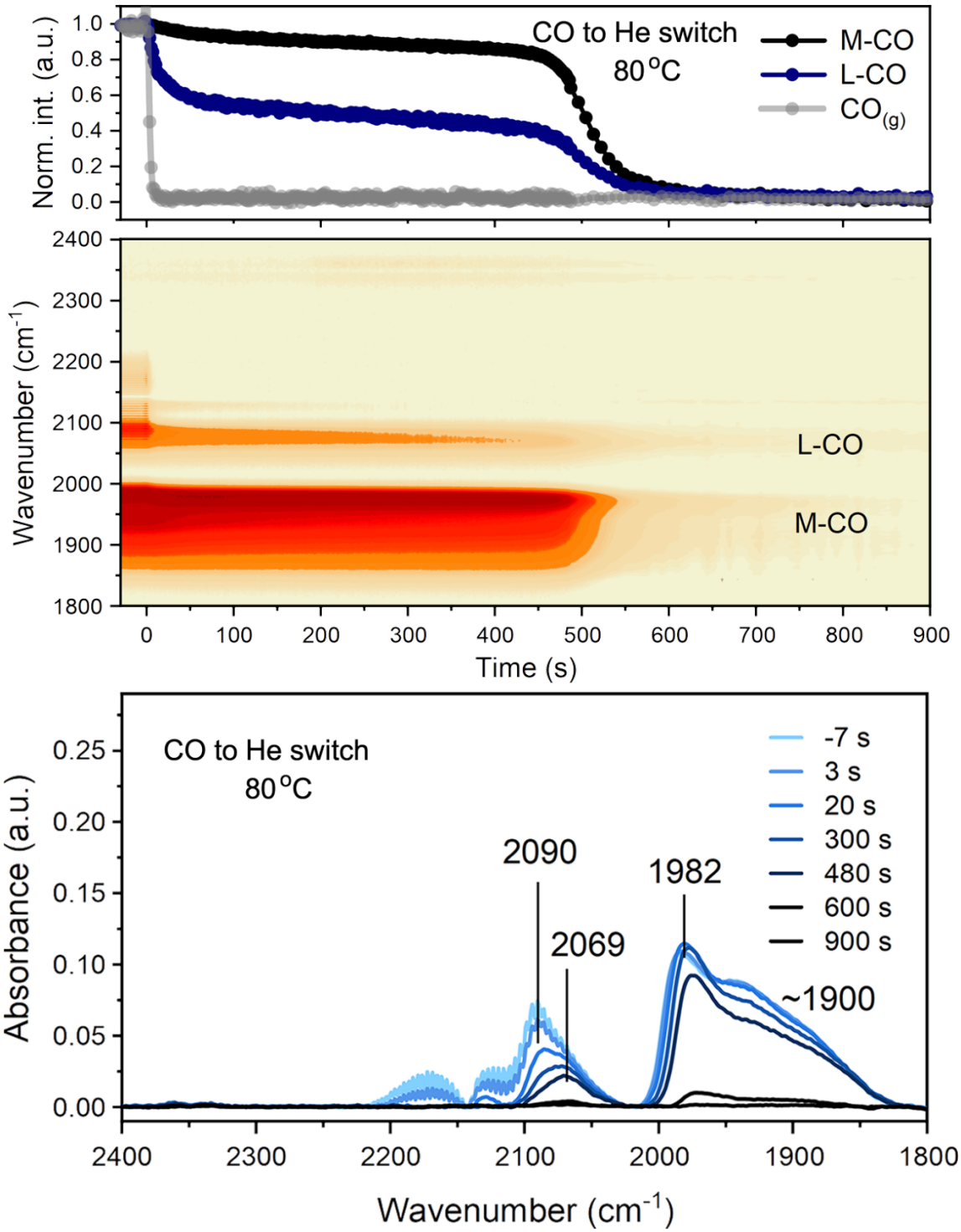

Figure C14. DRIFTS data for Pd/ZrO_2 catalyst acquired during a switch from CO to He at 80 °C. The top panel displays the evolution of normalized band area intensity over the time. The middle panel shows the changes in the respective spectral region as a function of time. The bottom panel display selected FTIR spectra acquired during the switch. In stark contrast to Pd/CeO_2, only a negligible signal of CO_2 was observed during exposure of Pd/ZrO_2 to pure CO. This implies that the amount of reactive oxygen in Pd/ZrO_2 sample is low. Furthermore, the kinetics of carbonyl disappearance is similar during $CO+O_2$ to He and CO to He switches, suggesting that in the absence of active interfacial sites pre-exposure to pure CO have little influence on the reactivity of adsorbed CO. This finding further supports the idea of ceria oxygen participation in CO oxidation on Pd/CeO_2 catalysts. Conditions: "$CO+O_2$" – 1% CO and 1% O_2 in He, total flow 100 ml/min.

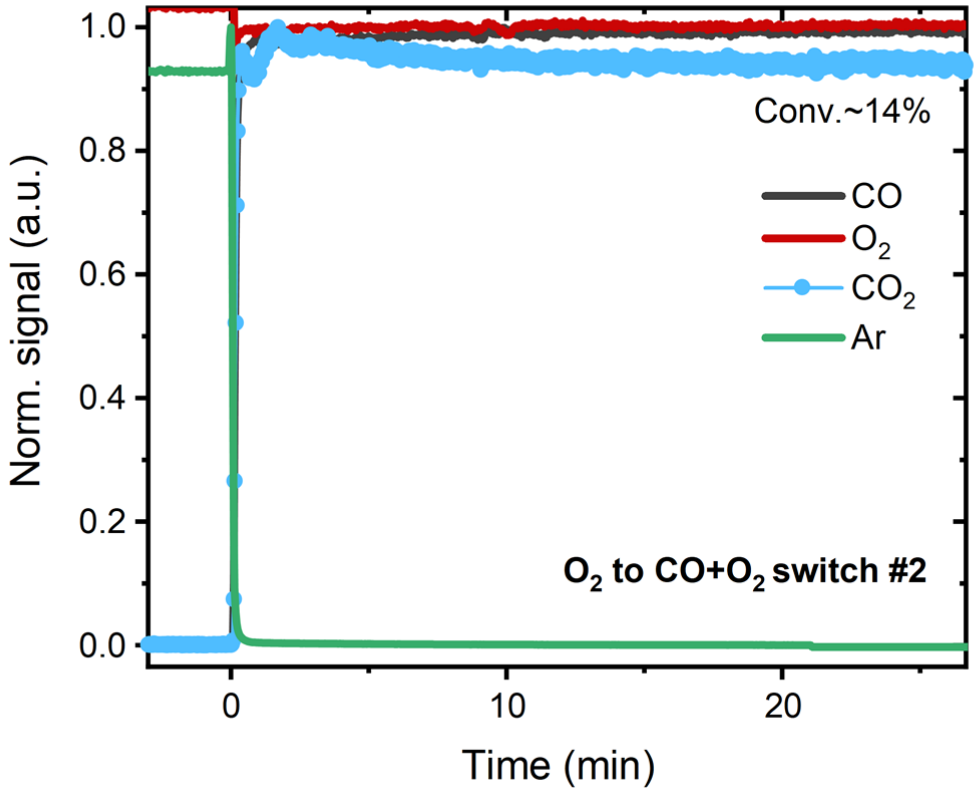

Figure C15. Mass-spectrometry data acquired during second chemical transient from O_2 to $CO+O_2$ mixture at 80 °C over Pd/CeO_2 catalyst followed by *operando* DRIFTS. Gas holdup time ~ 8 s. Conditions: "O_2" – 1% O_2 in He; "$CO+O_2$" – 1% CO + 1% O_2 in He, total flow 100 ml/min. The absence of transient high reactivity towards CO oxidation, which was seen during the first switch, is due to the absence of highly dispersed and/or single-atom Pd-oxo species. Apparently, these species cannot be regenerated in pure O_2 at 80 °C.

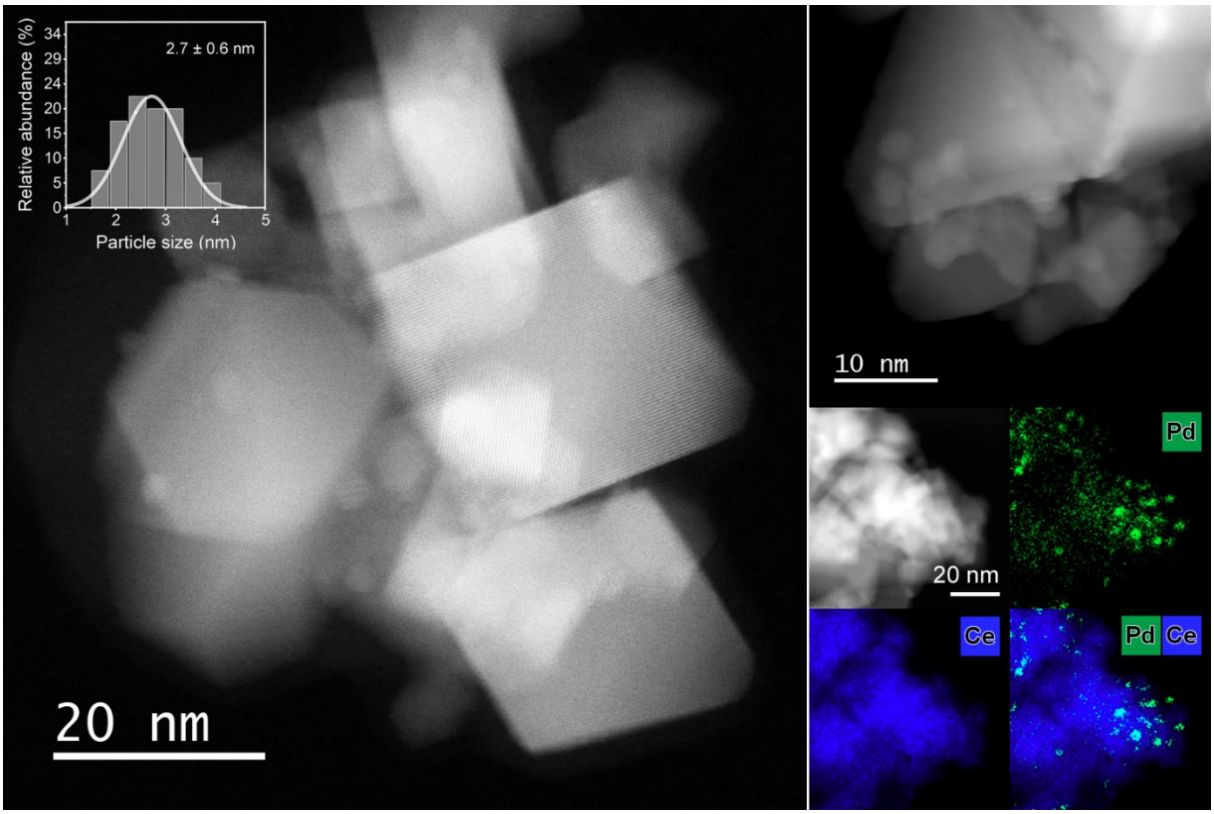

Figure C16. HAADF-STEM and EDX mapping images of used Pd/CeO_2 sample. Most of Pd is found in the form of small Pd-PdO nanoparticles of ~ 3 nm size.

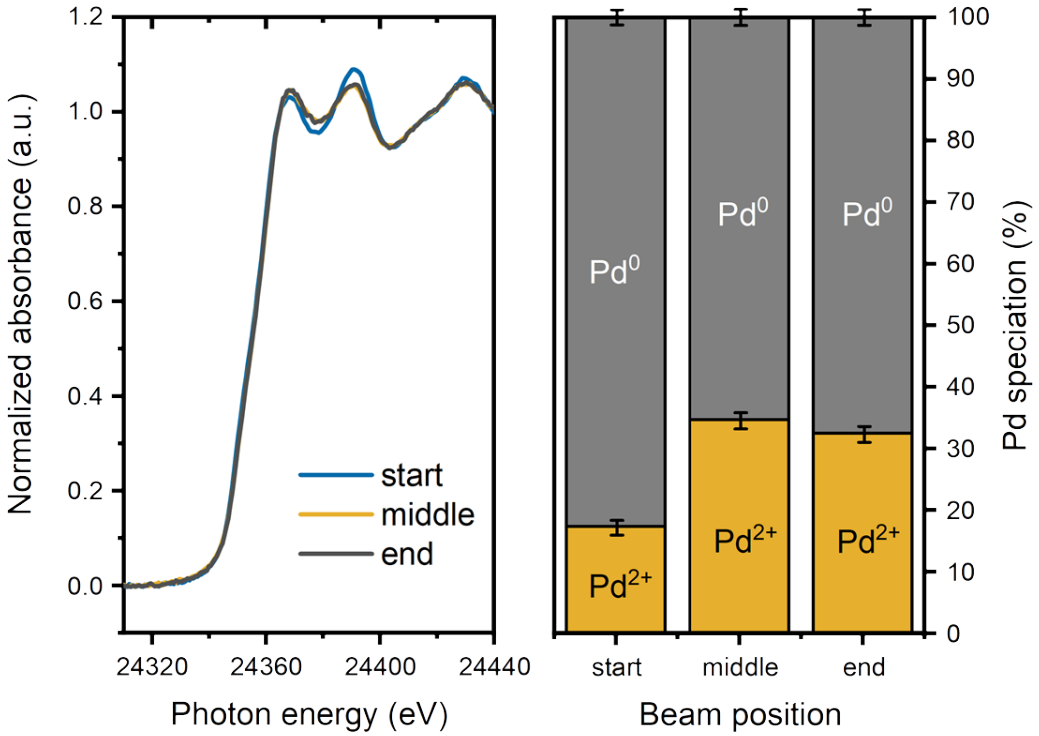

Figure C17. Operando XANES spectra at Pd K-edge acquired for Pd/CeO_2 sample during CO oxidation at 80 °C after the first light-off cycle (80 to 225 °C). Spectra were measured in different parts of the catalyst bed.

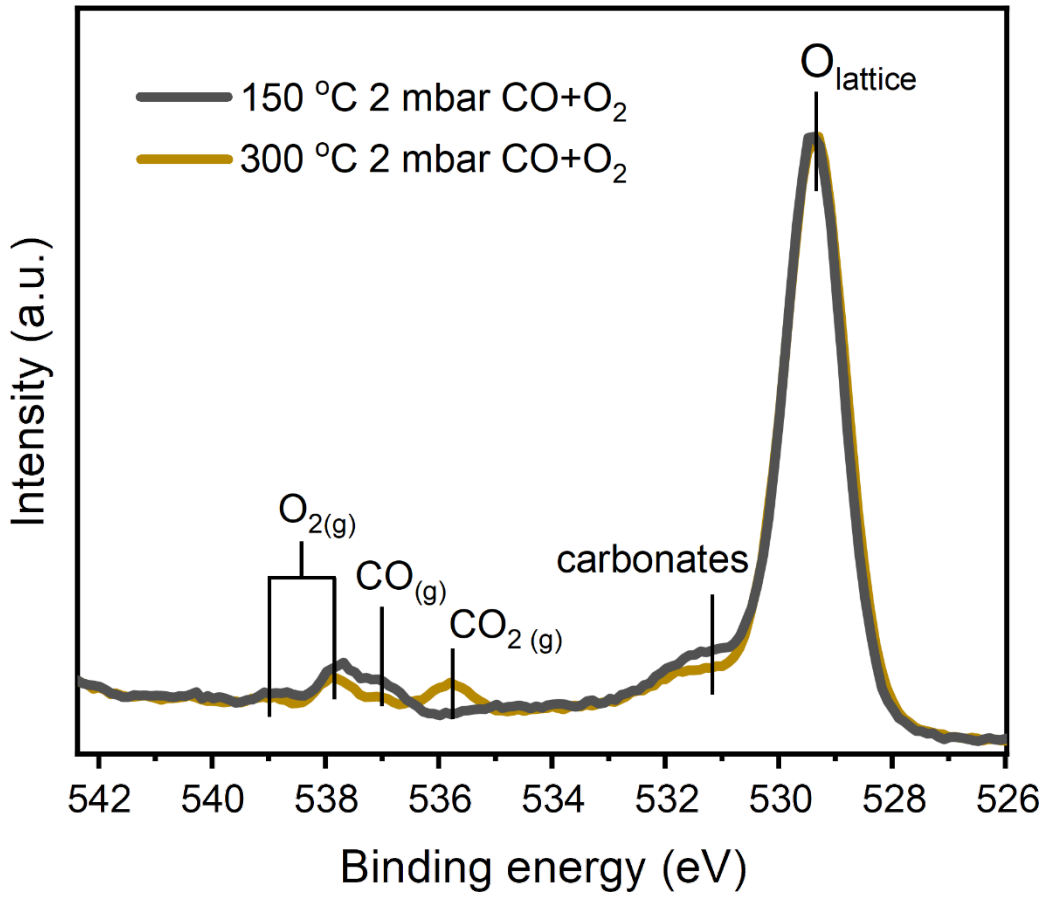

Figure C18. *In situ* NAP-XPS spectra of O 1s core-line acquired during CO oxidation ($CO+O_2$ =1+1 mbar) at 150 ºC and 300 ºC. As marked on the graph, at 300 ºC the CO conversion is nearly 100% in the NAP-cell. Lower conversion as compared to XAS or DRIFTS experiments is due to the lower loading of the catalyst as practically a few mg of the catalyst were drop casted on the sample holder. Another reason is the possible bypassing of the gas-phase reactants without a contact with the sample inside the NAP-cell.

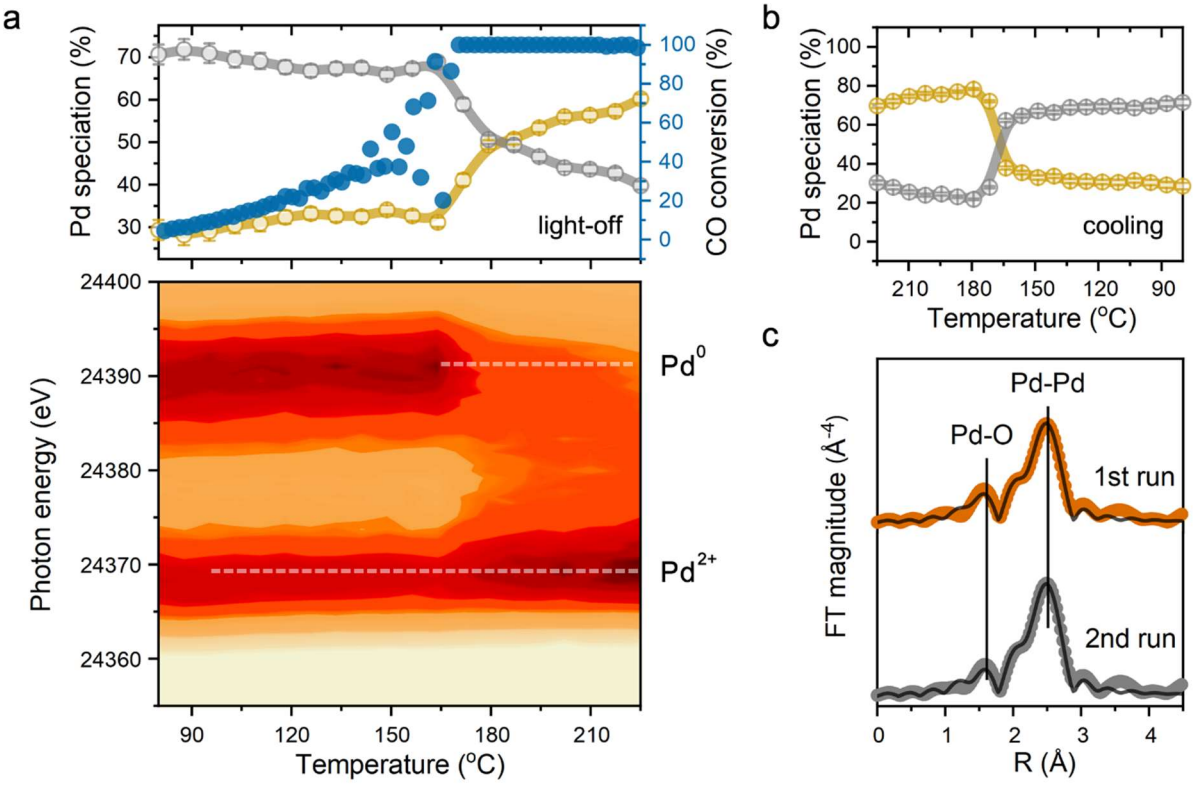

Figure C19. Evolution of Pd during CO oxidation as a function of temperature**.** a**)** *Operando* XAS at Pd K-edge during the second light-off in 1% CO and 1% O_2 in He (total flow 100 mL min^{-1}). XAS data acquired in the middle of the catalyst bed. Top panel shows the distribution of Pd states (grey-metallic, amber-oxidic), derived from linear combination fitting, and the CO conversion as a function of temperature. Bottom panel displays XANES region of Pd K-edge spectra as a function of temperature. b**)** Evolution of Pd oxidation state (grey-metallic, amber-oxidic) upon cooling in reaction mixture after second light-off test. c) R-space EXAFS spectra in the middle of catalyst bed cooled to 80 °C after the first and second reaction cycles.

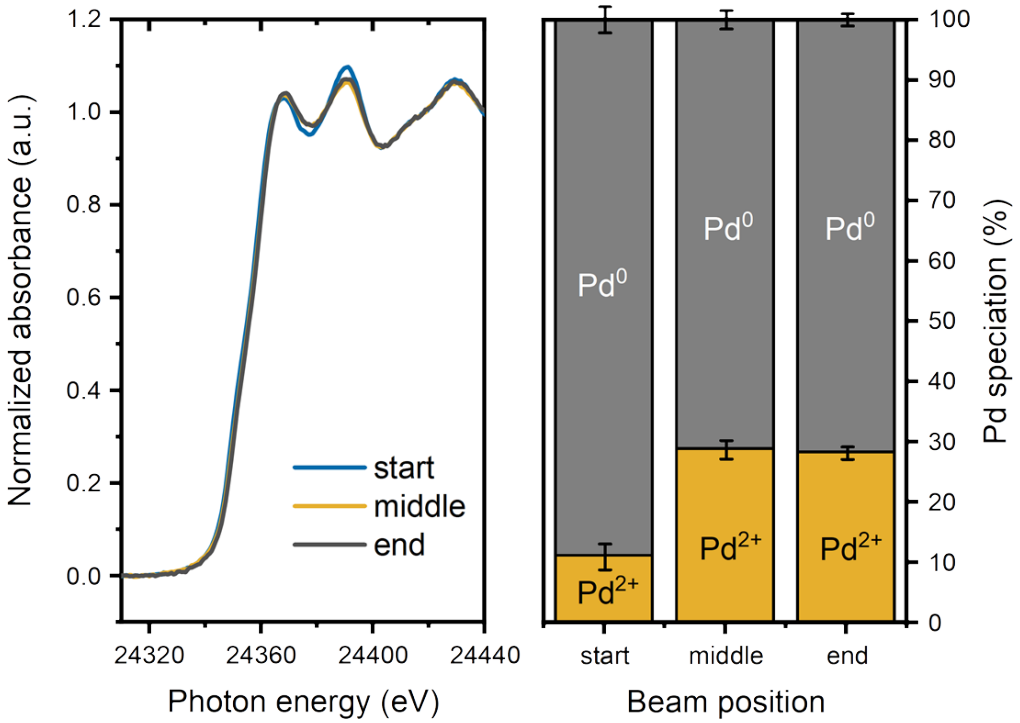

Figure C20. *Operando* XANES spectra at Pd K-edge acquired for Pd/CeO_2 sample during CO oxidation at 80 ºC after the second light-off cycle (80 to 225 ºC). Spectra were measured in different parts of the catalyst bed.

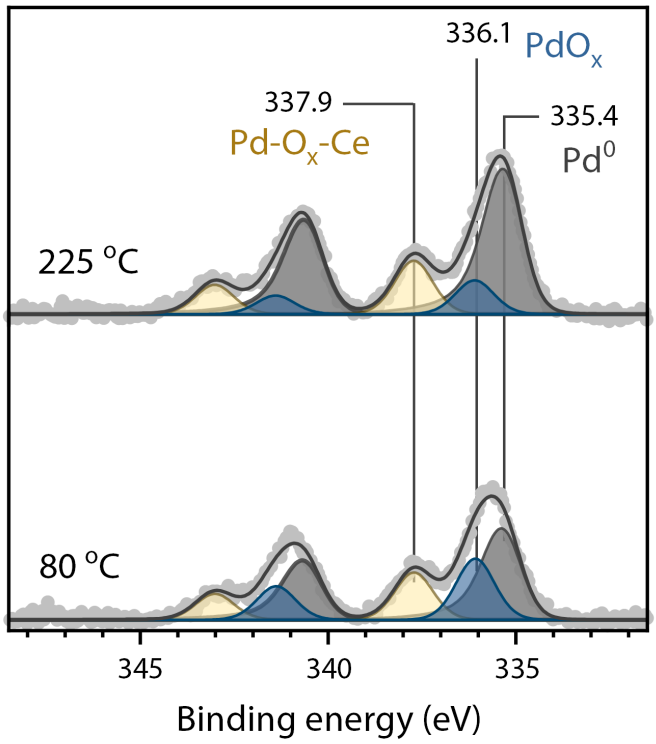

Figure C21. *In situ* NAP-XPS of Pd 3d core-level for the catalyst heated to 225 ºC and cooled to 80 ºC after experiments shown in **Fig. 5.5d**. The total pressure in NAP-cell was fixed to 2 mbar, for the reaction mixture 1 mbar CO and 1 mbar of O_2 was used.

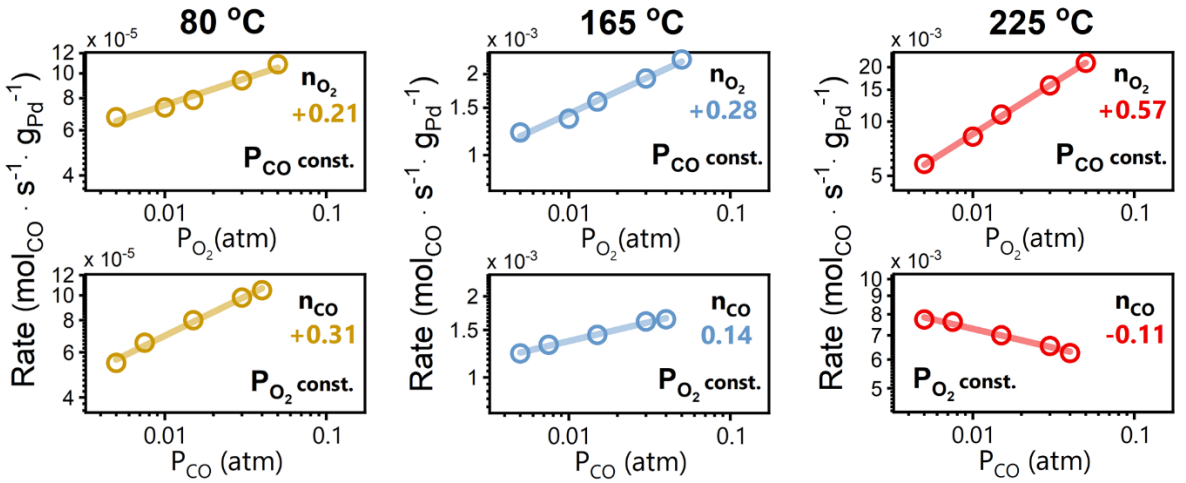

Figure C22. Reaction orders measured for Pd/CeO_2 catalyst as function of temperature. For each measurement a fresh catalyst was loaded and stabilized on the stream at least 14 h to reach steady state. When O_2 pressure was varied (5 to 50 mbar), the pressure of CO was constant (10 mbar). When CO pressure was varied (5 to 40 mbar), the pressure of O_2 was constant (10 mbar). Total flow was fixed to 200 ml/min, the loading of catalysts was varied to maintain low level of CO conversion (<5%). Sieved fraction (125 to 250 μm) was diluted with ~250-300 mg of SiC. The catalyst was pretreated in 20% O_2/He at 300 °C for 1 h.

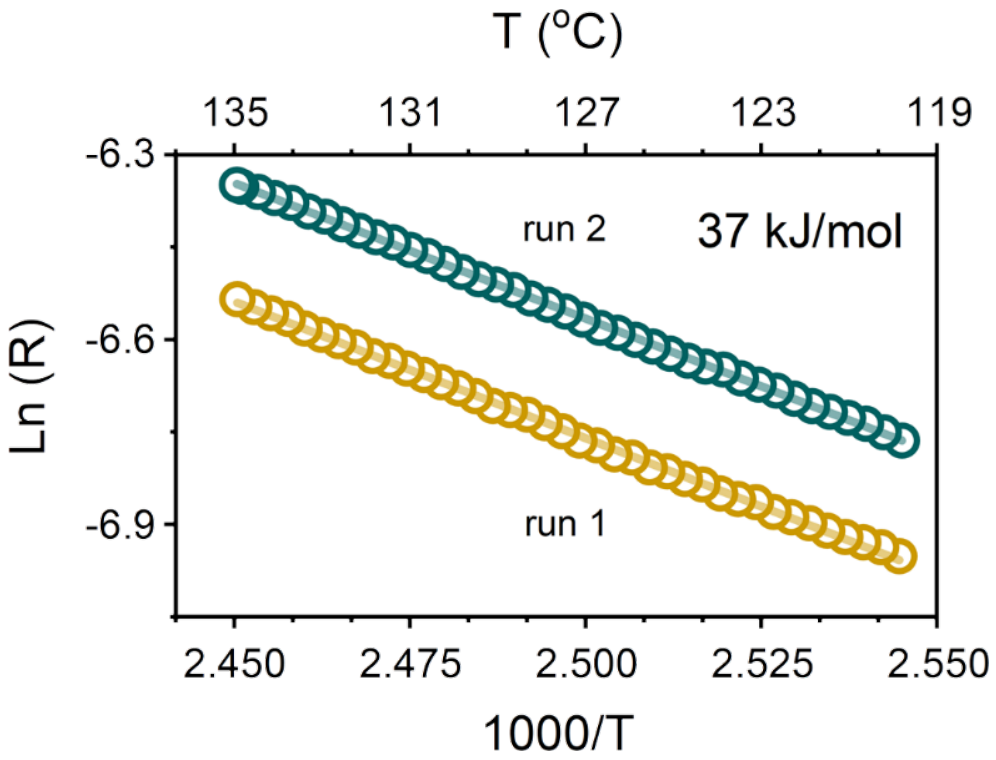

Figure C23. Arrhenius plot for catalytic activity of Pd/CeO_2 in CO oxidation at elevated temperatures. Yellow circles represent the low-temperature activity during the first light-off run (RT to 300 °C), cyan circles stand for the second run. Reaction conditions: 1% CO and 1% O_2 in He, (GHSV ~1,800,000 ml g_{cat}^{-1} h^{-1}). Total flow 150 ml/min.

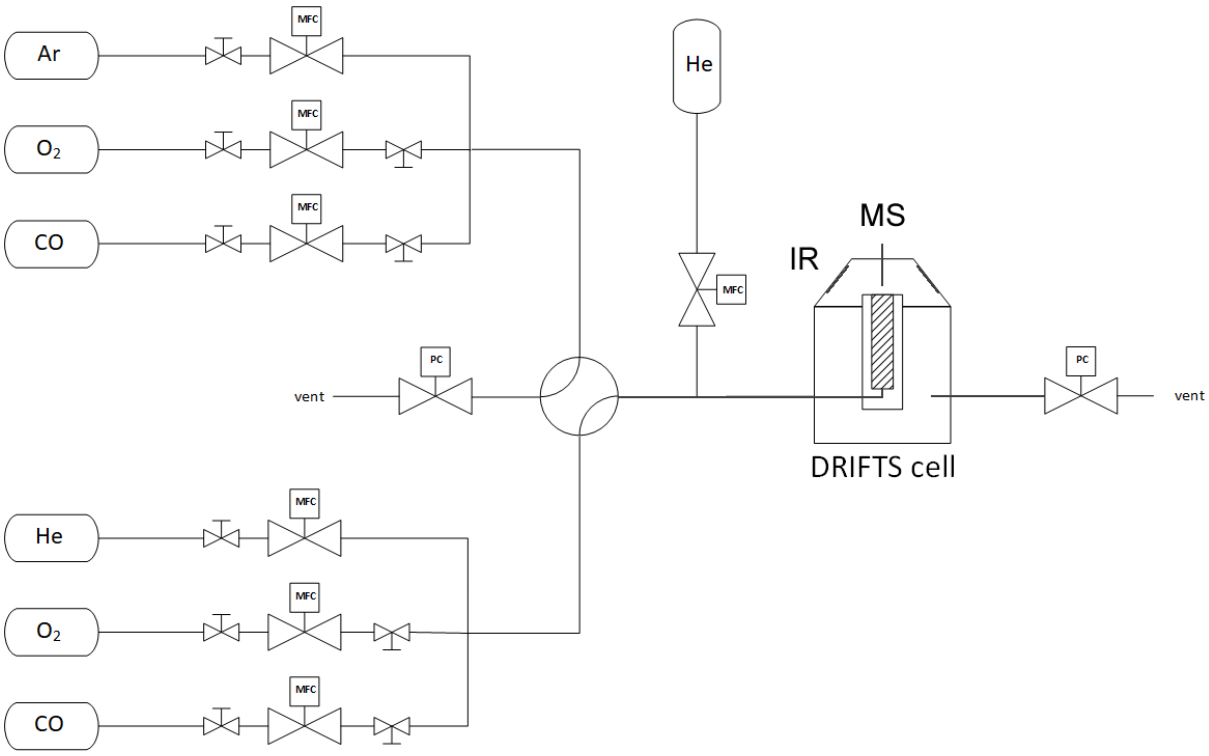

Figure C24. Scheme of the *operando* DRIFTS setup.

Table C1. EXAFS fitting results.

Sample	Path	R [Å]	CN	σ^2 [Å^2]	ΔE_0 [eV]	R-factor [%]
Pd/CeO_2 ex situ	Pd-O	2.02 ± 0.01	3.8 ± 0.4	0.001 ± 0.001	6.5 ± 1.2	1.7
	Pd-Pd (oxide)	3.02 ± 0.01	1.6 ± 1.1	0.004 ± 0.004		
	Pd-Pd (oxide)	3.42 ± 0.01	2.3 ± 1.5	0.004 ± 0.004		
Pd/CeO_2 O_2 80 °C	Pd-O	2.01 ± 0.01	4.1 ± 0.3	0.003 ± 0.001	4.1 ± 0.9	1.0
	Pd-Pd (oxide)	3.01 ± 0.01	2.7 ± 1.3	0.011 ± 0.003		
	Pd-Pd (oxide)	3.41 ± 0.01	5.1 ± 2.2	0.011 ± 0.003		
Pd/CeO_2 CO+O_2 80 °C	Pd-O	2.00 ± 0.02	2.5 ± 0.5	0.003 ± 0.003	1.4 ± 2.0	1.7
	Pd-Pd (metal)	2.77 ± 0.02	5.3 ± 1.6	0.010 ± 0.002		
	Pd-Pd (oxide)	3.01 ± 0.02	3.8 ± 2.1	0.010 ± 0.002		
	Pd-Pd (oxide)	3.40 ± 0.02	1.8 ± 1.4	0.010 ± 0.002		
Pd/CeO_2 CO+O_2 80 °C after 1st light-off - middle	Pd-O	1.97 ± 0.02	1.6 ± 0.7	0.006 ± 0.006	-2.6 ± 0.9	1.3
	Pd-Pd (metal)	2.74 ± 0.01	6.9 ± 0.9	0.008 ± 0.001		
Pd/CeO_2 CO+O_2 80 °C after 1st light-off - inlet	Pd-Pd (metal)	2.73 ± 0.01	9.8 ± 0.9	0.008 ± 0.001	-3.1 ± 0.7	1.4
Pd/CeO_2 CO+O_2 80 °C after 2nd light-off - middle	Pd-O	1.97 ± 0.02	1.7 ± 0.8	0.008 ± 0.007	-2.3 ± 0.8	1.0
	Pd-Pd (metal)	2.74 ± 0.01	7.3 ± 0.9	0.007 ± 0.001		
PdO	Pd-O	2.00 ± 0.01	4.0	0.002 ± 0.001	2.9 ± 1.3	2.1
	Pd-Pd (oxide)	3.04 ± 0.01	4.0	0.004 ± 0.001		
	Pd-Pd (oxide)	3.43 ± 0.01	8.0	0.004 ± 0.001		
Pd foil	Pd-Pd	2.74 ± 0.01	12.0	0.006 ± 0.001	-0.1 ± 0.5	0.3

S_0^2 values (0.68 for B18, Diamond and 0.82 for P65, DESSY) were derived from fitting the PdO reference (Sigma-Aldrich) and used for the fitting of Pd-CeO_2 samples. ΔE_0 was shared for all the shells, while σ^2 and ΔR values were shared within each shell for the same type of back-scattering atoms. The errors indicate the uncertainties of fitting results derived from Artemis software.

Table C2. XPS data quantification.

	Pd/Ce at.	Pd^0 (%)	PdO_x (%)	Pd^{2+}-O-Ce (%)
80 ºC O_2	0.044	0	13	87
80 ºC $CO+O_2$	0.047	5	35	60
150 ºC $CO+O_2$	0.041	47	7	46
225 ºC $CO+O_2$	0.039	53	6	40
300 ºC $CO+O_2$	0.028	53	5	42
80 ºC $CO+O_2$ cool	0.028	56	11	33

Table C3. Basic characterization.

	Pd loading (wt%, ICP)	BET, m^2g^{-1}
Pd/CeO_2	0.93 ± 0.02	39.8
Pd/ZrO_2	0.72 ± 0.01	6.2

Chapter 6

Tuning CO oxidation activity of Pd/CeO_2 catalysts by the size of the CeO_2 support

Abstract

Catalysis by atomically dispersed noble metals is an attractive strategy for achieving maximum metal utilization and high reactivity. A conventional approach to prepare single-atom catalysts requires sparse surface density of metal sites by using low metal loadings and nanosized supports with high surface area. Here we show that the size of the support (CeO_2) itself can influence the activity and stability of metal (Pd) single atoms during CO oxidation. Using flame spray pyrolysis, we prepared a set of Pd/CeO_2 catalysts differing in size from 4 to 18 nm. Their reactivity towards CO oxidation exhibits strong dependence on the particle size of the support, the optimum being around 8-9 nm. *In situ* and *operando* spectroscopic tools together with steady-state kinetic studies shed light on the origin of the observed structure sensitivity. Small-sized Pd/CeO_2 catalysts (~4 nm) exclusively contain single-atom Pd species, which are limited in their CO oxidation activity by oxygen poisoning in oxygen-rich reaction mixtures. Pd single atoms are unstable on the surface of large nanoparticles of CeO_2 (~13 nm) and form metallic Pd clusters, which are less active in low-temperature CO oxidation. In contrast to small Pd/CeO_2, single atoms of Pd on medium CeO_2 (~8-9 nm) are not poisoned by oxygen, benefiting the low-temperature activity. The reducibility of CeO_2 nanoparticles depends on size and strongly affects the activity and stability of Pd-oxo species through oxygen transfer at the Pd-CeO_2 interface. The support size-dependent catalytic behavior of Pd/CeO_2 catalysts was also demonstrated for sol-gel derived CeO_2. The insight that catalytic performance of metal-ceria systems can be tuned by the size of the support extends the toolbox for the design of ceria-based catalysts.

6.1 Introduction

Heterogenous catalysts consisting of transition metals deposited on a solid support constitute an important class of materials routinely used in many modern chemical processes. The intrinsic catalytic activity of such supported metal particles can be strongly dependent on their size. Classical examples of structure sensitivity in heterogeneous catalysis pertain to transition metals catalyzing hydrogenation reactions of molecules such as CO, CO_2 and N_2 in Fischer-Tropsch synthesis[1], CO_2 methanation[2], and methanol[3] and ammonia[4] syntheses. Haruta and co-workers showed the strong impact of gold particle size for oxidation reactions[5]. Small Au nanoparticles (<5 nm) are highly active in CO oxidation already at 0 °C, while larger nanoparticles are practically inactive under these conditions. Utilization of highly dispersed metal species is also beneficial in view of atom economy, in particular for catalysts based on expensive noble metals. In contrast to Au[6], Pt, Pd and Rh nanoparticles deposited on inert supports (Al_2O_3, SiO_2) are not very active in low-temperature CO oxidation and their intrinsic catalytic activity does not depend on metal particle size[7–9]. This is thought to relate to strong adsorption of CO on such transition metals, which results in a low O coverage and CO oxidation activity. On the other hand, when Pt, Pd and Rh nanoparticles are dispersed on redox-active supports such as TiO_2[10], FeO_x[11] and CeO_2[7,8], CO poisoning can be circumvented through O_2 activation at the metal-support interface.

The unusual catalytic properties of interfacial sites can be caused by metal-support interactions (MSIs)[12–15]. The particularly strong MSIs in metal-ceria systems also result in the stabilization of highly dispersed species of transition metals[16,17]. In some cases, atomic dispersion of metals on ceria can be achieved, giving rise to single-atom catalysts[18–21]. Recently, it was shown that isolated Pd atoms stabilized on CeO_2 exhibit a high CO oxidation activity at low temperature[22–26]. Maintaining Pd in the oxidized state appears not only to be critical for the high activity but also the high stability of single Pd atoms on CeO_2, because metallic Pd is prone to sintering[27,28]. The facile oxygen transport at the metal-support interface due to the reducibility of the CeO_2 support involving $Ce^{4+} \rightleftarrows Ce^{3+}$ redox transitions plays an important role in stabilization of Pd single atoms on CeO_2 during CO oxidation[27].

A conventional approach for the preparation of highly dispersed metal catalysts combines the use of a high-surface area support with a low loading of the catalytically active metal[29,30].

In a first approximation, one can assume that a higher support surface area and therefore smaller particle size of the supporting oxide should be beneficial for the dispersion of the active phase. However, strong indications have been found that the extent of metal-ceria interactions and the redox properties of CeO_2 depend on the size of the CeO_2 crystallites[31–34]. Based on density functional theory (DFT) calculations, Neyman and colleagues proposed that the unique redox chemistry of ceria nanoparticles smaller than ca. 5 nm stems from the reduced energy cost for removal of lattice oxygen atoms[35]. It has been experimentally demonstrated that nanostructuring of ceria facilitates oxygen spillover from the support to noble metals[36]. The group of Corma provided compelling evidence for the beneficial catalytic properties of nanosized ceria. A two-orders-of-magnitude increase of the low-temperature CO oxidation activity was achieved by supporting 2-3 nm Au nanoparticles on small ceria crystallites of ~4 nm instead of bulk CeO_2[37]. The improved activity was attributed to facile supply of reactive oxygen from nanosized ceria[38].The enhanced oxygen mobility at the interface between Pd and nanosized CeO_2 also contributes to an increased stability of single Pd atoms, which are highly active in low-temperature CO oxidation[27]. To the best of our knowledge, the effect of CeO_2 particle size on the activity and stability of highly dispersed Pd species in CO oxidation has not been addressed in a systematic manner. One of the reasons is the difficulty in synthesizing CeO_2 nanoparticles of controlled size via wet chemistry methods [32,39–41].

Here, we employed flame spray pyrolysis (FSP) to prepare a range of single-atom Pd/CeO_2 catalysts in which the particle size of the CeO_2 support was controlled in the 4-18 nm range. This was achieved by varying the injection feed rate of precursors during flame spray pyrolysis (FSP). We first prepared and characterized a set of CeO_2 supports and then applied this approach to synthesize Pd/CeO_2 samples in one step by FSP using a precursor solution containing both Ce and Pd. Extensive characterization of the as-prepared catalysts Pd/CeO_2 shows that Pd is predominantly present as atomically dispersed oxidized species. Catalytic activity measurements revealed that the CO oxidation performance is strongly dependent on the particle size of CeO_2 with an optimum observed for 8-9 nm nanoparticles. By combining *in situ* and *operando* diffuse-reflectance IR spectroscopy (DRIFTS) and near-ambient pressure X-ray photoelectron spectroscopy (NAP-XPS), the activity trends were interpreted in terms of differences in reducibility of the Pd-CeO_2 interface and the Pd

speciation. Similar activity trends were observed for a set of sol-gel prepared CeO_2 samples to which Pd was added by impregnation.

6.2 Results and Discussion

6.2.1 Flame spray pyrolysis preparation of CeO_2 nanoparticles

We prepared a set of ceria supports with different particle sizes using flame spray pyrolysis. Madler et al.[42] showed that the ceria particle size can be controlled by changing the injection rate of the liquid feed during FSP synthesis. This was explained by variations in the residence time and size of the precursor droplets sprayed in the flame, which strongly affect the crystallization process[42,43]. Using cerium acetate as a precursor and a mixture of 2-ethylhexanoic and glacial acetic acid (50:50 vol%) as solvent, we prepared CeO_2 samples at injection rates ranging from 1 to 10 ml/min. Synchrotron powder X-ray diffraction (XRD) patterns of the as-prepared samples (**Fig. 6.1a**) only exhibit the characteristic reflections of the cubic phase of ceria (*Fm*3*m*). The systematic broadening of the diffraction peaks upon decreasing the injection feed rate indicates a decrease in the CeO_2 crystallite size. In this way, the size of CeO_2 nanoparticles can be tuned in the range of 5 to 14 nm by adjusting the feed injection rate (**Table D1**). The redox properties of the obtained supports were studied using temperature-programmed reduction in hydrogen (H_2-TPR). For all CeO_2 samples, we can distinguish two main reduction features in the H_2 consumption profiles: a low-temperature peak (α) at ~300-325 °C and a broad feature (β) at 400-500 °C (**Fig. 6.1b**). As bulk reduction of CeO_2 usually occurs at higher temperature (*i.e.*, ~800 °C), the α and β features can be related to surface oxygen reduction[44]. A prominent β peak in TPR profiles is typical for CeO_2 with a high surface area, *i.e.*, with a crystallite size smaller than 20 nm[34,44]. The α feature becomes stronger with decreasing particle size. The appearance of this feature at substantially lower temperatures than the β one points to a presence of additional type of reactive oxygen species. Thus, the low-temperature α peak is a distinctive signature of very small ceria nanoparticles (<10 nm). The integral hydrogen consumption increases strongly when the particle size of CeO_2 decreases (**Fig. 6.1c**). This is in line with the earlier finding that small ceria nanoparticles are more reducible in this temperature range due to the enhanced surface-to-volume ratio[34]. Thus, FSP is a suitable method to prepare phase-pure CeO_2 nanoparticles of different size. These bare CeO_2 nanoparticles show a size-dependent

reducibility. In the following, we investigate the redox properties of Pd/CeO_2 catalysts as a function of CeO_2 particle size.

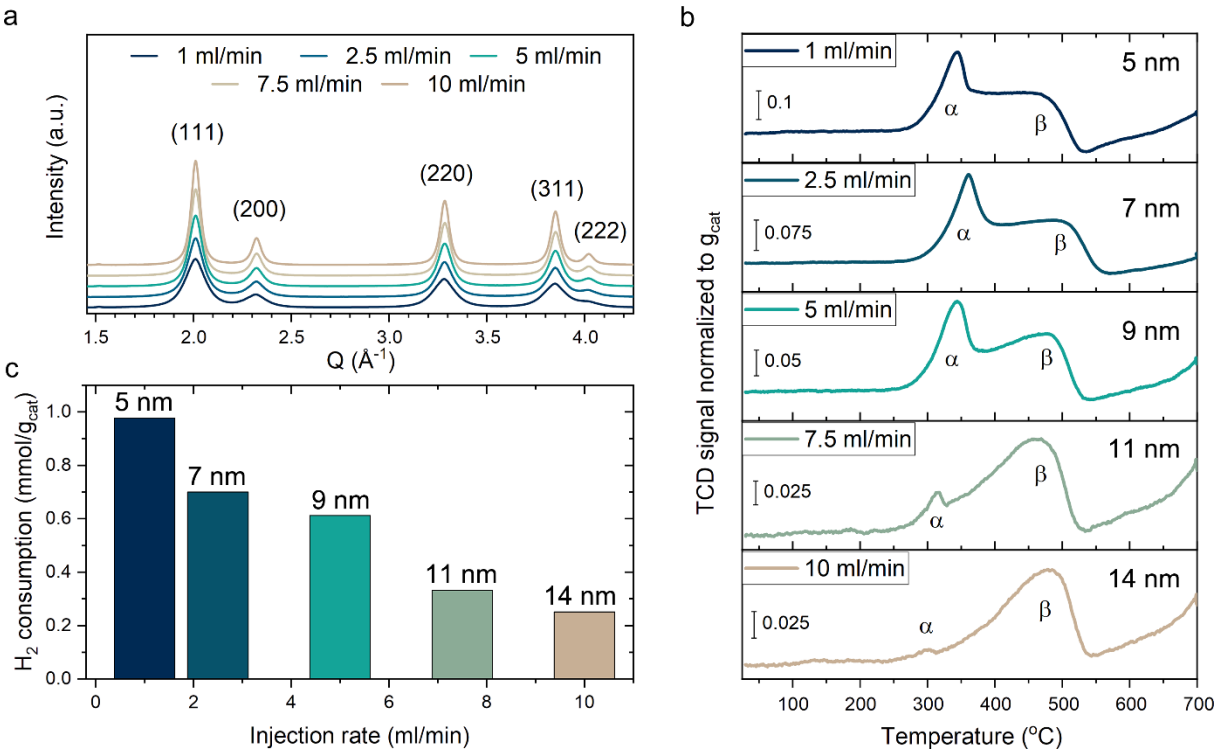

Figure 6.1. Characterization of CeO_2 powders prepared by FSP with variable injection feed rate of the liquid precursor (1 to 15 ml/min). a) Synchrotron powder XRD patterns acquired at λ = 0.18233 Å. b) H_2-TPR profiles of fresh FSP-CeO_2 prepared at different injection rates. c) Quantification of H_2 consumption for the FSP-CeO_2 supports.

6.2.2 Morphology and redox properties of FSP-made Pd/CeO_2

We have earlier shown that highly dispersed Pd-oxide on CeO_2 can be prepared by one-step FSP[27,45]. Here, we added Pd acetylacetonate to the solvent mixture for CeO_2 FSP synthesis to obtain Pd/CeO_2 with a Pd loading of 1 wt% and varied the injection rate from 1 to 15 ml/min. The resulting samples are denoted as PdFSP. High-resolution high-angle annular dark-field scanning transmission electron microscopy (HAADF-STEM) images shown in **Fig. 6.2a** and **Fig. D1** indicate that octahedra-like nanoparticles of PdFSP samples vary in size from 4 to 18 nm upon increasing the injection rate. The sizes of the resulting PdFSP nanoparticles (**Fig. D2**) are similar to those of the bare CeO_2 nanoparticles prepared at the same injection rate, indicating a minor influence of Pd on the crystallization of ceria during the FSP process. XRD only shows reflections due to CeO_2 for the PdFSP samples (**Fig. 6.2b** and **Fig. D3**), indicative of the high Pd dispersion. We found a good agreement between particle sizes of PdFSP estimated from BET surface measurements, XRD and TEM (**Table D2** and **Fig. D4**). For comparison, another set of samples was prepared using the same injection rates (1 to 15

ml/min) for bare CeO_2 supports followed by wet impregnation with 1 wt% Pd. These samples are denoted as PdFSPimp and their characterization is summarized in **Figs. D5-D8** and **Table D3**.

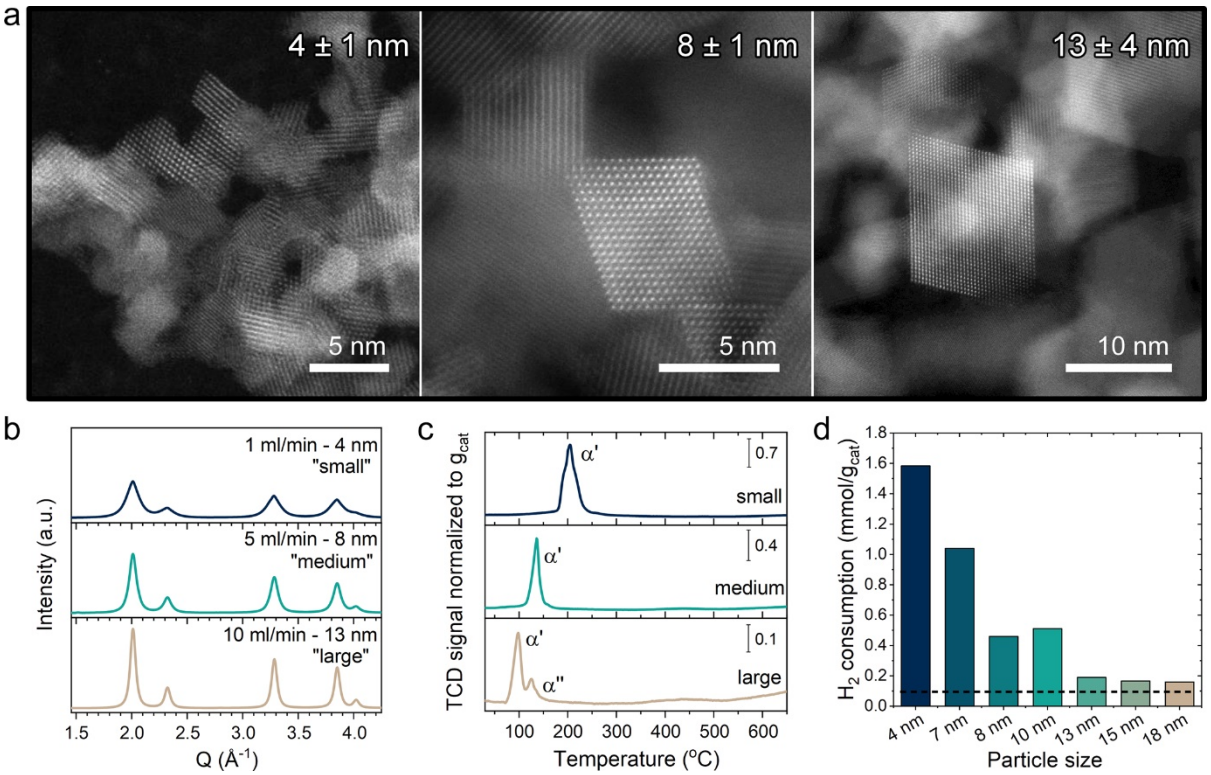

Figure 6.2. Characterization of Pd/CeO_2 samples prepared by FSP with different feed injection rate of the liquid precursor (1 to 15 ml/min). a) HAADF-STEM images of the small, medium, and large particles of PdFSP. b) Synchrotron powder XRD patterns acquired at λ = 0.18233 Å. c) H_2-TPR profiles of fresh PdFSP with different particle size. d) Quantification of H_2 consumption for PdFSP samples. The dashed line indicates the amount of H_2 required for reduction Pd-oxo species only.

The redox properties of PdFSP catalysts are different from the bare CeO_2 supports according to H_2-TPR (**Fig. 6.2c** and **Fig. D9**). The smallest PdFSP particles exhibit an intense H_2 consumption feature at ~200 °C (α'-peak), which indicates a strong interaction between CeO_2 and Pd, typical for highly dispersed Pd-oxo species[22]. As the size of the PdFSP particles increases, this feature shifts to lower temperature and finally splits into two peaks (α' and α''). We tentatively explain this by the presence of small PdO_x clusters on larger (>10 nm) ceria nanoparticles[22]. These findings indicate that the Pd-CeO_2 interactions become weaker with increasing size of the CeO_2 support. For the PdFSPimp samples, the reduction peaks are generally located at lower temperatures, suggesting a weaker stabilization of Pd by CeO_2 in comparison to the one-step made PdFSP samples (**Fig. D9**). Quantification of H_2-TPR data (**Fig. 6.2** and **Table D4**) reveals that the presence of Pd enhances the reducibility of nanosized CeO_2 [46]. The amount of consumed H_2 substantially exceeds the stoichiometry of

the reduction of Pd oxide (~0.9 mmol/g_{cat} for a Pd loading of 1 wt%). This is especially evident for the small PdFSP sample, which points to facile hydrogen spillover from Pd sites to CeO_2 and a higher reducibility of small CeO_2 nanoparticles. Conversely, the weaker interaction between Pd and large CeO_2 nanoparticles will decrease the Pd dispersion, hydrogen spillover and result in a lower reducibility of CeO_2. In contrast to bare CeO_2 whose reducibility was determined to be proportional to the surface-to-volume ratio, the H_2 consumption for PdFSP and PdFSPimp samples remains size-dependent after normalization to the surface area (**Table D4**). Thus, the redox properties and Pd-CeO_2 interactions in the PdFSP samples depend strongly on the size of the CeO_2 particles. In the next section, we study the influence of CeO_2 particle size on the structure of Pd sites in the prepared samples.

6.2.3 Speciation of Pd in as-prepared catalysts

We employed XPS and DRIFTS to investigate the nature of supported Pd species. We focused on three samples, namely PdFSP of small (4 nm), medium (8-9 nm) and large (13 nm) particle sizes. XPS of the Pd 3d core line region revealed that most of Pd in these samples (**Fig. 6.3** and **Fig. D10**) gives rise to a Pd $3d_{5/2}$ binding energy of 337.8 eV, corresponding to Pd^{2+} in strong interaction with CeO_2, likely in the form of highly, possibly atomically, dispersed Pd-oxo species[22,27,47]. For large PdFSP nanoparticles (> 10 nm), an additional state at ~336 eV is observed, which can be attributed to PdO_x ($x < 1$) clusters[27,48,49]. This latter finding is in line with the weaker MSIs for the large PdFSP nanoparticles indicated by the H_2-TPR results. The surface Pd/Ce atomic ratios determined by XPS (**Table D2** and **D3**) indicate a surface enrichment of Pd, as the particle size of the support increases. Hence, we surmise that clustering of Pd-oxo species on the surface of larger PdFSP nanoparticles is caused by the segregation of Pd from subsurface layers of CeO_2 during the FSP synthesis. Extended X-ray absorption fine structure (EXAFS) spectroscopy at the Pd K-edge was employed to investigate the coordination environment of Pd in the PdFSP samples (**Fig. 6.3b**). The relatively high first-shell coordination numbers (CN) for Pd-O (CN ~ 4, **Table D5**) emphasize the oxidized state of Pd in line with the XPS results. The real part of the Fourier-transformed EXAFS spectra of the PdFSP samples also contains a feature at ~2.65 Å. Although this distance is only ~0.1 Å shorter than the Pd-Pd distance in bulk Pd metal, we can attribute this shell to a Pd-Ce scattering path given the absence of metallic Pd as followed from XPS. Such assignment has also been used by Jeong et al. for a similar feature in EXAFS spectra of single-atom and clustered Pd species on small (~5 nm) CeO_2 nanoparticles[50]. As it is known

that metal ions can also be doped in CeO_2 during one-step FSP preparation[27,45], we used a structural model based on density functional theory data in which Pd is doped in the subsurface layer of CeO_2 in square planar configuration (**Fig. D11**) for fitting the EXAFS spectra. As shown in **Fig. 6.3b** and **Table D5**, this model adequately describes the experimental EXAFS data for small PdFSP nanoparticles with a Pd-Ce CN of ~2. For larger particle sizes, an additional Pd-Ce scattering path at ~3.2 Å could be added to the fit. This distance is characteristic for Pd single-atom species on and in the surface layers of CeO_2 [25,27,51,52]. The lower contribution of a short Pd-Ce path for medium and large PdFSP (**Table D5**) indicates that Pd tends to localize on the surface of CeO_2 as its particle size increases. In line with this, the EXAFS spectra for PdFSPimp samples contain a significant contribution of the long Pd-Ce distance (~3.20 Å), while the short one (~2.65 Å) is absent (**Figure D12-D13**). This indicates that Pd-oxo species are predominantly present on the CeO_2 surface.

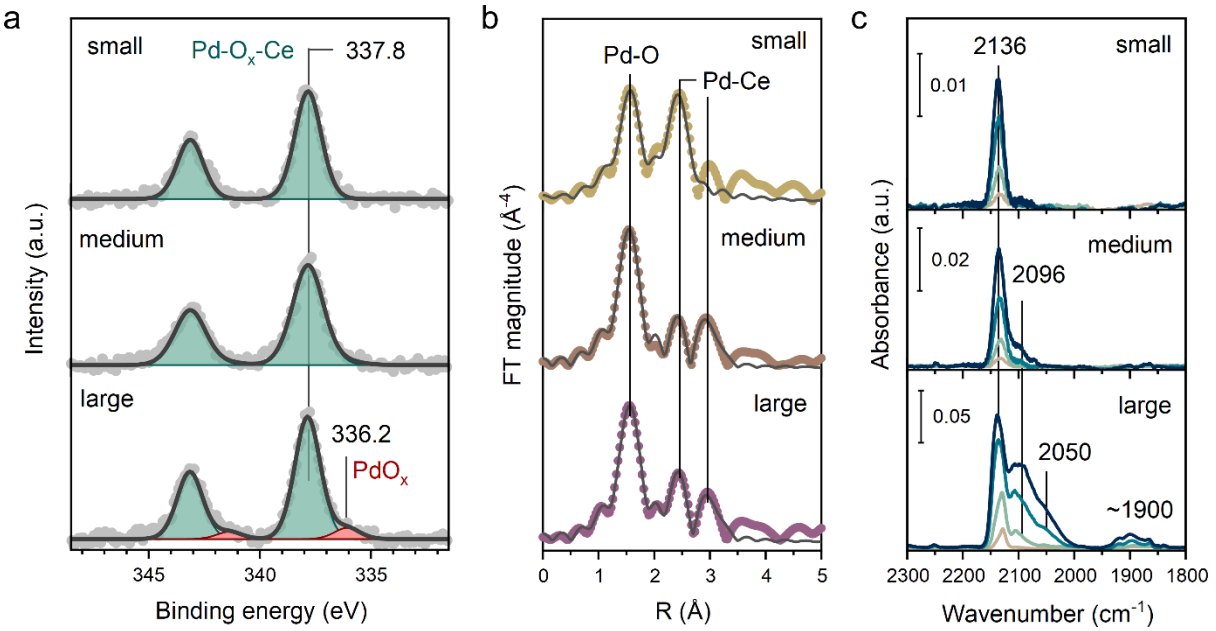

Figure 6.3. Spectroscopic characterization of PdFSP samples with small, medium, and large nanoparticles of CeO_2. a) XPS spectra of Pd 3d core line region acquired for fresh PdFSP samples. b) R-space k^3-weighted EXAFS spectra of fresh FSP samples acquired at the Pd K-edge. c) *In situ* DRIFTS during CO adsorption at -20 °C on fresh PdFSP samples. The CO was set to 0.3 ml/min, resulting in a partial pressure of 2 mbar in the DRIFTS cell.

DRIFTS of adsorbed probe molecules such as CO is a powerful method to study the speciation of metal sites[10]. An important advantage of this technique compared to XPS and XAS is the very high surface sensitivity. As highly dispersed Pd-oxo species readily react with CO at ambient temperatures[28] (see **Chapter 4**), we performed CO adsorption DRIFTS measurements at -20 °C. The DRIFTS spectra for small- and medium-sized nanoparticles of

PdFSP show a major IR feature at 2140 cm^{-1} in the CO stretching region (**Fig. 6.3c**), which can be assigned to CO adsorbed on single atoms of oxidized Pd[22,23,25,28]. The increasing intensity of this band with increasing CeO_2 particle size indicates a higher concentration of such isolated Pd ions. For large PdFSP nanoparticles, a band at ~2100 cm^{-1} can be seen, which has earlier been linked to partially reduced single atoms of Pd[27,28,53]. Furthermore, the observation of linear and bridged CO stretching bands at 2050 cm^{-1} and ~1900 cm^{-1} points to the presence of small metallic clusters of Pd [22,28]. The weaker Pd-CeO_2 interactions in large PdFSP nanoparticles is the likely reason for partial agglomeration of Pd single atoms into clusters of Pd during FSP synthesis. DRIFTS experiments of adsorbed CO on PdFSPimp samples revealed a similar trend, where the smallest CeO_2 nanoparticles contain only single-atom Pd species, while larger nanoparticles also contain Pd clusters (**Figure D14** and **Note D1**). Furthermore, the CO DRIFTS data for the PdFSPimp sample that was prepared by impregnation of 0.46 wt% Pd on large CeO_2 nanoparticles suggests that weak MSI is the likely reason for clustering of Pd on large CeO_2 (**Note D1**). These findings show that the size of CeO_2 nanoparticles strongly influences the Pd speciation in both one-step FSP-made and wet impregnated samples. Due to strong MSI in the PdFSP samples with a particle size of 8 nm and below, Pd is exclusively present as isolated sites on and in the CeO_2 surface. Weaker MSI in large CeO_2 particles (>10 nm) lead to coexistence of atomically dispersed Pd-oxo species and a small fraction of Pd clusters.

6.2.4 Catalytic activity in CO oxidation and reaction kinetics

We used CO oxidation to probe the activity of FSP-made Pd/CeO_2 catalysts. Prior to catalytic testing, all samples were calcined *in situ* at 300 °C in 20 % O_2 in He. The light-off tests were performed three times (**Fig. D15**) and the third run for each catalyst is shown in **Fig. 6.4a**. All catalysts exhibit room-temperature CO oxidation activity. The low-temperature activity is strongly influenced by the size of the CeO_2 nanoparticles. The small PdFSP particles display a lower activity at moderate temperature (~150 °C) than the medium and large PdFSP samples, which already achieve full conversion at this temperature. The optimal size of CeO_2 for low-temperature CO oxidation activity appears to be around 8 nm. Despite the difference in preparation method, the optimal support size for impregnated PdFSPimp catalysts is similar (~9 nm) and the activity trend remains the same (**Fig. D16**). To gain further insight into the observed size-dependent CO oxidation activity of PdFSP samples, we studied the reaction orders (**Fig. 6.4b** and **Table D6**). The order in CO was found to be positive for all

tested samples, indicating the absence of CO poisoning at low temperatures. This is usually explained by the participation of CeO_2 in the catalytic cycle of CO oxidation[8,15,22]. An unusually high reaction order in CO (+1.3) was determined for small PdFSP nanoparticles. The order in CO decreases as a function of CeO_2 size to values typical for single-atom Pd/CeO_2 catalysts (*i.e.*, in the range between 0 and +0.2)[27]. Catalysts with a high reaction order in CO can be especially relevant for automotive exhaust neutralizers, as the mixture entering the three-way catalyst during a cold-start is initially rich in CO[54]. Surprisingly, the reaction order in O_2 for small PdFSP is negative (-0.2), implying that oxygen poisons the catalyst. Such a behavior at low temperature (75 °C) has not been reported before for Pd/CeO_2 catalysts. The reaction order in O_2 becomes positive for the medium and large PdFSP samples with values approaching those typical for conventional Pd/CeO_2 catalysts (see **Chapter 5**). The CO and O_2 reaction orders of the PdFSPimp catalysts displayed a similar trend with respect to particle size. By varying the Pd loading for small PdFSP and large PdFSPimp samples, we found that the reaction orders did not change significantly as a function of the Pd content. (**Table D6**). Altogether, these results show that CO oxidation kinetics is strongly dependent on the particle size of CeO_2 in FSP-derived Pd/CeO_2 catalysts.

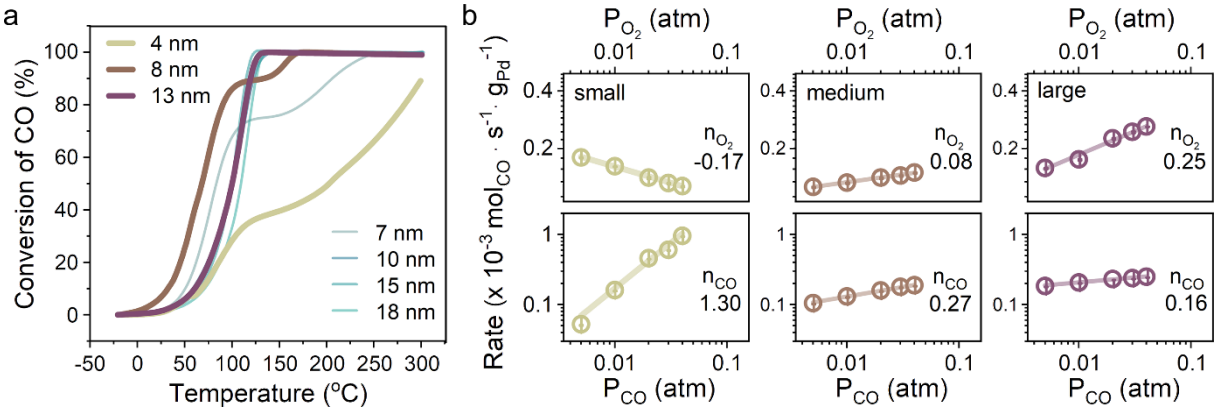

Figure 6.4. CO oxidation of small, medium and large PdFSP samples. a) CO oxidation light-off curves from -20 to 300 °C. Reaction conditions: 1% CO and 1% O_2 in He (GHSV ~180,000 ml g_{cat}^{-1} h^{-1}). b) Steady-state catalytic activity in CO oxidation as a function of pressure of reactants at 75 °C. Prior to measurement, catalysts were stabilized in the same reaction mixture at 75 °C for ~14 h.When O_2 partial pressure was varied (from 5 to 40 mbar), the partial pressure of CO was fixed (10 mbar). When CO partial pressure was varied (from 5 to 40 mbar) the partial pressure of O_2 was fixed (10 mbar). GHSV ~240,000 ml g_{cat}^{-1} h^{-1}, conversion kept below 5% for all experiments. Error bars represent five consequent measurements.

6.2.5 Pd state during CO oxidation

To explain the size-dependent reaction kinetics of CO oxidation on the PdFSP samples, we characterized the state of Pd under actual reaction conditions by *operando* DRIFTS at 75 °C.

During CO oxidation, the smallest CeO_2 nanoparticles can stabilize oxidized Pd single-atoms (**Fig. 6.5a**), as evident from the sole presence of a ~2140 cm^{-1} band in IR spectra. An increase in the O_2 partial pressure led to a slight decrease in the intensity of gas-phase CO_2 band, in line with the negative reaction order in O_2 determined for this sample. On the contrary, when the CO partial pressure was increased, a significantly higher CO_2 signal was registered together with a higher intensity of the band due to oxidized Pd single atoms (~2140 cm^{-1} IR band). As no other carbonyl bands were seen, we infer that the isolated nature of Pd is preserved even in a CO-rich feed. The higher activity of small PdFSP samples under CO-rich conditions can be explained by the higher CO coverage on Pd single atoms, which are poisoned by oxygen under leaner conditions. In such oxygen-rich mixtures, the IR spectra for the medium PdFSP sample contain more Pd single atoms as compared to the small PdFSP sample (**Fig. 6.5b**), which can explain the higher low-temperature CO oxidation activity of the medium PdFSP sample. A small fraction of semi-reduced (~2096 cm^{-1}) and reduced (~1975 cm^{-1}) Pd is also observed for the medium PdFSP sample. As demonstrated earlier (**Chapter 4**), these species play an important role in CO oxidation at elevated temperature. Contrary to small PdFSP, an increase in the O_2 partial pressure led to a slight decrease in the CO_2 gas-phase signal. As the bridged carbonyl band located at ~1975

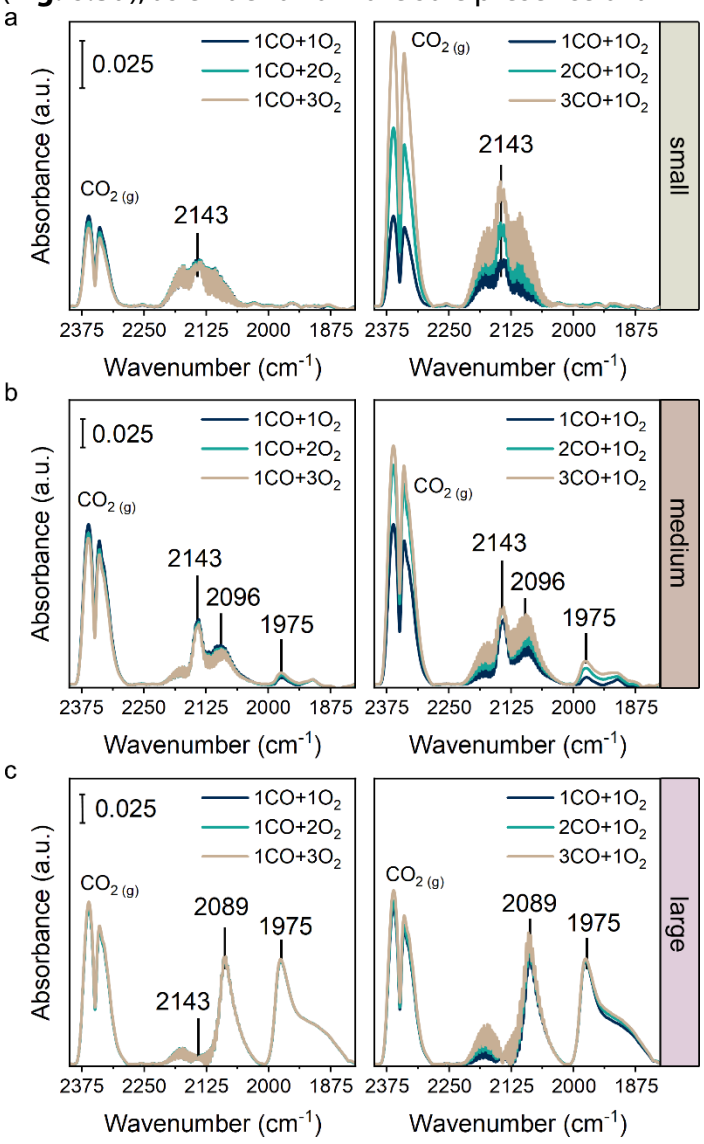

Figure 6.5. *Operando* DRIFTS study of CO oxidation at 75 °C for PdFSP sample with: a) small CeO_2 nanoparticles; b) medium CeO_2 nanoparticles; c) large CeO_2 nanoparticles. Reaction conditions: 1 to 3 vol% of CO and 1 to 3 vol% of O_2 in He at a total flow of 100 ml/min. Prior to changing the partial pressures the catalysts were stabilized on stream for ~30 min.

cm^{-1} increased in intensity, we attribute the lowered activity to some reduction and sintering of oxidized Pd single atoms during the DRIFTS measurements. When the CO partial pressure increased, a notable increase in the gas-phase CO_2 band was seen, which is in line with the positive reaction order in CO. CO-rich conditions led to reduction and sintering of Pd into metallic clusters. On the one hand, the absence of O_2 poisoning in medium PdFSP nanoparticles leads to a higher propensity of Pd single atoms to reduce under CO oxidation conditions. On the other hand, a lower oxygen coverage benefits the low-temperature activity due to a decreased competition between CO and O_2 for atomically dispersed Pd sites. The spectra for large PdFSP nanoparticles (**Fig. 6.5c**) reveal a rather low amount of Pd single atoms during CO oxidation. In contrast to small and medium PdFSP, the spectra are dominated by bands due to CO adsorbed on semi-reduced (~2090 cm^{-1}) and reduced (~1975 cm^{-1}) Pd clusters. These IR spectra resemble those acquired for a commercial CeO_2 wet impregnated with 1 wt% of Pd (see **Chapter 5**). This indicates that the properties of the large CeO_2 nanoparticles in large PdFSP are approaching those of conventional CeO_2 support. Due to the positive reaction order in O_2 for large PdFSP, an increase in O_2 partial pressure during DRIFTS led to a subtle increase in the gas-phase CO_2 band. In contrast to small and medium PdFSP nanoparticles, an increase in CO partial pressure caused only a small increase in the intensity of CO_2 and CO bands. This is consistent with the relatively low reaction order in CO. These trends were similar for large CeO_2 nanoparticles impregnated with less Pd (*i.e.*, 0.46 wt% in **Fig. D17**). Despite the substantially lower Pd surface concentration in this sample, the relative fraction of atomically dispersed Pd species remains very low under reaction conditions. Hence, the lower stability of single-atom Pd species on the surface of large CeO_2 nanoparticles is mainly caused by weaker MSI rather than by a higher Pd surface concentration.

We have recently shown that the extent of MSIs in Pd/CeO_2 catalysts can strongly influence the speciation of Pd during CO oxidation at elevated temperatures[27]. Under such conditions, the steady-state CO coverage is typically very low, rendering *operando* IR spectroscopy less useful to study the state of Pd. Instead, we used synchrotron-based *in situ* NAP-XPS to probe the state of Pd at the very surface using a low incident photon energy of 450 eV. **Fig. 6.6a** shows that the Pd speciation in small PdFSP nanoparticles did not change during exposure in a $CO+O_2$ mixture at 300 °C as compared to the as-prepared state. The strong MSIs in this sample lead to stable Pd in a highly dispersed oxidized state (E_b ~ 337.8 eV) during CO

oxidation at 300 °C. Consistent with this, *operando* DRIFTS spectra (**Fig. 6.6b**) show only minor changes in the Pd carbonyls at 75 °C after the catalyst was heated in the reaction mixture to 300 °C. A weak band at 1975 cm^{-1} suggests that a very small fraction of Pd clusters formed during CO oxidation at 300 °C. As DRIFTS probes only the Pd sites with adsorbed CO, this method can overestimate the relative fraction of reduced Pd species with respect to XPS. According to the EXAFS data (**Fig. 6.3**), a fraction of Pd atoms is doped in CeO_2 and thus cannot be probed by IR but can be seen in XPS. Finally, the molar extinction coefficients of multidentate carbonyls are generally an order of magnitude higher than those of linear ones[55]. From these considerations, we can conclude that the actual fraction of metallic Pd species after reaction of small PdFSP at 300 °C is minor. Exposure of the medium PdFSP catalyst to the CO oxidation mixture at 300 °C did not lead to significant changes in the Pd 3d spectra with only small fraction of PdO_x clusters (~7%) being formed (**Fig. 6.6a**). *Operando* DRIFTS spectra acquired after the reaction at 300 °C show that the intensity of single-atom Pd band (~2140 cm^{-1}) decreased, while bands related to reduced Pd species became more intense. The partial reduction of oxidized Pd single atoms during CO oxidation at elevated temperatures led to a decrease in the low-temperature CO oxidation activity. The weaker MSIs and absence of O_2 poisoning (reaction order in O_2 of +0.08, **Fig. 6.4**) in this sample lead to the formation of reduced Pd clusters that can significantly contribute to CO oxidation activity at moderate and elevated temperatures[27] (**Chapter 5**). The presence of both metallic and oxidized single-atom species can explain the high catalytic performance of medium-sized PdFSP catalyst over a wider temperature range during light-off tests. Analogous to medium PdFSP nanoparticles, the major component in the Pd 3d spectrum of large PdFSP during CO oxidation at 300 °C can be attributed to highly dispersed oxidized Pd (337.8 eV) (**Fig. 6.6a**). An additional component at ~336 eV points to a small fraction of $Pd^{\delta+}$ species (~8%). The increased intensity of bands related to CO adsorbed on hollow sites (~1900 cm^{-1}) in DRIFTS spectra after reaction at 300 °C (**Fig. 6.6b**) points to a larger size of the metallic Pd clusters. This, in turn, can explain the decrease in CO oxidation activity, because the number of interfacial sites decreases as the size of clusters or nanoparticles increases.

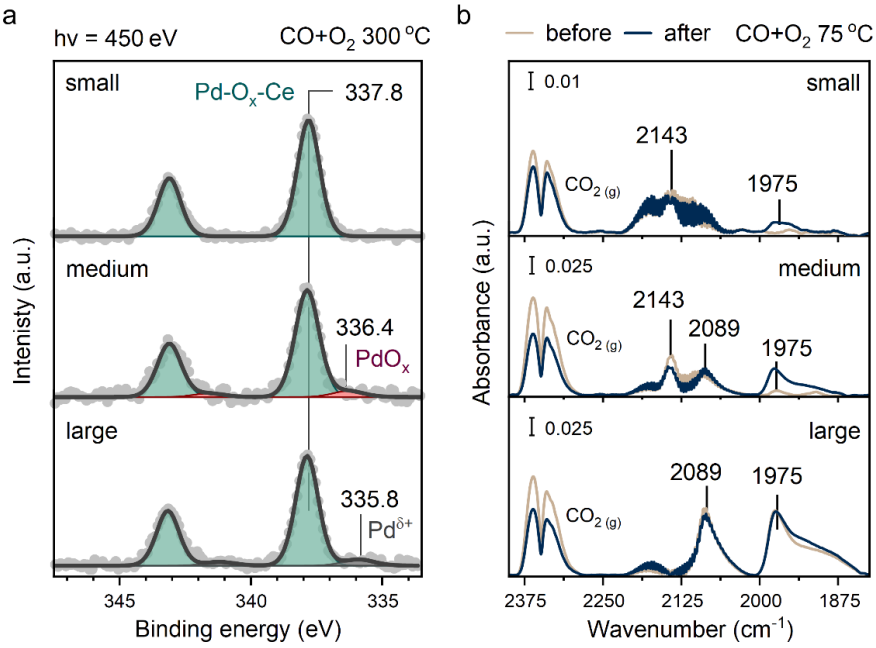

Figure 6.6. *In situ* NAP-XPS and *operando* DRIFTS characterization of PdFSP respectively during and after exposure to a CO oxidation feed mixture at 300 °C. a) Pd 3d core line spectra of the catalysts exposed to an equimolar $CO+O_2$ mixture at 300 °C. The total pressure in the NAP-cell was fixed to 0.13 mbar. All spectra were acquired at 450 eV resulting in a probing depth of ~0.5 nm. b) DRIFTS spectra acquired during CO oxidation at 75 °C before and after heating up to 300 °C in reaction mixture. Reaction conditions: 1% CO and 1% O_2 in He, total flow 100 ml/min.

Medium PdFSP shows the best catalytic performance in a wide temperature range. We explain this by the simultaneous presence of sufficient single-atom Pd species and metallic Pd clusters relevant respectively to low- and high-temperature performance in CO oxidation. The lower amount of surface Pd single-atom species in small PdFSP results in a lower low-temperature CO oxidation activity. At the same time, the lack of metallic sites in small PdFSP together with oxygen poisoning also limits CO oxidation at elevated temperatures. The large PdFSP performs worse than medium PdFSP at low temperature due to the very low concentration of single-atom Pd species, while the sample presents a high activity at elevated temperature due to metallic Pd. Taken together, these findings clearly show that the observed differences in Pd speciation as a function of CeO_2 particle size also lead to substantial changes in the CO oxidation activity. It has been earlier proposed that oxygen mobility at the Pd-CeO_2 interface can play an important role in defining the state of supported metal[27,56,57]. Hence, in the next section we investigate how the redox properties of Pd-CeO_2 interface are influenced by the different size of CeO_2.

6.2.6 Redox properties of Pd-CeO_2 interface

Temperature-programmed reduction in CO (CO-TPR) is widely used to investigate the redox properties of CeO_2-supported catalysts[23,48,58]. The high-temperature regime (T>200 °C) of the CO-TPR profiles for the PdFSP samples (**Fig. 6.7a**) contains features related to reduction of surface and bulk CeO_2 (**Fig. D18**), while the features at lower temperature can be assumed to be related to removal of oxygen atoms from oxidized Pd[23,48]. For small PdFSP nanoparticles, we can see an intense peak at ~175 °C, which can be related to reduction of lattice O atoms of CeO_2 in the vicinity of Pd-O-Ce interfaces[23]. For medium PdFSP, the main CO_2 evolution feature at 150 °C is substantially smaller than for small PdFSP, pointing at a lower amount of reactive oxygen in the former. The appearance of additional features at ~50 °C and 100 °C is indicative of the highly reactive nature of supported Pd-oxo species towards CO. This agrees with the high catalytic performance of this sample. For large PdFSP, the main reduction feature further decreases in intensity and shifts to lower temperatures, likely due to the presence of PdO_x clusters[59]. To quantify the amount of reactive oxygen present in these catalysts and estimate the extent of the involvement of lattice oxygen atoms of CeO_2, we performed CO pulsing titration experiments at 175 °C. The CO consumption decreases with the size of the PdFSP particles (**Table D7**). Normalization to the Pd content shows that CO consumption exceeds the amount expected when only PdO would be reduced. This is a strong indication that CeO_2 oxygen atoms are involved in CO oxidation at this temperature.

To probe the reactivity of Pd-CeO_2 interface towards CO, we used synchrotron-based surface-sensitive *in situ* NAP-XPS. Surprisingly, we observed that Pd only reduces partially upon exposure to CO at 175 °C regardless of particle size of CeO_2 (**Fig. 6.7b**). Deconvolution of the Pd 3d spectra shows that small PdFSP was most reduced (29% of PdO_x and Pd^0) among the three investigated samples. The incomplete reduction of Pd^{2+} in CO at 175°C indicates that the part of the O atoms titrated by CO-TPR and pulsing experiments does not originate from oxidized Pd. To follow the oxidation state of Ce in the surface region, we employed *in situ* resonance photoelectron spectroscopy (RPES) of Ce 4d-4f transitions[36,60]. **Fig. 6.7c** evidences a higher intensity of Ce^{3+}-related features in the valence band spectra of small PdFSP compared to the other two samples. This demonstrates a higher degree of CeO_2 surface reduction in small PdFSP (~13.9% Ce^{3+}) as compared to medium PdFSP (~5.4% Ce^{3+}) and large PdFSP (~5.2% Ce^{3+}).

From the above spectroscopic findings, CO-TPR and CO titration data, it emerges that small particles of PdFSP exhibit a higher reactivity of CeO_2 lattice oxygen atoms in comparison to larger ones. We propose that the particularly strong MSI in small PdFSP is caused by this high oxygen mobility. Earlier, we demonstrated that reverse oxygen spillover from CeO_2 to Pd aids the stabilization of Pd single atoms in an oxidized state under CO oxidation conditions[27]. Facile oxygen transport at the Pd-CeO_2 interface in small PdFSP can also explain the observed oxygen poisoning and strong stabilization of oxidized single-atom Pd species during CO oxidation even under CO-rich conditions. The weaker MSIs and lower oxygen mobility in medium and large ceria nanoparticles lead to lower oxygen coverage under reaction conditions and lower stability of atomically dispersed Pd species in these catalysts.

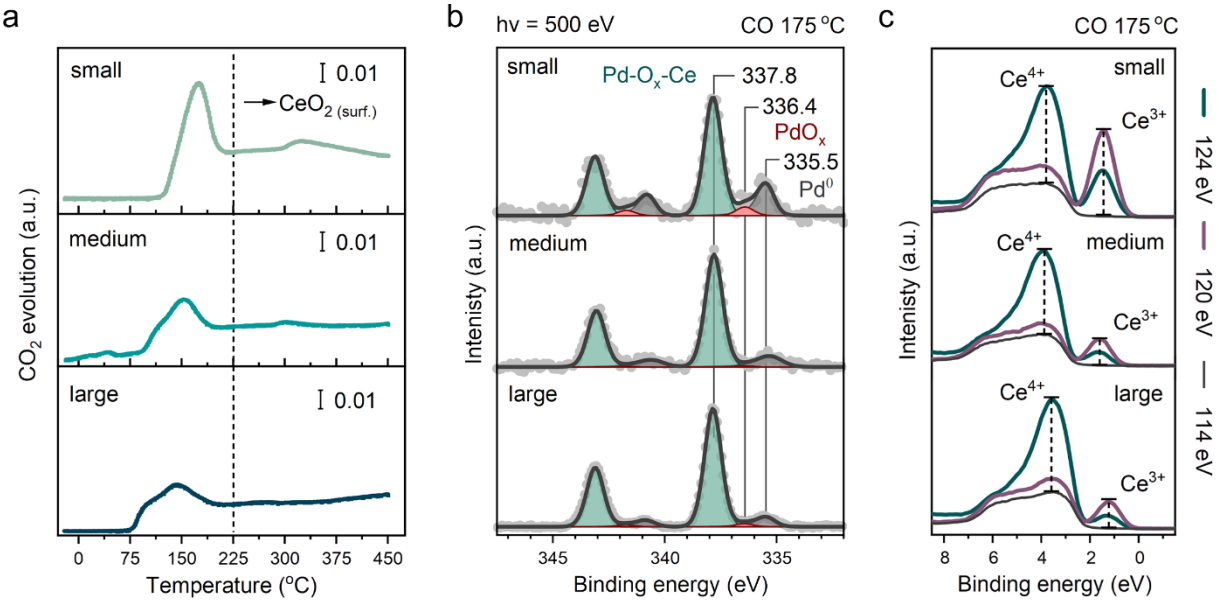

Figure 6.7. Reducibility of PdFSP catalysts with different size of CeO_2 support. a) CO-TPR profiles recorded from -20 to 450 °C. Conditions: 1.33 % CO in He, ramp rate 10 °C/min. b) *In situ* NAP-XPS Pd 3d core line spectra of the catalysts exposed to 1 mbar of CO at 175 °C. All spectra were acquired at 500 eV resulting in a probing depth of ~0.6 nm. c) *In situ* RPES valence band spectra of the catalysts exposed to 1 mbar of CO at 175 °C. The intensities of the Ce^{4+} and Ce^{3+} related features, which appear at the respective resonant energies (124 eV – Ce^{4+}; 120 eV – for Ce^{3+}; 114 eV – off resonance), were used to estimate the Ce^{3+} atomic fraction.

6.2.7 Tuning particle size of CeO_2 for optimization of Pd/CeO_2 catalysts

Although we have demonstrated a particle size effect of the CeO_2 support on the CO oxidation activity of Pd/CeO_2 catalysts, both one-step and Pd-loaded Pd/CeO_2 catalysts were prepared by FSP. To exclude a possible influence of FSP preparation of CeO_2, we also synthesized a set of CeO_2 supports by a polymer-assisted sol-gel method [61]. Different calcination temperatures were used to yield CeO_2 of different particle size. As the minimal

temperature for calcination is limited by the decomposition of the polyvinylpyrrolidone polymer (~400 °C), the smallest size of CeO_2 obtained in this way was 7 nm. An overview of the CeO_2 particle sizes is given in the appendix (**Figs. D19-D21** and **Table D8**).

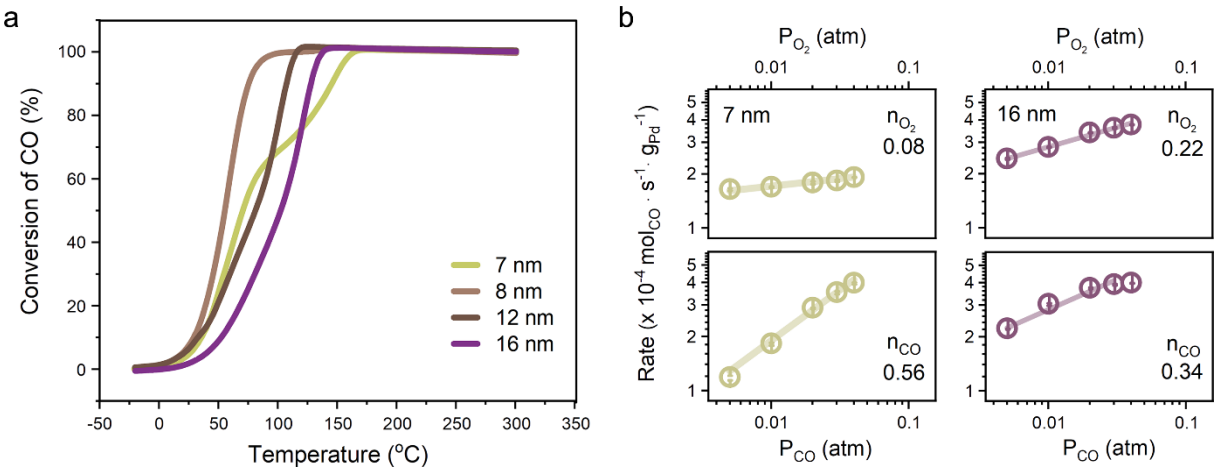

Figure 6.8. CO oxidation activity and reaction kinetics. a) CO oxidation light-off curves from -20 to 300 °C for PdSG samples. Reaction conditions: 1% CO and 1% O_2 in He (GHSV ~180,000 ml g_{cat}^{-1} h^{-1}). b) Steady-state catalytic activity of PdSG samples in CO oxidation as a function of pressure of reactants at 75 °C. When O_2 partial pressure was varied (from 5 to 40 mbar), the partial pressure of CO was fixed (10 mbar). When CO partial pressure was varied (from 5 to 40 mbar) the partial pressure of O_2 was fixed (10 mbar). Prior to the measurement catalysts were stabilized on the stream for ~14 h. GHSV ~400,000 ml g_{cat}^{-1} h^{-1}, conversion kept below 5%. Error bars represent five consequent measurements.

As compared to FSP method, the particle size distribution of CeO_2 of sol-gel prepared samples is slightly narrower. The shape of sol-gel prepared CeO_2 was close to spherical, in contrast to the mainly (111)-terminated octahedral-shaped particles obtained by FSP[62]. Wet impregnation of sol-gel derived CeO_2 with 1 wt% Pd yielded PdSG catalysts. As can be seen from **Fig. 6.8a**, all PdSG samples exhibit higher low-temperature CO oxidation activity than the FSP-made counterparts. We tentatively explain this by the stabilization of Pd species on other CeO_2 surface terminations than the (111) surface of the FSP CeO_2 particles. The facet-dependent properties of CeO_2 based catalysts are well-documented[53,63–65]. Despite the different shape of the sol-gel derived CeO_2 particles, the catalytic performance of PdSG catalysts shows a similar strong correlation with the CeO_2 particle size (**Fig. 6.8a**). We found that the optimal size for PdSG (8 nm) is similar to those found for PdFSP (8 nm) and PdFSPimp (9 nm) samples. Moreover, the reaction kinetics are also similar with small nanoparticles exhibiting a higher reaction order in CO and lower reaction order in O_2 as compared to larger ones (**Fig. 6.8b**). These results show that the strong impact of CeO_2

particle size on the CO oxidation performance of Pd/CeO_2 catalysts relates to an intrinsic effect of the size of the CeO_2 support.

6.3 Conclusions

Using FSP, a set of uniformly sized crystalline and phase-pure CeO_2 nanoparticles in the 4-18 nm range was obtained. The redox properties of these bare supports are dependent on their size, small nanoparticles being the most reducible. The single-atom Pd-loaded catalysts prepared by one-step FSP and wet impregnation of FSP-made CeO_2 displayed a unique structure sensitivity in CO oxidation. The size of the supporting CeO_2 nanoparticles strongly influences the Pd speciation and consequently the CO oxidation reaction kinetics. Detailed characterization by *operando* DRIFTS and *in situ* NAP-XPS revealed that atomically dispersed Pd species on small nanoparticles (~4 nm) of PdFSP are stable under reaction conditions. Yet these sites display low catalytic activity in O_2-rich mixtures due to oxygen poisoning caused by facile oxygen transport from CeO_2 to Pd single atoms. The lower oxygen mobility in large CeO_2 nanoparticles (~13 nm) leads to a positive reaction order in oxygen but renders Pd single atoms prone to reduction and sintering into clusters. This results in a limited low-temperature CO oxidation activity. The medium-sized CeO_2 nanoparticles (~8-9 nm) can stabilize single-atom Pd species explaining the high low-temperature CO oxidation activity. Moreover, these medium-sized particles also contain metallic Pd clusters under reaction conditions. These species contribute to a high CO oxidation activity at elevated temperature in contrast to the small-sized Pd/CeO_2 catalyst containing exclusively single Pd atoms. The moderate MSI and oxygen mobility in medium-sized PdFSP nanoparticles are the key parameters contributing to their optimal performance. It was also established that the CeO_2 particle size effect on the catalytic properties of Pd/CeO_2 nanocomposites is not limited to FSP preparation. The approach of fine-tuning the size of the support constitutes a new opportunity to optimize metal catalysts in which the redox properties of the support play a role through metal-support interfaces.

6.4 Materials and Methods

Catalyst preparation

FSP synthesis was performed using a TETHIS NPS10 apparatus. Cerium (III) acetate hydrate was dissolved in a mixture (50:50 vol%) of glacial acetic acid and 2-ethylhexanoic acid to yield a 0.15 M precursor solution for CeO_2 synthesis. To ensure complete solubility of cerium acetate, the mixture was mildly heated to 60-70 °C and stirred for 1 h. After cooling to ambient temperature, the solution was used to fill the syringe of the FSP apparatus. To sustain the flame, flows of 1.5 l/min of methane and 3.0 l/min of oxygen were used. Oxygen also served as a dispersion gas at a rate of 5 l/min. To obtain CeO_2 with different particle size, the liquid feed injection rate was varied (*i.e.,* 1, 2.5, 5, 7.5, 10, 12.5, and 15 m/min). At each injection rate, the overpressure at the nozzle was adjusted to 2.5 bar. PdFSPimp catalysts were obtained by wet impregnation of FSP-made CeO_2 supports with 1 wt% Pd (unless stated otherwise). For this purpose, an appropriate amount of $Pd(NO_3)_2{\cdot}2H_2O$ was dissolved in demineralized water (~10 ml) and the resulting solution was poured onto the support powder. The suspension was stirred and slowly heated without boiling until dry, followed by placing the sample in a drying oven overnight in order to remove the remaining water. The final step was calcination of the sample at 300 °C in air. The PdFSP samples were prepared by one-step FSP. For that an appropriate amount of Pd (II) acetylacetonate was dissolved together with cerium (III) acetate hydrate in a mixture (50:50 vol%) of glacial acetic acid and 2-ethylhexanoic acid to yield 0.15M (based on Ce content) precursor solution. The same parameters of FSP process as for the bare supports were applied to obtain the resulting materials.

The preparation of sol-gel derived CeO_2 was based on a method described by Riley et al.[61]. First, 5 g of polyvinylpyrrolidone (PVP-40,000) was dissolved in 100 ml of demineralized water upon mild heating (70 °C) and stirring. The solution was then cooled to ambient temperature and 3.1 g of cerium (III) nitrate was added. The solution was then heated to ~90 °C and left stirring until most of the water evaporated. To remove the remaining water, the samples were placed in a drying oven (110 °C) overnight. The obtained gel was then crushed and calcined. Different calcination temperatures were used to obtain different particle sizes of CeO_2. The temperatures used for calcination were 400 °C, 530 °C, 600 °C, 630 °C and 650 °C. After calcination the samples were impregnated with 1 wt% Pd analogous to the PdFSPimp samples. The resulting sol-gel derived Pd/CeO_2 catalysts are denoted as PdSG.

The reference 5 wt% Pd/SiO_2 sample was prepared by wetness impregnation of high surface area silica (Sipernat® 50) to represent PdO nanoparticles dispersed on the inert support.

Catalytic activity measurements

For the catalytic tests, the samples were pressed, crushed, and sieved to a fraction between 125 and 250 µm. The sieved fraction was then mixed with silicon carbide (200-300 mg) to avoid bypassing of the gas flow and formation of hot spots. This mixture was loaded in a quartz tube reactor and enclosed between two quartz wool plugs. The catalysts were pretreated *in situ* under a flow of 20 vol% O_2 in He at 300 °C for 1 h and then cooled to room temperature. The reactor was flushed with He and cooled to -20 °C by a home-made liquid nitrogen cooling system. The light-off CO oxidation catalytic tests followed by mass-spectrometry were performed from -20 °C to 300 °C at a ramp rate of 5 °C/min. The reaction mixture contained 1 vol% CO and 1 vol% O_2 in He, with a total flow of 150 ml/min. Repeated light-off cycles were performed on the same catalysts after cooling to -20 °C. CO conversion was estimated from the mass-spectrometry (Balzers TPG-300) data by following the CO (*m/z*=28), O_2 (*m/z*=32) and CO_2 (*m/z*=44) signals (*m/z*=44) and was verified by gas chromatography (GC). The GC analysis (Interscience Compact GC 4.0) of effluent was done using RT-Q-Plot and Molsieve columns and thermal conductivity detectors (TCDs). To determine the reaction orders, an appropriate amount of catalyst was loaded to maintain the CO conversion below 8%. The reference reaction mixture was 1 vol% O_2, 1 vol% CO in He at a total flow of 200 ml/min. Prior to changing the partial pressures of reactants (CO and O_2), the catalyst was stabilized in the reference reaction feed for ~14 h to reach the steady state. To determine the reaction orders, partial pressures of CO and O_2 were varied from 0.5 vol% to 4 vol%.

Characterization

Lab-based powder X-ray diffraction measurements were done on a Bruker Phaser D2 diffractometer with Cu Kα source. The crystallite size of PdFSP, PdFSPimp and PdSG samples was estimated using the DiffracEva software and the implemented Scherrer equation applied to the CeO_2 reflection at 47.5° corresponding to the (220) crystal plane. Synchrotron-based powder X-ray diffraction was performed at ID31 beamline (ESRF, Grenoble) at λ = 0.18233 Å. A Dectris Pilatus3X CdTe 2M detector was employed to acquire the data in Debye-Scherrer geometry. Using the GSAS II software, Rietveld refinement was employed to determine the crystallite size of FSP-made CeO_2 nanoparticles. The N_2 physisorption at -196

°C was performed using TriStar II 3020 apparatus. The Brunauer-Emmet-Teller (BET) method was employed to estimate the surface area of the prepared materials. The size of the nanoparticles was estimated using equation (1) assuming spherical nanoparticles and equation (2) assuming octahedral nanoparticles. A_s is the surface area determined by BET and ρ_p is the density of the material (7.2 g/cm^3). Better correlation with TEM and XRD data was found under assumption of octahedral shape of nanoparticles.

$$d_{BET}\,(nm) = \frac{6000}{A_s * \rho_p} \quad (1) \qquad d_{BET\,(octa)}(nm) = \frac{60000}{4 * A_s * \rho_p * \sqrt{2}} \quad (2)$$

ICP-OES was performed to determine the loading of Pd. The measurements were done on an AMETEK SpectroBlue apparatus. Around 25 mg of the sample was dissolved in 5 ml of concentrated H_2SO_4 at 200 °C. After cooling the solution, demineralized water was added for dilution. The solutions were prepared *in duplo* to verify the reproducibility of the results. A calibration line with concentrations between 0 and 2 mg/l of Pd was used.

Bright-field TEM images were collected on a FEI Tecnai 20 microscope operating at acceleration voltage of 200 kV. No less than 100 particles were counted to estimate the average particle size from TEM data.

X-ray absorption spectroscopy was performed at the B18 beamline of the Diamond Light Source. Data were collected at the Pd K edge (24350 eV) in fluorescence mode with simultaneous measurement of a Pd foil in transmission mode for energy referencing. The collected spectra were background subtracted and normalized using the Athena software package. EXAFS fitting of the k^3-weighted data was performed with the Artemis software. Scattering paths were calculated with FEFF6 using the crystal structures of Pd, PdO and DFT-optimized Pd models (**Figs. D9-D10**) The amplitude reduction factor S_0^2 was determined by fitting the first-shell Pd–Pd scattering paths in R-space EXAFS spectrum of Pd foil with the coordination number fixed to 12.

H_2 temperature-programmed reduction (H_2-TPR) was performed on a Micromeritics Autochem II 2920. The device was equipped with a U-shaped quartz reactor, a computer-programmed oven, and a thermal conductivity detector (TCD). Around 50-75 mg of catalyst was placed between two quartz wool plugs in the U-shaped reactor. Before the reduction each sample was pretreated *in situ* to remove adsorbed gasses and impurities. During the pretreatment the sample was heated to 300 °C in a 5 vol% O_2/He flow at 50 ml/min. After that the sample was cooled down to room temperature and flushed with a flow of helium

for 30 min. The reduction was performed using a 4 vol% H_2/He flow at 50 ml/min and ramping the temperature to 700 °C at a rate of 10 °C/min. The H_2 consumption registered by TCD was then plotted as H_2-TPR profile.

CO temperature-programmed reduction (CO-TPR) was performed using a home-built setup equipped with an online mass spectrometer (Balzers TPG-300). Typically, around 50 mg of the catalyst was placed in a quartz tube and fixed between plugs of glass wool. All samples were pretreated *in situ* using a 20 vol% O_2/He flow at 100 ml/min at 300 °C for 1h. After cooling of the sample to room temperature, the oxygen was turned off and for 20 minutes the reactor was flushed with He. The sample was then cooled to -20 °C by a home-built liquid nitrogen cooling system. Then the flow was switched to 1.33 vol% CO/He with a total flow of 150 ml/min and the reduction was performed by ramping up the temperature at 10 °C/min from -20 °C to 450 °C. The CO_2 MS signal (*m/z*=44) was used to plot the CO-TPR profiles.

CO pulsing experiments were performed using a home-build pulse setup equipped with a mass spectrometer (Balzers TPG-300). Typically, around 50 mg of the sample was fixed between two quartz wool plugs in a stainless-steel reactor tube. Each sample was pretreated *in situ* to remove adsorbates and impurities. During pretreatment the sample was heated to 300 °C for 1 h under a 33 vol% O_2/He flow at 60 ml/min. After that, the sample was cooled in pretreatment flow to 175 °C, followed by switching the flow to pure He and the catalyst was flushed for 1 h at 100 mL/min. After flushing, the flow of He was decreased to 25 ml/min and pulses of CO were introduced every 5 min by a 6-way valve with a sample loop of 100 µL. The amount of CO consumed by the sample was calculated from the peak areas of CO signal (*m/z*=28) and considering fragmentation of CO_2. CO pulsing was performed until no changes of the peak areas were registered.

Ultrahigh vacuum X-ray photoelectron spectroscopy (XPS) was performed using a Thermo Scientific K-Alpha spectrometer equipped with monochromatized Al Kα X-ray source operating at 72 W. Powder samples were deposited on a double-sided carbon tape and the spectra were measured at a pass energy of 50 eV. The dual-beam flood-gun was used to compensate the surface charging. All the spectra were processed using the CasaXPS software package. The binding energy scale was adjusted by the U''' component of the Ce 3d core line located at 916.7 eV as an internal energy reference[27,33,58]. The Pd to Ce surface atomic ratios were estimated using respective atomic sensitivity factors. The XPS spectra

were fitted using symmetric pseudo-Voigt function, referred to as GL (30) in CasaXPS software. For the Pd 3d spectra containing metallic component, an asymmetric pseudo-Voigt function referred to as LF (0.76, 1.5, 55, 300) in CasaXPS was used. The Ce 3d spectra were fitted according to the models reported earlier[48,60,66].

Surface-sensitive *in situ* resonant photoelectron spectroscopy (RPES) and near-ambient pressure X-ray photoelectron spectroscopy (NAP-XPS) were performed at the NAPP end station of CIRCE beamline at the ALBA Synchrotron. Photoelectron spectra were acquired using a SPECS Phoibos NAP-150 electron analyser featuring a differential pumping system that allowed *in situ* XPS measurements in a gaseous environment (in the mbar range). The experimental geometry implied a take-off angle of ~45°. The analysis chamber was pressurized using calibrated mass flow controllers and high-purity gases. To avoid charging effects, the samples were pelletized and fixed onto the stainless-steel sample holder. For $CO+O_2$ experiments (**Fig. 6.6**), an inert carbon diluent was added (20 wt%) to the sample powder prior to pelletizing. The pretreatment was performed by heating the samples to 300 °C in 1 mbar of O_2. The samples were then cooled to ambient temperature and a mixture of $CO+O_2$ (1:1) was introduced in the analysis chamber and the pressure was fixed to ~0.1 mbar. Subsequently, the samples were heated to 300 °C in the reaction mixture and stabilized for 30 minutes prior to spectra collection. The Pd 3d core-line spectra were recorded at 450 eV of incident photon energy and 10 eV of pass energy. After a linear background subtraction, the spectral lines were fitted in a similar manner to the lab-based XPS data. For the experiments shown in **Fig. 6.7**, the samples were not diluted with carbon diluent due to their sufficient conductivity in reducing atmosphere. After pretreatment in 1 mbar of O_2 at 300 °C, the samples were cooled to 175 °C and analysis chamber was filled with pure CO (1 mbar). After stabilization for 30 min, the Pd 3d spectra were acquired at 500 eV of incident photon energy and 10 eV of pass energy. The XPS data treatment was performed as described above. For the RPES study, a variable photon energy was used for selective excitation of Ce 4d–4f transitions related to Ce^{3+} and Ce^{4+} charge states[27,36,60]. We determined the energies required for the resonant enhancement of Ce^{3+} and Ce^{4+} features following the procedure described in **Chapter 4**. The Ce^{3+}/Ce^{4+} ratios were determined by the heights of the respective resonant peaks[27,36,60]. Following this approach, the concentration of Ce^{3+} at the very surface (<1 nm) can be obtained.

Diffuse reflectance infrared Fourier transform spectroscopy (DRIFTS) was carried out using Bruker Vertex 70V with an MCT-detector and Harrick-design in-situ DRIFTS cell. Typically, 25-50 mg of the sample powder was placed in the *in situ* cell. The thermocouple was in direct contact with the catalyst bed and the temperature was controlled by a PID thermocontroller (Harrick). The sample was pretreated *in situ* in 20 vol%O_2/He flow at 300 °C. After cooling to room temperature, the sample was evacuated and further cooled to -20 °C by liquid nitrogen. When the sample was stabilized at -20 °C, a background spectrum was collected. Then CO was admitted at 0.28 ml/min and a total pressure in the cell reached 2 mbar. Upon exposure of the sample to CO, a series of spectra, 50 scans per spectrum in the 3800 - 1000 cm^{-1} range and 2 cm^{-1} resolution, were acquired until no changes between the collected spectra were visible. For the *operando* DRIFTS experiments, the fresh sample was pretreated as described above. After cooling down to 75 °C the background spectrum was acquired, and the flow was switched to reaction mixture of 1 vol% CO + 1 vol% O_2 in He (total flow 100 ml/min). The catalyst was stabilized for ~30-40 minutes and then an *operando* IR spectrum (150 scans) was measured. Then DRIFTS spectra at different reaction stoichiometries were acquired.

6.5 References

1. Bezemer, G.L., Bitter, J.H., Kuipers, H.P.C.E., Oosterbeek, H., Holewijn, J.E., Xu, X., Kapteijn, F., van Dillen, A.J. & de Jong, K.P. *J. Am. Chem. Soc.* **128,** 3956–3964 (2006).
2. Vogt, C., Groeneveld, E., Kamsma, G., Nachtegaal, M., Lu, L., Kiely, C. J., Berben, P. H., Meirer, F. & Weckhuysen, B. M. *Nat. Catal.* **1,** 127–134 (2018).
3. van den Berg, R., Prieto, G., Korpershoek, G., van der Wal, L. I., van Bunningen, A. J., Lægsgaard-Jørgensen, S., de Jongh, P. E. & de Jong, K. P. *Nat. Commun.* **7,** 13057 (2016).
4. Honkala, K., Hellman, A., Remediakis, I. N., Logadottir, A., Carlsson, A., Dahl, S., Christensen, C. H. & Nørskov, J. K. *Science* **307,** 555–558 (2005).
5. Haruta, M., Kobayashi, T., Sano, H. & Yamada, N. *Chem. Lett.* **16,** 405–408 (1987).
6. Massimiliano Comotti, Wen-Cui Li, Bernd Spliethoff, and & Schüth*, F. J. *Am. Chem. Soci.* **128,** 917–924 (2005).
7. Ligthart, D. A. J. M., van Santen, R. A. & Hensen, E. J. M. *Angew. Chem. Int. Ed.* **50,** 5306–5310 (2011).
8. Cargnello, M., Doan-Nguyen, V. V. T., Gordon, T. R., Diaz, R. E., Stach, E. A., Gorte, R. J., Fornasiero, P. & Murray, C. B. *Science* **341,** 771–773 (2013).
9. Haneda, M., Todo, M., Nakamura, Y. & Hattori, M. *Catal. Today* **281,** 447–453 (2017).
10. DeRita, L., Dai, S., Lopez-Zepeda, K., Pham, N., Graham, G. W., Pan, X. & Christopher, P. *J. Am. Chem. Soc.* **139,** 14150–14165 (2017).
11. Liu, L., Zhou, F., Wang, L., Qi, X., Shi, F. & Deng, Y. *J. Catal.* **274,** 1–10 (2010).
12. Bruix, A., Rodriguez, J. A., Ramírez, P. J., Senanayake, S. D., Evans, J., Park, J. B., Stacchiola, D., Liu, P., Hrbek, J. & Illas, F. *J. Am. Chem. Soc.* **134,** 8968–8974 (2012).
13. Chen, A., Yu, X., Zhou, Y., Miao, S., Li, Y., Kuld, S., Sehested, J., Liu, J., Aoki, T., Hong, S., Camellone, M. F., Fabris, S., Ning, J., Jin, C., Yang, C., Nefedov, A., Wöll, C., Wang, Y. & Shen, W. *Nat. Catal.* **2,** 334–341 (2019).
14. van Deelen, T. W., Hernández Mejía, C. & de Jong, K. P. *Nat. Catal.* **2,** 955–970 (2019).
15. An, K., Alayoglu, S., Musselwhite, N., Plamthottam, S., Melaet, G., Lindeman, A. E. & Somorjai, G. A. *J. Am. Chem. Soc.* **135,** 16689–16696 (2013).
16. Farmer, J. A. & Campbell, C. T. *Science* **329,** 933–936 (2010).
17. Datye, A. K. & Votsmeier, M. *Nat. Mat.* **20,** 1049–1059 (2020).
18. Maurer, F., Jelic, J., Wang, J., Gänzler, A., Dolcet, P., Wöll, C., Wang, Y., Studt, F., Casapu, M. & Grunwaldt, J.-D. *Nat. Catal.* **3,** 824–833 (2020).
19. Datye, A. K. & Guo, H. *Nat. Commun.* **12,** 1–3 (2021).
20. Jones, J., Xiong, H., DeLaRiva, A. T., Peterson, E. J., Pham, H., Challa, S. R., Qi, G., Oh, S., Wiebenga, M. H., Pereira Hernandez, X. I., Wang, Y. & Datye, A. K. *Science* **353,** 150–154 (2016).
21. Fu, Q., Saltsburg, H., Flytzani-stephanopoulos, M. *Science* **301,** 935–938 (2003).
22. Kim, Y., Collinge, G., Lee, M.-S., Khivantsev, K., Cho, S. J., Glezakou, V.-A., Rousseau, R., Szanyi, J. & Kwak, J. H. *Angew. Chem. Int. Ed.* **60,** 2-9 (2021).
23. Jiang, D., Wan, G., García-Vargas, C. E., Li, L., Pereira-Hernández, X. I., Wang, C. & Wang, Y. *ACS Catal.* **10,** 11356–11364 (2020).
24. Spezzati, G., Su, Y.-Q., Hofmann, J. P., Benavidez, A. D., Delariva, A. T., McCabe, J., Datye, A. K. & Hensen, E. J. M. *ACS Catal.* **7,** 6887-6891 (2017).
25. Jeong, H., Bae, J., Han, J. W. & Lee, H. *ACS Catal.* **7,** 7097–7105 (2017).
26. Yuan, K., Guo, Y., Huang, L., Zhou, L., Yin, H.-J., Liu, H., Yan, C.-H. & Zhang, Y.-W. *Inorg. Chem.* **60,** 4207–4217 (2020).
27. Muravev, V., Spezzati, G., Su, Y.-Q., Parastaev, A., Chiang, F.-K., Longo, A., Escudero, C., Kosinov, N. & Hensen, E. J. M. *Nat. Catal.* **4,** 469–478 (2021).
28. Spezzati, G., Su, Y., Hofmann, J. P., Benavidez, A. D., DeLaRiva, A. T., McCabe, J., Datye, A. K. & Hensen, E. J. M.. *ACS Catal.* **7,** 6887–6891 (2017).
29. Resasco, J., Derita, L., Dai, S., Chada, J. P., Xu, M., Yan, X., Finzel, J., Hanukovich, S., Hoffman, A. S., Graham, G. W., Bare, S. R., Pan, X. & Christopher, P. *J. Am. Chem. Soc.* **142,** 169–184 (2020).
30. Beniya, A. & Higashi, S. *Nat. Catal.* **2,** 590–602 (2019).

31. Zhou, X. D. & Huebner, W. *Appl. Phys. Lett.* **79,** 3512–3514 (2001).
32. Paun, C., Safonova, O. V., Szlachetko, J., Abdala, P. M., Nachtegaal, M., Sa, J., Kleymenov, E., Cervellino, A., Krumeich, F. & van Bokhoven, J. A. *J. Phys. Chem. C* **116,** 7312–7317 (2012).
33. Parastaev, A., Muravev, V., Huertas Osta, E., van Hoof, A. J. F., Kimpel, T. F., Kosinov, N. & Hensen, E. J. M. *Nat. Catal.* **3,** 525-533 (2020).
34. Xu, J., Harmer, J., Li, G., Chapman, T., Collier, P., Longworth, S. & Tsang, S. C. *Chem.Com.* **46,** 1887–1889 (2010).
35. Migani, A., Vayssilov, G. N., Bromley, S. T., Illas, F. & Neyman, K. M. *J. Mater. Chem.* **20,** 10535–10546 (2010).
36. Vayssilov, G. N., Lykhach, Y., Migani, A., Staudt, T., Petrova, G. P., Tsud, N., Skála, T., Bruix, A., Illas, F., Prince, K. C., Matolı´n, V., Neyman, K. M. & Libuda, J. *Nat. Mater.* **10,** 310–315 (2011).
37. Carrettin, S., Concepción, P., Corma, A., López Nieto, J. M. & Puntes, V. F. *Angew. Chem. Int. Ed.* **43,** 2538–2540 (2004).
38. Guzman, J., Carrettin, S. & Corma, A. *J. Am. Chem. Soc.* **127,** 3286–3287 (2005).
39. Elias, J. S., Risch, M., Giordano, L., Mansour, A. N. & Shao-Horn, Y. *J. Am. Chem. Soc.* **136,** 17193–17200 (2014).
40. Yu, T., Joo, J., Park, Y. il & Hyeon, T. *Angew. Chem. Int. Ed.* **44,** 7411–7414 (2005).
41. Gu, H. & Soucek, M. D. *Chem.Mater.* **19,** 1103–1110 (2007).
42. Mädler, L., Stark, W. J. & Pratsinis, S. E. *J. Mater. Res.* **17,** 1356–1362 (2002).
43. Meierhofer, F., Mädler, L. & Fritsching, U. *AIChE Journal* **66,** e16885 (2020).
44. Giordano, F., Trovarelli, A., de Leitenburg, C. & Giona, M. *J. Catal.* **193,** 273–282 (2000).
45. Zhang, L., Spezzati, G., Muravev, V., Verheijen, M. A., Zijlstra, B., Filot, I. A. W., Su, Y.-Q., Chang, M.-W. & Hensen, E. J. M. *ACS Catal.* **11,** 5614–5627 (2021).
46. Zhu, H., Qin, Z., Shan, W., Shen, W. & Wang, J. *J. Catal.* **225,** 267–277 (2004).
47. Neitzel, A., Figueroba, A., Lykhach, Y., Skala, T., Vorokhta, M., Tsud, N., Mehl, S., Sevcikova, K., Prince, K. C., Neyman, K. M., Matolin, V. & Libuda, J. *J. Phys. Chem. C* **120,** 9852–9862 (2016).
48. Stonkus, O. A., Kardash, T. Y., Slavinskaya, E. M., Zaikovskii, V. I. & Boronin, A. I. *ChemCatChem* **11,** 3505–3521 (2019).
49. Slavinskaya, E. M., Kardash, T. Yu., Stonkus, O. A., Gulyaev, R. v., Lapin, I. N., Svetlichnyi, V. A. & Boronin, A. I. *Catal. Sci. Technol.* **6,** 6650–6666 (2016).
50. Jeong, H., Kwon, O., Kim, B. S., Bae, J., Shin, S., Kim, H. E., Kim, J. & Lee, H. *Nat. Catal.* **3,** 368–375 (2020).
51. Hinokuma, S., Fujii, H., Okamoto, M., Ikeue, K. & Machida, M. *Chem. Mater.* **22,** 6183–6190 (2010).
52. Wang, X., Chen, J., Zeng, J., Wang, Q., Li, Z., Qin, R., Wu, C., Xie, Z. & Zheng, L. *Nanoscale* **9,** 6643–6648 (2017).
53. Spezzati, G., Benavidez, A. D., DeLaRiva, A. T., Su, Y., Hofmann, J. P., Asahina, S., Olivier, E. J., Neethling, J. H., Miller, J. T., Datye, A. K. & Hensen, E. J. M. *Appl. Catal. B: Environ.* **243,** 36–46 (2019).
54. Lafyatis, D. S., Ansell, G. P., Bennett, S. C., Frost, J. C., Millington, P. J., Rajaram, R. R., Walker, A. P. & Ballinger, T. H. *Appl. Catal. B: Environ.* **18,** 123–135 (1998).
55. Vannice, M. A. & Wang, S. Y. *J. Phys. Chem.* **85,** 2543–2546 (1981).
56. Nilsson, J., Carlsson, P. A., Fouladvand, S., Martin, N. M., Gustafson, J., Newton, M. A., Lundgren, E., Grönbeck, H. & Skoglundh, M. *ACS Catal.* **5,** 2481–2489 (2015).
57. Ferri, D., Newton, M. A., Di Michiel, M., Chiarello, G. L., Yoon, S., Lu, Y. & Andrieux, J. *Angew. Chem. Int. Ed.* **53,** 8890–8894 (2014).
58. Pereira-Hernández, X. I., DeLaRiva, A., Muravev, V., Kunwar, D., Xiong, H., Sudduth, B., Engelhard, M., Kovarik, L., Hensen, E. J. M., Wang, Y. & Datye, A. K. *Nat. Commun.* **10,** 1358 (2019).
59. Slavinskaya, E. M., Gulyaev, R. v., Zadesenets, A. v., Stonkus, O. A., Zaikovskii, V. I., Shubin, Y. v., Korenev, S. v. & Boronin, A. I.. *Appl. Catal. B: Environ.* **166–167,** 91–103 (2015).
60. Skála, T., Šutara, F., Prince, K. C. & Matolín, V. *J. Electron Spectros. Relat. Phenomena* **169,** 20–25 (2009).
61. Riley, C., Canning, G., de La Riva, A., Zhou, S., Peterson, E., Boubnov, A., Hoffman, A., Tran, M., Bare, S. R., Lin, S., Guo, H. & Datye, A. *Appl. Catal. B: Environ.* **264,** 118547 (2020).
62. Feng, X., Sayle, D. C., Wang, Z. L., Paras, M. S., Santora, B., Sutorik, A. C., Sayle, T. X. T., Yang, Y., Ding, Y., Wang, X. & Her, Y.-S. *Science* **312,** 1504–8 (2006).

63. Trovarelli, A. & Llorca, J. *ACS Catal.* **7,** 4716–4735 (2017).
64. Aneggi, E., Wiater, D., de Leitenburg, C., Llorca, J. & Trovarelli, A. *ACS Catal.* **4,** 172–181 (2014).
65. Kim, Y., Lee, H. & Kwak, J. H. *ChemCatChem* **12,** 5164–5172 (2020).
66. Kato, S., Ammann, M., Huthwelker, T., Paun, C., Lampimäki, M., Lee, M.-T., Rothensteiner, M. & van Bokhoven, J. A. *Phys. Chem. Chem. Phys.* **17,** 5078–5083 (2015).

6.6 Appendix D

Table D1. Crystallite size determined via Rietveld refinement of synchrotron XRD data for FSP-made CeO_2 prepared at different injection rates

Injection rate (ml/min)	Rietveld refined size (nm)
1	5
2.5	7
5	9
7.5	11
10	14

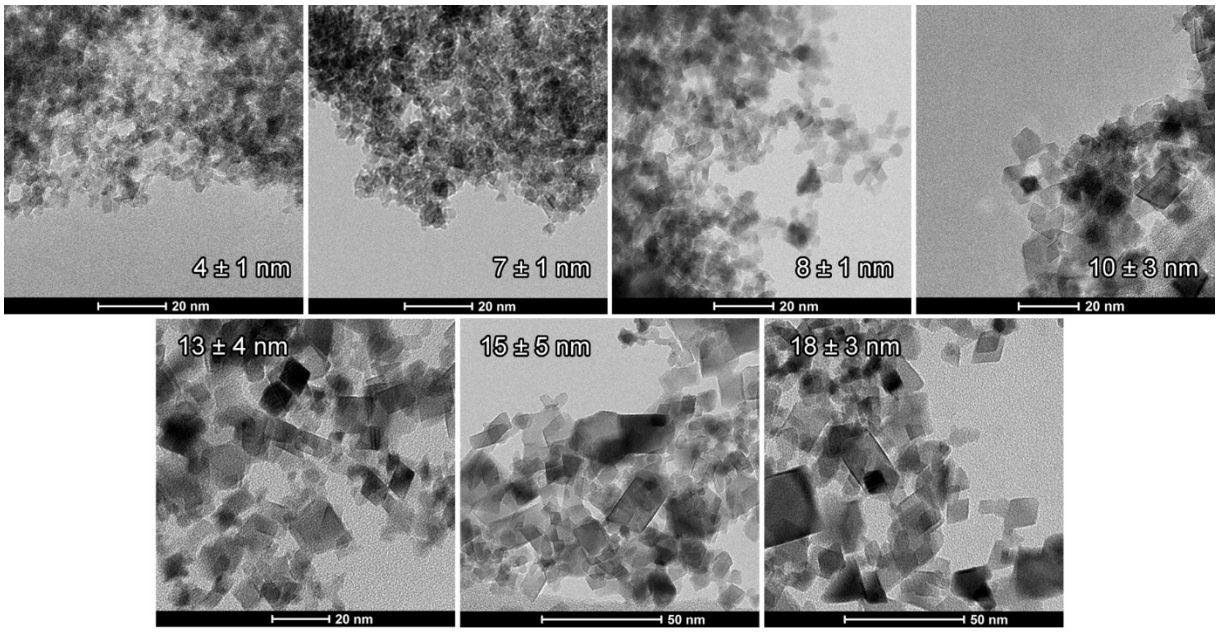

Figure D1. STEM images of one-step made PdFSP samples prepared at injection rates of 1, 2.5, 5, 7.5, 10, 12.5 and 15 ml/min. At higher injection rates particle size increases.

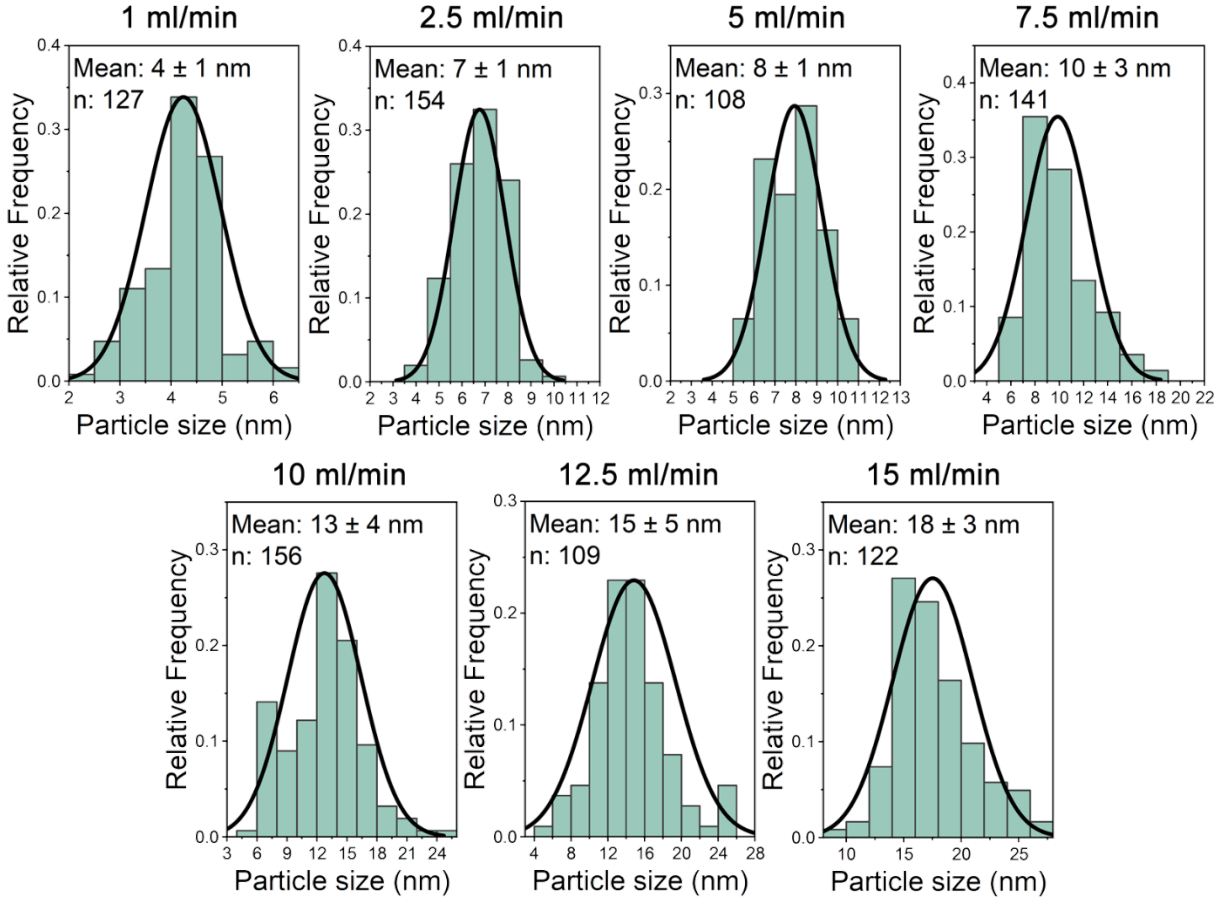

Figure D2. Particle size distributions for one-step made PdFSP samples prepared at injection rates of 1, 2.5, 5, 7.5, 10, 12.5 and 15 ml/min. At higher injection rates particle size distribution broadens.

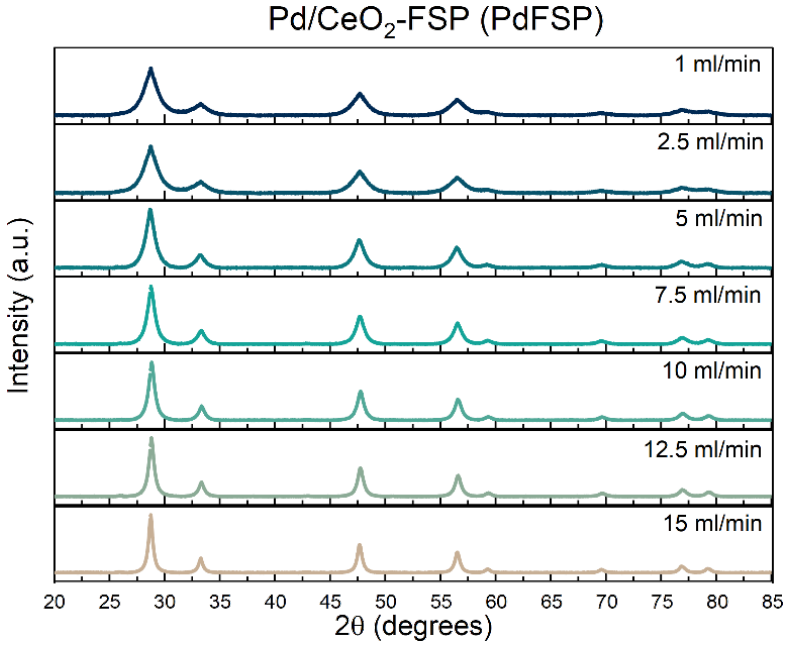

Figure D3. XRD patterns of PdFSP samples prepared at different injection rates.

Table D2. Characterization summary for PdFSP samples.

Injection rate (ml/min)	BET surface (m^2/g)	BET size (spherical) (nm)	BET size (octahedral) (nm)	XRD size (nm)	TEM size (nm)	Pd/Ce at. XPS	Pd loading ICP-OES (wt %)
1	284	3	5	5	**4 (±1)**	0.019	1.02 ± 0.01
2.5	211	4	7	7	**7 (±1)**	0.022	1.03 ± 0.02
5	206	4	7	8	**8 (±1)**	0.024	1.02 ± 0.03
7.5	135	6	11	11	**10 (±3)**	0.027	1.04 ± 0.05
10	117	7	13	14	**13 (±4)**	0.033	1.04 ± 0.05
12.5	99	8	15	16	**15 (±5)**	0.037	1.07 ± 0.01
15	76	11	19	19	**18 (±3)**	0.041	1.07 ± 0.01

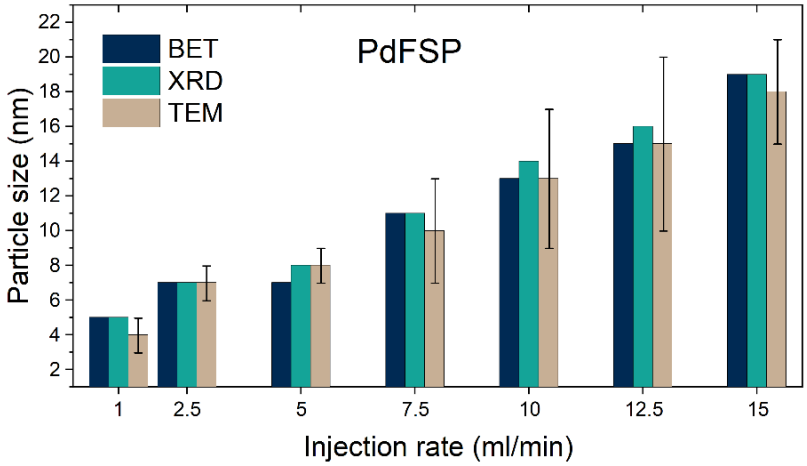

Figure D4. Particle sizes of PdFSP samples determined from XRD (Scherrer equation), surface area analysis (BET) and TEM.

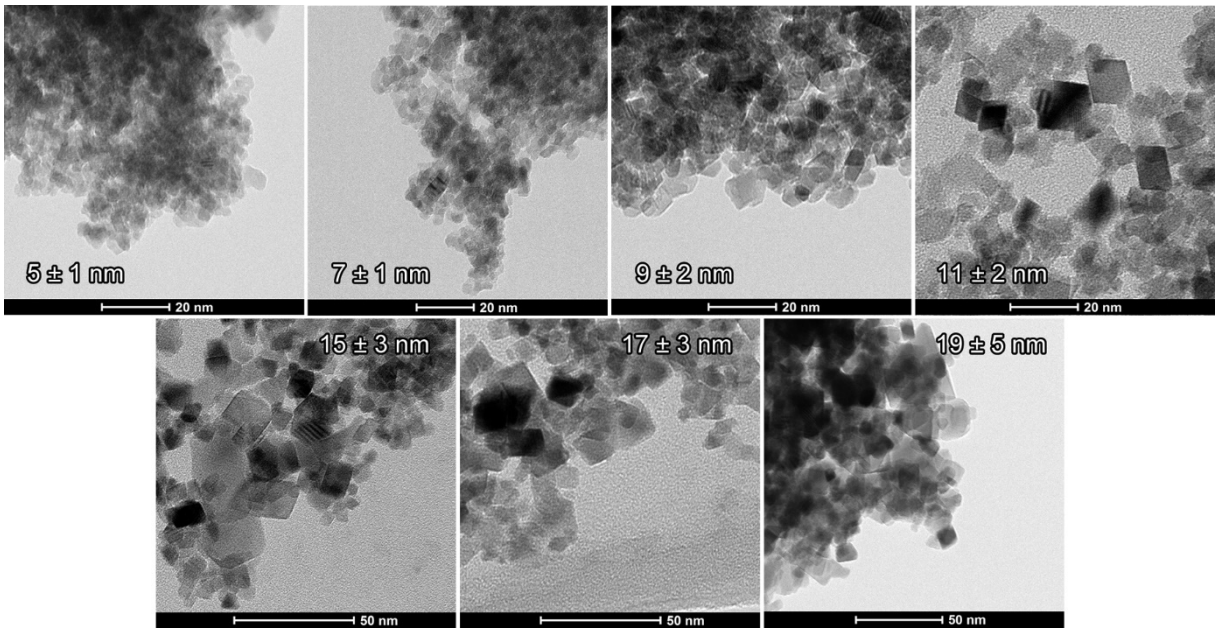

Figure D5. STEM images of PdFSPimp samples prepared by impregnation of FSP-CeO_2 made at injection rates of 1, 2.5, 5, 7.5, 10, 12.5 and 15 ml/min.

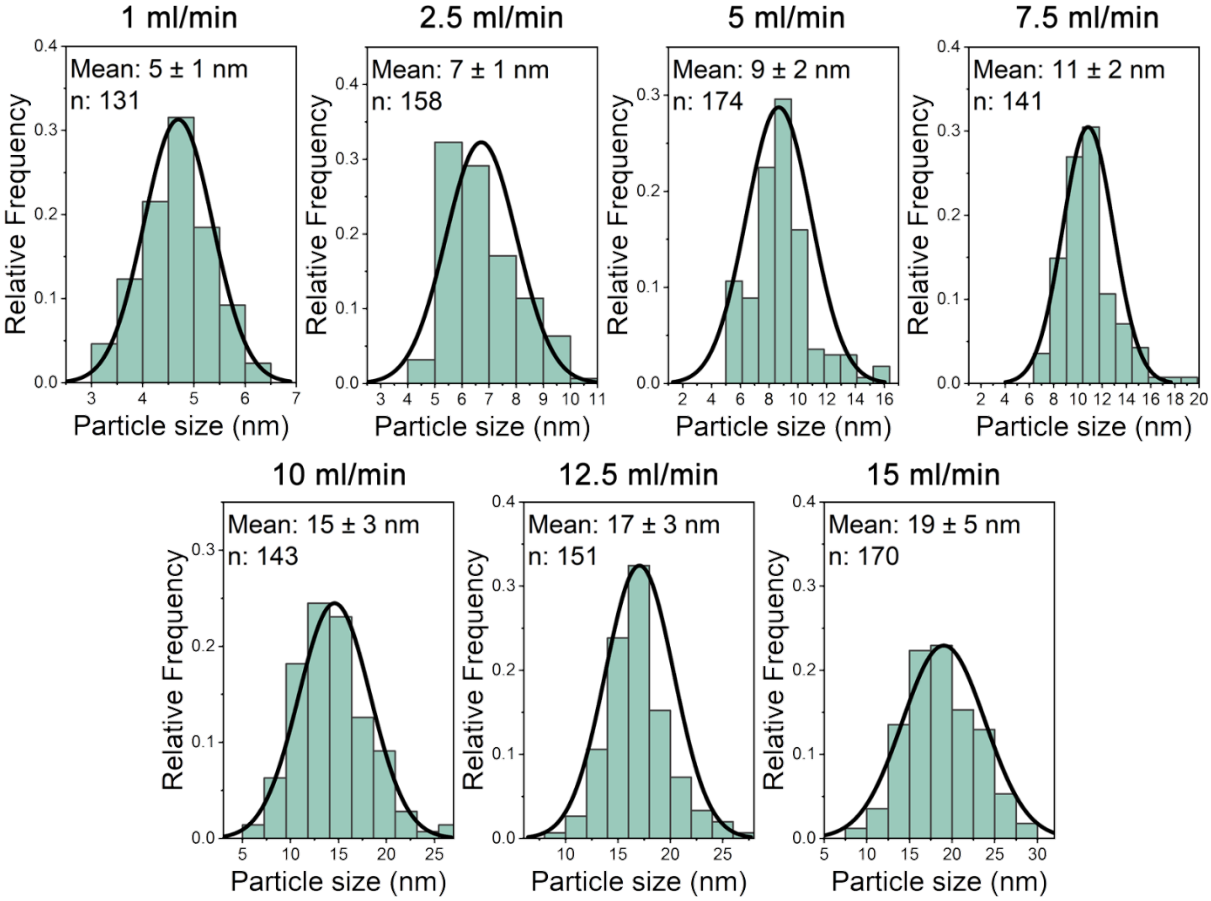

Figure D6. Particle size distributions for PdFSPimp samples prepared by impregnation of FSP-CeO_2 made at injection rates of 1, 2.5, 5, 7.5, 10, 12.5 and 15 ml/min. At higher injection rates particle size distribution broadens.

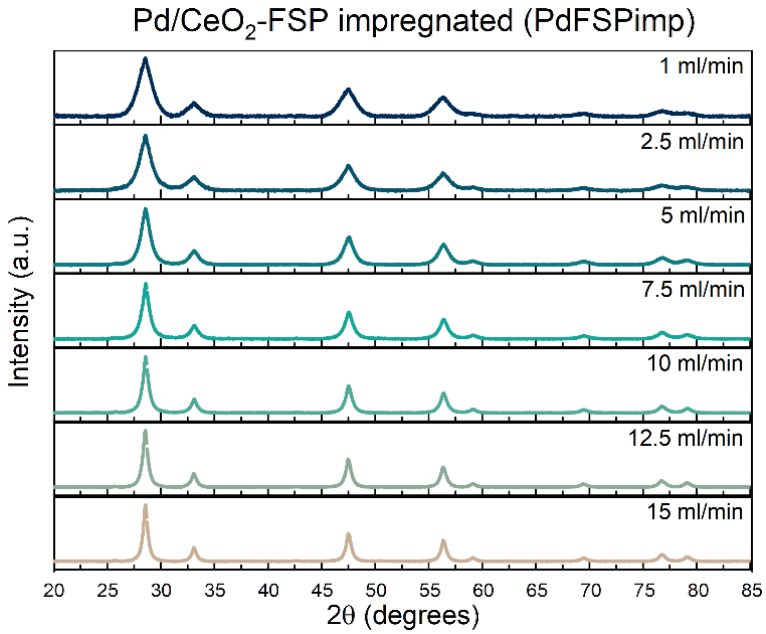

Figure D7. XRD patterns of PdFSPimp samples prepared by impregnation of FSP-CeO_2 made at different injection rates.

Table D3. Overview of characterization results for PdFSPimp samples. The slight decrease in surface area as compared to PdFSP samples is likely caused by the wet impregnation of Pd.

Injection rate (ml/min)	BET surface (m^2/g)	BET size (spherical) (nm)	BET size (octahedral) (nm)	XRD size (nm)	TEM size (nm)	Pd/Ce at. XPS	Pd loading ICP-OES (wt %)
1	177	5	8	6	**5 (±1)**	0.020	1.03 ± 0.01
2.5	183	5	8	7	**7 (±1)**	0.022	1.02 ± 0.01
5	129	6	11	9	**9 (±2)**	0.023	1.01 ± 0.01
7.5	117	7	13	11	**11 (±2)**	0.027	1.00 ± 0.01
10	97	9	15	15	**15 (±3)**	0.034	1.00 ± 0.01
12.5	86	10	17	16	**17 (±3)**	0.038	0.97 ± 0.01
15	72	12	20	19	**19 (±5)**	0.038	1.01 ± 0.04

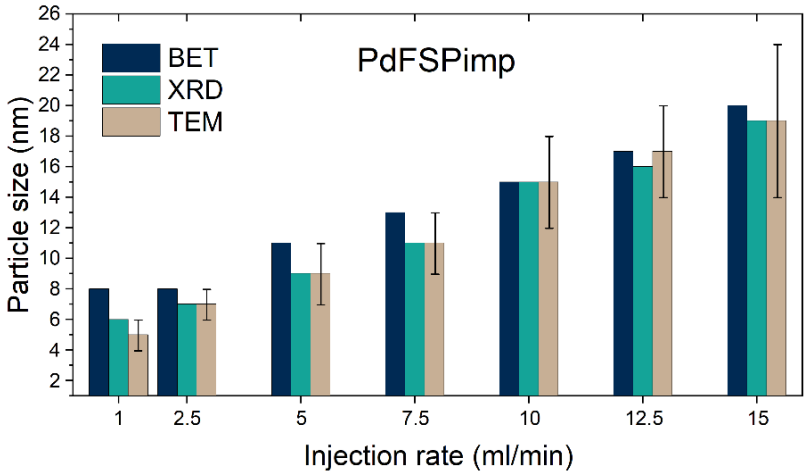

Figure D8. Particle sizes of PdFSPimp samples determined from XRD (Scherrer equation), surface area analysis (BET) and TEM.

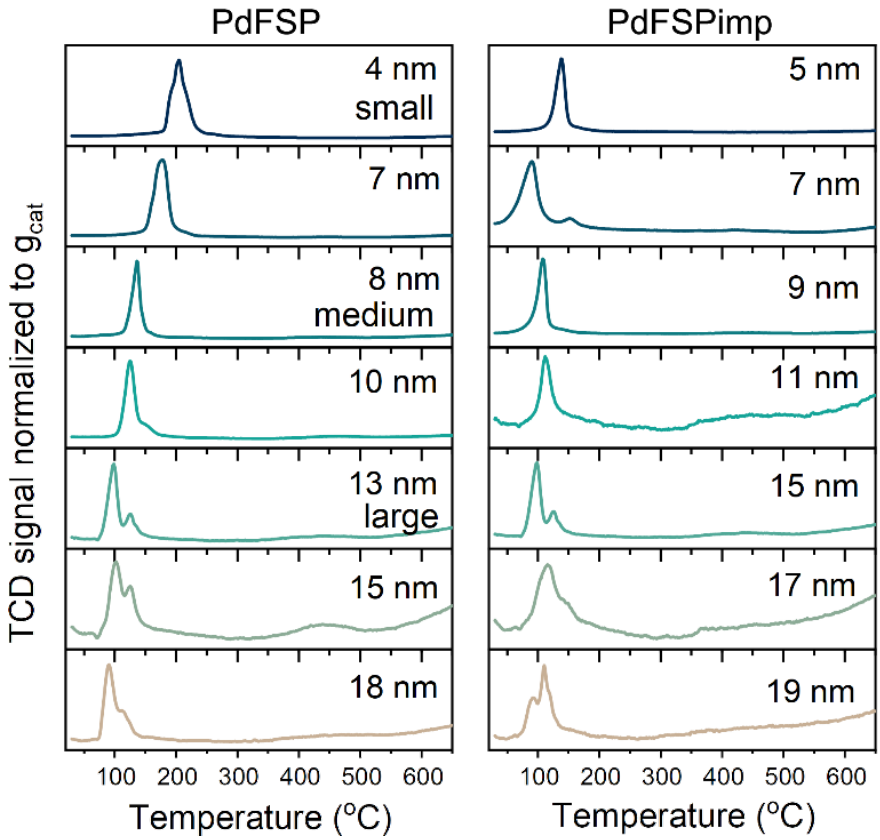

Figure D9. H_2-TPR curves for PdFSP and PdFSPimp samples.

Table D4. Quantification of H_2-TPR data.

	PdFSP				PdFSPimp		
Size TEM (nm)	**H_2/Pd_{total} (mol/mol)**	**H_2 (mmol/g_{cat})**	**H_2 (µmol/m^2)**	**Size TEM (nm)**	**H_2/Pd_{total} (mol/mol)**	**H_2 (mmol/g_{cat})**	**H_2 (µmol/m^2)**
4 (±1)	16.9	1.58	5.6	**5 (±1)**	13.5	1.27	7.2
7 (±1)	11.0	1.04	4.9	**7 (±1)**	4.7	0.44	2.4
8 (±1)	4.9	0.46	2.2	**9 (±2)**	4.1	0.39	3.0
10 (±3)	5.4	0.51	3.8	**11 (±2)**	2.9	0.27	2.3
13 (±4)	2.0	0.19	1.6	**15 (±3)**	1.3	0.12	1.2
15 (±5)	1.8	0.17	1.7	**17 (±3)**	1.3	0.12	1.4
18 (±3)	1.7	0.16	2.1	**19 (±5)**	1.1	0.11	1.5

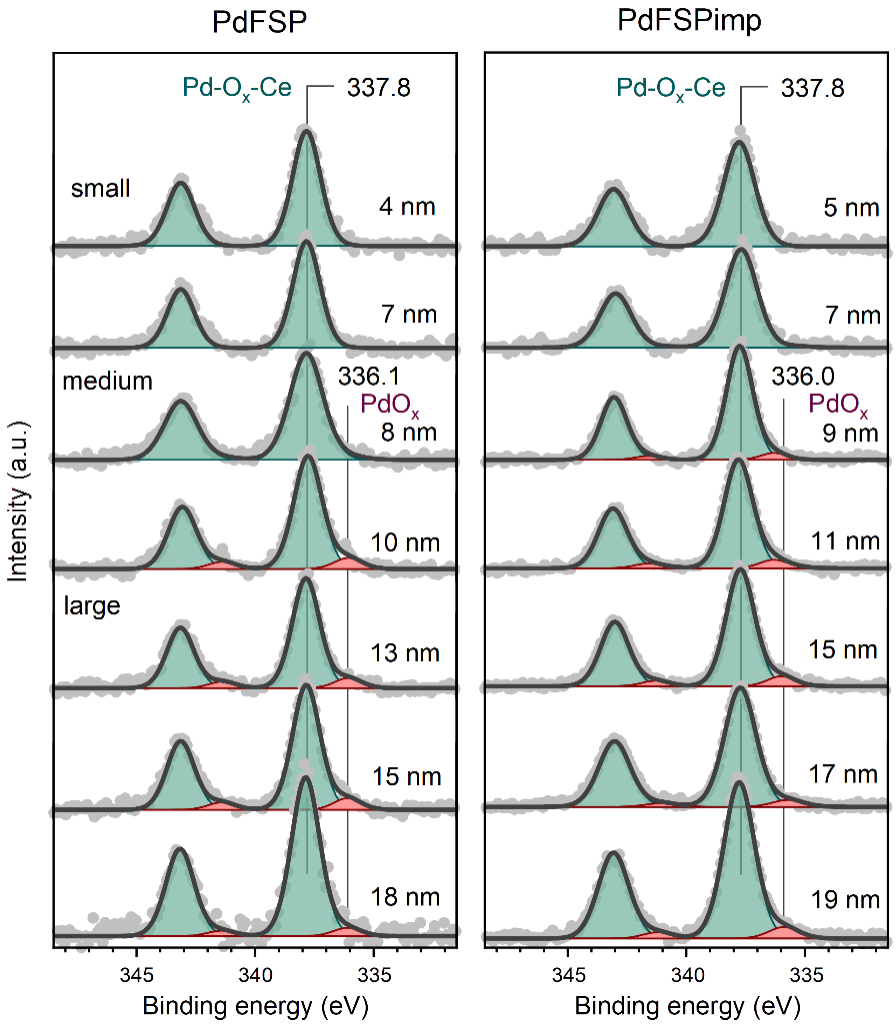

Figure D10. XPS spectra of Pd 3d core line region for PdFSP and PdFSPimp samples.

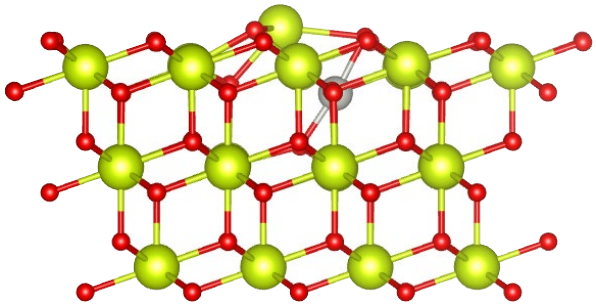

Figure D11. DFT-derived model in which Pd (grey atom) is doped in subsurface layer of (111) ceria facet. This model is different from the surface Pd-doped model proposed earlier (see **Chapter 4**), because here Pd is not exposed to the surface.

Table D5. EXAFS fitting summary. S_0^2 value (0.80) was determined from fitting of Pd foil spectrum and was used for the fitting of Pd-CeO_2 samples. ΔE_0 was shared for all the shells, while σ^2 and ΔR values were shared within each shell for the same type of back-scattering atoms. The errors indicate the uncertainties of fitting results derived from Artemis software

Sample	Path	R (Å)	CN	σ^2 (Å^2)	ΔE_0 (eV)	R-factor (%)
PdFSP – small	Pd-O	2.01 ± 0.01	3.8 ± 0.9	0.004 ± 0.002	2.9 ± 2.5	2.6
	Pd-Ce (doped)	2.65 ± 0.01	2.4 ± 0.9	0.005 ± 0.002		
PdFSP – medium	Pd-O	2.00 ± 0.01	4.1 ± 0.4	0.002 ± 0.001	2.3 ± 1.1	1.0
	Pd-Ce (doped)	2.65 ± 0.02	1.1 ± 0.4	0.009 ± 0.002		
	Pd-Ce (surface)	3.22 ± 0.01	3.4 ± 0.9	0.009 ± 0.002		
PdFSP – large	Pd-O	2.01 ± 0.01	3.9 ± 0.4	0.002 ± 0.001	2.7 ± 1.1	0.5
	Pd-Ce (doped)	2.66 ± 0.01	1.5 ± 0.4	0.007 ± 0.001		
	Pd-Ce (surface)	3.23 ± 0.01	2.4 ± 0.7	0.007 ± 0.00		
PdFSPimp – 7 nm	Pd-O	2.00 ± 0.01	4.1 ± 0.4	0.002 ± 0.001	0.1 ± 0.9	1.1
	Pd-Ce (surface)	3.19 ± 0.01	2.7 ± 1.0	0.006 ± 0.003		
PdFSPimp – 9 nm	Pd-O	2.01 ± 0.01	3.9 ± 0.4	0.001 ± 0.001	2.2 ± 1.1	0.8
	Pd-Ce (surface)	3.21 ± 0.01	3.8 ± 1.5	0.010 ± 0.003		
PdFSPimp – 13 nm	Pd-O	2.02 ± 0.01	4.1 ± 0.5	0.002 ± 0.001	1.8 ± 1.3	1.1
	Pd-Ce (surface)	3.21 ± 0.01	3.4 ± 1.2	0.006 ± 0.002		
Pd foil	Pd-Pd	2.74 ± 0.02	12.0	0.005 ± 0.001	3.6 ± 0.4	0.2

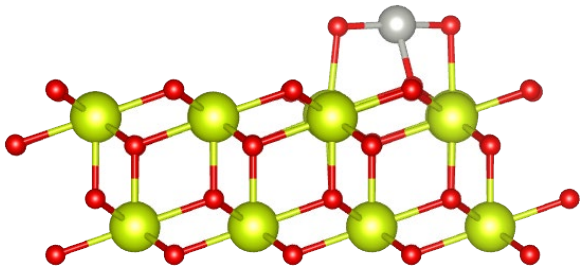

Figure D12. DFT-derived model in which Pd (grey atom) is stabilized on the (111) facet of CeO_2. This model represents surface Pd-oxo species (see **Chapter 4**).

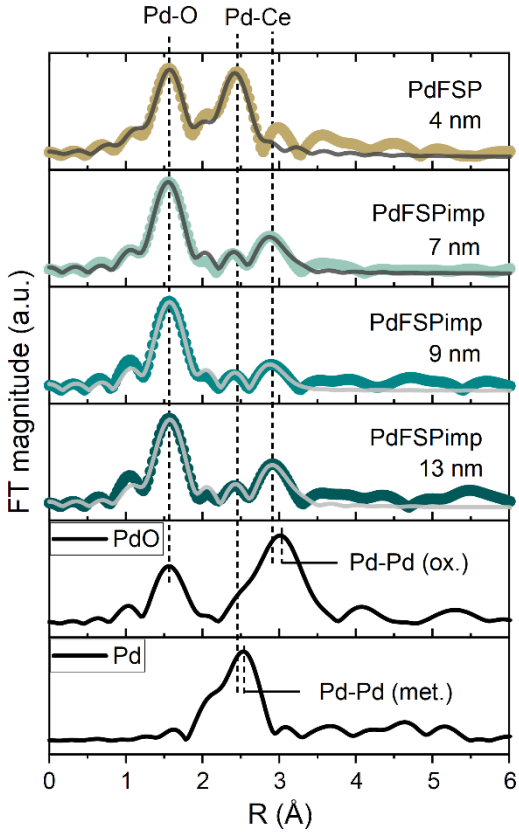

Figure D13. R-space k^3-weighted EXAFS spectra of samples acquired at Pd K-edge. As can be seen for PdFSPimp, the short Pd-Ce components (~2.65 Å) are diminished in contrast to spectra of PdFSP. This implies that Pd-oxo species are located predominantly in/on the surface ceria in impregnated catalysts.

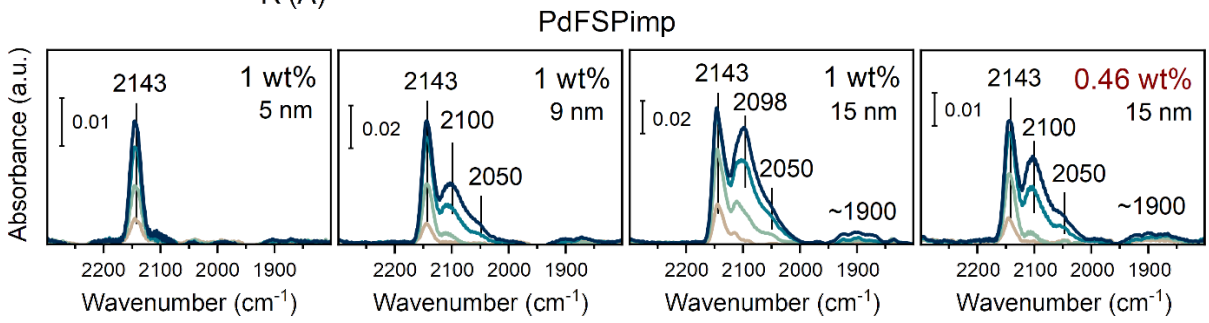

Figure D14. CO adsorption at -20 ºC followed by *in situ* DRIFTS for fresh PdFSPimp samples. Flow of CO was fixed to 0.3 ml/min yielding 2 mbar of total pressure in the *in situ* cell.

Note D1. As can be seen from **Fig. D14**, the single-atom nature of Pd sites manifested by ~2140 cm^{-1} band in spectra of small CeO_2 nanoparticles is preserved even for impregnated samples. Yet we note a slightly higher contribution of CO carbonyls related to Pd clusters in case of larger nanoparticles of PdFSPimp than for PdFSP. This can be explained by the higher Pd surface concertation due to impregnation preparation method of PdFSPimp. To account for differences in Pd surface concentration, we prepared a reference sample by impregnating large CeO_2 with a lower Pd loading (0.46 wt%) to reach the amount of Pd per unit of surface area (based on BET surface area analysis) as for the small nanoparticles. Although the overall intensity of CO bands decreased due to the lower concentration of Pd, we can still observe that some agglomerated Pd species are present (~2050 and ~1900 cm^{-1} bands). Thus, we infer that weaker MSI are the major cause of the lower stability of Pd single atoms on large CeO_2 instead of differences in the Pd surface concentration.

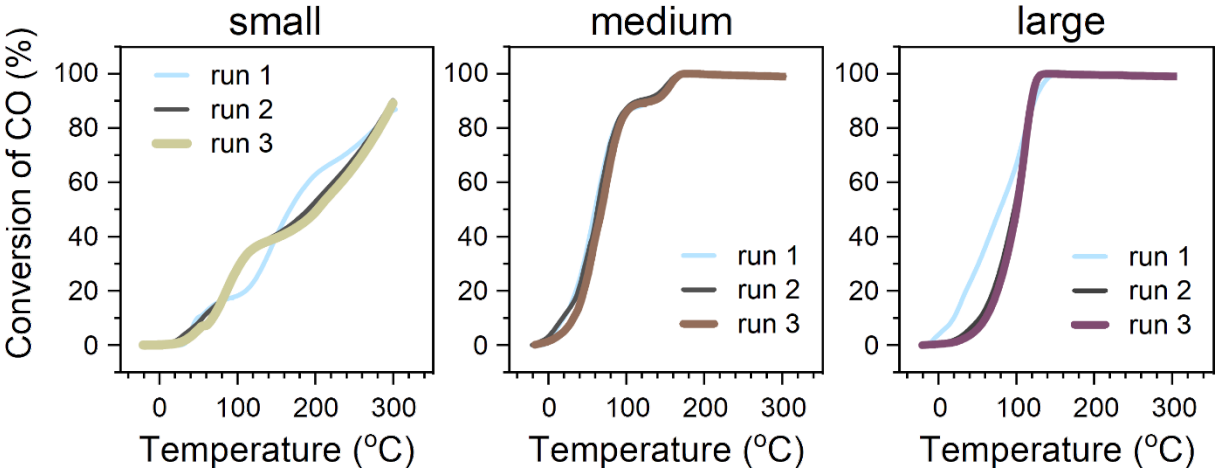

Figure D15. Three consecutive light-off runs for PdFSP samples. The partial loss in low-temperature (<100 °C) activity of medium and large PdFSP is likely due to reduction and clustering of Pd during CO oxidation.

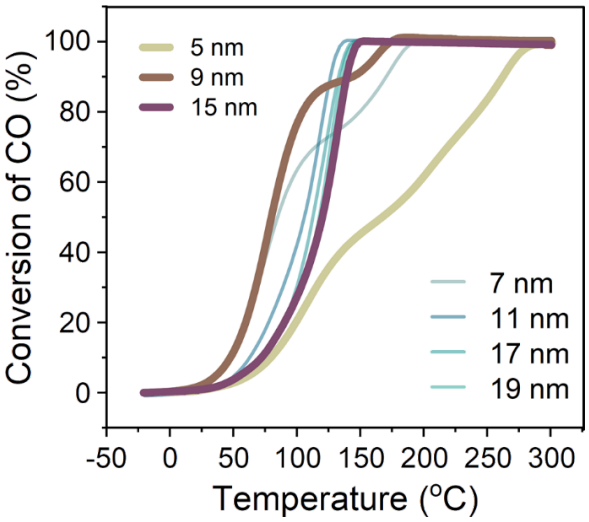

Figure D16. CO oxidation light-off curves from -20 to 300 °C for PdFSPimp samples. Reaction conditions: 1% CO and 1% O_2 in He (GHSV ~180,000 ml g_{cat}^{-1} h^{-1}).

Table D6. Reaction orders measured at 75 °C. All catalysts were stabilized on the stream at 75 °C for at least 14h prior to the measurements.

	CO	**O_2**
1 wt% Pd FSP – 4 nm (small)	1.30 ± 0.09	-0.17 ± 0.01
2 wt% PdFSP – 4 nm	1.09 ± 0.06	-0.11 ± 0.01
1 wt% Pd FSP – 7 nm	1.26 ± 0.06	-0.13 ± 0.01
1 wt% Pd FSP – 8 nm (medium)	0.27 ± 0.01	0.08 ± 0.04
1 wt% Pd FSP – 13 nm (large)	0.16 ± 0.03	0.25 ± 0.02
1 wt% Pd FSP – 18 nm	0.01 ± 0.01	0.27 ± 0.03
1 wt% PdFSPimp – 5 nm	1.02 ± 0.11	-0.07 ± 0.01
1 wt% PdFSPimp – 7 nm	0.75 ± 0.09	0.01 ± 0.01
1 wt% PdFSPimp – 9 nm	0.52 ± 0.06	0.05 ± 0.02
1 wt% PdFSPimp – 15 nm	0.20 ± 0.02	0.20 ± 0.01
0.46 wt% PdFSPimp -15 nm	0.27 ± 0.02	0.20 ± 0.01

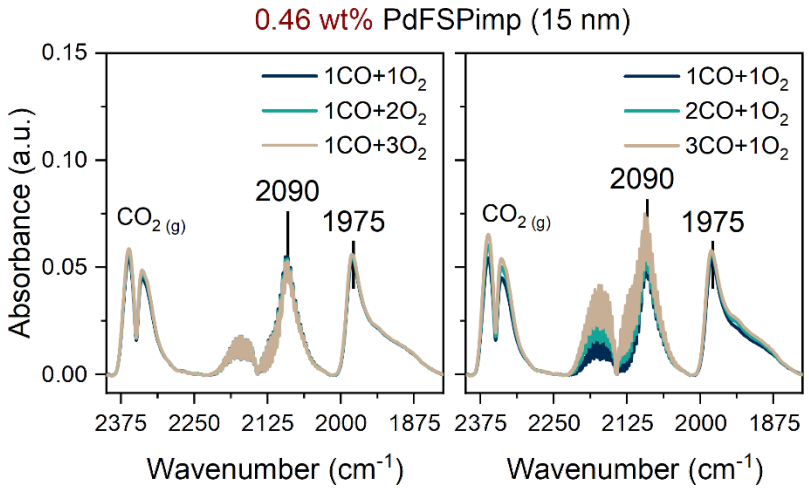

Figure D17. CO oxidation at 75 °C on 0.46%PdFSPimp-large sample followed by *operando* DRIFTS. Reaction conditions: 1%CO +1%O_2 in He, total flow of 100 ml/min. Due to the lower loading of Pd (0.46 wt%) in this sample than in large PdFSP (1 wt%), a lower intensity of the IR bands is noted. Yet, a similar extent of reduction and clustering of Pd is observed under actual CO oxidation conditions. Once again this points to the fact that the weaker MSI in PdFSP and PdFSPimp catalysts with large CeO_2 nanoparticles are the likely cause of the lower stability of single-atom Pd species.

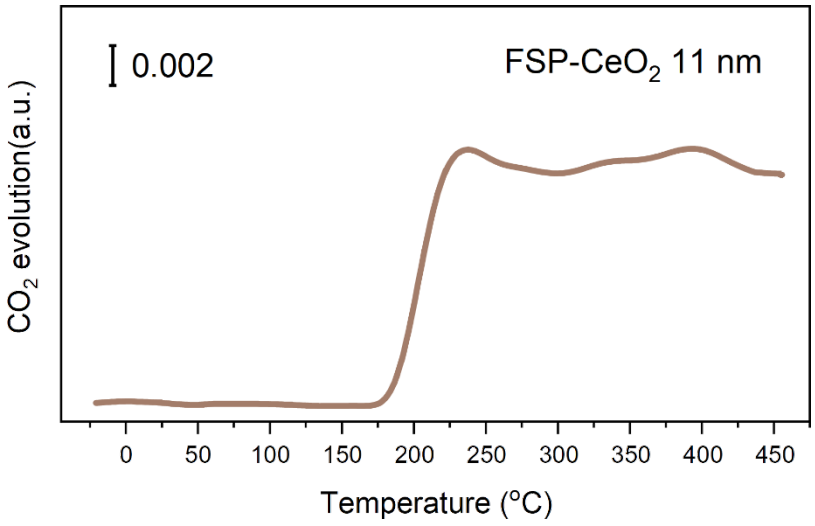

Figure D18. TPR-CO profile for bare FSP-CeO_2 recorded from -20 to 450 °C. Conditions: 1.33 vol% CO in He, ramp rate 10 °C/min.

Table D7. Pulsing CO titration at 175 °C.

	CO consumed (mmol g_{cat}^{-1})	**$CO_{cons.}/Pd_{total}$ (mol/mol)**
1 wt% Pd FSP – 4 nm (small)	1.02	10.9
1 wt% Pd FSP – 7 nm	0.87	9.3
1 wt% Pd FSP – 8 nm (medium)	0.54	5.8
1 wt% Pd FSP – 10 nm	0.45	4.8
1 wt% Pd FSP – 13 nm (large)	0.39	4.2
1 wt% Pd FSP – 15 nm	0.32	3.4
1 wt% Pd FSP – 18 nm	0.30	3.2
5 wt% PdO/SiO_2 (ref sample)	0.13	0.3

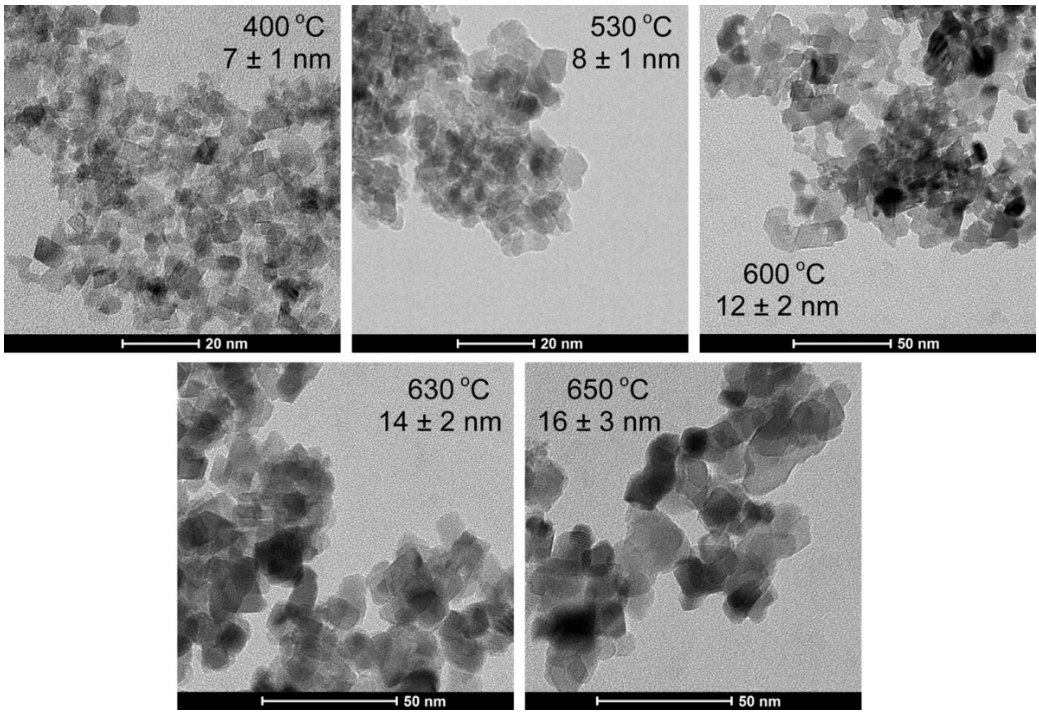

Figure D19. STEM images of PdSG samples prepared by impregnation of sol-gel-made CeO_2 calcined at different temperatures to yield different particle sizes of the support.

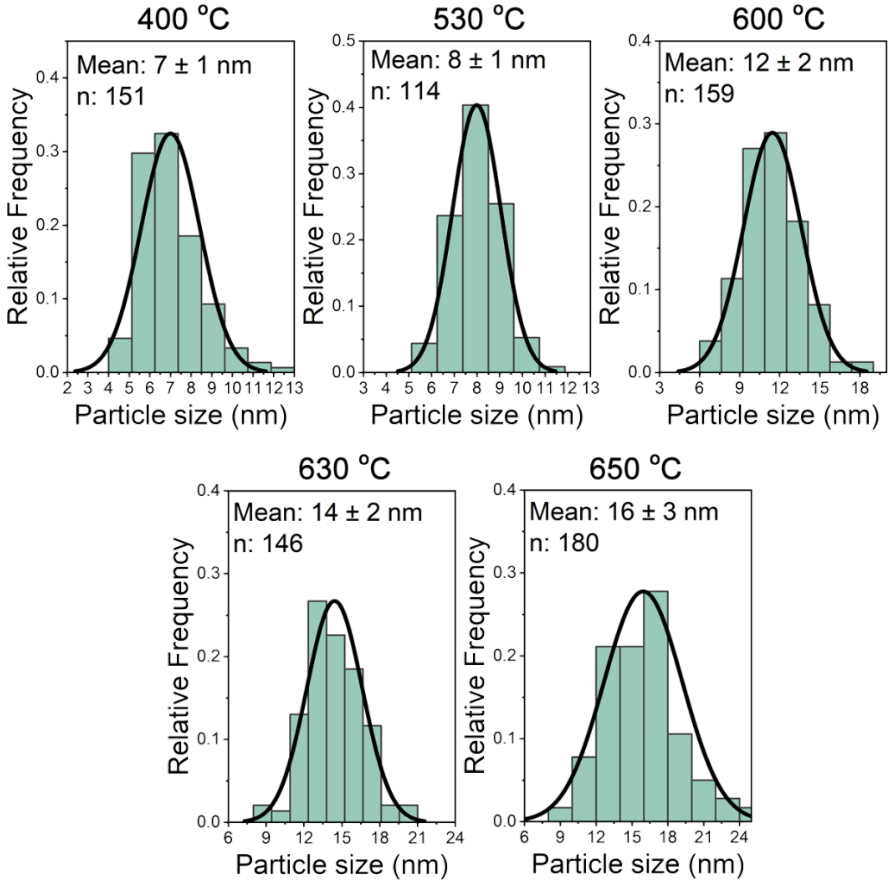

Figure D20. Particle size distributions for PdSG samples prepared by impregnation of sol-gel-made CeO_2 calcined at different temperatures to yield different particle sizes of the support.

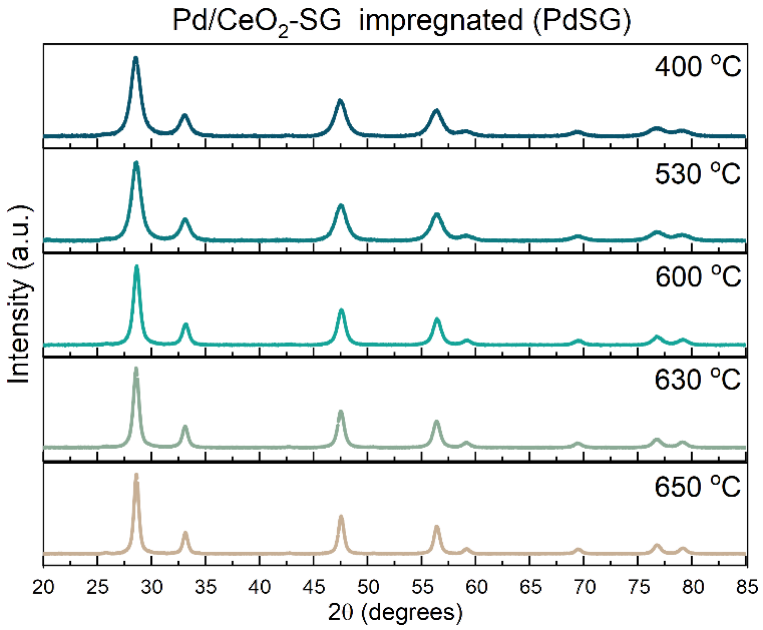

Figure D21. XRD patterns of PdSG samples prepared by impregnation of sol-gel-derived CeO_2 calcined at different temperatures.

Table D8. Characterization summary for PdSG samples

Calcination temperature (°C)	BET surface (m^2/g)	BET size (spherical) (nm)	XRD size (nm)	Size TEM (nm)	Pd loading ICP-OES (wt %)
400	144	6	7	**7 (±1)**	1.01 ± 0.01
530	131	7	8	**8 (±1)**	1.05 ± 0.01
600	81	11	12	**12 (±2)**	1.03 ± 0.01
630	61	14	14	**14 (±2)**	1.07 ± 0.01
650	47	17	17	**16 (±3)**	1.01 ± 0.01

Summary and outlook

Towards understanding the catalytic reactivity of metal-ceria interfaces

The global economic growth and rise in the standard of living are closely related to progress in catalytic technologies. The development of more efficient and environmentally friendly catalytic processes is essential for mitigating the anthropogenic footprint on the environment. As a scientific discipline heterogeneous catalysis has changed substantially in the past decades. The design of novel catalysts, initially based on trial-and-error approaches, can now benefit from molecular understanding of the chemical phenomena underlying the catalytic reactions. This would not be possible without the development and evolution of synthetic methods for nanomaterials, advanced spectroscopic and imaging characterization methods, and electronic structure calculations. Fundamental understanding of the functioning of catalysts is imperative for optimization of existing and design of new catalytic heterogeneous processes.

CO oxidation is one of the most studied heterogeneous catalytic reactions. Due to its seeming simplicity, it is often used to probe the reactivity of catalysts and for fundamental studies in heterogeneous catalysis. CO oxidation is also important for environmental catalysis. It is particularly relevant for automotive exhaust catalysts, for which abatement of CO and other toxic gases at low temperature constitutes the cold-start problem. Conventional noble metal catalysts in the form of small nanoparticles deposited on an inert support suffer from CO poisoning which limits the activity at low temperature (<150 °C). One of the promising solutions is the use of ceria-supported noble metal catalysts. Owing to facile $Ce^{3+} \rightleftarrows Ce^{4+}$ redox chemistry, ceria is capable of releasing and storing lattice oxygen depending on the reaction conditions. The supply of oxygen from ceria to noble metal atoms at the metal-support interface is commonly accepted as an explanation for the enhanced activity of these catalysts in low-temperature CO oxidation.

Recently, a new class of ceria-based catalysts in which noble metals are atomically dispersed over the support surface has been developed. The application of such single-atom catalysts (SACs) for automotive exhaust abatement is particularly appealing due to the highest possible utilization of expensive platinum group metals (PGMs). In contrast to conventional

catalysts that contain nanoparticles of PGMs, ceria-supported SACs are much less studied in the context of low-temperature CO oxidation. Evidence is however growing that the catalytic properties of atomically dispersed metals are significantly different from their bulky counterparts. Formulating structure-activity relationships for ceria-stabilized atomically dispersed PGMs is pivotal to their further development into technical catalysts. This work focused on the synthesis, the detailed characterization and reactivity of CeO_2-supported Pt and Pd catalysts for low-temperature CO oxidation. Special attention was paid to the characterization of the active components in the catalyst by vibrational and X-ray spectroscopy. As shown throughout this work, the properties of ceria have a profound effect on the catalytic performance of metal-ceria interface.

In **Chapter 2** the chemical properties of ceria were reviewed in the context of its application as a support for heterogeneous catalysts. We showed how modern methods allow for nanoscale-controlled synthesis of ceria, which is pivotal to fundamental studies that focus on structure-performance relationships. Literature evidences that redox properties of small ceria crystallites (<10 nm) differ from those of larger ones. The spectroscopy tools commonly used for characterization of ceria-based catalysts were reviewed with a focus on monitoring of the $Ce^{3+} \rightleftarrows Ce^{4+}$ redox dynamics. The importance of *in situ* and *operando* spectroscopy methods such as X-ray absorption spectroscopy (XAS) and X-ray photoelectron spectroscopy (XPS) for establishing structure-function relationships for ceria-based catalysts was emphasized. Strong metal-support interactions (MSI) in ceria catalysts comprising metal nanoparticles leads to unusual reactivity of interfacial metal sites. Finally, recent advances in the engineering of the catalysts with atomically dispersed metals on ceria were discussed.

In **Chapter 3**, the synthesis of single-atom Pt/CeO_2 catalysts using strong electrostatic adsorption (SEA), atom trapping (AT) and flame spray pyrolysis (FSP) was compared. In their as-prepared state, these catalysts did not display a high CO oxidation activity at low temperature (<150 °C). *In situ* diffuse reflectance IR spectroscopy (DRIFTS) indicated that the low activity can be explained by the strong adsorption of CO on ionic isolated Pt sites. CO oxidation activity at low temperatures increases substantially by activation in CO at 275 °C. Small Pt nanoparticles (<2 nm) formed after reductive treatment bind CO much weaker than single-atom Pt as evidenced by *in situ* DRIFTS. Among the activated catalysts, the AT-synthesized Pt/CeO_2 showed the highest low-temperature CO oxidation activity reaching full conversion at around 70 °C. CO-TPR indicated that the surface oxygen species in

activated AT catalyst can react at much lower temperature than in SEA and FSP catalysts. *In situ* near-ambient pressure XPS (NAP-XPS) revealed that CeO_2 lattice oxygen in the activated AT catalysts reacts with CO already at 50 °C. These results emphasize the role of ceria lattice oxygen in CO oxidation at low temperatures.

The catalytic properties of ceria-supported Pd single atoms investigated in **Chapter 4** were found to be different from Pt/CeO_2 SACs. Well-defined Pd/CeO_2(111) SACs prepared by wet impregnation of ceria nanorods (PdRods) and one-step FSP (PdFSP) displayed a high low-temperature CO oxidation activity already in the as-synthesized state. These Pd/CeO_2 SACs shared some similarities in the as-prepared state but detailed *in situ* spectroscopic characterization including DRIFTS and NAP-XPS revealed a very different Pd speciation during CO oxidation. The oxidized Pd single atoms on the surface of PdFSP catalyst are stable under reaction conditions, while they are prone to reduction and sintering in PdRods. By combining transient and steady-state kinetics studies, the pivotal role of atomically dispersed Pd-oxo species in low-temperature CO oxidation was revealed. Using *in situ* resonant photoelectron spectroscopy (RPES) and wide-angle X-ray scattering, the higher oxygen mobility in PdFSP catalysts was demonstrated. Facile reverse oxygen spillover from ceria to Pd in PdFSP was proposed to be responsible for preserving the oxidized nature of Pd single atoms sites, thereby preventing them from sintering.

Chapter 5 was dedicated to the identification of structure-activity relationships in a technical Pd/CeO_2 catalyst prepared by wet impregnation of a commercial ceria support. In contrast to the well-defined Pd/CeO_2 SACs discussed in **Chapter 4**, different types of species, including Pd oxide nanoparticles (<3 nm) and highly dispersed (sub-nm) Pd-oxo species, coexist in such Pd/CeO_2 catalyst in the as-prepared state. *In situ* and *operando* spectroscopic tools showed that the initially high CO oxidation activity at low temperature was due to Pd single atoms, although they reduce and sinter under reaction conditions. The resulting metallic Pd species display a lower low-temperature activity, as most of the sites are poisoned by CO as demonstrated by time-resolved *operando* DRIFTS experiments. Whereas at low temperature only sub-oxidized Pd sites in proximity to the Pd-CeO_2 interface are active, metallic Pd can contribute significantly to CO oxidation activity only at elevated temperature (>150 °C). This interpretation was supported by analysis of the reaction orders at different temperatures. Altogether these results highlight the utility of a multi-technique *operando* approach for establishing structure-activity relationships for technical catalysts.

Chapter 6 explores how the size of CeO_2 influences the catalytic properties of PdFSP SACs. A set of catalysts with the CeO_2 crystallite size ranging from 4 to 18 nm was prepared by adjusting the liquid injection rate during the FSP synthesis. In the as-synthesized state, small PdFSP (4 nm) and medium PdFSP (8-9 nm) contain only single-atom Pd species, while a minor fraction of Pd clusters is also present in large PdFSP (13 nm). The light-off CO oxidation performance of PdFSP catalysts is strongly influenced by the size of the support. Medium PdFSP (8-9 nm) was found to be the most active. *Operando* DRIFTS and reaction orders measurements showed that Pd single atoms in small PdFSP are particularly stable during CO oxidation. Nevertheless, poisoning by oxygen limits their activity under oxygen-rich conditions. Large PdFSP lacks single-atom Pd species under reaction conditions. The metallic Pd clusters display a positive reaction order in oxygen and are active at elevated temperature (>150 °C). The absence of oxygen poisoning and the high concentration of Pd single atoms in medium PdFSP are the likely reasons for its high CO oxidation activity. *In situ* RPES and CO titration experiments showed that the reducibility of PdFSP catalysts changes as a function of the ceria particle size. High oxygen mobility in small PdFSP explains the observed oxygen poisoning and high stability of oxidized Pd single atoms during CO oxidation. The dependence of CO oxidation activity on ceria particle size is not limited to FSP-prepared catalysts: a set of sol-gel derived CeO_2 of different size impregnated with Pd showed a similar activity trend with respect to ceria particle size. In conclusion, this work demonstrates that the catalytic performance of metal-ceria catalysts can be tuned by varying the size of the ceria support.

As common to scientific research, answering one question leads to new ones that require deeper investigation. The synthesis strategies used for preparing Pt/CeO_2 SACs described in **Chapter 3** can be extended to other transition metals. Recent literature hints that this is indeed possible[1–3]. Systematic studies on application of AT and FSP for preparation of transition metal SACs for CO oxidation would be valuable. It would be also interesting to investigate the stability of small Pt nanoparticles that are formed during the activation treatment of the Pt/CeO_2 SACs under aging conditions relevant to the application in three-way catalysis (>800 °C). It is known that small Pt clusters can redisperse through the formation of volatile PtO_2 under oxidative conditions. Addressing these issues is crucial for successful implementation of such catalysts in automotive exhaust catalysis.

The multi-technique *in situ* and *operando* approach used in **Chapter 5** for characterization of a conventional Pd/CeO_2 catalyst revealed that the catalytic role of different species in CO oxidation is dynamic and strongly depends on the reaction conditions. The presence of multiple catalytic sites can be important for practical applications. It is, for example, relevant for three-way catalysis where different redox reactions take place simultaneously. Accordingly, this hints at a potential limitation of uniform single-atom catalysts or more generally catalysts that contain one type of active sites. Different active sites might be required for optimum performance in a wide range of reaction conditions, as relevant to transient operation in environmental catalysis applications. The logical step forward would be to apply the multi-technique *operando* approach for conventional Pd/CeO_2 catalysts using model exhaust gas mixtures. Investigation of the catalytic role of different Pd sites in the abatement of CO, NO_x and hydrocarbons would be a valuable contribution to the field.

Preparation of stable Pd/CeO_2 SACs as semi-model systems for fundamental studies using one-step FSP was demonstrated in **Chapters 4** and **6**. As part of Pd atoms can reside in the subsurface layers of ceria, the utilization of noble metal atoms in such catalysts is not ultimate. One possible solution to this is doping of ceria with cheaper transition metals (*e.g.*, Fe, Cu or Mn) to activate the lattice oxygen, followed by impregnation of such modified supports with Pd. Furthermore, it would be interesting to systematically investigate the effect of particle size of CeO_2 on the CO oxidation activity of Pt and Ni SACs, the other two transition metals that share group 10 in the periodic table. Usually, these catalysts are not very active in low-temperature CO oxidation. As the oxygen mobility in ceria changes as a function of crystallite size and has a strong impact on CO oxidation kinetics, the reactivity of single-atom Pt/CeO_2 and Ni/CeO_2 may be improved. Another interesting research direction would concern exploiting the ceria particle size effect for other catalytic reactions where oxygen transport at metal-support interface plays a role. Recently, we showed that catalytic activity of cobalt-ceria-zirconia catalysts for CO_2 hydrogenation depends on the size of the support in the 10-100 nm range[4]. Different extent of MSI and oxygen spillover effects underly the observed activity trends. It would be also interesting to explore whether the support size-dependence of catalytic properties exclusively relates to ceria-based materials. As other reducible oxides such as FeO_x, TiO_2, Co_3O_4 and Mn_3O_4 can be prepared by FSP and used as supports, it would be revealing to explore the impact of their crystallite size on the

catalytic properties. This would substantially extend the toolbox for preparation of catalysts and fine-tuning of their performance for specific applications.

To date, most spectroscopic approaches are based on determining the structure and electronic state of the supported metals, traditionally assumed to be the active component of the catalysts. As shown throughout this work, the nature of the metal-support interface in ceria-based catalysts often governs the overall activity. Hence, the speciation and electronic structure of both the metal and the support at the interface needs to be studied in detail. X-ray based *in situ* spectroscopy has seen an immense progress in the past decades. Surface science techniques such as NAP-XPS and RPES (**Chapters 4** and **6**) can provide extreme sensitivity to even minute changes in the valence state of elements. Using hard X-ray based spectroscopy tools (**Chapter 5**), one can study catalysts in a wide range of pressures and temperature, including the very conditions realized in practical applications. This comes, however, at the expense of surface sensitivity, as compared to the soft X-ray regime. This downside of bulk-sensitive XAS and XRD can be alleviated using nanosized materials, in which the surface-to-bulk ratio is maximized (**Chapter 4**). The properties of such nanosized ceria supports appear to be very different from their bulkier counterparts as discussed in **Chapter 6**. Despite the insights obtained in this work, further in-depth fundamental studies of nanosized CeO_2 based catalysts are necessary. A promising approach involves time-resolved XAS to follow the electronic states of supported metal and Ce, while simultaneously tracking the catalytic performance as a function of transiently changing reaction conditions. This combination will enable identification of the active sites and spectator species which is essential for establishing structure-activity relationships.

References

1. Alcala, R., DeLaRiva, A., Peterson, E. J., Benavidez, A., Garcia-Vargas, C. E., Jiang, D., Pereira-Hernández, X. I., Brongersma, H. H., ter Veen, R., Staněk, J., Miller, J. T., Wang, Y. & Datye, A. *Appl. Catal. B: Environ.* **284,** 119722 (2021).
2. Zhang, L., Spezzati, G., Muravev, V., Verheijen, M. A., Zijlstra, B., Filot, I. A. W., Su, Y.-Q., Chang, M.-W. & Hensen, E. J. M. *ACS Catal.* **11,** 5614–5627 (2021).
3. Kang, L., Wang, B., Bing, Q., Zalibera, M., Büchel, R., Xu, R., Wang, Q., Liu, Y., Gianolio, D., Tang, C. C., Gibson, E. K., Danaie, M., Allen, C., Wu, K., Marlow, S., Sun, L., He, Q., Guan, S., Savitsky, A., Velasco-Vélez, J. J., Callison, J., Kay, C. W. M., Pratsinis, S. E., Lubitz, W., Liu, J. & Wang, F. R. *Nat. Commun.* **11,** 4008 (2020).
4. Parastaev, A., Muravev, V., Huertas Osta, E., van Hoof, A. J. F., Kimpel, T. F., Kosinov, N. & Hensen, E. J. M. *Nat. Catal.* **3,** 526–533 (2020).

Acknowledgements

Doing my PhD research in IMC group was a unique experience full of memorable moments. As essential as the scientific part, this section of my thesis is dedicated to many people who were beside me during these past four years and without whom this document would simply not exist.

First, I would like to thank my promotors. Emiel, thank you for giving me the opportunity to do research in your group. These years were one of the best in my scientific life and largely this is due to the great environment that you and other members of IMC had created. Since the very first email I received from you, I have always admired your ability to respond and act promptly, regardless of how difficult the task at hand is. Your hard-working attitude and very broad scientific interests have always inspired me, and I hope will continue to stimulate new generations of PhD students at IMC. Despite your natural desire to be involved in all the aspects of ongoing work, you were always able to provide enough academic freedom for my research endeavors. It is a very valuable experience, and I am very grateful for that. I particularly enjoyed our trip to Reading, where we had insightful scientific discussions with colleagues from Johnson Matthey that were followed by late-evening beers in authentic British pubs. As our collaboration with JM continues, I hope that another opportunity for such a trip would present itself. Abhaya, I am very happy that I have had a chance to work with you and your colleagues on this fascinating ceria project. Thank you for those fruitful scientific discussions we had and your contribution to my research project. Your deep expertise and, more importantly, your keenness to share it with others in a very clear and concise manner are exemplary. I hope that the longstanding collaboration with IMC had only strengthened in the past years and we will continue working together on deciphering the intricate chemistry of ceria-based catalysts.

Special thanks go to my copromotor. Nikolay, your energy and passion at work never ceased to amaze me. Occasionally, these virtues would almost make us realign the mirrors to “gain some counts” by recalling some console commands from the good old DUBBLE at a beamline we have never been before (*N.B.* no end-stations were harmed). At the same time, your scientific vigor could lead to exciting and daring “Friday night experiments” that

provide unique insights and broaden the knowledge of what is experimentally possible. I am certain, that one day one of those experiments will finally lead to a major scientific breakthrough! Although you got involved in my project somewhat at a later stage, your contribution is concrete. Your constructive and detailed feedback on my writing helped me to see the logic of the process. Of course, there is plenty of room for improvement on my side. I learnt a lot from you and truly enjoyed the time we spent at work and outside of it during these past years.

I am grateful to prof. van der Schaaf, prof. Weber, prof. van Bokhoven and prof. Grunwaldt, for taking time to read this thesis, providing me with feedback and taking part in the defense ceremony.

Dear Evgeny and Sasha, thank you for being my paranymphs. You have always been not only great colleagues but also good friends. When I started my project, you were the people that I would go to if I needed help or some advice. I warmly remember those days when we used to leave Helix just before its closure and then would stay outside for hours discussing work and just life in general. Often with some beers of course. I am very happy that we shared those nice moments and glad that we remain in touch.

Giulia, I am very grateful to you for those years we worked together. Your help and guidance in the lab made the start of my project truly enjoyable. You are a very open, kind, and friendly person, who helped me and many others to accommodate in the group very quickly and with great comfort. I wish you all the best for your new life in Italy and hope to see you soon! Yaqiong, thank you for all the fruitful discussions we had. It was a pleasure to work with you and I hope we will continue collaborating in the future! Long, we worked together and also had some good time in Albarella and Reading. You were always very friendly and nice to talk to. All the best wishes for your career in China!

Jan Philipp, thank you for the guidance during the first stages of my project and getting me acquainted with DRIFTS and NAP-XPS. I am happy to know that your interest and expertise in surface science and materials chemistry had led you to an appointment as a full professor at TU Darmstadt. Freddy and Marco, my NAP-XPS buddies, thank you for your help with repairs and keeping the machine up and running. Freddy, thank you for your guidance during my first NAP-XPS experiments. I enjoyed our beamtrips to Diamond and Alba, as well as our discussions about band bending, core-hole clock spectroscopy, and many other things that I have not heard about before.

Emma, a big thank you goes to you for the help with the things that everybody hates the most – paperwork and administrative matters. I am especially grateful for your efforts with HF process. For both of us it was something new, but you did your absolute best to make it work as smoothly as possible. I would also like to thank our team of technicians: Adelheid, Brahim, Tiny and Thijs. Your constant support and assistance make lives of PhD students much easier. Adelheid, thanks for the help with ICP measurements. It is always great to enter your sparkling clean part of the lab. Brahim, thank you for keeping FTIR and Raman up and running. Special thanks go to Tiny. Your creativity and problem-solving skills are legendary. I am sure they saved many PhD projects over the years. You are always there when someone needs help. It has always been a pleasure to come up with some workarounds together with you. Johan, I did not have a chance to work with you and it seems like a missed opportunity. I wish you good health and happiness. Thijs, I hope you will enjoy working at IMC! Gabriela, I did not work much with you, but I really enjoyed those friendly talks during PhD defenses. Robert, thank you for those thought-provoking questions you asked during seminars.

I was very lucky to work with bright and motivated master students. Wesley, Bianca and Yannis, it was a pleasure to guide you through your projects and I am very proud of the results you achieved. You grew into independent researchers in a very short time, and I hope you will benefit from this experience. I wish you all the best in your future endeavors! Job, you are very talented, no doubts you will become a great scientist!

My dear officemates, Longfei, Xiaofeng, Nitin and Bianca, thank you for keeping a friendly atmosphere and sharing the space with me. Longfei, if I ever felt somewhat busy, I would always look at you and quickly realize that I have plenty of free time. Your productivity and enthusiasm have always motivated me, good luck with your new position at UU! Xiaofeng, I hope that your move to TU Darmstadt had made your scientific life a little bit easier and I wish you all the best for your PhD.

A very special thank you goes to the "lunch group". Wilbert, Giulia, Monica, Sasha, Arno, Tobias and Evgeny, we always had a great time regardless of how and where we would spend it. Wilbert, you are the most communicative person I have ever seen. It was great to share nightshifts with you – talking is the best way to keep each other awake! Also thank you for introducing me to Pusphaira, the football club I am part of ever since. I wish you and Leonie happy times. Arno, Monica and Tobias, thank you for your sense of humor that kept the welcoming vibe in the group. We had some great fun together! Sasha and Elisabet, thank

you for your hospitality and kindness when I joined the group. Luke, you are a very knowledgeable person whom everyone would like to have around especially during pub quizzes.

I am very grateful to my external collaborators. Alessandro, your friendliness has no limits. Thank you for sharing your knowledge and for those nice experiments we did together. Hopefully there are many more to come! Carlos and Nacho, I am very glad that I had a chance to work with you at your beamline, this experience was truly unique. Fu-Kuo, I am very thankful to you for the TEM measurements that you performed on our challenging samples. Xavier, I think we made a great team, and I am very proud of our joint work. Thank you, dear colleagues, your expertise and willingness to help contributed significantly to my project. I am looking forward to continuing our fruitful collaboration!

There are many other people who I would like to express gratitude to. Andrey and Georgy, thank you for all the talks we had and your friendliness. Andrey, you were especially thoughtful showing me on the very first day of my arrival the best (in terms of quality-price balance) Italian pizza place in Eindhoven. Funnily enough, I never visited it again, although the pizza was good. Alexey, your planning skills are fantastic, I always admired that. Michel, we had a great time during CAIA and MCEC schools, thank you for being kind and friendly to me. Bart, Robin, Jan, Roderigh and Ivo, thanks for the advices you gave me and nice time we had during MCEC meetings. Jiadong you are a hard-working person, and it was great to collaborate with you. Jérôme, thank you for sharing your expertise in SSITKA and also for the nice time we had during beamtrips. Remember, there is always enough time for another switch! Hao, your motivation and productivity are difficult to overestimate. I am sure you will succeed with your challenging project. Tim and Dimitra, I really like your calm and well-balanced approach to do research, best wishes for your PhD! Ferdy, it was great to have you during the beam time at Alba. Thank you for decorating the control room for my birthday on the last night of the experiments! Rim, thank you for the TEM measurements you performed for me and my students during these last few years. Your curiosity and creativity will serve you well during your PhD. It was great to have on the football pitch such teammates as Miao, Yue and Younes, you are forever in the history of “Bulls of Hensen”. Yujie and Jiachun, thank you for the beamtrips we had together, I hope this experience will be instrumental for your projects. Anna and Angelina, you are very dedicated PhD students, I

am certain that you will do well with your research. Valentin, I am glad that you joined the group and looking forward to working together on the JM project.

There are many members of IMC who are not listed here but contributed in one way or another. I thank you for that and wish you to succeed in your current and future activities.

I would also like to thank my colleagues from Boreskov Institute of Catalysis. Prof. Boronin, Andrey, Lidiya, Dmitriy, Roman, Tatyana, S.V. and E.M., thank you for giving me an opportunity to work with you. I learnt a lot during that time and this knowledge helped me during these past years. I am very glad that we stay in touch.

Finally, my dear Floriane, I cannot express in words how much I am grateful for your patience and endless support. These past years were not the easiest, we have spent some time apart and gone through many things that brought us closer together. I am so happy that I met you, and you know how much you mean to me! I am also glad that now I will be able to return the favor and support you during your PhD.

В заключение я хочу поблагодарить мою семью за поддержку и терпение в течение этих четырех лет. Дорогие мама, папа, брат, я вас очень люблю. Несмотря на расстояние между нами, я всегда чувствую, что вы рядом. Спасибо вам за все!

List of publications

Publications within the scope of this thesis:

- **Muravev, V.**, Spezzati, G., Su, Y., Parastaev, A., Chiang, F., Longo, A., Escudero, C., Kosinov, N., Hensen, E.J.M., Interface dynamics of Pd–CeO_2 single-atom catalysts during CO oxidation, *Nature Catalysis,* 4**,** 469–478 (2021).
- **Muravev, V.**, Kosinov, N., Hensen, E.J.M., Metal-support interfaces in ceria-based catalysts, *Comprehensive Inorganic Chemistry III* (book chapter). Elsevier, Amsterdam, 2021.
- Zhang, L.*, Spezzati, G.*, **Muravev, V.*,** Verheijen, M. A., Zijlstra, B., Filot, I. A. W., Su, Y.-Q., Chang, M.-W. & Hensen, E. J. M., Improved Pd/CeO_2 Catalysts for Low-Temperature NO Reduction: Activation of CeO_2 Lattice Oxygen by Fe Doping, *ACS Catalysis,* 11**,** 5614–5627 (2021). **(* equal contribution)**
- Pereira-Hernández, X.I.*, DeLaRiva, A.*, **Muravev, V.***, Kunwar, D., Xiong, H., Sudduth, B., Engelhard, M., Kovarik, L., Hensen, E.J.M., Wang, Y., Datye, A.K., Tuning Pt-CeO_2 interactions by high-temperature vapor-phase synthesis for improved reducibility of lattice oxygen, *Nature Communications*, 10 (1), 1358 (2019). **(* equal contribution)**
- Parastaev, A., **Muravev, V.**, Huertas Osta, E., van Hoof, A.J.F., Kimpel, T.F., Kosinov, N., Hensen, E.J.M., Boosting CO_2 hydrogenation via size-dependent metal–support interactions in cobalt/ceria-based catalysts, *Nature Catalysis,* 3, 526-533 (2020).
- Boronin, A.I., Slavinskaya, E.M., Figueroba, A., Stadnichenko, A.I., Kardash, T.Y., Stonkus, O.A., Fedorova, E.A., **Muravev, V.**, Svetlichnyi, V.A., Bruix, A., Neyman, K.M., CO oxidation activity of Pt/CeO_2 catalysts below 0° C: platinum loading effects, *Applied Catalysis B: Environmental*, 286, 119931 (2021).
- Zhu, J., Su, Y., Chai, J., **Muravev, V.**, Kosinov, N., Hensen, E.J.M., Mechanism and Nature of Active Sites for Methanol Synthesis from CO/CO_2 on Cu/CeO_2, *ACS Catalysis*, 10, 11532-11544 (2020).
- Stadnichenko, A.I., **Muravev, V.**, Koscheev, S.V., Zaikovskii, V.I., Aleksandrov, H.A., Neyman, K.M., Boronin, A.I., Study of active surface centers of Pt/CeO_2 catalysts prepared using radio-frequency plasma sputtering technique, *Surface Science*, 679, 273-283 (2019).
- Slavinskaya, E.M., Stadnichenko, A.I., **Muravev, V.**, Kardash, T.Y., Derevyannikova, E.A., Zaikovskii, V.I., Stonkus, O.A., Lapin, I.N., Svetlichnyi, V.A., Boronin, A.I., Transformation of a Pt–CeO_2 Mechanical Mixture of Pulsed-Laser-Ablated Nanoparticles to a Highly Active Catalyst for Carbon Monoxide Oxidation, *ChemCatChem*, 10, 2232-2247 (2018).
- Stadnichenko, A.I., **Muravev, V.**, Svetlichnyi, V.A., Boronin, A.I., Platinum state in highly active Pt/CeO_2 catalysts from the X-ray photoelectron spectroscopy data, *Journal of Structural Chemistry*, 58, 1152-1159 (2017).

Publications outside the scope of this thesis:

- Jiang, L., van Deursen, P.M.G., Arjmandi-Tash, H., Belyaeva, L.A., Qi, H., He, J., Kofman,V., Wu, L., **Muravev, V.**, Kaiser, U., Linnartz, H., Hensen, E.J.M., Hofmann, J.P., Schneider G.F., Reversible hydrogenation restores defected graphene to graphene, *Science China Chemistry,* 64, 1047–1056 (2021)
- Su, Y.-Q., Zhang, L., Wang, Y., Liu, J.-X., **Muravev, V.**, Alexopoulos, K., Filot, I.A.W., Vlachos, D.G., Hensen, E.J.M., Stability of heterogeneous single-atom catalysts: a scaling law mapping thermodynamics to kinetics, *npj Computational Materials,* 6 (1), 144 (2020).
- Su, Y.-Q., Zhang, L., **Muravev, V.**, Hensen, E.J.M., Lattice oxygen activation in transition metal doped ceria, *Chinese Journal of Catalysis*, 41, 977-984 (2020).
- Su, Y.-Q., Wang, Y., Liu, J.-X., Filot, I.A.W., Alexopoulos, K., Zhang, L., **Muravev, V.**, Zijlstra, B., Vlachos, D.G., Hensen, E.J.M., Theoretical approach to predict the stability of supported single-atom catalysts, *ACS Catalysis*, 9, 3289-3297 (2019).

Conference contributions:

- **Muravev, V.**, Hensen, E.J.M., Support size-effects in single-atom Pd/CeO_2 catalysts, CHAINS 2020, December 2020, Veldhoven, The Netherlands (oral presentation).
- **Muravev, V.**, Hensen, E.J.M., Operando NAP-XPS Unveils Pd Speciation and Reducibility of Nano-Sized Ceria during CO Oxidation, 17th International Congress on Catalysis 2020, June 2020, San Diego, CA, USA (accepted oral presentation, cancelled due to COVID-19).
- **Muravev, V.**, Hensen, E.J.M., Operando NAP-XPS Unveils Pd Speciation and Reducibility of Nano-sized Ceria during CO Oxidation, NCCC, March 2020, Noordwijkerhout, The Netherlands (oral presentation).
- **Muravev, V.**, Hensen, E.J.M., CO oxidation over Pd/CeO_2 powder catalysts: insights with Operando Near-Ambient Pressure XPS, EuropaCat 2019, August 2019, Aachen, Germany (oral presentation).
- **Muravev, V.**, Hensen, E.J.M., Operando Near-Ambient Pressure XPS study of CO oxidation over Pd/CeO_2 powder catalysts, NCCC, March 2019, Noordwijkerhout, The Netherlands (oral presentation).
- **Muravev, V.**, Hensen, E.J.M., NAP-XPS study of CO oxidation over Pd/CeO_2 powder catalysts, 3rd International Conference on Fundamentals and Applications of Cerium Dioxide in Catalysis, June 2018, Barcelona, Spain (oral presentation).

Curriculum Vitae

Valerii Muravev was born in Biysk, Russia on the 22nd of July 1994. He received his high school degree in 2012 at the Specialized Educational Scientific Center on Physics, Mathematics, Chemistry and Biology of Novosibirsk State University (SESC NSU). He then enrolled in the Chemical Department of Natural Sciences at Novosibirsk State University (NSU). During his studies he was involved in teaching inorganic chemistry at the annual summer school of SESC NSU. From 2015 onwards, he was working as a research assistant at the Boreskov Institute of Catalysis under supervision of prof.dr. A.I. Boronin on the application of X-ray photoelectron spectroscopy (XPS) for characterization of catalysts. In 2017, he defended his diploma thesis entitled *"Redox properties of model and powder $Pt_xCe_{1-x}O_{2-\delta}$ catalysts studied by XPS"* and graduated from NSU with a specialization in catalysis and adsorption. In August 2017, he joined the Inorganic Materials and Catalysis group at Eindhoven University of Technology as a PhD candidate. Under supervision of prof.dr.ir. E.J.M. Hensen, prof.dr. A.K. Datye and dr. Nikolay Kosinov, he studied interfacial chemistry of metal-ceria catalysts using advanced *in situ* spectroscopic tools. The main results of his research are summarized in this thesis.